

# Particle Size Distribution II



ACS SYMPOSIUM SERIES 472

# Particle Size Distribution II

## Assessment and Characterization

**Theodore Provder, EDITOR**

*The Glidden Company  
(Member of ICI Paints)*

Developed from a symposium sponsored  
by the Division of Polymeric Materials:  
Science and Engineering  
at the 199th National Meeting  
of the American Chemical Society,  
Boston, Massachusetts,  
April 22–27, 1990



American Chemical Society, Washington, DC 1991

Particle size distribution  
II



Library of Congress Cataloging-in-Publication Data

Particle size distribution II: assessment and characterization /  
Theodore Provder, editor.

p. cm.—(ACS symposium series; 472)

“Developed from a symposium sponsored by the Division of Polymeric  
Materials: Science and Engineering at the 199th National Meeting of  
the American Chemical Society, Boston, Massachusetts, April 22–27,  
1990.”

Includes bibliographical references and indexes.


ISBN 0–8412–2117–0

1. Particle size determination—Congresses.

I. Provder, Theodore, 1939– . II. American Chemical Society.  
Division of Polymeric Materials: Science and Engineering.  
III. American Chemical Society. Meeting (199th: 1990: Boston, Mass.)  
IV. Title: Particle size distribution 2. V. Title: Particle size  
distribution two. VI. Series.

TA418.8.P34 1991  
620'.43—dc20

91–25166  
CIP

The paper used in this publication meets the minimum requirements of American National  
Standard for Information Sciences—Permanence of Paper for Printed Library Materials, ANSI  
Z39.48–1984. 

Copyright © 1991

American Chemical Society

All Rights Reserved. The appearance of the code at the bottom of the first page of each  
chapter in this volume indicates the copyright owner's consent that reprographic copies of the  
chapter may be made for personal or internal use or for the personal or internal use of  
specific clients. This consent is given on the condition, however, that the copier pay the stated  
per-copy fee through the Copyright Clearance Center, Inc., 27 Congress Street, Salem, MA  
01970, for copying beyond that permitted by Sections 107 or 108 of the U.S. Copyright Law.  
This consent does not extend to copying or transmission by any means—graphic or  
electronic—for any other purpose, such as for general distribution, for advertising or  
promotional purposes, for creating a new collective work, for resale, or for information  
storage and retrieval systems. The copying fee for each chapter is indicated in the code at the  
bottom of the first page of the chapter.

The citation of trade names and/or names of manufacturers in this publication is not to be  
construed as an endorsement or as approval by ACS of the commercial products or services  
referenced herein; nor should the mere reference herein to any drawing, specification,  
chemical process, or other data be regarded as a license or as a conveyance of any right or  
permission to the holder, reader, or any other person or corporation, to manufacture,  
reproduce, use, or sell any patented invention or copyrighted work that may in any way be  
related thereto. Registered names, trademarks, etc., used in this publication, even without  
specific indication thereof, are not to be considered unprotected by law.

PRINTED IN THE UNITED STATES OF AMERICA  
**American Chemical Society  
Library**

1155 16th St. N.W.  
Washington, D.C. 20036  
In Particle Size Distribution II: Provder, T.;  
ACS Symposium Series; American Chemical Society: Washington, DC, 1991.

# ACS Symposium Series

**M. Joan Comstock, *Series Editor***

***1991 ACS Books Advisory Board***

**V. Dean Adams**  
Tennessee Technological  
University

**Paul S. Anderson**  
Merck Sharp & Dohme  
Research Laboratories

**Alexis T. Bell**  
University of California—Berkeley

**Malcolm H. Chisholm**  
Indiana University

**Natalie Foster**  
Lehigh University

**Dennis W. Hess**  
Lehigh University

**Mary A. Kaiser**  
E. I. du Pont de Nemours and  
Company

**Gretchen S. Kohl**  
Dow-Corning Corporation

**Michael R. Ladisch**  
Purdue University

**Bonnie Lawlor**  
Institute for Scientific Information

**John L. Massingill**  
Dow Chemical Company

**Robert McGorin**  
Kraft General Foods

**Julius J. Menn**  
Plant Sciences Institute,  
U.S. Department of Agriculture

**Marshall Phillips**  
Office of Agricultural Biotechnology,  
U.S. Department of Agriculture

**Daniel M. Quinn**  
University of Iowa

**A. Truman Schwartz**  
Macalaster College

**Stephen A. Szabo**  
Conoco Inc.

**Robert A. Weiss**  
University of Connecticut

# Foreword

**T**HE ACS SYMPOSIUM SERIES was founded in 1974 to provide a medium for publishing symposia quickly in book form. The format of the Series parallels that of the continuing ADVANCES IN CHEMISTRY SERIES except that, in order to save time, the papers are not typeset, but are reproduced as they are submitted by the authors in camera-ready form. Papers are reviewed under the supervision of the editors with the assistance of the Advisory Board and are selected to maintain the integrity of the symposia. Both reviews and reports of research are acceptable, because symposia may embrace both types of presentation. However, verbatim reproductions of previously published papers are not accepted.

# Preface

**T**HE RENAISSANCE IN PARTICLE SIZE DISTRIBUTION ANALYSIS was discussed in the preface for *Particle Size Distribution*, written on November 5, 1985, from three perspectives:

1. commercialization of instrumental methods used previously in a few academic and industrial laboratories by skilled individuals,
2. revitalization of older instrumental methods, and
3. evolution of research-grade instrumentation into low-cost equipment that requires a minimum of skill to use.

A fourth perspective can be added:

4. instrumental methods that fail in the marketplace.

Hydrodynamic chromatography (HDC) was invented by Hamish Small in an industrial laboratory and first reported in 1976. The technology was licensed to an instrument company for commercialization. Five years ago HDC was in the process of trying to gain a foothold in the marketplace. In 1991, HDC is not a viable commercial instrument. It failed in the marketplace, primarily because the separation mechanism, which required fractionation and separation of particles in a packed column, had a flaw that was not fully overcome: During the fractionation process some of the particles being separated would deposit on the column packing. Recovery of the injected sample was less than 100%.

The basic concept of HDC was a good one. Since 1986, a new chromatographic technique for particle size distribution analysis, capillary hydrodynamic fractionation (CHDF), has become a commercial reality. In this technique, separation and fractionation of  $<1\text{-}\mu\text{m}$  particles occurs in empty fine capillaries. Such separation avoids the problem of particle deposition on a packed bed. Theory refinement and prototype instrument development took place in the academic laboratory of Cesar Silebi. This development was accelerated into commercialization by a joint venture

between the academic laboratory and an instrumentation company. The method is gaining acceptance in the marketplace because of ease of use and fast analysis time.

Revitalization of older instrumental methods by redesign, modernization with advanced electronics, and user-friendly, computer-aided analysis have extended the product life cycle and created spin-off products. Disc centrifuge photosedimentometry (DCP) in the line-start mode has been a good example of this. Within the past year a spin-off product, an X-ray sedimentometer, has been commercialized. This disc centrifuge uses the homogeneous start method with X-ray detection to achieve analysis of dense materials such as pigments in a very short time. It is expected to replace the older gravitational sedimentation methods for this type of analysis. Competitive Darwinian marketplace forces have caused a consolidation of instrument vendors for some techniques. The DCP method and the sedimentation field flow fractionation (SdFFF) method are each commercially available from one instrument vendor in North America.

The renaissance in the field of particle size distribution analysis and characterization continues. The chapters in this book reflect the current activity in measurement techniques, methodology, and application to a variety of particulate systems and dispersions, with topics divided into five sections.

The first section deals with light-scattering methods. The classical turbidity method is re-examined for its potential to provide particle size distribution data and for its potential as an on-line process analysis method. The dynamic light-scattering method also is explored as an on-line process analysis method in two chapters that use quite different approaches. Another chapter describes a hybrid method of particle size analysis, using Fraunhofer diffraction and Mie scattering to cover a wide dynamic range.

The second section reports on refinements to the DCP methodology. The chapters in the third section report on the use of SdFFF and flow FFF to separate and fractionate a variety of particulate systems. The chapters in the fourth section are concerned with the new technique of CHDF in terms of theory, instrumentation, methodology, and application. The fifth section reports on a variety of methods to characterize particles. These methods include electrophoretic characterization of particles, image analysis procedures and fractal analysis of particles, and electrozone sensing analysis of magnetic particles.

Because of the continuing commercial availability of new methods, low-cost instruments for routine analysis, and highly specialized techniques, particle size distribution analysis and particle characterization will continue to grow and prosper. I hope that this book will be a useful guide to those first becoming acquainted with this field and will spur further activity among experienced practitioners in particle size analysis and characterization.



I thank the authors for their effective oral and written communications and the reviewers for their helpful critiques and constructive comments.

**THEODORE PROVDER**  
The Glidden Company  
(Member of ICI Paints)  
Strongsville, OH 44136

**July 11, 1991**

# Chapter 1

## Turbidimetric Techniques

### Capability To Provide the Full Particle Size Distribution

Theodora Kourti, John F. MacGregor, and Archie E. Hamielec

McMaster Institute for Polymer Production Technology, Department of Chemical Engineering, McMaster University, Hamilton, Ontario L8S 4L7, Canada

A detailed theoretical investigation on the capability of turbidimetric methods to provide an estimate of the particle size distribution (PSD) in suspensions of non-absorbing particles is presented. It is shown that turbidimetric methods are not expected to provide the full PSD in certain cases. The type of information that can be extracted from a turbidimetric method is strongly related to the  $(m, a)$  values of the system under consideration. ( $m$  is the ratio of the refractive index of the suspended particles to that of the medium;  $a$  is proportional to the ratio of the particle diameter to the wavelength of the light in the medium.) Therefore, results and conclusions cannot be extrapolated from one system to another without knowledge of how these parameters affect the results. For small values of  $m$  ( $m < 1.15$ ), only the weight average diameter can be estimated for suspensions of submicron non-absorbing particles using the specific turbidity method. The turbidity ratio method is not recommended for these systems. Experimental results corroborate these findings.

A relatively large number of methods are available for the determination of particle size in suspensions (1). Turbidimetric techniques are experimentally simple and they have been widely used in the last 35 years. There are numerous reports of the use of turbidimetry for the determination of either the particle size or the particle size distribution (PSD) for a variety of latex systems such as polystyrene (2), poly(vinyl acetate) (3-8) and poly(styrene butadiene) (9).

Specific turbidity is the most widely used turbidimetric technique for particle size determination. It relates the particle size distribution (PSD) of a suspension to the turbidity (measured at given wavelength) and the particle volume fraction  $\phi$ . For a suspension of spherical, non-absorbing, isotropic particles, in the absence of multiple scattering, specific turbidity is given by:

$$\frac{\tau}{\phi} = \frac{3}{2} \frac{\int_0^{\infty} D^2 K\left(\frac{D}{\lambda_m}, \frac{n_p}{n_m}\right) f(D) dD}{\int_0^{\infty} D^3 f(D) dD} \quad (1)$$

0097-6156/91/0472-0002\$06.00/0  
© 1991 American Chemical Society

where  $f(D)$  is the normalized particle size distribution.  $K(D/\lambda_m, n_p/n_m)$  or  $K_{\text{scat}}$  is the scattering coefficient, which is a function of two parameters,  $\alpha$  and  $m$ .  $\alpha = \pi(D/\lambda_m)$ ,  $D$  is the particle diameter and  $\lambda_m$  the wavelength of the light in the medium.  $m = n_p/n_m$ , where  $n_p$ ,  $n_m$  are the refractive indices of the particles and the medium, respectively.  $\lambda_m = \lambda_0/n_m$ , where  $\lambda_0$  is the wavelength of the incident beam in vacuo.  $K_{\text{scat}}$  exhibits an oscillatory dependence on  $\alpha$  and  $m$ , and in the general case can be calculated from the rigorous Mie theory (10). For very large particles  $K_{\text{scat}} = 2.0$ , while for particles very small compared to the wavelength,  $K_{\text{scat}}$  is proportional to the 4th power of the particle diameter. For a monodisperse suspension the specific turbidity is simply given by:

$$\frac{\tau}{\phi} = \frac{3}{2} \frac{K\left(\frac{D}{\lambda_m}, \frac{n_p}{n_m}\right)}{D} \quad (2)$$

It is clear from Equation 1 that the specific turbidity of a suspension at given wavelength is a function of the ratio of the refractive indices of the particles to the medium, the particle size distribution and the relative size of particles to the wavelength. In principle the PSD can be estimated from Equation 1 from specific turbidity measurements at different wavelengths, when the optical properties ( $n_p$  and  $n_m$ ) are known. If a continuous set of measurements of  $\tau$  vs.  $\lambda_m$  was available, one could theoretically deconvolve Equation 1 to yield  $f(D)$ . However, in practice, one usually only has turbidity measurements at a finite number of wavelengths. For a small number of turbidity measurements, a convenient approach is to approximate  $f(D)$  by an assumed form having only a few parameters, substitute this form in Equation 1 and solve for these parameters. The logarithmic normal distribution is very frequently used to describe the PSD in colloidal suspensions (4,11,12). For suspensions with log-normal PSD one can estimate the mean  $D_g$  and the variance of the distribution from at least two specific turbidity measurements (two turbidity measurements and the particle volume fraction (13)). The turbidity of a suspension can be measured with any spectrophotometer after certain modifications (14) have been made. The particle volume fraction can be measured either via gravimetry or densitometry (7). Descriptions of the experimental procedure and of the algorithm used for the conversion of specific turbidity measurements to particle size distribution can be found in several sources (12,14-16). The estimation of the full PSD is impossible for particles that are either very large or very small compared to all of the wavelengths used for the turbidity measurements; in these cases, one can obtain only the surface-volume average or the turbidity average diameter, respectively (17).

There has been a controversy in the literature, on whether turbidimetric techniques are at all capable of providing a valid estimate of the particle size distribution of a suspension (3,4). When attempting to estimate the PSD in poly(vinyl acetate) latexes in our laboratories using specific turbidity measurements and assuming log-normal distributions we observed (5,6,16) that the parameters of the estimated distribution were so highly correlated that effectively an infinite number of distributions could adequately explain the data. However, all these alternative solutions were found to correspond to distributions having the same weight average diameter. We also observed that the behaviour of the solution during the parameter estimation was very dependent: i) on the value of  $m$  of the suspension; ii) on the actual particle size of the suspension and iii) on the turbidimetric technique used. These observations and the controversy in the literature motivated an investigation of the capability of turbidimetry to determine the PSD in polydisperse systems.

### The Behaviour of Specific Turbidity for Polydisperse Systems

As a first step, it is important to see if, from a theoretical point of view, with no experimental errors, and for a known distributional form, it is possible from turbidity measurements to (i) determine the full particle size distribution for any system (i.e. any value of  $m$ ) and for any particle size range in the submicrometer (and near micrometer) region, or (ii) determine an average particle size, and if so what kind of average. It is also important to investigate the sensitivity of the method to various experimental errors. These issues are investigated here with a theoretical analysis and simulation studies. Our conclusions will be verified with an experimental investigation.

Theoretical values of specific turbidities for suspensions with log-normal particle size distributions, covering the submicrometer range and polydispersities up to 3.0, were calculated at various wavelengths for two systems, with different  $m$  values: i) Poly(styrene) particles suspended in water,  $m \sim 1.2$ ; and ii) Poly(vinyl acetate) particles suspended in water,  $m \sim 1.1$ . Details can be found in Kourti (16). The log-normal distribution can be described by two parameters:  $D_g$  and  $\sigma$ .  $D_g$  is the median and geometric mean of the PSD and  $\sigma$  is the geometric mean standard deviation (4,11,12,17). Constant specific turbidity curves at two wavelengths (400 nm and 600 nm) are plotted on a  $D_g$ - $\sigma$  plane for poly(vinyl acetate) latexes in Figure 1. A constant specific turbidity curve at certain wavelength defines distributions which, under no experimental error, give the same specific turbidity at that wavelength. A particle size distribution is defined when constant specific turbidity curves at two wavelengths intersect at a point on  $D_g$ - $\sigma$  plane.

From Figure 1, one can observe that intersections of constant specific turbidity curves at two wavelengths are very clearly defined for large  $D_g$  values (points F, G, K). For small  $D_g$  values the specific turbidity curves stay very close together for a wide range of ( $D_g$ ,  $\sigma$ ) values around the true intersection (points H, D, I) indicating that the parameters are highly correlated and that, with small experimental error one may not be able to distinguish between alternative solutions. For very small  $D_g$  values, curves at two wavelengths look as if they are coincident (curves corresponding to points A, B). These observations imply that for poly(vinyl acetate) latexes with certain particle size distributions (certain  $D_g$ ,  $\sigma$  values), it would be extremely difficult to obtain any estimate of the full PSD from specific turbidity measurements taken at wavelengths between 400-600 nm.

For some of the distributions [( $D_g$ ,  $\sigma$ ) points] that lie on the nearly coincident specific turbidity curves around the point of intersection of case D (Figure 1) the corresponding number, ( $D_N$ ), weight, ( $D_W$ ), and turbidity, ( $D_t$ ), average diameters were calculated for each wavelength (16). It was observed that all the distributions defined by the nearly coincident curves (at both wavelengths) have weight average diameters numerically close to the weight average diameter of the distribution corresponding to the intersection ( $D_g = 0.455 \mu\text{m}$  and  $\sigma = 0.2$ ). In other words, the constant specific turbidity curves define almost constant  $D_W$  curves for a wide region around the point of intersection. (For a wide range of  $D_g$  and  $\sigma$  values around the intersection, the difference between their corresponding weight average and that of the distribution of the intersection was less than 5%. The differences in the turbidity or number average diameters were much larger). A similar behaviour was observed for all the other cases where the specific turbidity curves are nearly coincident. Finally, in case A it was observed that constant specific turbidity curves define constant turbidity average diameters.

The question now, is whether or not it is possible to estimate the true particle size distribution, even assuming that it is known to be of a log-normal form, if the specific turbidities at different wavelengths correspond to curves that stay very close together on a  $D_g$ - $\sigma$  plane. The parameters ( $D_g$ ,  $\sigma$ ) are expected to be very highly correlated in these regions. Of course, theoretically a solution is possible since the curves, although very close to each other, do not overlap. The difficulty arises in practice where one deals with experimental measurements having some error. The estimation of the true particle size

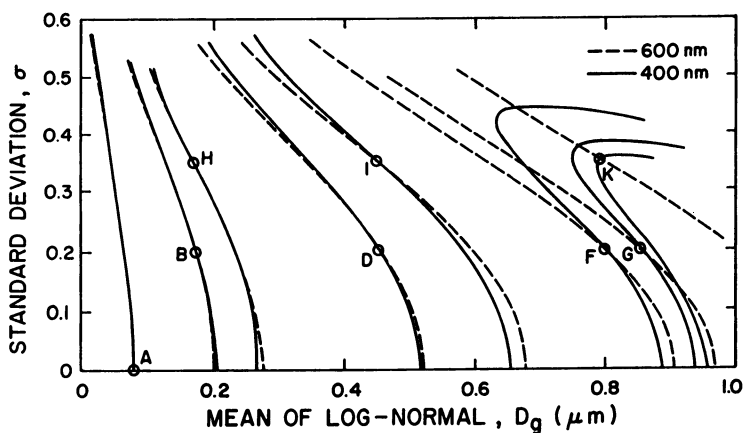


Figure 1. Constant specific turbidity curves at two wavelengths (600 nm and 400 nm), on a  $D_g$ - $\sigma$  plane for poly(vinyl acetate) latexes.

distribution is then expected to be extremely difficult, if not impossible, in these ( $D_g$ ,  $\sigma$ ) regions.

To investigate the behaviour of the solution in the presence of small measurement errors, simulation studies were performed.

**Estimation of the Parameters of the PSD When Error is Present.** A very small error (less than  $\pm 1.0\%$ ) was added to the specific turbidities calculated at 3 wavelengths for a poly(vinyl acetate) suspension with log-normal particle size distribution ( $D_g = 0.455 \mu\text{m}$  and  $\sigma = 0.2$ ). Using the specific turbidities with added error as observations, we tried to re-estimate the parameters of the distribution. The non-linear estimation routine, based on a Levenberg-Marquardt procedure (16), used as a termination criterion a relative change of less than  $10^{-9}$  in all the parameter estimates, or in the residual sum of squares. The results are summarized in Table I.

Notice that the individual confidence limits for the estimated parameters are very large and the zero value is included in the estimate of  $\sigma$ . The correlation of the parameters was extremely high ( $-0.9998$ ). A maximum of  $\pm 1.0\%$  error in the specific turbidities, resulted in 13.5% and 11.5% error in the estimated  $D_g$  and  $D_N$  values, respectively. However, the weight average diameter of the estimated distribution is very close to that of the true one.

The 75%, 90% and 95% approximate joint confidence regions for the parameters ( $D_g$ ,  $\sigma$ ) are plotted in Figure 2. Also shown are the true parameter values, the estimates from Table I, and the true constant specific turbidity curves at wavelengths 400 and 600 nm.

TABLE I. Results from Parameter Estimation With a Small Error (less than 1.0%) in Specific Turbidity

Parameters	Estimated Values	% Error from true solution
$D_g$ ( $\mu\text{m}$ )	$0.394 \pm 0.228$	13.4
$\sigma$	$0.289 \pm 0.306$	44.5
$D_N$ ( $\mu\text{m}$ )	0.411	11.5
$D_w$ ( $\mu\text{m}$ )	0.528	0.9

The  $(1-\alpha)$  approximate joint confidence regions were estimated from

$$S(D_g, \sigma)_{1-\omega} = S(D_g, \sigma)_{\min} \left( 1 + \frac{p}{n-p} F_{\omega}(n, n-p) \right) \quad (3)$$

where  $S(D_g, \sigma)_{\min}$  is the residual sum of squares corresponding to the estimated ( $D_g$ ,  $\sigma$ ),  $p$  is the number of parameters that were estimated ( $p = 2$ ),  $n$  is the number of observations ( $n = 3$ ) and  $F_{\omega}(v_1, v_2)$  gives the upper  $\omega\%$  of an F distribution with  $v_1$ ,  $v_2$  degrees of freedom.

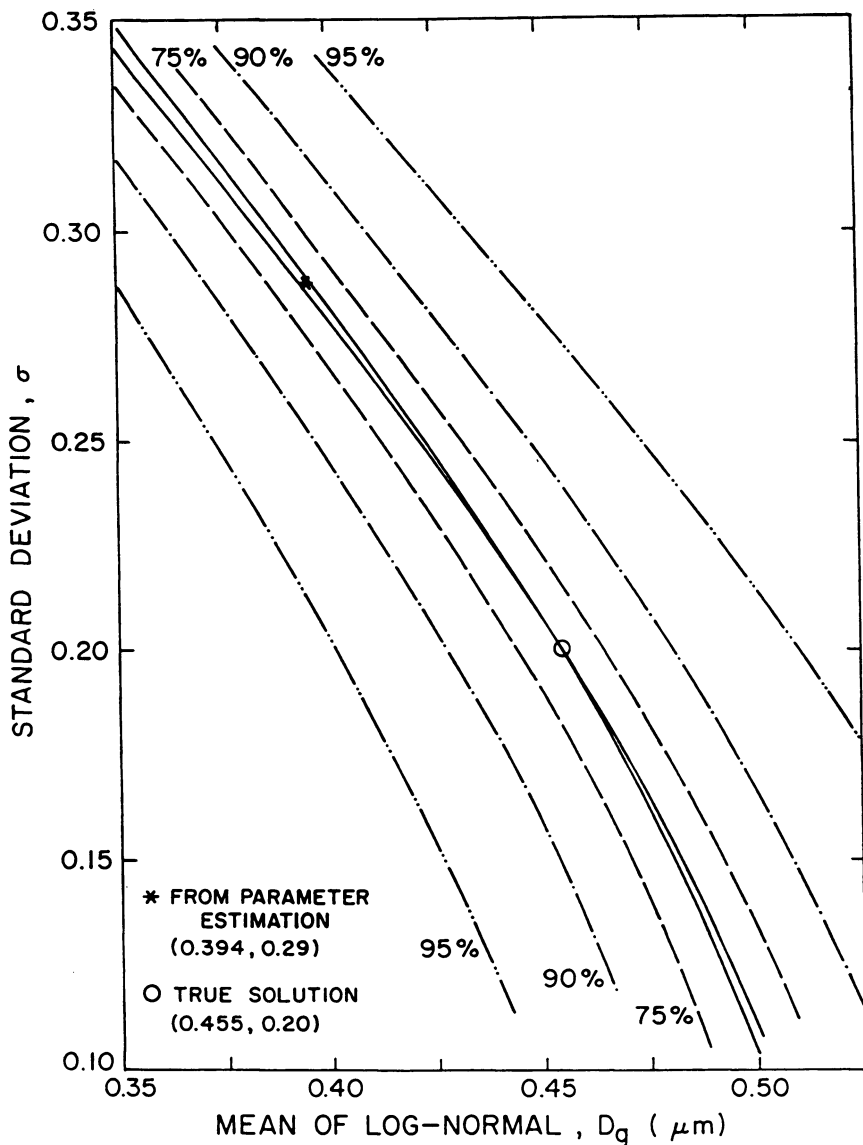


Figure 2. 75, 90 and 95% approximate joint confidence regions for the estimated parameters for a small error in the specific turbidity. Poly(vinyl acetate) latex. True solution:  $D_g = 0.455$  and  $\sigma = 0.2$ .

The high negative correlation observed between  $D_g$  and  $\sigma$  is evident from Figure 2. The approximate joint confidence regions for poly(vinyl acetate) correspond to narrow elongated regions along the constant specific turbidity curves which are almost coincident. Under random experimental error, the estimates of the particle size distribution are expected to lie anywhere in the elongated 95% confidence region (i.e., anywhere along the almost coincident specific turbidity curves). To verify this speculation, we investigated the behaviour of the parameter estimation in the presence of random error, for some of the cases of Figure 1 (corresponding to points B, D, F, H, I, K).

Adding a small random error (less than 3%) to the theoretically calculated specific turbidities we tried to re-estimate the parameters of the log-normal distributions. For each one of the true distributions we run 8-10 simulations assuming a different random error each time. The results are shown in Figure 3, where the true solution (that can be obtained with no measurement error) is the intersection marked with an asterisk. The full circles show the solutions ( $D_g$ - $\sigma$  pairs) that we obtained; their location indicates the region where one should expect to find the solution if experimental error is present. Notice that for small particles these solutions lie in an elongated region around the almost coincident specific turbidity curves, while for case K the estimates stay in a small area enveloping the true solution.

**Specific Turbidity Behaviour for Systems With Different Value of  $m$ .** The behaviour of the specific turbidity curves for polystyrene (Figure 4) with different  $m$  value is, on qualitative basis, similar to that of poly(vinyl acetate). For large particles specific turbidity curves at two wavelengths define clearly the corresponding PSD while for small particles these curves are almost coincident. On a quantitative basis, however, one can observe that, for polystyrene, intersections are very clearly defined for  $D_g$  values as small as  $0.4 \mu\text{m}$  and  $\sigma = 0.2$ , while for poly(vinyl acetate) clear intersections are only observed for larger  $D_g$  values ( $D_g > 0.7 \mu\text{m}$ ). As a result, under random error, the estimates for the polystyrene cases are very close to the true solution for  $D_g$  values as small as  $0.4 \mu\text{m}$ .

The maximum % deviations from the true solution observed in the estimated  $D_g$ ,  $D_N$  and  $D_w$  values, when a 3% error was introduced in the specific turbidity measurements, are summarized in Table II. Notice that for the cases where the specific turbidity curves stay close together around their intersection very large deviations from the true solution were observed in the estimated  $D_g$  and  $D_N$ ; however, the estimate of the  $D_w$  is always very close to the true value. It is clear from the above that for the wavelengths used, for poly(vinyl acetate) latexes ( $m \approx 1.1$ ) a successful estimate of the PSD can be obtained only for suspensions with large particles, while for polystyrene (where the value of  $m$  is larger) the region where a successful estimate of the PSD can be obtained can be extended to smaller sizes.

TABLE II. Maximum % Error in Estimated Parameters (With Respect to The True Solution) For Experimental Error 3%

parameter	Poly(vinyl acetate) Latexes Cases (point in Fig. 3)						Polystyrene Latexes Cases (point in Fig. 4)				
	B	D	F	H	I	K	B	C	D	E	F
$D_g$	62.0	37.0	13.6	45.2	46.5	7.6	27.0	15.0	10.0	4.8	8.6
$D_N$	57.0	32.0	11.3	44.5	39.0	6.1	24.0	13.0	7.7	4.0	8.0
$D_w$	2.0	3.0	3.6	0.7	4.6	7.4	0.9	2.1	4.3	5.1	3.6



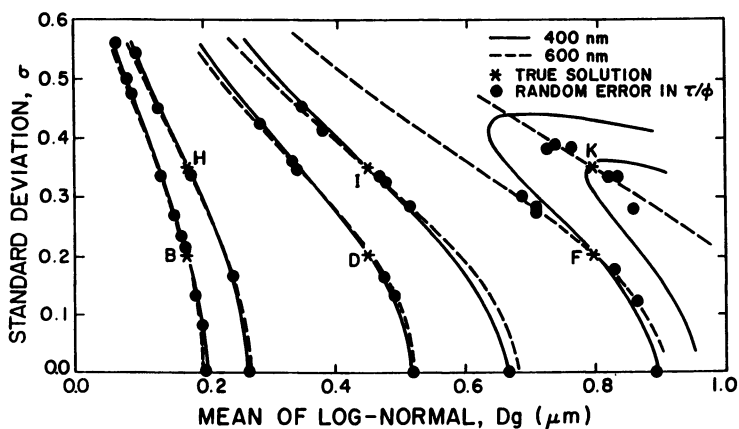


Figure 3. Estimates of the particle size distribution when a random error (up to  $\pm 3\%$ ) was added to the specific turbidities. Poly(vinyl acetate) latex.

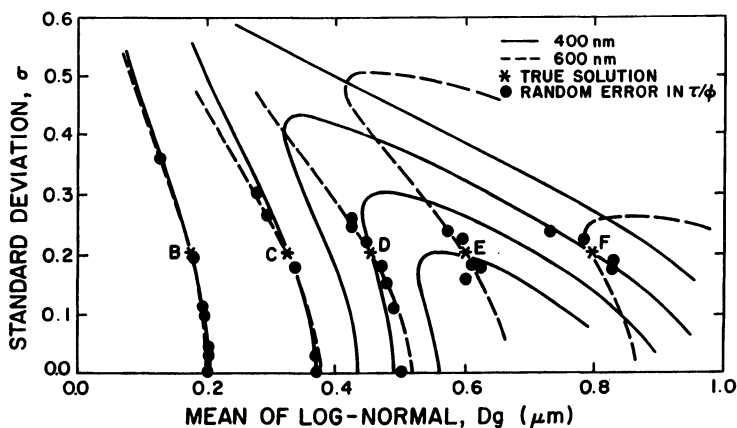


Figure 4. Estimates of the particle size distribution when a random error (up to  $\pm 3\%$ ) was added to the specific turbidities. Polystyrene latex.

### The Diameter Exponent and The Apparent Diameter

It is clear that the specific turbidity behaviour depends: i) on the particle sizes covered by the PSD of the suspension and ii) on the value of  $m$  of the suspension. To explain this behaviour we will make use of two concepts: the diameter exponent and the apparent diameter.

From specific turbidity measurements one can estimate a single diameter for a suspension, an apparent diameter. For a monodisperse suspension the apparent diameter, is the true diameter of the particles. For a polydisperse suspension the apparent diameter, obtained by treating the system as a monodisperse one, is sometimes numerically close to a meaningful average of the particle size distribution (weight average, volume to surface average, etc.). The apparent diameter estimated for a polydisperse suspension from a specific turbidity measurement (see Appendix A) can be defined as (see Equation 2):

$$\frac{\tau}{\phi} = \frac{3}{2} \frac{K\left(\frac{D_{ap}}{\lambda_m}, \frac{n_p}{n_m}\right)}{D_{ap}} \quad (4)$$

The relation between the apparent diameter and an average diameter of the particle size distribution has been discussed by Meehan and Beattie (18) and it is briefly outlined below.

For a monodisperse suspension, at a given wavelength, the dependence of the scattering coefficient on the diameter can be approximated by:

$$K_{scat} = K\left(\frac{D}{\lambda_m}, \frac{n_p}{n_m}\right) = k'(D/\lambda_m)^z \quad (5)$$

and

$$R_{scat} = K\left(\frac{D}{\lambda_m}, \frac{n_p}{n_m}\right) \frac{\pi D^2}{4} = k D^y \quad (6)$$

where  $y = z + 2$ ;  $k'$ ,  $k$  are proportionality constants.  $R_{scat}$  is the scattering cross section (17). For constant  $D$ ,  $K_{scat} = k_0 \lambda_0^{-z}$ , and therefore  $z$  has been termed "the wavelength exponent" (19). The turbidity of a monodisperse suspension with  $N$  particles per  $\text{cm}^3$  is given as:

$$\tau = N k D^y \quad (7)$$

In a polydisperse system at a given wavelength:

$$\tau = \sum_i n_i R_{i,scat} = \sum_i n_i k_i D_i^{y_i} \quad (8)$$

and

$$\Phi = \frac{\pi}{6} \sum_i n_i D_i^3 \quad (9)$$

where  $n_i$  is the number fraction of particles with diameter  $D_i$ .

When the sizes of the particles in a polydisperse system are such, that  $k$  and  $y$  do not change significantly with the diameter (i.e.,  $k_1 \sim k_2 \sim k_3 \sim k$  and  $y_1 \sim y_2 \sim y_3 \sim y$ ), then:

$$\frac{\tau}{\Phi} \sim k^n \frac{\sum_i n_i D_i^y}{\sum_i n_i D_i^3} \sim k^n \overline{D}^{\frac{y-3}{3}} \quad (10)$$

Comparing Equations 4 and 10, we conclude that the apparent diameter obtained by treating the system as monodisperse, would correspond to the  $(y,3)$  average diameter of the particle size distribution. The exponent  $(y-3)$  had earlier been termed "the radius exponent" by Heller and Pangonis (15), and as they pointed out, it has the value of 3 (i.e.  $y=6$ ) in the Rayleigh regime, and zero ( $y=3$ ) at the specific turbidity maxima and minima, regardless of the  $m$  values.

Specific turbidity measurements result in turbidity average diameters ( $D_\tau = D_{63}$ ) when  $y=6$ , and weight average diameters ( $D_w = D_{43}$ ) when  $y=4$ . For very large particles, where the scattering coefficient is constant ( $K_{\text{scat}}=2$ ),  $z=0$  and  $y=2$ , specific turbidities are always proportional to  $(1/D_{32})$ . With broad distributions of sizes, where the value of  $y$  changes throughout the distribution it is impossible to assign any meaningful average to the apparent diameter. This is especially true for higher  $m$  values due to irregular (oscillating) variations of  $K_{\text{scat}}$  with  $\alpha$  at high  $m$  values (Figure 5).

At constant wavelength, from Equations 5 and 6 we can write:

$$\ln(K_{\text{scat}}) = z \ln \alpha + \ln k_c' \quad (11)$$

or

$$\ln(R_{\text{scat}}) = y d \ln \alpha + \ln k_c$$

The value of  $y$  can be obtained for any  $\alpha$  at any  $m$  value from the slope of  $\ln(R_{\text{scat}})$  vs  $\ln \alpha$ , and the value of  $z$  from the slope of  $\ln(K_{\text{scat}})$  vs  $\ln \alpha$ ; ( $y=z+2$ ). Several authors (18,19) have tabulated values of  $y$  for several pairs of  $m$  and  $\alpha$  values. Values of  $y$  calculated for a wide range of  $\alpha$  values for  $m = 1.05, 1.0, 1.15$  and  $1.2$  are plotted in Figure 6. The scattering coefficient  $K(D/\lambda_m, n_p/n_m)$  was calculated directly from the Mie theory and the slope  $z$  of  $\ln(K_{\text{scat}})$  vs  $\ln \alpha$  at a given  $\ln \alpha$  was calculated using a central difference derivative formula (16).

Notice in Figure 6 that for all  $m$  values the  $y$  vs  $\alpha$  behaviour is almost identical for  $\alpha < 1.6$ . Hence, in this regime apparent diameters for systems with different  $m$  values, but the same distributions will be identical. For  $\alpha < 0.5$ ,  $y$  approaches the limiting value of 6, thereby yielding turbidity average diameters. For  $0.5 < \alpha < 1.6$  the  $y$  value falls from 6 to  $\sim 4.4$ . Specific turbidities for particle size distributions with  $\alpha$  values in this range are expected to give an apparent diameter numerically between the turbidity and the weight average diameter. Then the  $y$  value falls abruptly, for  $\alpha$  values up to  $\alpha \sim 1.6$  exhibits an indentation (corresponding to the first inflection point of the  $K_{\text{scat}}$  vs.  $\alpha$  curve) and then it decreases monotonically for  $m = 1.05$  while it starts oscillating for  $m = 1.2$ , following the corresponding  $K_{\text{scat}}$  vs.  $\alpha$  oscillatory behaviour. For small values of  $m$  ( $m = 1.05, 1.1, 1.15$ ), the value of  $y$  is approximately 4.0 ( $4.2 \leq y \leq 3.8$ ) for a very wide range of  $\alpha$  values

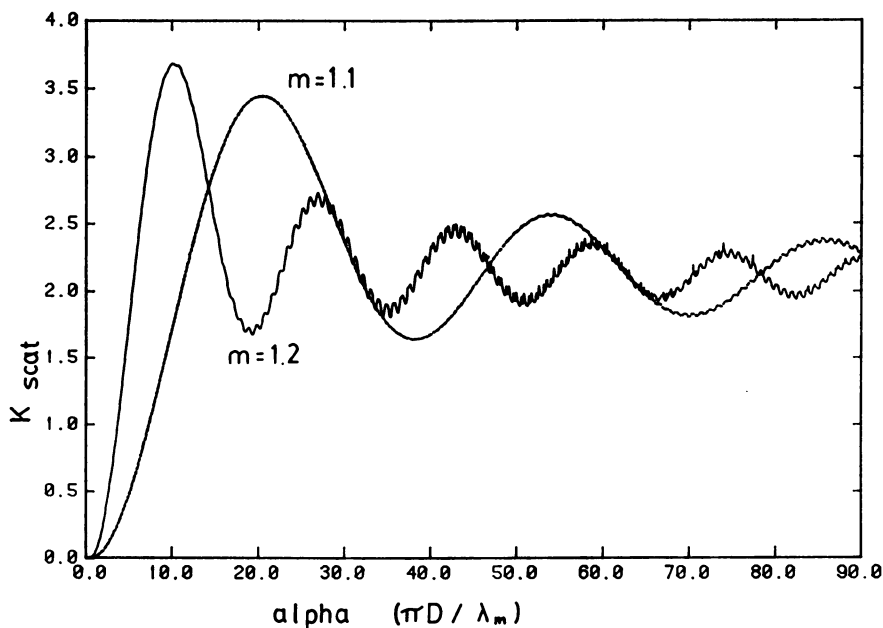


Figure 5. The scattering coefficient as a function of  $\alpha$  ( $\alpha = \pi D/\lambda_m$ ), for  $m = 1.1$  and  $m = 1.2$ .

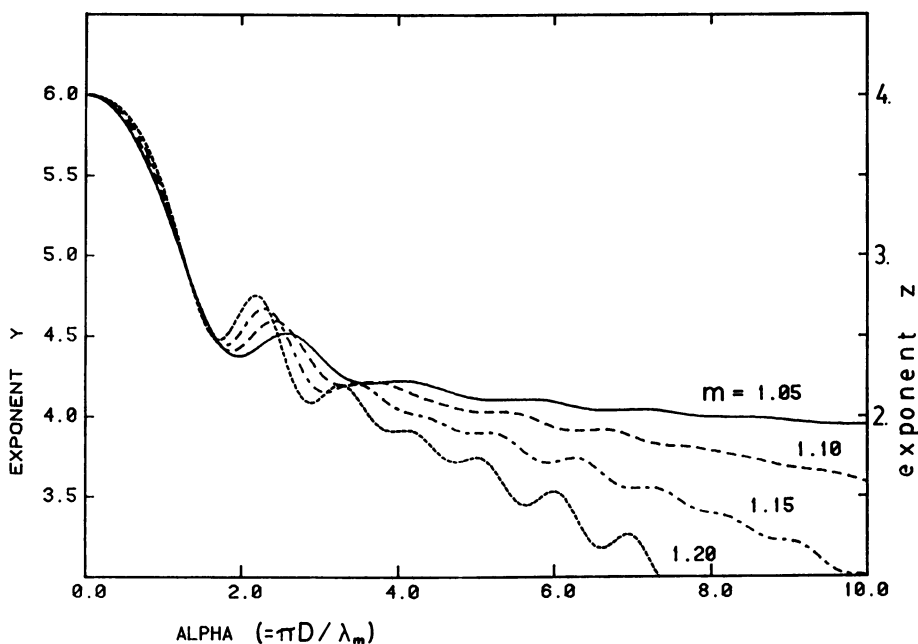


Figure 6. The exponents  $y$  and  $z$  as a function of  $\alpha$ , for  $m = 1.05, 1.1, 1.15$  and  $1.2$ .

(for  $m = 1.05$ ,  $3.0 \leq \alpha \leq 14$ ; for  $m = 1.15$ ,  $3 < \alpha < 6$ ). Hence, for small values of  $m$  and for particle size distributions with  $\alpha$  values in the above region, apparent diameters obtained from specific turbidity readings would be numerically very close to the weight average diameter. For  $m = 1.2$ , the apparent diameter can be assigned to the weight average only in a relatively narrow regime ( $3.0 \leq \alpha \leq 4.3$ ).

### Explanation for the Specific Turbidity Behaviour

A constant specific turbidity curve is a curve of constant apparent diameter. On a  $D_g$ - $\sigma$  plane, at given  $(\lambda_m, m)$ , all the points on a constant specific turbidity curve correspond to log-normal distributions with the same apparent diameter.

For  $m = 1.1$ , the apparent diameter is expected to be numerically very close to the weight average diameter of the suspension ( $y \sim 4.0$ ), for any type of particle size distribution (bimodal, unimodal) provided that the particles in the suspension correspond to  $\alpha$  values between 3.0 and 8.0 (Figure 6). For particles suspended in water the particle diameters corresponding to these  $\alpha$  values are:

for	$\lambda_0 = 400 \text{ nm}$	$0.28 \mu\text{m} \leq D \leq 0.76 \mu\text{m}$
	$\lambda_0 = 600 \text{ nm}$	$0.42 \mu\text{m} \leq D \leq 1.14 \mu\text{m}$

(For suspensions with log-normal particle size distributions the  $\alpha$  regime for which the apparent diameter, obtained from specific turbidity measurements, are numerically close to the weight average of the PSD can be extended further (16).

It is clear from the above that for suspensions with  $m = 1.1$  and particles with diameters up to  $0.8 \mu\text{m}$  (and for any type of distribution), specific turbidities at both 400 and 600 nm result in apparent diameters numerically close to the weight average of the suspension, and therefore numerically close to each other. Therefore, constant specific turbidity curves at these two wavelengths, plotted against the parameters that define the PSD, stay close to each other and pass through those points that define constant weight average diameters. For log-normal distributions, on a  $D_g$ - $\sigma$  plane, these curves pass through points for which  $D_w = D_g \exp(3.5\sigma^2) = \text{constant} = D_{ap}$  where  $D_{ap}$  is the apparent diameter corresponding to the specific turbidity assuming the suspension is monodisperse. This is the case observed previously for the poly(vinyl acetate) distributions corresponding to points B, H, D and I (Figure 1).

For systems with larger particles ( $D_g > 0.7 \mu\text{m}$ ,  $\sigma > 0.2$ ) where the  $y$  value varies significantly within the distribution, specific turbidity measurements result in different apparent diameters at the two wavelengths; therefore, the constant specific turbidity curves on a  $D_g$ - $\sigma$  plane intersect at a wider angle and more clearly define the particle size distribution (point K, Figure 1).

For poly(styrene), where  $y$  remains close to 4.0 for only a very narrow range of  $\alpha$  values ( $m = 1.2$ , Figure 6), a constant weight average trend is expected only for narrower distributions of particles with  $\alpha$  values in the above range. This is the case for the distributions corresponding to points B and C (Figure 4).

Distributions of very small particles ( $\alpha < 1.6$ ) give almost the same apparent diameter for  $m = 1.1$  or  $m = 1.2$ , and hence the identical behaviour of specific turbidity for poly(vinyl acetate) and poly(styrene) at 600 nm (cases A and B).

From the above discussion, it is clear that the difference in the specific turbidity behaviour on a  $D_g$ - $\sigma$  plane, observed between polystyrene and poly(vinyl acetate) suspensions, is due to the different values of  $m$  of these systems which means a different wavelength exponent behaviour. For small values of  $m$  ( $m = 1.05, 1.10$ ), the wavelength exponent  $y$  changes very slowly with  $\alpha$  (for  $\alpha > 3.0$ ) and remains very close to 4 for a wide  $\alpha$  regime. Therefore, polydisperse systems with small values of  $m$  and particles covering the above  $\alpha$  regimes are expected to exhibit a specific turbidity behaviour on a  $D_g$ - $\sigma$  plane,

similar to that of poly(vinyl acetate) latexes. Specific turbidity curves, at different wavelengths, are expected to stay close together around the point of true solution defining constant weight average diameter trends. In this case the estimation of the full PSD is impossible.

### The Weight Average Diameter from The Apparent Diameter: Experimental Verification

Particle size distributions were synthesized by mixing monodisperse poly(vinyl acetate) latexes. These distributions were covering particle size from 60 to 420 nm (16). Their apparent diameters calculated from specific turbidity measurements are shown in Table III, together with their true weight average diameter. (More than one value for  $D_{ap}$  of a sample indicates repeated measurements.) It can be seen that for all the cases the apparent diameters at 440 nm and 500 nm are remarkably close to the true weight average diameter. This experimental observation verifies our conclusions from the theoretical analysis. It is obvious that with the apparent diameters so close to each other, the parameters of the PSD can not be estimated since the sample appears monodisperse within experimental error (with a diameter equal to the weight average diameter).

### The Turbidity Ratio Method

The difficulties that are encountered in the estimation of the PSD using specific turbidity measurements have been discussed so far. Another turbidimetric method that has been utilized by researchers for the determination of particle size in polydisperse systems is the turbidity ratio. In this approach the particle size distribution is related to the ratio of two turbidity measurements at two wavelengths, one of which is chosen as basis:

$$\frac{\tau_{\lambda_{o1}}}{\tau_{\lambda_{ob}}} = \frac{\int_0^{\infty} D^2 K\left(\frac{D}{\lambda_m}, \frac{n_p}{n_m}\right)_{\lambda_{o1}} f(D) dD}{\int_0^{\infty} D^2 K\left(\frac{D}{\lambda_m}, \frac{n_p}{n_m}\right)_{\lambda_{ob}} f(D) dD} \quad (12)$$

where subscripts  $\lambda_{o1}$ ,  $\lambda_{ob}$  denote that the quantities  $\tau$ ,  $n_p$ ,  $n_m$ ,  $\lambda_m$  are evaluated at the corresponding wavelengths.

Wallach and Heller (2) reported a successful application of the method in estimating the PSD in polystyrene suspensions with large particles ( $0.65 < D < 1.3 \mu\text{m}$ ). When Maxim et al (3) however, applied the method for poly(vinyl acetate) latexes with particles in the submicrometer range, it was stated that the turbidity ratio "leads to multivalued solutions and unless prior estimates of the answer are available from some other technique, there are no criteria for choosing between alternative solutions". Similar observations with Maxim et al (3) are reported by Haseler (14) for small values of  $m$  ( $m = 1.15$ ). In the analysis that follows, it will be shown that this technique is extremely sensitive to experimental error for suspensions with small values of  $m$  ( $m < 1.15$ ) and particle sizes in the submicrometer range, and therefore should not be used for the determination of the PSD in such systems.

TABLE III. The Apparent Diameter for  $m = 1.095$  for Poly(vinyl acetate) Suspensions with Known Distributions

distribution	$D_w$ (true)	$D_{ap}$ at 440 nm	$D_{ap}$ at 500 nm
DV1	136	–	136
		134	137
		134	136
DV2	163	159	160
		158	159
DV3	194.3	195	196
		196.5	197
		196	193
DV4	227	226	232
		227	230
		229	232
BDV5	253.2	255	263
		254	262
DV6	340.2	338	342
		336	344
		341	340
DV7	309.3	300	302
		303	306

A minimum of three turbidity measurements at three wavelengths, one of which is chosen as basis, are required in principle for the determination of a two-parameter particle size distribution. A wavelength that very frequently (2,3) has been chosen as basis is  $\lambda_{ob} = 546$  nm, and it is usually recommended that the other two wavelengths are widely separated. We therefore chose  $\lambda_{01} = 350$  nm,  $\lambda_{02} = 700$  nm, and calculated turbidity ratios ( $\tau_{350}/\tau_{546}$  and  $\tau_{700}/\tau_{546}$ ) for several log-normal distributions, for  $m = 1.1$ . When constant turbidity ratio curves were plotted for these two wavelengths on a  $D_g$ - $\sigma$  plane, they looked as if they were coincident for very long ( $D_g$ ,  $\sigma$ ) regions and there seemed no way to define the point of their true intersection. In other words, a large number of distributions significantly different from each other have, even under ideal conditions (i.e., no experimental error), turbidity ratios that are almost equal to each other at more than one wavelength. This is illustrated in Table IV where turbidity ratios were calculated at two wavelengths for some ( $D_g$ ,  $\sigma$ ) pairs, located along these almost coincident curves; their values were compared with those of the (0.500, 0.15) pair for the two wavelengths and the % differences are given. Notice that these differences are all below 0.5%. The sensitivity of the method to experimental error is obvious; errors as small as 0.5% on the turbidity ratio measurements will result in estimated distributions very much different from the true ones. Notice also that the weight average diameters of these distributions are not necessarily very close to the true one; in other words, neither the correct distribution nor a correct weight average can be obtained.

TABLE IV. Turbidity Ratios for Some Poly(vinyl acetate) Suspensions With Log-normal Particle Size Distributions; Basis:  $\lambda_{0b} = 546$  nm

$D_g$ ( $\mu\text{m}$ )	$\sigma$	$D_w$ ( $\mu\text{m}$ )	$\lambda_{01} = 350$ nm		$\lambda_{02} = 700$ nm	
			ratio	% diff.	ratio	% diff.
0.500	0.15	0.541	2.5017		0.5763	
0.465	0.20	0.535	2.5012	0.02	0.5755	0.13
0.425	0.25	0.529	2.4989	0.11	0.5753	0.18
0.380	0.30	0.520	2.4973	0.17	0.5753	0.18
0.330	0.35	0.507	2.5005	0.05	0.5749	0.24
0.285	0.40	0.499	2.4934	0.33	0.5758	0.08

To explain the turbidity ratio behaviour, we will make again use of the diameter exponent. Suppose that in a suspension with a value of  $m = 1.1$  and a relatively broad particle size distribution, the particle diameters are between  $D_1 = 0.3 \mu\text{m}$  and  $D_q = 0.8 \mu\text{m}$  with number fractions  $n_1, n_2, \dots, n_q$ . From Equations 8 and 12 the turbidity ratio can be written:

$$\frac{\tau_{350}}{\tau_{546}} = \frac{k'_1 n_1 D_1^{4.2} + \dots + k'_q n_q D_q^{3.6}}{k_1 n_1 D_1^{4.6} + \dots + k_q n_q D_q^{3.9}} \quad \text{and} \quad \frac{\tau_{700}}{\tau_{546}} = \frac{k''_1 n_1 D_1^{4.4} + \dots + k''_q n_q D_q^{4.1}}{k_1 n_1 D_1^{4.6} + \dots + k_q n_q D_q^{3.9}}$$

where  $k'_i, k''_i, k_i$  denote that the  $k$  values are different at different wavelengths. The exponents  $y$  have been calculated for the  $\alpha$  values corresponding to each wavelength, for water medium.

From these ratios, it can be seen that, even for a broad distribution and turbidity measurements at two widely separated wavelengths, the diameter exponents between the numerators and the denominator do not differ significantly. Therefore, the turbidity ratio cannot be very sensitive to the distribution characteristics; different distributions with their main populations on the same regimes, are expected to give the same turbidity ratios. The difference between the exponents will become even smaller, for wavelengths closer to 546 nm than the ones used above, and for narrower particle size distributions. Hence for  $m = 1.1$ , where the diameter exponent changes very slowly with  $\alpha$ , the turbidity ratio does not change significantly for different distributions in the submicrometer range. (For  $m = 1.05$ , these problems are expected to occur in wider particle size regimes.) Therefore, small experimental errors may result in estimates significantly different from the true particle size distribution. If the wavelengths at which the turbidity measurements are taken are not widely separated from the wavelength used as basis, then the turbidity ratio will be practically independent of the particle diameter.

The turbidity ratio is expected to be a stronger function of the particle size distribution in  $(m, \alpha)$  regions where the diameter exponent changes significantly with  $\alpha$ . For



$m = 1.2$  and larger  $\alpha$  values the turbidity ratio technique can be used successfully for the determination of the full PSD. The above analysis explains why the reports of Wallach and Heller (2) and Maxim et al (3), on the capability of the method to determine the PSD, for systems with different  $m$  values and different particle sizes contradict each other.

The specific turbidity has an advantage over the turbidity ratio method, as a result of the different properties measured by the two methods. The turbidity ratio utilizes only turbidity measurements, while in the specific turbidity, the particle concentration is also measured. The particle concentration is always proportional to the third moment of the PSD. In the cases where  $y$  does not change significantly with  $\alpha$ , specific turbidity is proportional to  $D_{y3}^{(y-3)}$ . Although the PSD determination is not possible in these cases, an apparent diameter, corresponding to the  $D_{y3}$  average of the distribution, can always be obtained. On the contrary, the turbidity ratio will be almost independent of the diameter in these cases and no reliable estimate of the particle size can be obtained. (the turbidity ratio is proportional to the  $(y_1 - y_2)$ th power of  $D_{y_1 y_2}$  but when  $(y_1 = y_2)$ , then  $y_1 - y_2 \approx 0$ , and  $D^\circ = 1.0$ )

### Concluding Remarks

Turbidimetric methods cannot be expected to provide information on the full PSD in many situations. The estimation of the true PSD (even assuming that it is known to be of a log-normal form) is extremely difficult even under very small experimental error, in  $(m, \alpha)$  regions where the value of the wavelength exponent changes very slowly with the value of  $\alpha$ . In these regions the parameters that define the PSD are highly correlated and small experimental errors result in large errors in the parameter estimation. In these regimes, improving deconvolution algorithms for Equation 1, does not alter the fundamental regression problem caused by the high correlation among the parameters. Therefore, the type of information about the PSD that can be extracted from any turbidimetric method and its sensitivity to experimental error are strongly related to the  $m$  and  $\alpha$  values of the suspension. Unfortunately this consideration has not often been taken into account and one of the controversies (3,4) in the literature resulted when workers tried to extrapolate observations and conclusions, correct for their system and the turbidimetric method they used, to systems with different  $m$  and  $\alpha$  values and for a different method. (Discussions on the inconsistencies and conflicts reported in the literature and their resolution can be found in Kourti (16,17).)

This study however indicated that specific turbidity is a very reliable method (and for non-absorbing particles, more reliable than the turbidity ratio). It can always provide information on the particle size of a polydisperse suspension; that is, a correct average diameter can be obtained even when the estimation of the full PSD is not possible. More specifically, for suspensions of non-absorbing particles: i) the turbidity average diameter and the volume-surface average diameter ( $D_{32}$ ) can be estimated for very small and very large particles, respectively, for any value of  $m$ . ii) for suspensions with values of  $m < 1.15$  and distributions covering a values smaller than approximately 8.0, the weight average diameter ( $D_w$ ) can be correctly estimated (numerically  $D_w$  is equal to the apparent diameter obtained by treating the system as monodisperse). For the other  $(m, \alpha)$  regimes, the estimation of the full PSD of non-absorbing particles should be possible. For these cases it has been shown (16,17) that the assumption of a log-normal PSD will result in a correct estimate (within 1%) of the weight average diameter; for continuous distributions (i.e., not widely separated bimodals) it will also provide the correct location of the main body of the distribution on weight basis.

Our choice to use log-normal distributions for this analysis, and the choice of the wavelengths (400-600 nm) for the specific turbidities, do not affect the main conclusion of this investigation for suspensions of non-absorbing particles (i.e., that information on the full PSD of a suspension is impossible whenever specific turbidities at different wavelengths result in the same apparent diameters). We covered so many distributions

with different sizes (i.e., a wide range of  $\alpha$  values), that the actual values of the wavelengths do not put any restriction.

We chose to work with polystyrene ( $m \approx 1.2$ ) and poly(vinyl acetate) latexes ( $m \approx 1.1$ ) at wavelengths that these latexes do not absorb because a large number of studies in the literature are for non-absorbing particles and systems with  $m$  values between 1.1 and 1.2 (17). Systems with  $1.0 < m < 1.15$  are expected to behave like poly(vinyl acetate), and systems with  $m > 1.2$  like the polystyrene latexes.

With the above analysis it was demonstrated for the first time, that theoretically, turbidimetric techniques are not expected to provide information on the full PSD of the suspension in certain cases and these cases have been identified. These are the ( $m, \alpha$ ) regimes where the various turbidity functions are more sensitive to experimental errors, and they are determined by the behaviour of the wavelength exponent; in these regimes, the wavelength exponent is not a strong function of the particle size. This conclusion is general, and not restricted only to non-absorbing particles.

The conclusions from the above analysis corroborate and explain experimental results reported in the literature (17) and our experimental observations.

### Literature Cited

1. Barth, H.G., and S-T. Sun, Analytical Chemistry, **57** (1985) 151R.
2. Wallach, M.L., and W. Heller, J. Phys. Chem., **68** (1964) 924.
3. Maxim, L.D., Klein, A., Meyer, M.E., and C.H. Kuist, J. Polym. Sci. Part C, **27** (1969) 195.
4. Zollars, R.L., J. Colloid Interface Sci., **74** (1980) 163.
5. Kourti, T., Penlidis, A., Hamielec, A.E., and J.F. MacGregor, ACS PMSE Div. Preprints, **53** (1985) 147.
6. Kourti, T., Penlidis, A., MacGregor, J.F., and A.E. Hamielec, In Provder, Th. (Ed.), Particle Size Distribution - Assessment and Characterization, ACS Symposium Series, **332**, Washington, D.C., 1987.
7. Gossen, P.D., Kourti, T., Penlidis, A., MacGregor, J.F., and A.E. Hamielec, PRP-6 Automation Preprints. 6th International IFAC/IFIP/IMEKO Conference on Instrumentation and Automation in the Paper, Rubber, Plastics and Polymerization Industries, Akron, Ohio, U.S.A., 1986.
8. Gossen, P.D., On-Line Particle Size Measurement and Mathematical Modelling of Continuous Poly(vinyl acetate) Emulsion Polymerization, Master's Thesis. Dept. Chem. Eng., McMaster University, Hamilton, Ontario, Canada, 1988.
9. Maron, S.H., Pierce, P.E., and Ulevitch, I.N., J. Coll. Sci., **18** (1963) 470.
10. Van de Hulst, H.C., Light Scattering by Small Particles, J. Wiley and Sons, Inc., New York, 1957.
11. Kerker, M., The Scattering of Light and Other Electro-magnetic Radiation. Academic Press, New York, 1969.
12. Yang, K.C., and R. Hogg, Analytical Chemistry, **51** (1979) 758.
13. Kourti, T., MacGregor, J.F., and A.E. Hamielec, J. Colloid Inter. Sci., **120** (1987) 292.
14. Haseler, S.C., Part. Charact., **2** (1985) 14.
15. Heller, W., and W.J. Pangonis, J. Chem. Phys., **26** (1957) 498.
16. Kourti, T., Polymer Latexes: Production by Homogeneous Nucleation and Methods for Particle Size Determination, Ph.D. Thesis, McMaster University, Hamilton, Ont., Canada, 1989.
17. Kourti, T. and MacGregor, J.F., "Particle Size Determination Using Turbidimetry: Capabilities, Limitations and Evaluation for On-Line Applications", This volume.
18. Meehan, E. J. and Beattie, W.H., J. Phys. Chem., **64** (1960) 1006.
19. Heller, W., Bhatnagar, H.L., Nakagaki, M., J. Chem. Phys., **36** (1962) 1163.

## Appendix A

Due to the oscillatory character of the specific turbidity vs diameter curve, one specific turbidity value at given wavelength corresponds to more than one diameter. If there is not a priori information on the particle size range in the suspension, specific turbidity measurements at more than one wavelength are needed to uniquely define the correct diameter of a monodisperse system (or, the apparent diameter of a polydisperse system). At each wavelength a specific turbidity measurement defines a set of diameter values. For a monodisperse suspension there is a value common to all sets and this is the true diameter of the suspension.

For a polydisperse suspension the sets of diameters obtained at different wavelengths, do not in general have a common value. However, in some cases the polydisperse suspensions exhibit a behaviour somewhat similar to monodisperse ones; these are the cases where the apparent diameter can be assigned to a meaningful average of the PSD of the suspension. In these cases, each one of the sets of diameters obtained at several wavelengths contains a diameter with a value that (although not constant, i.e., not common to all sets), appears to change slowly with the wavelength. That diameter corresponds to an average of the PSD and its value at each wavelength gives the correct apparent diameter of the suspension for that wavelength.

This behaviour is observed for suspensions of submicron particles whenever the apparent diameters are close to  $D_t$  or  $D_w$  of the PSD, or for suspensions of very large particles (where  $K_{\text{scat}} \approx 2.0$ ) when the apparent diameter is close to  $D_{32}$ .

In this work, in the discussion of the apparent diameter and its relation to averages of the PSD,  $D_{\text{ap}}$  represents the correct value of the apparent diameter at given wavelength, selected in the manner explained above.

Finally, for practical purposes, if it is known that the particles in the suspension have diameters in the submicron or near micron range (i.e.,  $D < 2\text{-}3 \mu\text{m}$ ), one specific turbidity at one measurement can be used to define the particle size of a monodisperse or, the apparent diameter of a polydisperse suspension, because there is a monotonic relation between the specific turbidity and the particle diameter in that regime (i.e., from the set of all values available for that measurement we choose the one corresponding to a diameter  $D$ , such that  $0 \leq D \leq 2\text{-}3 \mu\text{m}$ ).

RECEIVED May 14, 1991

## Chapter 2

# Latex Particle Size Distribution from Turbidimetry Using Inversion Techniques Experimental Validation

A. Brandolin<sup>1</sup>, L. H. Garcia-Rubio<sup>1,3</sup>, Theodore Provder<sup>2</sup>, M. E. Koehler<sup>2</sup>,  
and C. Kuo<sup>2</sup>

<sup>1</sup>Chemical Engineering Department, University of South Florida,  
Tampa, FL 33620

<sup>2</sup>Dwight P. Joyce Research Center, The Glidden Company,  
Strongsville, OH 44136

A method is reported for the estimation of the size distribution of particle suspensions from spectral turbidity data. The proposed method is based on existing solutions to Fredholm integral equations of the first kind and the generalized cross validation technique. The capabilities of the proposed method are experimentally demonstrated through the recovery of the particle size distribution of polystyrene, poly(methyl methacrylate), and several copolymer latices. It is shown that the proposed method yields good recoveries of the shapes and the averages of the particle size distributions.

The optical spectral extinction (turbidity) of a latex contains information that, in principle, can be used to estimate the size distribution (PSD) of the suspended particles. Several authors have approached this problem using different techniques (1-4). More recently (5), regularization techniques have been applied to estimate the PSD of polystyrene latices. The regularization techniques require that the model relating the PSD and the turbidity be formulated in an integral form

$$\tau(\lambda_0) = \frac{\pi}{4} \int_0^{\infty} Q_{\text{ext}}(\lambda_0, D) D^2 f(D) dD \quad (1)$$

Eq.[1] can be recognized as a Fredholm integral equation of the first kind where:  $\tau(\lambda_0)$  is the turbidity measured at a wavelength in vacuo  $\lambda_0$ ;  $Q_{\text{ext}}$  is the extinction efficiency,  $D$  is the diameter of the particles; and  $f(D)$  is the number density of particles in the sample such that  $f(D)dD$  is the number of particles per unit volume with diameters between  $D$  and  $D+dD$ .

<sup>3</sup>Corresponding author

0097-6156/91/0472-0020\$06.00/0  
© 1991 American Chemical Society

The corresponding discrete model for Eq. [1] can be written in matrix form as

$$\underline{r} = A \underline{f} + \underline{\epsilon} \quad (2)$$

where:  $\underline{r}$  is a (mx1) vector containing the turbidity measurements at m different wavelengths; A is a (mxn) matrix whose elements  $a_{ij}$  are given by

$$a_{ij} = \frac{\pi}{4} Q_{\text{ext}}(\lambda_i, D_j) D_j^2 w_{ij} \quad (3)$$

the  $w_{ij}$ 's are weighting coefficients and they depend on the quadrature formula used in the approximation to Eq. [1];  $\underline{f}$  is a (nx1) vector whose elements are the ordinates of the PSD at each  $D_j$  diameter; and  $\underline{\epsilon}$  is a (mx1) vector that accounts for the quadrature and measurements errors at each wavelength. The regularized solution to Eq. [2] is (5-6)

$$\hat{\underline{f}}(\gamma) = [\hat{f}_1(\gamma), \dots, \hat{f}_n(\gamma)]^T = (A^T A + \gamma H)^{-1} A^T \underline{r} \quad (4)$$

where  $H = K^T K$  is a (nxn) matrix that constrains the squares of the second difference of the estimated solution  $\hat{\underline{f}}(\gamma)$ ; and  $\gamma$  is a parameter  $> 0$  that must be chosen appropriately to obtain solutions close to the true PSD's. The effect of the parameter  $\gamma$  on the solution is very important, if  $\gamma$  is too small the solution will be oscillatory, on the other hand if  $\gamma$  is too large the features of the solution will be lost. The selection of the parameter  $\gamma$  is accomplished using the generalized cross validation technique (GCV) (7-8). The method consist in minimizing the following objective function with respect to  $\gamma$

$$V(\gamma) = m \frac{|[I - A(A^T A + \gamma H)^{-1} A^T] \underline{r}|^2}{\text{Trace} \{ [I - A(A^T A + \gamma H)^{-1} A^T] \}^2} \quad (5)$$

Through the application of Eqs [4] and [5], it is possible to recover the particle size distribution directly from turbidity measurements. The potential of this technique, its sensitivity and limitations have been demonstrated with simulation experiments using unimodal and bimodal particle size distributions of varying breadth and mean particle diameters (5-8). In this paper, the capabilities of the proposed method are experimentally demonstrated through the recovery of the particle size distribution of synthetic polymer latices having a broad range of particle size distributions and polydispersities. The types of polymers have been selected to test the performance of the proposed turbidimetric technique with a variety of optical properties. Strongly absorbing polymers such as polystyrene (PS) and styrene-butadiene copolymers (PSB) and polymers containing weak chromophores such as poly(methyl methacrylate) (PMMA) and vinyl acetate-butyl acrylate copolymers (PVABA) have been analyzed. The results from the application of the regularized

solution to Eq. [1] are discussed within the context of each latex system.

### Experimental:

#### Materials:

Narrow PSD polystyrene standards were purchased from Polysciences (Warrington, PA); Poly(methyl methacrylate) latices were obtained from Glidden Corporation (Strongsville, Ohio); The vinyl acetate copolymers were kindly provided by Dr. A. Rudin from the University of Waterloo (Waterloo, Ontario, Canada) and the styrene-butadiene latices were provided by Dr. G. Poehlein from Georgia Tech. (Atlanta, Ga).

#### Optical Properties:

The optical properties for polystyrene were obtained from the data of Inagaki et al, (9); The values for poly-methyl methacrylate are from the data reported by Ritsco et al, (10). The absorption coefficients for the vinyl acetate copolymers were estimated from transmission measurements and the refractive index values reported by Devon and Rudin (11). The refractive indexes for the styrene-butadiene copolymers were estimated as a weighted sum of the refractive indexes of polystyrene and polybutadiene. The refractive index values for water were calculated from the equation given in (11).

#### Experimental Procedures:

The UV/VIS turbidity spectra were recorded in a Perkin Elmer 3840 photodiode array UV/VIS spectrophotometer equipped with a thermoelectric cell holder and a temperature controller with temperature programming capabilities. All measurements were taken at 25 °C in a 1-cm path length cell. The latices were diluted in distilled water until the linear range of the instrument was reached. Several replications were taken under different sample preparation conditions to ensure reproducibility of the results. As a precaution, and in order to avoid variability in the background, water spectra were always taken using distilled water from the same batch utilized in the dilutions of the original sample. Moreover, the background spectra were always taken shortly after or before the latex was measured in order to compensate for any instrument drift. The background corrected spectra were used for the analysis with the software developed in house. The disc centrifuge photosedimentometer analysis of the poly(methyl methacrylate) latices were conducted at Glidden with a Brookhaven DCP-1000 Particle Size Analyzer (12).

#### Effect of Small Molecules:

A source of concern in the turbidimetric analysis of polymer latices, particularly at short wavelengths (200-300nm), is the presence of chromophoric groups such as residual monomer, unreacted initiator, stabilizers, etc. In general, if chromophores are present in the water phase, their contribution can be readily identified because their extinction efficiency per unit mass is high. In these cases it is possible to remove the small molecule contributions through dilution and through the use of standard deconvolution techniques. If the chromophores are dissolved and/or bound to the

polymer particles then, the optical properties of the particles will be modified accordingly. For these cases it is necessary to resolve the scattering and the deconvolution problems simultaneously. For the latices analyzed here, the distinctive absorption pattern due to the monomers, initiators and/or emulsifiers could not be identified (see Figs. 1,4 and 8). On the other hand, the presence of small quantities of residual monomer and initiator in the polymer particles cannot be ruled out at this point (see Refs. 11-13). The contribution of these chromophoric groups may be reflected on smaller than expected  $D_n$  values. However, the excellent recoveries of the measured spectra with a single set of optical parameters suggests that, although chromophores other than the polymer may be present, their contribution to the overall extinction spectra is small.

### Results and Discussion:

In order to test the potential of the proposed regularization technique (Eqs [4] and [5]) for the deconvolution of the PSD from turbidity measurements, the analysis of the polymer latices has been divided into three groups: The first group consist of well characterized, commercially available, narrow polystyrene standards; the second group consists of poly(methyl methacrylate) latices for which the PSD has been independently measured by disc centrifuge photosedimentometry (DCP). These latices have been previously utilized in comparative particle size analysis studies (13). The third group, consist of styrene-butadiene and vinyl acetate-butyl acrylate copolymer latices. The vinyl acetate-butyl acrylate copolymer latices were analyzed as blind samples.

### Narrow PSD Polystyrene Standards:

From the point of view of scattering measurements, polystyrene latices constitute an ideal optical system. Polystyrene is not only a strong chromophore but the refractive index differences between the suspending medium and the polymer are significant throughout the complete measurement range. Figure 1 shows typical turbidity spectra for the samples analyzed. The large differences in the spectra, observed as functions of the particle diameter, are a consequence of the optical properties of polystyrene.

From the point of view of the numerical inversion technique, narrow distributions are always difficult to recover (5-8). The reason being that the identification of sharp peaks requires the inclusion of high frequencies (ie; small  $\gamma$ 's in Eqs [4] and [5]) making it difficult to separate the distributions from the measurement noise. Nevertheless, as it can be appreciated in Figures 2-3 and in Table I, the regularization technique yields adequate results. First, there is good agreement between the average particle diameters reported by the manufacturer and the values calculated from the recovered size distributions. Second, although the numerical deconvolution of narrow distributions is expected to be unstable, and therefore to show oscillatory behaviour (5-6), the particle size distributions are recovered with only mild oscillations at the tails. The smaller-than-expected oscillations are due to the fact that the actual measurement noise (Fig. 1) is considerably smaller

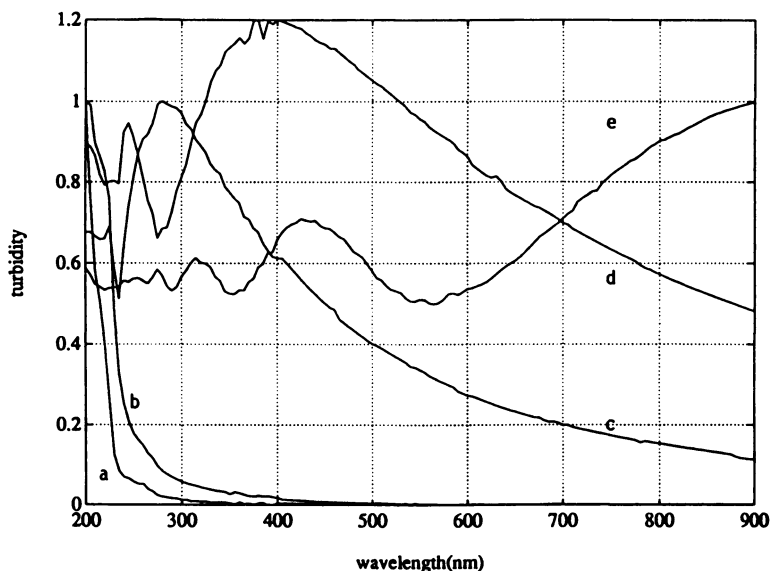


**Figure 1:** Normalized Measured Turbidity Spectra of Commercial Polystyrene Latices: a).  $D_n = 50\text{nm}$ ; b).  $D_n = 120\text{nm}$ ; c).  $D_n = 530\text{nm}$ ; d).  $D_n = 1050$  and e).  $D_n = 2790$ .

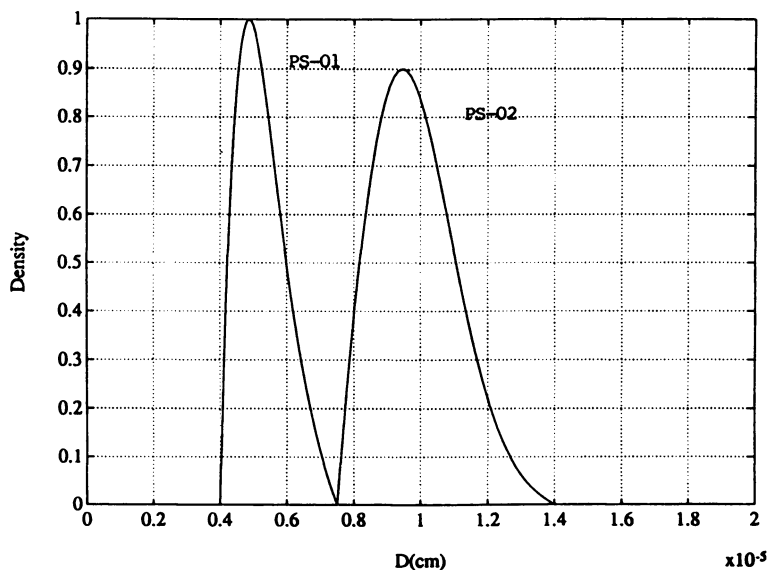


**Figure 2:** Particle Size Distributions estimated from Turbidity Measurements and Eqs. [4] and [5]: Narrow Polystyrene Latices PS-01 and PS-02.



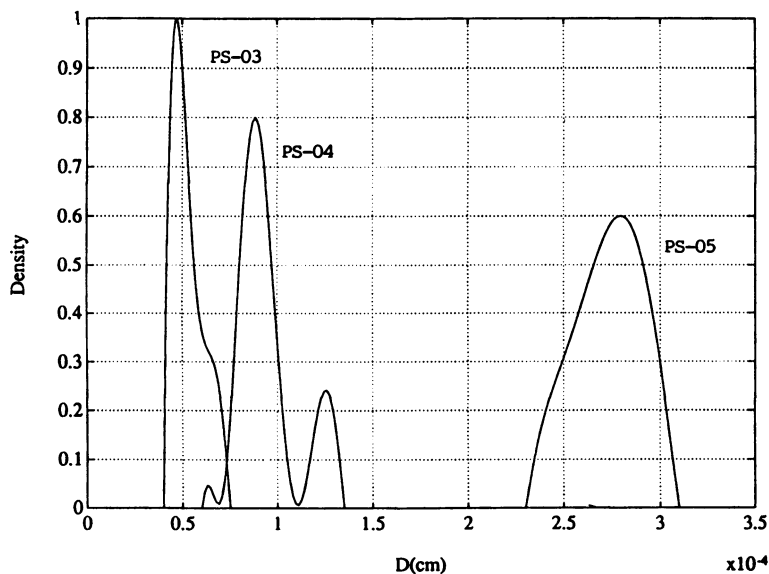


**Figure 3:** Particle Size Distributions estimated from Turbidity Measurements and Eqs. [4] and [5]: Polystyrene Latices PS-03, PS-04 and PS-05.

**Table I:** Particle Size Averages in nm for Commercial Polystyrene Standards

	Turbidimetry				Manufacturer	
	D <sub>n</sub>	D <sub>w</sub>	D <sub>r</sub>	D <sub>w</sub> /D <sub>n</sub>	D(nominal)	S.D (nm)
PS-01	47	55	57	1.17	50	9
PS-02	98	103	104	1.05	120	6
PS-03	524	570	586	1.09	530	5
PS-04	937	1028	1059	1.10	1050	70
PS-05	2730	2744	2757	1.01	2790	60

than the values used for the simulation studies (5). It is interesting to notice that not all the distributions are narrow and that some of them show bimodal character, where the smaller peaks are clearly distinguishable from the oscillations due to the numerical technique.

**Poly(Methyl Methacrylate Latices):**

In this group, a series of seven latex samples were analyzed. Five of the samples were previously characterized in a comparative study of particle size analysis techniques (10). Two additional replicate samples (68ar and 68br) have been included in the series. In principle, the only difference between original and replicate samples is that the replicate samples were filtered prior to shipping. The measured turbidity spectra for typical PMMA latices are shown in Fig 4 and the recovered particle size distributions are shown in Figs 5-7 and in Table II.

In contrast with polystyrene, the optical properties of PMMA make the problem of particle size determination, by scattering techniques and by turbidimetry in particular, a difficult one. PMMA has rather weak chromophores with small refractive index differences relative to water (11, 13). In addition, the PMMA latices analysed appear to aggregate upon dilution with distilled water. The extent to which PMMA latices aggregate can be appreciated in Fig 5, where the weight based PSDs for samples 68a and 68ar are shown. Notice that the extent of aggregation is different in each case, and that the main population from each distribution spans approximately the same diameter range and yields similar particle size averages (Table II). The aggregation observed could explain discrepancies reported in the literature between turbidimetry and other techniques and why turbidity and light scattering average diameters are consistently higher than the averages obtained with techniques like DCP (13). In spite of these difficulties, Eqs [4] and [5] yield adequate results. The average diameters, calculated from the recovered distributions are certainly within two standard deviations of all the values previously reported for the same samples (see reference (13) and Table II). Figures 6 and 7 show the PSD for all the PMMA samples analysed. Comparison of turbidimetry and DCP results (13), indicate that the PSDs estimated from turbidimetry are broader and biased towards smaller particle diameters. Differences in the shape of the PSDs estimated from turbidimetry and other techniques, can be explained on the basis of the biases particular to each technique. Standard light scattering methods, in which absorption is not considered, will tend to emphasize large particles. However, if the absorbing portion of the spectrum is considered, small particles having large surface to volume ratios will dominate the spectrum, resulting in smaller  $D_n$  values and larger variances. Other measurement techniques, like DCP, rely on the effectiveness of the fractionation mechanism, the resolution of which, generally decreases as a function of the particle diameter. As a result, the PSDs estimated from DCP will tend to have smaller variances. Although fractionation techniques have limited resolution for small particles, multimodal distributions are better resolved through fractionation because discrete elements of the overall population are selectively sampled. On the other hand, scattering and

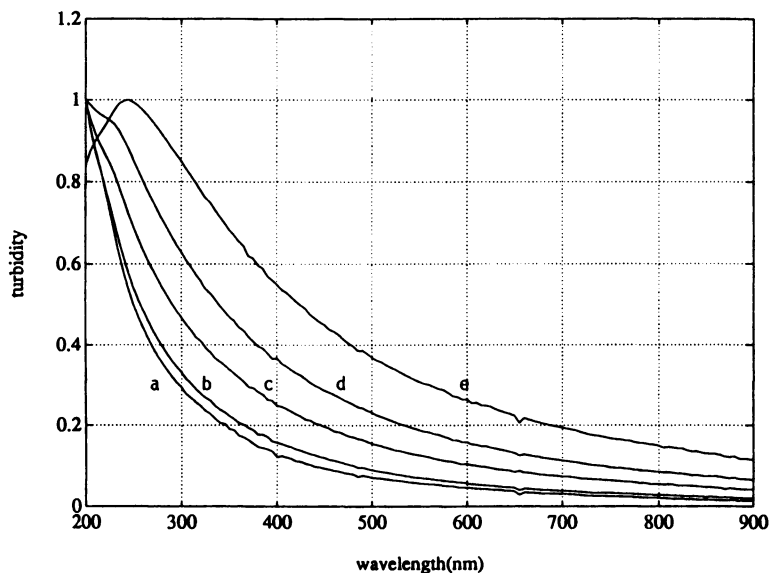


**Figure 4:** Turbidity Spectra Typical of Poly(Methyl Methacrylate) Latices: a). PMMA68a; b). PMMA68b; c). PMMA93a; d). PMMA8a and e). PMMA8c.

**Table II:** Particle Size Averages in nm for Poly-Methyl Methacrylate Latices

	Turbidimetry				DCP			
	D <sub>n</sub>	D <sub>w</sub>	D <sub>r</sub>	D <sub>w</sub> /D <sub>n</sub>	D <sub>n</sub>	D <sub>w</sub>	D <sub>r</sub>	D <sub>w</sub> /D <sub>n</sub>
PMMA68a	120	256	300	2.13	233	247	275	1.06
PMMA68ar	121	262	307	2.16				
PMMA68b	109	189	215	1.73	182	192	237	1.05
PMMA68br	108	187	212	1.73				
PMMA08a	463	554	594	1.20	550	566	667	1.03
PMMA08c	590	741	788	1.26	658	686	817	1.04
PMMA93a	341	434	468	1.27	418	432	459	1.03

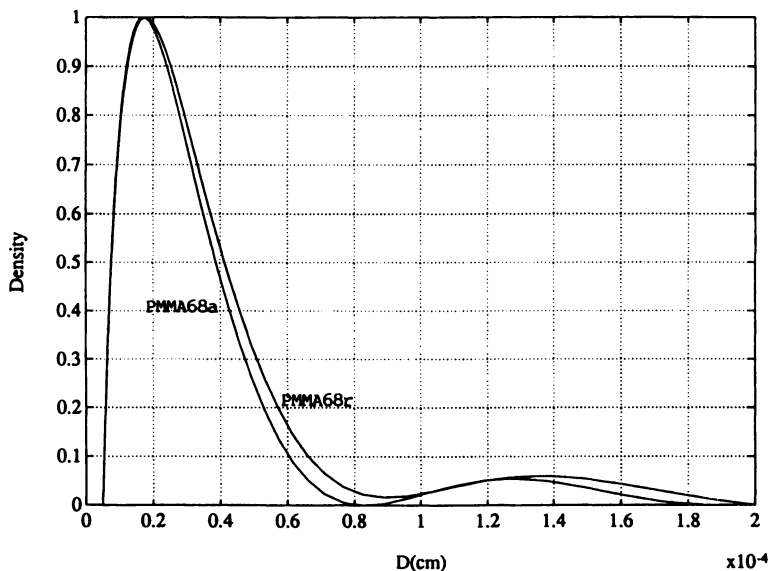


**Figure 5** : Comparison between the Weight Particle Size Distribution results for latices PMMA68a and PMMA68r suggesting the presence of aggregates.

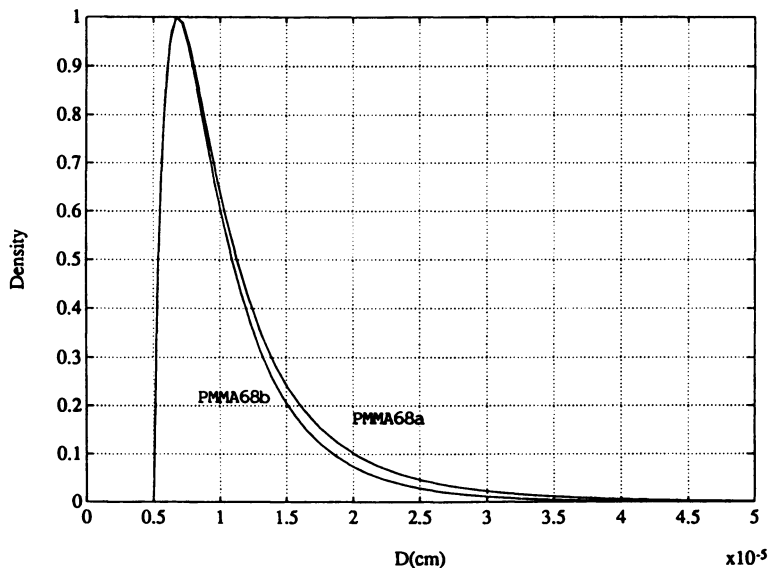


**Figure 6** : Comparison between the Particle Size Distribution results corrected for aggregation for latices PMMA68a and PMMA68b.

turbidimetry techniques, sample the whole population simultaneously resulting in the absorption and scattering effects being averaged over the whole population. How much the small particles are emphasized in turbidimetry depends on the magnitude of the absorption coefficients. Therefore, the importance of having good estimates of the optical properties cannot be understated. The averages reported in Table II were obtained using literature values for the refractive indexes (10) and absorption coefficients estimated from solution data.

#### Styrene-Butadiene Latices:

Styrene butadiene latices have been extensively used in the past for the evaluation of light scattering methods (14). Therefore, they provide a reasonable basis to assess potential applications for the proposed turbidimetry technique. In this particular case, changes in the PSD for grafting reactions have been analyzed as function of conversion for two sets of grafting conditions (15).

From the particle size analysis point of view, styrene-butadiene latices represent an intermediate case between poly(methyl methacrylate) and polystyrene. Unfortunately in our case, the styrene-butadiene copolymer contained a significant fraction of gel and therefore the determination of the absorption coefficients via transmission measurements was not possible. The refractive index, however, could be readily estimated as a weighted sum of the refractive indexes of polystyrene and polybutadiene (Table III). Because the absorption coefficient of polybutadiene could not be adequately measured, the PSD was determined using only the non-absorbing portion of the spectrum (280-900 nm). The results obtained are shown in Table III. Notice the good agreement between the value provided for the seed latex and the value calculated from the recovered PSD. The PSD's showed no special features retaining their shape through the reaction. Thus suggesting that no significant particle nucleation has taken place as a result from the grafting conditions.

#### Vinyl Acetate-Butyl Acrylate Latices:

A series of four vinyl acetate-butyl acrylate copolymer latices were analyzed as blind samples. At the time of the analysis only the polymer composition was known (85:15).

As in the case of styrene-butadiene copolymers, the absorption coefficient for the vinyl acetate-butyl acrylate copolymers is unknown over the measurement range (200-900nm). Initially, the refractive indexes of the copolymer were approximated as a weighted sum of the refractive indexes of polyvinyl acetate and polybutyl acrylate (19). Subsequently, the refractive indexes were estimated from solution measurements. In terms of optical properties, PVABA polymers are similar to PMMA latices (Fig 8). The chromophores present in PVABA copolymers are weak, however, the refractive indexes relative to water are larger than PMMA. As a consequence, the balance of optical properties allows easier recoveries of the PSDs. The results from the application of Eqs [4] and [5] together with the solution estimates of the refractive indexes, are shown in Table IV and in Fig 9. A number of interesting features are clearly

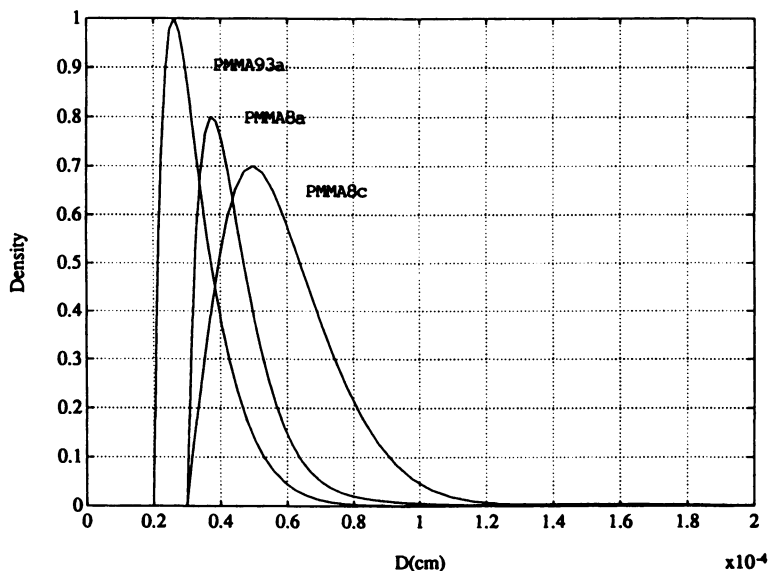


**Figure 7:** Results from the Turbidimetric analysis of Poly-Methyl Methacrylate latices: PMMA8a; PMMA8c and PMMA93a.

**Table III:** Particle Size Averages in nm for Styrene-Butadiene Copolymer Latices

	Turbidimetry				Data Ref(15)			
	Dn	Dw	Dr	Dw/Dn	D	Cw	Pw	Run
PSB-01	62	101	111	1.63	122	0.0	7.0	Seed
PSB-02	67	121	133	1.79	-	42.2	31.4	3
PSB-03	70	118	129	1.69	-	98.3	49.2	3
PSB-04	67	114	125	1.71	-	49.3	52.6	5
PSB-05	-	-	160	-	-	98.2	65.9	5

Cw: % Conversion of Styrene in the Grafting Process

Pw: Weight percent of Styrene in the Latex

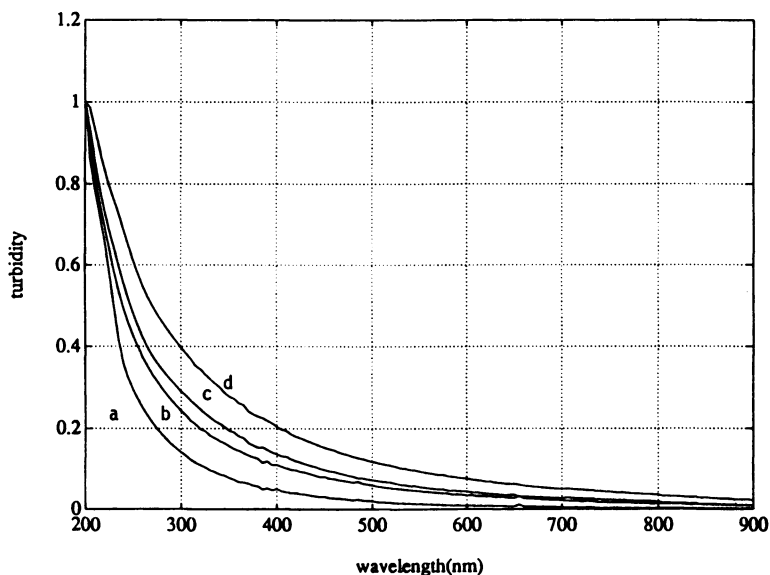


**Figure 8:** Normalized Measured Turbidity Spectra of Poly-Vinyl Acetate-Butyl Acrylate Latices: a) PVABA-01; b) PVABA-02; c) PVABA-03 and d) PVABA-04.

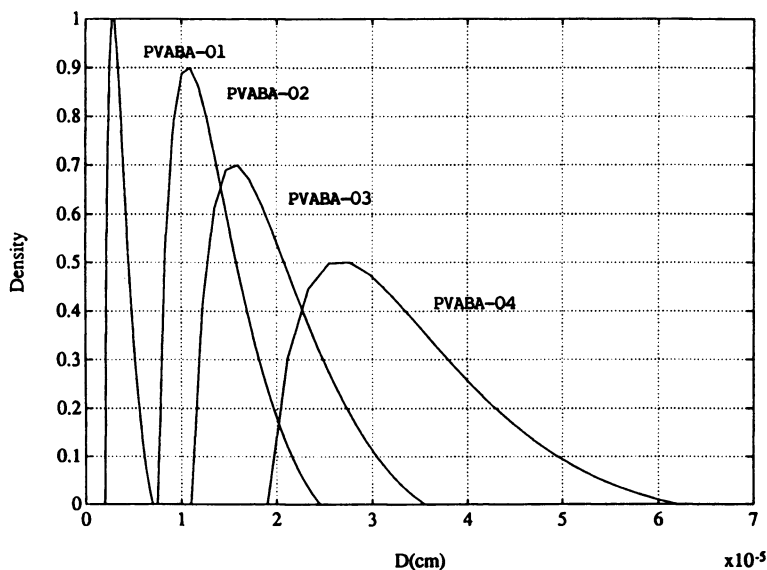


**Figure 9:** Particle Size Distributions of Poly-Vinyl Acetate-Butyl Acrylate Copolymer Latices estimated from Turbidity Measurements and Eqs. [4] and [5].

**Table IV:** Particle Size Averages for Vinyl Acetate-Butyl Acrylate Copolymer Latices

	Turbidimetry				Manufacturer			
	Dn	Dw	Dr	Dw/Dn	Dn	Dw	Dr	Dw/Dn
PVABA-01	38	46	49	1.21	54	-	-	-
PVABA-02	137	164	172	1.20	148	158	162	1.07
PVABA-03	199	238	250	1.20	233	239	242	1.03
PVABA-04	342	410	430	1.20	390	405	411	1.04

distinguishable: In agreement with DCP results, the PVABA latices appear to be unimodal. The bimodal character reported before (17) was due to the initial approximation used for the refractive indexes. The refractive index values reported in the literature (18) include only a small fraction of the wavelength range used, whereas, the refractive indexes obtained from solution data cover the same wavelength range used for the turbidity measurements. As a consequence, the agreement between DCP and turbidimetry improved considerably (Table IV). The results from Eq. [1] also indicate that the PSD's obtained from turbidimetry span a broad range of particle diameters and polydispersities. As in the case of PMMA latices, the distributions appear to be biased to smaller particle diameters. Nevertheless, as it can be appreciated in Table IV, the averages obtained from turbidimetry are reasonably close to the DCP values (16). The agreement for this set of samples is surprising when it is considered that no information on the PSD was available and that the optical properties were roughly approximated.

#### **Summary and Conclusions:**

From the results obtained, it is evident that the regularized solution to Eq. [1], is capable of yielding both, the moments and the shape of the particle size distribution of a variety of latices. The latices analyzed contain polymers that cover a significant range of optical properties that test the capabilities of the proposed method; from small refractive index differences and weakly absorbing chromophores, where scattering techniques are known to have low resolution; to large refractive index differences and strongly absorbing materials, where the use of scattering techniques is optimal. It is highly significant that the moments calculated from the regularized solution are in reasonable agreement with the results obtained using other techniques (13).

The differences in shape observed between some DCP and turbidimetry measurements can be explained on the basis of the biases particular to each measurement technique and the uncertainty associated with the optical properties of the latices analyzed. One interesting aspect of the turbidimetry technique is its apparent sensitivity to small particles. In spite of the differences in shape observed between the turbidimetry and the results from other techniques, it is evident that the leading moments of the PSD are adequately recovered. This, added to the simplicity and robustness of turbidity measurements, makes turbidimetric techniques coupled with their



interpretation by means of the regularized solution of Eq. [1], a viable alternative for the characterization of polymer latices.

#### Acknowledgments:

This research was supported by NSF Grants RII 8507956 and INT-8602578. A. Brandolin is with a Fellowship from Consejo Nacional de Investigaciones Cientificas y Tecnicas de la Republica Argentina. The Authors wish to acknowledge Dr. D. Peramunage for the turbidity measurements of the polystyrene standards and Dr. F. K. Hansen from the University of Oslo, Norway for his useful suggestions regarding possible aggregation of the poly(methyl methacrylate) latices.

#### Literature Cited:

1. Wallach, M. L., Heller, W. and Stevenson, A. F., J. Chem. Phys. **34**, 1796 (1961).
2. Wallach, M. L. and Heller, W., J. Phys. Chem. **68**, 924 (1964).
3. Zollars, R. L., J. Coll. Interface Sci. **74**, 163 (1980).
4. Melik, D. H. and Fogler, H. S., J. Coll. Interface Sci. **92**, 161 (1983).
5. Elicabe, G. E. and Garcia-Rubio, L. H., J. Coll. Interface Sci. **129**(1), 192 (1989).
6. Twomey, S., "Introduction to the Mathematics of Inversion in Remote Sensing and Indirect Measurements". Elsevier, New York, (1979).
7. Golub, G. H., Heath, M. and Wahba, G., Technometrics **21**, 215 (1979).
8. Elicabe, G. E. and Garcia-Rubio, L. H., To be published in: ACS Symposium Series on Polymer Characterization by Interdisciplinary Methods. (1989).
9. Inagaki, T., Arakawa, E. T., Hamm, R. N. and Williams, M. W., Physical Review B **15**, 3243 (1977).
10. Ritsco J. L; Brillson L. J; Bigelow R. L and Fabish, T. J., J. Chem. Phys. **69**(9), 3931 (1978).
11. Devon M. J. and Rudin A., J. Appl. Polym. Sci. **34**, 469 (1987).
12. Koheler M. E., Zander R. A., Gill T. and Provder T., ACS Symposium Series No 332. Particle Size Distribution Assesment and Characterization, Chapter 12., T. Provder Ed., (1987).
13. Koheler M. E., and Provder T., ACS Symposium Series No 332 Particle Size Distribution Assesment and Characterization. Chapter 16, T. Provder Ed., (1987).
14. Maron, S. H., Pierce, P. E. and Ulevitch, I. N., J. Colloid Sci. **18**, 470 (1963).
15. Xizhen Qian and Poehlein G., 'An Approach for Reliable Determination of Grafting Efficiency of Styrene onto Butadiene Seed". Report, School of Chemical Engineering, Georgia Institute of Technology, (1990).
16. Rudin A., Private Communication, University of Waterloo, Canada (1990).
17. Brandolin A., Garcia-Rubio L. H., Provder T., Koehler M. E and Kuo C., "Latex Particle Size Distribution from Turbidimetry Using Inversion Techniques: Experimental Validation", Presented at the ACS Symposium on Particle Size Analysis. ACS NATIONAL Meeting, Boston, Massachusetts, April 23-27, 1990.
18. Huglin M. B., Ed., "Light Scattering From Polymer Solutions". Academic Press, NY, (1972).

RECEIVED January 14, 1991

## Chapter 3

# Particle Size Determination Using Turbidimetry Capabilities, Limitations, and Evaluation for On-Line Applications

Theodora Kourti and John F. MacGregor

McMaster Institute for Polymer Production Technology, Department  
of Chemical Engineering, McMaster University, Hamilton, Ontario  
L8S 4L7, Canada

A critical discussion on the use of turbidimetric methods for particle size determination in polydisperse suspensions, with emphasis on latexes, is presented, and the potential of these methods for on-line particle size determination during latex production is evaluated. The advantages, disadvantages and limitations of several turbidimetric techniques that have been used for the estimation of an average size or the full particle size distribution are discussed. Some conflicts and inconsistencies reported in the literature and an existing controversy are resolved. Also, some observations reported concerning the type of average of the PSD that can be estimated from one specific turbidity measurement are shown to be coincidental and therefore should not be generalized. Specific problems arising when turbidimetry is used for latex particle size determination are discussed, and the use of the method for on-line particle size measurements during latex production is evaluated.

For almost four decades turbidimetric techniques have been used widely for the determination of particle size in suspensions (1-49). Turbidimetry is experimentally simple, can be used for a wide range of particle sizes (from lower submicrometer to many micrometers) and does not disturb the system under investigation. It is also fast, reproducible and inexpensive. These advantages make it a very attractive method for the determination of particle size in suspensions. It is the fastest and experimentally the simplest of the light scattering methods and is promising for on-line applications.

There are numerous reports on the use of turbidimetric techniques for the determination of either an average size or the particle size distribution (PSD) in polydisperse suspensions, in a variety of systems, such as silver bromide sols in water (3,4,19), poly(styrene) latexes (10,29,34), poly(vinyl acetate) latexes (14-17,21,24,26,27), homogenized milk, oil in water emulsions (11,18,42), coupler dispersions (22), minerals (39). There are even attempts to use turbidimetry for the determination of particle size in polymer blends (25,49). A wide range of wavelengths have been utilized for the turbidity measurements; particle size determination from turbidity measurements at wavelengths in the infrared regime has been widely reported (11, 18, 19, 22). The determination of particle size using on-line turbidimetry has also attracted a lot of attention (14-16, 19, 24, 27, 31, 45). Some of the work reported in the literature on the application of the method to different materials has been summarized (in order of decreasing value of  $m$ ) in Table I.

0097-6156/91/0472-0034\$08.50/0  
© 1991 American Chemical Society

Very frequently, workers tried to compare turbidimetry with other particle sizing methods. There are numerous reports where the average diameters or the particle size distributions estimated by turbidimetry and by other methods, were in good agreement. There are some reports (12,22) however, on "failure" of some turbidimetric techniques to provide the full PSD. There is a controversy in the literature (12,16,17) on whether or not turbidimetry can provide the true PSD. The controversies and contradictory reports in the literature motivated a detailed investigation on the capability of the method to provide the full PSD, and this investigation is presented in another chapter in this volume (28). The main conclusion from this investigation was that it is impossible to generalize turbidimetric methods across refractive indices and particle size ranges. The capability of a turbidimetric method to provide an average particle size or the particle size distribution of the suspension and its sensitivity to experimental error cannot be discussed without relating it to the  $m$  and  $a$  values of the suspension, and conclusions cannot be extrapolated from one  $(m,a)$  regime to another and from one method to another. A critical review (27) of the work reported on turbidimetry indicated that contrary to the above conclusion, there is a tendency in the literature to generalize or extrapolate conclusions and observations across methods and  $(m,a)$  regimes, and that most of the conflicts and the existing controversy arise from this tendency. The observations reported by each investigator were correct and could be justified for their system, by taking into account our analysis in (28). By checking the  $(m,a)$  values of these systems, turbidimetry was expected to succeed in providing the PSD in the cases that was reported as a successful method, and was expected to fail in the cases that it failed. However, although their observations were correct, conflicts arose when these investigators extrapolated their observations to other systems (other  $m, a$  regimes) and other methods.

The objective of this chapter is to give an insight into turbidimetry. The methods available for particle size determination using turbidimetry are discussed. After a brief theoretical background the advantages and limitations of each method are given and the  $(m, a)$  regimes where the estimation of the full PSD is possible are identified. The sensitivity of the results to experimental error is investigated. Several publications on turbidimetry are critically discussed in order to highlight the limitations of some approaches that are not widely used, and to point out some coincidental observations that may result to misleading conclusions. Finally, the potential of the method for on-line applications is investigated and problems related to applications for latex systems are discussed.

### General Definitions

Turbidity gives a measure of the attenuation of a beam of light traversing a suspension of particles:

$$\tau = \frac{1}{\ell} \ln \frac{I_0}{I} \quad (1)$$

where  $I_0$  and  $I$  represent intensities of the incident and transmitted beams, respectively, and  $\ell$  is the length of the optical path (cell length, cm). The turbidity of a suspension can be measured with any spectrophotometer, after certain modification have been made (22).

For a suspension of spherical, non absorbing, isotropic particles, in the absence of multiple scattering,

TABLE I: Particle Size Determination in Polydisperse Systems using Turbidimetry

AUTHORS	System	m	Wavelengths (nm)	Particle Size D( $\mu$ m)	Turbidimetric Method	Assumed PSD	Other Methods
Meehan and Beatlie (4)	stable silver bromide sols in water	1.7	1. 436, 546 2. 450, 800	D < 0.25	Specific Turbidity	1. Apparent Diameters 2. Log-normal (ZOLD)	EM
Haseler and Parkin (19) <sup>a</sup>	silver bromide grains	1.7	infrared (2.22 $\mu$ m)	D < 0.8	Specific Turbidity	Apparent Diameter ( $D_v$ )	EM
Yang and Hong (39)	Minerals: TiO <sub>2</sub> Al <sub>2</sub> O <sub>3</sub> Al(OH) <sub>3</sub> SiO <sub>2</sub>	1.9 1.33 1.86 1.163	436, 546, 650, 800	0.1 < D < 10	Specific Turbidity	Log-normal on weight basis	Centrifugal sedimentation
Wallach and Heller (10) <sup>a</sup>	poly(styrene) latexes d	1.2	440-610 basis: 546	0.65 < D < 1.3	Turbidity Ratio	Positively Skewed <sup>e</sup>	EM
Maron et al (9) <sup>a</sup>	poly(butadiene-styrene) latexes	1.17, 1.15	350-1000	D < 0.4	Specific Turbidity	Apparent Diameters	EM
Gledhill (7) <sup>a</sup>	Kodacolor dispersions	1.166, 1.21	400-800	0.05 < D < 1.0	Specific Turbidity and Wavelength Exponent	Log-normal on weight basis	EM
Haseler (22) <sup>a</sup>	coupler dispersions	1.15	400, 700 400 nm, 2.22 $\mu$ m	D < 1.0	Specific Turbidity	Log-normal	-
Wales (6) <sup>a</sup>	Latexes: Hevea, cis-polyisoprene	1.136	650, 800, 950, 1100	D < 2.0	Specific Turbidity	Log-normal on weight basis	Coulter Counter EM
Bagchi and Vold (13)	Styrene divinylbenzene copolymer latexes	-	400-600	12 < D <sub>N</sub> < 50	Specific Turbidity	Apparent Diameter ( $D_{32}$ )	EM (standard latexes)

Kubota et al (20)	latexes	—	400, 700	$2 < D < 40$	Specific Turbidity	Apparent Diameter ( $D_{32}$ )	EM
Melik and Fogler (36) <sup>a,b</sup>	octacosane suspensions	1.15	436, 546	$D < 3.0$	Turbidity Ratio and Wavelength Exponent	1. Log-normal 2. One parameter positively skewed	EM
Maxim et al (11) <sup>a</sup>	poly (vinyl acetate)	1.1	320-720	$0.1 < D < 1.0$	Turbidity Ratio	Positively Skewed <sup>d</sup>	EM
Zollars (16,17) <sup>a</sup>	poly (vinyl acetate)	1.1	300,600	1. $D_w: 0.20$ 2. $D_i: 0.11$	Specific Turbidity	Log-normal	1. Disc-Centrifugation, 2. Angular Light Scattering
Kourti et al (21,26,27)	poly (vinyl acetate)	1.1	400-600	$D < 0.2$	Specific Turbidity	Log-normal ( $D_{ap} = D_w$ )	HDC
Kiparissides (15) <sup>a</sup>	poly (vinyl acetate)	1.1	350-700	$D < 0.4$	Method of Moments	Moments of PSD	HDC
Walstra (11) <sup>c</sup>	cow's milk, paraffin oil in (water + glycerol)	1.1 1.05	300-1700	$0.1 < D < 10.0$ $0.1 < D < 40.0$	Specific Turbidity	1. log-normal 2. an upper limit function 3. exponential type	Coulter Counter

a. This work is briefly discussed in this chapter. For detailed discussions, see Kourti (27).

b. See also (35).

c. For similar systems, see also (18, 42) and references in them.

d. For polystyrene suspensions, see also (22).

e. This distribution (which was also utilized by Heller and his collaborators (5, 10, 38) cannot describe polydisperse systems (maximum polydispersity,  $D_w/D_N = 1.5$ ).

EM: Electron Microscopy.

HDC: Hydrodynamic Chromatography.

$$\tau = N \int_0^{\infty} \frac{\pi D^2}{4} K\left(\frac{D}{\lambda_m}, \frac{n_p}{n_m}\right) f(D) dD \quad (2)$$

where  $N$  is the number of particles per  $\text{cm}^3$  and  $f(D)$  is the normalized particle size distribution.  $K(D/\lambda_m, n_p/n_m)$  or  $K_{\text{scat}}$  is the scattering coefficient, which is an involved function of two parameters,  $\alpha$  and  $m$ .  $\alpha = \pi(D/\lambda_m)$  is defined as the relative size of the particle diameter to the wavelength of the light in the medium and  $m = n_p/n_m$  is the ratio of the refractive index of the particles to the refractive index of the medium.  $\lambda_m = \lambda_0/n_m$  where  $\lambda_0$  is the wavelength of the incident beam in vacuo; both  $n_p$  and  $n_m$  are evaluated at  $\lambda_0$ . Another parameter which is useful in the light scattering theory is the phase shift,  $\rho$ , suffered by a wave passing through the centre of a sphere (40);  $\rho = 2\alpha m - 1$ .

The scattering coefficient exhibits an oscillatory dependence on  $\alpha$ , with a series of successive minima and maxima, and approaches the value of 2 at large  $\alpha$  values (see, for example, Figure 5 of reference (28), this volume). The first maximum occurs at lower  $\alpha$  values, the larger the value of  $m$ . The numerical value of  $K_{\text{scat}}$  at the first maximum is larger, the larger the  $m$  value. When  $K_{\text{scat}}$  is plotted against  $\rho$ , the  $\rho$  position of the extremes (minima and maxima) of the main oscillation, is almost independent of the value of  $m$  (30,50). In the general case the scattering coefficient can be calculated from the rigorous Mie theory (1,30,50). A large number of approximating formulas have been developed which, for certain  $(m, \alpha)$  regimes, give  $K_{\text{scat}}$  within 1% accuracy from the true value (40). Simplified expressions can also be used in the two extreme cases:

a) For particles, which are very small compared to the wavelength both outside ( $\alpha < 1$ ) and inside ( $|m\alpha| < 1$ ) the particle (50), the Rayleigh scattering theory gives:

$$K\left(\frac{D}{\lambda_m}, \frac{n_p}{n_m}\right) = \frac{8}{3} \left(\frac{m^2 - 1}{m^2 + 2}\right)^2 \alpha^4 \quad (3)$$

A discussion concerning the  $m$  and  $\alpha$  regions where the Rayleigh theory is valid can be found in (40,41).

b) For particles very large compared to the wavelength, the scattering coefficient approaches a constant value independent of  $m$  (1,30,50):

$$K\left(\frac{D}{\lambda_m}, \frac{n_p}{n_m}\right) = 2 \quad (4)$$

For a monodisperse suspension of non absorbing spheres, at a given wavelength, the dependence of the scattering coefficient on the diameter can be approximated by (3,4):

$$K_{\text{scat}} = K\left(\frac{D}{\lambda_m}, \frac{n_p}{n_m}\right) = k'(D/\lambda_m)^2 = k'_c \alpha^2 \quad (5)$$

where  $k'$ ,  $k'_c$  are proportionality constants. For constant  $D$ ,  $K_{\text{scat}} = k'' \lambda_0^{-z}$ , and therefore  $z$  has been termed "the wavelength exponent" (8). At constant  $\lambda_m$ , we can write:

$$\ell n(K_{\text{scat}}) = z \ell n \alpha + \ell n k'_c \quad (6)$$

The value of  $z$  can be obtained for any  $\alpha$  at any  $m$  value from the slope of  $\ln(K_{\text{scat}})$  vs.  $\ln \alpha$ . The turbidity of a monodisperse suspension is given as:  $\tau = NkD^y$  where  $y = z + 2$ . Several authors (4,8) have tabulated values of  $y$  or  $z$  for several pairs of  $(m, \alpha)$  values. (In the notation of Ref. (8),  $z \approx n$ ). Values of  $y$  are plotted as a function of  $\alpha$  in Figure 1 for several values of  $m$ .

For a polydisperse system, at a given  $\lambda_m$ , from Equations 2 and 5:

$$\tau = N \int_0^{\infty} k D^y f(D) dD \quad (7)$$

where both  $k$  and  $y$  are functions of  $D$ . When the particle sizes in the suspension are such that  $k$  and  $y$  do not change significantly with  $D$ , then:

$$\tau = k \int_0^{\infty} D^y f(D) dD \quad (8)$$

where  $k$  and  $y$  are constants. In these cases, turbidity is proportional to the  $y$ th moment ( $J_y$ ) of the particle size distribution. The value of  $y$  (i.e., the order of the moment) depends on the  $\alpha$  and  $m$  values of the suspension. For  $\alpha < 0.5$ , where  $y$  approaches the limiting value of 6 ( $z = 4$ ; compare Equations 3 and 5), turbidity is proportional to the sixth moment of the particle size distribution. Notice (Figure 1) that for values of  $m$  between 1.1 and 1.2, the  $y$  vs  $\alpha$  behaviour is almost identical (i.e., independent of the value of  $m$ ) for  $\alpha < 1.6$ . For small values of  $m$  ( $m = 1.05, 1.1, 1.15$ ) the value of  $y$  is approximately 4.0 ( $4.2 \leq y \leq 3.8$ ) for a very wide range of  $\alpha$  values (for  $m = 1.05, 3 < \alpha < 14$ ; for  $m = 1.15, 3 < \alpha < 6$ ). For suspensions with particle size distributions in the above  $(m, \alpha)$  regions, turbidity should be approximately proportional to the 4th moment of the PSD. Finally, for very large particles, turbidity is proportional to the 2nd moment of the PSD.

### Estimation of the Particle Size Distribution Using Turbidimetry

The turbidity of a suspension of spherical particles is a function of both the number concentration of particles and the particle size distribution (PSD). A number of approaches (30) have been used to eliminate the unknown number of particles and relate the turbidity measurements to the particle size distribution only. The most widely used approaches are briefly outlined below and their advantages and disadvantages are discussed. It has been shown (28) that the estimation of the full PSD is not always possible when using turbidimetry, and that this is related to the  $(m, \alpha)$  values of the suspension, and to the technique employed. Here, the  $(m, \alpha)$  regimes where the estimation of the full PSD is practically possible are given for each one of the methods. When the estimation of the full PSD is not possible or only an estimate of an average diameter is desirable, an apparent diameter can be estimated by treating the system as monodisperse. The potential of each method to provide an apparent diameter that corresponds to a meaningful average of the PSD is also discussed.

### Specific Turbidity

Specific turbidity has been the most widely used turbidimetric technique. Extensive discussions on the method can be found in several sources (4, 11, 27, 30, 39). Successful applications for particle (or droplet) size distribution determination, have been reported by several researchers (4, 11, 39). The theoretical background of the method is briefly outlined here.

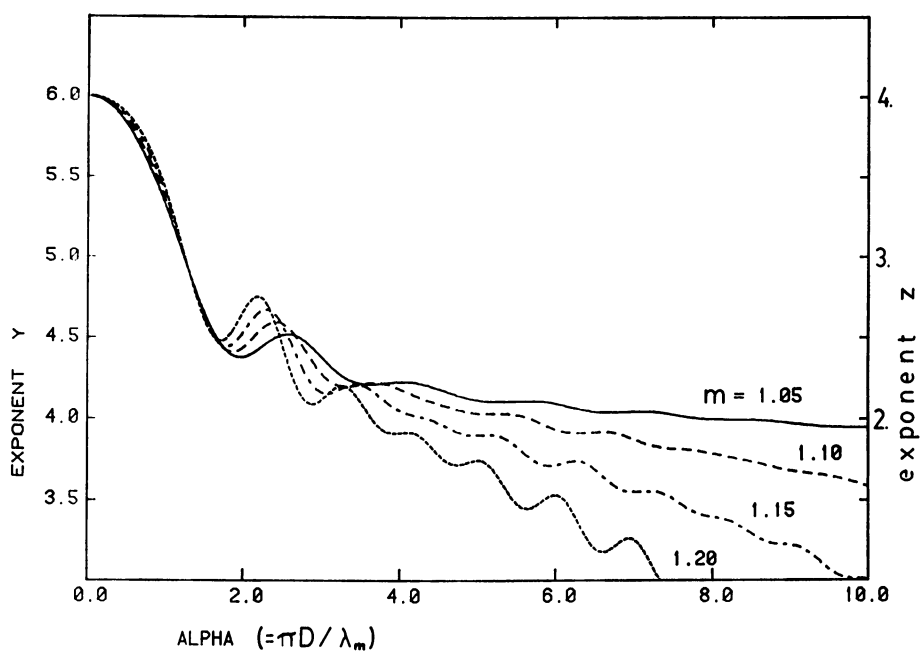


Figure 1. The exponents  $y$  and  $z$  as a function of  $\alpha$  ( $\alpha = \pi D / \lambda_m$ ), for  $m = 1.05, 1.1, 1.15$  and  $1.2$ .



The volume fraction,  $\phi$ , of the spherical particles in a polydisperse suspension is:

$$\phi = N \int_0^{\infty} \frac{\pi D^3}{6} f(D) dD \quad (9)$$

The particle volume fraction can be measured using gravimetric analysis or densitometry (24, 45).

The specific turbidity is defined as the ratio of the turbidity of the suspension to the volume fraction of the suspended particles, and it is independent of the particle number concentration:

$$\frac{\tau}{\phi} = \frac{3}{2} \frac{\int_0^{\infty} D^2 K\left(\frac{D}{\lambda_m}, \frac{n_p}{n_m}\right) f(D) dD}{\int_0^{\infty} D^3 f(D) dD} \quad (10a)$$

Alternatively, the specific turbidity of a suspension can be written as:

$$\frac{\tau}{\phi} = \int_0^{\infty} \frac{\tau}{\phi}(D) F(D) dD \quad (10b)$$

where,  $\tau/\phi(D)$  is the specific turbidity corresponding to particles with diameter  $D$ , and  $F(D)$  is the normalized PSD on weight basis. For a suspension of spheres with a known size distributional form a minimum of two specific turbidity measurements are required for the estimation of a two parameter particle size distribution, from Equations 10a or 10b, when the optical properties of the suspension are known.

For a monodisperse suspension, specific turbidity is simply:

$$\frac{\tau}{\phi} = \frac{3}{2} \frac{K\left(\frac{D}{\lambda_m}, \frac{n_p}{n_m}\right)}{D} \quad (10c)$$

The diameter  $D$  of the particles in a monodisperse suspension can be calculated from one or more specific turbidity measurements (see Appendix A of Ref. 28, in this volume) when the optical properties of the suspension are known.

The estimation of the parameters of the particle size distribution, from Equations 10a or 10b is impossible whenever turbidity measurements at two or more wavelengths are proportional to the same moment,  $J_y$ , of the PSD (Equation 8). In these cases, specific turbidity becomes proportional to  $J_y/J_3$  or, more simply, proportional to the  $(y-3)$ rd power of the  $D_{y3}$  average diameter (28) for all the wavelengths used, and only the  $D_{y3}$  average can be correctly estimated (27, 28). Notice (Equation 9) that  $\phi$  is always proportional to the third moment,  $J_3$ , of the PSD. An apparent (average) diameter can be calculated for a polydisperse system using Equation 10c. For a polydisperse system, Equation 10c can be written as:

$$\frac{\tau}{\phi} = \frac{3}{2} \frac{K(\alpha_{av}, m)}{D_{av}} \quad (11)$$

where  $\alpha_{av} = \pi D_{av}/\lambda_m = \pi D_{av} n_m/\lambda_0$ .  $D_{av}$  is the apparent diameter of the suspension at  $\lambda_0$ , the wavelength at which the turbidity measurement was taken, and corresponds to the  $D_{y3}$  average of the PSD. An average diameter is determined in the following situations:

i) For distributions with particles very small compared to the wavelength (for all the wavelengths used for the turbidity measurements), where the Rayleigh equation applies. Substitution of Equation 3 in 10a gives:

$$\frac{\tau_{\lambda_0}}{\phi} = L_{\lambda_0} \frac{\int_0^{\infty} D^6 f(D) dD}{\int_0^{\infty} D^3 f(D) dD} = L_{\lambda_0} D_{\tau}^3 \quad (12)$$

where  $D_{\tau}$  (or  $D_{63}$ ) is a "turbidity average" diameter and  $L_{\lambda_0} = 4\pi^4 \lambda_m^{-4}((m^2-1)/(m^2+2))^2$ ; the subscript  $\lambda_0$  denotes that  $\tau$ ,  $\lambda_m$ ,  $m$  are evaluated at  $\lambda_0$ . Notice that for monodisperse suspensions in the Rayleigh regime, specific turbidity is simply proportional to the volume of a particle:  $\tau/\phi \propto D^3$ .

ii) For very large diameters where  $K_{scat} = 2$ . Substitution in Equation 10a gives:

$$\frac{\tau}{\phi} = 3 \frac{\int_0^{\infty} D^2 f(D) dD}{\int_0^{\infty} D^3 f(D) dD} = \frac{3}{D_{32}} \quad (13)$$

where  $D_{32}$  is the volume-surface average (or Sauter mean) diameter. For monodisperse suspensions of large particles, specific turbidity is simply given by:  $\tau/\phi = 3/D$ .

iii) For suspensions and particle size distributions in the  $(m, \alpha)$  regimes where the exponent  $y$  is very close to 4.0 ( $3.8 < y < 4.2$ ) and specific turbidities result in apparent diameters numerically very close to the weight average ( $D_w$  or  $D_{43}$ ) of the true PSD (27,28). The  $(m, \alpha)$  values where this happens can be read from a  $y$  vs.  $\alpha$  plot. (For example, from Figure 1, we read: for  $m = 1.05$ ,  $3.0 < \alpha < 14$ ; for  $m = 1.15$ ,  $3.0 < \alpha < 6.0$ .) If the whole distribution covers  $\alpha$  values in this regime for both of the wavelengths used, then only the weight average of the distribution can be correctly estimated. This is true for any type of distribution (multimodal or unimodal, continuous distribution of mixture of two populations). This is a very useful property of the specific turbidity: the weight average diameter of suspensions can be correctly estimated even though the PSD determination is impossible. The  $\alpha$  range where this property applies may be extended further when the distribution is log-normal. This information is useful when an average diameter of the PSD is sufficient to describe a process (i.e., for routine measurements to follow the progress of the reaction), because the weight average of the distribution can be determined with simple measurements. For suspensions with  $m = 1.1$  and log-normal distributions of submicrometer particles, for example, it has been observed (27) that the mean average of the apparent diameters estimated from specific turbidities at 400 nm and 600 nm is within 5% the true weight average diameter of the

PSD (27,28). Therefore, monitoring these two apparent diameters gives information on the weight average of the PSD.

### Turbidity Ratio

The ratio of two turbidity readings taken at different wavelengths is a quantity independent of the particle number concentration.

$$\frac{\tau_{\lambda_{01}}}{\tau_{\lambda_{02}}} = \frac{\int_0^{\infty} D^2 K\left(\frac{D}{\lambda_m}, \frac{n_p}{n_m}\right) f(D) dD}{\int_0^{\infty} D^2 K\left(\frac{D}{\lambda_m}, \frac{n_p}{n_m}\right) f(D) dD} \quad (14)$$

where subscripts  $\lambda_{01}$ ,  $\lambda_{02}$  denote that the quantities  $\tau$ ,  $n_p$ ,  $n_m$ ,  $\lambda_m$  are calculated at these wavelengths;  $\lambda_{01}$ ,  $\lambda_{02}$  are wavelengths in vacuo. For a two parameter, known particle size distributional form, a minimum of three turbidity measurements at different wavelengths (one of which is chosen as reference) are required, in principle, for the estimation of these parameters.

For monodisperse suspensions, Equation 14 reduces to the ratio of the scattering coefficients at two wavelengths and the particle diameter could be estimated from one turbidity ratio (2 turbidity measurements) in regimes where the ratio is a monotonic function of particle size. However, an indentation exists in the turbidity ratio vs. a curve, at the lower  $\alpha$  regime, due to the first inflection point of the  $K_{\text{scat}}$  vs.  $\alpha$  curve. (In polydisperse suspensions, this indentation vanishes). Also, for larger particles, the turbidity ratio vs.  $\alpha$  curve exhibits an oscillatory behaviour. Therefore, a reading at a third wavelength (two turbidity ratios) is advised, to uniquely define the particle size.

The method gives no information on the particle size in the following cases:

- i) For very large particles, where the scattering coefficient is constant; substitution of  $K_{\text{scat}} = 2$  in Equation 14 gives a ratio equal to unity.
- ii) For very small particles, where the Rayleigh Equation 3 applies, the turbidity ratio is independent of the particle size.
- iii) When, for all the wavelengths used, turbidities are approximately proportional to the same moment of the PSD. This case is observed for suspensions with very small  $m$  values ( $m \sim 1.15, 1.1, 1.05$ ) when the particle sizes of the suspension correspond to a regime of  $\alpha$  values below the first  $K_{\text{scat}}$  maximum, where the exponent  $y$  changes very slowly with  $\alpha$ . For these small values of  $m$  this  $\alpha$  regime is very wide. This in turn means that even for broad distributions, turbidities at widely separated wavelengths will be proportional to approximately the same moment of the PSD, and their ratio will be almost independent of the particle size. In other words, the method is so sensitive to experimental error in these regimes, that practically gives no information on the particle size. Kourti et al. (27) showed that for  $m = 1.1$  and submicrometer particles, the estimation of the true PSD from turbidity measurements at 350 and 700 nm (with reference  $\lambda_0 = 546$  nm) is impossible for measurement errors as small as 0.5%.

The turbidity ratio method should therefore be avoided for the estimation of the particle size, for systems of very small or very large particles, and for systems with small  $m$  values ( $m < 1.15$ ) and  $\alpha$  values below approximately 10. In this regime the method offers no information on the size of the suspension (i.e., neither the PSD nor an average can be estimated).

### Methods Similar to Turbidity Ratio

Alternatively to Equation 14, some authors (5, 36) use the ratio:

$$\left(\frac{\tau\lambda}{\phi}\right)_{\lambda_{01}} / \left(\frac{\tau\lambda}{\phi}\right)_{\lambda_{02}}$$

or in the DQ (dispersion-quotient) method, the ratio (30):

$$DQ = \tau_{\lambda_{01}} \lambda_{02}^2 / \tau_{\lambda_{02}} \lambda_{01}^2$$

The restrictions and limitations for these approaches are the same with those that apply for the turbidity ratio, described by Equation 14.

### The Wavelength Exponent

In this approach, the change of the turbidity of a suspension with the wavelength is recorded and related to the size of the suspended particles. The concentration of the scattering material does not need to be known; the only requirement is that the suspension should be dilute enough to avoid multiple scattering. The method is described in detail in Bateman et al. (37), Heller et al. (8), and Kourti (27).

Melik and Fogler (36) describe a combination of the wavelength exponent and the turbidity ratio method, where it is claimed that the two parameters of the particle size distribution can be estimated from only two turbidity measurements. However, it has been shown (27,35) that the turbidity ratio and the wavelength exponent are not two different methods, but are theoretically equivalent for the determination of the parameters of the PSD. The functions used in these two "techniques" to convert the turbidity measurements to particle size distributions can be derived from each other, and in case of no measurement error use of either method gives identical results. At least three turbidity measurements are required for the determination of a two parameter PSD using either of the methods or their combination. Otherwise (two turbidity measurements only), an infinite number of solutions will be obtained. The claims of (36) are shown (35) to be incorrect.

Although the turbidity ratio and the wavelength exponent technique are theoretically equivalent for the determination of the PSD, the formulation of the turbidity ratio method, is less complex than that of the wavelength exponent. Consequently, the turbidity ratio method requires less computation to calculate the particle size distribution, and the error propagation is smaller. It should be also noted that, in the (m, a) regions where the estimation of the particle size in a suspension is not possible using the turbidity ratio method, the wavelength exponent method also fails.

### Other Methods

Several other approaches have appeared in the literature for the determination of the particle size distribution or an average diameter in polydisperse suspensions. Most of these methods, however, have serious limitations and have not found a wide application. Some of these approaches are discussed briefly below. Extensive discussions can be found in Kourti (27).

**The Method of Moments.** In this method no assumption on the shape of the PSD is made (14,15), and only the moments of the unknown PSD are calculated, from turbidity ratio measurements. The main idea behind this technique was to approximate the term  $K(D/\lambda_m, n_p/n_m) \pi D^2/4$  in Equation 2 with a polynomial form:

$$K\left(\frac{D}{\lambda_m}, \frac{n_p}{n_m}\right) \frac{\pi D^2}{4} \sim \sum_{i=0}^P C_{i\lambda} D^i \quad (15)$$

By substituting this form in Equation 2 turbidity can be expressed as a sum of P moments of the unknown PSD. Using P turbidity ratios (P+1 turbidity measurements) one can estimate the P moments. ( $J_0$  of the normalized distribution is unity). The PSD is then represented analytically using a set of its moments, by modifying a gamma distribution which serves as a basis (14,15,27). The  $C_{i\lambda}$  coefficients were estimated as follows: the left hand side of this equation was calculated exactly from the Mie theory for a set of 20 diameters (between 0.04 and 0.8  $\mu\text{m}$ ) and a given wavelength. The value of P was set equal to 6 and the coefficients  $C_{i\lambda}$  were estimated for that wavelength. The procedure was repeated for 7 wavelengths (350 to 800 nm). The method was applied for particle size determination in poly(vinyl acetate) latexes.

The expansion of the scattering coefficient to a power series of  $\alpha$  (which for constant  $\lambda_m$ , results in a power series of D) has been widely used in the literature; however, in all cases, these approximations are applicable for small  $\alpha$  and  $m\alpha$  values and the coefficients of  $\alpha^i$  (or  $D^i$ ) are known functions of the optical constants and can be calculated (40) (i.e., no estimation of  $C_{i\lambda}$  is necessary). Approximating formulas for the calculation of  $K_{\text{scat}}$  for larger  $m$  and  $\alpha$  values include more involved functions of  $\alpha$  (or  $\rho = 2\alpha(m-1)$ ) than a simple power series expansion (40). The  $\alpha$  values corresponding to the diameters and wavelengths reported in (14,15) were very large ( $\alpha$  as large as 9.5) for the power series expansion to apply. Furthermore, as it has been shown (27,28), the term  $K_{\text{scat}} D^2$  can be set proportional to  $D^y$ , and the value of  $y$  changes as a function of the particle size. For poly(vinyl acetate) latexes in particular, and for a very wide range of  $\alpha$  values, the value of  $y$  is very close to 4.0. For most of the diameters used for the calculation of the above term in that study (14,15) at each wavelength, the  $\alpha$  values were such that  $y$  was close to 4.0. It is clear that a reasonable value from the parameter estimation is expected only for  $C_{4\lambda}$ , since all the other coefficients are practically equal to zero. From the results reported by Kiparissides (14), only  $C_{4\lambda}$  seems to have a consistent value for all the wavelengths; the estimated values of all the other coefficients change, both sign and value, randomly (27). It should be clear that with meaningless estimates of the  $C_{i\lambda}$  coefficients the correct estimation of the moments of the PSD is impossible.

**Multimodal Distributions From Turbidity Spectra.** Gulari et al. (33,34) tried to estimate particle size distributions in polystyrene suspensions ( $m \sim 1.2$ ), from a large number of turbidity measurements (using very small wavelength steps, at the wavelength range between 300 and 800 nm). In each case, the unknown particle size distribution was assumed to be the sum of 20 equally spaced delta functions. The mass fraction and position of each diameter was optimized using a non-linear least squares minimization process. The suspensions used to test the method were synthesized by mixing two or three monodisperse latexes, with particle diameters approximately 1  $\mu\text{m}$  separated from each other. The distributions were resolved on weight basis. In each distribution the weight fraction of the small particle population was significant. The method however may not give satisfactory results i) when a very small weight fraction of the small particles is present, ii) for suspensions with ( $m, \alpha$ ) values different than that above, as for example, suspensions with submicron particles and  $m = 1.1$  and iii) for suspensions containing some particle populations with particle diameters very close to each other compared to the

assumed  $\Delta D$  interval. The reader should keep in mind that the resolution of the method depends on the location of the assumed delta functions (number and width of  $\Delta D$  intervals) and of course on the number of measurements (observations) available.

An attempt to determine the PSD from multiple turbidity measurements and without assuming a distributional form is also reported by Elicabe and Garcia-Rubio (48). Again,  $f(D)$  is solved at a finite number of points. A regularization technique is utilized for the parameter estimation. Simulations were used to test the technique for the estimation of unimodal and bimodal PSD's of varying breadth and mean diameter. When no a priori information is available for the choice of the regularization parameter, the estimation of  $f(D)$  at a finite number of points is expected to give satisfactory results only for certain suspensions (i.e., corresponding to certain  $m$  and  $\alpha$  values). For example, it is not expected to work (i.e., results will be questionable) in  $(m, \alpha)$  regimes where  $y$  is a very slow function of  $\alpha$ . In (48a) satisfactory results are reported for broad distributions with particle diameters in the micron range (distributions with  $D_{\max} = 1.45 \mu\text{m}$  or  $2.25 \mu\text{m}$ ). For  $m = 1.2$  the results were not satisfactory for distributions covering sizes from 50nm to 325nm, that is, a regime where a large number of latex particle diameters are expected to be found.

### The Choice of the Particle Size Distributional Form

If a continuous set of measurements of  $\tau$  vs.  $\lambda$  was available, one could theoretically deconvolve Equations 10a and 14 to yield  $f(D)$ . However, in practice, one usually only has turbidity measurements at a finite number of wavelengths. If no distributional form is assumed for  $f(D)$ , then one could either solve for  $f(D)$  at a finite number (33,34,48) of points (less or equal to the number of specific turbidity or turbidity ratio measurements made), or approximate  $f(D)$  via polynomials, etc., and solve Equations 10a or 14 via collocation methods. Alternatively, for a small number of turbidity measurements, a convenient approach is to approximate  $f(D)$  by an assumed form having only a few parameters. This form is then substituted into Equations 10a or 14 and its parameters are estimated from the turbidity measurements. The assumed distributional form is one that is expected to occur from a knowledge of similar cases.

Typical Distributional Functions. An extensive review on the distributional forms that have been used to describe the PSD in various suspensions can be found elsewhere (27,30,38). The most frequently used distribution function is the logarithmic normal distribution (16,27,30,39). This distribution represents satisfactorily most of the colloidal populations that are frequently skewed.

$$f(D) = \frac{1}{\sqrt{2\pi} \sigma D} \exp\left(-\frac{(\ln D - \ln D_g)^2}{2\sigma^2}\right) \quad (16)$$

$D_g$  is both the median and the geometric mean diameter;  $\sigma$ , is the standard deviation of  $\ln D$  and it is termed the geometric mean standard deviation. The  $n$ th moment of the log-normal distribution, is given by (53):

$$J_n = E(D^n) = \exp\left(n(\ln D_g) + (n\sigma)^2/2\right) \quad (17)$$

The number ( $D_N$ ), volume-surface ( $D_{32}$ ), weight ( $D_w$ ), and turbidity ( $D_t$ ), average diameters can be calculated as (27):

$$D_N = \frac{J_1}{J_0}; \quad D_{32} = \frac{J_3}{J_2}; \quad D_w = \frac{J_4}{J_3}; \quad D_t = \left(\frac{J_6}{J_3}\right)^{1/3} \quad (18)$$

Some workers (3,4) had termed as logarithmic normal, the distribution with the frequency function:  $f'(D) = Df(D)$ . Notice that the two distribution functions are related as:  $f(D)dD = f'(D)d\ln D$  (43,55,56). Therefore, if  $f'(D)$  is used, then Equation 2 should be integrated with respect to  $\ln D$  (as was done by Gledhill (7)), and not with respect to  $D$ . This distribution described by  $f'(D)$ , has been called a Zeroth-Order Logarithmic Distribution (ZOLD).

When applying Equation 10b, a particle size distribution on weight basis must be used. Many workers (6,7,39) have used log-normal distributions on weight basis. If the number distribution is log-normal, then the weight distribution is also log-normal with the same geometric standard deviation  $\sigma$  (51,53); the log-normal distribution on weight basis, corresponding to Equation 16 is:

$$F(D) = \frac{1}{\sqrt{2\pi} \sigma D} \exp\left(-\frac{(\ln D - \ln D_{wm})^2}{2\sigma^2}\right) \quad (19)$$

where  $D_{wm}$  is both the median and the geometric mean diameter on weight basis.  $D_{wm}$  and  $D_g$  are related by:

$$D_{wm} = D_g \exp(3\sigma^2) \quad (20)$$

Heller and his collaborators (5,10,38) adopted another type of distribution also described by two parameters. However, it should be emphasized that the maximum polydispersity for that distribution, is  $D_w/D_N = 1.5$  (27). Therefore, even though the distributional form can describe positively skewed distributions, it can not successfully describe highly polydisperse systems.

**Error in the Assumed Distributional Form.** Wallach and Heller (10) studied experimentally the error introduced in the estimated PSD when the assumed distributional form is different from the true one. They were trying to estimate the PSD of 3 suspensions with positively skewed, negatively skewed and symmetrical distributions, using the turbidity ratio method and assuming a distributional form which can describe only positively skewed distributions. In the cases of negatively skewed and symmetrical PSD's, the estimates of the parameters chosen to describe the distribution had a significant error; however a careful examination of the results showed (27) that despite the error in the parameters, when the results were plotted against the true solution, the estimated PSD covered successfully the main body of the true distribution. This behaviour was expected since the polydispersities of the 3 synthesized distributions and the assumed distribution were very small; no distributions with very long tails to small or large particles were studied.

Yang and Hong (39) studied the error on the estimated PSD when the true distribution is different from the assumed log-normal form. The estimated distribution was compared to the true one on a weight basis; the distributions studied were broad, covering particle sizes from 0.1  $\mu\text{m}$  to 10.0  $\mu\text{m}$ . It was found that "the estimated distribution conformed quite closely to the central portion of the true distribution (on weight basis) and was not strongly biased towards either of the tails".

American Chemical Society  
Library

1155 16th St., N.W.

Washington, D.C. 20036

Kourti (27) showed that for suspensions with continuous distributions, the weight average diameter of the PSD estimated when assuming a log-normal form (on number or weight basis), is, in general, within 1.0% from the weight average of the true PSD. The weight average diameter obtained with a log-normal assumption is very close to the true one, even in the case that the true distribution is significantly different from a log-normal shape. For distributions with no long tails to either small or large particles, the estimated log-normal distribution will cover the main body of the true PSD on a number basis. When the true and estimated distributions are plotted on a weight basis, the main body of the true distribution was covered by the estimated distribution, in all cases, even when the true distribution had long tails.

It is important to note that when the distributional form is assumed, the shape of the distribution (i.e., a constraint) is forced upon the solution. The expected result is a PSD with the assumed shape that will envelope the true distribution; the details of the true PSD are not expected to be resolved. The estimation of the location of the main body of the distribution is therefore the most satisfactory result expected in this case.

Thus, it can be concluded that for suspensions with continuous PSD's whenever the form of the distribution is unknown, the assumption of a log-normal distribution is a safe approach.

**Other Considerations.** It should be noted that Equation 16 gives the normalized PSD, and that the formulas for the calculation of the average diameters of the estimated PSD as a function of  $D_g$  and  $\sigma$ , given in Equations 17 and 18, are correct only if the upper limit of the PSD,  $D'_{max}$ , is such that:

$$\int_0^{D'_{max}} f(D) dD = 1.0$$

If it is known a priori (from another method such as electron microscopy, dynamic light scattering, particle chromatography, or simply filtering of the suspension) that particle sizes smaller than  $D_{min}$  and/or larger than  $D_{max}$  do not exist, then this additional information should be utilized in the parameter estimation, and all the integrations should be done between  $D_{min}$  and  $D_{max}$ . A log-normal envelope, characterized by  $D_g$  and  $\sigma$  can still be estimated; however the PSD should be normalized before each iteration in the parameter estimation. Furthermore the calculation of the various moments and averages also requires normalization of the PSD; this calculation should be done using explicit equations and not Equation 17. Equation 17 is used if integration is done from  $D_{min} = 0$  to  $D_{max} = \infty$ . The log-normal distribution estimated with previous knowledge of  $D_{min}$  and  $D_{max}$  is expected to be a more accurate estimate of the true PSD, since the contribution of tails of very large particles to the theoretically calculated specific turbidity is eliminated.

#### Effect of Errors on The Estimated PSD

The determination of the particle size distribution of a suspension using turbidimetry involves the following: i) determination of the particle concentration in the original sample (for the specific turbidity technique); ii) dilution of the sample (to avoid multiple scattering); iii) taking turbidity measurements at two or more wavelengths; iv) an assumption on the type of the particle size distribution; v) theoretical calculation of scattering functions (requires knowledge of the value of  $m$  at the different wavelengths); and vi) estimation of the parameters of the particle size distribution. It is obvious that there are many sources of experimental error or uncertainty with a minor or a major effect on the estimated distribution.



These sources can be grouped as follows: i) experimental errors in measurements: these are due to errors in the turbidity measurements and in the calculations of the solids volume fraction (i.e., dilution, gravimetry, etc.) for specific turbidity; ii) uncertainty (or error in the estimation) of the  $m$  values and the dependence of the  $m$  on the wavelength, and iii) error in the assumed distributional form. Simulation studies were performed (27) to investigate the sensitivity of the estimated particle size distribution to such errors. The results for i) and ii) are briefly summarized in this section. The effects of error in the assumed distributional form have already been discussed earlier in this chapter.

Another significant source of error in the turbidity measurements is the forward scattering. The error due to forward scattering arises when the spectrophotometers are not properly designed to reject this additional source of light. A discussion on forward scattering is included in a later section of this chapter. This error may be significant in practice. For the simulations reported here we assumed properly designed spectrophotometers and our conclusions are not affected by this assumption.

**Error in the Value of  $m$ .** It has been demonstrated (27) that turbidimetric methods are extremely sensitive to errors in the value of  $m$ . This sensitivity is however dependent upon the  $(m,a)$  values of the suspension and the turbidimetric technique employed. In certain  $(m,a)$  regimes, the effect of this error on the estimated parameters of the PSD is small, while in others it is much higher. The users should be cautious on that, and should never rely on observations reported for the magnitude of this effect, if these observations are for systems with different  $(m,a)$  values than the system under investigation. (For example, 1% error in the value of  $m$  resulted in 5.5% and 0.6% error in the values of  $D_N$  and  $D_W$ , respectively, for a distribution with  $D_g = 0.8 \mu\text{m}$  and  $\sigma = 0.35$ ; the same error in  $m$  resulted in 47.0% and 2.3% error in  $D_N$ ,  $D_W$ , respectively, for a distribution with  $D_g = 0.175 \mu\text{m}$  and  $\sigma = 0.35$ .) Whenever there is uncertainty in the value of  $m$  of the suspension to be analysed, a sensitivity analysis should accompany the solution, to indicate the degree of confidence in the results. Alternatively the results should be corroborated with another method that is not sensitive to the optical properties of a suspension.

**Error in Measurements.** The effects of measurement errors (measurements of specific turbidity or turbidity ratio) on the estimated PSD have been discussed in detail elsewhere (27,28). The effect depends, again, on the  $(m,a)$  values of the suspension. It is serious for suspensions of particles with  $(m,a)$  values corresponding to regimes where the exponent  $y$  changes slowly with particle size. In other regimes, the effect of a measurement error up to  $\approx 3\%$  is negligible.

The errors in the specific turbidity measurements encountered in practice are due to: i) reproducibility error in transmittance or absorption readings from the spectrophotometer; the average value for such error observed in our laboratory was approximately 2.0% and ii) error in the calculation of the particle volume fraction (due to error in gravimetric analysis or error in dilution); this error is always small and obscured by the reproducibility error.

### Resolution of a Controversy in Literature

The analysis presented in (27, 28) helped to resolve a controversy that appeared in the literature on whether the true PSD of a suspension can be estimated from turbidimetric techniques. Details can be found in (27). This conflict arose between Maxim et al. (12) and Zollars (16,17). Maxim et al. tried to estimate the full PSD in commercial suspensions with submicron particles and  $m=1.1$ , using turbidity ratio measurements. They observed a high correlation of the parameters of the distribution, and stated that a valid estimate of the true distribution is impossible under experimental error. According to the analysis presented in (28) their observations are justified (and were expected) for the  $(m, a)$  values of the suspension and for the method they used. Zollars used a simula-

tion study with no experimental error to re-estimate the parameters of log-normal particle size distributions from theoretically calculated specific turbidities. Of course, the parameters were correctly re-estimated. The author stated that "turbidimetry does not exhibit multiple solutions as reported by other investigators". The observations of Zollars (16, 17) are also justified for this specific case. Both the workers were correct for the types of cases they were studying. However, their findings cannot be extrapolated over turbidimetric methods and (m,a) regimes. This extrapolation caused the controversy.

### Estimation of Average Diameters

Many workers have tried to use turbidimetry to estimate an average of the PSD of a poly-disperse system. The concept of the "apparent" diameter was introduced almost 30 years ago and theoretically explained in a very careful work by Meehan and Beattie (3,4). (A discussion on this matter can also be found in (27) and in this volume (28).) It was concluded that: i) An apparent diameter can be obtained, treating the system as a monodisperse one. This apparent diameter corresponds to an average of the unknown particle size distribution; ii) The kind of average obtained by a light scattering method depends on the value of  $m$  of the suspension, on the type of the particle size distribution, and on the actual size of the particles in suspension. Different kinds of averages are obtained for different particle size regimes; and iii) Different kinds of averages are yielded by different light scattering methods.

There are numerous reports (3,4,7,10,11,13) where it is either discussed or experimentally shown that the type of average obtained from the apparent diameter depends on the turbidimetric technique employed and the  $m$  and  $a$  values of the suspension. At this point, it should be emphasized, however, that specific turbidity is the only method that gives apparent diameters that correspond to meaningful averages of the PSD. Furthermore there is a known correspondence between these averages and well defined (m, a) regimes. Thus, by applying specific turbidity, one may obtain the following averages: i) the turbidity average for very small particles ( $a < 0.5$ ) and any value of  $m$ , ii) the volume-surface average for very large particles and any  $m$  value, and iii) weight average for a combination of (m, a) values ( $m < 1.2$ ) which can be identified very easily for the system under investigation. Therefore, specific turbidity was the only method used by workers when only an average of the PSD was desired.

Wallach and Heller (10) suggested that the ratio of the apparent diameters estimated at two wavelengths can provide a rough idea on the polydispersity of the system. However, this is not always true. It has already been shown that, sometimes, especially for small  $m$  values ( $m \sim 1.1$ ), the apparent diameters corresponding to very broad distributions or to bimodal distributions do not change significantly with the wavelength, leaving the impression that the system is monodisperse.

Turbidity Average Diameters. These averages can be obtained from specific turbidity measurements, for any value of  $m$ , provided that all the diameters of the particles in the suspension correspond to  $a$  values that are small (Rayleigh regime). The turbidity average diameter can be obtained from one specific turbidity measurement.

It should be noticed that, in the Rayleigh regime, for the same type of suspension (i.e., same  $m$ ) the ratio of two turbidity average diameters estimated at the same wavelength is independent of the value of  $m$ . One can therefore monitor the relative increase in the turbidity average diameter of a suspension (for example, the change as a function of time due to reaction or crystallization process) by simply monitoring specific turbidity even if the value of  $m$  is not known.

A practical application of the specific turbidity method to monitor on-line particle growth in polydisperse systems by following turbidity average diameters is reported by Haseler and Parkin (19). The authors were careful to choose long wavelengths (infrared

regime) so that the Rayleigh scattering theory could be applied even for the largest particles in their system, with diameters as large as 0.8  $\mu\text{m}$  (27).

Maron et al. (9) tried to determine experimentally the type of average diameters obtained from specific turbidity measurements. Their observations that a correct turbidity average can be obtained for a values as large as 4.74 are rather coincidental of the polydispersities of the systems investigated. This is explained in detail in (27). The reader should be cautious in that the term "weight" average used in (9) is in fact the "turbidity" average as can be deduced from the definition in the original publication (54), where electron microscopy results were presented for the latexes used in (9).

**Volume-Surface Average Diameters.** Volume-surface average diameters can be obtained from specific turbidity measurements of suspensions of large particles. A number of researchers used turbidimetric techniques for the determination of average particle size of polydisperse suspensions with particle diameters beyond the submicron regime (ranging from 2-4  $\mu\text{m}$  to 30-50  $\mu\text{m}$ ).

Bagchi and Vold (13) verified experimentally the Mie theory, that for very large particles, specific turbidity varies linearly with the inverse of the volume surface average diameter ( $1/D_{32}$ ). A linearity observed with respect to the inverse of other averages was coincidental and attributed to the fact that the degrees of polydispersity of the latexes investigated were very similar (27). Kubota et al. (20) discussed this coincidental linearity and presented more experimental results from suspensions of various polydispersities, verifying that only the specific turbidity vs ( $1/D_{32}$ ) curves are linear, as was theoretically expected.

A claim of Dobbins (44) and Dobbins and Jizmagian (47) that the volume-surface average diameter can be obtained from one specific turbidity measurement in any particle size regime has been refuted. Kourti (27) showed that their observations, that "the specific turbidity is primarily dependent on the  $D_{32}$  diameter and only weakly dependent on the type of the distribution", were coincidental of the types of distributions that they used for their investigation. (These distributions had also their weight averages close to each other and covered the same particle size regime.) Therefore, their implications that the  $D_{32}$  diameter can always be estimated from one specific turbidity measurement cannot be supported. This is true only for very large particles. Similar claims by Haseler (22) are also discussed in (27). It has been shown that in the examples reported in (22), the estimated  $D_{32}$  was close to the true one because the location of the whole distribution was correctly estimated, and not because specific turbidity results always in a correct  $D_{32}$  as claimed in (44,47). Furthermore, it was shown (27) that, in fact, when estimation of the full PSD is attempted, it is  $D_w$  that is correctly estimated with the log-normal assumption even when the true and estimated distributions do not conform well, and that the  $D_{32}$  average is correct only when the estimated log-normal distribution conforms well with the true distribution.

Bohren and Huffman (52) calculated the average extinction coefficient for Gaussian distributions. They showed that only for very broad distributions ( $\sigma = 5000 \text{ nm}$ ) and  $\alpha$  values larger than 12.0, the value of  $K_{\text{scat}}$  is approximately 2.2, which means that in these cases the apparent diameter would be close to the  $D_{32}$  average.

Recently, Garcia-Rubio (32) suggested that the specific turbidity of a polydisperse system can be expressed as

$$\frac{\tau}{\phi} = \frac{3}{2} \frac{K(\alpha_{\text{av}}, m)}{D_{32}} \quad (21)$$

where

$$K(\alpha_{av}, m) \int_0^{\infty} D^2 f(D) dD = \int_0^{\infty} D^2 K(\alpha_{av}, m) f(D) dD \quad (22)$$

where  $\alpha_{av}$  corresponds to an average diameter  $D_{av}$ . It was also suggested that the two parameters  $\alpha_{av}$  and  $D_{32}$  can be used to interpret turbidity data over a wavelength range. The  $D_{32}$  diameter will correspond to the true PSD whereas  $\alpha_{av}$  will correspond to the average diameter "seen" by the measurements "averaged over the wavelength range".

However, by definition, the only correct form for the calculation of an average diameter from specific turbidity measurements is that of Equation 11. Equation 22 is only valid for very large diameters, where  $K(\alpha, m) = 2$ , independent of particle size. In any other case if one estimates the two parameters in Equation 22, that is,  $\alpha_{av}$  and  $D_{32}$ , "over a range of wavelengths", these estimates will be highly correlated. Their numerical estimates will depend on wavelength range used and the  $D_{32}$  estimate will not, in general, correspond to the volume-surface average of the true PSD

**Weight Average Diameters.** For suspensions with small values of  $m$  (usually  $m < 1.2$ ), and particle sizes corresponding to certain  $\alpha$  values, the apparent diameters obtained from specific turbidity measurements are numerically close to  $D_w$ . The apparent diameter assigned to  $D_w$  is essentially the only correct estimate of the particle size that can be obtained in these  $(m, \alpha)$  regimes. (These  $(m, \alpha)$  regimes have been identified earlier in this chapter in the discussion under Specific Turbidity.) This is an extremely useful information for such systems, since a meaningful average can be obtained very easily, with very small error and for any type of PSD. Simple rules can be derived to give information from simple measurements for routine analysis. For example, it has been shown (27) that the mean average of the apparent diameters at 600 nm and 400 nm, obtained for a variety of polydisperse poly(vinyl acetate) latexes ( $m \sim 1.1$ ) with distributions in the submicrometer regime is numerically very close to the true weight average of the distribution. Similar rules of thumb could be derived for other suspensions with small  $m$  values

Cheesman (46) observed that when the specific turbidity measurements were taken at a certain wavelength, then the apparent diameter of polydisperse systems was within 4% of the true weight average diameter. The wavelength had to be such, that the  $\alpha$  value calculated from the apparent diameter ( $D_{ap}$ ) as  $\alpha = \pi D_{ap} / \lambda_m$  was equal to an  $\alpha$  value near the first point of inflection of the specific turbidity vs.  $\alpha$  curve (plotted for  $m$  equal to the value of  $m$  of the system). For  $m = 1.1$ , this  $\alpha$  value was chosen (46) to be 2.7 and for  $m = 1.2$ , to be 2.2. He suggested a technique, in which the specific turbidity is measured at several wavelengths, the apparent diameter is estimated for each wavelength and the corresponding  $\alpha$  values are calculated. The value of the apparent diameter that results to an  $\alpha$  value closer to  $\alpha = 2.7$  (for  $m = 1.1$ ) is assigned to the weight average of the distribution in the suspension. The observations of Cheesman are theoretically supported. Near the inflection point (which corresponds to the first ripple of the  $y$  vs.  $\alpha$  curve, (Figure 1)) the value of  $y$ , for almost any value of  $m$  is close to 4.5. If the weight average corresponds to this  $\alpha$  value, then the distribution is located around it and the value of  $y$  varies between 4 and 4.5. In other words, the wavelength is chosen such that the entire distribution is brought to an  $\alpha$  regime where  $y$  is close to 4.0 and the apparent diameter is the weight average diameter. Using wavelengths between 280 nm and 1300 nm, he claimed that weight average diameters between 0.18  $\mu\text{m}$  and 0.85  $\mu\text{m}$  could be estimated for  $m = 1.1$ . The approach of (27) mentioned earlier, is a much simpler way to estimate  $D_w$  for submicron particles for  $m = 1.1$ ; it requires only two specific turbidity measurements, and taking the mean value of the apparent diameters at 400 and 600 nm.

Experimental Investigation of the Potential of the Method for On-line Applications to Latex Reactors

Kourti (27) carried out an extensive experimental investigation in order to demonstrate the conclusions from the theoretical analysis of (27, 28) and to investigate the potential of turbidimetry for on-line applications in latex reactors. The method was tested for its capability to provide the full PSD or an accurate and precise average particle diameter, and capability to follow particle growth during emulsion polymerizations. Special attention was paid to any limitations or problems arising when the method is applied to latex systems.

A variety of latexes were analysed for particle size such as poly(vinyl acetate), poly(methyl methacrylate), polystyrene and poly(styrene butadiene). These were produced by emulsion polymerization either in pilot scale or industrial reactors. Distributions which were synthesized from monodisperse latexes of known particle size and from commercially available standards were used to test for the accuracy and the precision of the method. Latex samples with unknown PSD were analysed by turbidimetry and the results were compared with results from dynamic light scattering, hydrodynamic chromatography and electron microscopy.

The conclusions from the theoretical investigation, regarding the inability of the method to provide an estimate of the full PSD for submicron particles and low values of  $m$ , have been verified experimentally. It has also been shown that for particles in the lower submicron range, specific turbidity is more sensitive to particle size changes than the turbidity ratio. This study showed that turbidimetry is a simple and consistent method with very good reproducibility and that in spite of the limitations mentioned earlier, it can yield extremely useful results.

Turbidity or specific turbidity at a single wavelength can be used to follow successfully the reaction history, both in batch and continuous latex reactors and to study qualitatively the effects of various parameters (emulsifier levels, agitation, impurities) on the latex particle size. A correct weight average diameter (and for very small particles a turbidity average) can always be obtained from specific turbidity. A meaningful average diameter may be acceptable for control purposes and a good tool for on-line monitoring of a process. Results from specific turbidity showed very good agreement with results from other methods. This is demonstrated in Figures 2 and 3.

In Figure 2, diameters obtained using off-line turbidimetry and dynamic light scattering are plotted as a function of reaction time for three batch emulsion polymerizations of vinyl acetate (H6, H7 and H8). It can be seen that both of the methods follow successfully the particle growth during the reaction. In these soap free polymerizations we were studying the effect of the initial initiator concentration and of the impurities on the reaction rate and the particle size. Run H6 served as a base case. In Run H7 we changed the initiator concentration (leaving the other parameters the same as in H6) and this had an effect on the particle size which was detected by the two methods. Run H8 has the same recipe with H6 but higher content of impurities. The presence of impurities affects the particle size and this effect was also detected by the two methods. The particle size of the final latex (100% conversion) was also measured by electron microscopy and the results are given for each run. The results from all three methods agree remarkably well for these monodisperse samples.

Figure 3 shows weight average diameters for several polydisperse suspensions, corresponding to three different types of latex. The values obtained by DLS are plotted against those obtained by turbidimetry. The agreement between the two methods is excellent.

The above investigation that covered a variety of latex samples from a variety of polymerization conditions showed that specific turbidity has an excellent potential for on-line applications. It is consistent, reproducible, can detect small changes in the particle size during the polymerization. These characteristics combined with the fact that the

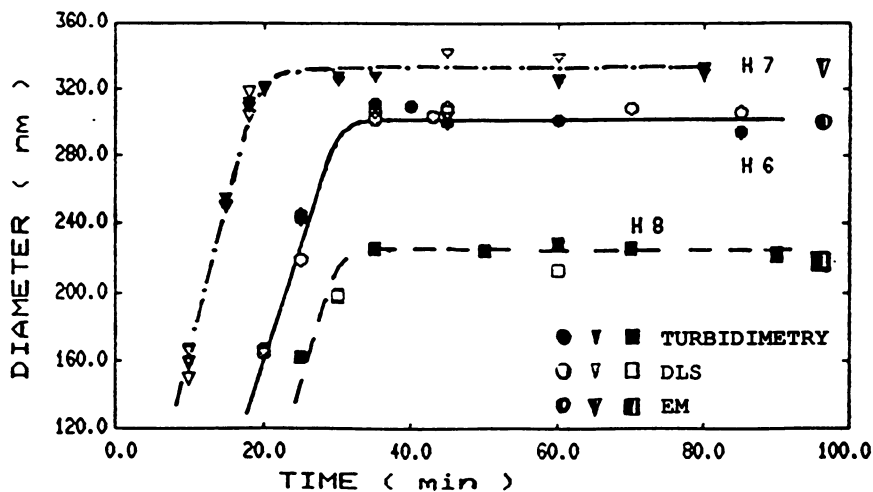


Figure 2. Particle growth in three batch runs (H6, H7, H8) as estimated by turbidimetry, dynamic light scattering (DLS) and electron microscopy (EM).

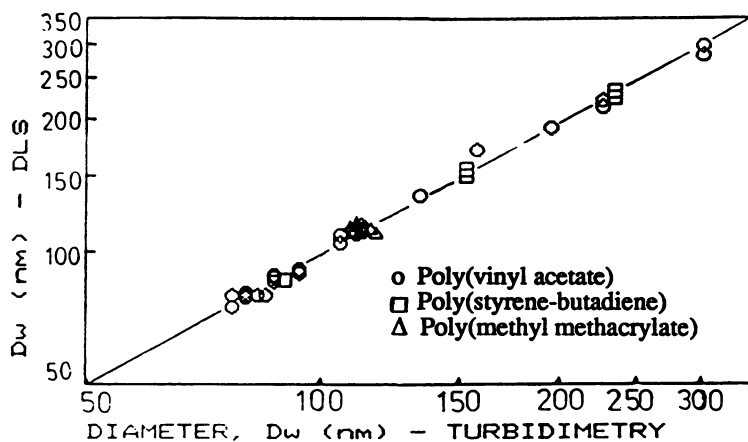


Figure 3. Weight average diameters from a variety of latexes as estimated from dynamic light scattering plotted against the values estimated by turbidimetry.

method is fast and experimentally simple make it an excellent candidate for on-line applications.

#### Requirements for On-line Measurements and Data Analysis

From the discussions so far it has been concluded that specific turbidity is the most reliable turbidimetric method for particle size determination in latexes with submicron non-absorbing particles. Depending on the latex characteristics (values of  $m$  and  $\alpha$ ), there are two approaches for particle size determination, using specific turbidity. The first one involves parameter search for the determination of the parameters of a log-normal distribution; this approach guarantees a correct estimate of the weight average diameter and the location of the PSD. The second one provides an average diameter by treating the system as monodisperse. In this case, the apparent diameter can be estimated from one specific turbidity measurement using either a table look up, or a one parameter search, or by fitting a polynomial to a certain size regime of a diameter vs specific turbidity curve. Both of these approaches can be pursued on line (27).

Turbidity measurements at two (or more) wavelengths and measurement of the particle volume fraction will provide the specific turbidities. Two spectrophotometers at fixed wavelengths (with flow through cells) connected in series (or, a scanning spectrophotometer), can be used for the turbidity measurements. The polymer volume fraction can be calculated using information from a densitometer (see discussion below) connected in series with the reactor and the spectrophotometers. The latex must be diluted before entering the spectrophotometer. The sampling system must acquire a known amount of latex and dilute to a known dilution. The degree of dilution must be considered in the specific turbidity calculations.

Calculation of Polymeric Volume Fraction. The polymeric volume fraction can be calculated (24, 45, 64) from the density of the reacting mixture; this can be measured on-line, using a vibrating U-tube densitometer [a DPR-YWE model by Anton Paar, Austria, is used in our laboratories (Y-mode oscillator, PTE-98-EV-72 excitation cell) with a DPR-2000 electronic board]. This calculation is relatively easy for batch reactors, if the polymerization recipe is known. For continuous reactors however, one should consider parameters such as the feedrates of monomer, water, soap and initiator concentrations and the residence time in the reactor to calculate it. The complications in this calculation for homopolymers are discussed in (64). Once the solids volume fraction in the latex is calculated, the degree of dilution should be considered in order to calculate the solids volume fraction of the sample in the spectrophotometer.

For monomer free particles, the particle volume fraction in the spectrophotometer is: (polymer volume fraction in latex)/(degree of dilution). The degree of dilution is defined as the ratio of the final volume of the dilute sample to the volume of the sampled latex. The particle volume fraction however is different when the particles are swollen with monomer. In this case, which applies for samples of latex at low monomer conversions and low degrees of dilution or for non-water soluble monomers, some corrections (discussed in (27)) must be applied. For high degrees of dilution and water soluble monomers, it is safe to assign the polymer volume in the sample, to the particle volume.

Optical Properties. The refractive indices of the particles and the medium, at the wavelengths at which the turbidity readings are taken must be known for the calculation of  $m$ . If the value of  $m$  of the suspension is not accurately known, or it changes with conversion (as for example, for multicomponent polymerizations with composition drift), then this can be accounted for by using some type of calibration. The calibration approach is particularly useful when the particles are non-homogeneous spheres (i.e., copolymers) or whenever unreacted monomer is present in the particles and the medium.

**Degree of Dilution.** The degree of dilution required to avoid multiple scattering varies. It depends on the solids concentration of the original sample, the size and the refractive index of the particles, and may have any value from 20 to 10,000. In some processes, the degree of dilution may need to change with conversion. For a known process (routine analysis), the on-line density measurements can give an idea of the conversion and therefore the degree of dilution can be adjusted following some kind of calibration (i.e., information from the densitometer is utilized on-line to control the dilution factor). Alternatively, the degree of dilution can be adjusted simply from feedback from the reading of the spectrophotometer. An acceptable turbidity range is predefined, for which the sample is not too dilute or too concentrated. If the reading is out of this range, the dilution factor is properly adjusted.

**Other Considerations:** In continuous reactors, the densitometers, the sampling system and the spectrophotometers are connected at the outlet of the reactor. To monitor the particle growth correctly, the density measurement (particle volume fraction) and the turbidity measurement must be assigned to the same time. Therefore, the time delays between the sample acquisition and the actual measurements, as well as between the reactor exit and the instruments, should be accounted for.

Finally, the user should keep in mind that the waste dilute latex which is created should be treated before being disposed. The waste is water with traces of monomer and low concentrations of polymer. Care should be taken, to polymerize the monomer and precipitate the polymer, before disposing the waste water.

#### On-line Particle Size Measurements – A Historical Perspective

Hamielec and Wright (61) suggested the use of turbidimetry for on-line latex particle size determination as early as 1973 and an attempt for on-line sampling for turbidity measurements has been reported by Hamielec and co-workers in 1976 (62). On-line turbidity measurements in fully automated systems have been reported by Kiparissides (14, 15), Zollars (16) and by Haseler and Parkin (19). All of these workers were measuring turbidity only. In (14-16) no quantitative results from on-line determination of particle size are reported. In (19) turbidity average diameters were obtained; that setup however, requires prior knowledge of the volume fraction of the particles. Up to this point, there was no mention for a way to determine the polymeric volume fraction on-line. In (14-16, 62) turbidity was measured with the objective to determine the PSD in poly(vinyl acetate) latexes. It has already been demonstrated however, that this is impossible using only turbidity measurements (i.e., utilizing the turbidity ratio method); specific turbidity must be used, to obtain at least the weight average of the PSD, for this latex with  $m = 1.1$ .

An experimental setup to combine on-line determination of the particle volume fraction with on-line turbidity measurements, which would make the on-line determination of particle size during a vinyl acetate polymerization possible, was first suggested by Pollock (63). However, no results are reported on particle sizing in that work.

The setup suggested for on-line particle size measurements by (14-16, 63) has a serious disadvantage: it requires continuous flow of diluted latex through the spectrophotometer. For specific turbidity measurements this means that a known amount of latex is continuously mixed with a known amount of diluent. Both the latex and diluent have to be pumped at constant flowrates. This in turn requires a very small amount of latex to be pumped at the exit of the reactor, at flow rates as small as 10 ml/min., for long periods of time. A peristaltic pump tried by Gossen (45) for this setup failed (coagulation of latex due to high shear, and chemical attack of tube by monomer). Other types of pumps tried in the same laboratory also failed (64). Another problem with continuous dilution of latex is that it creates an enormous amount of waste (very dilute latex) that requires treatment before being disposed. This would cause problems in large scale



operations. The setup suggested in (62) utilizes discrete sampling but it has serious disadvantages (64).

A system suggested by Gossen (45) utilizes discrete sampling and it is currently used in our laboratories. The sampling system has been designed to collect a sample of known volume from the latex reactor and dilute it to a known degree of dilution. The turbidity of the dilute sample is then measured. Information on the particle volume fraction is provided by on-line densitometry. The layout is briefly described elsewhere in this volume (65), where results are shown from the on-line application of specific turbidity to monitor particle growth during poly(vinyl acetate) production in continuous pilot plant reactors, for a period of 10 hours. Samples were taken at discrete intervals of 5 min. The weight average diameters showed excellent agreement with results from on-line dynamic light scattering. These results, obtained by Gossen, is the first published successful effort (66) to combine on-line turbidity and density measurements and to monitor, on-line, weight average diameters during latex production in pilot scale reactors, in a fully automated manner.

#### Other Considerations When Using Turbidimetric Techniques

**Optical Properties of Latex Suspensions.** Turbidimetric methods are sensitive to errors in the value of the optical properties of the suspension (i.e., the refractive indices of the particles and the medium). The optical properties of latex suspensions with non-homogeneous particles should be calculated carefully in order to avoid errors in the value of  $m$ . Such errors are more likely to occur when dealing with carboxylated particles, latex samples withdrawn at low conversions, or latex particles produced by multicomponent polymerizations. Carboxylated particles swell in the water phase; their density and refractive index depend on the degree of swelling and therefore these properties should be adjusted accordingly. In samples withdrawn at low conversions, latex particles may be swollen with monomer; the amount of monomer associated with the particles (and therefore the refractive index of the particles and the medium) depends on the conversion, the solubility of monomer and on the degree of dilution of the original sample. Again, appropriate corrections should be made. Finally, the refractive index of particles produced by multicomponent polymerizations depends on their composition, and may change during the reaction (due to composition drift). When monitoring particle growth during multicomponent polymerizations using on-line turbidimetry, on-line gas chromatography can be utilized to provide information on the composition of the particles. The refractive index can be calculated from the particle composition utilizing some type of calibration. On-line densitometry combined with on-line gas chromatography can provide information on the particle volume fraction. More details on this topic can be found in (27).

Using turbidimetry for particle size determination in cases where the refractive index is not accurately known is risky and therefore the method is not recommended for cases where the refractive index of the particles changes during the reaction, unless this change can be accurately predicted (i.e., via calibration). Dynamic light scattering (DLS) with a laser beam of 670 nm is independent of the refractive index of the particles for particle diameters roughly up to 300 nm. This regime covers a large number of latexes produced by seeded polymerizations or copolymerizations and therefore use of DLS would be a good solution to the problem of particle size determination in multicomponent polymerizations.

**Forward Scattering.** For the determination of particle size from turbidity measurements, it is assumed that the detector measures the attenuation of the beam of the source light. However, all the spectrophotometers measure the attenuated light from the source plus a certain amount of light scattered at small angles. A detection system may have to be designed to reject forward scattering, so that theoretical calculations of turbidity can be legitimately compared with the measured values. The larger the particles the greater the

possible discrepancy between the true and the measured (or apparent) turbidity. For small particles however and particles comparable to the wavelength the difference between the true and apparent turbidity is minute (50).

Errors in turbidity measurements due to forward scattering are discussed in a number of references, where suggestions are given for the modifications of the spectrophotometers (19, 37, 39, 42, 57-60). Also, several empirical approaches have been suggested to account for the difference between true and apparent turbidity (13,39). In (39) for example, a correction factor (R) was estimated, equal to the ratio of measured to theoretically expected turbidity for several suspensions with known particle diameters. This factor was then used to correct the turbidity of suspensions with unknown particle sizes. The user should be careful however, because this factor can only be used for unknown suspensions with particle sizes and values of  $m$  in the same range with those of the suspensions that it has been estimated for. A calibration was also used in (13) to relate apparent specific turbidity with the true particle size for large latex particles (4 to 50  $\mu\text{m}$ ) where forward scattering is significant.

Bohren and Huffman (52) suggest that although conventional spectrophotometers are not usually designed to reject scattered light at small angles, such instruments may be adequate for scattering measurements if the particles are not too large. For monodisperse polystyrene latexes ( $m=1.2$ ) and diameters 109, 312, and 1050 nm, at wavelengths between 300 and 600 nm these authors used a conventional spectrophotometer suggesting that the forward scattering should not be that significant. The error due to forward scattering should not be significant for small latex particles, and Walstra (60) suggested that sometimes errors attributed for forward scattering (59) were in fact due to extremely high optical densities that the investigators had included in their results.

The user can get an idea of the accuracy of the turbidity measurements by comparing experimental and theoretical results for monodisperse standards with known diameters, covering the range of particle diameters that plans to analyze. Before proceeding to any modifications of the instrument one should assess whether the accuracy of the turbidimetric results is satisfactory for the purpose for which they will be used. For example, if the purpose is to use turbidimetry as a reproducible and inexpensive way to monitor particle size during a reaction or to detect the effect of various parameters (emulsifier, impurities) on the particle size of the latex, then the accuracy of the spectrophotometer with no modifications may be satisfactory. For kinetic studies and more accurate determinations of larger particles, one may consider modifications of the spectrophotometer and the use of a correction formula (60), that accounts for the angle of acceptance of the detector, for the calculation of the scattering coefficient.

**The Choice of the Wavelength.** The successful determination of the PSD or of an average particle size of a suspension using turbidimetry, depends on the  $m$  and  $a$  values of the suspension and the turbidimetric technique used. The value of  $m$  of a suspension can be changed by adding other substances in the medium (i.e., glycerol (4,11) in water medium). The range of  $a$  values covered by the PSD can be manipulated by changing the wavelengths at which the turbidity measurements are taken. As a general rule, wavelengths widely separated from each other are desirable when the estimation of the full PSD is required; this way the range of  $a$  values covered by the PSD changes significantly from one wavelength to another, the exponent  $y$  changes, and the probability of the turbidity being proportional to the same moment of the PSD at both wavelengths is reduced.

It is important to note that the value of  $m$  is a function of the wavelength. When wavelengths widely separated from each other are used, the value of  $m$  at each wavelength must be accurately known in order to obtain correct estimates of the particle size. If only one value for  $m$ , estimated at, say,  $\lambda_0'$  is available and the user plans to keep it constant for all the wavelengths, then, one should choose to work with wavelengths on

both sides of  $\lambda_0'$  and as close to  $\lambda_0'$  as possible. (Use equal number of shorter and longer wavelengths; this way the effects of using constant  $m$  almost cancel each other.)

In this work we are dealing only with scattering and have avoided using short wavelengths ( $\lambda_0 < 300$  nm), where some of the polymer particles may absorb light. The advantage of working with scattering only, for latex analysis, becomes evident from the following. Most of the monomers used for latex production absorb at short wavelengths. At low conversions there is residual monomer in the medium and/or the particles; this residual monomer (which may exist even after diluting the original sample) will absorb light. This extra absorption may cause errors in the calculation of the particle size if it is not accounted for. However this requires knowledge of the relative amount of monomer and polymer in the original sample (i.e., conversion), the partition coefficient of the monomer between the water and the polymer phase, the degree of dilution of the original sample and the value of the refractive indices of the polymer and the monomer (which are complex numbers when both absorption and scattering occur). Most of the time all this information may not be available, especially when dealing with multicomponent polymerizations. Therefore, the use of short wavelengths may not be practical if one wants to monitor particle growth during the reaction, from low to high conversions.

**Corroboration of Results.** When the behaviour of a turbidimetric method at a certain ( $m, \alpha$ ) regime is not known, its capability to provide the correct estimate of particle size in a suspension should be corroborated with results from other sizing methods for the same suspension. It is not correct to assume that the results obtained by a turbidimetric technique for a suspension are reliable because this method gave reliable results for another suspension with known PSD. In other words it is not correct to assume that the results obtained from a turbidimetric method, on the full PSD of an unknown poly(vinyl acetate) latex are correct, because this method gave correct results for polystyrene latex with known PSD. Unfortunately similar extrapolations from system to system have been reported in the literature. The results of the turbidimetric method for poly(vinyl acetate) should be corroborated by another method (as for example, dynamic light-scattering, hydrodynamic fractionation, etc.). Furthermore, this second method must be chosen carefully. For example Wales (6) used coulter counter measurements to corroborate results from turbidimetry. Some discrepancies were observed between the two methods. His work is discussed in detail in (27). From this discussion it became clear that in particle size regions where both coulter counter and turbidimetry are capable of providing a valid estimate of the PSD the two methods compare favorably. The discrepancies observed for distributions of small particles were not due to forward scattering as claimed in (6); rather they were due to the fact that coulter counter can not detect small particles. Similar discrepancies were observed by Walstra (11). Coulter counter should not be used to corroborate results from other techniques when dealing with distributions of small particle sizes (i.e., submicron particles), or PSD with tails of small particles.

### Concluding Remarks

Turbidimetry is an experimentally simple method for particle sizing with a very good potential for on-line applications. However, to make the best use of the method one should be aware of its limitations and work within these limitations. This way the results will always be meaningful. Our experience with the method, can be summarized as follows:

Turbidimetric methods can not be expected to provide information on the full particle size distribution in many situations. In order to decide the type of information about the PSD that can be extracted from any turbidimetric method one must consider both the value of the refractive index ratio ( $m$ ) of the suspension and the  $\alpha$  values covered by the distribution (particle sizes, wavelengths at which measurements are taken). The

same PSD that can be successfully estimated for one system may be impossible to estimate for another system with a different  $m$  value.

The specific turbidity is a "safer" method that the turbidity ratio or the wavelength exponent, for the determination of the particle size (average size or full PSD) in a suspension. This is because it involves two independent measurements of the particle size via two different properties of the suspension (turbidity and solids volume fraction), while the other turbidimetric techniques are based on turbidity measurements only. In certain ( $m$ ,  $\alpha$ ) regimes, turbidity is a very slow function of a certain average of the distribution. In these regimes, information on the full particle size distribution is impossible, but using specific turbidity a meaningful average of the particle size distribution (turbidity, weight or surface-volume) can always be estimated. On the contrary, in these regimes, the turbidity ratio can provide no reliable estimate of the particle size of the suspension, because it is extremely sensitive to experimental error and practically independent of the particle size. Therefore, the claim of Zollars (16) that "all turbidimetric methods (i.e. specific turbidity, turbidity ratio) are based on the same fundamental principles. Therefore any weaknesses or limitations in one technique should be inherent in all turbidimetric techniques", is not justified.

As a general rule, if the volume fraction of the particles in the suspension can be measured, then specific turbidity is the best choice among the turbidimetric techniques for particle size determination. The turbidity ratio or the wavelength exponent method should be used only if the particle volume fraction is unknown. However, these last two methods should be avoided for i) suspensions with values of  $m$  smaller than 1.15 and submicron particles and ii) regardless the value of  $m$ , for suspensions with very small particles ( $\alpha < 1$ ) or very large particles ( $\alpha > 100$ ). In these cases, if the particle volume fraction is not known, then it is better to choose another sizing method, as for example dynamic light scattering (when dealing with submicron particles) or capillary-hydrodynamic fractionation, coulter counter or field flow fractionation (when dealing with small and large particles). In cases i) and ii), reliable information on the full PSD cannot be obtained by any turbidimetric technique. Using the specific turbidity, however, a very good estimate of the weight average diameter can be obtained for any type of distribution in the first case (from the mean value of the apparent diameters at 400 nm and 600 nm), while in the second case, the turbidity average diameter can be obtained for suspensions of very small particles and the surface-volume average for suspensions of very large particles. In any other ( $m$ ,  $\alpha$ ) regimes (where measurements at different wavelengths do not result in the same apparent diameters), the specific turbidity method with the assumption of log-normal distribution results in a very good estimate of the weight average diameter. For continuous unimodal distributions and not widely separated bimodals it will also provide the correct location of the main body of the distribution on weight basis. Bimodal distributions consisted of two separate narrow distributions (or mixtures of monodisperse latexes) can be resolved only when the contribution of the small particles on weight basis is significant. For any type of bimodal distribution, the weight average of the distribution estimated assuming log-normal form will be correct (but the location of the distribution not).

If the shape of the distribution in the suspension is not assumed an estimate of the full PSD can be obtained if a large number of turbidity measurements is available. However, in the regimes where  $y$  changes slowly with an estimation of the full PSD is, again, impossible (i.e., using a different algorithm does not eliminate the problem of high correlation).

Although this analysis was focussed on latexes, turbidimetry can be applied for particle size determination in other systems in polymer science. Attempts to utilize turbidimetric techniques for the determination of the particle size distribution of the dispersed phase in polymer blends (in the form of thin films) have been reported (25,49). Again, the information obtained on the PSD depends on the technique utilized, the size of the dispersed phase and the wavelengths used. The specific turbidity method is expected

to perform better than the turbidity ratio, especially when wavelengths in the IR regime are utilized, and therefore the  $\alpha$  values of the system are small. Multiple scattering is one of the main problems when dealing with polymer blends. For analysis on a routine basis, however, it may be possible to account for multiple scattering utilizing a calibration approach.

Finally, on-line latex particle size measurements using turbidimetry are possible. An extensive discussion on this topic can be found in (45, 64). In our experience discrete sampling has more advantages than continuous sampling both in batch and continuous reactors. Discrete sampling with sampling cycles of 2-4 min is feasible; we believe that sampling at such intervals is frequent enough to give a satisfactory picture of the process history, when monitoring emulsion polymerization in industrial scale reactors.

#### Literature Cited

- Heller, W., and Pangonis, W.J., J. Chem. Phys., **26**, 498 (1957).
- Heller, W., J. Chem. Phys., **26**, 1258 (1957).
- Beattie, W.H., Ph.D. Thesis, University of Minnesota, 1958.
- Meehan, E.J. and Beattie, W.H., J. Phys. Chem., **64**, 1006 (1960).
- Wallach, M.L., Heller, W., and Stevenson, A.F., J. Chem. Phys., **34**, 1796 (1961).
- Wales, M., J. Phys. Chem., **66**, 1768 (1962).
- Gledhill, R.J., J. Phys. Chem., **66**, 458 (1962).
- Heller, W., Bhatnagar, H.L., Nakagaki, M., J. Chem. Phys., **36**, 1163 (1962).
- Maron, S.H., Pierce, P.E., and Ulevitch, I.N., J. Colloid Sci., **18**, 470 (1963).
- Wallach, M.L. and Heller, W., J. Phys. Chem., **68**, 924 (1964).
- Walstra, P., J. Colloid Interface Sci., **27**, 493 (1968).
- Maxim, L.D., Klein, A., Meyer, M.E., and Kuist, C.H., J. Polym. Sci. Part C, **27**, 195 (1969).
- Bagchi, P., and Vold, R.D., J. Colloid Interface Sci., **53**, 194 (1975).
- Kiparissides, C., "Modelling and Experimental Studies of a Continuous Emulsion Polymerization Reactor", Ph.D. Thesis, McMaster University, Hamilton, Ontario, Canada, 1978.
- Kiparissides, C., MacGregor, J.F., Singh, S., and Hamielec, A.E., CJChE., **58**, 65 (1980).
- Zollars, R.L., J. Colloid Interface Sci., **74**, 163 (1980).
- Zollars, R.L., J. Disp. Sci. and Techn., **2** (2&3), 331 (1981).
- Shaw, A.T., and Darling, D.F., in Particle Size Analysis 1981, (N.G. Stanley-Wood and T. Allen, Eds) p. 355 Wiley Heyden, Ltd., 1982.
- Haseler, S.C., and Parkin, E.M.L., in Particle Size Analysis 1981, (N.G. Stanley-Wood and T. Allen, Eds) p. 403. Wiley Heyden Ltd., 1982.
- Katsuyuki Kubota, Shinya Hayashi and Hedeharu Mandai, J. Colloid Interface Sci., **98**, 581 (1984).
- Kourti, T., Penlidis, A., Hamielec, A.E., and MacGregor, J.F., ACS PMSE Div. Preprints, **53**, 147 (1985).
- Haseler, S.C., Part. Charact., **2**, 14 (1985).
- Barth, H.G., and Sun, S-T., Analytical Chemistry, **57**, 151R (1985).
- Gossen, P.D., Kourti, T., Penlidis, A., MacGregor, J.F. and Hamielec, A.E., Preprints, 6th International IFAC/IFIP/IMEKO Conference on Instrumentation and Automation in the Paper, Rubber, Plastics and Polymerization Industries, Akron, Ohio, 1986.
- Cielo, P., Cole, K., and Favis, B.C., Preprints, 6th International IFAC/IFIP/IMEKO Conference on Instrumentation and Automation in the Paper, Rubber, Plastics and Polymerization Industries, Akron, Ohio, 1986.

26. Kourti, T., Penlidis, A., MacGregor, J.F. and Hamielec, A.E., in Particle Size Distribution – Assessment and Characterization, (Th. Provder, Ed.) p. 242. ACS Symposium Series **332**, Washington, D.C., 1987.
27. Kourti, T., Polymer Latexes: Production by Homogeneous Nucleation and Methods for Particle Size Determination, Ph.D. Thesis, McMaster University, Hamilton, Ontario, Canada, 1989.
28. Kourti, T., MacGregor, J.F. and Hamielec, A.E., "An Investigation of the Capability of Turbidimetric Techniques to Provide the Full Particle Size Distribution", This volume.
29. Gulari, Es., Gulari, Er., ACS PMSE Div. Preprints, **53**, 137 (1985).
30. Kerker, M., The Scattering of Light and Other Electro-magnetic Radiation, Academic Press, N.Y. 1969.
31. Bradolin, A. and Garcia-Rubio, L.H., "On-Line Particle Size Distribution Measurements for Latex Reactors", This Volume.
32. Garcia-Rubio, L.H., in Particle Size Distribution – Assessment and Characterization, (Th. Provder, Ed.) p. 161. ACS Symposium Series, **332**, Washington, D.C., 1987.
33. Gulari, Er., Annapragada, A., Gulari, Es. and Jawad, B., in Particle Size Distribution – Assessment and Characterization, (Th-Provder, Ed.) p. 133. ACS Symposium Series, **332**, Washington, D.C., 1987.
34. Goulari, Es., Bazzi, G., Gulari Er., and Annapragada, A., Part. Charact., **4**, 96 (1987).
35. Kourti, T., MacGregor, J.F., Hamielec, A.E., J. Colloid Interface Sci., **120**, 292 (1987).
36. Melik, D.H., and Fogler, H.S., J. Colloid Interface Sci., **92**, 161 (1983).
37. Bateman, J.B., Weneck, E.J., and Eshler, D.C., J. Colloid Sci., **14**, 308 (1959).
38. Stevenson, A.F., Heller, W., and Wallach, M.L., J. Chem. Phys., **34**, 1789 (1961).
39. Yang, K.C. and Hogg, R., Analytical Chemistry, **51**, 758 (1979).
40. Walstra, P., Brit. J. Appl. Phys., **15**, 1545 (1964).
41. Heller, W., J. Chem. Phys., **2**, 1609 (1965).
42. Goulden, J.D.S., Brit. J. Appl. Phys., **12**, 456 (1961).
43. Espenscheid, W.F., Kerker, M. and Matijevic, E., J. Phys. Chem., **68**, 3093 (1964).
44. Dobbins, R.A., AIAA J., **1**, 1940 (1963).
45. Gossen, P.D., On-Line Particle Size Measurement and Mathematical Modelling of Continuous Poly(vinyl acetate) Emulsion Polymerization, Master's Thesis, Dept. of Chemical Engineering, McMaster University, Hamilton, Ontario, Canada, 1988.
46. Cheesman, G.C.N., in Particle Size Analysis (Groves, M.J., Ed.), Heyden, London, England, 1978.
47. Dobbins, R.A. and Jizmagian, G.S., J. Opt. Soc. Am., **56**, 1345 (1966).
48. Eliçabe G.E. and Garcia-Rubio, L.H.-  $\alpha$ : "Latex Particle Size Distribution from Turbidimetry Using a Combination of Regularization Techniques and Generalized Cross-Validation", In Polymer Characterization (C. Craver and T. Provder, Eds.), Advances in Chemistry Series, 227, American Chemical Society, Washington, D.C., 1990; b: J. Colloid Interface Sci., **129**, 192 (1989).
49. Belanger, C. Cielo, P., Favis, B.D. and Patterson, W.I., Analysis of Polymer Blend Morphology by Transmission and Reflection Light Scattering Techniques, in Polyblends 89, National Research Council Canada (L.A. Utracki, Ed.), 1989.
50. Van de Hulst, H.C., Light Scattering by Small Particles, J. Wiley and Sons, Inc., New York, 1957.
51. Herdan, G., Small Particle Statistics, (2nd Edition), Butterworths, London, 1960.
52. Bohren, C.F. and Huffman, D.R., in Absorption and Scattering of Light by Small Particles, J. Wiley and Sons, New York, 1983.

53. Irani, R.R. and Callis, C.F., Particle Size: Measurement, Interpretation and Application, J. Wiley and Sons, N. Y., 1963.
54. Maron, S.H., Moore, C., and Powell, A.S., J. Appl. Phys., **23**, 900 (1952).
55. Yan, J.F., J. Colloid Interface Sci., **49**, 152 (1974).
56. Honig, E.P., J. Phys. Chem., **69**, 4418 (1965).
57. Cumprecht, R.O., and Sliepcevich, C.M., J. Phys. Chem., **57**, 90 (1953).
58. Tabibian, R.M., Heller, W., and Eppel, J.N., J. Colloid Sci., **11**, 195 (1956).
59. Heller, W., and Tabibian, R.M., J. Colloid Sci., **12**, 25 (1957).
60. Walstra, P., Brit. J. Appl. Phys., **16**, 1187 (1965).
61. Hamielec, A.E. and Wright, J.D., Chemistry in Canada, (Dec. 1973), p. 27-29.
62. Ray, S.W., Minicomputer Control of a Latex Reactor, Master Eng. Thesis, McMaster University, Hamilton, Ontario, Canada, 1976.
63. Pollock, M.J., Modelling and Control of Sustained Oscillations in the Continuous Emulsion Polymerization of Vinyl Acetate, Ph.D. Thesis, McMaster University, Hamilton, Ontario, Canada, 1984.
64. Gossen, P.D., On-Line Instrumentation for Latex Production, Ph.D. Thesis, McMaster University, Hamilton, Ontario, Canada, 1991.
65. Nicoli, D.F., Kourti, T., Gossen, P.D., Wu, J-S. and MacGregor, J.F., "On-Line Latex Particle Size Determination by Dynamic Light Scattering, Designed for an Industrial Environment", This volume.
66. These results were first presented in the "Symposium on Particle Size Analysis in Polymer Science", organized by the PMSE division, during the 199 ACS National Meeting, in Boston, MA, (April 1990).

RECEIVED May 14, 1991

## Chapter 4

# On-Line Particle Size Distribution Measurements for Latex Reactors

A. Brandolin and L. H. Garcia-Rubio<sup>1</sup>

Department of Chemical Engineering, University of South Florida,  
Tampa, FL 33620

The on-line measurement of the particle size distribution has been an outstanding problem in the design, analysis and control of latex reactors. Most available techniques have long time delays associated, primarily, with sample preparation and/or the actual measurements. Recent developments in the interpretation of turbidity spectra have resulted in a technique for the measurement of the complete particle size distribution with instrumentation that can be easily implemented in a plant environment. In this paper, the effects of process variables such as sampling time and dilution factors are analyzed within the context of continuous on-line turbidity measurements. Important results for the design of sampling/measurement strategies are presented and discussed.

The on-line measurement of the particle size distribution has been an outstanding problem in the design, analysis and control of latex reactors. Most available techniques have long time delays due to the sample preparation and to the time it takes to conduct the actual measurements. Recent developments in the interpretation of turbidity spectra (1) have resulted in a spectrophotometric technique for the estimation of the complete particle size distribution with instrumentation that can be easily implemented in a plant environment (1,2). In this paper, some alternatives for the design of a continuous sampling and measurement system are explored.

One of the major problems with the design of continuous measurement systems using spectrophotometric techniques is the considerable dilution required for the measurements. The dilution steps not only increase the delays associated with the measurements but also may

<sup>1</sup>Corresponding author



increase the experimental errors and bias the interpretation of the data. Errors in the dilution steps generally will reflect in the estimation of the particle concentration and, depending on the interpretation equation, the average particle diameter may also be affected. The dilution steps have inherently two effects: 1). Shift the data in time relative to the populations existing in the reactor and, 2) Average the data over the dilution interval with a concomitant loss in resolution. These two effects can bias the interpretation of the PSD data. Therefore, it is important to investigate, through realistic simulations of complete reactor-measurement systems, the sampling and dilution strategies (i.e.: batch versus continuous sampling). For this purpose, the continuous emulsion polymerization of styrene has been investigated as a base case. The particle size distributions, generated in the reactor as function of time, are sampled and diluted using batch and continuous strategies. Then, the turbidity spectra for the distribution at the exit of the dilution vessel is deconvoluted to estimate the PSD in the reactor. Figure 1 shows a block diagram for the direct simulation and the deconvolution steps. A continuous dilution system coupled with turbidity measurements is demonstrated. Because of the continuous recording of the data, and because the complete size distribution is obtained for every measurement point, the continuous system offers a suitable alternative for the measurement and control of the particle size distributions.

#### **Reactor Model:**

For the simulation of the reactor, a generalized stirred tank reactor model has been implemented (the detailed descriptions of emulsion polymerization processes and the mathematical model for the continuous emulsion polymerization reactor are given in (3-5)). The continuous reactor model is based on the birth time distribution of particles (4) and on the physical and chemical processes known to take place during emulsion polymerization reactions (5). Thus, the model can simulate the emulsion polymerizations of vinyl acetate and methyl methacrylate which have high radical desorption rates and may exhibit sustained oscillatory behavior, as well as, the emulsion polymerization of styrene which presents low desorption rates with very attenuated or non-oscillatory behavior. The output from the reactor model consists of latex properties such as particle size distribution, total particle surface area, total number of particles and free emulsifier concentration.

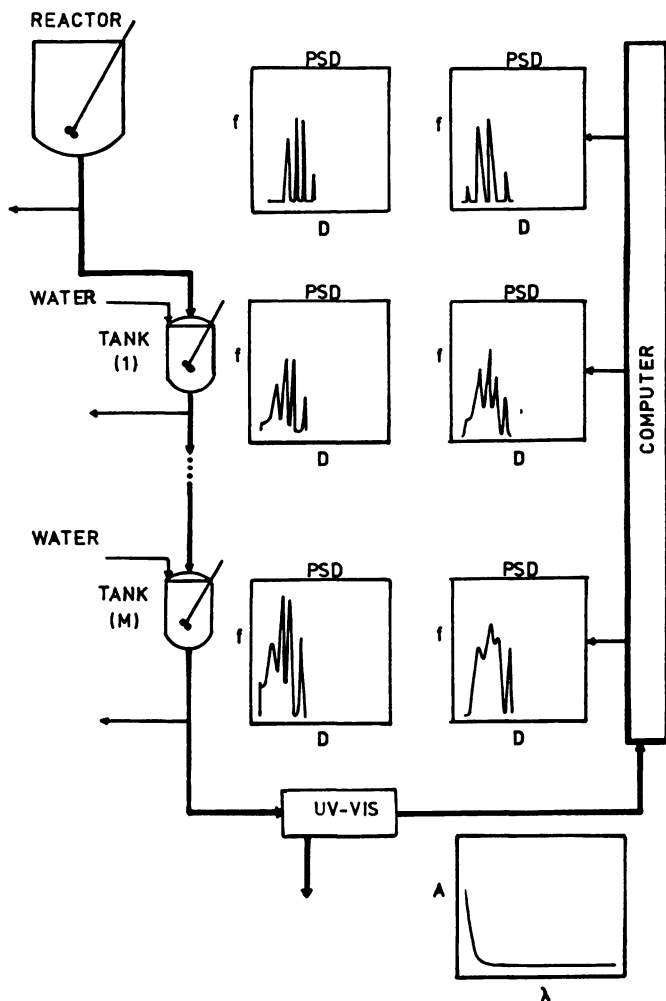


**Figure 1:** Block Diagram for the Direct Simulation and Deconvolution steps of a Latex Reactor-Measurement System.

**Sampling and Measurement Systems:**

The delays associated with the traditional techniques for sampling and measurement of particle size distribution make them suitable only for off-line measurements. Examples of such techniques are: electron microscopy, disc centrifuge photosedimentometry and hydrodynamic chromatography. A good review of the techniques available for determining particle size distribution is given in (6). On-line measurements of the particle size distribution have only recently become a real possibility through the development of turbidimetry (1,2,7) and dynamic light scattering (8,9) techniques.

Zollars (7), presented an on-line system based on turbidity measurements for; the estimation of the particle size distribution, the refractive index and the concentration of particles. Zollars considered the effect of the residence time in the dilution step and assumed a two parameter log-normal distribution to interpret the turbidity data. This method will give reasonable approximations whenever unimodal distributions are being generated in the reactor. However, because the shape of the PSD is fixed, the values for the particle size distribution will not be reliable for cases where secondary nucleations occur and multi-modal distributions are present.

Dynamic light scattering has also been proposed as a suitable alternative for on-line measurements of the particle size distribution in latex polymerizations (8,9). With dynamic light scattering, a single average diameter is typically measured. The dilution step plus measurement consuming 10-15 minutes. Dynamic light scattering was proven useful in monitoring the average particle diameter during batch polymerizations of vinyl acetate. Throughout the course of the reaction, three to five samples were taken, the difference in the average diameter between each sample ranged from 50 to 100%, implying that the delay times associated with the measurements could lead to inaccurate control actions if the particle diameter was to be controlled on the basis of these measurements.

**Simulation of the Sampling-Dilution System:**

A viable on-line dilution system consists of  $M \geq 1$  dilution vessels in series of equal volume and ideal residence time distribution. In this system, a stream from the reactor is continuously diluted and passed through a diode array spectrometer where a complete uv-vis spectrum (200-900 nm) is recorded at the desired measurement intervals. Depending upon the desired wavelength resolution, the measurement times could range between 0.1 second to several seconds. Therefore, for most applications to latex reactors, the measurements can be considered instantaneous relative to the dilution times.

The following mass balances must be solved in order to predict the particle size distribution at the exit of the "M" dilution vessel:

$$\frac{dn^k(t, D_j)}{dt} = \frac{n^{k-1}(t, D_j)R_f - n^k(t, D_j)}{\theta^*} \quad (1)$$

for  $j=1, \dots, ND$  and  $k=1, \dots, M$

$$R_f = (Cd/Cr)^{0.5} \quad (2)$$

where "k" and "j" represent the dilution vessels and discretized diameters respectively,  $R_f$  is the dilution factor and  $\theta^*$  is the mean residence time in each dilution vessel.  $Cr$  is the polymer mass concentration in the reactor and  $Cd$  is the concentration expected at the exit of the dilution system.

If the system is operated in a batch mode, Eq. [1] becomes;

$$n^k(t, D_j) = n^{k-1}(t, D_j)R_f \quad (3)$$

for  $k=1, \dots, M$  and  $j=1, \dots, ND$

For simulation purposes, the diameter  $D$  was discretized with the minimum and maximum particle diameters considered to be the micelle diameter and 150 nm respectively. These limits can be easily changed in accordance with the particle diameters predicted by the reactor model.

Because the polymer mass concentration and the particle size distribution in the reactor vary continuously during the course of the polymerization, it is not feasible to use a constant dilution factor and at the same time attain the linear range for the spectrophotometer (ie;  $\tau_{\max} < 1$ ). For example, in some cases, the polymer mass concentration in the reactor increases continuously until the first peak in conversion is reached, then it becomes almost constant. A dilution factor appropriate for the higher concentrations will lead to noisy turbidity spectra at the beginning of the

polymerization. In other cases, the use of a dilution factor selected on the basis of the polymer mass concentration at the beginning of the reaction will lead, after the first peak in conversion, to concentrated solutions which are not useful for the analysis because of multiple scattering effects.

In order to obtain measurements within the linear range of the spectrophotometer, with a continuous dilution system, two strategies are possible: the dilution factor may be up-dated according to the polymer mass concentration predicted by the reactor model or, if a reactor model is not available, a feedback loop can be incorporated to increase the dilution factor until the turbidity spectra is within the appropriate range for analysis.

#### **Recovery of the Particle Size Distribution in the Reactor:**

##### **Deconvolution of the Turbidity Spectra:**

For the purpose of simulation, the "measured" turbidity spectra ( $\tau$ ) were generated using the particle size distributions ( $f$ ) calculated at the exit of the dilution vessel with the following expression (1):

$$\tau = A f \quad (4)$$

where matrix A depends on the diameter, the wavelentgths and the optical properties for water (10) and the polymer in question (11). Then, the particle size distribution was recovered through the following expression (1,2):

$$f = (A + \gamma H)^{-1} A \tau \quad (5)$$

where H contains the information known about the particle size distribution, and  $\gamma$  is the so called "Regularization Parameter" selected such that the correct particle size distribution can be recovered (1-2).

##### **Time Deconvolution of the Particle Size Distribution:**

Once the size distribution at the exit of the dilution process is recovered, the particle size distribution in the polymerization reactor can be calculated integrating equation [1] between  $t-\Delta t$  and  $t$ , and solving for  $n^{k-1}(t, D_i)$ , which is assumed constant throughout the dilution step (ie; changes in the particle size distribution through the dilution period are assumed to be negligible).

$$n^{k-1}(t, D_j) = \frac{n^k(t, D_j) - n^k(t - \Delta t, D_j)e^{-\Delta t/\theta^k}}{R_j(1 - e^{-\Delta t/\theta^k})} \quad (6)$$

for  $j = 1, \dots, ND$  and  $k = 1, \dots, M$ .

where  $k$  represents the dilution vessels and  $j$  the points at which the size distribution was discretized. Note that if there are "M" dilution steps in series, "M+1" successive PSD must be known at the exit of the dilution system in order to recover the size distribution in the reactor.

### Simulation Results:

#### Styrene Polymerization.

Experiment 3 in reference (12) has been simulated to demonstrate the predictive capabilities of the model. The model parameters and reactor conditions are given in references (5) and (12). The results are shown in Fig. 2. In agreement with the experimental results, the model predicts a peak in conversion after 1.6 residence times followed by a damped oscillatory behaviour (Fig. 2a). The corresponding number average particle diameters vs. time are shown in Fig. 2b. The observed oscillations are produced by the periodic washing out of the emulsifier (Fig. 2c). At the beginning of the reaction, the model predicts an initial particle generation, then, this first population of particles shifts towards larger diameters indicating that no new particles are being produced. A second particle generation is observed when the emulsifier is again able to form new micelles. This cycle continues and as a result, several particle populations may coexist at the same time. The best sample times for a batch dilution system can be selected by analysing the shape of the conversion versus time curves.

#### Batch Dilution:

There are two factors that should be addressed in order to select batch sampling times. First, the shape of the particle size distribution and the diameter range change very rapidly along the ascendent portions of the conversion curve, specially before its first maximum, therefore it would be desirable to take as many samples as the dead times permit. Second, each oscillation in the conversion trajectory implies a new generation of particles eventually leading to multimodal distributions. Therefore, if a sample is taken just before a minimum in conversion it will not represent the shape of the particle size distribution that exists in the reactor at the

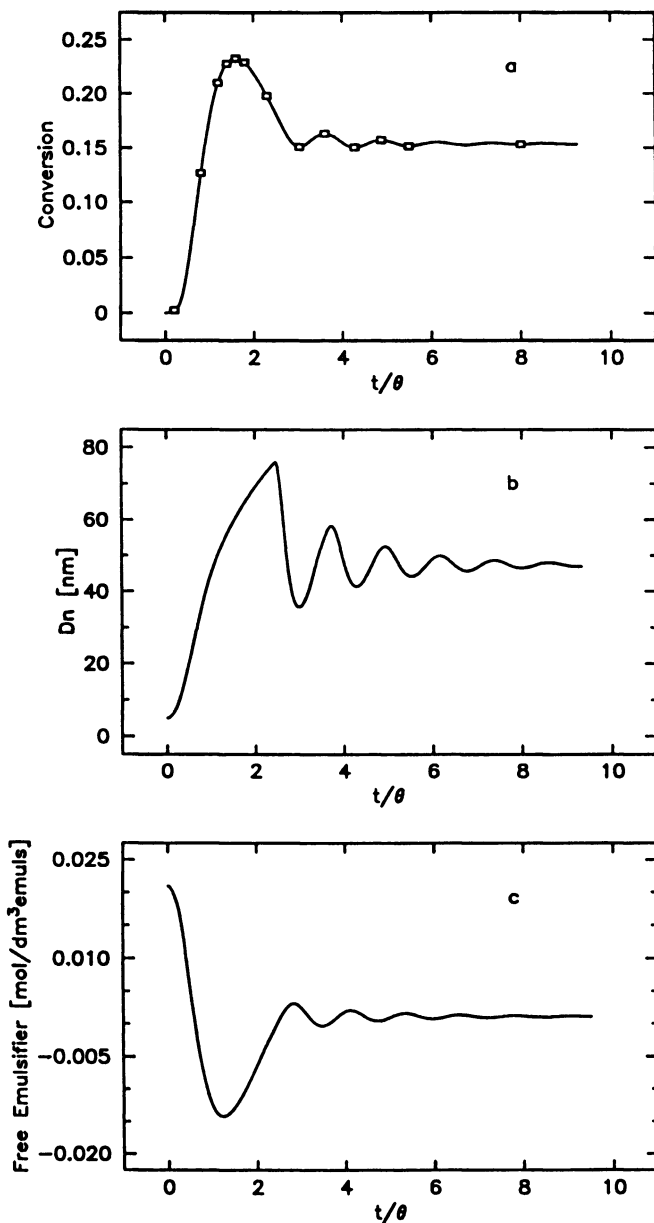


**Figure 2:** Simulation Results for a Continuous Styrene Emulsion Polymerization. a) Conversion; b) Number Average Particle Diameter; c) Emulsifier Concentration. The data is from Ref(12).

measurement time. Thus, the sampling intervals must not exceed the elapsed time between minima and maxima in conversion. Also, notice that in accordance with the model predictions, the total number of particles is of the order of  $1 \cdot 10^{18} \text{ l/dm}^3$ . For typical polystyrene latices, measurement concentrations are in the order of  $1 \cdot 10^{18} \text{ l/dm}^3$ . Clearly, a careful design of the dilution system is required even if samples are to be captured in a batch mode.

#### **Continuous Dilution System:**

In order to investigate the capabilities of continuous dilution, a system of two equal-volume dilution vessels has been considered. It is further assumed that the mass of polymer can be obtained independently (ie; using a densitometer). Under these conditions Eq.[2] can be used to determine the dilution factor. Figure 3 shows the dilution factor calculated with Eq. [2] as function of time. The points along the conversion trajectory, where the particle size distribution in the reactor has been compared to the PSD estimated at the exit of the dilution system, are indicated in Figure 2a. Three mean residence times in the dilution vessels ( $\theta^*$ ) have been used: 1/3, 1/6 and 1/15 of the reactor's mean residence time ( $\theta$ ).

In the reactor, when the conversion reaches its first maximum ( $t/\theta=1.6$ ), the first generation of particles has been completed resulting in a unimodal PSD (Fig. 4a). The PSD is located at diameters larger than the particle diameters observed for newly formed particles ( $D(\text{new})=5 \text{ nm}$ ). At the exit of the dilution system, for residence times in the dilution system comparable to the reactor residence time (ie;  $\theta^*/\theta=1/3$ ), the particle size distribution observed will contain two populations: a population containing small particle diameters reflecting the PSD existing at the beginning of the reaction, and a second population, very similar in shape and location to the unimodal particle size distribution existing at the same time in the reactor. As the residence time in the dilution system is decreased (Figs. 4a-4c), the PSD at the exit of the dilution vessels will eventually sample only the PSD existing in the reactor at the measurement time (Fig. 4c). It is evident that the PSD at the exit of the dilution system contains information about the initial particle generations. Clearly, assuming the PSD at the exit of the sampling system to be identical to the PSD in the reactor could be misleading.

A similar analysis for longer reaction times indicates that the differences between the PSD in the reactor and the PSD observed at the exit of the dilution vessel are smaller and independent of the residence times in the dilution system (Fig. 5). This is because only small oscillations in conversion have been occurring in the reactor.

Figures 6 and 7 show the differences between the



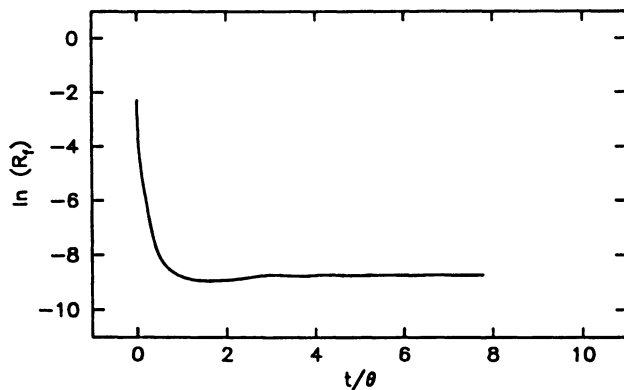


**Figure 3:** Dilution Factor  $R_f$  calculated as function of time.

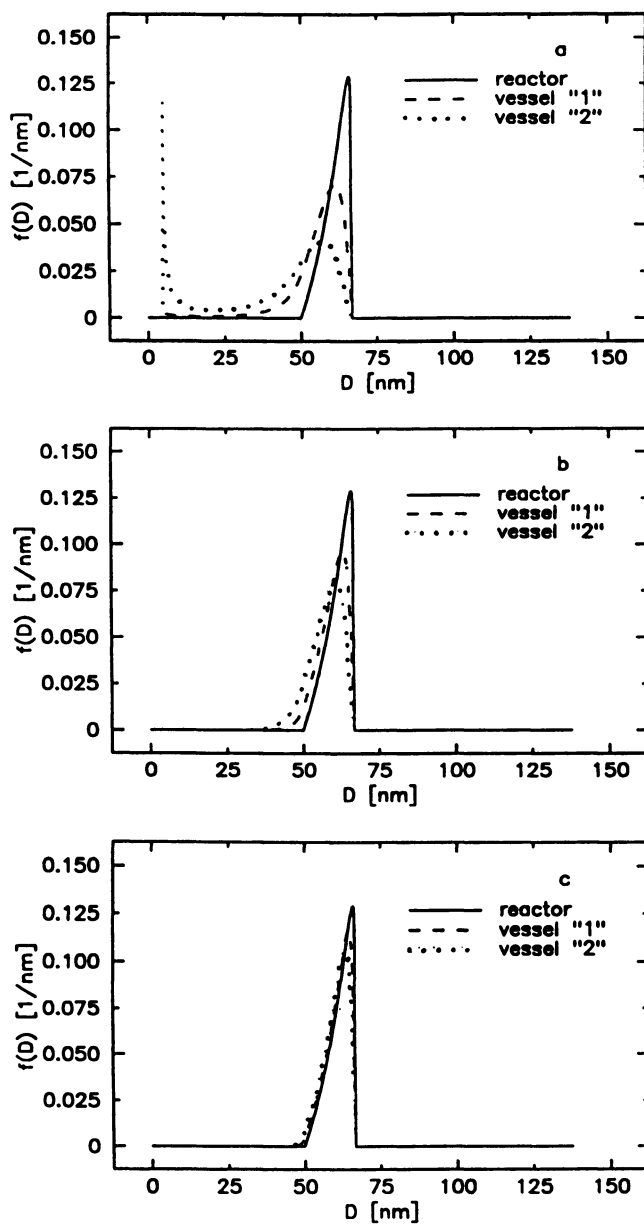


**Figure 4:** Particle Size Distributions at  $t/\theta = 1.6$  as sampled in: Reactor; Dilution Vessel No 1; Dilution Vessel No 2. a)  $\theta/\theta^* = 1/3$ ; b)  $\theta/\theta^* = 1/6$ ; c)  $\theta/\theta^* = 1/15$ .

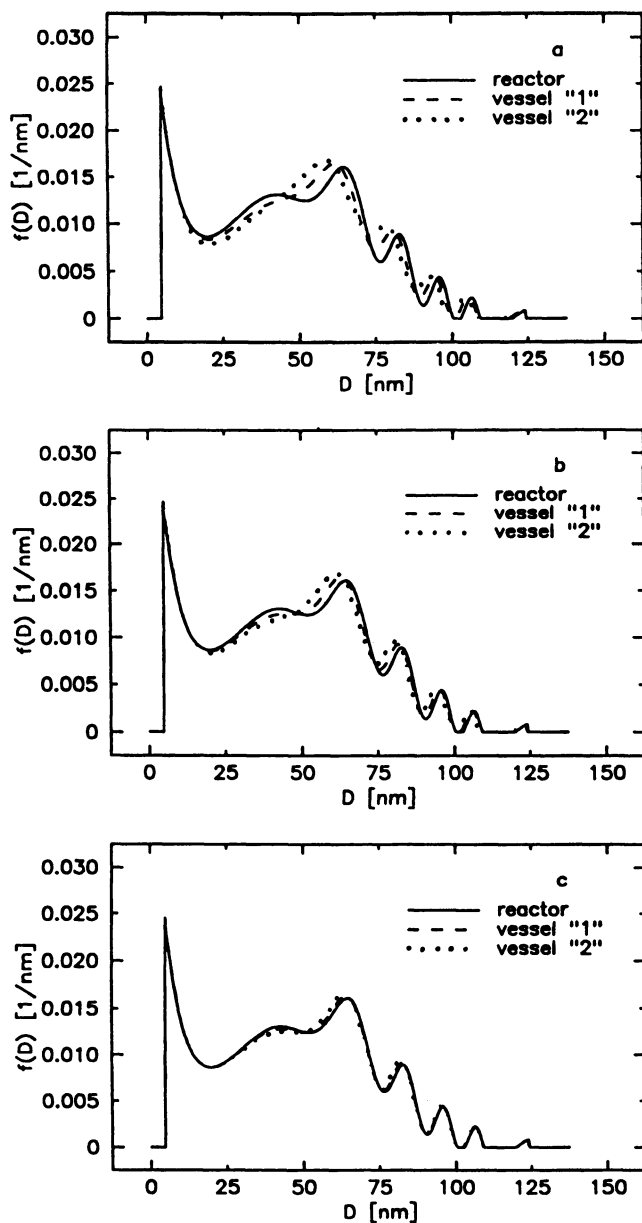


**Figure 5:** Particle Size Distributions at  $t/\theta=8.0$  as sampled in: Reactor; Dilution Vessel No 1; Dilution Vessel No 2. a)  $\theta/\theta^*=1/3$ ; b)  $\theta/\theta^*=1/6$ ; c)  $\theta/\theta^*=1/15$ .

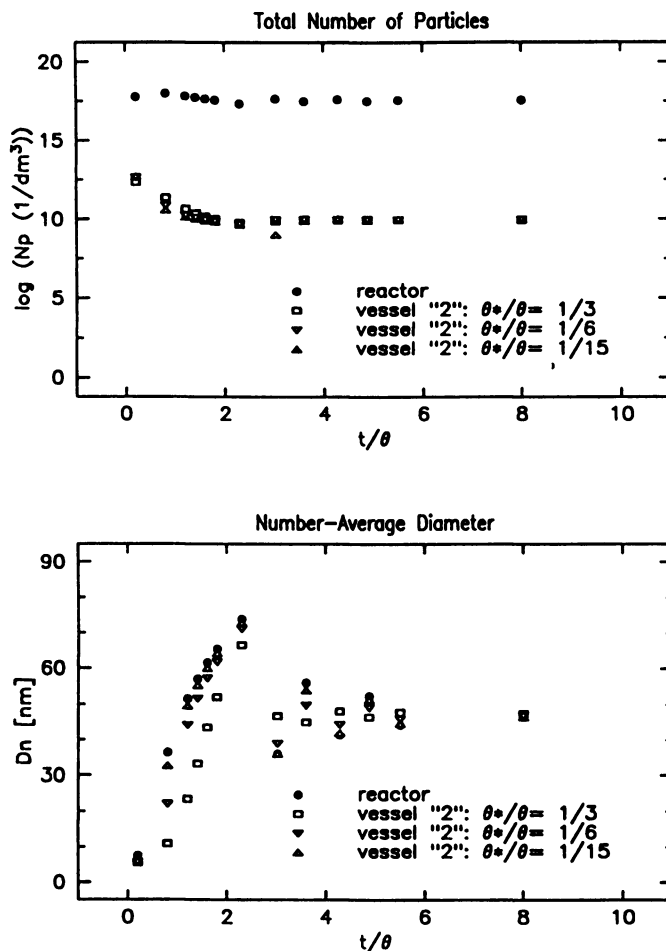


**Figure 6:** Comparison between Leading Moments of the Particle Size distribution in the reactor and at the exit of the second dilution vessel, for several residence times in the Dilution System.

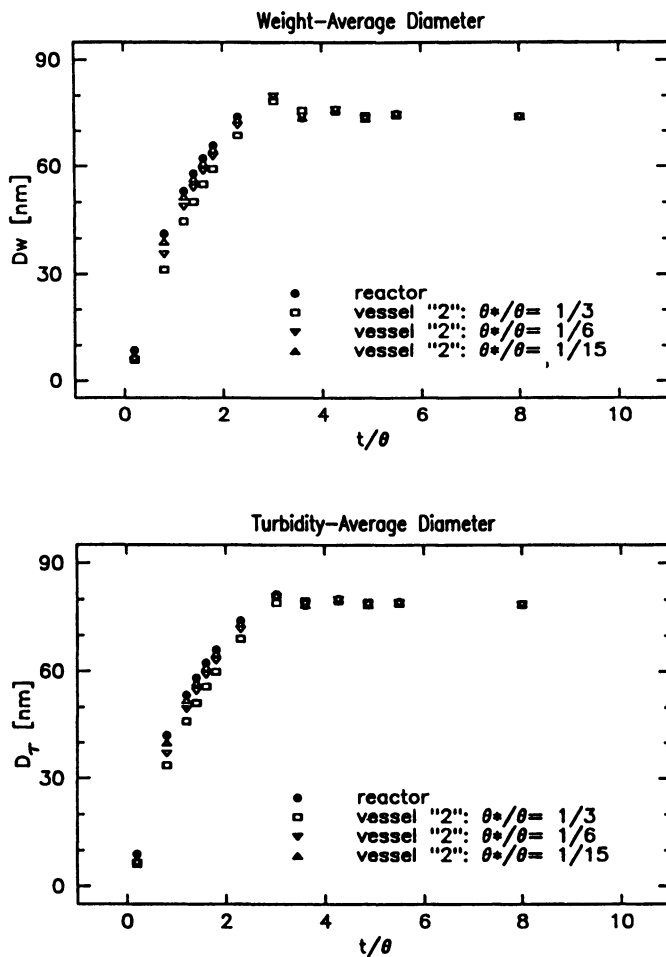


**Figure 7:** Comparison between Leading Moments of the Particle Size distribution in the reactor and at the exit of the second dilution vessel, for several residence times in the Dilution System.

leading moments of the reactor particle size distribution and the PSD at the exit of the dilution system for three residence times  $\theta^*$ . Notice that smaller differences are observed for the higher moments. This is because they depend mainly on the large diameters and these are well represented at the exit of the dilution system for all  $\theta^*/\theta$ . On the other hand, the lower moments of the PSD will be more affected because of the presence of small diameter particles present in the dilution system but no longer present in the reactor.

In order to solve the problems of sampling more than one population in the dilution system and simultaneously recover the PSD in the reactor at the measurement time, it is necessary to perform a deconvolution along the time axis after the PSD at the exit of the dilution system has been recovered. Figures 8-10 demonstrate that it is possible to recover the PSD's at the exit of the dilution system and in the reactor, even for cases in which both distributions are complex and very different from each other. Figure 8 shows the deconvolution in frequency and in time at  $t/\theta=1.6$  (first maximum in conversion). The PSD at the exit of the dilution system shows a bimodal distribution with a narrow population in the small diameter range, the recovered distribution shows good agreement for the larger diameters and indicates the presence of small particles. The recovered PSD reflects the population existing in the reactor at the measurement time. The oscillations present in the PSD are a characteristic of the numerical method and appear when narrow distributions are recovered (1-3). Figure 9 shows the results for a smaller residence times in the dilution system. Clearly, the recoveries in frequency and in time are in good agreement with the simulated PSD. Figure 10 demonstrates that it is possible to recover complex distributions present in the reactor after several residence times. Figures 11 and 12 show the moments of the simulated and recovered particle size distribution in the reactor for different residence times in the dilution system. The agreement between the simulated and recovered  $D_r$  and  $D_w$  is excellent, as expected for higher moments of the PSD. However, it is important to note that, because the higher moments of the distribution are rather insensitive to the delays in the dilution system, considerable errors in the interpretation of the PSD in the reactor are likely to occur if a single average is measured.

### **Summary and Conclusions:**

Through a realistic simulation of the complete reactor-measurement system it has been demonstrated that the on-line measurement of the particle size distribution in continuous emulsion polymerization reactors is possible using a uv-vis spectrophotometer connected to an appropriate dilution system. The dilution must be designed

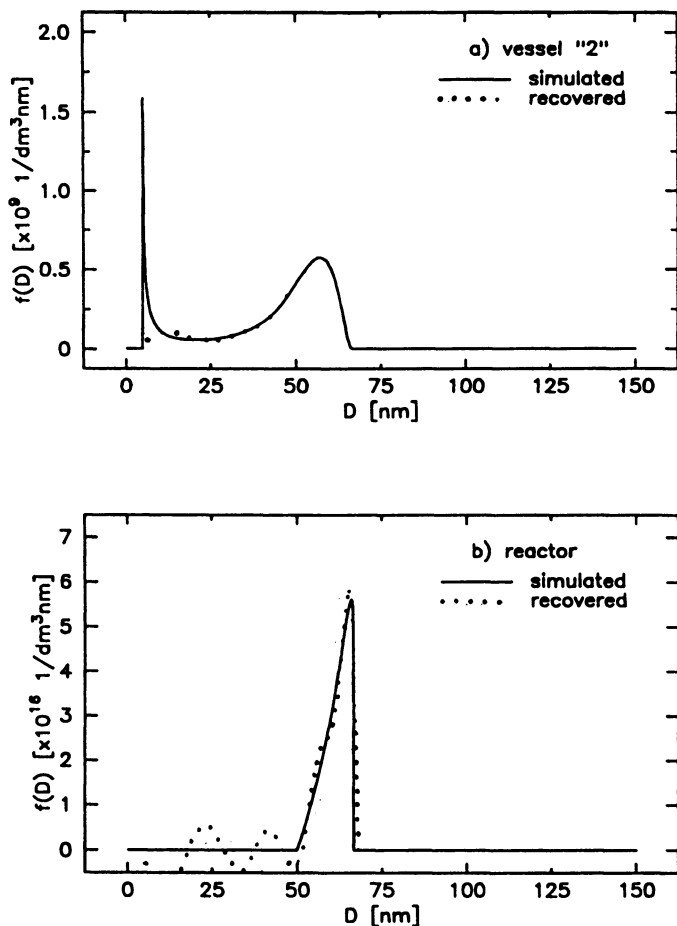


**Figure 8:** Comparison between Simulated and Recovered Particle Size Distributions at  $t/\theta=1.6$ : a) Exit of the Dilution Vessel No 2; b) Reactor.  $\theta/\theta^*=1/3$ .

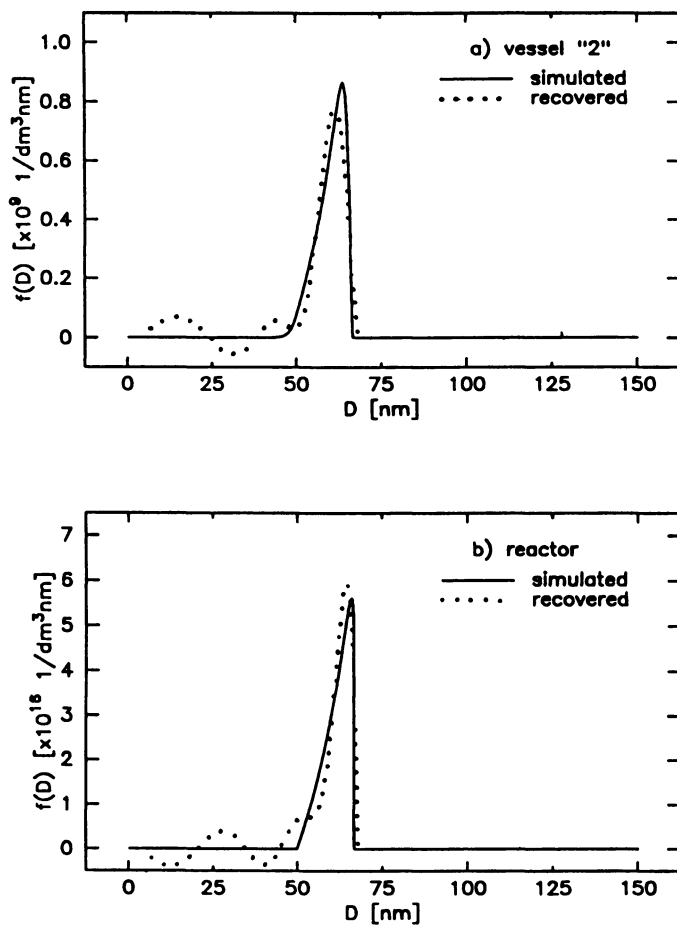


**Figure 9:** Comparison between Simulated and Recovered Particle Size Distributions at  $t/\theta=1.6$ : a) Exit of the Dilution Vessel No 2; b) Reactor.  $\theta/\theta^*=1/15$ .



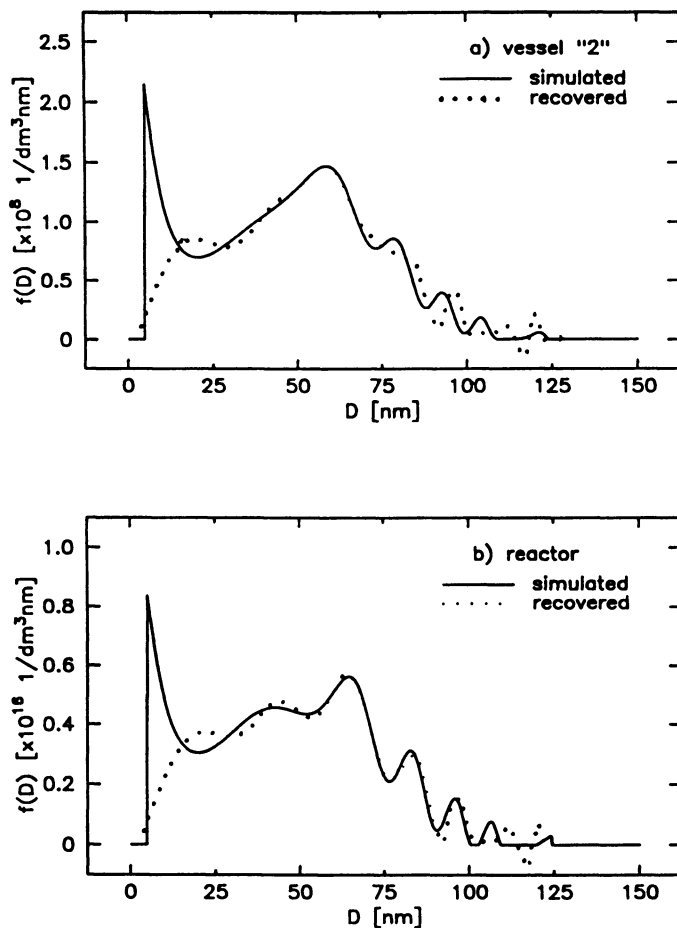


**Figure 10:** Comparison between Simulated and Recovered Particle Size Distributions at  $t/\theta=8.0$ : a) Exit of the Dilution Vessel No 2; b) Reactor.  $\theta/\theta^*=1/3$ .

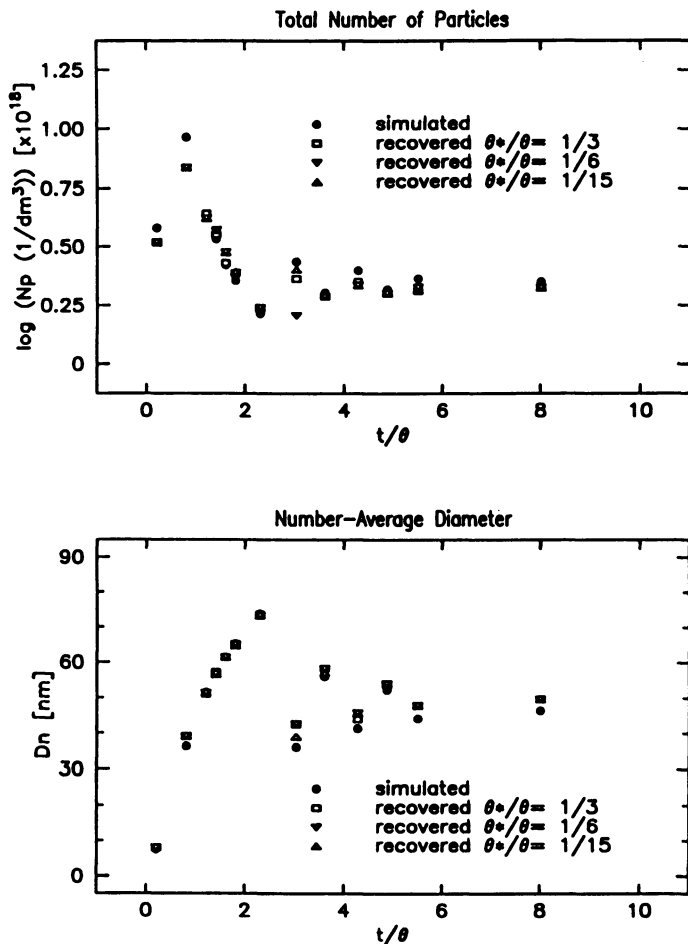


**Figure 11:** Comparison between Simulated and Recovered Leading Moments of the Particle Size Distributions in the Reactor System for several residence times in the Dilution System.

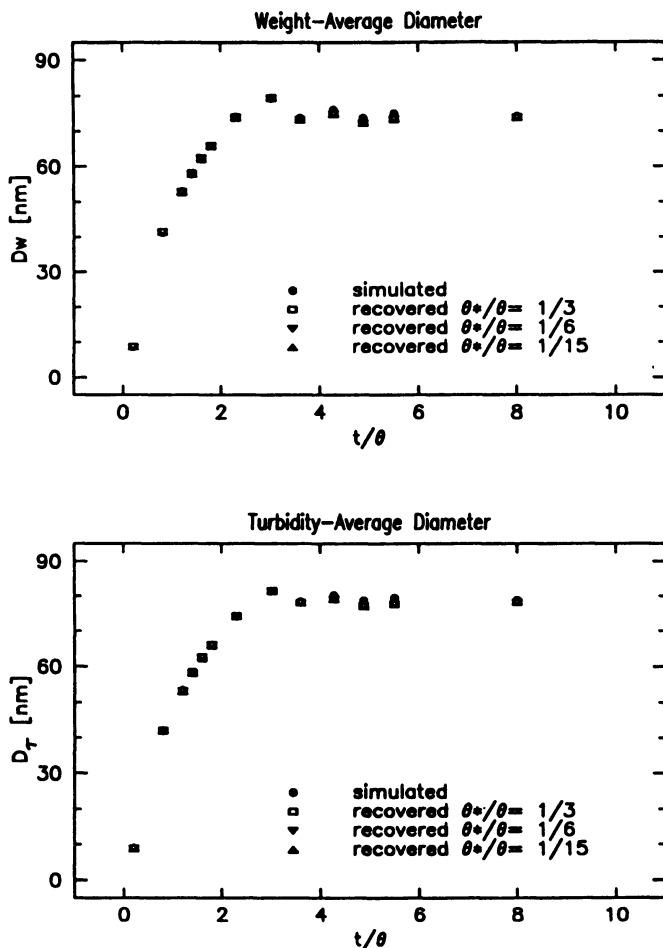


**Figure 12:** Comparison between Simulated and Recovered Leading Moments of the Particle Size Distributions in the Reactor for several residence times in the Dilution System.

to deal with varying flows and flow ratios ranging between  $1 \cdot 10^{-4}$  to  $1 \cdot 10^{-6}$ . The recovery of the PSD in the reactor requires two deconvolution steps. First, the turbidity spectrum must be deconvoluted in frequency in order to obtain the PSD at the exit of the dilution system and then, the PSD must be deconvoluted in time to recover the PSD in the reactor.

From the results presented here, it is evident that the particle size distribution at the exit of the dilution system does not necessarily represent the PSD existing in the reactor at the same time. The larger the residence time in the dilution system, the greater the difference between both distributions. It is also important to notice that a single average diameter, as determined with standard turbidity or dynamic light scattering measurements, may be misleading since these measurements sample higher moments of the PSD.

Clearly, since the complete PSD is recovered, the approach suggested here could be an important tool for the control of latex reactors and for the understanding of the nucleation phenomena.

#### **Acknowledgments:**

This research was supported by the National Science Foundation under Grants RII 8507956 and INT-8602578. Adriana Brandolin received a scholarship from Consejo Nacional de Investigaciones Cientificas y Tecnicas de la Republica Argentina.

#### **Literature Cited:**

1. Elicabe, G.; Garcia-Rubio, L. H. J. Coll. Interphase Sci., 1989, 129, 1.
2. Elicabe, G.; Garcia-Rubio, L. H. Proc. ACS Div Polym. Mats.: Sci and Eng., 1988, 59, 165.
3. Brandolin, A.; Garcia-Rubio, L. H., "Simulation of Reactor-Sampling Systems for Latex Reactors", Internal Report, Center for Materials Development, University of South Florida, U.S.A. 1990.
4. Kiparissides, C.; MacGregor, J. F.; Hamielec, A. E. J. Appl. Polym. Sci. 1979, 23, 401.
5. Rawlings, J. B.; Ray, W. H. Polymer Eng. Sci. 1988, 28, 257
6. Stock, R.S. "Determination of the particle size distribution in polymer latex using quasielastic light scattering and dielectric spectroscopy", Ph.D. Thesis University of Wisconsin-Madison, Wisconsin, U.S.A. 1986.
7. Zollars, R. L. J. Coll. Interphase Sci., 1980, 74, 163.
8. Kourti, T.; MacGregor, J. F.; Hamielec, A.E.; Nicoli, D. F.; Elings, V. B. Proc. ACS Div Polym. Mats.: Sci and Eng., 1988, 59, 160.

9. Nicoli, D. F.; Elings, V. B. Private Communication, 1989.
10. Maron, S. H.; Pierce, P. E.; Ulevitch, I. N. J. Colloid. Sci. 1963, 18, 1470.
11. Inagaki, T.; Arakawa, E. T.; Hamm, R. N.; Williams, M. W. Physical Review B 1977, 15, 3243.
12. Brooks, B. W., Kropholler, H. W.; Purt, S. N., Polymer 1978, 19, 193.

RECEIVED January 14, 1991

## Chapter 5

# On-Line Latex Particle Size Determination by Dynamic Light Scattering Design for an Industrial Environment

David F. Nicoli<sup>1</sup>, Theodora Kourti<sup>2</sup>, Paul Gossen<sup>2</sup>, Jau-Sien Wu<sup>1</sup>, Yu-Jain Chang<sup>1</sup>, and John F. MacGregor<sup>2</sup>

<sup>1</sup>Nicomp Particle Sizing Systems, 75 Aero Camino, Santa Barbara, CA 93117

<sup>2</sup>Department of Chemical Engineering, McMaster University, Hamilton, Ontario L8S 4L7, Canada

The use of on-line dynamic light scattering (DLS) in monitoring latex particle growth in a continuous pilot scale reactor is reported. The weight average diameter of the latex is measured simultaneously using on-line turbidimetry and the results from the two methods are compared. A new design for the on-line DLS apparatus involving the use of a remote sensor and fiber optics, for a more robust performance in industrial environments, is described.

Dynamic light scattering (DLS) also known as photon correlation spectroscopy (PCS) has been widely used during the past twenty years for the determination of the mean particle size or the particle size distribution (PSD) of suspensions with particle diameters in the submicrometer size range (1-16). This technology was confined exclusively to off-line quality control measurements in laboratories. However, the need for on-line measurements has increased recently, especially in the latex industry where the PSD determines the physical properties and therefore the end use of the latex product. Recently, a device for automatic sample acquisition and dilution was developed, designed to interface with a DLS based particle sizing instrument, permitting the on-line use of the method to monitor particle growth during latex production. Results from an on-line application of DLS to a batch latex reactor were shown in our previous publications (17,18) where an average particle diameter was monitored during the production of a poly(vinyl acetate) latex with a narrow particle size distribution. With a short time of data collection the DLS method can provide reasonable size information for such narrow distributions (19). By contrast to batch reactors the PSDs of latexes produced in continuous reactors are usually broad (sometimes bimodal or multimodal) and longer times of data collection are required to analyze these more complex distributions. Furthermore, application of the DLS method to continuous reactors requires continuous use of the sampling system for several hours (or days), without clogging of the components of the fluid circuit. Here we test the capability of this on-line DLS system to function successfully in monitoring latex particle growth in a continuous pilot scale reactor. Results are shown for 10 hours of continuous operation with samples withdrawn every 10 min for particle size analysis by DLS. The particle growth was also monitored independently using on-line turbidimetry, and results from the two methods are compared. In both the batch and continuous applications the automatic sampler diluter was used in conjunction with a modified Nicomp 370/Autodilute Submicron Particle Sizer (NICOMP Particle Sizing Systems, Santa Barbara, CA).

Instruments used for on-line industrial applications must be robust and able to endure harsh environments. We also report here a new design for the DLS apparatus used for on-line particle size determination which is better suited for industrial environments. This design involves the physical separation of the sampling and sensing system (which includes sampling

0097-6156/91/0472-0086\$06.00/0  
© 1991 American Chemical Society

valves, autodiluter, laser source and scattering cell) from the photomultiplier detector, auto-correlator and computer that controls the system and computes the particle size distribution. The sampling and sensing system is located near the reactor in the plant while the central controller is in the analytical laboratory; the two systems communicate with fiber optics.

### Theoretical Background Of DLS

Dynamic light scattering is used to measure the size of submicrometer particles suspended in a liquid medium. The suspension is illuminated by a beam of light and the scattered light intensity is measured as a function of time.

The suspended particles diffuse in random walk fashion due to collisions with molecules of the surrounding liquid medium (Brownian motion). As a result, when the colloidal dispersion is illuminated by a coherent light source the phases of each of the scattered waves (arriving at a detector at fixed angle) fluctuate randomly in time due to the fluctuations of the positions of the particles responsible for scattering. Because these waves mutually interfere, the net intensity of the scattered light,  $I(t)$ , fluctuates randomly in time around a mean value. The technique makes use of the fact that the time dependence of the intensity fluctuations (calculated from the autocorrelation function of the scattered intensity) can be related to the translational diffusion coefficient of the particles and then to the particle size through the Stokes-Einstein equation. Details of the theory of DLS and the experimental setup and examples of applications of the technique can be found in a number of texts (1-4). Here we present only a brief review.

The autocorrelation function  $G^{(2)}(t')$  of the scattered light intensity can be expressed in terms of the normalized first order autocorrelation function,  $g^{(1)}(t')$ :

$$G^{(2)}(t') = \langle I(t)I(t+t') \rangle = B(1 + \beta |g^{(1)}(t')|^2) \quad (1)$$

where  $I(t)$  is the intensity at time  $t$ , and  $t'$  is the time delay. The  $\langle \rangle$  symbol indicates a running sum of products taken at different times,  $t$ . For  $t' \rightarrow \infty$ ,  $G^{(2)}(\infty) = \langle I(t) \rangle^2$ , which is the square of the average scattered intensity and it is equal to the baseline of the autocorrelation function,  $B$ .  $\beta$  is an instrument related constant ( $0 < \beta < 1$ ). For suspensions of uniform particle size,  $g^{(1)}(t')$  is a simple exponentially decaying function of  $t'$ :

$$g^{(1)}(t') = \exp(-\Gamma t') \quad (2)$$

The decay constant  $\Gamma$  is proportional to the translational diffusion coefficient  $D$ , by:

$$\Gamma = D K^2 \quad (3)$$

where  $K$  is the scattering wavevector, which depends on the wavelength of the light source ( $\lambda_0$ ), the solvent refractive index ( $n$ ) and the scattering angle,  $\theta$ :

$$K = 4\pi n \sin(\theta/2)/\lambda_0 \quad (4)$$

For random diffusion of non-interacting particles, the single particle diffusion coefficient ( $D$ ), is obtained from the above equations. If the medium is a newtonian fluid, and the particles are spheres,  $D$ , can be related to the hydrodynamic radius  $R$  via the Stokes-Einstein equation:

$$R = kT/6\pi\eta D, \quad (5)$$

where  $k$  is Boltzmann's constant,  $T$  is the temperature ( $^{\circ}\text{K}$ ) and  $\eta$  is the shear viscosity of the medium. Thus, the particle size of a monodisperse suspension can be easily obtained from the measured autocorrelation function via equations (1) to (5).

For suspensions with broad unimodal or with multimodal distributions, the conversion of the autocorrelation data to PSD is a relatively difficult task and remains an area of active research (4-14). For a polydisperse suspension,  $g^{(1)}(t')$  is a weighted sum of exponentially decaying functions, each of which corresponds to a different particle diffusivity with decay constant  $\Gamma_i$ .

$$g^{(1)}(t') = \int_0^{\infty} F(\Gamma) \exp(-\Gamma t') d\Gamma \quad (6)$$

$F(\Gamma)$  is the normalized distribution of the decay constants of the scatterers in the suspension. The problem of obtaining the PSD from the raw data, in effect, reduces to solving equation (6) for  $F(\Gamma)$ , an ill conditioned problem. A number of algorithms for inverting this equation have been proposed (4-13). There have been also several attempts to improve the resolution of the method (10,11,14). The approach used with significant success in commercially available instruments (Nicomp 370 and others) is based on a Laplace transform inversion of  $g^{(1)}(t')$  using a nonlinear least squares procedure (with a non negative constraint). A review of most of the available algorithms for the determination of  $F(\Gamma)$  from DLS data and an evaluation of their performance for suspensions of unimodal and bimodal distributions can be found in Stock and Ray (15). The particle size distribution of the suspension, on mass or number basis can be easily calculated from the estimated distribution of the decay constants (3,4,14).

Fortunately, in practice one often encounters simple unimodal particle size distributions for which  $F(\Gamma)$  is approximately Gaussian in shape. For these cases the much simpler method of cumulants analysis (16) usually provides a good fit to the autocorrelation function data, yielding moments of the distribution  $F(\Gamma)$ . In this approach,  $\ln g^{(1)}(t')$ , (a linear function for a monodisperse sample) is fitted to a quadratic or cubic function of  $t'$ . The advantage of the cumulants analysis is that it is computationally fast and settles rapidly with improving statistical accuracy in the autocorrelation function. The method gives very accurate results for decay distributions with negligible high order central moments (15).

Commercially available DLS instruments usually employ two approaches to convert the autocorrelation data to PSD: i) the method of cumulants and ii) an algorithm that inverts equation (6), solves for  $F(\Gamma)$  and yields an estimate of the full particle size distribution. The Nicomp 370 computes distributions utilizing both of these approaches and selects one of the computed distributions based on a goodness of fit criterion (19). The first approach is termed Gaussian analysis and the second, Nicomp distribution analysis. The former uses a second order cumulants fit to the data. A chi-squared fitting error parameter ( $\chi^2$ ) is used to test whether this assumption is reasonable. The analysis is a two parameter fit, to estimate the mean diffusivity and a coefficient of variation (measure of the variance) of the distribution of the diffusion coefficients. The mean diffusivity is converted to an intensity weighted mean diameter ( $D_{\text{cm}}$ ). The resulting distribution of diffusion coefficients is converted to a particle size distribution based on intensity, volume (mass), or number weighting and the corresponding average diameters are calculated. The Nicomp distribution analysis employs an algorithm based on a variation of Provencher's technique (7-9). This approach makes no assumption about the shape of the distribution and utilizes a non-linear least squares parameter estimation. It requires longer times to settle because of its greater sensitivity to the noise in the autocorrelation function.

A variety of polydisperse latexes with known particle size distributions were previously analyzed (off-line) in a Nicomp 370 in order to test the accuracy of the above techniques. For unimodal distributions (both broad and narrow) the Gaussian analysis gave a good estimate of the location of the main body of the true particle size distribution on a weight (volume) basis and a good estimate of the weight (volume) average diameter (the estimated value was always within 8% of the true one). The mean diffusion coefficient estimated from the cumulants analysis was correct even for distributions for which the Gaussian assumption does not hold (for example, bimodal distributions). The weight average diameter estimated from the Nicomp analysis was sometimes substantially different from the true one (10-15% error). Furthermore, when the estimated distribution was overlaid with the true one, the larger particles were correctly estimated, but the smaller ones were not included. Detailed discussions and explanations for this behavior can be found in Kourti (19). The Nicomp analysis can detect some bimodal distributions (two populations of particles with significantly different diameters) in a short time, and this is useful when analyzing samples from processes where secondary nucleation may take place. The results from the Gaussian analysis showed better reproducibility and, as expected, settled faster than those obtained from the Nicomp distribution analysis. It was concluded that whenever the value of  $\chi^2$  is small and at the same time the Nicomp analysis does not yield a bimodal distribution with widely separated peaks, the Gaussian analysis can be used to obtain a reliable estimate of the weight average diameter and the main location of the PSD in a short time. Finally, it was shown (19) that for routine analysis,  $D_{\text{cm}}$  (calculated from the mean diffusion coefficient) together with the coefficient of variation estimated from the Gaussian analysis can be used successfully to monitor particle growth during latex production (both for monodisperse and polydisperse latex). In processes where secondary nucleation is likely to occur, the display from the Nicomp analysis can be used, in parallel with the Gaussian analysis to detect the presence of a second generation of particles.



Another objective of our earlier study was to determine how fast the estimated averages of the PSD settle to final values using the two approaches. The Nicomp 370 instrument collects scattered intensity data continuously with a particle size distribution estimated and displayed approximately every 30-45 seconds. It was shown (17,18,19) that 4-5 min of data acquisition is enough for both  $D_{\text{sum}}$  and the weight average diameter from the Gaussian analysis to settle. When the true distribution was bimodal it was observed (19) that the Nicomp analysis displayed two peaks (i.e., gave an indication that the distribution is bimodal) at time less than 2 min. (A bimodal is generally detected immediately. If the intensity contribution of one of the peaks is very small (less than 2%), this peak may later disappear, due to an unfavorable signal to noise ratio)). Although short times of analysis in the Nicomp approach usually yield the correct shape of the PSD, it is very difficult to resolve the correct sizes for the bimodal distribution. Determination of the correct size requires longer analysis times. It is more difficult to resolve accurately the exact volume (mass) ratio of the two populations; more than one solution is possible. However, all of these solutions (which fluctuate with time around a correct mean value) yield the same mean diffusion coefficient (19) and the same intensity average diameter.

The results obtained from a variety of latexes showed that the DLS method can provide estimates of the PSD for polydisperse latexes with narrow or broad continuous distributions in less than 5 - 10 min, at any monomer conversion. For widely separated bimodals, the shape of the distribution is displayed to warn for possible secondary generations. The method is fast, consistent and reproducible and (as discussed below) possesses some other advantages that make it an excellent candidate for on-line applications.

### Suitability Of DLS For On-Line Applications

In order to qualify for on-line applications, a particle sizing technique must possess certain characteristics. It must be fast; the time required for the particle size measurement must be short enough to allow sufficient time for the appropriate control action to be calculated and implemented. Second, the instrumentation must be simple; complicated parts will clog with latex over time (latex is made to adhere). Finally, the measurements must have good reproducibility and no drift should occur with time due to clogging or other malfunction of the components of the fluid circuit.

The DLS technique for particle sizing has a number of inherent advantages over other methods, which make it well suited for automated, on-line applications. First, it is an absolute technique, requiring no calibration. The particle diffusion coefficient and the corresponding particle radius can be calculated directly from the theory. Furthermore the scattering wavevector  $K$  (Equations 3,4) which relates the time scale of the intensity fluctuations to the particle diffusivity,  $D$ , depends on three parameters (laser wavelength, scattering angle and refractive index of diluent), all of which can be held constant over time. The calculation of the corresponding hydrodynamic particle radius  $R$  from  $D$ , (Equation 5) depends on two additional parameters which can also be held constant over time (temperature,  $T$ , and viscosity of diluent,  $\eta$ ). Hence, any well designed DLS instrument should yield consistent, reproducible results over extended periods of time, requiring no calibration.

Second, the diffusion coefficient  $D$ , depends only on the size of a particle (Equation 5) and is independent of its composition (density, molecular weight and refractive index). While the refractive index of the particles will certainly influence the average scattered intensity, it will not affect the particle diffusivity (i.e., the behavior of the intensity fluctuations). Finally, the measured particle diffusivity (and hence the computed particle size, or full PSD) is independent of the concentration of the particles in the suspension, provided that the original suspension is diluted sufficiently to eliminate the effects of multiple scattering and interparticle interactions (either electrostatic repulsions or Van der Waals attractions) on the autocorrelation function.

Clearly, these three intrinsic characteristics of the DLS technique make it ideally suited for on-line measurements, where acquisition and dilution of fresh concentrated samples must be performed automatically and must be immune from maintenance requirements over long periods of time.

For suspensions of submicron particles DLS has a significant advantage over another particle sizing method based on turbidimetry. For latexes of submicron particles for which the ratio of the refractive index of the particles to that of the medium is approximately 1.1, specific turbidity is the only turbidimetric technique that provides reliable results. This technique requires

knowledge of the solids fraction in the sample (19-21). To apply the specific turbidity technique on-line for particle sizing, a known quantity of latex sample must be captured and diluted to a known final volume. A weight average particle diameter can be determined from the optical turbidity of the resulting dilute suspension, provided that the degree of dilution and the optical properties of the suspension are known. By contrast, DLS does not require that the particle concentration in the suspension be known (i.e., it does not require exact dilution of the original latex). Because of the need of exact dilution the sampling system required for turbidimetry is more complicated than that required by DLS. In case of clogging of the metering valve in the former, the dilution factor may change and the calculated particle size will be wrong. In DLS the sampling device is simple and very robust.

The second advantage of DLS over turbidimetry is that the latter method is extremely sensitive to errors in the value of the refractive index,  $n_p$ , of the particles. DLS is independent of  $n_p$  for most latexes. More specifically, the estimated particle size is independent of the refractive index of the particles for monodisperse suspensions. For polydisperse suspensions with any type of PSD, the intensity weighted distribution is independent of  $n_p$ . For distributions expressed on volume or number basis, the error due to uncertainties in the value of the refractive index will be very small in two cases: i) for any type of distribution (unimodal or bimodal - continuous or with separated peaks) with particle sizes smaller than approximately 350 nm (for a laser wavelength of 670 nm), and ii) for any continuous submicron PSD. The error will be larger (but not as large as in turbidimetry) for widely separated bimodal distributions covering regimes beyond 300 nm.

### Sampling Device And Autodilution

On-line particle size analysis using DLS instrumentation requires a proper sampling device capable of automatically acquiring a quantity of concentrated suspension from the reactor and diluting to an optimal final concentration. This concentration must be sufficiently low to avoid multiple scattering and interparticle interactions but large enough to yield a high signal to noise ratio in the autocorrelation function after a relatively short time of data acquisition (typically, just several minutes). The optimal dilution factor can be expected to vary significantly with the properties of the starting concentrated suspension. The average intensity of the scattered light from a diluted sample depends strongly on the PSD, the particle concentration and the ratio of the refractive index of the particles to that of the diluent (water). This requires that the automatic dilution system possess a very wide dynamic range, capable of achieving dilution factors ranging from 100:1 or smaller to 100,000 : 1 or greater. For example, early in the polymerization in a batch reactor the size of particles is small and the polymer concentration low; in this case a relatively low dilution factor is needed. Near the end of the reaction, when the particles have grown and the mass of polymer has increased, higher dilution factors are needed. Furthermore, for the same polymer concentration and the same PSD, different degrees of dilution may be needed for different polymers.

On-line application of DLS was made possible by using a combination of a sampling device and autodilution mechanism which were described in detail in previous reports (17-19). The autodilution mechanism is well suited to meet the requirements discussed above. A modified version of this computer controlled mechanism, designed to operate in industrial environments, is described later.

In fully automatic mode the sampling cycle commences with the capture of an arbitrary small quantity of concentrated sample from the latex reactor. Following a short predilution step, the partially diluted sample is then passed to the Autodiluter, where the dilution factor is allowed to increase continuously until the scattering intensity falls to a preset level appropriate for the digital autocorrelator. After a predetermined delay to achieve temperature equilibration in the scattering cell, the autocorrelation function is measured by the Nicomp analyzer. At a predetermined time the particle size distribution results are printed, the raw data stored on diskette and the system is flushed with fresh diluent. The computer controller then awaits the preprogrammed start of the next measurement cycle.

Because of its design, our on-line DLS based system with Autodilution should yield results of comparable accuracy and reproducibility to those obtained in an off-line laboratory setting. That is, once a fresh latex sample has been captured and prediluted by the sampler / prediluter device, its treatment by the Autodilution /DLS device is identical to that which occurs on a lab bench when concentrated samples are introduced manually into the system.

### On-Line Application Of DLS To A Continuous Latex Reactor

In our previous work the DLS technique was used to monitor on-line the particle growth during the production of poly(vinyl acetate) latex in a batch reactor (17,18). The sampling cycle in that first application was 17 min, of which approximately 5 minutes were devoted to data collection and analysis. Here, we report the use of on-line DLS to monitor particle growth during poly(vinyl acetate) latex production in a continuous stirred tank reactor. On-line turbidimetry is also used to measure the size of the latex particles simultaneously with DLS, and the results from the two methods are compared (22).

A simplified schematic diagram of the experimental setup is shown in Figure 1. The reactor is a 500 ml jacketed stainless steel vessel. Steam heated water circulates in the jacket. The reaction temperature is controlled by manipulating the flow of steam to the jacket. The reactants (initiator solution, emulsifier solution, monomer and water) are pumped from storage tanks to the reactor using four positive displacement pumps; they are mixed in the reactor by a pitched blade agitator. This small reactor is the first in a series (train) of continuous pilot scale reactors used for the production of poly(vinyl acetate) latex. This reactor is used as a "seed" reactor. In simple terms this is the reactor where the particles are nucleated. The other reactors where the latex particles grow have larger volume (1 gallon). The rationale for the use of a seed reactor has been discussed elsewhere (24) and is beyond the scope of this report. For this work we used the seed reactor only to produce a low solids latex, at relatively high conversion (90 to 100 %). The residence time in this seed reactor was approximately 8 minutes, and the reaction temperature was 60 °C.

The latex exits from an overflow tube at the top of the reactor and then flows through an on-line densitometer. Two sampling devices are used to withdraw latex samples from the exit of the densitometer for on-line particle size analysis by turbidimetry and DLS. A detailed description of the reactor setup and the apparatus used for sampling and measurements by turbidimetry, can be found in Gossen (23). The sampling system for on-line DLS measurements has been described before (17,18) and will also be shown later in Figure 3. Filtered, deionized, distilled water (which may also contain hydroquinone, a radical scavenger) is the diluent for DLS and turbidimetry. This water is at room temperature and quenches the reaction in the sample; we assume no further growth of the particles after sampling. The sampling cycle was 5 min for turbidimetry and 10 min for DLS, with 4 minutes of the latter devoted to data collection and analysis. The remaining time is devoted to sample autodilution, temperature equilibration and flushing of the system.

The particle size of the produced latex depends on several parameters, such as the temperature of the reaction, the concentrations of monomer, emulsifier and initiator and the presence of impurities. During this experiment, we deliberately manipulated some of these parameters in order to cause changes in the mean particle size of the latex and thus to ascertain whether turbidimetry and DLS could detect these changes.

In Figure 2 we plot the measured variables (solids volume fraction and average particle diameters (in nm) as measured by DLS and turbidimetry) and the manipulated variables (concentrations of emulsifier and initiator, and the monomer fraction in the feed streams), as a function of elapsed time. The diameters plotted are weight average diameters obtained by turbidimetry and intensity ( $D_{\text{int}}$ ) and weight average diameters (calculated from the Gaussian analysis), obtained by DLS. The fact that the weight and intensity averages are significantly different from each other indicates that the particle size distributions are relatively broad, as expected for latex produced in a continuous reactor.

Initially, the manipulated variables were kept constant for several hours, from the start of the reaction to the point at which the reactor reached steady state. At time  $t = 4$  hours (point A) we increased the emulsifier concentration and the monomer feed fraction. The combination of these two changes seems to have no significant net effect on the weight average diameter, while the solids fraction increases, as expected, due to the monomer fraction increase. (The net effect on the particle size was not significant because the two step changes had an opposite effect on the particle size: higher monomer concentration should result in larger particles but higher emulsifier concentration should result in smaller particles). At  $t = 5$  hours (point B) a large decrease in the emulsifier concentration combined with a small decrease in the monomer feed fraction, resulted in an increase in the average particle size, as expected. (Decreasing the emulsifier concentration results in a decrease in the concentration of free soap and therefore in a decrease in the concentration of micelles, which in turn results in a smaller number of generated particles and therefore larger particles). The change in the solids fraction (due to the decrease

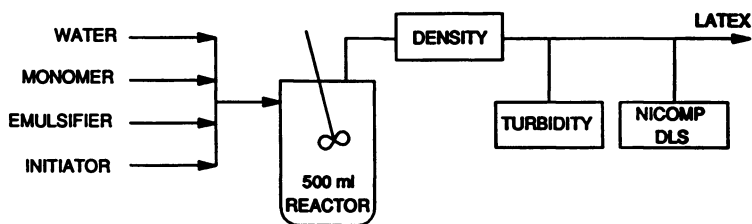


Figure 1. Simplified schematic diagram of the experimental setup for on-line density measurements and particle size measurements, using DLS and turbidimetry, during latex production.

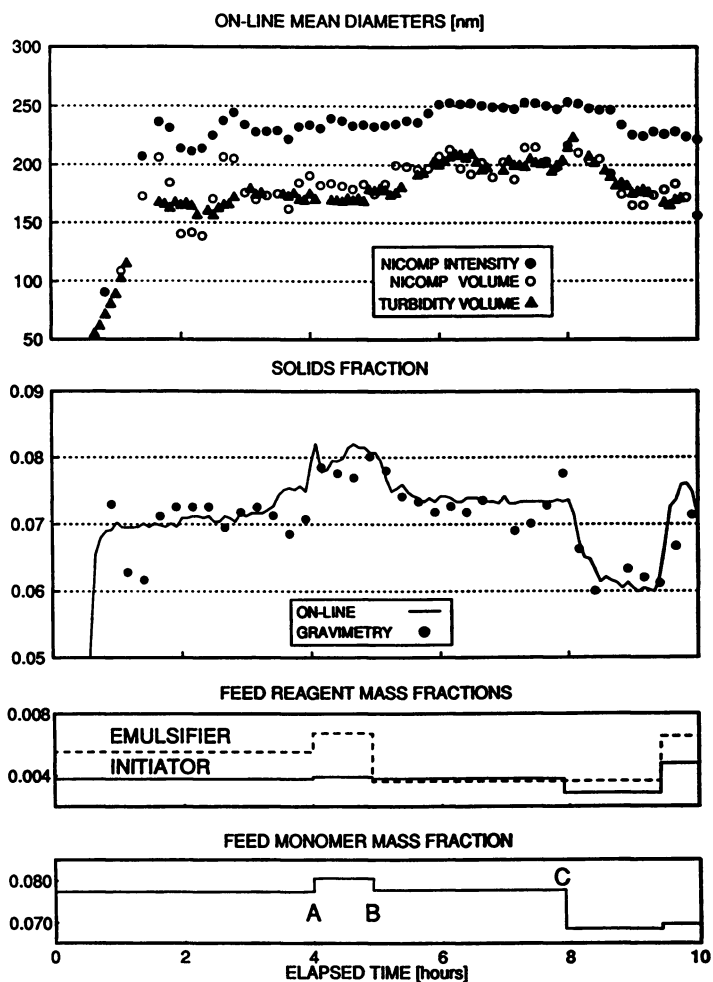
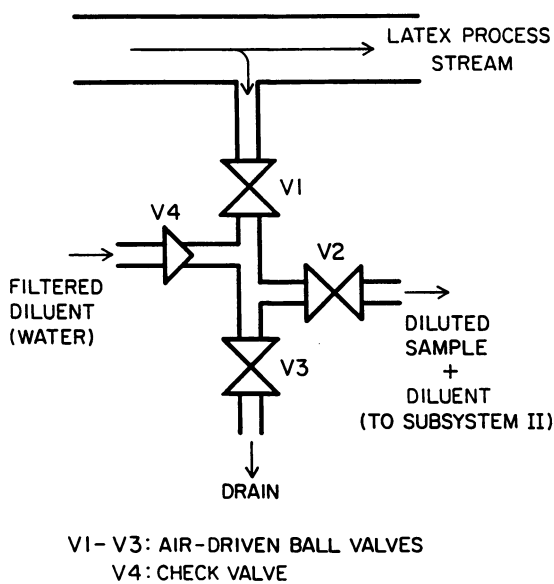


Figure 2. Measured and manipulated variables plotted as a function of reaction time.



**Figure 3.** Sampler and prediluter (subsystem I) for on-line DLS measurements.

in monomer concentration) was detected almost immediately, while the change in the average particle size was detected approximately 25 minutes later. The averages which we monitor are calculated from the higher moments of the distribution; therefore, in the presence of new, larger particles in the reactor, these averages are expected to change faster than others (i.e., number average). The delay of 25 minutes (approximately 3 reactor residence times) does not mean that the effect of the step change on particle size went undetected for this length of time; it simply means that several residence times were required for the changes in the emulsifier concentration to affect the weight average of the particle size distribution.

At  $t = 8$  hours (point C), a decrease in the monomer feed fraction and in the initiator concentration resulted, eventually, in smaller particle sizes and, of course, in smaller solids fraction. The effect on the particle size can be explained as follows. A decrease in the monomer feed fraction means less polymer per particle (smaller volume) for the same number of particles. A decrease in the initiator concentration has a positive effect on the particle stability (less salt present in the medium) and, at reaction temperature of  $60^\circ\text{C}$ , is expected either to have no effect on the particle size or, to result in a decrease in the particle size (19). Therefore, the overall effect is expected to be a decrease in particle size. The change in the solids fraction, again, is detected almost immediately; the change in the particle size is also detected relatively quickly by the weight averages. The intensity average diameter is expected to reflect these changes later, because of the higher moments of the PSD that are used for its calculation.

Because of the high dilutions we used and the high solubility of vinyl acetate, we were dealing with monomer free particles at all conversions. The two methods showed comparable results in following the changes in the particle size due to the step changes in the manipulated variables. In both cases we plot average diameters. The weight average is the only average we can obtain from turbidimetry for poly(vinyl acetate) latex with small particles (19-21). From the DLS analysis we obtain the weight and intensity averages, and their ratio can give an idea of the spread of the distribution.

The weight average diameter obtained from turbidimetry shows a smooth response. The fluctuations in the diameter values are very small when the system reaches steady state. Notice that the intensity average from DLS also shows a smooth behavior, but the weight average from DLS fluctuates around a mean value when the system reaches steady state. This behavior is expected. These fluctuations are within the standard deviation of the fluctuations observed for a single sample. It was shown (19) that when average diameters obtained from DLS, for a given sample, are plotted as a function of the time of data accumulation, the variance of the fluctuations around a mean value is higher for the weight average than it is for the intensity average. The high variance in the volume weighted averages is observed because this average is calculated from  $D_{\text{w, max}}$  and the coefficient of variation (a measure of the breadth of the distribution). While the intensity weighted mean diameter converges relatively quickly to its final value, the coefficient of variation requires longer times to settle and varies more because of the presence of aggregates, dirt and other effects; these variations significantly influence the weight average diameter.

Both the DLS and turbidimetry samplers performed continuously for 10 hours with no clogging of the sampling valves. In turbidimetry the sampler/diluter operated continuously for 100 cycles at 5 minute intervals, without any problems. (To date it has operated flawlessly for over 500 cycles without need for maintenance). The performance of the DLS sampling device was similar.

### Modification Of On-Line DLS Instrumentation For Industrial Environments

The particle size results reported here for the emulsion polymerization of vinyl acetate in a continuous pilot-scale reactor, were obtained using a commercial DLS instrument (Nicom Model 370/Autodilute Submicron Particle Sizer, Particle Sizing Systems, Santa Barbara, CA), modified for use with a valve sampler / prediluter attached directly to an effluent line exiting the continuous reactor. This apparatus is very similar to that employed for an earlier study (17,18). Following our initial work with the continuous reactor, we have modified our on-line instrument to make it better suited to more demanding industrial environments. The valve sampler / prediluter (subsystem I) remained unchanged, but we have physically separated into two packages, or modules, the functions previously performed by the Nicom 370 instrument. One module (subsystem II) now includes the functions of autodilution and illumination of the sample cell and is designed to be located close to the process reactor or effluent line. The other

module (subsystem III) performs the functions of scattered light detection, autocorrelation and PSD analysis, and is typically located in a central control facility. This configuration which is more effective for typical process environments, is now described in detail.

**Subsystem I: Sampler and Prediluter.** The sampling device, shown in Figure 3, consists of three pneumatically-operated ball valves and a low-pressure check valve, connected to form a simple mixing chamber (all parts of stainless steel). The valves are powered by compressed air (80 PSI), controlled by electrically-operated solenoid actuators (see subsystem II below). Air driven valves were chosen because they are explosion proof and therefore meet the safety needs for a typical latex production facility. Filtered water (0.2-0.4  $\mu\text{m}$ , large area filter) feeds the mixing chamber and is used to predilute a quantity of fresh, concentrated latex which is captured by opening the ball valve connected to the process reactor or output stream. This low pressure water supply also serves to transmit the prediluted aliquot of latex to an autodilution mechanism located in subsystem II.

**Subsystem II: Remote Autodilution and Light Scattering Sensor.** The fluid output of the sampler/prediluter above, consisting of fresh, prediluted latex followed by diluent, is first pulled into an autodilution mechanism and then into a flow-through light scattering cell by an electrically powered gear pump (flow rate adjustable, 50-200 ml/min), as shown in Figure 4. The proprietary autodiluter (patents issued and pending, 26) provides a continuous dilution of the latex sample until the intensity of the scattered light falls to an optimal, preset value. The final particle concentration is chosen to be sufficiently low to avoid multiple scattering and interparticle interactions, but large enough to yield an acceptable light scattering level and a high autocorrelation counting rate.

A laser beam is focussed into the scattering cell which contains the diluted sample. A 5-mW laser diode ( $\lambda = 670 \text{ nm}$ ) is used as the illuminating source. A portion of the scattered light is captured at a  $90^\circ$  angle and transmitted to subsystem III for subsequent detection, autocorrelation and analysis. The scattering cell consists of a 7 mm square, polished-glass, flow-through cuvette in thermal contact with a black-anodized aluminum cell holder. The temperature of the latter is held constant ( $\pm 0.2^\circ\text{C}$ ) by a thermoelectric (Peltier) element, using a feedback controller. A cable consisting of just two optical fibers is used to provide all communications between the remote sensor (subsystem II) and the central controller - analyzer (subsystem III).

Optical fiber #1 is used to convey the scattered light signal directly to the a PMT detector, located in subsystem III. Judicious use of a pinhole aperture together with the optical fiber allows light to be collected from approximately one coherence area, resulting in a high correlation efficiency. Optical fiber #2 provides digital communication from the controller in subsystem III to subsystem II (encoded signals which set the sample cell temperature, activate the laser diode, operate the flow pump and control the three electrically-powered solenoid actuators which activate the air-driven ball valves in the sampler/prediluter of subsystem I). The use of optical fibers rather than electrical conductors for communication between subsystems II and III is advantageous for three principal reasons: 1) immunity to electrical interference in potentially harsh process environments; 2) explosion-proof operation (providing safety in the presence of flammable monomer vapors, with only subsystem II needing to be housed in a special enclosure); 3) simplification of the remote sensor hardware, where the detector and the preamplifier / discriminator can be transferred to subsystem III, thereby improving the economics of multiplexing (with several remote sensors able to feed one centralized detector / autocorrelator / analyzer).

**Subsystem III: Central Detector, Autocorrelator and PSD Analyzer.** This last subsystem, shown in Figure 5, contains the most critical elements of the on-line particle sizing system. Its main components include a photomultiplier (PMT) detector and preamplifier / discriminator (with computer-controlled sensitivity); a 64 channel, 7 bit digital autocorrelator with measured baseline and dedicated microcomputer (MOT 6809) for signal management; and main system computer (MOT 68000) for deconvolution of the autocorrelation function and associated particle size distribution analysis (using both the cumulants analysis and the Nicomp analysis for multimodal PSDs). A XT or AT type computer (IBM-compatible, operating under MS/DOS) provides i) serial communication with this central control unit, subsystem III, ii) control of the sampler / prediluter and control of the remote autodiluter / light scattering sensor (subsystem II) by optical fibers, and iii) display and data storage capabilities.

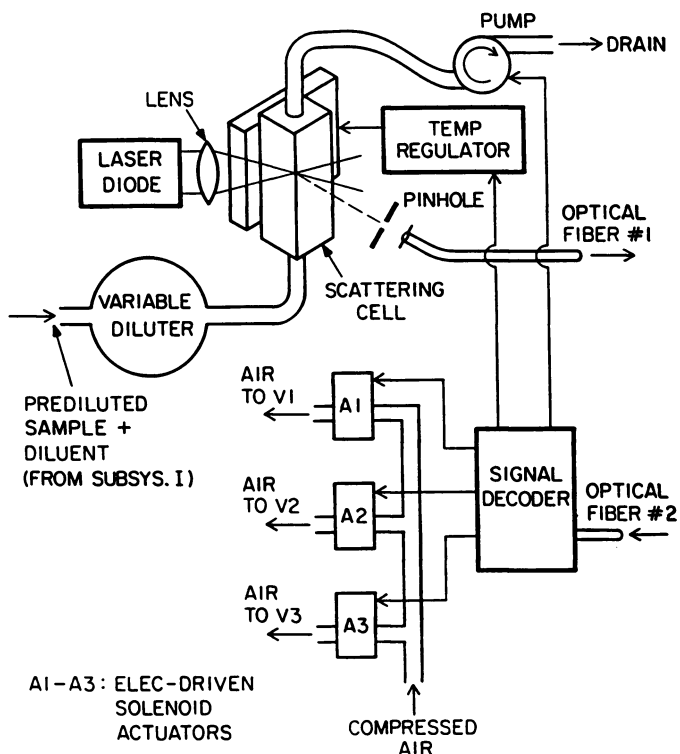


**Figure 4.** Autodilution and light scattering sensor (subsystem II) for on-line DLS measurements.

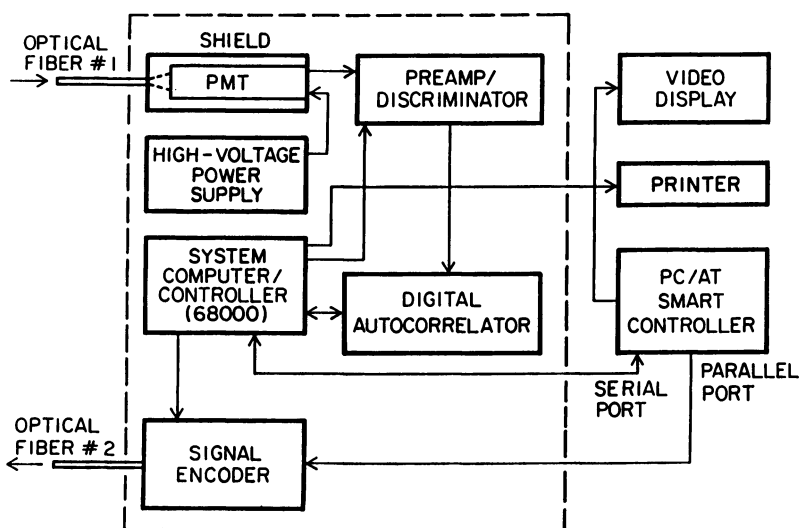


**Figure 5.** Photomultiplier detector, autocorrelator and PSD analyzer (subsystem III) for on-line DLS.



### Concluding Remarks

On-line DLS has been applied in combination with on-line turbidimetry to measure particle growth in latex reactors. Weight and intensity average diameters were monitored as function of time. On-line DLS gives results comparable with off-line DLS. Therefore the method can be applied on-line to perform analysis of similar quality. The weight average diameters obtained using DLS for poly(vinyl acetate) latex were in very good agreement with the values obtained using on-line turbidimetry.

The new modifications described here for the on-line DLS instrument should result in more robust performance in industrial environments.

### Literature Cited

1. Chu, B. (1974). Laser Light Scattering, Academic Press, New York.
2. Pecora, R. (Ed.) (1985). Dynamic Light Scattering. Applications of Photon Correlation Spectroscopy, Plenum Press, New York.
3. Berne, B.J. and Pecora, R., Dynamic Light Scattering, John Wiley, New York, 1976.
4. Dahneke, B.E. (Ed.) Measurement of Suspended Particles by Quasi - Elastic Light Scattering, Wiley - Interscience, New York, 1983.
5. Pike, E.R. In Scattering Techniques Applied to Supramolecular and Non-Equilibrium Systems. (S.H. Chen, R. Nossal, and B.Chu, Eds). Plenum Press, New York, 1981.
6. Ostrowsky, N., Sornette, D., Parker, P. and Pike, E.R., Opt. Acta, **28**, 1059 (1981).
7. Provencher, S.W., Hendrix, J., and De Mayer, L., J.Chem. Phys., **69**, 4273 (1978).
8. Provencher, S.W., Macromolekulare Chemie, **180**, 201 (1979).
9. Provencher, S.W., Computer Phys. Commun. **27**, 213-227, 229-242 (1982).
10. Morrison, I. D., Grabowski, E.F., and Herb, C. A., Langmuir, **1**, 496-501 (1985).
11. Herb, C.A., Berger, E.J., Chang, K., Morrison, I.D. and E.F. Grabowski In Particle Size Distribution - Assessment and Characterization (Provder, Th., Ed.), ACS Symposium Series, 332, Washington, D.C., 1987. 89-104.
12. Gulari, E., Gulari, E., Tsunashima, Y., and Chu, B., J.Chem.Phys., **70**, 3965 (1979).
13. Gulari, E., Gulari, E., Tsunashima, Y., and Chu, B., Polymer, **20**, 347 (1979).
14. Bott, S.E. In Particle Size Distribution - Assessment and Characterization, (Provder, Th., Ed.), ACS Symp. Series, 332, Washington, D.C., 1987. 74-88.
15. Stock, R.S. and Ray, W.H., J. Polym. Sci.: Polym. Phys. Edit. **23**, 1393 (1985).
16. Koppel, D.E., J. Chem. Phys., **57**, 4814 (1972).
17. Kourti, T. MacGregor, J.F., Hamielec, A.E., Nicoli, D.F., and Elings, V.B., " On-Line Particle Size Determination in a Latex Reactor using Dynamic Light Scattering", ACS PMSE Division Proceedings, **59**, 160 (1988).
18. Kourti, T. MacGregor, J.F., Hamielec, A.E., Nicoli, D.F., and Elings, V.B., In Polymer Characterization. Advances in Chemistry Series, **227**, (C.Craver and T.Provder, Eds.), Chapter 7, ACS Washington, D.C., 1990.
19. Kourti T., "Polymer Latexes: Production by Homogeneous Nucleation and Methods for Particle Size Determination", Ph.D. Thesis, McMaster University, Hamilton, Ontario, Canada, 1989.
20. Kourti, T., MacGregor, J.F., and A.E. Hamielec, " An Investigation on the Capability of Turbidimetric Techniques to Provide the Full PSD", ACS Symposium Series, 1991 (This volume).
21. Kourti, T., and MacGregor, J.F., " Particle Size Determination using Turbidimetry: Capabilities, Limitations, Evaluation for On-line Applications", ACS Symposium Series, 1991 (This volume).
22. These results were first shown in the 199 ACS National Meeting, in the Symposium for Particle Size Assessment and Characterization, held in Boston, Ma., in April 1990.
23. P.D. Gossen, "On-Line Instrumentation for Latex Reactors", Ph.D. Thesis, McMaster University, Hamilton, Ontario, Canada, 1991.
24. Pollock, M.J., " Modelling and Control of Sustained Oscillations in the Continuous Emulsion Polymerization of Vinyl Acetate", Ph.D. Thesis, McMaster University, Hamilton, Ontario, Canada (1983).
25. D. F. Nicoli and V. B. Elings, U.S. Patent #4,794,806; Jan. 3, 1989, "Automatic dilution systems". Foreign Patents Pending.

RECEIVED May 14, 1991

## Chapter 6

# Fiber Optic Dynamic Light Scattering from Concentrated Dispersions

## Potential for On-Line Particle Size Measurement

John C. Thomas

Brookhaven Instruments Corporation, 750 Blue Point Road,  
Holtsville, NY 11742

The method of fiber optic dynamic light scattering is outlined and its application to particle size measurement in concentrated dispersions is described. We present results of particle size measurements during emulsion polymerization and crystallization reactions. These results indicate that the fiber optic dynamic light scattering technique has potential for use in on-line particle sizing applications.

Particle size plays a fundamental role in most industrial applications of polymeric and colloidal materials. To satisfy the demand for particle size information, a large range of techniques is available (1-3). These all have their relative advantages and disadvantages, which, ultimately determine their suitability for a particular application. For example, during the last ten or so years, dynamic light scattering (*DLS*) has enjoyed wide usage, particularly in the sub-micrometre size range. The popularity of the *DLS* technique arises because it is rapid, absolute and, with modern instrumentation, simple to use (3,4). The principal disadvantage of the technique is its inherent low resolution.

One characteristic that most particle sizing techniques have in common is that they may only be applied to dilute systems, i.e., typically much less than 0.1% solids. This precludes their use in on-line or at-line applications where the solids concentration is more often in the range ~20%-70%. It also has the undesirable consequence that particle size is invariably measured under physical conditions which are vastly different from those under which the material is produced and ultimately used. In the case of polymeric materials, many sensors

NOTE: This chapter is Part 4 in a series.

0097-6156/91/0472-0098\$06.00/0  
© 1991 American Chemical Society

are available for monitoring parameters such as temperature, pressure, flow, density, viscosity, composition etc. directly in the reactor (5). However, sensors for monitoring particle size under these conditions are essentially non-existent.

A fast, non-invasive technique such as light scattering is a prime candidate for development as an on-line sizing technique. Indeed, *DLS* has been used to follow particle size during emulsion polymerization using a sophisticated dilution scheme (6). The primary disadvantages of this approach would appear to be the long time delay between measurements (10-12 minutes) and the plumbing required to achieve the dilution.

With the aid of fiber optics it is possible to perform *DLS* measurements directly on concentrated dispersions (7-10). Here an optical fiber carrying the incident light has its tip placed in the sample and either the same or a different fiber collects the backscattered light from the sample. These measurements are complicated by the possibility of multiple scattering, particle interactions and a changing heterodyne/homodyne ratio in the detected signal (9). Nevertheless, it is possible to determine useful information in many situations. In the following we outline the method of fiber optic dynamic light scattering (*FODLS*) and present some typical results of these measurements on concentrated dispersions.

### Basic Theory Of *DLS*

The fundamental quantity measured in a *DLS* experiment is the photocount autocorrelation function (*ACF*) of the scattered light

$$g^{(2)}(\tau) = \frac{\langle n(0)n(\tau) \rangle}{\langle n \rangle^2} \quad (1)$$

$n(\tau)$  is the photon count measured at time delay  $\tau$ . The dynamics of the scattering system are manifested in the electric field *ACF*,  $g^{(1)}(\tau)$ . The relationship between  $g^{(1)}(\tau)$  and  $g^{(2)}(\tau)$  depends on the method of detection being used.

*DLS* measurements may be performed in the homodyne or heterodyne mode. Homodyning occurs when only scattered light falls on the photodetector. In heterodyning a strong, unscattered local oscillator signal is superimposed on the scattered light at the photodetector. In general, when a local oscillator signal is present, there will be a mixture of homodyne and heterodyne components in the measured  $g^{(2)}(\tau)$  and

$$g^{(2)}(\tau) = 1 + \frac{b[2\langle n_s \rangle n_{LO} g^{(1)}(\tau) + \langle n_s \rangle^2 |g^{(1)}(\tau)|^2]}{\langle n \rangle^2} \quad (2)$$

Here  $b$  is an instrumental constant of order 1,  $n_{LO}$  is the (constant) local oscillator count rate,  $\langle n_s \rangle$  is the average scattered light count rate, and

$$\langle n \rangle = n_{LO} + \langle n_s \rangle \quad (3)$$

is the total photon count rate.

For a dilute suspension of monodisperse, non-interacting spheres

$$|g^{(1)}(\tau)| = \exp(-\Gamma\tau) \quad (4)$$

and the decay constant is

$$\Gamma = K^2 D \quad (5)$$

where  $D$  is the particle diffusion coefficient and

$$K = \frac{4\pi n \sin(\theta/2)}{\lambda_0} \quad (6)$$

is the magnitude of the scattering vector. Here  $n$  is the refractive index of the suspending liquid,  $\theta$  is the scattering angle and  $\lambda_0$  is the laser wavelength. For spheres,  $D$  is related to the particle radius,  $r$ , by the Stokes-Einstein relationship

$$D = \frac{k_B T}{6\pi\eta r} \quad (7)$$

Here  $k_B$  is the Boltzmann constant,  $T$  the absolute temperature and  $\eta$  is the viscosity of the suspending liquid. This equation provides the basis for particle sizing with *DLS*.

Note that the relative amplitude of the two time-dependent terms in Equation 2 is determined by the ratio  $n_{LO}/\langle n_s \rangle$ . When  $n_{LO}/\langle n_s \rangle \gg 1$ , the first term dominates and heterodyning occurs. Conversely, when  $n_{LO}/\langle n_s \rangle \ll 1$ , the second term dominates and homodyning occurs. Note also that, since the homodyne term is basically the square of the heterodyne term, it will decay twice as rapidly as the latter term. Thus, the fundamental practical difference between a homodyne and a heterodyne measurement is that the *ACF* decays twice as rapidly in the former case as it does in the latter case.

The complexity of *FODLS* measurements on concentrated dispersions makes it difficult to model the *ACF*. Here we resort to simply determining a mean decay constant,  $\Gamma_{av}$ , using the method of cumulants (11-12) and calculate an apparent diffusion coefficient,  $D_{app}$ , and particle size using Equations 5 and 7 respectively.

### Experimental Arrangement

Figure 1 shows the optical setup used in this work. It is based on a three-port, single-mode fiber optic system containing a 1:1 beam splitting directional coupler. The output of the 5mW HeNe laser is coupled into the fiber on the two-port side, passes through the coupler, out the fiber on the one-port side and

into the sample being measured. Backscattered light from the sample returns up the same fiber to the coupler at which point half goes back towards the laser and is lost and half goes to the photomultiplier detector (*PMT*). The output of the photomultiplier goes through an amplifier-discriminator (*A/D*) and on to a Brookhaven Instruments *BI-2030AT* digital correlator. The correlator computes the *ACF* of the scattered light.

The fiber optic system generates a large backscattered signal from reflections at the fiber end face and from scattering within the coupler. This constitutes a local oscillator signal which beats with the light scattered from the sample and gives rise to a heterodyne component in the detected signal.

### Results and Discussion

To test the operation of the *FODLS* system, measurements of  $D_{app}$  were made on an ~170nm diameter latex sphere sample as a function of volume fraction,  $\phi$ , over the range  $5.8 \times 10^{-5}$  to 0.43, i.e., four orders of magnitude. As reported earlier (9), we observed a pronounced variation of  $D_{app}$  with  $\phi$ . These results are reproduced in Figure 2, which shows  $D_{app}$  and the amplitude of the time-dependent component of the *ACF* as a function of  $\phi$ .  $D_{app}$  is normalized to  $D_o$ , the value of the diffusion coefficient measured in dilute suspension in a normal *DLS* experiment.

From these data we were able to draw a number of conclusions. At the lowest concentration measured, the backscattered light was insignificant compared with the inherent local oscillator signal from the fiber. In this case the time dependence of  $g^{(2)}(\tau)$  is dominated by the second (heterodyne) term in Equation 2 and our data analysis, which arbitrarily assumed a homodyne signal, would yield a value for  $D_{app}$  which is half the true value,  $D_o$ . This is what was observed. With increasing  $\phi$ ,  $\langle n_s \rangle$  increases because there is more scattered light, whereas  $n_{LO}$  remains constant, so that the third (homodyne) term in Equation 2 contributes more and more to the time dependence of  $g^{(2)}(\tau)$  and the second (heterodyne) term contributes less and less. Eventually the homodyne term will dominate and the value obtained for  $D_{app}$  will approach  $D_o$ . This occurs at  $\phi > 10^{-3}$ . Beyond this point any changes in  $D_{app}$  cannot be due to the changing heterodyne/homodyne mix and are ascribed to the dynamics of the concentrated suspension. Thus, the decrease in  $D_{app}$  which occurs for  $\phi > 10^{-1}$  is due to the behavior of the suspension. Note that, in the region  $10^{-3} < \phi < 10^{-1}$ ,  $D_{app}$  is fairly constant and within 10-20% of  $D_o$ . This means that, over a range of two orders of magnitude in  $\phi$ , a reliable value for  $D_{app}$ , and hence particle size, can be obtained.

To assess the potential of the *FODLS* technique for monitoring particle size in a process situation, measurements were made over the course of a latex emulsion polymerization reaction and compared with the particle size measurements obtained from *DLS* on the diluted samples (10). The *FODLS* measurements were made with a commercial instrument, the Brookhaven Instruments *BI-FOQELS*, which has an optical setup similar to that of Figure 1. The *DLS* measurements were made with a Brookhaven Instruments *BI-90* Particle Sizer. The reaction was a standard styrene-acrylonitrile polymerization

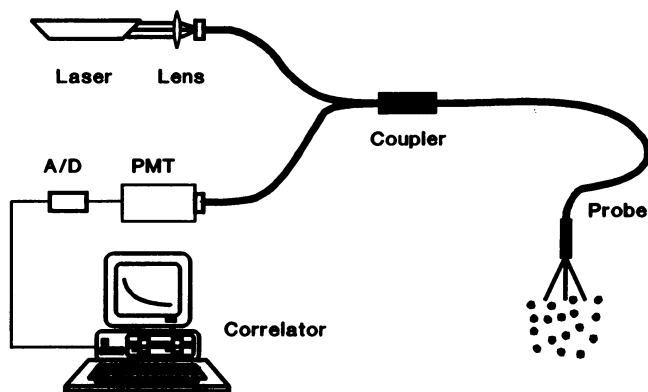


Figure 1. Experimental setup for *FODLS* experiments. (Reproduced with permission from Ref. 10. Copyright 1990 Optical Society of America.)

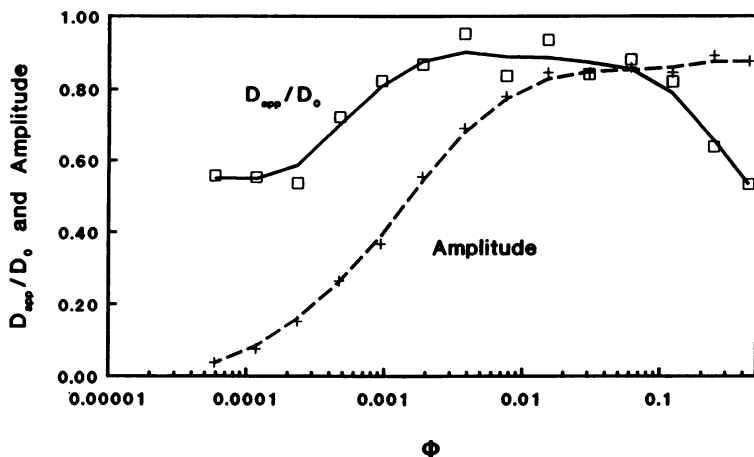


Figure 2. Apparent diffusion coefficient,  $D_{app}$  (□), and time-dependent amplitude (+) of the *ACF* as a function of the volume fraction,  $\phi$ , for  $\sim 170$  nm latex spheres. (Reproduced from Ref. 9. Copyright 1989 American Chemical Society.)

and aliquots were drawn periodically from the reactor after the initiator was added. The *FODLS* measurements were made directly on the undiluted samples and the *DLS* measurements were made on a diluted portion of the samples.

Figure 3 shows the particle size determined by *FODLS* and *DLS* as a function of reaction time. Evidently the *FODLS* results parallel the *DLS* results and reliably follow the growth of the latex particles during the reaction. In particular, the *FODLS* measurements clearly detect the point where the latex particle size reaches its maximum and the reaction is complete. Thus the *FODLS* technique is able to monitor particle size in a situation where both the size and the concentration of the particles are changing.

**Table I.** *FODLS* measurements of particle size during pigment crystallization

Sample	T (°C)	Time (hr)	Diameter (nm)	
			<i>FODLS</i>	<i>DLS</i>
a	40	1.5	203 ± 24	196
b	60	"	182 ± 16	173
c	80	"	208 ± 14	220
d	100	"	252 ± 23	264
e	"	4	231 ± 12	224
f	"	8	249 ± 10	248
g	"	16	252 ± 14	256
h	"	28	251 ± 12	254
i	"	52	303 ± 30	253

The *FODLS* technique has also been used to study the effect of temperature and incubation time on the growth of crystals of pigment material (Horn, D. and Weise, H.; personal communication). Table I shows both *FODLS* and *DLS* results of particle size measurements during crystallization of red pigment material. Samples *a*, *b*, *c* and *d* were incubated for 1.5 hrs at 40°C, 60°C, 80°C and 100°C respectively. Samples *e-i* were held at 100°C and incubated for different times. The measurements were made at 23°C and the pigment concentration was approximately 0.6% by weight. The *FODLS* measurements were made directly on the undiluted material using a *BI-FOQELS*. The samples were then diluted 250 fold and *DLS* measurements were performed at a scattering angle of 90° using a *BI-2030AT* correlator and an ALV goniometer. The *FODLS* results are the mean and standard deviation of 10 measurements and the *DLS* results are from one measurement on each sample.

As can be seen from Table I, the *FODLS* particle size results agree well with those from *DLS* and faithfully monitors the particle size during the crystallization process. Furthermore, the *FODLS* data are highly reproducible;

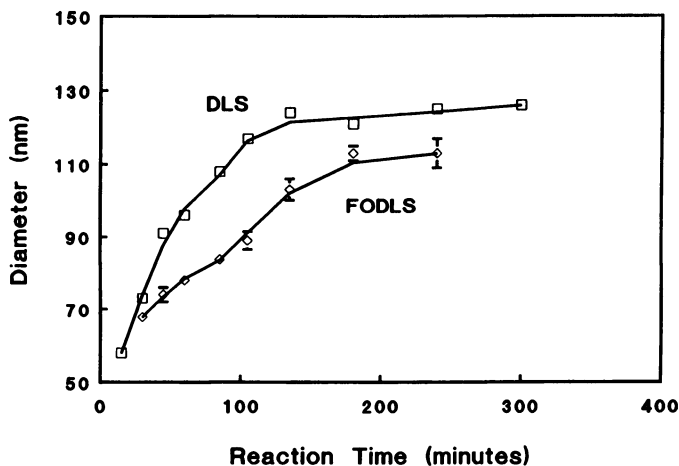


Figure 3. Latex particle size as a function of reaction time [ $\square$ , determined by standard *DLS* measurements on diluted sample;  $\diamond$ , determined by *FODLS* measurements directly on undiluted sample]. (Reproduced with permission from Ref. 10. Copyright 1990 Optical Society of America.)

the coefficient of variation in the data is  $\sim 12\%$ . Here *FODLS* yields essentially the same results as normal *DLS*, but without the need for sample dilution.

### Conclusion

In general, the interpretation of results from *FODLS* experiments is a complicated task. However, the present work has demonstrated unequivocally that there are situations in which useful and reliable data may be readily obtained from these measurements.

Perhaps the greatest attraction of *FODLS* is the ability to make measurements in highly concentrated samples since this is a fundamental requirement for on-line measurements in process control applications. Over certain ranges of particle concentration and size, close agreement between *FODLS* and *DLS* results will occur and interpretation of *FODLS* data is straightforward. More generally, the *FODLS* results may be expected to exhibit a complicated dependence on particle concentration and size, such as is seen in Figure 2. In this case the most fruitful approach would be to construct a standard reference curve ( $D_{app}$  or  $r$  as a function of reaction time etc.) with *FODLS* for each process and use this to interpret subsequent *FODLS* measurements on the same process. In any event, *FODLS* will yield a reliable *relative* measurement which may be suitable for process control.

Another attraction of *FODLS* is the use of optical fibers to deliver the laser beam and collect the scattered light. This makes it convenient to do *FODLS* measurements in a plant or remote environment. It is only necessary to route an optical fiber to the measurement site and the delicate optics and electronics associated with the measurement may be housed in a clean, air-conditioned control room.



To conclude, the present work indicates that the *FODLS* technique is useful for monitoring particle size in samples which are orders of magnitude too concentrated for ordinary *DLS* measurements to be made. This opens up the possibility of performing on-line or at-line particle size measurements with dynamic light scattering.

### Acknowledgment

We remain indebted to Dr. D. Horn and Dr. H. Weise, BASF, Polymer Research Div., ZKM-G 201, Ludwigshafen, West Germany, for providing the *BI-FOQELS* data on the pigment crystallization.

### Literature Cited

1. Barth, H. G., Ed.; Modern Methods of Particle Size Analysis; Wiley-Interscience: New York, 1984.
2. Provder, T., Ed.; Particle Size Assessment and Characterization; ACS Symposium Series No. 332; American Chemical Society: Washington, DC, 1987.
3. Dahneke, B. E., Ed.; Measurement of Suspended Particles by Quasielastic Light Scattering; Wiley-Interscience: New York, 1983.
4. Thomas, J.C. Chem. in Aust. 1985, 52, 464-466.
5. Chien, D. C. H.; Penlidis, A. JMS - Rev. Macromol. Chem. Phys. 1990, C30, 1-42.
6. Kourti, T.; MacGregor, J. F.; Hamielec, A. E.; Nicoli, D. F.; Elings, V. B. Proc. ACS PMSE Symposium 1988, 58, p 169.
7. Auweter, H.; Horn, D. J. Coll. Int. Sci. 1985, 105, 399-409.
8. Thomas, J. C.; Tjin, S. C. J. Coll. Int. Sci. 1989, 129, 15-31.
9. Thomas, J. C. Langmuir 1989, 5, 1350-5.
10. Thomas, J. C.; Dimonie, V. Appl. Opt. 1990, 29, 5332-5335.
11. Koppel, D. E. J. Chem. Phys. 1972, 57, 4814-20.
12. Brown, J. C.; Pusey, P. N.; Dietz, R. J. Chem. Phys. 1975, 62, 1136-44.

RECEIVED January 14, 1991

## Chapter 7

# Extremely Wide Dynamic Range, High-Resolution Particle Sizing by Light Scattering

S. E. Bott and W. H. Hart

Scientific Instruments Division, Coulter Electronics, Inc., 29 Cottage  
Street, Amherst, MA 01002

Light diffraction is one of the most commonly employed methods of measuring sizes of particles in the range of  $0.1\mu\text{m}$  to around  $1000\mu\text{m}$  (1,2). The popularity of the method stems from its ability to make quick, facile, precise measurements as well as its adaptability to measuring samples presented in various forms, for example, stirred or pumped suspensions of particles in any clear liquid, aerosols, dry powders in an air stream, particles adhering to a glass slide, etc (3,4).

Diffraction measurements are based on sensing the angular patterns of light scattered by particles of different sizes when they are exposed to a collimated beam of light. Because the patterns of light scattered by particles of different sizes are highly characteristic of the particle size, a mathematical analysis of the pattern of light scattered from a sample of particles can extract an accurate, reproducible measure of the size distribution.

The aforementioned flexibility of the method in measuring particles presented in a variety of ways, combined with the remoteness of the detection method (i.e. the light source and detectors are located far from the particles and therefore do not perturb the system under measurement) gives diffraction the potential for making measurements of very broadly dispersed distributions of particles. This article presents work done by the authors in extending the potentially large dynamic range of diffraction measurements as well as extending the size range over which the light scattering methods can accurately resolve particle size distributions.

When a beam of light is projected onto a particle, in the limit of particle size much greater than the wavelength of the light, the interactions of the particle with light can be broken down into three phenomena: reflection, refraction and diffraction. The first two phenomena are experienced daily; the last is a bending of light around a particle as the particle interrupts or blocks part of the planar wavefronts of the light incident on the particle. It should be noted that in the general case, encompassing particles of arbitrary size and light of any wavelength, the interaction of light with particles, collectively termed *scattering*, does not separate into the three distinct phenomena mentioned above.

The extent of the bending of the light around a particle depends on the ratio of

0097-6156/91/0472-0106\$06.00/0

© 1991 American Chemical Society

the wavelength of the light to the particle size. In general, larger particles diffract the light into smaller scattering angles (i.e. into the nearly forward direction) while the diffracted light from smaller particles is sent into larger scattering angles, where the scattering angle is defined as the angle between the direction of propagation of the incident light and the direction from which the diffracted light is observed.

To quantify the diffracted light, an optical system such as that shown in Figure 1, is used. The Fourier lens in this system, located at its focal length from the plane of the detector array, or Fourier plane, serves to focus all the undiffracted light into a single point in the center of the array of sensing detectors. This undiffracted light is generally used only to monitor the beam strength. All light that is diffracted from any of the particles in the beam into a given scattering angle, is focused by the Fourier lens into a thin annulus, centered around the point where the undiffracted light is focused. Light diffracted into small angles produces annuli of small radius; that diffracted into larger angles results in annuli of larger radii.

A detection system comprising an array of annular detectors measures the pattern of light diffracted from the particles in the beam. Figure 2 shows the diffracted light pattern, as a function of scattering angle for particles of 550 and 275 $\mu\text{m}$ . If particles of more than one size are in the beam, the composite diffraction pattern will be the linear superposition of the patterns corresponding to the individual particles.

In the limit of particles much larger than the wavelength of light and small scattering angles, the pattern of diffracted light is described by the *Fraunhofer Diffraction* approximation (5). In the more general case, including higher scattering angles and arbitrary ratio of light wavelength to particle size, various other approximations can be used to calculate the scattered light pattern. For the specific case of isotropic spherical particles of arbitrary size, an exact general expression for the scattered light pattern is given by the *Mie* theory (6).

The general relationship between the light pattern measured at  $n$  discrete detectors and the distribution of the particles in  $m$  selected size classifications is given by:

$$\begin{bmatrix} f_1 \\ \vdots \\ f_n \end{bmatrix} = \begin{bmatrix} a_1^1 & \dots & a_1^m \\ \vdots & \dots & \vdots \\ a_n^1 & \dots & a_n^m \end{bmatrix} * \begin{bmatrix} x_1 \\ \vdots \\ x_m \end{bmatrix} \quad (1)$$

where  $f_i$  is the light flux measured at the  $i$ th detector,  $a_i^j$  is the amount of light flux due to particles of size classification  $j$ , diffracted into the  $i$ th detector and the  $x_j$ ,  $j=1,m$  are the desired volumes of particles of each size classification. In this equation, the  $\{a_i^j\}$  are calculated using the Fraunhofer diffraction approximation, the Mie theory or some other expression relating particle size to diffraction pattern. Equations of the form of (1) have standard means of solution (7,8).

In a diffraction measurement, the choice of angles covered by the  $n$  detectors generally determines the number and range of the  $m$  size classifications covered by the instrument. As a general rule of thumb, the dynamic range of scattering angles covered by an instrument roughly equals the dynamic range of sizes which the instrument is capable of measuring. (The dynamic range of a sample is defined as the ratio of the largest to the smallest particle contained in significant percentage in a sample. Dynamic range in scattering angle refers to the ratio of the largest to the smallest scattering angle over which light can be sensed in a single measurement.)

Thus an instrument which measures angles from 0.03° to 3°, a dynamic range of 100:1, would be expected to measure particle size from around 8 $\mu\text{m}$  to around 800 $\mu\text{m}$ ,

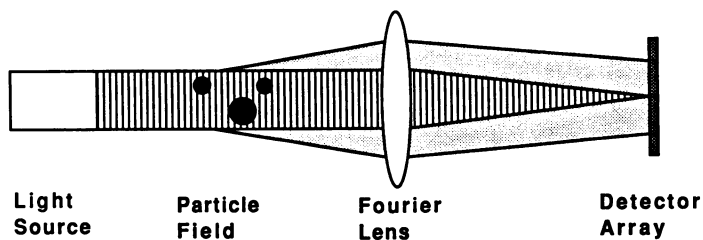


Figure 1. Optical train for conventional diffraction measurement.

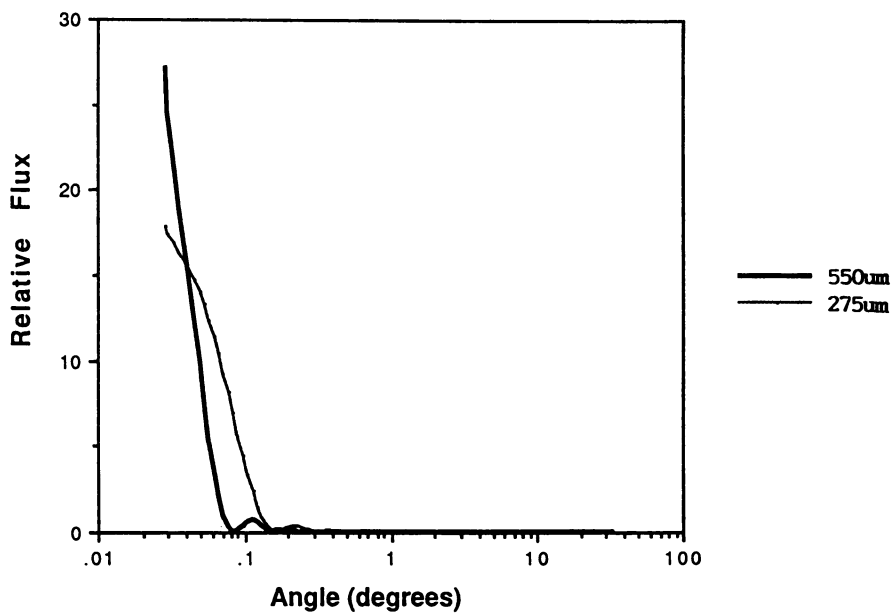


Figure 2. Scattered light flux (intensity/area) pattern for 275µm and 550µm particles.

also a dynamic range of 100:1. (The center of the size range covered by a measurement of a given angular range would depend on the wavelength of light used; however, the dynamic range of the size measurement would always be about the same as the dynamic range of angles over which the measurement was made.) This rule of thumb breaks down for small particles as will be seen later.

From the rule of thumb given above, it is apparent that to increase the dynamic range of a sizing measurement, the angular range over which the scattered light is measured must be increased. Hence, historically, the first commercial light diffraction instruments covered a dynamic range of around 100:1. Several years later commercial instruments covering a dynamic range of several hundred to one became available. The instrument used by the authors covers a dynamic range exceeding several thousand to one.

### **Broad Size Distributions**

Many important classes of particles are dispersed in extremely broad distributions, distributions whose dynamic range may exceed 1000:1. Although diffraction offers the potential of measuring over such an extremely broad dynamic range, there are some physical problems which make this wide dynamic range difficult, in practice, to achieve. Figure 3 is a log-log plot of the diffraction pattern expected for equal volumes of a large (700 $\mu\text{m}$ ) and small (1 $\mu\text{m}$ ) particles. In order to accurately measure these particles, diffraction patterns similar to these must be measurable by the instrument.

The difficulties with measuring samples which contain particles of sizes as disparate as those shown in Figure 3 are twofold. The first part lies in the tremendous range of light fluxes which must be sensed. The detectors must be able to sense light levels with high precision over many orders of magnitude to accurately characterize two diffraction patterns like those shown. This difficulty is frequently addressed by using a detector array which has detectors of increasing sizes for the larger angles. In this way, the high light flux levels (flux is light power per unit area), which occur primarily at small scattering angles, are detected by very small detectors; conversely, the lower flux levels at higher scattering angles are detected by larger detectors. The signal levels are thus balanced by tailoring the detector sizes to the light level they are likely to sense.

Figure 4A shows the amount of light flux for a mixture of 275 and 5 $\mu\text{m}$  particles, recorded by a series of detectors increasing in area geometrically with scattering angle. Note that in this graph the ordinate is plotted on a linear rather than a log scale. Figure 4A can be contrasted with Figure 2, to illustrate the effect of employing detectors of increasing sizes to balance the light levels recorded by the detectors. The improvement made possible by the geometrically scaled detector sizes, is apparent in the additional oscillations which become visible for the 275 $\mu\text{m}$  particles in this weighted flux pattern. As Figure 4A also shows, the composite diffraction pattern resulting from a mixture of particles of different sizes is the sum of the diffraction patterns for the individual particles, weighted by the amount of particles of each size.

The second and more persistent difficulty in measuring scattering patterns over an extremely wide dynamic range is in the enormous difference in the shape of the diffraction patterns of the small versus large particles. It is this characteristic difference in the shape of the patterns for different sized particles which permits the measurement to distinguish between particles of different sizes. However, distinguishing between the diffraction patterns of the two large particles requires measuring the light patterns extremely accurately at small ( $<0.1^\circ$ ) scattering angles. Conversely, distinguishing between the two small particles requires measuring the very small amount of curvature difference in the diffraction patterns at high scattering angles.

Figure 4B shows the true (ideal) diffraction pattern which would be exhibited by 164 $\mu\text{m}$  particles. To extract all the information about the particle size that is intrinsically

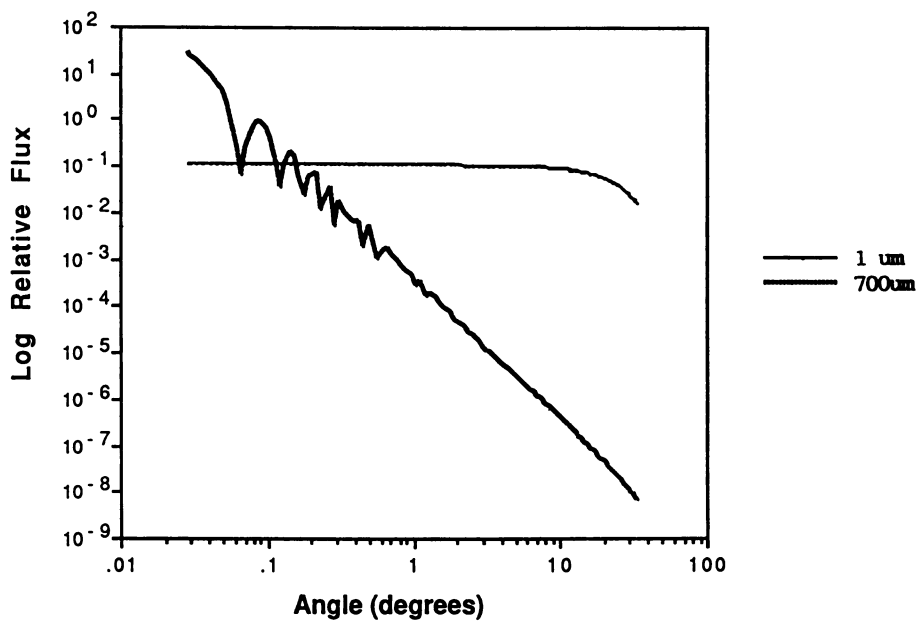


Figure 3. Light flux patterns for 1 $\mu\text{m}$  and 700 $\mu\text{m}$  particles.

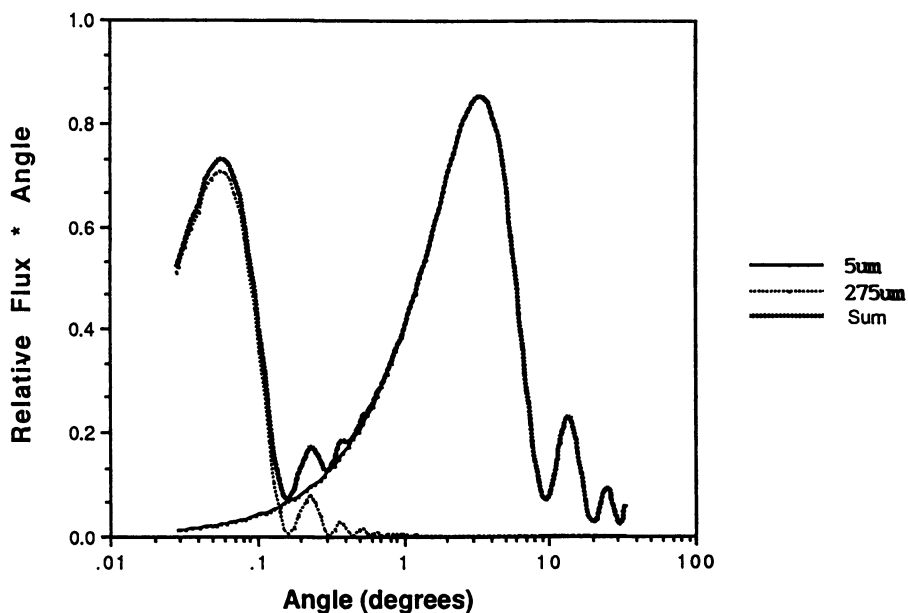


Figure 4A. Weighted light flux patterns for  $5\mu\text{m}$  and  $275\mu\text{m}$  particles. Flux pattern for mixture of the two particles is the linear superposition of the individual light fluxes.

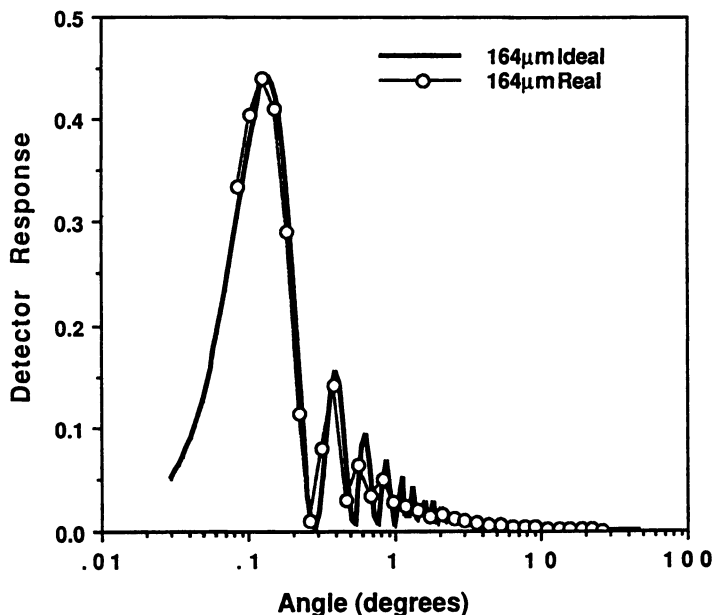


Figure 4B. Ideal light flux pattern and light flux pattern measured by 32 discrete detectors for  $164\mu\text{m}$  particles.

contained in the diffraction pattern, an instrument would need to have enough detectors to characterize the pattern through all the oscillations exhibited by the pattern. Superimposed on the true diffraction pattern is the pattern which would be measured by a real instrument containing 32 discrete light detectors spaced geometrically across the angular range of interest. As is apparent from the graph, these 32 detectors are sufficient to capture most, but not all, of the character of the true diffraction pattern. Additional detectors, located between those shown would permit the true diffraction pattern to be more completely measured.

To measure the diffraction pattern accurately at both high and very low angles requires a large number of detectors spread over a very wide area on the plane of the detector. Because of the expense of constructing a suitable detector array and because of the added difficulty of the optical aberrations (blur) which occur when a lens is used to form an image over such a wide part of the Fourier plane, the angular range over which diffraction patterns are conventionally measured in particle sizing measurements is generally limited to a range of several hundred to one, i.e. the largest angle measured is, at most, several hundred times the smallest angle measured in a single measurement. As discussed earlier, this limits the dynamic range of a size measurement to a similar several hundred to one.

If all the particles to be measured fall within the several hundred to one size range which the limits of the angular range of the scattering measurement permit, the limitations in the angular range should have little effect on the recovered size distribution. However, for wide dynamic range samples, the foregoing condition will not always be met. In addition, limited dynamic range may also adversely affect samples for which part of the size distribution falls outside of the range of the measurement even if the dynamic range of the distribution does not necessarily exceed the dynamic range of the measurement. This is worrisome, since many samples comprise unknown particle size distributions which might contain particles outside the range of the instruments. It might be expected that out of range material would be ignored by the diffraction measurement; however, out of range material still contributes scattered light within the measurement range and therefore will result in measurement anomalies of the sort discussed below. Obviously an important advantage of the widest possible angular scattering range is immunity to problems of this sort.

To test the effects of limited angular range, restricted size range diffraction measurements on a size distribution which does not fall completely within the measurement range, the following experiment was performed. The diffraction pattern expected for a 1:1 mixture of 275 and 5  $\mu\text{m}$  spheres was calculated over a large angular range: 0.03 to 35°. Noise corresponding to 1% of the light flux signal strength was added to the diffraction pattern to simulate the noise levels generally contained in such measurements. This computer simulated data was then analyzed over the full angular range, and the amount of material in 72 size classes from .8 to 800  $\mu\text{m}$  was reported. That result was compared to a similar analysis covering a more conventional, limited angular range of .03 to 3.5° analyzed over a correspondingly smaller range of size classifications: 8 - 800 $\mu\text{m}$ . The histogram plotted with a fine line in Figure 5 is the size distribution recovered using the full angular range measurement, the histogram plotted with a bold line is the result with the limited angular range measurement.

The important result is that in the limited angular/size range result, the 5 $\mu\text{m}$  particles, though out of the size range over which the analysis is performed, are not simply ignored by the analysis. Instead, an artifact peak at around 150 $\mu\text{m}$  is reported, as a result of the presence of the 5 $\mu\text{m}$  particles. Using the broader angular range, the bimodal size distribution is accurately recovered.

The source of the artifact peak can be found by referring again to Figure 4. The composite diffraction pattern shown is a result of the sum of the individual diffraction patterns from the two populations of particles. Although the larger and smaller particles diffract light predominantly into the lower and higher scattering angles, respectively, the



population of smaller particles does diffract a significant amount of light into the .03 - 3° angular range dominated by the larger particles' diffraction pattern. This light leads to the reporting of the 150µm artifact.

Note that if the analysis of the data from the limited angular range measurement is extended to include a wider range of size classifications, other artifacts will be introduced by the attempt to size particles whose dominant diffraction peak falls out of the range over which the diffraction is sensed.

### **Double Fourier Lens Optical Collection System**

Although to the knowledge of the authors it has not been previously done, the restricted angular range used by many diffraction instruments can be extended straightforwardly by adding a second Fourier lens to capture light diffracted into higher scattering angles. Such a measurement system is shown schematically in Figure 6. The addition of the second Fourier lens helps to prevent artifacts such as those described above, in addition to extending the dynamic range of the measurement.

### **Loss of Resolution at Small Size End**

An examination of Figure 7 shows that for small particles, especially particles below around 0.5µm in diameter, the diffraction patterns are rather similar. For this reason, the diffraction patterns of small particles do not provide as much information about particle size as do the more oscillatory, information rich, patterns exhibited by larger particles. The diffraction patterns for very small particles are all characterized by an even scattering intensity out to a fairly high angle, followed by a region at higher angle in which the scattered light intensity falls off slightly with angle. The basic similarity in the diffraction patterns for small particles means that the resolution of diffraction measurements in this size regime is intrinsically limited.

The resolution of the measurement can be extended by measuring to as high a scattering angle as possible, in order to detect small differences in the shape of the pattern in the region in which the patterns are falling in amplitude. However, because of the basic similarity in the shape of the patterns, measurements at higher angles provide diminishing returns.

### **Polarization Intensity Differential Scattering (PIDS)**

The authors have devised an alternate method for characterizing particles in the submicrometer size range. This method is based on a particular feature of the scattered light pattern for particles smaller than the wavelength of the incident light, more specifically, on the sensitivity of scattering by these small particles to the polarization of the incident light. Various methods have been used previously which exploit the polarization sensitivity of scattering to size small particles (2,10). Figure 8 shows the experimental geometry. The incident light may be polarized either perpendicular to or parallel to the scattering plane, i.e. the plane defined by the light beam and a line from the scattering volume to the detector.

Heuristically, the origin of the polarization sensitivity of the scattering of small particles can be understood in the following way. Light is a transverse electromagnetic wave, i.e. the electric and magnetic fields of the light oscillate in a direction perpendicular to the direction of propagation of the beam. If a small particle is located in a light beam, the oscillating electric field induces in the particle an oscillating dipole moment; the electrons in the atoms comprising the particle move back and forth with respect to the relatively stationary particle. The direction of induced motion of the electrons will be in the direction of oscillation of electric field, and therefore perpendicular to the direction of propagation of the light beam. Because of the transverse nature of light, the oscillating dipole radiates light in all directions except in the direction of oscillation; there is, by definition, no component of transverse

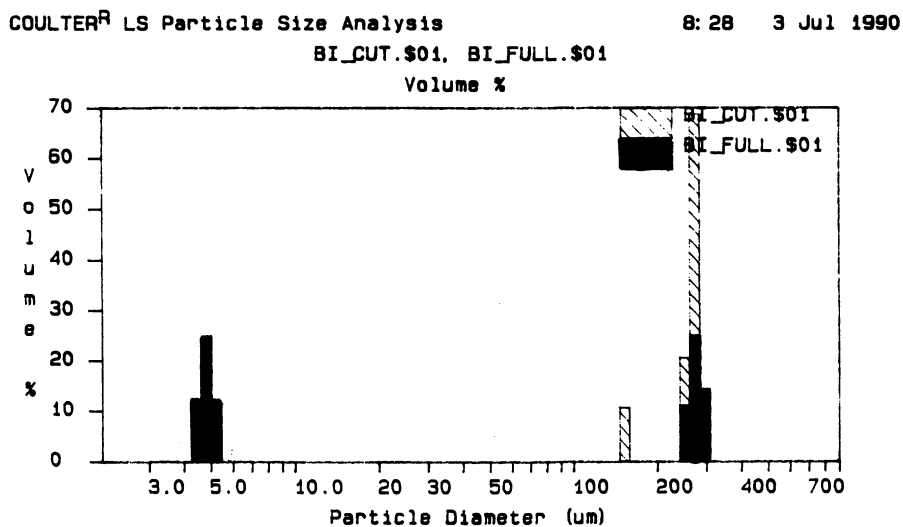


Figure 5. True distribution and recovered distribution showing artifact peak (150 $\mu$ m) resulting from inadequate dynamic range.

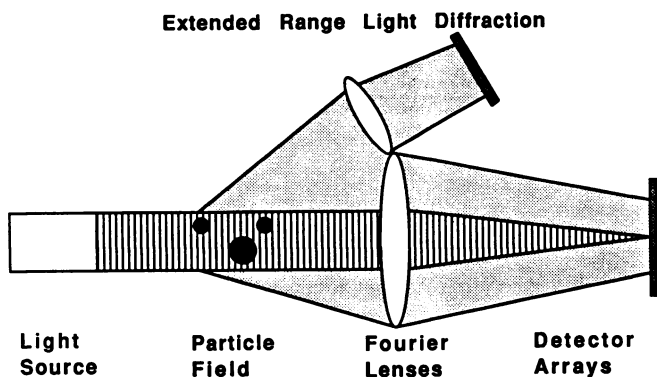


Figure 6. Optical train for wide dynamic range diffraction measurement.

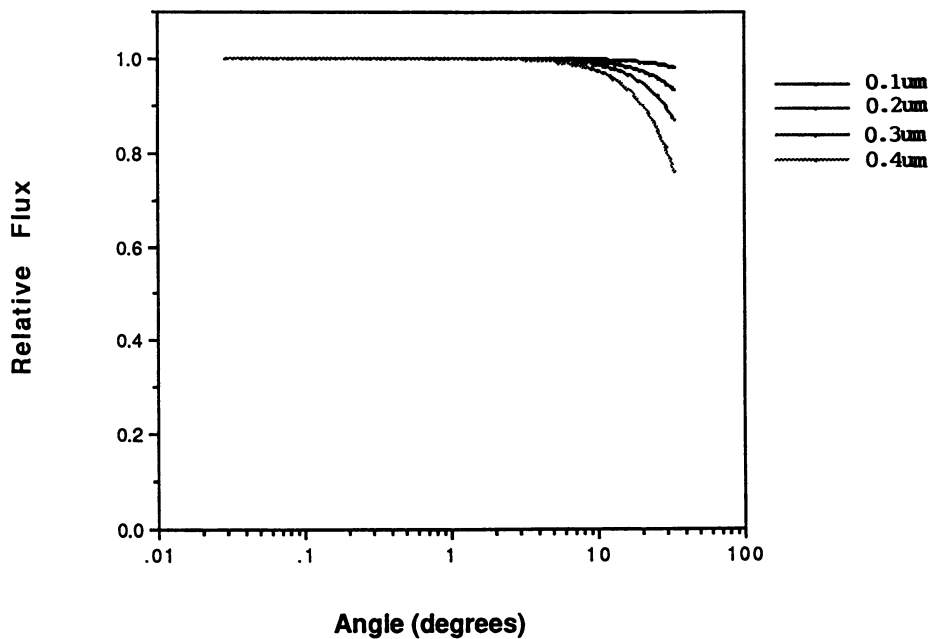


Figure 7. Light flux patterns for small particles.

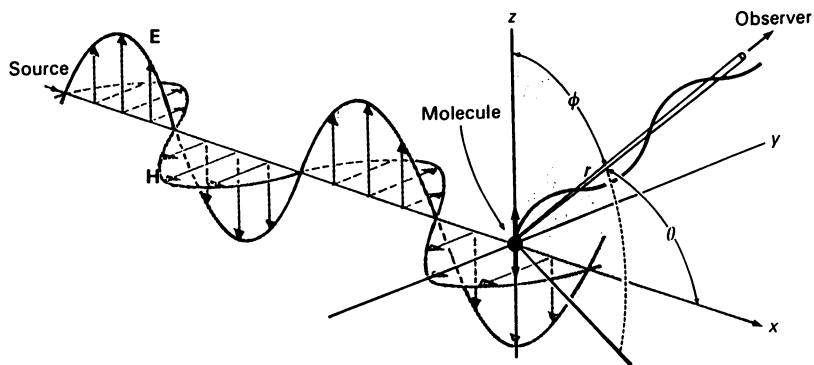


Figure 8. Experimental geometry for PIDS scattering measurement.

oscillation of the electrons in this direction. Referring again to Figure 8, the light is polarized in the  $x$ - $z$  plane; the scattering intensity in the direction of the  $\pm z$  axis will be zero. If the light were polarized in the  $x$ - $y$  plane, there would be appreciable scattered light intensity in the  $z$  direction, since the direction of oscillation of the electrons would then be perpendicular to the  $z$  axis. Thus the scattering response of the small particle is heavily dependent on the polarization of the light. The electric field from an oscillating dipole is shown in Figure 9.

The foregoing explanation was predicated on the particles being much smaller than the wavelength of the light. As the particle size increases (or, equivalently, as the light wavelength decreases), the particle will no longer act like a simple dipole and the scattering pattern will become more complex. Figure 10 is a plot, as a function of scattering angle, of the difference in scattered light intensity for incident light polarized perpendicular to vs parallel to the scattering plane. This difference is termed a PIDS signal. For the smaller particle, the scattering pattern is a roughly quadratic curve centered at  $90^\circ$ . For particles which are larger, the pattern shifts somewhat to the left. For still larger particles (or again, shorter light wavelengths), the pattern will shift further to the left and secondary peaks will appear. Since the PIDS signal is dependent on particle size relative to the light wavelength, by measuring the PIDS signal at a variety of light wavelengths, valuable information about the particle size distribution can be obtained.

The physics described above can be utilized to measure submicrometer particles in a measurement system such as that shown in Figure 11. A white light source is collimated to form a beam of light. One filter on a carousel containing several filter-polarizers selects light of one particular wavelength and of polarization either perpendicular to or parallel to the scattering plane. The symmetry of the scattering pattern around  $90^\circ$  scattering angle is measured for that filter-polarizer by several detectors. The filter wheel is rotated to measure, sequentially, the scattered light pattern resulting from the other filter-polarizers (covering the two polarizations at other selected light wavelengths) on the carousel. The PIDS pattern for each of several light wavelengths can in this way be measured and recorded by the instrument.

Figure 12 show the PIDS patterns, for three light wavelengths, expected for particles of 0.1-0.4 $\mu\text{m}$ . These PIDS patterns are in marked contrast to the diffraction patterns for particles of similar sizes, shown in Figure 7. Without delving into the mathematics, it is clear that the PIDS patterns are much more characteristic of particle size in this range, than are the diffraction patterns. The similarity between the diffraction patterns for small particles restricts the resolution and accuracy with which the particles can be sized. Conversely, the extremely characteristic PIDS patterns for various small particles makes it easy to identify the size of particles by observing the PIDS signals.

Although it is beyond the scope of this article, a mathematical analysis must be used to reduce the PIDS patterns at several wavelengths to a size distribution. Such an analysis must also combine conventional diffraction data with the additional information present in the PIDS signals. Figures 13 and 14 show size distributions recovered for two small (0.137 and 0.359  $\mu\text{m}$ ) polystyrene latex spheres (PSL) using diffraction alone, Figure 13, and diffraction in conjunction with PIDS, Figure 14. Results were obtained using the Coulter model LS130 particle analyzer.

The diffraction results show that the method is fairly insensitive to particle size in this size regime. The results for particles of both sizes are reported as a single broad peak centered at around 0.25 $\mu\text{m}$ . Using PIDS in addition to the diffraction, the two PSLs are reported as the correct, narrow peaks, with mean sizes quite close to the nominal sizes.

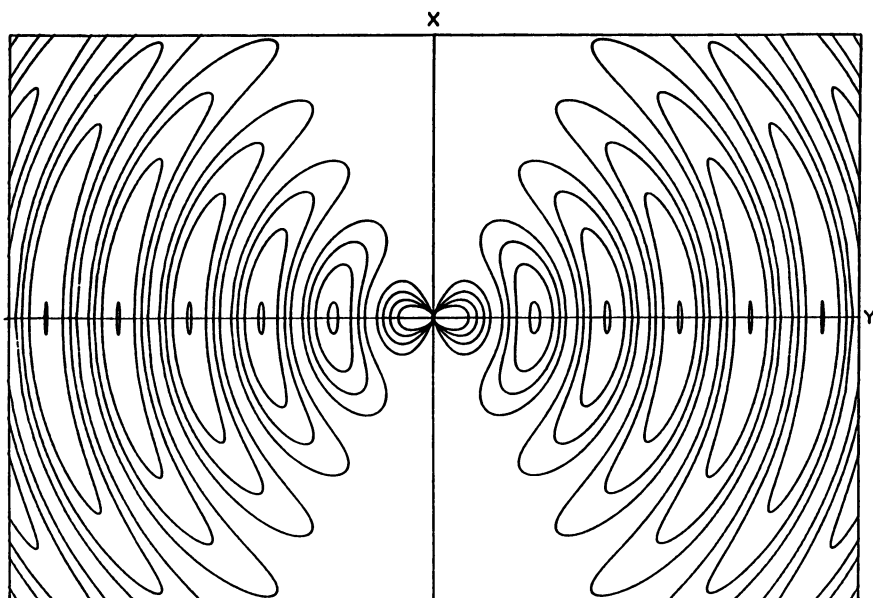
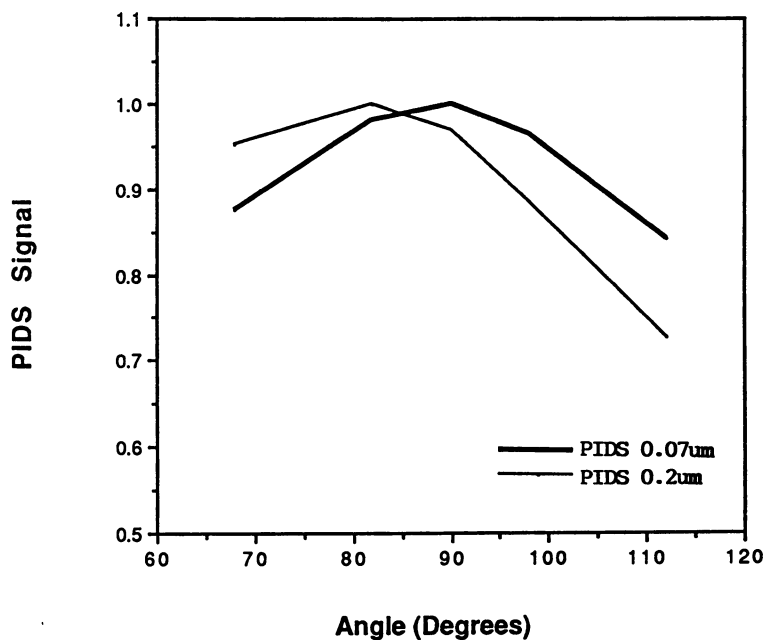


Figure 9. Electric field from oscillating dipole.

Figure 10. PIDS signal for particles much smaller ( $0.07\mu\text{m}$ ) than light wavelength ( $0.45\mu\text{m}$ ) and particles comparable to light wavelength ( $0.2\mu\text{m}$ ).

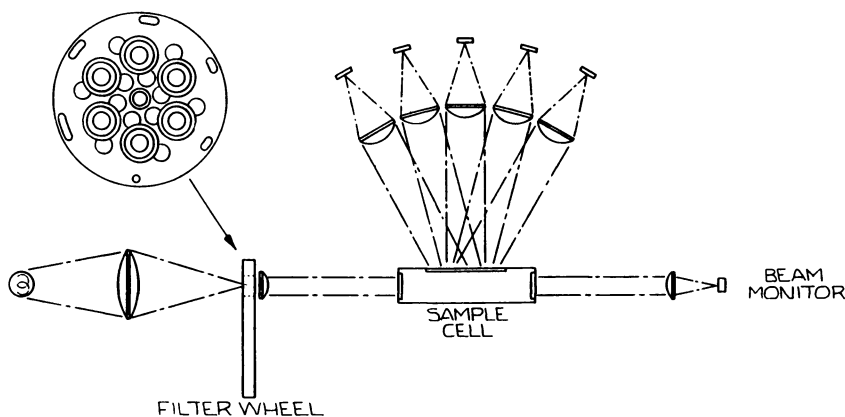


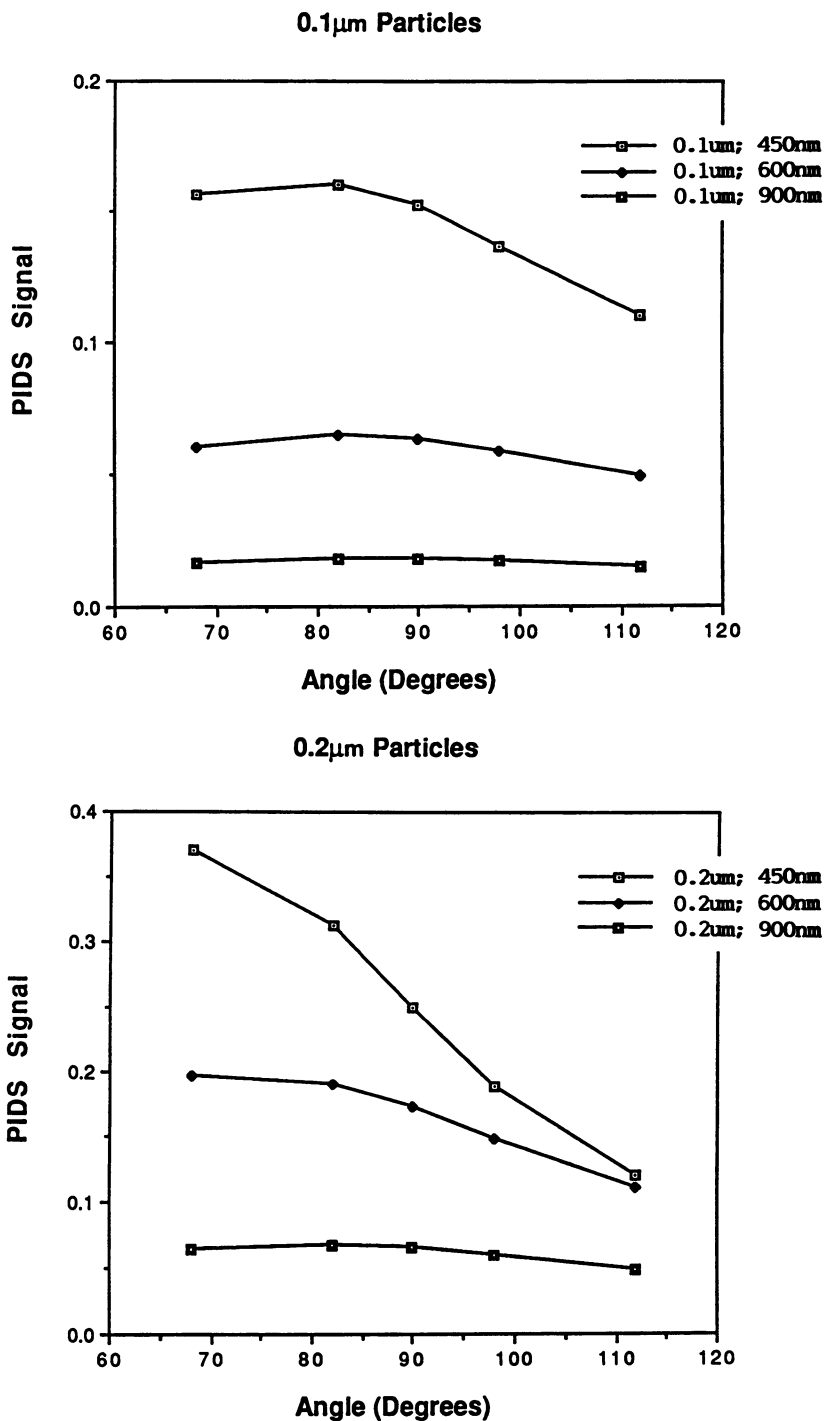
Figure 11. Optical train for PIDS measurement.

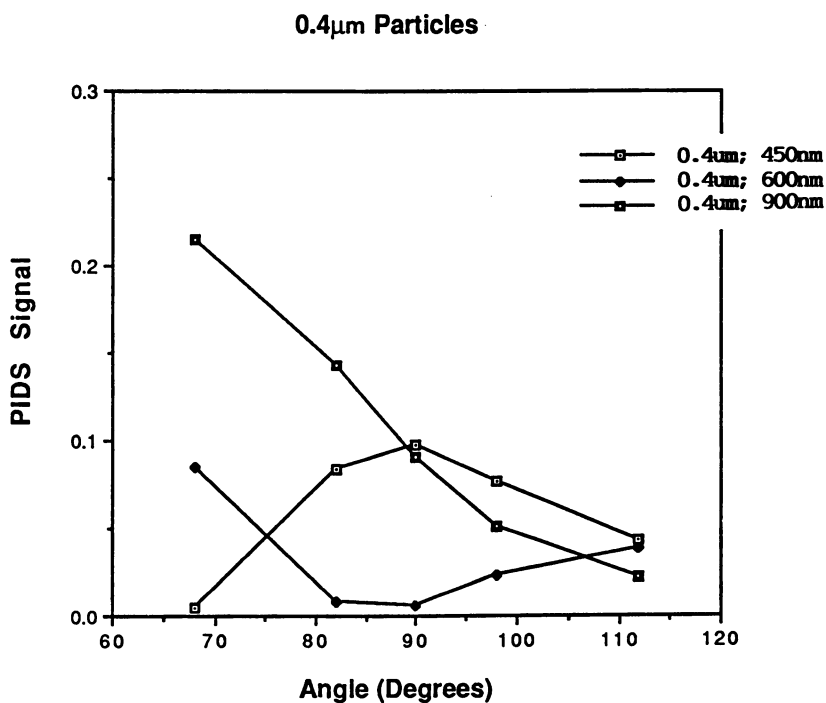
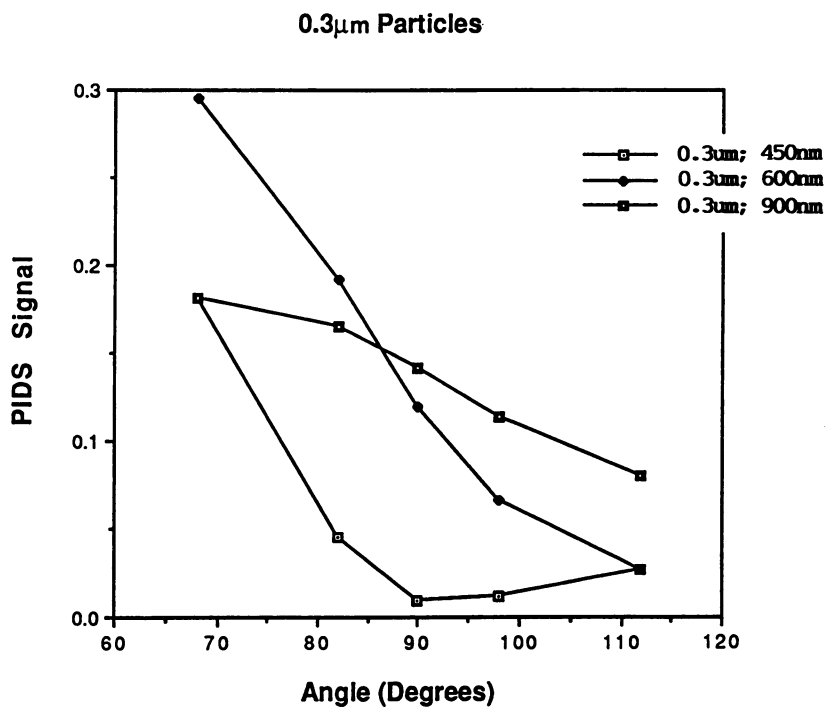
## Conclusion

The dynamic range of a diffraction sizing measurement can be extended by extending the angular range over which the diffracted light is measured. An new optical scheme employing two sets of Fourier collection optics, of different optical powers, has been presented. The new scheme extends the angular range over which the diffraction pattern can be accurately characterized in a single measurement. The use of the second optical train has been shown to help alleviate certain artifacts that occur when broad size distributions are measured with conventional single collection train optics.

A new polarization sensitive light scattering scheme, PIDS, has been described for measurements of submicrometer particles. This scheme extends the useful sizing range for diffraction instruments down to  $0.1\mu\text{m}$ . Using graphical comparisons of scattered light patterns, reasons for the higher sizing resolution of PIDS versus simple diffraction have been outlined. In addition, experimental data using the PIDS measurement on submicrometer polystyrene latex spheres demonstrates the considerably better resolution and accuracy of PIDS versus conventional diffraction for particles less than  $0.4\mu\text{m}$ .

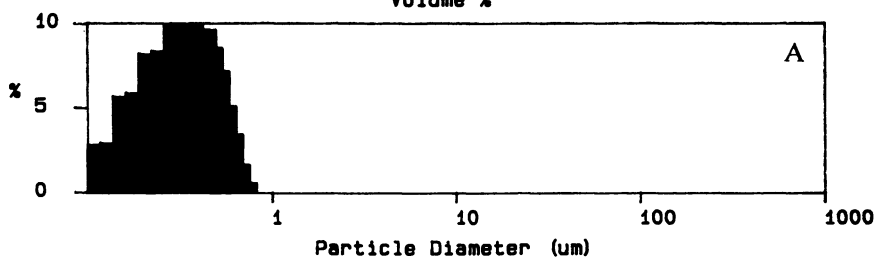
Using a combination of the double Fourier lens collection system and the new polarization sensitive scattering method for submicrometer particles, a single the entire size range from  $0.1\mu\text{m}$  to around  $1000\mu\text{m}$  can be measured in a single measurement

Figure 12. PIDS patterns for small particles. *Continued on next page.*

Figure 12. *Continued.*



COULTER<sup>®</sup> LS Particle Size Analysis Fri Dec 08 07: 42: 17 1989.  
137P096.\$04  
Volume %



COULTER<sup>®</sup> LS Particle Size Analysis Fri Dec 08 08: 07: 26 1989.  
359P096.\$05  
Volume %

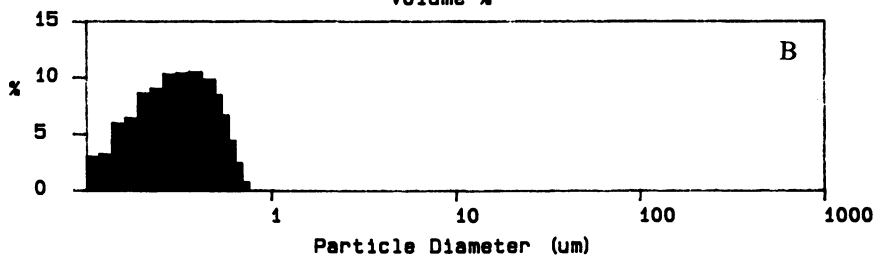
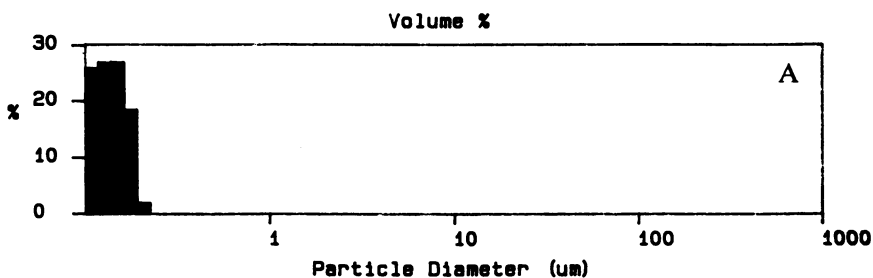


Figure 13. 0.137 $\mu\text{m}$  (A) and 0.359 $\mu\text{m}$  (B) polystyrene latex spheres measured with diffraction alone.

COULTER<sup>®</sup> LS Particle Size Analysis      Fri Dec 08 08: 22: 17 1989.  
137PSN63.\$02



COULTER<sup>®</sup> LS Particle Size Analysis      Thu Dec 07 17: 44: 18 1989.  
359NMTST.\$06

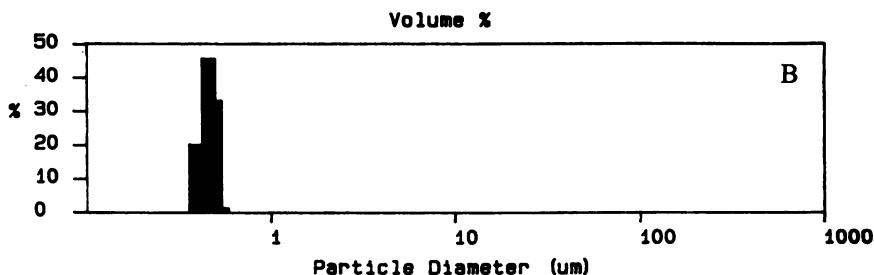


Figure 14. 0.137 $\mu\text{m}$  (A) and 0.359 $\mu\text{m}$  (B) polystyrene latex spheres measured with PIDS plus diffraction.

### Literature Cited

1. B. Olsson, H. Jaegfeldt, K. Hed and H. Lundback, *J. Aerosol Sci.*, **19** (7) (1988).
2. J.K. Singer, J.B. Anderson, M.T. Ledbetter, I.N. McCave, K.P.N. Jones and R. Wright, *Journal of Sedimentary Petrology*, **58**(3) (1988).
3. VI. Ovod, V.Y. Shoyuko, E.I. Moshkovskii and A.B. Lyashcheko, *Sov. PDG. Metall. Met. Ceram.*, **23** (11) (1984).
4. L.G. Dodge and S.A. Cerwin, "Extending the Applicability of Diffraction-Based Drop Sizing Instruments", in *Liquid Particle Size Measurement Techniques*, J.M. Tishkoff, R.D. Ingebo and J.B. Kennedy, Eds. (ASTM STP 848, 1984).
5. M. Born and E. Wolf, *Principles of Optics* (Pergamon Press, Oxford, 1983).
6. M. Kerker, *The Scattering of Light and Other Electromagnetic Radiation* (Academic Press, NY, 1969).
7. C.L. Lawson and R.J. Hanson, *Solving Least Squares Problems* (Prentice-Hall, Inc., NJ, 1974).
8. E.D. Hirtleman, *Part. Charact.*, **4**, 128 (1987).
9. A.F. Stevenson, W. Heller and M. Wallach, *J. Chem. Phys.*, **34**, 1789 (1961).
10. H.N. Frock, "Particle Size Determination Using Angular Light Scattering", in *Particle Size Distribution*, T. Provder, Ed. (ACS Symposium Series 332; American Chemical Society: Washington D.C., 1987; p. 146).

RECEIVED January 25, 1991

## Chapter 8

# Instrumental Particle Size Analysis Procedures for Parenteral Solutions

### Some Practical Issues

M. J. Groves

Institute for Tuberculosis Research (M/C 964), College of Pharmacy,  
University of Illinois at Chicago, 115 South Sangamon Street,  
Chicago, IL 60607

Particulate contamination in solutions intended for injection into the human body is physiologically undesirable but inevitable. Mobile particulate contaminants have a wide size spectrum, from the visible ( $>50\ \mu\text{m}$ ) to molecular levels ( $<0.001\ \mu\text{m}$ ). Attempts to limit the presence of particulates by visual inspection methods have produced notoriously variable results. In 1975, a limit test based on the filtration procedure used for measuring particulates in hydraulic oils was published in the United States Pharmacopoeia (USP XIX) for large-volume ( $>100\text{-mL}$ ) injection solutions (infusions). In 1985, this test was followed by a method based on the HIAC/Royco light extinction (blockage) instrument for small-volume ( $\leq 100\text{-mL}$ ) injections. When this method was initially introduced, both producers and users of the instrument experienced some major problems. Subsequent resolution of these issues is discussed in this chapter to demonstrate that practical problems will tend to dissipate if adequate education and information are provided at all levels of the process.

Parenteral solutions, that is, sterile solutions of drugs and electrolytes intended for injection into the human body, will inevitably contain small quantities of mobile, undissolved, solid or liquid particulate contaminants. By its very nature, a parenteral solution should contain very small amounts of extraneous particulates, because it will have been repeatedly filtered through filters of a nominal pore size at or below 200 nm, and it is packaged in containers (and their associated seals) that have been repeatedly rinsed in clean water with very low levels of particulates. Nevertheless, these solutions may contain particulates with a size spectrum ranging from the molecular level (e.g.,  $<10\ \text{nm}$ ) to the visible region ( $>50\ \mu\text{m}$ ). Because of the nature of the filtration process, it is likely

0097-6156/91/0472-0123\$06.00/0  
© 1991 American Chemical Society

that there will be a discontinuity at around the nominal pore size of the filtration medium, but particles larger than this size will be present by chance contamination or by interactions between components of the solution or between the solution and components of the container. This "contamination" must be put in context. If a solution contains 1000 particles per mL with diameters corresponding to a 2- $\mu\text{m}$ -diameter sphere and the particles have a mean density of 1.2 g/mL, the solid contamination corresponds to approximately 5 parts per billion by weight. Currently, solutions are being commercially prepared two to three orders of magnitude cleaner than this level of particulates, which actually corresponds to the limit allowed by the British Pharmacopoeia 1988 at 2  $\mu\text{m}$  when measured by the Coulter principle.

Physiologically, these particles are undesirable although inevitable. The body defense mechanisms for dealing with low levels of particulates involving phagocytosis of extraneous bacteria or other particles introduced into the body can be invoked. However, rigid particles much larger than 5–7  $\mu\text{m}$  will occlude blood capillaries. Nevertheless, as discussed elsewhere (1–3), the defense systems can be overwhelmed by particulates and enough capillaries can be blocked to deny the vital blood supply to essential organs. These situations, however, are encountered only in extreme cases (e.g., intravenous drug abuse) and are generally considered to be substantially irrelevant in modern medical practice. Some workers have suggested that particulates can produce profound physiological effects, even leading to death (4–6). More recently, reversible effects noted experimentally on isolated rat heart (7–9) have been attributed to particulates. However, it will never be possible to demonstrate unambiguously the physiological dangers associated with the administration of low levels of unwanted, inadvertent particulates. Compendia throughout the world have expressed a desire to limit particulates administered to the patient without clear evidence as to the hazard. The issue is now one of relative "quality," with limits placed on amounts allowed by the compendia. The enumeration of particles is a direct measure of the success of manufacturing procedures used to prepare, package, and process the parenteral solution. The problem then becomes how to determine particulates present at very low levels with accuracy and precision.

### **Probable Size Distributions in Parenteral Solutions**

The dominant feature of a very dilute suspension of insoluble particulate matter repeatedly passed through filtration systems is that very few particles at sizes above the nominal pore size of the filters are present and that the numbers of particles increase exponentially as the particle size decreases. This unusual type of distribution has been discussed elsewhere (2, 3, 10–14) but approximates to a power law in that a linear relationship exists between the logarithm of the "size" and the logarithm of the cumulative number of particles per unit volume. Here, clearly, size is determined by the method of analysis used to measure the particles. For

example, by Coulter, size would be the diameter of a sphere of equivalent volume, and by light extinction, it would be the size of a sphere of equivalent cross-sectional area. Although an approximation, this distribution can be tested statistically and provides a means for calculating single numerical parameters as a measure of the particulate levels (22). Although the particulates in any parenteral solution cover a wide spectrum of size, the analyst should only be concerned with particles of sizes between approximately 1  $\mu\text{m}$  and 100  $\mu\text{m}$ . Below 1  $\mu\text{m}$  the physiological significance of the particulates becomes extremely dubious, and the numbers of visible particles (approximately 50  $\mu\text{m}$  and larger) present in a quality parenteral solution are very low or nonexistent. (Japanese compendial authorities are currently suggesting that entire lots of solutions containing as little as one visible particle in one container should not be used.)

Compendia throughout the world measure particulates over a size range of 2–25  $\mu\text{m}$  by different methodologies. The basic question hinges on the relative merits of the methodologies selected by the various authorities.

### Concerns about Particulates

The first commercially prepared injectable solutions appeared in the early 1890s, and the British Pharmacopoeia of 1898 contained a number of injection monographs. The solutions were not sterilized and were only intended for subcutaneous administration. The United States Pharmacopoeia (USP) introduced injection monographs in 1905. Sterilization of injections was not required until the 1930s, and in 1936, the National Formulary (later merged into the USP) introduced a test for “clarity” based on optical inspection of ampouled products.

Over the next decade increasing concern was expressed by the various compendia about the presence of visible particulates. The USP XII suggested that injection solutions should be substantially free of visible particulates, but the ambiguity of the term “substantially free” and the difficulty of carrying out any test based on discrimination by human observers were noted from a legal standpoint, and the requirement was abandoned. Although the undesirability of extraneous particulate matter in drug solutions introduced into the veins was recognized much earlier, the situation came to a head with the publications by the Australians Garvan and Gunner in the early 1960s (4–6). This surgeon/anaesthetist team drew attention to physiological and pathological effects produced by particulate debris encountered in locally (Australian) made intravenous fluids. These studies provoked a renewed interest in the field. Coincidentally, problems encountered by a large manufacturer in the United States resulted in deaths due to contaminated intravenous solutions. This situation resulted in the 1966 Symposium organized by the Food and Drug Administration (1). The resulting proceedings of the symposium reads today, with

modern hindsight, as a curious mixture of science and emotion. It established the undesirability of particulates but failed to establish an unequivocal methodology for particulate quantitation. As a result, a National Coordinating Committee on Large Volume Parenterals was established with representation from industry, regulatory bodies, academia, and compendia.

The particulate insult to the patient was considered to be a function of volume of injectable. Ultimately, this group recommended an inspection method based on membrane filtration followed by microscopy. The methodology was essentially an earlier method for determining particulates in hydraulic oils and, in a refined form, is still in the Pharmacopoeia today (USP XXII, <788>). Instrumental methods were used elsewhere, however. The Coulter Counter had been used in the UK in 1964 (14) and was the basis of initial studies in Australia (15). The HIAC counter (16) originated from the need for an automatic instrumental method for determining particles in hydraulic oil and was also evaluated in the United States, the United Kingdom, and Australia (17). This instrument is featured in the current (1988) British Pharmacopoeia, together with the Coulter method. In the United States, the HIAC was introduced industrially in the mid-1970s because of problems experienced in measuring an amorphous precipitate that occurred in high concentrations of dextrose solutions and that was otherwise difficult to quantitate by microscopy. The compendial authorities allowed this alteration in test methodology as a special case. The HIAC was then introduced in the USP XXI (1985) for the small-volume (<100 mL) injections, which up to that point had been neglected officially although some evidence suggested that small-volume injections could also be a significant source of particulates. Surprisingly, as will be discussed later, this innovation caused a considerable amount of concern in the industry, despite the fact that some sections had been using the instrument for over a decade as a release specification for injectable solutions containing high concentrations of dextrose.

### Current Issues with Particulate Detection Methods

**The Microscopic Method.** The method described in the current USP XXII <788> is applied to solutions with volumes in excess of 100 mL and is basically an adoption of an earlier method. It has both advantages and disadvantages. As officially described, the work must be done in an ultra-HEPA (high efficiency particulate air) filtered environment; a sample of 25 mL is removed from the container after mixing and passed through a membrane filter. After washing with water, the filter is allowed to dry and is examined with a microscope using incident light. Particles with linear dimensions exceeding 10 and 25  $\mu\text{m}$  are counted and, after subtracting any blank values, reported as the number per mL equal to or larger than the size threshold. With this method, the longest linear dimension is measured; therefore, the method discriminates in favor of fibrous particulates. The major advantage of this method is that the

operator actually sees the particulates and can make judgements about the nature of the contamination. However, the Pharmacopoeia does not, in fact, use the method for that purpose; it is used purely as a counting procedure.

The present procedure has some major problems and could be improved considerably (23) by taking the total contents of a container rather than a small sample. Furthermore, improvements in microscopy by using epidiastopic illumination and an improved eyepiece graticule and in the filter by using new precision all-glass membrane filters have been proposed (24). Perhaps the most serious criticism of the microscopic method, quite apart from difficulty in counting the amorphous particulates found in dextrose solutions, is the fact that oil droplets are absorbed into the composition of the filter and are not detected. This fact became evident when solutions containing excess silicone lubricant were examined by light extinction instruments and gave appreciably higher counts. Such results demonstrated that this contaminant had not been counted previously by microscopy. Indeed, some "authorities" went so far as to deny that oil droplets are, in fact, particulates, although this argument appears somewhat tenuous (22).

An improved methodology is currently being evaluated and will be proposed for consideration by the compendial authorities. The inability to detect oils and some doubts about the accuracy of measurement of 10  $\mu\text{m}$  by optical microscopy are serious constraints on the method; nevertheless, the fact that particulate morphology can be readily seen and even, with improved instrumentation, identified suggests that the method will be retained in <788> but not necessarily used for quantitation. Some critics have suggested that the method is inexpensive to operate. On the contrary, it is labor intensive, requires a highly trained operator as well as expensive HEPA-filtered facilities, and overall is less than satisfactory.

**The Coulter Principle.** Although not used for this purpose in the United States to any significant degree, a compendial method based on use of the Coulter Counter has been used in the United Kingdom since the 1973 edition of the British Pharmacopoeia. In the United Kingdom, Coulter Counters are used in hospital hematological laboratories so instruments are available for use by hospital pharmaceutical quality control areas. The instrument is undoubtedly well researched and established in the field (14, 15, 17-19). Practically, however, the device has a problem in that electrolyte is essential for detection of particulates, and for some parenteral solutions, electrolyte must be added prior to evaluation. This procedure is an additional stage in the analysis, and industrially, the HIAC instrument tends to be preferred because it is faster overall.

**Light Extinction Methodology.** The HIAC/Royco light extinction instrument was allowed by the USP for evaluation of particle burden in large-volume dextrose solutions. The method has been used extensively in the industry

as a release specification (Barber, T., personal communication). Nevertheless, when the USP XXI introduced a procedure to limit particulates in small-volume injectables, a considerable amount of discussion ensued. The instrument is based on the blockage or extinction of light caused by the passage of an obscuring particle between a light source and a suitable detector. Although originally devised in the early 1960s for use with hydraulic oils (16), the principle is attractive because it can be used in-line, does not require electrolyte, and is effective at detecting particles above the wavelength of the illuminating white light, that is, above approximately 1  $\mu\text{m}$ . Again, well supported by literature (17, 20, 21), the instrumental principle has been used extensively by the pharmaceutical industry.

Some issues about the machine have surfaced (Barber, T. A.; Lannis, M. D.; Williams, J. G.; Ryan, J. R. *J. Parent. Sci. Technol.*, in press):

- sensitivity to flow rate and subthreshold interference by particles below a set threshold level
- sensitivity to coincident passage when particles pass through the sensing zone together
- sensitivity to shape
- sensitivity to relative refractive index between the particle and the carrying fluid

The first two issues are actually irrelevant for parenteral solutions, which are by definition clean and do not contain significant quantities of particulates. The possibility of small ( $<10 \mu\text{m}$ ) oil droplets being present in a solution has been discussed by Barber, but a solution containing this amount of material must be regarded as aberrant and contaminated to the point of being undesirable. Shape and relative refractive index are certainly effects that reduce the count measured by the machine, but for comparative purposes, the instrument is useful because it allows the analyst to judge the quality of a filtered solution being passed through the instrument.

Although the method was originally intended to be official on January 1, 1985, the date that the USP XXI became legally effective, a concern was expressed to the authorities by a number of individuals and organizations. It was unfortunate that at about this time the only U.S. supplier of instruments based on the light extinction principle was also undergoing a major reorganization, including a move from California to Virginia. For a while, the net effect of this reorganization was an inability to supply new instruments or effectively service existing machines. The USP therefore extended the deadline, initially for six months and eventually for one year, so that the method did not become official until January 1, 1986. A comparison of the  $<788>$  in the USP XXI (1985) and the USP XXII (1990) shows that the official method has been improved and developed considerably during the intervening four years, and indeed, the



development process is still continuing. Unfortunately, manufacturers themselves have continued to develop their own instruments; the net effect of these solo developments is a range of devices in laboratories with different sensitivities and resolutions, not all of which are suitable for the required purpose. Accordingly, <788> was modified to include procedures to determine sensor resolution, sample volume accuracy, and calibration, as well as allowing sample pooling. Although operated in a clean environment, it may be noted that this is probably not completely necessary.

As manufacturers improved their product, the education and experience base of the parenteral industry also increased, and complaints about the method diminished (Gallelli, J., personal communication). In addition, alternative suppliers of light extinction methods have been identified so that, in a competitive environment, improvements in both equipment and data processing have now appeared. Overall, the environment has improved for users, manufacturers, regulatory authorities, and compendial authorities. The Food and Drug Administration (FDA) has maintained a watching brief. Admitting that only the light extinction method can be used in FDA laboratories has again provided some unofficial guidance to parenteral manufacturers (25).

This developmental phase between 1986 and 1990 has been beneficial all around and has mainly come about by an educational process initiated at the bench and carried through to management. Information has been provided by educators, other users, and instrument manufacturers. As information diffused, so concerns diminished. This is not to say that concerns have disappeared altogether, but it is anticipated that the recent proposal to extend the light extinction methodology to large-volume parenterals in the USP (26) will be less traumatic.

### **Future Concerns**

As experience increases, it becomes evident that no one method (microscopy, light extinction, or any other based on different principles) is ideal. It is irrelevant, for example, to complain that results obtained by one method do not correlate with those obtained by another, because of course, each method is based on different principles of detection and measures different particle parameters. Pharmacopoeial limits, therefore, must be set with reference to the detection method employed in the monograph. Extending the evaluation of all particulates to one unified methodology will be a step forward, but that method itself would require considerable improvement.

Standards of cleanliness are substantially based on those proposed by Vessey and Kendall (15) 25 years ago, and it is time to reassess the relevance of these standards in today's technical environment. For example, detection and counting particles based on 5-mL samples (as specified in <788> for small-volume injections) will be extremely difficult if

solutions containing less than 1 particle of 25- $\mu\text{m}$  diameter in 100 mL of a parenteral became common place. Instruments must be modified to count the particulates in the whole contents of a container. By using information obtained from measurements of the whole size distribution between limits already well established for light extinction instruments (e.g., 1–100  $\mu\text{m}$ ), statistical tests of the validity of the log–log distribution law can be established (13, 22). The instruments can be used to determine whether an unacceptable level of contamination or an undue amount of a particular species is present in the system. If unacceptable amounts of a particular species are present, the pharmacopoeial monograph could require the use of a chemical or a physical limit test as a second stage of evaluation. Particle detection is not specific, neither is it designed or intended to be, and it is more appropriate to apply other tests to limit extraneous silicone oil, plasticizers such as phthalates, or undissolved preservatives such as benzyl alcohol. However, the instruments could be used to provide a warning during the first or screening stage that the product may have a problem.

Finally, instruments should be less affected by factors such as morphology or transparency of the particulates. This ideal instrument remains to be devised and tested. In the meantime, we need to learn how to apply what we already have and how to correctly interpret the data that we are obtaining. These provide serious challenges for the present as well as for the future.

### Literature Cited

1. *Proc. Nat. Symp. & Safety of Large Volume Parenteral Solutions* Food and Drug Administration, Washington, D.C., 1966.
2. Groves, M. J. *Parenteral Products*, Heinemann Medical, London, 1973.
3. Groves, M. J. *Parenteral Technology Manual*, 2nd Ed.; Interpharm Press, Buffalo Grove, IL, 1988.
4. Garvan, J. M.; Gunner, B. W. *Med. J. Austral.*, 1963, 2, 140–144.
5. Garvan, J. M.; Gunner, B. W. *Med. J. Austral.*, 1964, 2, 1–8.
6. Garvan, J. M.; Gunner, B. W. *Brit. J. Clin. Pract.*, 1971, 25, 119–130.
7. Robinson, L. A.; Braimbridge, M. V.; Hearse, D. J. *J. Thorac. Cardiovasc. Surg.* 1984, 87, 48–58.
8. Hearse, D. J.; Erol, C.; Robinson, L. A.; Maxwell, M. P.; Braimbridge, M. V. *J. Thorac. Cardiovasc. Surg.* 1985, 89, 428–438.
9. Robinson, L. A.; Harwood, D. L. *Circulation*, 1986, 74, Suppl. 11–400.

10. Groves, M. J. *Analyst*, **1969**, *94*, 992–998.
11. Groves, M. J.; Wong, J. *Pharm. Technol.* **1986**, *10*(11), 32–40.
12. Groves, M. J.; Wong, J. *Drug Dev. Ind. Pharm.* **1987**, *13*(1), 193–199.
13. Groves, M. J.; Mühlen, E. *J. Parent. Sci. Technol.* **1987**, *41*(4), 116.
14. Groves, M. J.; Major, J. F. G. *Pharm. J.* **1964**, *193*, 227–229.
15. Vessey, I.; Kendall, C.E. *Analyst* **1966**, *91*(4), 273–278.
16. Carver, L. D. *Ann. N.Y. Acad. Sci.* **1969**, *158*(3), 710–720.
17. Groves, M. J.; Wana, D. *Powder Technol.* **1977**, *18*, 215–222.
18. Taylor, S. A.; Spence, J. *J. Pharm. Pharmacol.* **1983**, *35*(12), 769–773.
19. Spence, J. *Anal. Proc. (London)* **1981**, *18*(12), 509–511.
20. Knapp, J. Z.; DeLuca, P. P. *J. Parent. Sci. Technol.* **1988**, *42*, 1 S Supplement, Technical Report No. 9.
21. Borchert, S. J.; Abe, A.; Aldrich, D. S.; Lloyd, E. F.; Freeman, J. E.; White, R. D. *J. Parent. Sci. Technol.* **1986**, *40*(5), 212–241.
22. Groves, M. J. *Proc. PDA Int. Conf. on Particle Detection, Metrology and Control*, **1990**, 82–102.
23. Draftz, R. G. *Proc. PDA Int. Conf. on Particle Detection, Metrology and Control*, **1990**, 458–466.
24. Bares, D.; Lannis, M. *Proc. PDA Int. Conf. on Particle Detection, Metrology and Control*, **1990**, 467–501.
25. Munson, T. E. *Proc. PDA Int. Conf. on Particle Detection, Metrology and Control*, **1990**, 827–832.
26. Gallelli, J. F. *Proc. PDA Int. Conf. on Particle Detection, Metrology and Control*, **1990**, 805–815.

RECEIVED February 15, 1991

## Chapter 9

# Measurement of Particle Size Distributions with a Disc Centrifuge Data Analysis Considerations

Michael J. Devon<sup>1</sup>, Theodore Provder<sup>2</sup>, and Alfred Rudin<sup>3,4</sup>

<sup>1</sup>Dow Chemical Canada Inc., P.O. Box 3030, Sarnia, Ontario N7T 7M1,  
Canada

<sup>2</sup>The Glidden Company, 16651 Sprague Road, Strongsville, OH 44136

<sup>3</sup>Guelph-Waterloo Centre for Graduate Work in Chemistry, Department  
of Chemistry, University of Waterloo, Waterloo, Ontario N2L 3G1, Canada

The disc centrifuge with an optical detector measures particle size distributions of various types of particles over a wide dynamic size range, .01 to 50  $\mu\text{m}$  based on Stokes' Law for centrifugation. Generally the extinction efficiency of particles is a function of particle size, refractive index and an optical correction based on Mie scattering theory is required to ensure that the photodetector response is proportional to particle concentrations. It is shown that such corrections can be simplified if experimental conditions are adjusted to prevent the largest particles from sedimenting in short spin times. When this is done, data acquired on an equal time interval basis can be used to obtain valid particle size distribution averages.

The disc centrifuge (1,2) with an optical detector is an excellent instrument for the measurement of particle size distributions of species with sizes from several micrometers down to less than 0.1  $\mu\text{m}$ . A small sample is injected into the center of a spinning disc containing a known volume of fluid. The particles sediment toward the outer edge of the rotor where they pass through the light beam of the optical detector. The hydrodynamic sizes of the particles that are being detected can be calculated from Stokes' Law, as described below, and the time between injection and the arrival of the particular species at the detector light beam. The instantaneous output of the detector is used to estimate the number of particles in the beam, and thus to measure the particle size distribution.

It is recognized, however (3-5), that the uncorrected output of the detector is proportional to the number of particles only for large particles or for a very narrow particle size distribution.

<sup>4</sup>Corresponding author

0097-6156/91/0472-0134\$06.00/0  
© 1991 American Chemical Society

Generally the extinction efficiency of particles is a function of particle size and refractive index as well as the wavelength of the light beam. A valid optical correction method has been proposed (6) but its application is somewhat tedious without the approximation of a single wavelength computation of extinction efficiency for the whole distribution. In this article we delineate the experimental conditions under which the optical correction may be simplified allowing for data acquisition on a straight time basis and simplifying data collection. The disc centrifuge method of particle size analysis without the use of explicit optical corrections is shown to provide reliable information for the particle size distributions of various polymer emulsions.

### Theory

The disc centrifuge operates by forcing particles radially outward through a spin fluid under high centrifugal force. The particles settle at rates determined by their sizes and densities. At a specific radial distance the particles interrupt a light beam and the particle size and relative concentrations of the particles are calculated from known parameters. Particle settling is described by Stokes' Law for centrifugation.

$$D^2 = \frac{6.299 \times 10^9 \eta \log(R/R_0)}{t \omega^2 \Delta \rho} \quad (1)$$

where t = centrifuge time in minutes  
 D = particle diameter in micrometers  
 $\omega$  = centrifugal speed in rotations per minute  
 $\Delta \rho$  = density difference between particles and spin fluid in g/mL  
 $\eta$  = spin fluid viscosity in poises  
 R = fixed distance from the center of the disc cavity to where the photodetector is located  
 R<sub>0</sub> = starting distance of particles from the center of the disc cavity, determined by the volume of spin fluid used in the rotor.

The most generally applicable method for turbidity axis calibration in the turbidity-time raw data plot of the disc centrifuge is the technique described by Oppenheimer (6). The turbidity,  $\tau$ , of a uniform dispersion illuminated by monochromatic light with incident intensity I<sub>0</sub> is given by

$$\frac{I}{I_0} = e^{-(\tau \ell)} \quad (2)$$

where I is the transmitted intensity and  $\ell$  is the path length. From eq. (2):

$$\tau(t) = \frac{1}{\ell} \ln \frac{I_0}{I(t)} = \frac{1}{\ell} \ln \frac{1}{T(t)} \quad (3)$$

where  $T(t)$  is the transmittance at time  $t$ . The turbidity is related to the particle diameter  $D$ , and to the number of particles in the light path at time  $t$  by the expression (7)

$$\tau(t) = \frac{(2.303)D^3 F_N(D) Q_{\text{ext}}(D, m, \lambda)}{16 R^2 \ell_n(R/R_0)^2}, \quad (4)$$

where

- $F_N(D)$  =  $(dn/dD)$  is the differential number distribution of particles between  $D$  and  $D+dD$  at the center of the detection zone
- $Q_{\text{ext}}(D, m, \lambda)$  = the extinction coefficient which includes absorption and scattering effects
- $m$  = relative refractive index; ratio of particle refractive index to that of the medium.
- $\lambda$  = wavelength in the medium.

Time is related to diameter,  $D$ , in eq. (4) through Stoke's Law, eq. (1). For a fixed detector position at radius  $R$ , the turbidity is proportional to the differential volume distribution  $D^3 F_N(D)$ . The term  $R^2 \ell_n(R/R_0)$  in the denominator of eq. (4) is a radial dilution factor. The turbidity will decrease as the particles spread radially outward in the disc cavity. In the disc centrifuge experiment raw data are obtained as a function of time. For a fixed detector position,  $R$ , and fixed spin fluid volume corresponding to  $R_0$ , the denominator in eq. (4) is a constant.

The procedure for estimating  $Q_{\text{ext}}$  involves calculations using Mie theory (8) for given values of diameter, wavelength and refractive index ratio of the polymer and spin fluid. A computer program eliminates the more tedious aspects of curve fitting in the calculation of  $Q_{\text{ext}}$ . Each polymer has a different refractive index.  $Q_{\text{ext}}$  itself is also a function of the particle size and the wavelength of the light source. For polychromatic light, which normally is used, it is usually necessary to integrate the product of  $Q_{\text{ext}}$  and the wavelength response of the instrument over the range of wavelengths. Oppenheimer (6) showed, however, that for low relative refractive indices a single-wavelength computation of  $Q_{\text{ext}}$  is a good approximation. This approximation to the integrated extinction coefficient will be designated as  $\bar{Q}_{\text{ext}}(D, m)$ . The calculation of the extinction efficiencies for a wide range of diameters is a slow process for a microcomputer. Also, the wavelength dependence of refractive index is not readily available for all materials that may be analyzed on the instrument.

An assumption made in disc centrifuge analysis is that the turbidity is proportional to the negative logarithm of the transmittance:

$$\tau \propto -\ln T \approx (1-T) = \frac{I_0 - I(t)}{I_0}, \quad \text{for} \quad \frac{(T-1)^2}{2} \ll 1 \quad (5)$$

The percentage error in this assumption is given by:

$$\% \text{ Error} = \{[\ln T - (T-1)] / \ln T\} \times 100 \quad (6)$$

If the transmittance level is 80%, the error will be less than 10% in turbidity. The actual expression used for the normalized differential volume distribution utilizing eqs.(5) and (4) is as follows:

$$D^3 F_N(D) dD = \frac{\{(I_0 - I(t)) / I_0\} \bar{Q}_{ext}(D, m) dD}{\int_{D_L}^{D_H} \{(I_0 - I(t)) / I_0\} \bar{Q}_{ext}(D, m) dD} \quad (7)$$

where  $D_L$  and  $D_H$  are the smallest and largest particle diameters in the sample particle size distribution.

For particles of constant density the normalized differential volume distribution can be considered the normalized differential weight distribution of particle sizes,  $F_w(D)$ ,

$$F_w(D) dD = D^3 F_N(D) dD. \quad (8)$$

The formulae for the calculation of distribution averages are shown in Table I both in discrete and integral form where  $F_N(D)$  is defined by eq.(7) for integration in diameter space.

Equation(4) can be rearranged and set up for integration of the turbidity function in time space. From Stoke's Law, eq.(1)

$$D^2 t = K \quad (9)$$

$$dt = -(2K/D^3) dD \quad (10)$$

where  $K$  is a constant. Utilizing eq.(4) and the definition of  $\bar{Q}_{ext}(D, m)$ ,

$$F_N(D) D^3 dt = \frac{16 \ell R^2 (R/R_0) \tau(t) dt}{(2.303) \bar{Q}_{ext}(D, m)} \quad (11)$$

Substitution of eqs.(10) and (5) into eq.(11) and normalization yields

$$F_N(D) dD = \frac{\{(I_0 - I(t)) / I_0\} \bar{Q}_{ext}(t, m) dt}{\int_{t_0}^{t_f} \{(I_0 - I(t)) / I_0\} \bar{Q}_{ext}(t, m) dt} \quad (12)$$

where  $t_0$  and  $t_f$  correspond to the time of appearance of the largest and smallest particle diameters in the sample, respectively, in the center of the detection zone. Thus the product of the diameter and the turbidity extinction coefficient ratio yields the number average diameter in time space.

$$\bar{D}_N = \frac{\int_{D_L}^{D_H} D F_N(D) dD}{\int_{D_L}^{D_H} F_N(D) dD} = \frac{\int_{t_0}^{t_f} \{(I_0 - I(t)) / I_0\} D(t) \bar{Q}_{ext}(t, m) dt}{\int_{t_0}^{t_f} \{(I_0 - I(t)) / I_0\} \bar{Q}_{ext}(t, m) dt} \quad (13)$$

It follows that the weight average diameter in time space is given by

$$\bar{D}_w = \frac{\int_{D_L}^{D_H} D [D^3 F_N(D)] dD}{\int_{t_0}^{t_f} \{[(I_0 - I(t))/I_0] / \bar{Q}_{ext}(t, m)\} dt} \quad (14)$$

In this work the proportionality between the integrated extinction coefficients ( $\bar{Q}_{ext}$ ) and the slope of a Stokes Law plot (i.e. particle diameter versus spinning time) is investigated for a range of diameters. The manner in which the extinction coefficient varies with diameter (i.e. increasing  $\bar{Q}_{ext}$  with increasing diameter up to 1.1  $\mu\text{m}$ ) is similar to the manner in which time and diameter are related (i.e. increasing inverse time with increasing diameter) through Stokes' Law (eq.1)). The range over which this relationship holds true is determined by the conditions used in the disc centrifuge measurement. It turns out that this range is dependent on the time for the initial appearance of the sample at the photodetector.

The relationship that is observed between  $\bar{Q}_{ext}$  and time of appearance of the particles at the photodetector under favorable operating condition permits elimination of the explicit expression for the extinction efficiency from eq.(12) and the simplification of the data handling in this analysis.

We have calculated the extinction coefficients for a number of different types of latex particles (polystyrene, poly(vinyl acetate) and acrylic copolymers) and then used these coefficients to calculate distribution averages for different polymers that have been analyzed with the disc centrifuge. These averages are then compared to those that are computed without the explicit use of the extinction coefficient, but a simplified form of the extinction coefficient.

Ultimately the reliability of the disc centrifuge for latex particle size analysis is determined by the precision and accuracy of the results obtained. We have determined the minimum number of points required for precise measurements and are able to confirm accuracy by measurements on standards of known diameter.

### Experimental

Particle size measurements were performed with an ICI-Joyce Loebel Disc Centrifuge Mk III with the photodetector attachment. A very important step in the operation of the centrifuge is the formation of a density gradient within the spin fluid to allow better and more efficient separation of the suspended particles. The buffered line start method has been widely used (9). For this work, however, the external gradient method of Holsworth and Provder (10), was preferred because of its simplicity. A hypodermic syringe is used to form the density gradient external to the disk. For spin conditions in which 15 mL of aqueous spin fluid were used:



exactly 15 mL of water were drawn into a 25 mL syringe. Air bubbles were then expelled from the syringe. With the needle pointing down, an additional 1 mL of methanol was drawn into the syringe. This entire volume was then injected into the spinning disc cavity of the disc centrifuge. Centrifuge speeds were chosen so that particles passed the detector at times between 1 and 25 minutes after injection. Speeds were used 3200 to 8534 rpm, depending on the particular sample.

Commercial acrylic, vinyl acetate copolymer and polystyrene latex samples were diluted to between 0.25 and 0.5% weight concentrations with a 80% water - 20% methanol mixture. The spin fluid in all cases was water and the density gradient within the spin fluid was formed with methanol. The output of the optical detector was acquired with a minicomputer data acquisition system and converted to particle size distributions. Distribution averages are calculated according to the formulae listed in Table I.

Calculations of the integrated extinction efficiencies,  $\bar{Q}_{\text{ext}}$ , for the particle size range of 100 to 1000 nm were done at 50 nm intervals with a microcomputer by the method described by Oppenheimer (6). The output of this program was fitted to a third degree polynomial to allow calculation of  $\bar{Q}_{\text{ext}}$  for each measured diameter. The calculation of  $\bar{Q}_{\text{ext}}$  was done for several aqueous spin fluids and polymer types. The wavelength dependence of the refractive indices of the spin fluids was taken from the literature (11). Refractive indices and densities of solvent mixtures are best determined experimentally. However, the refractive index of the mixture,  $\eta_m$ , may be calculated if the density of the mixture,  $\rho_m$ , the densities of the components of the mixture,  $\rho_1$ ,  $\rho_2$ , and the refractive indices of the components,  $\eta_1$ ,  $\eta_2$ , are known accurately (12). The simplest formula to use in this case is the empirical Gladstone-Dale equation:

$$\frac{1}{\rho_m} (\eta_m - 1) = (w_1 / \rho_1) (\eta_1 - 1) + (w_2 / \rho_2) (\eta_2 - 1) \quad , \quad (15)$$

where  $w_1$  and  $w_2$  are the weight fractions of the components of the spin fluid mixture. The wavelength dependence of the refractive index of the polymers also was taken from the literature (13), where possible, or measured via the method of Devon and Rudin (14).

### Results and Discussion

We have investigated the proportionality between the extinction coefficients and the slope of the Stokes' Law plot. Stokes' Law plots for polystyrene and polymethyl methacrylate at a given set of spin parameters are shown in Figure 1.

Figure 2 illustrates the relationship between particle diameter and the integrated extinction coefficient. The polystyrene integrated extinction coefficient includes data for three different spin fluids (water, 4% aqueous sucrose and 7% aqueous methanol).

TABLE I

## FORMULAE FOR THE CALCULATION OF DISTRIBUTION AVERAGES

(A general definition of a statistical moment of particle size taken about

zero is

$$U_j = \sum n_i D_i^j,$$

where  $n_i$  is the number fraction of particles per unit volume of the sample with diameter  $D_i$ .

## NUMBER MEAN

$$\bar{D}_N = \frac{U_1}{U_0} = \frac{\sum n_i D_i}{\sum n_i} = \int D F_N(D) dD$$

## SURFACE MEAN

$$\bar{D}_S = \left( \frac{U_2}{U_0} \right)^{1/2} = \left( \frac{\sum n_i D_i^2}{\sum n_i} \right)^{1/2} = [\int D^2 F_N(D) dD]^{1/2}$$

## VOLUME MEAN

$$\bar{D}_V = \left( \frac{U_3}{U_0} \right)^{1/3} = \left( \frac{\sum n_i D_i^3}{\sum n_i} \right)^{1/3} = [\int D^3 F_N(D) dD]^{1/3}$$

## SPECIFIC SURFACE MEAN

$$\bar{D}_{SS} = \frac{U_3}{U_2} = \frac{\sum n_i D_i^3}{\sum n_i D_i^2} = \frac{\bar{D}_V^3}{\bar{D}_S^2} = \frac{\int D^3 F_N(D) dD}{\int D^2 F_N(D) dD}$$

## WEIGHT MEAN

$$\bar{D}_W = \frac{U_4}{U_3} = \frac{\sum n_i D_i^4}{\sum n_i D_i^3} = \frac{\int D^4 F_N(D) dD}{\int D^3 F_N(D) dD}$$

## TURBIDITY MEAN

$$\bar{D}_T = \left( \frac{U_6}{U_3} \right)^{1/3} = \left( \frac{\sum n_i D_i^6}{\sum n_i D_i^3} \right)^{1/3} = [\int D^6 F_N(D) dD / \int D^3 F_N(D) dD]^{1/3}$$

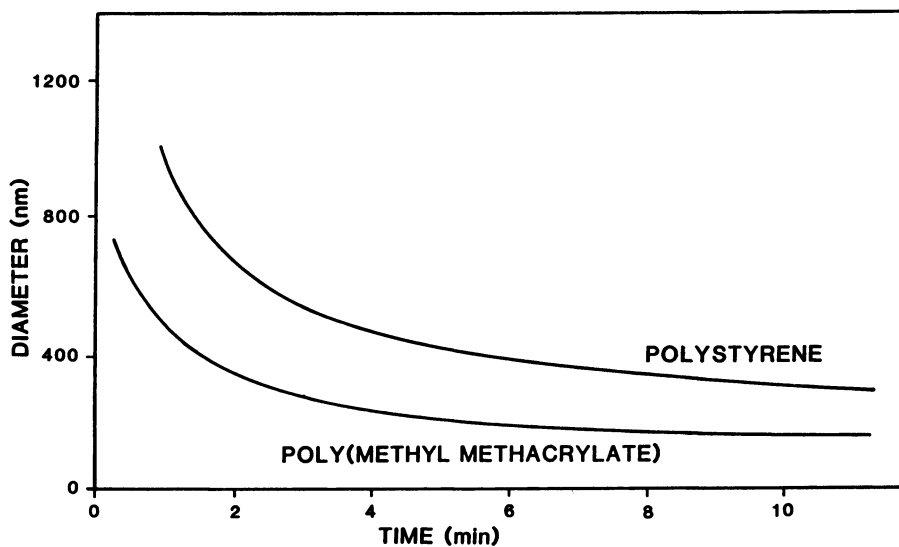


Figure 1: Stokes' Law Plot for Polystyrene and Polymethyl Methacrylate Latexes

Spin Parameters: spin fluid viscosity = 0.9584 cP  
spin fluid density = 0.9978 g/mL  
rotational speed = 8534 rpm  
spin fluid volume = 15 mL

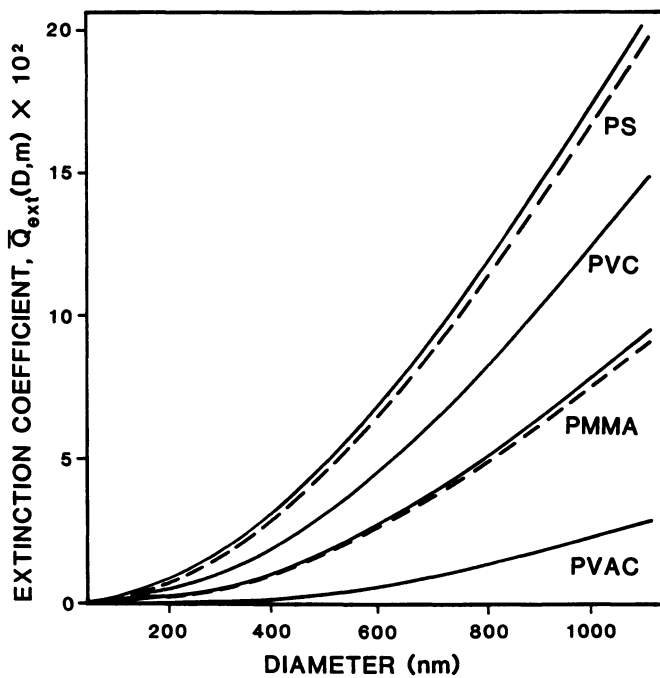


Figure 2: Relations between particle diameter and calculated extinction efficiency of Polystyrene, Polyvinyl chloride, Polymethyl Methacrylate and Polyvinyl Acetate Latexes.

The poly(methyl methacrylate) integrated extinction coefficient includes data for two spin fluids (water and 7% methanol in water). This figure shows that the different aqueous spin fluids have little effect on the integrated extinction efficiencies because their refractive indices hardly differ. The different relations for the different polymers result from differences in their refractive indices.

The extinction coefficients from Figure 2 were then compared to the Stokes' Law relationship by combining the inverse time plot and the extinction coefficient for the same polymer onto the same plot. The curves superimpose (Figures 3-8) over a range of diameters. Deviations occur at the larger diameters in some of the plots (Figure 3,6,7). The onset of the deviation between the two curves occurs when the large diameter particles appear at the detector after short spin times. The range over which the two curves superimpose is determined by the type of polymer and the operational spin parameters. Therefore, improved fits at these diameters can be obtained by changing the operational spin parameters in a manner that ensures that larger diameters appear at longer times (Figure 8). Figures 3, 4, 6 and 7 show the values of the critical time ( $t_c$ ) above which the two curves will superimpose and below which the two curves diverge.

Inverse time and extinction coefficient, for a particular polymer run under a particular set of spin conditions, are related through a constant, A, according to the following equation:

$$\frac{1}{\bar{t}} = A \bar{Q}_{\text{ext}} \quad (16)$$

The constant, A, that fits the extinction efficiency to inverse time can be related to operational spin parameters. For example, a good fit is obtained for a polystyrene sample with a disc rotational speed of 8534 rpm instead of a 6400 rpm (Figures 4,5).

The relationship between the fitting constants  $A_1$  and  $A_2$  for any two respective spin conditions is derived as follows from eqs. (9) and (16):

$$\frac{1}{\bar{t}} = A \bar{Q}_{\text{ext}} = \frac{D^2}{K} \quad , \quad (17)$$

where K is the Stokes Law constant:

$$K = \frac{6.299 \times 10^9 \eta \log (R/R_0)}{\omega^2 \Delta \rho} \quad . \quad (18)$$

Thus for two disc spin conditions:

$$\frac{A_1 \bar{Q}_{\text{ext}}}{A_2 \bar{Q}_{\text{ext}}} = \frac{D^2/K_1}{D^2/K_2} \quad . \quad (19)$$

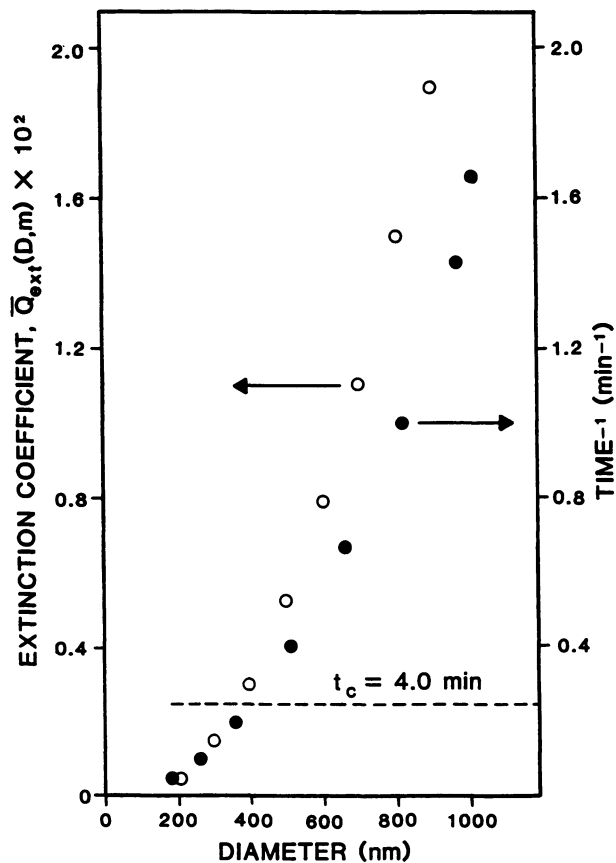


Figure 3: Extinction coefficient and Inverse Time vs. Diameter for Poly(vinyl acetate) Latex.  
 Spin Parameters: spin fluid viscosity = 1.055 cP  
 spin fluid density = 0.9857 g/mL  
 rotational speed = 6400 rpm  
 spin fluid volume = 20 mL

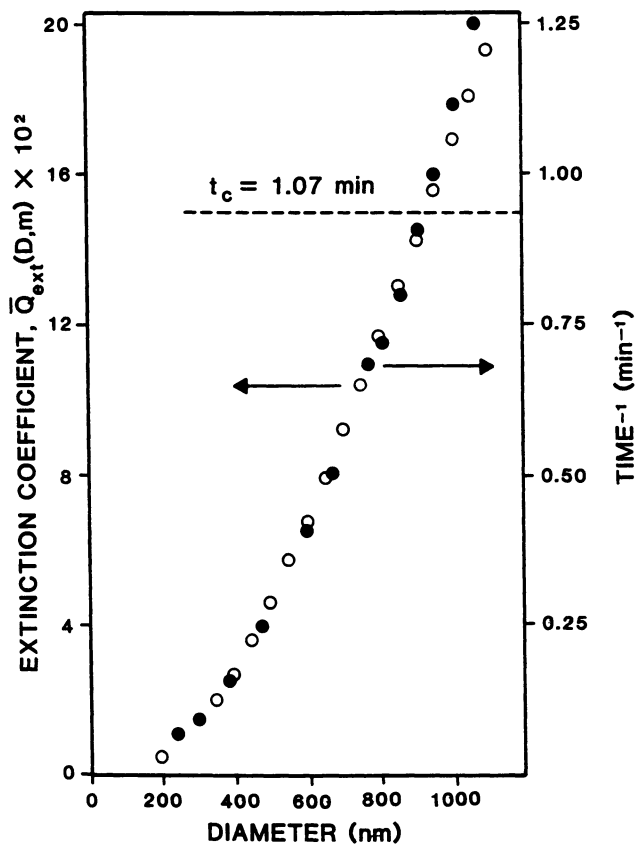


Figure 4: Extinction coefficient and Inverse Time vs. Diameter for Polystyrene Latex.

Spin Parameters: spin fluid viscosity = 0.9589 cP  
 spin fluid density = 0.9978 g/mL  
 rotational speed = 8534 rpm  
 spin fluid volume = 15 mL

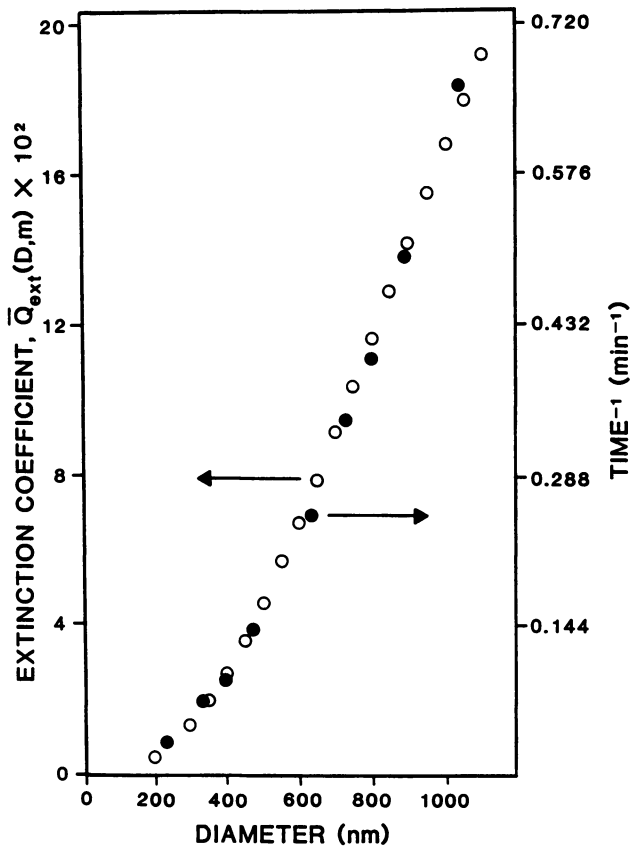


Figure 5: Extinction coefficient and Inverse Time vs. Diameter for Polystyrene Latex.

Spin Parameters: spin fluid viscosity = 0.9589 cP  
 spin fluid density = 0.9978 g/mL  
 rotational speed = 6400 rpm  
 spin fluid volume = 15 mL



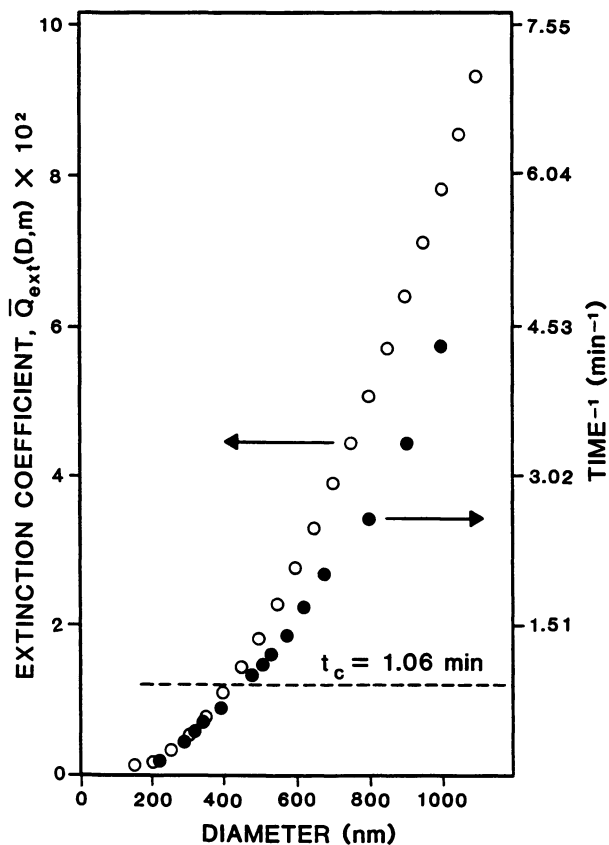


Figure 6: Extinction coefficient and Inverse Time vs. Diameter for Poly(methyl methacrylate) Latex.  
 Spin Parameters: spin fluid viscosity = 0.9548 cP  
 spin fluid density = 0.9978 g/mL  
 rotational speed = 8534 rpm  
 spin fluid volume = 15 mL

**American Chemical Society  
 Library**

1155 16th St., N.W.

In Particle Size Distribution by Prodyer, T.;  
 ACS Symposium Series 477; American Chemical Society: Washington, DC, 1991.

Washington, D.C. 20036

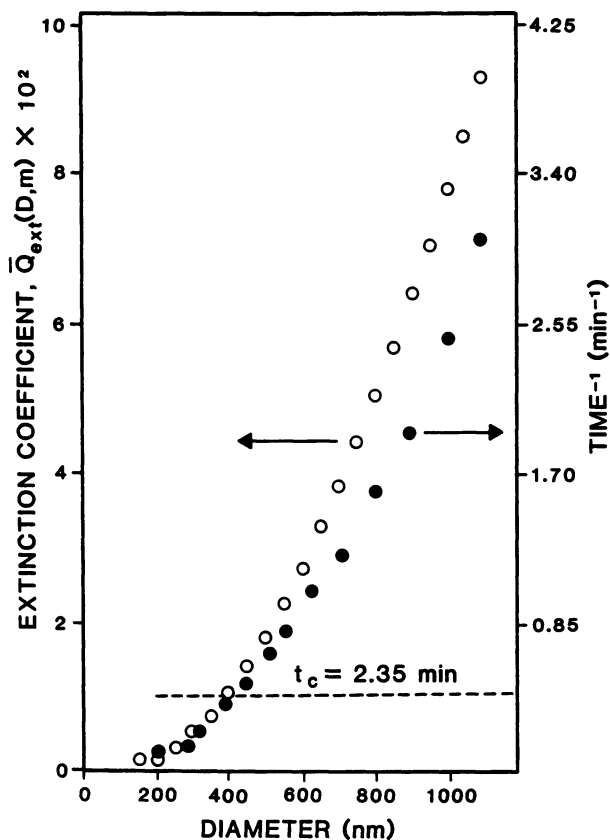


Figure 7: Extinction coefficient and Inverse Time vs. Diameter for Poly(methyl methacrylate) Latex.  
 Spin Parameters: spin fluid viscosity = 0.9548 cP  
 spin fluid density = 0.9978 g/mL  
 rotational speed = 6400 rpm  
 spin fluid volume = 15 mL

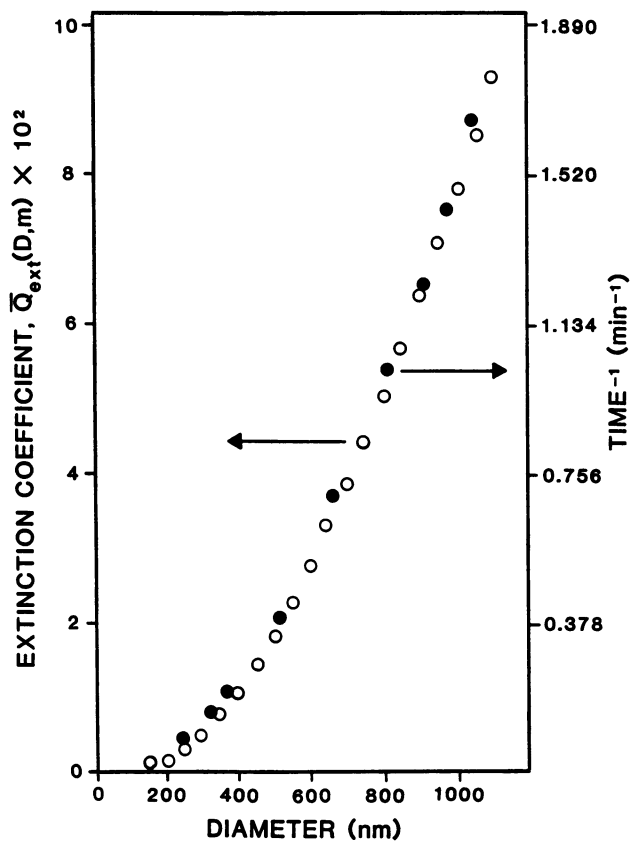


Figure 8: Extinction coefficient and Inverse Time vs. Diameter for Poly(methyl methacrylate) Latex.  
 Spin Parameters: spin fluid viscosity = 0.9548 cP  
 spin fluid density = 0.9978 g/mL  
 rotational speed = 4265 rpm  
 spin fluid volume = 15 mL

Then for two disc spin conditions where only the rotational speeds can vary:

$$\sqrt{\frac{A_1}{A_2}} = \frac{\omega_1}{\omega_2} \quad (20)$$

Similar proportionalities exist for other operational spin parameters such as viscosity of the spin fluid and spin fluid volume.

The relationship between the extinction coefficient of the particles and their appearance time at the detector allows a substitution of the extinction efficiency in equation (12). From equation (17) the relationship between the extinction efficiency and the diameter,  $D(t)$ , is as follows:

$$\bar{Q}_{\text{ext}}(t,m) = D^2(t)/KA \quad (21)$$

Substitution of eq. (21) into eq. (12) leads to

$$F_N(D)dD = \frac{\{(I_0 - I(t))/I_0\}D^2(t)dt}{\int_{t_0}^{t_f} \{(I_0 - I(t))/D^2(t)\}dt} \quad (22)$$

which is now only a function of time and diameter and explicitly independent of the extinction coefficient. Thus over the ranges of experimental data where  $t > t_c$  there is a fixed relationship between  $\bar{Q}_{\text{ext}}(t,m)$  and diameter.

Figure 9 shows a typical raw photosedimentometer trace. The distribution averages are calculated with eqs. (12) and (22). The averages for typical size distributions that would result from different emulsion polymerization systems are contained in Table II. A comparison of averages as measured with eqs. (12) and (22) shows that the deviations are generally small. The most significant deviations occurred with the larger diameter vinyl acetate copolymer. This latter sample was run on the disc centrifuge in such a manner that there was only a very short interval between the start of the run and the initial detection of particles. Thus, some of the larger particles appeared at the detector in time less than  $t_c$ .

It was reported previously that the extinction coefficient may be considered constant generally, if the operational spin parameters in eq. (1) are chosen such that the initial sample appearance time at the photodetector is greater than five minutes (15). With broadly distributed samples, this may be a difficult condition to achieve since delaying the appearance of the large particles will most likely result in an unreasonable lengthening of the time of the experiment.

The above method of interpretation of disc centrifuge results ultimately can be evaluated by running mixtures of commercial polystyrene latexes of essentially monodisperse particle size distributions. Table III contains data from a mixture of such polystyrene latexes. The experimental averages are calculated in time space and are seen to agree well with the expected values.

TABLE II  
OPTICALLY CORRECTED DIAMETER AVERAGES  
FROM EQ.12 AND FROM EQ.22

Average (nanometers)	EQ.12	EQ.22	% Deviation
1) PVAc (a) Copolymer 1	DISTRIBUTION SKEWED TO LARGE DIAMETERS		
$\bar{D}_N$	136	130	-4.4
$\bar{D}_S$	138	132	-4.3
$\bar{D}_V$	141	134	-5.0
$\bar{D}_{SS}$	145	138	-4.8
$\bar{D}_W$	151	144	-4.6
$\bar{D}_T$	158	154	-2.5
2) PVAc (a) Copolymer 2	DISTRIBUTION SKEWED TO LARGE DIAMETERS		
$\bar{D}_N$	268	283	+5.6
$\bar{D}_S$	281	298	+6.1
$\bar{D}_V$	297	315	+6.1
$\bar{D}_{SS}$	333	354	6.3
$\bar{D}_W$	385	411	+6.7
$\bar{D}_T$	462	491	+6.3
3) PVAc (a) Copolymer 3	DISTRIBUTION SKEWED TO LARGE DIAMETERS		
$\bar{D}_N$	219	225	+2.7
$\bar{D}_S$	224	232	+3.6
$\bar{D}_V$	232	242	+4.3
$\bar{D}_{SS}$	248	263	+6.0
$\bar{D}_W$	277	298	+7.6
$\bar{D}_T$	325	352	+8.3
4) Butyl Acrylate/Methyl Methacrylate Copolymer	NARROW DISTRIBUTION		
$\bar{D}_N$	498	498	0
$\bar{D}_S$	502	502	0
$\bar{D}_V$	505	506	+0.2
$\bar{D}_{SS}$	513	514	+0.2
$\bar{D}_W$	522	523	+0.2
$\bar{D}_T$	531	532	+0.2

**TABLE III**  
 COMPARISON OF ACTUAL AND CALCULATED  
 AVERAGES FOR A POLYSTYRENE MIXTURE  
 (nanometers)

Size of Components of Mixture	Weight Fraction	Number Fraction	Averages	
			Calculated	Experimental
1091	0.106	0.014		
726	0.258	0.114	$\bar{D}_N$	523
497	0.634	0.872	$\bar{D}_W$	623

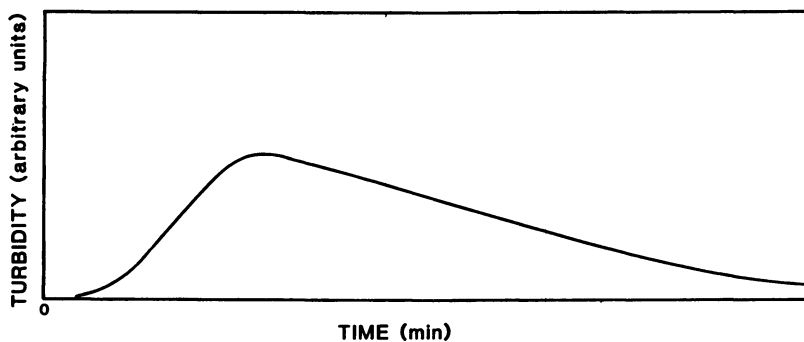


Figure 9: Polyvinyl acetate emulsion - raw  
 photosedimentometer trace.

Parameters: spin fluid viscosity = 1.055 cP  
 spin fluid density = 0.9857 g/mL  
 polymer density = 1.19 g/mL  
 rotational speed = 8534 rpm

### Conclusions

Since the extinction efficiency of polymer particles is a function of refractive index, particle size and wavelength an optical correction is generally required for photodetector response data. However, such corrections can be simplified if experimental conditions are adjusted to prevent the largest particles from sedimenting in short spin times. When this is done, data can be acquired and treated without the explicit use of the extinction coefficient as shown in eq.(22).

### Acknowledgements

The authors thank the Natural Sciences and Engineering Research Council of Canada for financial support and L. E. Oppenheimer for making the computer program of reference (6) available to us.

### References

1. Kaye, B. H., British Patent 895222, 1962.
2. Hildreth, J. D. and Patterson, D., J. Soc. Dyers Colourists, 1964, 80, 474.
3. Beresford, J., J. Oil Colour Chem. Assoc. 1967, 50, 594.
4. Brugger, K., Powder Technol. 1976, 13, 215.
5. Svarovsky L., and Svarovsky, J., J. Phys. D., 1975, 8, 16.
6. Oppenheimer, L. E., J. Colloid Interface Sci. 1983, 92, 350.
7. Devon, M. J., Meyer, E., Provder, T., Rudin, A., Weiner, B. B., ACS Symposium Series, this volume.
8. Mie, G., Ann. Phys. Leipzig, 1908, 25, 377.
9. Jones, M. H., U. S. Patent 3,475,968, 1969.
10. Holsworth, R. M., Provder, T., U. S. Patent 4,478,073, 1984.
11. Timmermans, J., The Physico-Chemical Constants of Binary Systems in Concentrated Solutions. Interscience, New York, 1959.
12. Huglin, M. G., Light Scattering from Polymer Solution, Academic Press, 1972.
13. Brandrup, J. and Immergut, E. H., Ed., Polymer Handbook 2nd edition, Wiley Interscience, New York, 1975.
14. Devon M. J., and Rudin, A., J. Appl. Polym. Sci., 34, 1987, 469.
15. Provder, T., and Holsworth, R. M., Am. Chem. Soc. Div. Org. Coat. Plast. Chem. Preprints, 1876, 36, 150.

RECEIVED May 29, 1991

## Chapter 10

# Detector Slit Width Error in Measurement of Latex Particle Size Distributions with a Disc Centrifuge

Michael J. Devon<sup>1</sup>, Edwin Meyer<sup>2</sup>, Theodore Provder<sup>2</sup>, Alfred Rudin<sup>3,5</sup>, and Bruce B. Weiner<sup>4</sup>

<sup>1</sup>Dow Chemical Canada Inc., P.O. Box 3030, Sarnia, Ontario N7T 7M1, Canada

<sup>2</sup>The Glidden Company, 16651 Sprague Road, Strongsville, OH 44136

<sup>3</sup>Guelph–Waterloo Centre for Graduate Work in Chemistry, Department of Chemistry, University of Waterloo, Waterloo, Ontario N2L 3G1, Canada

<sup>4</sup>Brookhaven Instruments Corporation, 750 Blue Point Road, Holtsville, NY 11742

An expression for the turbidity is derived for a polydisperse distribution of particles in a detection zone having a finite slit width. It is shown that the turbidity is proportional to the differential volume distribution and decreases as the particles spread radially outward by a dilution effect. Furthermore, the first moment of the diameter about the turbidity - extinction coefficient ratio in time space yields the number average diameter. This paper reports an investigation of possible errors in particle size distribution and averages resulting from the finite size of the detector slit width. The previously reported derivation of turbidity accounting for the finite slit width by Treasure and Coll and Haseler is not rigorously correct. A more rigorous derivation is presented in this paper along with an error analysis of the effect of finite slit width on particle size values. Mixtures of nearly monodisperse latexes with closely spaced sizes analyzed by the disc centrifuge over a range of normal operational variables demonstrate that the error due to finite slit width is well within the observable experimental error of the method and as a practical matter can be neglected.

The disc centrifuge with an optical detector is a reliable instrument for the measurement of particle size distributions of polymer latexes in the normal size ranges produced in emulsion polymerizations (1-4).

In this instrumental technique, particle size can be related by Stoke's Law to the time required for the species to appear at the location of an optical detector subsequent to the injection of the whole sample into the spin fluid. The optical detector gives a turbidity signal as a function of time which can be related to particle concentration.

<sup>5</sup>Corresponding author

0097-6156/91/0472-0154\$06.00/0  
© 1991 American Chemical Society



The width of the detector light beam defines the sampling increment for measurement of a differential particle size distribution. The size of the sampling increment can affect the accuracy of the calculated particle size distribution if the particles that are viewed at any given sedimentation time are polydisperse in size. This problem has been considered by Treasure(5). More recently, Coll and Haseler(6) have concluded that differential size distributions obtained with the disc centrifuge under constant rotor speed operation are volume distributions.

This article reports an investigation of the effects of possible errors resulting from the finite size of the detector slit. The materials used were all polymer latexes, with narrow particle size distributions. Blends of such latexes produce samples with predictable average particle sizes. Mixing of nearly monodisperse latexes with similar particle sizes ensures that the detector slit contained particles with different sizes. To determine the significance of the slit width error, particle size distributions were measured and compared with predicted values.

The versatility of the disc centrifuge also permitted a second experiment to assess the need to account for the finite size of the slit width. A sample of a bimodal particle size distribution was characterized under different spinning conditions such that the separation of the two peaks in the sample was increased or decreased. The particle size averages were compared from these runs with different degrees of overlap of the two components of the mixture in order to verify that the slit width error can be neglected in normal analyses of particle size distributions of polymer emulsions.

### Theory

The cited analysis of the error due to the finite size of the detector slit(5) does not appear to us to be entirely correct. Following is a derivation of an expression for the turbidity based on the differential volume distribution of particles in the disc centrifuge detection zone.

The disc centrifuge operates by forcing particles radially outward through a spin fluid under high centrifugal force. The particles settle at rates determined by their sizes and densities. At a specific radial distance the particles interrupt a light beam and the particle size and relative concentrations of the particles are calculated from known parameters. Particle settling is described by the Stoke's Law Equation.

$$D^2 = \frac{6.299 \times 10^9 \eta \log(R/R_0)}{t \omega^2 \Delta \rho} \quad (1)$$

where t = centrifuge time in minutes  
 D = particle diameter in micrometers  
 $\omega$  = centrifugal speed in rotations per minute  
 $\Delta \rho$  = density difference between particles and spin fluid in g/mL

- $\eta$  = spin fluid viscosity in poises  
 $R$  = fixed distance from the center of the disc cavity to where the photodetector is located  
 $R_0$  = starting distance of particles from the center of the disc cavity, determined by the volume of spin fluid used in the rotor.

For randomly placed particles and very dilute concentrations where multiple scattering is negligible

$$T = \frac{I}{I_0} = e^{-\tau \ell} = e^{-2.303A} \quad , \quad (2)$$

where  $T$  is the transmittance,  $I$  is the transmitted light intensity in the spin fluid medium measured at the photodetector,  $I_0$  is the initial beam intensity in the spin fluid medium in the absence of particles measured at the photodetector,  $\ell$  is the path length,  $\tau$  is the observed turbidity, and  $A$  is the absorbance.

For monodisperse spheres and a monochromatic idealized point light source the turbidity is a function of diameter and given by (7)

$$g_b \tau(D) = N(\pi D^2/4) Q_{\text{ext}}(D, m, \lambda) \quad , \quad (3)$$

where

- $N$  = number of particles per unit volume  
 $Q_{\text{ext}}(D, m, \lambda)$  = extinction coefficient which includes absorption and scattering efforts  
 $m$  = relative refractive index; ratio of particle refractive index to that of the medium  
 $\lambda$  = wavelength in the medium

In a typical disc centrifuge the light source is not monochromatic and  $Q_{\text{ext}}(D, m, \lambda)$  is replaced by the integrated extinction coefficient,  $\bar{Q}_{\text{ext}}(D, m)$  as shown by Oppenheimer(8).

$$\bar{Q}_{\text{ext}}(D, M) = A \int_{\lambda_1}^{\lambda_2} Q_{\text{ext}}(D, m, \lambda) \cdot P(\lambda) d\lambda \quad , \quad (4)$$

where

- $A$  = normalizing factor  
 $P(\lambda)$  = product of spectral irradiance of the light source and spectral response of the detector.

For a real disc centrifuge the finite slit width implies a finite acceptance angle. Thus, as shown in Figure 1 the slit has a finite length  $\Delta R$  along the radius  $R$ , that contributes to the signal. There is also a finite slit height  $h$ . As Treasure(5) points out there is a spread in particle diameters  $\Delta D$  that contributes to the turbidity signal because of the finite slit width  $\Delta R$ . To calculate the particle size distribution of a sample

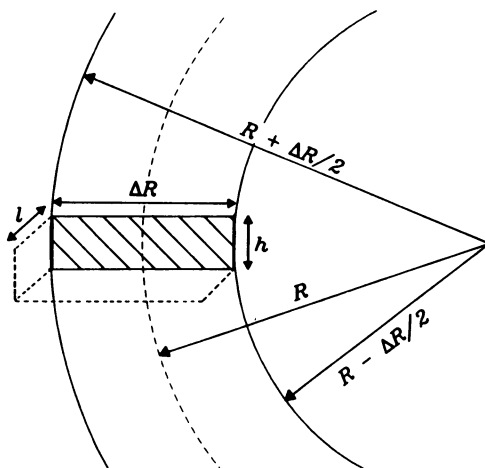


Figure 1. Geometry of Finite Slit Width in Detector Zone

fractionated by the disc centrifuge an expression must be derived for the turbidity involving the total particle cross-section in the beam. The number of particles in the distribution that is sampled by the detector beam will be determined by the experimental conditions and Stoke's Law.

From eq.(2) the product of the turbidity and the path length is proportional to the absorbance. The absorbance in the detector zone can be defined as

$$\frac{\tau \ell}{2.303} = A = \frac{\sigma(R, \Delta R) \bar{Q}_{\text{ext}}(D, m) V_p}{A_{\text{det}}}, \quad (5)$$

where

$\sigma(R, \Delta R)$  = particle cross section in the annular ring between  $R - \Delta R/2$  and  $R + \Delta R/2$

$A_{\text{det}}$  =  $\Delta R h$ , area of the detector zone from Figure 1

$V_p$  = volume fraction of particles in the detector zone.

From Figure 1 it can be seen that

$$V_p = \frac{\text{volume of detector zone}}{\text{volume of annulus}} = \frac{\Delta R h \ell}{\pi \ell [(R + \Delta R/2)^2 - (R - \Delta R/2)^2]} \quad (6)$$

$$V_p = h/2\pi R \quad (7)$$

Substituting eq.(7) into eq.(5) gives the following expression for the turbidity:

$$\tau = \frac{\sigma(R, \Delta R) \bar{Q}_{\text{ext}}(D, m) (2.303)}{2\pi R \Delta R \ell} \quad (8)$$

The total particle cross section in the beam (in units of length, squared) is given by

$$\sigma(D_{\text{max}}, D_{\text{min}}) = \int_{D_{\text{min}}}^{D_{\text{max}}} \left( \frac{dN}{dD} \right) \left( \frac{\pi D^2}{4} \right) dD, \quad (9)$$

where

$D$  = particle diameter

$D_{\text{min}}, D_{\text{max}}$  = the smallest and largest particles in the detector beam, respectively

$\frac{dN}{dD}$  = differential number distribution of particles between  $D$  and  $D + dD$ .

To proceed further it is necessary to know or assume a functional form for  $(dN/dD)$ . Treasure<sup>(5)</sup> makes the reasonable assumption that

$$\frac{dN}{dD} = f + g (D/D_{mid}) , \quad (10)$$

where  $D_{mid}$  is the particle diameter at the slit midpoint at radius  $R$  as shown in Figure 1 and  $f$  and  $g$  are appropriate constants. In essence this amounts to a linear gradient of particle concentration over the slit width  $\Delta R$ . Defining  $D_{max}$  and  $D_{min}$  as

$$D_{max} = D_{mid} + \Delta D; \quad D_{min} = D_{mid} - \Delta D \quad (11)$$

and inserting eq.(10) into eq.(9) and integrating gives

$$\sigma(D, \Delta D) = \frac{f\pi}{12} [(D+\Delta D)^3 - [D_{mid}-\Delta D]^3] + \frac{g\pi}{16D_{mid}} [(D_{mid} + \Delta D)^4 - (D_{mid}-\Delta D)^4] \quad (12)$$

Retaining only first order terms in  $\Delta D$  gives

$$\sigma(D, \Delta D) = (f + g) (\pi D_{mid}^2) (\Delta D/4) \quad (13)$$

From eq.(10)

$$f + g = \left( \frac{dN}{dD} \right)_{mid} \quad (14)$$

Substituting eq.(14) into eq.(13) yields

$$\sigma(D, \Delta D) = \left( \frac{dN}{dD} \right)_{mid} (\pi D_{mid}^2) (\Delta D/4) \quad (15)$$

It is important to note that eq.(15) differs from Treasure's result<sup>(5)</sup> as well as Allen's results<sup>(4)</sup> in which  $\sigma(D, \Delta D)$  is proportional to  $D^3$  rather than proportional to  $D^2 \Delta D$ .

The first order result of eq.(15) is independent of the functional form assumed for  $(dN/dD)$ . One can assume that

$$(dN/dD) = \text{const} \quad (16)$$

or

$$(dN/dD) = f + gD^2/D_{mid}^2 \quad (17)$$

Equation (15) provides an expression for the total particle cross section in terms of particle diameter. To utilize this equation for the disc centrifuge instrument in the turbidity expression in eq.(8), the expression must be transformed from particle diameter space to radial distance space of the photodetector zone. To accomplish this Stoke's Law is utilized and written as

$$D^2t = K\ell_n(R/R_0) , \quad (18)$$

where K is defined by eq.(1). The differential of eq.(18) with respect to R yields

$$2DdD = KdR/Rt \quad (19)$$

which can be transformed to

$$dD = \left( \frac{dR}{R} \right) \frac{D}{2\ell_n(R/R_0)} \quad (20)$$

Equation (19) and (20) apply at a fixed time t. We are considering a snapshot of the distribution of particle diameters in the detection zone at an instant of time. Thus,  $\sigma(D, \Delta D)$  is converted to  $\sigma(R, \Delta R)$  by use of eqs.(15) and (20).

$$\sigma(R, \Delta R) = \left( \frac{dN}{dD} \right)_{mid} \left( \frac{\pi D_{mid}^2}{8} \right) \frac{\Delta R}{R\ell_n(R/R_0)} \quad (21)$$

From eq.(21), it can be seen that  $\sigma(R, \Delta R)$  varies as  $D^3$  no matter how small the slit becomes (assuming that geometric optics still hold). To get a correction for the non-infinitesimal character of the slit, the higher order terms must be kept if they are significant. For the typical physical size of the slit these higher order terms are not significant.

By generalizing the subscript mid and substituting eq.(21) into eq.(8) we obtain the following expression for the turbidity

$$\tau(D) = \frac{\left( \frac{dN}{dD} \right) D^3 \bar{Q}_{ext}(D, m) (2.303)}{16\ell R^2 \ell_n(R/R_0)} \quad (22)$$

For a fixed detector position, R, the turbidity is proportional to the differential volume distribution,  $(dN/dD)D^3$ . This result agrees with that of Coll and Haseler(6), although they did not use an integration procedure. Instead they used a quasi-chain rule approach which was not rigorously correct. Equation (22) also demonstrates that the turbidity will decrease as  $R\ell_n(R/R_0)$ . This is a dilution effect as the particles spread radially outward.

In the disc centrifuge experiment, raw data are obtained as a function of time. For a fixed detector position, R, and fixed spin fluid volume corresponding to  $R_0$ , eq.(22) can be rewritten as

$$\tau(t) = K_1 \left( \frac{dN}{dD} \right) D^3 \bar{Q}_{\text{ext}}(D, m) \quad (23)$$

Rearranging eq.(23) provides the following expression for the normalized differential weight distribution in diameter space for particles of constant density

$$F_w(D) dD = \left( \frac{dN}{dD} \right) D^3 dD = \frac{[\tau(D)/\bar{Q}_{\text{ext}}(D, m)] dD}{\int_{D_L}^{D_H} [\tau(D)/\bar{Q}_{\text{ext}}(D, m)] dD} \quad (24)$$

where  $D_L$  and  $D_H$  are the smallest and largest particle diameters in the sample particle size distribution.

In diameter space the weight average diameter is obtained by taking the first moment of  $F_w(D)$ .

$$\bar{D}_w = \frac{\int_{D_L}^{D_H} D F_w(D) dD}{\int_{D_L}^{D_H} F_w(D) dD} = \frac{\int_{D_L}^{D_H} [\tau(D) D / \bar{Q}_{\text{ext}}(D, m)] dD}{\int_{D_L}^{D_H} [\tau(D) / \bar{Q}_{\text{ext}}(D, m)] dD} \quad (25)$$

Equation (23) can be rearranged for integration in time space as follows:

$$\left( \frac{dN}{dD} \right) D^3 dt = \frac{\tau(t)}{K_1 \bar{Q}_{\text{ext}}(D, m)} dt \quad (26)$$

Taking the derivative of the Stoke's Law expression, eq.(1), with respect to time provides the relation

$$dt = -(2K/D^3) dD \quad (27)$$

Substitution of eq.(27) into eq.(23) and rearrangement provides the following expression

$$\left( \frac{dN}{dD} \right) D^3 \left( \frac{-2K}{D^3} \right) dD = \frac{\tau(t)}{K_1 \bar{Q}_{\text{ext}}(D, m)} dt \quad (28)$$

Rearrangement and normalization yields an expression for the differential number distribution in time space.

$$F_N(D) dD = \left( \frac{dN}{dD} \right) dD = \frac{[\tau(t)/\bar{Q}_{\text{ext}}(t, m)] dt}{\int_{t_0}^{t_f} [\tau(t)/\bar{Q}_{\text{ext}}(t, m)] dt} \quad (29)$$

where  $t_0$  and  $t_f$  correspond to the time of appearance of the largest and smallest particle diameters in the sample, respectively, in the center of the detection zone.

Thus taking the product of the diameter and the turbidity extinction coefficient ratio yields the number average diameter in time space.

$$\bar{D}_N = \int_{D_L}^{D_H} D F_N(D) dD = \frac{\int_{t_0}^{t_f} [\tau(t)D(t)/\bar{Q}_{\text{ext}}(t,m)] dt}{\int_{t_0}^{t_f} [\tau(t)/\bar{Q}_{\text{ext}}(t,m)] dt} \quad (30)$$

The result obtained in eq.(30) agrees with that of Allen(4). It follows that weight average diameter in time space is given by

$$\bar{D}_W = \int_{D_L}^{D_H} D [D^3 F_N(D)] dD = \frac{\int_{t_0}^{t_f} [\tau(t)D^4(t)/\bar{Q}_{\text{ext}}(t,m)] dt}{\int_{t_0}^{t_f} [\tau(t)D^3(t)/\bar{Q}_{\text{ext}}(t,m)] dt} \quad (31)$$

For latexes often  $\bar{Q}_{\text{ext}} \propto D^3$ . Weiner et al showed this to be true for polystyrene latexes in water for  $140 \text{ nm} < D < 320 \text{ nm}$ .(9) In this special case the weight average diameter is given by the first moment of the diameter about the normalized turbidity in time space

$$\bar{D}_W = \int_{D_L}^{D_H} \tau(t)D(t) dt / \int_{D_L}^{D_H} \tau(t) dt \quad (32)$$

and the number average is given by

$$\bar{D}_N = \int_{t_0}^{t_f} [\tau(t)/D^2(t)] dt / \int_{t_0}^{t_f} [\tau(t)/D^3(t)] dt \quad (33)$$

### Experimental

Particle size measurements were performed with an ICI-Joyce Loebel Disk Centrifuge Mk III with the photodetector attachment. A very important step in the operation of the centrifuge is the formation of a density gradient within the spin fluid to allow better and more efficient separation of the suspended articles. The method of Holsworth and Provder(10), known as the external gradient method, was used for the formation of a density gradient within the spin fluid on the disk. The spin fluid used here was either water or a 20% glycerol-80% water mixture. The latexes were dispersed in a 80:20 (w/w) water methanol mixture and sonicated for 2 minutes to ensure a uniform dispersion. Centrifuge speeds were chosen so that particles appeared at the detector at least two minutes after injection of the dispersion into the spin fluid. It has been shown



that optical correction can be simplified for latex particles if the appearance time at the detector from the large particles exceeds at least two minutes (3,11). The output of the optical detector was recorded at 2.5 V full scale and was digitized for data processing with a microcomputer. In all cases stable sedimentation conditions were achieved.

### Polymerizations

Acrylic latices with narrow particle size distributions were synthesized by a seeded continuous addition emulsion polymerization procedure. The emulsions were prepared in a thermostated glass reactor fitted with a stirrer, condenser and a glass tube for purging with nitrogen. A typical emulsion polymerization recipe is listed below for the seed and subsequent stages. Particle sizes other than that described were prepared by adjusting the polymerization procedure. Particle diameters for a particular recipe can be calculated a priori from the seed particle diameter and the emulsion recipe using eq.(34):

$$D_p = D_s \left[ \frac{W_s + W_1}{W_s} \right] \quad (34)$$

where

- $D_s$  = seed particle diameter  
 $D_p$  = projected diameter for final particle  
 $W_s$  = seed polymer weight fraction  
 $W_1$  = weight fraction of polymer to be added on.

The concentration of surfactant in these polymerizations is purposely kept low to ensure that there is not a second generation of particles that would broaden the particle size distribution.

### **Recipe for Emulsion Polymerization of Seed Polymer**

water	290 g
anionic surfactant (sodium dodecyl benzene sulfonate)	0.2 g
ammonium persulfate initiator	0.3 g
t-butyl hydroperoxide (70%)	0.19 g
sodium formaldehyde sulfoxylate	0.159 g

### **Monomer Emulsion:**

water	26.6 g
anionic surfactant (sodium benzene sulfonate)	0.04 g
butyl acrylate	39 g
methyl methacrylate	39 g

In a one litre reaction kettle the water, surfactant, initiator and 5 g of the monomer emulsion were combined with stirring under a nitrogen blanket, at 78°C. After 15 minutes the remaining monomer emulsion was added at a rate of 1 g/min. and the reaction temperature was raised to 85°C. Fifteen minutes after the monomer addition was completed, the mixture was cooled. At 55°C the

t-butyl hydroperoxide and then the sodium formaldehyde sulfoxylate dissolved in 5 ml of water were added. The emulsion was filtered through a 100 mesh screen to remove any coagulum. The weight average particle size was determined to be 90 nm.

#### Recipe for Emulsion Polymerization of Polymer Particle from the Seed Particle

water	200 g
ammonium persulfate initiator	0.84 g
seed polymer emulsion	12.4 g

#### Monomer Emulsion:

water	47 g
anionic surfactant (siponate DS-10)	0.16 g
methyl methacrylate	70 g
butyl acrylate	70 g

In a one litre reactor kettle, water, initiator and seed emulsion are combined with stirring under a nitrogen blanket at 85°C. Monomer emulsion is added to the reactor at 1 g/min and when the addition is complete, the reactor is held at 85°C for 30 minutes, cooled at 25°C and the latex is filtered through a 100 mesh screen. For this example cited the number average particle size was determined to be 356 nm and weight average diameter was equal to 378 nm.

#### Results and Discussion

Table I lists particle size averages for the narrow distribution latexes and their blends. Figure 2 illustrates a typical number distribution of particles that results from mixing two nearly monodisperse latexes. This figure illustrates that the two samples (T4 and T6) that compose the mixture (T10) are not resolved with the spin conditions that have been used. It is evident then that the centrifuge slit contains particles from each distribution at some particular time in the run. A correction for the finite width of the detector slit should be applied here (4), strictly speaking. However, the data in Table I for T10 and other mixtures show that neglect of this correction does not cause significant errors in the measured values of  $\bar{D}_n$  and  $\bar{D}_w$ .

Table II summarizes the results of the particle size measurements of a mixture of two nearly monodisperse latices (T2 and T5). The two sample peaks for this sample were made to overlap by changing the spin conditions of the centrifuge. With increasing extent of overlap the magnitude of the slit width error should increase. No large change in the particle size averages is observed, however, as the overlap was caused to increase.

Our results on many sample mixtures of narrow particle size distributions indicated that the effect of slit width upon error in diameter for the disc centrifuge is small. This tends to make the need to integrate the total particle cross section in the region of the beam less urgent. Our data show that such corrections can be

TABLE I - PARTICLE SIZE DATA FOR NEARLY MONODISPERSE SAMPLES

SAMPLE	WEIGHT PERCENT	$\bar{D}_N$	$\bar{D}_W$	$\bar{D}_N$	$\bar{D}_W$
		EXPERIMENTAL (nm)		CALCULATED (nm)	
T1		356	378		
T2		446	469		
T3		332	349		
T4		603	633		
T5		443	463		
T6		545	555		
T7		174	178		
T8		153	161		
T9	0.516 T1 + 0.484 T3	339	361	343	364
T10	0.615 T4 + 0.385 T6	570	592	575	603
T11	0.560 T7 + 0.440 T8	162	170	163	171
T12	0.621 T2 + 0.379 T5	439	461	445	467

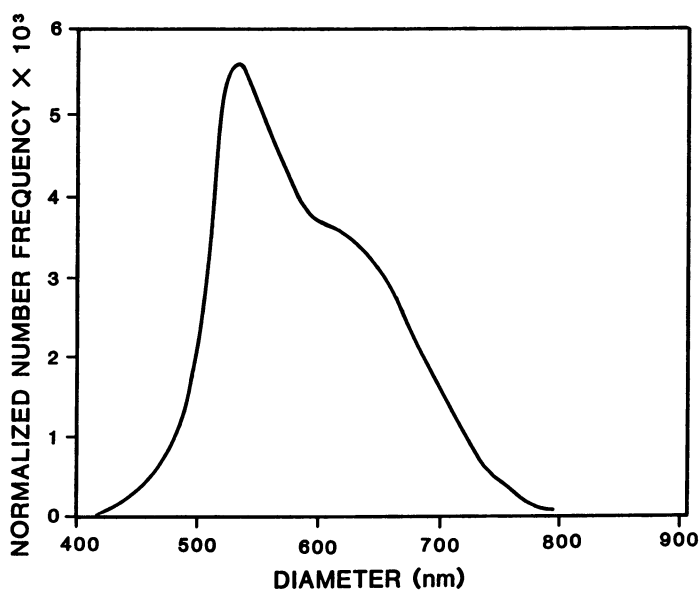


Figure 2. Particle Size Distribution for Sample T10 of Table I.

neglected, as a practical matter. The reason that this correction is small is outlined below. The photodetector slit width is 0.46 mm (as measured by a measuring microscope). For our disc cavity the range of particle diameters from the middle of the slit to the edges of the slit can be calculated using Stokes Law (eq.1) and the geometric dimensions of the disc recorded in Table III. The working expression is analogous to eq.(1) and is given by

$$D_{\pm} = \frac{6.299 \times 10^9 \eta \log \left( \frac{R \pm \Delta R / 2}{R_0} \right)}{t \omega^2 \Delta \rho} \quad (35)$$

where

$\Delta R$  = slit width  
 $D_{\pm}$  = particle diameters (in micrometers) at the inside and outside edges of the detector slit.

The percentage deviation of the particle size at either end of the slit from those at the center of the slit is given by eq.(36).

$$\% \text{ Deviation} = \left( \frac{D_{\pm} - D}{D} \right) \times 100 \quad (36)$$

where D is the particle diameter at the center of the slit. Substitution of eq.(35) into eq.(36) leads to

$$\% \text{ DEVIATION } (\pm) = \left[ \frac{\log \{ (R \pm \Delta R / 2) / R_0 \}}{\log (R / R_0)} - 1 \right] \times 100 \quad (37)$$

The percent deviation in diameter for particles in the slit will range from -8.14% to +7.95% of the diameter of the particles at the center of the slit. Since these deviations nearly cancel, the difference between the average size of the particles in the slit and the size of particles at the center of the slit is negligible. Therefore, the error in assuming that the average particle size in the slit is the particle size at the center of the slit also is negligible and well within the experimental errors from variation in technique that contribute to errors in particle size.

### Conclusions

An expression for the turbidity has been derived for a polydisperse distribution of particle sizes in a detection zone having a finite slit width. The turbidity is proportional to the differential volume distribution and decreases as the particles spread radially outward, a dilution effect. It also is shown that integrating the first moment of the diameter about the turbidity - extinction coefficient ratio in time space yields the number average diameter. Using bimodal mixtures of closely spaced narrow particle size distribution acrylic latexes, it is shown that under conditions of decreasing peak separation on a time basis, no change in particle

TABLE II - PARTICLE SIZE DATA FOR BIMODAL SAMPLE

PEAK SEPARATION (min)	$\bar{D}_N$ (nm)	$\bar{D}_W$ (nm)	% CHANGE IN $\bar{D}_W$
7.4	429	454	-
4.7	428	451	0.7
3.0	414	438	3.5
1.1	425	449	1.1

TABLE III - GEOMETRIC DIMENSIONS OF DISC CAVITY

R	=	4.82 cm (5 mL position)
R <sub>0</sub>	=	4.28 cm (15 mL position)
$\Delta R$	=	0.046 cm
R + $\Delta R/2$	=	4.843 cm (4.548 mL position)
R - $\Delta R/2$	=	4.797 cm (5.450 mL position)

a The radial distances associated with the spin fluid volumes are calculated by assuming the disc cavity is cylindrical and having knowledge of the disc cavity dimensions. Once two radial distances corresponding to two volumes are known, any other volumes can be calculated from these values corresponding to other radial distances (see reference 12). For this specific case the volumes  $V_{\pm}$  corresponding to  $R \pm \Delta R/2$  is given by

$$V_{\pm}(\text{mL}) = 5 + \frac{10\Delta R[\pm R - \Delta R/4]}{R^2 - R_0^2}$$

size averages were observed that could be attributed to the effect of finite width of the detector slit that was outside the expected experimental error of the method. Therefore, slit width error can be neglected in normal analyses of particle size distributions of latexes.

### Acknowledgement

This research was supported by the Natural Sciences and Engineering Research Council of Canada. The authors acknowledge stimulating and helpful discussions with Walter Tscharnuter and Mark Koehler.

### Literature Cited

1. Beresford, J., J. Oil Colour Chem. Assoc., 1967, 50, 594.
2. Langer, G., Colloid Polymer J., 1979, 257, 522.
3. Provder, T. and Holsworth, R. M., ACS Org. Coat. Plast. Div. Preprints, 1976, 35, 150.
4. Allen, T., Particle Size Measurements, 3rd Ed., Chapman and Hall, London, 1981.
5. Treasure, C. R. G., Whiting and Industrial Powder Research Council, Welwyn (England), Tech. Paper No. 50, 1964.
6. Coll, H. and Haseler, S. C., J. Colloid Interf. Sci., 1984, 99, 591.
7. Van de Hulst, H. L., Light Scattering of Small Particles, Wiley and Sons, New York, 1950, p. 129.
8. Oppenheimer, L. E., J. Colloid Interface Sci., 1983, 92, 350.
9. Weiner, B. B., Fairhurst, D., and Tscharnuter, W. W., ACS Symposium Series, this volume (1991).
10. Holsworth, R. M. and Provder, T., US Patent 4,473,073, 1984.
11. Devon, M. J., Provder, T., and Rudin, A. ACS Symposium Series, this volume (1991).
12. Koehler, M. E., Zander, R. A., Gill, T., Provder, T. and Niemann, T. F., ACS Symposium Series No. 332, T. Provder, Ed., 1987, p. 180

RECEIVED May 29, 1991

## Chapter 11

# Particle Size Measurements with a Disc Centrifuge

## A Density-Gradient Method with Light-Scattering Corrections

Finn Knut Hansen

Department of Chemistry, University of Oslo, P.O. Box 1033, Blindern,  
0315 Oslo 3, Norway

An improved technique for particle analysis by disk centrifugation utilizing an externally produced density gradient and with corrections for the wavelength and angular distribution of the transmitted light has been developed. The sedimentation constant is calculated from the radial dependence of spin fluid viscosity and density. Light scattering corrections are calculated by means of calibration curves, representing the efficiency of light scattering as a function of size and relative refractive index of particles. Calibration curves for the white light in the photosedimentometer are obtained by integration across the wavelength distribution of the lamp, the sensitivity distribution of the photo diode and the angular distribution of the forward scattered light obtained from Mie theory. Coefficients of variation below 2% may be calculated using different spin fluid volumes to estimate the instrument variance.

Sedimentation methods based on gravitational or centrifugal sedimentation are still superior in many people's opinion in dealing with wide and/or multimodal size distributions. Such particle size distributions are often found in products of the polymer industry (paint binders, PVC pastes, glue binders etc.) where the presence or absence of undersized/oversized particles is of crucial importance to the product quality.

Several papers dealing with this technique have been published (1-10) in which the theoretical basis for the method is established, and also expressions for the size distributions are developed. These are based either on gravimetric (i.e. sampling and weighing) or light scattering (i.e. turbidity) methods, where either a laser or an ordinary lamp is used as a light source. With monochromatic light (lasers) calculations of light scattering coefficients as a function of particle size and refractive index is relatively easy, using the Mie theory. However, there are also several problems with a laser

0097-6156/91/0472-0169\$06.00/0  
© 1991 American Chemical Society

instrument, one of these is stability of the light intensity, another is the fact that the turbidity function oscillates very strongly with particle size, especially when the refractive index is high. This means that particle size (i.e. density and time) have to be very correct to avoid large errors in the distribution such as artifact peaks due to turbidity oscillation. Therefore, most producers prefer using a white light source. This sort of "smoothes" out the maxima and minima, but introduces the problem of calculating correct calibration curves.

This problem has been treated by Oppenheimer (6) who introduced the average extinction coefficient  $Q_{ext}^*$  by integrating over the range of wavelength sensitivity. He showed that it is necessary to include this factor to obtain correct size distributions, and more the larger the particle size. A second problem with the detector system in the disk centrifuge is that some forward scattering will be included in the turbidity signal due to a finite angle of acceptance in the photo cell. This problem may become important with large particle sizes or/and refractive index. In this paper, these problems are solved by numerical integration of the theoretical equations.

When extremely narrow sized particle suspensions (such as Dynosphers), or very low density products ( $< 1 \text{ g/cm}^3$ ) are to be analyzed by a disk centrifuge, we have not succeeded to obtain stable conditions using the ordinary start techniques such as the buffered line or homogenous start. Turbulence will most often occur in the disk cavity during the run, thus invalidating the results. By using a density gradient in the disk however, stable conditions can be obtained (9,10). The added difficulty of calculating the particle sizes in a density gradient system is also treated in this paper.

The essential part of the work reported here was done several years ago (1982) at Dyno Industrier A.S, Norway, and has been an important component in the development of Dynospheres monosized particles. In view of recent developments in size analysis techniques, it is felt that the fundamental treatments presented still has considerable actuality.

### Experimental

A Joyce Loebl Disk Centrifuge Mk II with the standard photo-sedimentometer with a white light source has been used. The density gradient was produced by means of a Beckman Density Gradient Former with two parallel 30 ml glass syringes and a mixing chamber with a magnetic stirrer. The two components most often used were 15% w/w glycerol/water mixture (heavy component) and water (light component). When particles with diameters below ca.  $1 \mu\text{m}$  were to be analyzed, 0.15% sodium dodecyl sulfate (SDS) was added to both components to avoid coagulation in the disk. The spin fluid volume was usually 30 ml. In order to measure emulsions of low density liquids a gradient consisting of methanol and water was used.

The latex was diluted with a solution of 0.15% SDS in deionized water. Of this suspension 0.5 ml was injected into the disk center. The particle concentration in the injected sample was varied dependent on particle size; larger particles required larger concentrations. The disk speed was also adjusted to the particle size in order to give sedimentation times between 4 and 16 minutes. In this man-



ner, polystyrene and polyacrylate particles from 0.5 to 20  $\mu\text{m}$  could be measured. Particles above 20  $\mu\text{m}$  could also be analyzed by this method, provided the spin fluid was thickened with hydroxyethyl cellulose (HEC) in order to decrease the rate of sedimentation.

A similar gradient method was developed to analyze size distributions of alkyd emulsions. Because these droplets have densities close to water, a gradient consisting of water (heavy component) and methanol (light component) was applied. The samples were diluted in 50% w/w methanol/water with a nonionic stabilizer, such as Triton X-100.

Data Logging and Presentation. The output from the Disk Centrifuge was fed into a 12-bit A/D-converter connected to a microcomputer where 480 voltage values were logged at equal time intervals (variable). To minimize signal noise, each data value was calculated as an average of a number (20-100) of measurements. In this way, an accuracy better than 12 bits could be obtained and facilitated detection of small peaks in the distribution.

At the end of the run, the data was saved automatically to a disk file together with key data for the run, such as time interval, run-ID, gradient type etc. Peaks were selected manually on-screen. The program sets the baseline as the straight line between the first and last peak limits. The time values between the limits were converted to diameters as described below. The gradient constants (Table I) were read from a disk file together with density and refractive index. From the diameters and voltage values, relative particle numbers were calculated. From the D/N-data were also calculated statistical parameters for each peak separately and for the joint distribution. The distribution curve together with the statistical parameters may be output in a report, to be used in product documentation.

The computer program was originally written in BASIC for a DEC PDP-11 computer, but has later been converted to PASCAL on a PC.

### Theory and calculation

Particle size distributions are calculated in two steps. First the particle diameters are calculated from the sedimentation time (the x-axis), then particle numbers can be calculated from the joint turbidity signal from the photo cell (the y-axis) by means of a size- and refractive index dependent calibration curve.

Sedimentation in a density gradient. The sedimentation rate is represented by Stoke's law. Figure 1 shows the disk and the size parameters used in this work. Stokes equation is easily integrated from  $r_0$  to  $r_1$  when the spin fluid density and viscosity are independent of radius  $r$ , giving a simple logarithmic dependence between time  $t$  and  $r$ . When density and/or viscosity are not constant, the particle diameter may still be represented by,

$$D = 2a = K / (n \sqrt{t}) \quad (1)$$

Where  $a$  is the particle radius and  $n$  the disk speed (frequency). The "constant",  $K$ , or its square,  $K^2$ , is given by the integral (10),

$$K^2 = \frac{9}{2\pi^2} \int_{r_0}^{r_1} \frac{\eta}{(\rho_p - \rho_w)r} dr \quad (2)$$

Where  $\rho_p$  and  $\rho_w$  are the densities of the particles and spin fluid, respectively and  $\eta$  is the spin fluid viscosity. The dependence of  $\eta$  and  $\rho_w$  on  $r$  may be found from the radial distribution of volume (or weight) fractions. The gradient former produces a linear density gradient as function of volume, as long as the partial molar volumes are constant (ideal mixing), but even if this is not so, the weight fractions will always be linear. Therefore, weight fractions of the components in the disk cavity may be calculated from the disk geometry and from these density and viscosity as separate functions.

If the volume fraction is linear, the expression for the volume fraction  $\phi$  in the disk at a radius  $r$  (in circular coordinates) is,

$$\phi = \phi_0 + (\phi_2 - \phi_0) (r^2 - r_0^2) / (r_2^2 - r_0^2) \quad (3)$$

The radius  $r_2$  is an instrument constant, while the inner radius  $r_0$  is dependent on the spin fluid volume  $V$ ,

$$r_0^2 = r_2^2 - V/(\pi l) \quad (4)$$

where  $l$  is the inner thickness of the disk cavity (Figure 1).  $\phi_0$  and  $\phi_2$  are the volume fractions at the outer and inner spin fluid surface, respectively. These are dependent on the composition of the light and heavy liquid in the gradient former, on the spin fluid volume and on the type of syringes used in the gradient former. They may be described by the following equations (derived from a nomogram in the gradient former's manual),

$$\phi_0 = \phi_1^1 + (\phi_1^1 - \phi_1^0) (125 - s'V)/150 \quad (5)$$

$$\phi_2 = \phi_1^1 + (\phi_1^1 - \phi_1^0) 125/150 \quad (6)$$

$\phi_1^0$  and  $\phi_1^1$  are the volume fractions of the heavy component in the light and heavy liquid (0 and 1 if pure liquids are used) and  $s'$  is the gradient former's scale value pr. ml of gradient, inversely proportional to the inner cross-section of the syringe. From the above equations, it is possible to calculate the volume or weight fractions as a function of radius in the disk. The weight fraction,  $w$ , is for an ideal system,

$$w = 1/[1 + (1-\phi) c_0/(\phi \rho_A)] \quad (7)$$

where  $\rho_A$  is the density of the other pure component (i.e.  $w=1$ ). The following equations were found to satisfactorily represent the viscosity,  $\eta$ , and density,  $\rho$ ,

$$\log \eta = (a_0 + a_1 w + a_2 w^2)/(273 + \tau) + b_0 + b_1 w + b_2 w^2 \quad (8)$$

$$\rho = c_0 + c_1 w + c_2 w^2 + c_3 w^3 - (d_0 + d_1 w + d_2 w^2) (\tau - 20) \quad (9)$$

Here  $\tau$  is the temperature ( $^{\circ}\text{C}$ ). The coefficients are constants for a given system. By combining the above equations, eq.(2) may be integrated and the instrument constant K determined.

**Density and viscosity data.** For both the glycerol/water (A) and the methanol/water (M) gradient the constants in eqs.(8) and (9) were determined by least squares fit to literature data. These are given in Table I below. The reason that the 0-constants are not exactly the same, even if water is the one pure component in both gradients, is that this gives the best fit all over. The physical dimensions of the disk are,

$$r_2 = 50.8 \text{ mm (2")}, \quad r_1 = 48.2 \text{ mm}, \quad l = 6.35 \text{ mm}$$

Because of the complexity of the equations, the integration of eq.(2) was performed numerically by Simpson's formula.

Table I. Constants in the viscosity and density equations

Constant Gradient A			Constant Gradient M		
	Gradient A	Gradient M		Gradient A	Gradient M
$a_0$	880.2	863.5	$c_0$	0.9981	0.9977
$a_1$	781.5	766.2	$c_1$	0.2338	-0.1536
$a_2$	-565.0	-1028	$c_2$	0.0535	0.0157
			$c_3$	-0.01167	-0.0750
$b_0$	-5.0036	-4.9404	$d_0$	0.000205	0.00006
$b_1$	-1.5695	-1.395	$d_1$	0.000475	0.0015
$b_2$	2.605	2.032	$d_2$	0.000250	-0.00084

**Particle numbers from turbidity.** The Joyce-Loebl disk centrifuge utilizes a photosedimentometer with a tungsten lamp as the light source. The light beam is concentrated by a lens and passed through a small hole and then through the disk as indicated in Figure 1. On the other side of the disk is a photodiode inside a small compartment. The light beam passes through a narrow slit in the compartment, parallel to the disk circumference. The signal from the photodiode is amplified and presented as a voltage output. The output is adjusted to 0 by adjusting the voltage to the lamp, and thus the light intensity. According to Joyce-Loebl, the output is proportional to optical density in the range 0-0.15, leading to a voltage of 0-1 V. Even if the voltage is proportional to the difference between the scattered intensity,  $I$ , and the reference intensity,  $I_0$ , instead of  $\log(I/I_0)$ , the error in this approximation will be less than 15% as long as the output signal is kept below 1 Volt.

When calculating the particle concentration from the light intensity signal we will be using the turbidity expression (11),

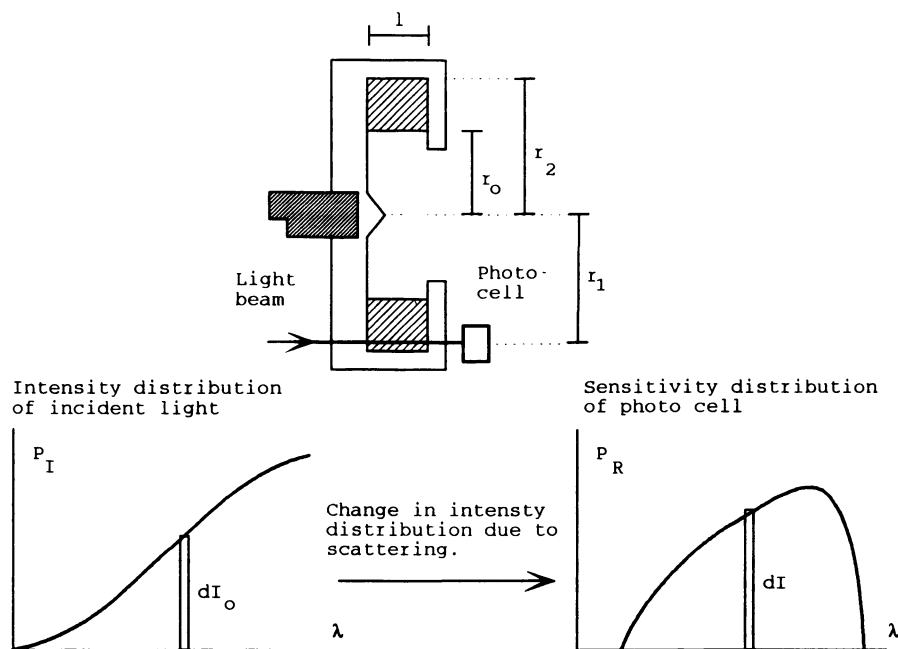


Figure 1. Schematic drawing of the Joyce-Loebl disk with the important dimensions and distribution curves representing the emitted and measured light intensity.

$$\ln(I/I_0) = -\pi N a^2 Q_{sca} \quad (10)$$

where  $N$  is the particle number,  $a$  is the particle radius and  $Q_{sca}$  is the efficiency factor for scattering. For particles that adsorb light,  $Q_{sca}$  must be exchanged with the extinction efficiency  $Q_{ext}$ . The efficiencies may be calculated from the Mie theory for any particle size if the wavelength of the incident light and the refractive indexes are known.

To calculate  $N$  from eq.(10), we must consider the problems with this type of instrument, mainly stemming from the fact that the optical system is not constructed for accurate light scattering measurements:

1. The light source is an ordinary lamp, and is therefore emitting a continuous distribution of wavelengths.
2. The photo diode's sensitivity is dependent of wavelength.
3. The photo diode accepts some forward scattered light due to the geometry of the sensor slit.
4. The light may be partly polarized, due to the optical arrangement (prism).

There are also other possible error sources due to the arrangement of the optical system in addition to spreading in the measured distributions due to the width of the injected particle band and the light beam. These may be corrected for, as will be shown.

The first two problems are the most serious; the third problem will be most important with particles of large diameters and/or large refractive index. The last problem is considered to be small compared to the others, and we will assume in all calculations that the light is unpolarized.

For calculation of the total wavelength distribution of the optical density, refer to Figure 1. At a wavelength  $\lambda$  the emitted intensity from the lamp between  $\lambda$  and  $\lambda+d\lambda$  will be denoted  $dI_0$ , which may be expressed by,

$$dI_0 = I_0 P_I d\lambda \quad (11)$$

where  $P_I$  is the normalized intensity distribution function defined so that the integral of  $P_I d\lambda = 1$ . When light passes the particle suspension, the attenuation due to scattering is

$$-dI/dx = N C_{sca} dI \quad (12)$$

where  $C_{sca}$  is the scattering cross section  $= Q_{sca} \pi a^2$ . The transmitted intensity between  $\lambda$  and  $\lambda+d\lambda$  is then,

$$dI = dI_0 \exp(-N \pi a^2 Q_{sca} d\lambda) \quad (13)$$

The incremental response from the photocell in this wavelength interval is set equal to

$$dR = dI S(\lambda) \quad (14)$$

where  $S(\lambda)$  is the amplification at the given wavelength  $\lambda$ . The total

response from the photocell is obtained by integrating across the wavelength distribution. The output signal (voltage) may be set equal to the difference in response with and without particles,

$$U = R_0 - R = \int_{\lambda_1}^{\lambda_2} S(\lambda) dI_0 - \int_{\lambda_1}^{\lambda_2} S(\lambda) dI_0 \exp(-N\pi a^2 Q_{sca} l) \quad (15)$$

As long as the scattered intensity is small,  $\exp(-x)$  may be approximated by  $1-x$ . By inserting  $I_0$  from eq.(11) and rearranging we obtain,

$$U = N\pi a^2 l I_0 \int_{\lambda_1}^{\lambda_2} S(\lambda) P_I Q_{sca} d\lambda - N\pi a^2 l I_0 S_0 \bar{Q}_{sca} \quad (16)$$

where  $\bar{Q}_{sca}$  is the mean value of  $Q_{sca}$  over the wavelength distribution and  $S_0$  is the total amplification.  $\bar{Q}_{sca}$  is therefore expressed by,

$$\bar{Q}_{sca} = \int_{\lambda_1}^{\lambda_2} P_S P_I Q_{sca} d\lambda \quad (17)$$

where  $P_S = S(\lambda)/S_0$ . Also  $S_0$  is normalized so that the integral of  $P_S P_I = 1$ . This expression corresponds to that given by Oppenheimer for  $Q_{ext}^*$  (6). The values for  $Q_{sca}$  is calculated from the light scattering coefficients by means of Mie theory (11) by a computer program.

The photo diode's responsivity curve (Amperes/Watt) is given by the manufacturer (PIN 5D/B, originally /SB) (United Detector Technology, Inc.). The responsivity is 0 below 0.30  $\mu\text{m}$  and above 1.10  $\mu\text{m}$ . Therefore 15 values were read from the curve in the region 0.35 - 1.05  $\mu\text{m}$  at 0.05  $\mu\text{m}$  intervals and stored in an array  $Re(\lambda)$ .

The intensity distribution of the light source is dependent on its color temperature, which again is dependent on the supply voltage. The voltage may vary because this instrument uses supply voltage to adjust the recorder. We have found, however, that the instrument has been fairly stable, and that supply voltage is usually ca. 3 V, corresponding to a color temperature of ca. 2250 K (lamp type M29, 6V, 10W) (13). The spectral distribution may be calculated from Planck's emission equation, (12),

$$E_\lambda = \frac{C_1 \lambda^{-5}}{\exp(C_2/\lambda T) - 1} \quad (18)$$

where  $T$  is absolute temperature and  $C_1$  and  $C_2$  are constants given by,

$$C_1 = 3.7403 \times 10^{10} \mu\text{W } \mu\text{m}^4/\text{cm}^2, \quad C_2 = 14384 \mu\text{m } ^\circ\text{K}$$

Planck's equation is valid for a black body, but the tungsten filament has an emissivity lower than a black body, in the range  $E/E(\text{black}) = 0.47 - 0.36$  at  $\lambda = 0.4 - 1.1 \mu\text{m}$  (12). We have neglected this effect because of the uncertainties of the other factors, also it is the variation that is important, not the absolute value.  $E_\lambda$  is calculated from eq.(19) for the same 15 wavelengths as the photo diode responsivity, and the mean value of  $\bar{Q}_{sca}$  may then be calculated for any value of  $\alpha$  and  $m$  from a slightly modified eq.(17),

$$\bar{Q}_{sca} = \frac{\int_{\lambda_1}^{\lambda_2} E_\lambda \text{Re}(\lambda) Q_{sca} d\lambda}{\int_{\lambda_1}^{\lambda_2} E_\lambda \text{Re}(\lambda) d\lambda} \quad (19)$$

Where  $\lambda_1 = 0.35 \mu\text{m}$  and  $\lambda_2 = 1.05 \mu\text{m}$ . When a detector used to measure the transmission also views some of the forward scattered light, the efficiency of scattering is reduced by the fraction of light scattered through the cone of half-angle,  $\Phi$ , so that

$$Q_{eff} = Q_{sca} - (1/\alpha^2) \int_0^\Phi (i_1 + i_2) \sin \theta d\theta \quad (20)$$

where  $i_1$  and  $i_2$  are the angular intensity functions ((11)-p.392). If we consider eq.(20) we may write

$$\bar{Q}_{eff} = \bar{Q}_{sca} - \bar{I}_{sca} \quad (21)$$

where  $I_{sca}$  may be averaged across the wavelength interval in the same way as  $Q_{sca}$ . The particle numbers,  $N$ , may then be calculated from eq.(16) when  $\bar{Q}_{eff}$  is used instead of  $\bar{Q}_{sca}$ .

Calibration curves for  $\bar{Q}_{eff}$ . To calculate  $N$ ,  $Q_{eff}$  must be calculated for the particle radius,  $a$ , and averaged across the wavelength interval and forward scattered cone. These calculations include double numerical integrations, and for each point in the integration, the scattering coefficients and angular intensity functions must be evaluated numerically. It has not been feasible to do this in real-time on a microcomputer. An alternate procedure that has been used here, is to do the calculations in advance, and store a selection of values for  $\bar{Q}_{eff}$  in a lookup table (calibration curve). The values must be sufficiently close to give satisfactory results by interpolation.

Curves for  $Q_{sca}$  are usually calculated as a function of the dimensionless parameters  $\alpha$  and  $m$ . The curves are of the well-known oscillating type, with an overlaid complex ripple structure. Ideally, we would want to calculate calibration curves for  $\bar{Q}_{eff}$  as a function of particle size, for different values of  $m$ . This means we will for each value of  $a$ , integrate over the  $\alpha$ -interval  $\alpha_1 - \alpha_2$  given by the wavelength interval  $\lambda_1 - \lambda_2$ . Because the x-location of the

curves are very dependent of  $m$ , this will lead to a great number of calibration curves. It is possible to improve upon this situation by using the parameter  $\rho$  defined by

$$\rho = 2\alpha(m-1) \quad (22)$$

This makes the maxima and minima in the curve appear (approximately) at the same values of  $\rho$ , the first maximum in the curve is at  $\rho=4$ . The ripple structure, however, is a more complex function of  $\alpha$  and  $m$ . It will partly disappear when we integrate across the wavelength interval, and still more when correction for the forward scattering is included.

When we want to calculate  $\rho$  from particle size, we must choose one value of  $\lambda$ . An average wavelength  $\bar{\lambda}$  is therefore calculated by integration in the same way as  $\bar{Q}_{sca}$  in eq.(19). The calibration curves for  $\bar{Q}_{eff}$  are calculated at fixed intervals in  $\rho$  and  $m$ . In the integrations described above, values for  $\alpha$  for each value of  $\lambda$  is calculated from

$$\alpha = \frac{\rho}{2(m-1)} \times \frac{\bar{\lambda}}{\lambda} \quad (23)$$

We have chosen a constant value for  $m$  in the integrations, corresponding to the value at  $\bar{\lambda}$ . We believe that the error introduced by this is small. The value of  $\bar{\lambda}$  is between 0.80 and 0.86  $\mu\text{m}$ , dependent of the color temperature of the lamp. At 2250 K,  $\bar{\lambda}=0.8461 \mu\text{m}$ , which has been used in this work.

When the calibration curves are used to calculate  $\bar{Q}_{eff}$  from  $m$  and  $a$ , the same value of  $\bar{\lambda}$  is used to calculate  $\alpha$  and  $\rho$ . For polymer particles and emulsions the relative refractive index,  $m$ , is between 1.08 and 1.20. Values for  $\bar{Q}_{eff}$  at 60  $\rho$ -values from 0 to 12.0 in 60 steps of 0.2 were calculated in this  $m$ -interval in steps of 0.01 (13 curves). The values were stored in a disk file. Above  $\rho=12.0$ , a constant value of  $\bar{Q}_{eff}$  equal to the last value (at 12.0) is used. Because the calibration curves are stored in  $\rho$ -coordinates, the difference in form between adjacent curves is relatively small. To calculate  $\bar{Q}_{eff}$  for any particle radius,  $a$ , the calibration curve for the  $m$ -value closest to the that of the dispersed particles is chosen. The corresponding value of  $\rho$  is calculated from eq.(22), using  $\bar{\lambda}$  as the wavelength. The value for  $\bar{Q}_{eff}$  is calculated by interpolation between the 4 closest  $\rho$ -values by the equation,

$$y = y_1 + cd_1 + c(c-1)d_2/2 + c(c-1)(c-2)d_3/6 \quad (24)$$

where

$$\begin{aligned} c &= (x-x_1)/h \\ d_1 &= y_2 - y_1 \\ d_2 &= y_3 - y_2 - d_1 \\ d_3 &= 2(y_3-y_2) - d_1 - (y_4-y_3) \end{aligned}$$

Here  $x$  and  $y$  are the variables,  $y_1 \dots y_4$  the  $y$ -values of the 4 points and  $h$  is the interval between the  $x$ -values. At high  $\rho$ , it is probable that a simple linear interpolation is sufficient, and above  $\rho=12.0$ , no interpolation is necessary.



Statistical data from particle numbers. When particle numbers,  $N$ , are calculated at equal time intervals we get a particle size distribution where the  $D$ -axis intervals are steadily increasing according to eq.(1).

$$dD = - (n/K)^2 D^3 dt \quad (25)$$

The difference in size between 2 adjacent datapoints increases proportional to the particle volume. This fact must be considered when the statistical parameters of the distribution are calculated, by multiplying each particle number with  $D^3$ . When absolute particle numbers are not calculated, it is not necessary to know the total amplification in the system. This means that a relative particle number  $N'$  may be calculated from a simplified eq.(16) (6),

$$N' = U / (D^2 \bar{Q}_{eff}) \quad (26)$$

The relative standard deviation of the size distribution, i.e. the coefficient of variation,  $CV$ , is an important parameter for characterization of particle suspensions. When  $CV$  decreases, however, the systematic error of the instrument becomes increasingly important. In order to measure low values of  $CV$ , we have to make an estimate of the systematic error. The total variance may be written,

$$CV^2 = CV_D^2 + CV_s^2 + CV_e^2 \quad (27)$$

where  $CV_D$  is the  $CV$  of the particle distribution,  $CV_s$  is the systematic error and  $CV_e$  is the random error, which is assumed to be small in these type of measurements. It may be estimated by repeated experiments. We will assume that  $CV_e = 0$ . The systematic error mainly stems from two sources; one is the width of the injected particle band, the other is the width of the light beam, both will lead to a peak broadening. A third effect is the lateral diffusion and possible turbulence. For particles in the micron range, diffusion will be very small, but turbulence may have an influence, especially with larger particles. It is, however, difficult to calculate the exact magnitude of this.

The  $CV$  for systematic error (peak broadening),  $CV_s$ , may be measured for a particular system by using different spin fluid volumes. When different settings are used on the gradient former, different volumes are produced, but the gradients will always have the same radial composition (same starting composition). The variance due to systematic error should therefore be the same on the time axis, independent of gradient volume. However, because  $CV$  is calculated relative to the (mean) particle diameter,  $CV_s$  will increase with decreasing  $V$  because the centrifugation time is decreasing, while  $CV_D$  should be constant.

It is therefore possible to estimate  $CV_s$  by using two or more different gradient volumes with the same narrow sized particle sample. It is, however, necessary to know the connection between centrifugation time and gradient volume. This may be obtained by calculating the constant  $K$  in eq.(1) as a function of  $V$  by means of eq.(2) etc. or by measuring the centrifugation time. The connection between  $CV_s$  and the systematic standard deviation  $\sigma_{st}$  on the time axis may be estimated from eq.(25).

$$CV_S = \sigma_s/D - (-n^2/K^2) D^2 \sigma_{st} - \sigma_{st}/t \quad (28)$$

Because  $\sigma_{st}$  will be independent of gradient volume for a given system, we may write,

$$CV_I^2 = (\sigma_{st}/t)^2 + CV_D^2 \quad (29)$$

By plotting  $CV_I^2$  as a straight line against  $1/t^2$ ,  $CV_D$  can be estimated from the intercept on the y-axis and  $\sigma_{st}$  as the derivative. The correction may then be applied to all samples run at any condition.

### Results and discussion

The effect of the different averaging processes performed in this work is illustrated in Figure 2. In (A)  $Q_{sca}$  for the m-values 1.10 and 1.20 is plotted as a function of  $\rho$ , and in (B)  $\bar{Q}_{sca}$  is smoothed by integration according to eq.(19). Compared to (A) we see a considerably smoothing from the integration over the wavelength interval, but still some oscillation and ripple effect is left. When we include the forward scattering, most of this variation is smoothed out as shown in the curves for  $\bar{Q}_{eff}$  (C). Still the first maximum appears for m=1.20, but this becomes increasingly lower as m is decreasing, because the effect from the forward scattered light becomes increasingly important. The half-angle for forward scattering was  $4^\circ$  (total angle of acceptance= $8^\circ$ ). This has been calculated from the width of the slit in the detector housing and the distance from the disk, but is somewhat uncertain, also because the distance from the inner and outer part of the disk compartment varies. A decreasing angle will lower the effect of forward scattering. Also higher refractive indexes as for instance with inorganic material will lower the effect.

The present method has been used for many years with satisfactory results for both monosized polystyrene latexes from 0.5 to 100  $\mu\text{m}$  diameter and with CV values 0.5-5%, and alkyd emulsions in the 1  $\mu\text{m}$  size range with broader size distributions (CV = 20-30%). The method produces good results when compared to other methods such as electron microscopy, Coulter Counter and Fraunhofer diffraction. This indicates that the integration of the density gradient and the curves for  $\bar{Q}_{eff}$  are fairly correct, although it is difficult to accurately measure the latter experimentally. Some uncertainty exists with respect to the exact magnitude of the correction for forward scattering due to the width of the light beam, but several experiments have showed that the general curve form is correct.

In Figure 3 is shown results from running a 0.5  $\mu\text{m}$  monosized polystyrene latex (SS-92) at two different spin fluid volumes (15 and 30 ml). In this figure both the raw data (time) curves are shown and the measured CV-values are plotted against  $1/t^2$ . As seen, the line almost goes through the origin, meaning that the observed CV is almost totally due to systematic error. From this plot  $CV_D$  is estimated to 0.5% and  $\sigma_{st}$  to 22.8 minutes. This means that  $CV_S = 0.99\%$  at 30 ml and 2.16% at 15 ml spin fluid. It is therefore very difficult to accurately measure CV for very monosized particle latexes on the disk centrifuge.

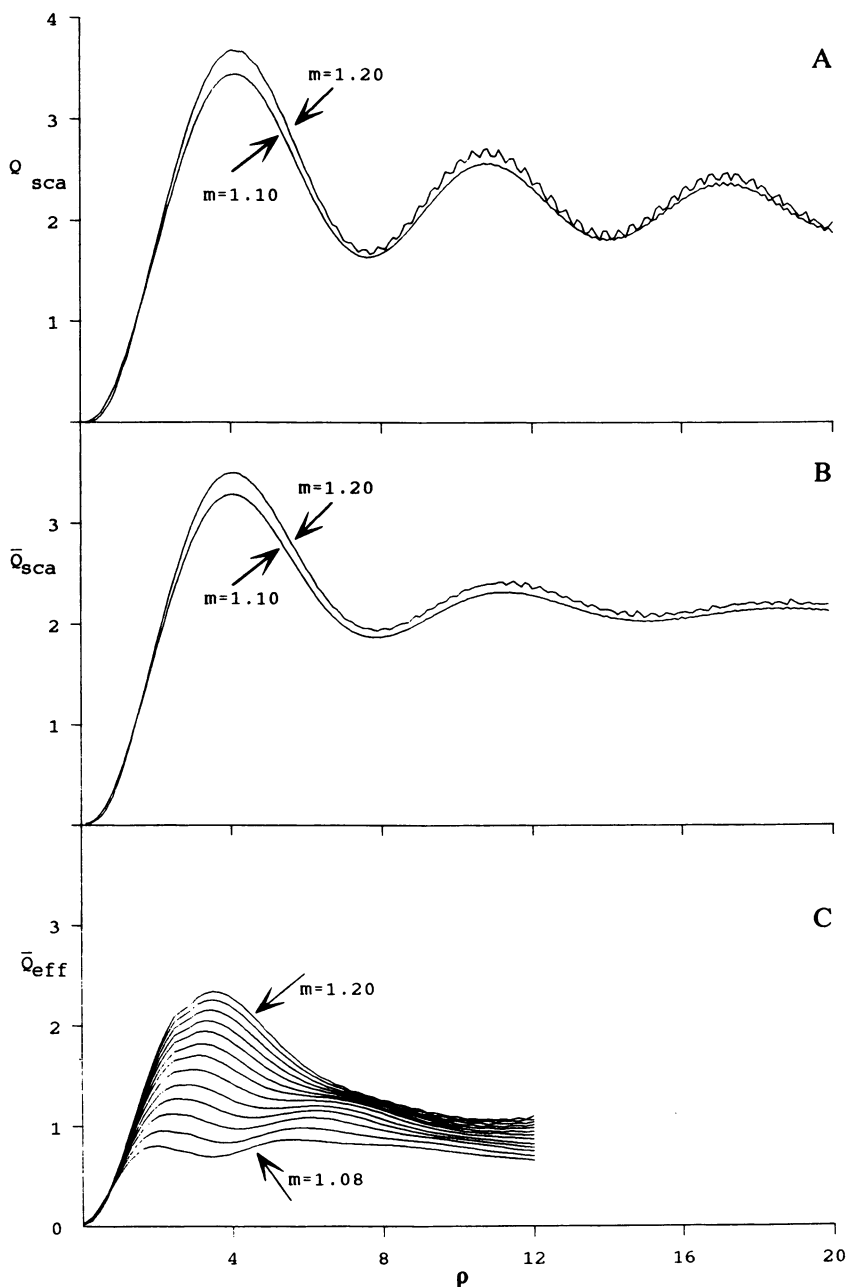


Figure 2. The efficiency factors for light scattering as a function of the parameter  $\rho = 2\alpha(m-1)$ . The three curves represent (A) the factor for monochromatic light, (B) averaged across the emitted and detected intensity distributions, and (C) also averaged across the forward scattered angle.

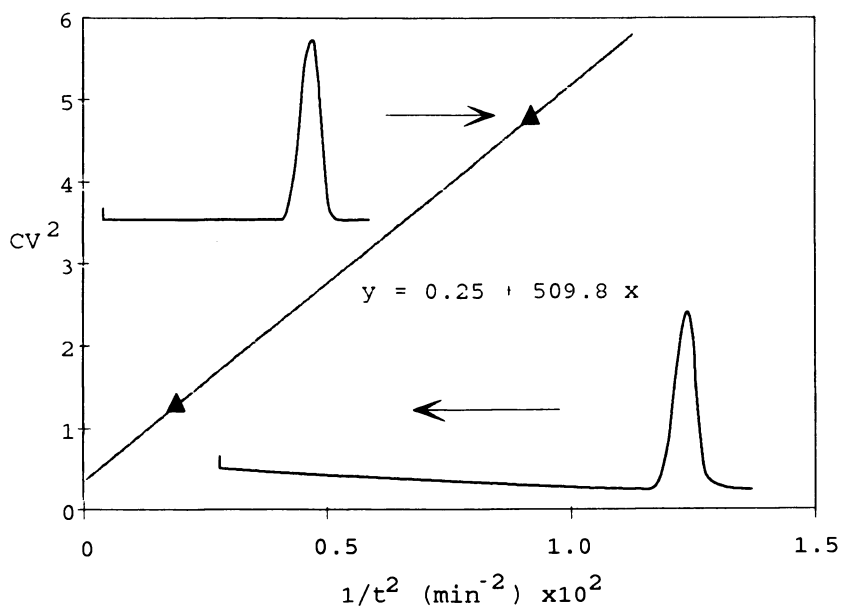


Figure 3. Centrifugation curves for a monosized seed of  $0.5 \mu\text{m}$  diameter run at two different volumes of gradient A (15 and 30 mL). Variance ( $\text{CV}^2$ ) plotted as a function of  $1/t^2$  in order to estimate the instrument variance.

Acknowledgement

The author would like to thank Dyno Industrier A.S for the permission to publish this work and specially Mr. Ø.Aasen who has transferred the hardware arrangement to a PC and rewritten the program in PASCAL.

Literature cited

1. M.J.Groves, B.M.Kaye and B.Scarlett, *Brit.Chem.Eng.*, **9**, 742-744 (1964)
2. N. Fisher, *Polymer Eng. Sci.*, **14**, 332-337 (1974)
3. M.J.Groves, H.S.Yalabik and J.A.Tempel, *Powder Techn.* **11**, 245-255 (1975)
4. T.Provder and R.M.Holsworth, *Organic Coatings and Plastics* **36**, 150-156 (1976)
5. P.Hauser and B.Honigmann, *Farbe und Lack* **81**, 1005-1011 (1975) and **83**, 886-890 (1977)
6. L.E.Oppenheimer, *J.Colloid Interface Sci.* **92**, 350-357 (1983)
7. M.E.Koehler, R.A.Zandler, T.Gill and T.F.Niemann, "Particle Size Distribution", T.Provder ed., *ACS Symp.Series.* **332**, 180-190 (1985)
8. R.M.Holsworth, T.Provder and J.J.Stanley, *ibid.*, 191-201
9. H.Coll and L.Oppenheimer, *ibid.*, 202-214
10. H.Coll and C.G.Searles, *J.Colloid Interface Sci.* **110**, 65-72 (1986)
11. M. Kerker, "The Scattering of Light and Other Electromagnetic Radiation", *Acad.Pres.*, 1969
12. *CRC Handbook of Chemistry and Physics*, CRC Press, Inc., 59th ed., 1979
13. Joyce-Loebl, private communication.

RECEIVED January 14, 1991

## Chapter 12

# Particle Size Analysis with a Disc Centrifuge Importance of the Extinction Efficiency

Bruce B. Weiner, D. Fairhurst, and W. W. Tscharnuter

Brookhaven Instruments Corporation, 750 Blue Point Road,  
Holtsville, NY 11742

Comparison of standard samples is made between mass distributions obtained gravimetrically and those obtained from a disc centrifuge photosedimentometer with full extinction efficiency corrections. The excellent agreement between theory and experiment suggests that accurate results are readily obtainable for many types of materials. Some form of light scattering is used in most particle sizers. For particles less than a few microns in size light scattering corrections are necessary to obtain accurate size distribution information. Calculations of the full extinction efficiencies for correcting turbidity data obtained with a broad spectrum source are reviewed. Examples for carbon black, quartz powder, and polystyrene latex are given.

Most particle sizing instrument specifications concern size range, reproducibility, resolution, ease-of-use, and, occasionally, accuracy; accuracy in determining the size, not the amount. Yet the amount is just as important as the size. The aim of an accurate particle size distribution measurement is to produce either a differential or cumulative size distribution with the amount at each size in terms of either the volume, mass or number of particles. This information is needed to calculate the common statistics that characterize the distribution. These statistics--the mean is the simplest example--are just as much a function of the amount as they are of the particle size. Yet most attention is focused on the sizing capabilities of a technique.

Most commercially available submicron particle sizing instruments either use light scattering to determine both the size and the amount or just the amount. The former category includes photon correlation spectroscopy (PCS) and multiangle light scattering (MLS). The latter category includes disc centrifuge photosedimentometry (DCP), cuvette centrifuge photosedimentometry (CCP), sedimentation field-flow fractionation (SdFFF), and two forms of chromatography: hydrodynamic (HDC) and capillary hydrodynamic fractionation (CHDF).

In all these techniques, except PCS, a light intensity is measured. It must then be converted into size distribution information, and this process involves

0097-6156/91/0472-0184\$06.00/0  
© 1991 American Chemical Society

light scattering corrections. With PCS the intensity autocorrelation function is measured, and, for broad distributions, light scattering corrections are then applied to transform from intensity-weighted to volume- and number-weighted distributions.

Light scattering corrections are of two types: the extinction efficiency and the particle scattering factor. Extinction efficiency is associated with turbidity measurements. It is an important correction for DCP, CCP, SdFFF, HDC, and CHDF measurements. The scattering factor is associated with the angular pattern of intensity measurements. It is an important correction for PCS and MLS measurements. Both types of corrections are calculated from Mie scattering theory or, in certain limiting cases, from simpler analytic functions.

This paper will focus on the extinction efficiency and its importance in the determination of particle size distributions. A spherical model for particle shape is assumed not only for simplicity but also because light scattering corrections are then readily calculable from Mie theory and its limiting forms. Fortunately, many submicron applications involve either spheres (latexes, liposomes, monoclonal antibodies) or relatively compact shapes approximating spheres (silver halides, ceramics, some pigments).

### Theory

A brief review of the well-known theory for extinction efficiencies <sup>1</sup> is presented here. For sufficiently dilute systems the intensity  $I$  of the transmitted light is related to the incident intensity  $I_0$  by,

$$I = I_0 \cdot \exp[-\tau L] \quad (1)$$

where  $L$  is the path length and  $\tau$  is called the extinction coefficient in the light scattering literature and the turbidity in much of the chemical and particle sizing literature. Turbidity arises from two sources: absorption and scattering. Separately or in combination these two sources are the cause for the extinction of the transmitted light.

Turbidity is related to the number of particles  $N$  per unit detected volume, the particle's geometric cross-sectional area  $A$ , and the extinction efficiency  $Q_{\text{ext}}$  by,

$$\tau = N \cdot A \cdot Q_{\text{ext}} \quad (2)$$

All of these variables are a function of particle size  $D$ . (Here  $D$  is the diameter of the assumed sphere. In general  $D$  is some characteristic length, often an equivalent spherical diameter determined by the particular technique used to measure it.) In particular the area  $A$  is proportional to  $D^2$ .

The extinction efficiency is a function of  $D$ , the wavelength of light in the medium  $\lambda$ , the particle refractive index  $n_p$ , and the refractive index of the suspending medium  $n_0$ . The two refractive indices are also, in principle, a function of  $\lambda$ . In practice, however, they are often taken as constant, especially  $n_p$ , since the wavelength dependence may not be known. Absorption is accounted for by specifying the imaginary part of both refractive indices, although choosing a medium that absorbs is usually counterproductive. Given  $\lambda$ ,  $n_p$ , and  $n_0$  the numerical value of  $Q_{\text{ext}}$  is calculated for each  $D$  using spherical Mie theory.

According to Mie theory for spheres, the extinction efficiency is given by,

$$Q_{\text{ext}} = (2/x^2) \cdot \sum (2n+1) \cdot \text{Re}(a_n + b_n) \quad (3)$$

Here  $x$ , the size parameter, is equal to  $\pi D/\lambda$ . Both  $a_n$  and  $b_n$ , the partial wave scattering amplitudes, and, therefore,  $Q_{\text{ext}}$ , are functions of  $x$  and  $m$ , where  $m = n_p/n_o$ . The scattering amplitudes can be written in terms of Riccati-Bessel functions. Numerical algorithms are used to calculate the final results. The algorithms in the appendix of the Bohren and Huffman book in reference 1 are particularly useful for this purpose.

Commercially available DCP instruments use a tungsten-halogen lamp, a broadband source. This type of source is very compact and stable, reaches operating conditions in a few seconds, is inexpensive, rugged, and produces an intense beam of light. Since it is not monochromatic the calculation of an appropriate extinction efficiency is more difficult. However, once calculated, its use in Equation 2 is straightforward.

If a light source is not monochromatic, then  $Q_{\text{ext}}$  is replaced by a weighted average. The weighting function is proportional to the product of the wavelength dependence of the source and detector. Following Oppenheimer<sup>2</sup> we write the average, integrated extinction efficiency as

$$Q^*_{\text{ext}} = B \cdot \int P(\lambda) \cdot Q_{\text{ext}}(\lambda) d\lambda \quad (4)$$

where the asterisk denotes the integrated efficiency,  $B$  is a normalizing factor, and  $P(\lambda)$  is the product of the source and detector wavelength sensitivities.

In principle these sensitivities should be measured for each source-detector combination. Oppenheimer shows a measured curve for a particular tungsten-halogen lamp and photodiode detector used for his DCP measurements. In practice the source dependence is reasonably well described by the Planck blackbody radiation law modified by the wavelength dependence of the quartz envelope used to house the lamp. And the detector dependence is dominated by the near-infrared wavelength dependence of the silicon photodiode and the glass material covering the active part. The  $P(\lambda)$  is sufficiently similar in either case that the final, corrected distribution results agree to within experimental error.

Limiting cases are useful as guidelines. For large particles  $Q_{\text{ext}}$  approaches the Fraunhofer value of 2. For small particles in the Rayleigh regime  $Q_{\text{ext}}$  varies as  $D$  for strong absorbers like carbon black and  $D^4$  for nonabsorbers like polystyrene latex. Thus,  $Q_{\text{ext}}$  as a function of  $D$  must increase, then peak, then approach a constant value. For strong absorbers the approach is nearly linear. For weak absorbers and for nonabsorbers two kinds of periodicity are apparent provided  $m$  is roughly less than or equal to 2.5. The low frequency periodicity is termed the interference structure. The high frequency periodicity is termed the ripple structure, and it is appears for  $m$  greater than roughly 1.3 or 1.4. In this study  $m \leq 1.2$ , and the ripple structure is not of concern. Absorption dampens both types of periodicity. So does integrating over wavelengths from a polychromatic source. The wavelength dependence of the refractive index as well as a small, but unquantified, amount of absorption become less important, and this represents an advantage in using a multi-wavelength source.



### **Extinction Efficiency Calculations**

Figure 1 shows the integrated extinction efficiency versus diameter for carbon black in water. Carbon black is a strong absorber. Not surprisingly then, the efficiency is very nearly linear in the Rayleigh regime. It reaches a peak around 600nm, and decreases smoothly toward the Fraunhofer limit of 2. For the results plotted here the refractive index of carbon black<sup>3</sup> was taken as  $1.84 \cdot (1 - 0.46i)$  and that for water as 1.33.

Figure 2 shows the extinction efficiency versus diameter for natural quartz (density 2.62 g/cm<sup>3</sup>) in 10% sucrose. The refractive index of natural quartz is 1.545, and it varies by no more than 0.01 from 400nm to 1100nm, the range over which the source-detector shows non-zero sensitivity. It will be shown below that variations of 0.01 or less in the refractive index do not result in significant differences in the final size distribution results. The value for pure water was increased by 0.015 refractive index units to account for the 10% sucrose. The wavelength dependence was assumed to be the same as for pure water<sup>4</sup>,  $1.3242 + 3,046/\lambda^2$ , where  $\lambda$  is in nanometers. Temperature variations of a few degrees give rise to variations in refractive index in the 3rd place. Thus, they are ignored.

Three curves are shown. The integrated extinction efficiency is shown as a filled-circle curve fitted by the method of cubic splines to values calculated every 200nm in diameter and every 100nm in wavelength. The open-circle curve is a cubic spline fit to a single wavelength calculation at 700nm. The smooth curve is a cubic spline fit to a single wavelength calculation at 254nm, a popular wavelength used in RI detectors. Notice the characteristic wiggles after the first peak. Such a curve places a greater demand on the accuracy with which the refractive indices and their wavelength dependencies must be known.

Figure 3 shows the extinction efficiency versus diameter for polystyrene in water. The refractive index for bulk polystyrene<sup>5</sup> is  $1.5663 + 7,850/\lambda^2$ . Notice also that the integrated extinction efficiency curve is smoother than the single wavelength curve.

Figure 4 shows the integrated extinction efficiency versus diameter for polystyrene in water calculated every 20nm from 140nm to 320nm. The data are plotted on a log-log scale. A linear fit with a slope of 3.05 shows that a simple cubic power law for  $Q^*_{ext}$  vs  $D$  is reasonable in this size range.

### **Materials and Methods**

The standard BCR66 quartz powder sample was obtained courtesy of T. Allen, and it may be purchased from the Duke Scientific Company, Menlo Park, California. A stock suspension was made up at approximately 0.5% w/v in 0.2 $\mu$  filtered milliQ water using approximately 0.1% w/v tetra sodium pyrophosphate as surfactant. A density of 2.62 g/cm<sup>3</sup> was used for the natural quartz powder.

BCR66 samples were run on a Brookhaven Instruments model BI-DCP disc centrifuge photosedimentometer using 16ml of a 10% w/w sucrose solution as spin fluid and 1ml of a 5% sucrose solution as the buffer layer. The gradient between these two was formed using an external gradient method described in the literature<sup>6</sup>. Samples were run for about 60 minutes at 852 RPM. Results shown below represent the average of three runs. The run-to-run reproducibility was approximately  $\pm 2\%$ .

Narrow, emulsifier-free polystyrene latex suspensions were purchased from the Interfacial Dynamics Corporation, Portland, Oregon. Lot #10-65-53 was labeled  $0.300\mu \pm 2.5\%$ , and Lot #10-95-38 was labeled  $0.121\mu \pm 5.5\%$ . The labeled values are the result of TEM measurements on 500 randomly

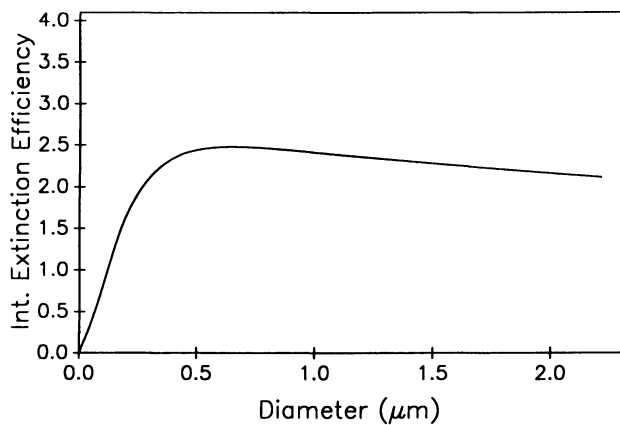


Figure 1. Integrated extinction efficiency of carbon black in H<sub>2</sub>O as a function of diameter.

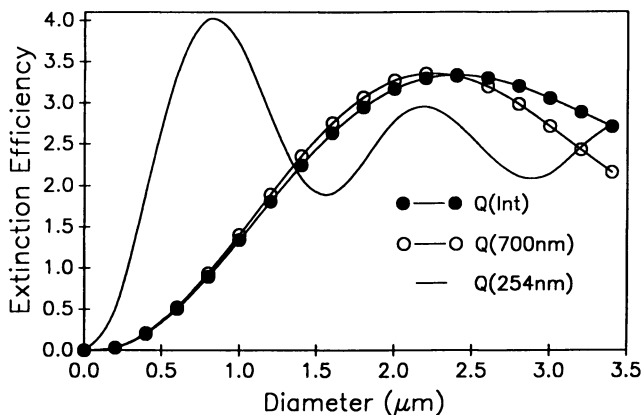


Figure 2. Extinction efficiency of natural quartz powder in H<sub>2</sub>O as a function of diameter.

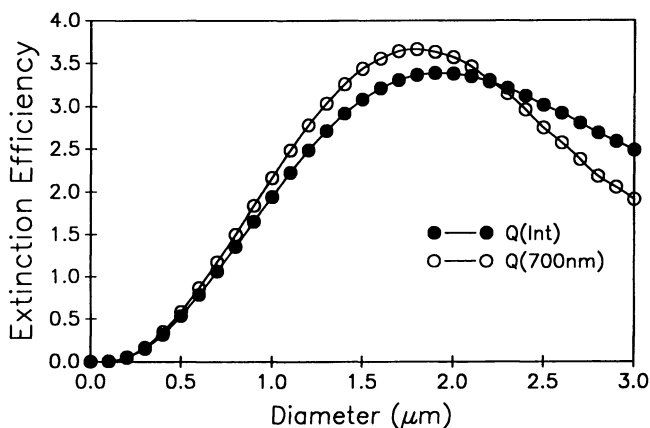


Figure 3. Extinction efficiency of polystyrene latex in  $\text{H}_2\text{O}$  as a function of diameter.

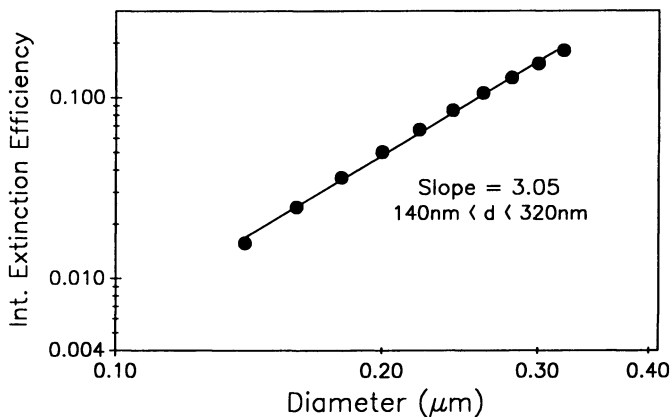


Figure 4. Log-log plot of the integrated extinction efficiency of PS latex in  $\text{H}_2\text{O}$  as a function of diameter from 140 to 320nm.

selected particles. Emulsifier-free particles were selected because it was felt that they would be easier to dry.

To determine the percent solids a stock suspension was made from the concentrate by accurately diluting 2g with 20g of milliQ water. Twenty drops were then weighed on an aluminum dish. The sample was then evaporated slowly at room temperature to constant dry weight over a period of one week. The mean and standard error of 7 samples for each lot are shown in Table I.

**Table I. Solids Content of Two Standard Latexes**

	Lot 10-65-53, Std. 1	Lot 10-95-38, Std. 2
<b>Labeled</b>	<b>9.30 ± 0.10% w/w</b>	<b>10.10 ± 0.10%</b>
<b>Measured</b>	<b>8.90 ± 0.02%</b>	<b>9.98 ± 0.02%</b>

All subsequent mixtures were prepared gravimetrically using the measured percent solids for calculations.

PCS results on the unmixed polystyrene samples were obtained as pooled averages from 8 runs on one instrument and 6 runs on another. The instruments were two Brookhaven BI-90 submicron particle sizers. Pooled data showed no instrument-to-instrument variations. Each run took just over 4 minutes. Samples were made by diluting one drop of the concentrates into 5ml of aqueous solutions of 10mM NaCl and 0.1% v/v Triton X-100. All solutions were prepared using milliQ water, pH 5.3, which had been filtered through a 0.2 $\mu$  filter. Sample cells were cleaned repeatedly using the same diluent.

The individual and mixed latexes were each run twice on two different disc centrifuge photosedimentometers, Brookhaven Instruments model BI-DCP. Pooled data showed no instrument-to-instrument variations. Samples were prepared as follows: 1 drop of the concentrate was diluted into 3ml of a 0.2 $\mu$  filtered aqueous solution of 0.1% v/v Triton X-100 followed by 30 seconds of sonication, after which 3ml of MeOH was added. An external gradient was formed using 15ml of milliQ water and 1ml of MeOH as described previously. Disc rotation speed was 8000RPM, and run times varied from about 12 minutes for the larger particles to about 60 minutes for the smaller particles. Temperature was monitored and recorded throughout the runs. Deviations of no more than two degrees centigrade were noted. The mean temperature was used for calculating fluid viscosity and density.

## **Results and Discussion**

Data analysis for a disc centrifuge using the line start method is well known<sup>7</sup>. In particular, all the data presented here were analyzed using the Treasure<sup>8</sup> correction. The Treasure correction arises from the finite size range in the detector due to the finite detector aperture. Treasure was the first to note that, apart from any variation of  $Q_{ext}$  with diameter, this leads to a volume rather than a surface area distribution as might be expected from a cursory examination of Equation 1.

It is difficult to prove that a submicron particle sizing method is accurate using carbon black. Such particles are neither spherical nor solid, and carbon black standards are not available. Thus, proving that extinction efficiencies have been properly accounted for is impossible. However, the BCR66 quartz powder standard and polystyrene standards do provide a means for testing.

**BCR Results.** The BCR66 standard consists of 11 data points from about  $0.35\mu$  to  $3.5\mu$ . The cumulative percent undersize values are known to within several percent. These values are an average from several laboratories using the Andreasen pipette method. Although tedious and difficult for small particles that also diffuse, this method relies on direct gravimetric analysis to determine the weight of particles that has sedimented a known distance.

Figure 5 shows the mass percent undersize versus the Stokes Diameter for BCR66. The filled circles represent the standard data. The smooth curve was obtained using the DCP method described in the experimental section and the integrated extinction efficiency shown in Figure 2. The agreement is excellent.

The dashed curve shows the results calculated without any extinction correction. A significantly more coarse distribution is obtained. Since the refractive index of PS is close to that of natural quartz, it might be expected that the full PS extinction correction would yield acceptable results. As shown by the dotted curve in Figure 5, it does not.

Allen<sup>7</sup> also measured the particle size distribution of BCR66 using a disc centrifuge fitted with a tungsten-halogen lamp and silicon diode detector. Instead of correcting theoretically for the extinction efficiency as we have done in this paper, he chose to calculate the extinction efficiency as a function of diameter given the BCR66 size distribution and the uncorrected DCP data. In other words, he constructed a calibration curve.

Figure 6 in the Allen paper shows the extinction curve constructed for calibration. It does not resemble our Figure 2. Figure 7 in the Allen paper shows the cumulative percent undersize versus diameter for BCR66 with and without the extinction correction. Even with the extinction correction the cumulative distribution does not agree nearly as well with the standard BCR66 data as our data shown in Figure 5. These differences are puzzling.

**Latex Results.** The results of particle size measurements on the individual latex standards are shown in Table II.

**Table II. Unmixed Latex Standards: Diameter**

Technique	Std. 1(nm)	Std. 2(nm)
<b>LABEL</b>	<b>300 ± 1</b>	<b>121 ± 1</b>
<b>PCS</b>	<b>313 ± 1</b>	<b>151 ± 1</b>
<b>DCP</b>	<b>316 ± 2</b>	<b>151 ± 2</b>

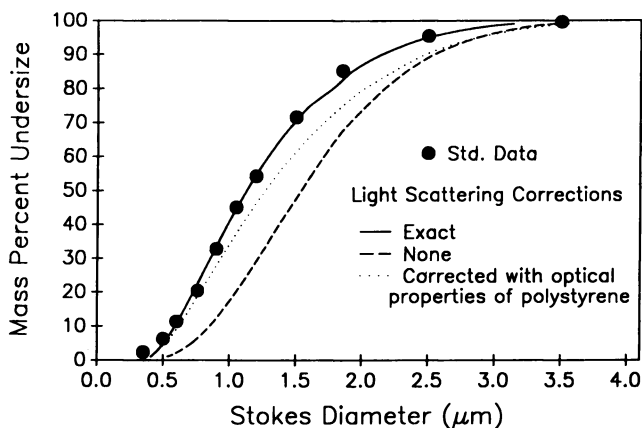


Figure 5. Cumulative undersize distribution by mass for BCR66, a natural quartz powder standard, in  $H_2O$  as a function of diameter and different optical corrections. The data was measured with a disc centrifuge.

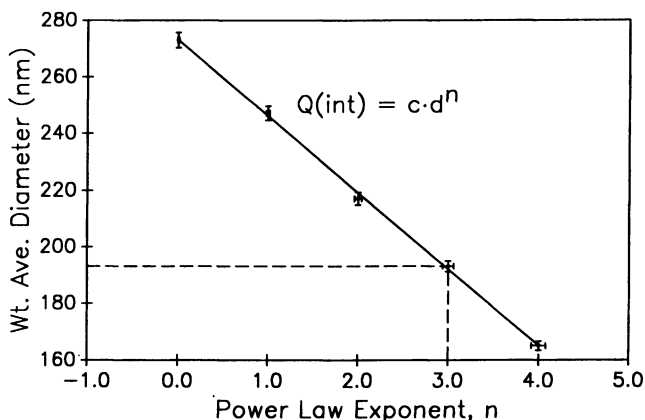


Figure 6. Weight average diameter of a bimodal suspension as a function of the power law exponent used to calculate the correction due to extinction efficiency. The raw data was measured with a disc centrifuge using a 23.9%/76.1% by weight mixture of 151/314nm PS in  $H_2O$ .

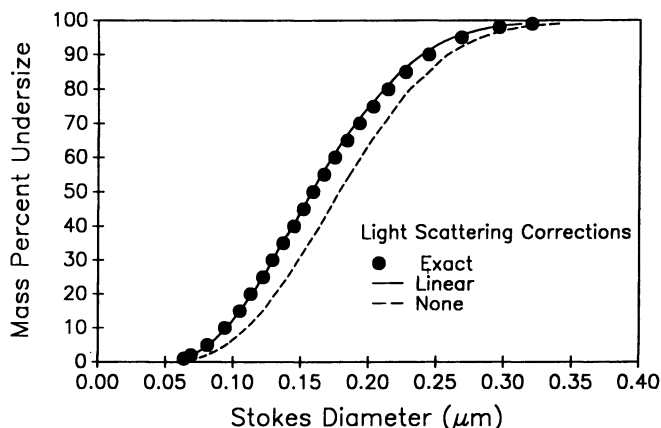


Figure 7. Cumulative undersize distribution by mass of a typical carbon black in  $H_2O$  as a function of diameter and different optical corrections. The data was measured with a disc centrifuge.

The uncertainties are the standard deviation of the mean values. PCS measurements in this size range are least subject to error. The DCP results depend on the density used for the particle. Here a value of  $1.045\text{g/cm}^3$  was used for both samples. Furthermore, this same density has been used in our laboratory on several Duke Scientific latex standards. And agreement between the labeled values and those found with the DCP are usually within 2%.

On this basis we find the supplier's values are suspect. Further measurements made by the supplier on Std. 2 revealed an error in calibration. A new value of 149nm was subsequently reported. Std. 1 was never remeasured by the supplier.

Mixtures of these two latexes were made with nominal 2:1, 1:1, and 1:2 ratios by weight. More exact ratios were calculated by weighing the samples used to make the mixtures. These exact ratios, along with the weight average diameters calculated gravimetrically and those obtained from the DCP, are presented in Table III.

**Table III. Mixed Latex Standards: Weight Average Diameters**

Mixture	DCP Results(nm)	Grav. Results(nm)
69.1/30.9	$265 \pm 5$	$264 \pm 3$
46.5/53.5	$225 \pm 2$	$227 \pm 3$
23.9/76.1	$195 \pm 2$	$190 \pm 3$

The DCP results were calculated using the sizes determined from each mixture and the extinction efficiency shown in Figure 3. The gravimetric results were calculated using the values 314.5nm and 151nm for the diameters and the

percents by weight determined gravimetrically and shown in the first column of Table III. The agreement is excellent with the worst case differing by only 2.5%, yet still within one standard deviation of the mean. The other two cases agree to better than 1%.

Oppenheimer<sup>2</sup> also tested his extinction efficiency calculations using a mixture of latexes. His sizes also varied by a ratio of about 2:1 as ours do; however, he chose sizes in a range over which the extinction efficiency is nearly linear in the diameter. The extinction efficiency in the size range we have chosen varies as the cube of diameter. A given relative error in size would lead to three times the same relative error in the calculated extinction efficiency. And the final weight-average diameter would show a much greater sensitivity to the extinction correction. The excellent agreement obtained in this work is a more sensitive test of the extinction efficiency calculations than that of Oppenheimer.

#### Effects of Ignoring the Treasure Correction and Refractive Index Variations.

The weight average diameter for the 23.9/76.1 mixture was recalculated from the DCP data using different power laws for the extinction efficiency. The results are shown in Figure 6. Using the full extinction correction the answer is 195nm in excellent agreement with 190nm obtained gravimetrically as shown in Table III. The same result is obtained using an exponent of 3 in the power law as shown in Figure 6.

The vertical bars represent the 1% random error in the mean value obtained in this work. The horizontal bars represent the error in the power law exponent obtained by varying the refractive index by  $\pm 0.01$ . A variation of this magnitude would occur by ignoring, as we have done, the wavelength dependence of the refractive index in carbon black or quartz powder; or that due to temperature differences of many degrees; or that due to slight chemical heterogeneities from sample-to-sample. Clearly these errors yield results within the experimental error of the measurement. Thus, they can be ignored.

The Treasure correction varies linearly with the diameter. Ignoring this correction is equivalent to changing the power law exponent by one. Here the systematic errors are clearly much greater than the random errors, and ignoring this correction is never justified.

**Carbon Black.** Figure 7 shows the mass percent undersize versus the Stokes Diameter for a carbon black sample. The smooth curve was obtained using the integrated extinction efficiency shown in Figure 1. The filled circles represent values calculated assuming  $Q$  varies as  $D^1$ . The agreement is excellent as it should be since the full curve in Figure 1 is very nearly linear up to several hundred nanometers. The dashed curve represents the uncorrected results. As expected, a coarser distribution results.

## **Conclusions**

Extinction efficiency corrections are crucial for accurate interpretation of DCP measurements and for any other technique which utilizes a turbidimetric method of detection. Indeed, without appropriate extinction efficiency corrections particle size distribution data are of questionable value. These corrections can be calculated sufficiently accurately for a broadband source using the bulk refractive index for polystyrene latex and natural quartz. The excellent agreement obtained in this work between theory and experiment suggests that other materials are also amenable to this treatment.



Literature Cited

1. Van de Hulst, H.C. Light Scattering by Small Particles; Dover Publications: New York, 1981. Bohren, C.F.; Huffman, D.R. Absorption and Scattering of Light by Small Particles; Wiley-Interscience Publications: New York, 1983.
2. Oppenheimer, L.J. J. Colloid and Interface Sci. 1983, 92, 350.
3. Medalia, A.I.; Richards, L.W. J. Colloid and Interface Sci. 1972, 40, 233.
4. Kerker, M. The Scattering of Light and other Electromagnetic Radiation; Academic Press: New York, 1969; p. 324.
5. Boundy, R.H.; Boyer, R.F. Styrene: Its Polymers, Copolymers and Derivatives; American Chemical Society Monograph Series; Reinhold Publishing Corp.: New York, 1952; p. 524.
6. Holsworth, R.M.; Provder, T.; Stansbrey, J.J. In Particle Size Distribution: Assessment and Characterization; Provder, T., Ed.; ACS Symposium Series 332; American Chemical Society: Washington D.C., 1987; Chapter 13.
7. Allen, T. Powder Technology 1987, 50, 193.
8. Coll, H.; Haseler, S.C. J. Colloid and Interface Sci. 1984, 99 591.

RECEIVED May 7, 1991

## Chapter 13

# Particle Separation and Size Characterization by Sedimentation Field-Flow Fractionation

J. Calvin Giddings<sup>1</sup>, Marcus N. Myers<sup>1</sup>, Myeong Hee Moon<sup>1</sup>, and Bhajendra N. Barman<sup>2</sup>

<sup>1</sup>Field-Flow Fractionation Research Center, Department of Chemistry, University of Utah, Salt Lake City, UT 84112

<sup>2</sup>FFFractionation, Inc., P.O. Box 58718, Salt Lake City, UT 84158-0718

This chapter provides, first, an overview of particle characterization by field-flow fractionation (FFF) and describes how FFF works, the applicable size range, the properties that can be characterized, and the underlying theory. Second, a number of applications of sedimentation FFF are shown to illustrate the applicability of this FFF technique to diverse particulate materials in both sub-micron and supramicron size ranges. The materials examined include uniform and broad latex populations, dense inorganic and metallic particles, elongated Teflon particles, and plate-like clay particles. It is shown that self-consistent particle size distributions can be obtained under different experimental conditions and that narrow fractions can be collected and further examined and characterized by microscopy or other means. The high speed of steric FFF is illustrated by a one minute run of 3-15  $\mu\text{m}$  copper particles.

Field-flow fractionation (FFF) is a family of separation methods in which particles with different properties are eluted from the thin FFF flow channel at different times and their relative amounts recorded (1-5). The properties that control elution times depend on the FFF subtechnique utilized: particle size in the case of flow FFF, mass and density for sedimentation FFF, sedimentation coefficients for cyclical-field FFF, etc. In each case the concentration versus elution time curve can be converted into a property distribution curve: mass distribution, size distribution, sedimentation coefficient distribution, etc. Because FFF is capable of yielding so many kinds of information on so many categories of particles and doing these tasks both flexibly and with high resolution, the FFF family has emerged as the most versatile and effective single methodology available for detailed particle characterization. For highly complex colloids, fractions can be collected and further characterized by electron microscopy, elemental analysis, and other complementary techniques.

0097-6156/91/0472-0198\$06.00/0  
© 1991 American Chemical Society

For perspective, it is useful to describe the range of applicability of FFF. At the small diameter end of the spectrum, we have applied flow FFF to particles (e.g., globular proteins) as small as  $0.005\ \mu\text{m}$  (5 nm) and below. At the large diameter extreme, sedimentation FFF operating in the steric mode has been applied in our laboratories to particles up to  $500\ \mu\text{m}$  (0.5 mm) in diameter. The total mass range covered is over  $10^{15}$ . Applications have been made throughout this range. While most work has been done with aqueous suspensions of particles, we have applied sedimentation FFF to nonaqueous suspensions as well (6). (Nonaqueous sedimentation FFF work has also been reported by Yonker et al. (7).) More recently, we have demonstrated that thermal FFF is applicable to various categories of particles suspended in organic liquids (8).

The particulate materials that have been subjected to FFF analysis have now involved work in so many laboratories, both academic and industrial, that they cannot be compiled without serious omissions. While most of the analyzed materials are industrial intermediates or products, many of them proprietary, there have been many applications of FFF to biological and environmental materials. The particles range from high density metal and low density latex microspheres to various "soft" and highly deformable particles such as those constituting emulsions, biological cells, and liposomes. A listing of many of the particulate materials studied by FFF in our laboratories, as shown in Table I, is suggestive of the broad scope of the methodology. (Polymers, analyzed by thermal and flow FFF, are not listed in this table.)

### Principles of FFF

Field-flow fractionation is generally carried out in a ribbon shaped channel only a few hundred  $\mu\text{m}$  thick and 0.25-1 m in length. The channel contains no packing material. Accordingly, flow through the channel is even and predictable, assuming a parabolic flow profile between the two major channel faces (see Figure 1). The velocity of parabolic flow approaches zero at both walls and reaches a maximum at the midpoint between the walls.

The essence of FFF is to apply a field or gradient across the thin dimension of the channel perpendicular to flow such that it will drive entrained particles into particular cross sectional positions or distributions within the channel. Particles driven close to a wall will be displaced very slowly by flow because of the low flow velocity near the bounding surfaces as shown in Figure 1 (9). Particles positioned further from the wall are displaced more rapidly. Because the applied field causes different particle populations to accumulate in different distributions, they are swept along at different mean velocities. With unequal velocities, the populations migrate differentially and are thus separated (2-5).

The field most widely used for FFF particle characterization is sedimentation (hence sedimentation FFF). While gravity has had limited use for particles over  $1\ \mu\text{m}$  in diameter (10), the sedimentation forces are usually generated in a centrifuge custom designed for FFF work. Here the FFF channel, rather than having a flat configuration as suggested in Figure 1, encircles the axis of rotation like a rotating belt, held in place in a specially designed basket. Rotating seals are used to bring the liquid stream into and out of the channel. Following separation, the particles are

Table I. Some Particles Characterized by FFF Methods in FFFRC and FFFractionation Laboratories\*

---

<b>latex</b>	<b>inorganic</b>
polystyrene (s,f)	gold (s)
polyvinylchloride (s)	copper (s)
polybutadiene (s)	silver (s)
polyurethane (s)	palladium (s)
polymethylmethacrylate(PMMA) (s)	selenium (s)
styrene-butadiene (s)	nickel (s)
grafted polybutadiene - PMMA (s)	glass beads (s,f)
vinyltoluene t-butadiene (s)	silica (s,f)
epoxy-acrylic latex (s)	hematite (s)
	Teflon (s)
<b>emulsions</b>	clay (s)
soybean oil (s)	limestone (f)
safflower oil (s)	zirconia (s)
perfluorocarbon (s)	paint pigments (s,f)
milk (s)	<b>biological</b>
liposomes (s)	red blood cells (s,f)
	white blood cells (s,f)
<b>environmental</b>	HeLa cells (s)
fly ash (s)	yeast cells (s)
coal liquefaction residue (s)	human lens particles (s)
ground coal (f)	albumin microspheres (s)
coal dust (s)	casein particles (s)
waterborne colloids (s)	viruses (T2, Q $\beta$ , PBCV, T4D, P22) (s,f)
diesel soot (s)	gypsy moth NP virus (s)
pollen grains (f)	mitochondria (s)
	lysosomes (s)

---

\*Letters s and f in parentheses represent sedimentation FFF and flow FFF methods, respectively.

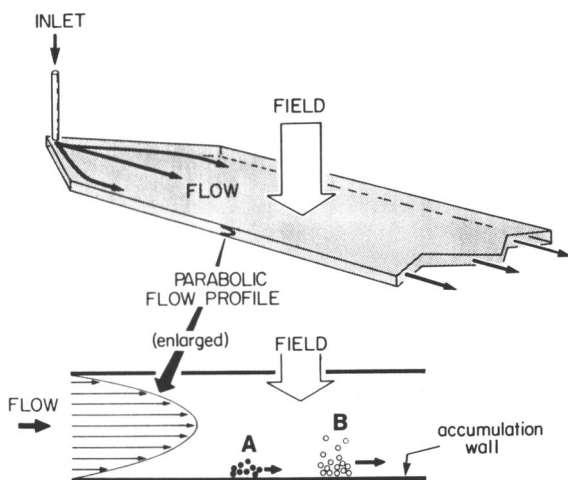


Figure 1. Structure of thin FFF channel (upper) and an enlarged edge view (lower) showing the different distributions of two particulate species A and B that are undergoing differential migration and separation in the channel. (Reproduced with permission from Ref. 9. Copyright 1989 John Wiley & Sons.)

eluted from the channel, through the seals, and into a detector where relative concentrations can be recorded.

Because of the rapidly growing importance of sedimentation FFF in particle characterization, the applications shown later in this chapter will be based entirely on this FFF technique.

We note that flow FFF is also being increasingly developed for particle analysis. In flow FFF, a cross flow of fluid moving in a direction perpendicular to the channel flow serves as the driving force to displace particles across the thin dimension of the channel. The flow FFF channels have permeable walls to facilitate the cross flow. The apparatus and methodology for this "universally" applicable FFF approach are described more completely in an accompanying report.

We have very recently discovered that the FFF subtechnique of thermal FFF is applicable to particles suspended in organic liquids. This method, in which a temperature gradient serves as a driving force for transverse displacement, has been applied widely to polymer analysis in the past. The device consists of a thin channel sandwiched between specially coated and polished copper blocks, one heated and one cooled so that a controllable temperature gradient can be applied across the channel (11).

Other variants of FFF exist but have been less well developed. One of these is cyclical-field FFF, in which the direction of the field is cycled back and forth during the run (12). Separation in cyclical-field FFF is governed mainly by differences in a transport coefficient, which, depending on the field, might be the sedimentation coefficient or the electrophoretic mobility.

### Theory of FFF

There are a number of different operating modes of FFF, each associated with its own theory. The principal operating modes for particle analysis are normal FFF, steric FFF, hyperlayer FFF, and cyclical-field FFF. (Any one of these modes can be used with a sedimentation field.) It is not our purpose to detail all of these theories here. Instead we will describe in a general way how the theories are formulated and what they accomplish. A few key equations for normal and steric FFF will be given.

Providing the forces acting on particles are known, transport in the FFF system is highly predictable because of the uniform channel geometry, the even application of the field, and the well understood flow profile. The first objective of theory is to describe the velocity and thus the retention time of different populations of particles making up the particulate sample. For particles distributed over different streamlines, the velocity of downstream transport can be calculated by averaging the velocity of particles occupying the different stream laminae (2-4). By a somewhat more complicated procedure, band broadening, representing the axial dispersion of particles and thus having an important bearing on resolution, can also be calculated (13).

FFF has been widely applied in the normal mode of operation, generally applicable to particles of submicron size. Here the distribution of particles relative to the accumulation wall of the channel, fixed by the balance between field-driven transport toward the accumulation wall and diffusive transport in the opposite direction, is exponential in nature (2-5)

$$\frac{c(x)}{c_0} = e^{-x/\lambda w} \quad (1)$$

where  $c(x)$  is the concentration of particles at distance  $x$  above the accumulation wall,  $c_0$  is the concentration at the wall,  $w$  is the channel thickness, and  $\lambda$  is the retention parameter. The latter is a dimensionless parameter given by

$$\lambda = \frac{kT}{Fw} \quad (2)$$

where  $kT$  is thermal energy and  $F$  is the force exerted on a single particle by the field. Separation is based on different levels of force  $F$ , which lead to different distributions  $c(x)$  as expressed in Equation 1.

The mean retention time  $t_r$  of a population of like particles obtained by the above mentioned averaging procedure is given by

$$\frac{t_r}{t^0} = \frac{1}{6\lambda[\coth(1/2\lambda) - 2\lambda]} \rightarrow \frac{1}{6\lambda} \quad (3)$$

where  $t^0$ , the void time, is the time needed to elute a tracer material moving with the average fluid velocity. The final part of Equation 3, shown by the arrow, is a simple form approached by  $t_r/t^0$  for  $\lambda \ll 1$ .

For most fields,  $F$  is a predictable function of particle properties, particularly particle mass and size. Thus for a sedimentation field

$$F = m \frac{\Delta\rho}{\rho_p} G \quad (4)$$

or equivalently

$$F = \frac{1}{6}\pi d^3 \Delta\rho G \quad (5)$$

where  $m$  is the particle mass,  $d$  is the effective spherical particle diameter,  $\Delta\rho$  is the particle density ( $\rho_p$ ) less the carrier density ( $\rho$ ), and  $G$  is the acceleration.

For flow FFF,  $F$  is given by

$$F = 3\pi\eta d_s U \quad (6)$$

where  $\eta$  is viscosity,  $U$  is the velocity of cross flow, and  $d_s$  is the Stokes diameter.

The above force equations, used in conjunction with eqs 2 and 3, provide a direct theoretical link between particle properties (such as  $m$ ,  $d_s$ , and  $\Delta\rho$ ) and retention time  $t_r$ . Thus measured retention times can be used to calculate relevant properties. The observed distribution of retention times, represented by the recorded elution profile or fractogram, can then be used to obtain property distributions, such as the

particle size distribution (PSD). Particle densities can also be obtained by sedimentation FFF.

For steric and hyperlayer FFF, applicable primarily to particles over 1  $\mu\text{m}$  in diameter,  $t_r$  is given by (14)

$$\frac{t_r}{t^0} = \frac{w}{3\gamma d} \quad (7)$$

where  $\gamma$  is the steric correction factor. For steric FFF,  $\gamma < 2$ ; for hyperlayer FFF,  $\gamma \geq 2$ .

### Experimental

The experiments reported here were carried out on several different (but closely related) sedimentation FFF devices. The apparatus for systems I and II is the model S101 colloid/particle fractionator from FFFractionation, Inc. (Salt Lake City, UT). Systems III, IV, and V are research devices used in the Field-Flow Fractionation Research Center (FFFRC) laboratories. Important features and essential components of these systems are provided in Table II. For all runs, small (sub-milligram) samples in suspension were injected into an aqueous carrier stream that enters and flows through the channel. Detection in all systems is based on light scattering of the emerging components within the flow cell of a UV detector designed for liquid chromatography. Particle size distributions were obtained from FFFractionation and FFFRC software. The runs shown here were made either at constant field strength or under conditions of power programming, a unique form of field programming yielding uniform fractionating power (15). Here, the field strength  $G$ , after being held constant for time  $t_1$ , decreases as the following power function of the elapsed time  $t$  from the start of the run

$$G = G_0 \left( \frac{t_1 - t_a}{t - t_a} \right)^8 \quad (8)$$

where  $G_0$  is the initial acceleration and  $t_a$  is a constant.

### Illustrative Applications

Figure 2 illustrates the resolution of six polystyrene latex particles in the diameter range 0.20 to 0.86  $\mu\text{m}$  using system I and a power programmed run with parameters  $G_0 = 380.2$  gravities (1500 rpm),  $t_1 = 13$  min,  $t_a = -104$  min, flow rate  $\dot{V} = 6.37$  mL/min, and stop-flow time  $t_{sf} = 12$  min. The aqueous carrier solution contained 0.05% (w/v) sodium dodecyl sulfate (SDS) and 0.01% (w/v) sodium azide.

While mixtures of narrow latex standards, as resolved in Figure 2, are in no sense typical of industrial samples, an attempt to resolve such standards provides an important resolution test. Even for broad distributions, high resolution is necessary for distinguishing subtle population changes, discerning bimodal and trimodal distributions, accurately measuring the tails of a distribution, and generally obtaining



Table II. Description of SdFFF Devices

Features/Components	SdFFF Systems				
	I	II	III	IV	V
Channel length (tip to tip), breadth, thickness (cm)	89.4 1.9 0.0254	89.4 2.0 0.0254	90.5 2.0 0.0254	90.0 2.0 0.0254	90.0 1.0 0.0127
Void volume (mL)	4.25	4.52	4.50	4.20	1.40
Channel radius (cm)	15.1	15.1	15.3	15.75	15.1
Detectors	UV at 254 nm	UV at 254 nm	UV at 254 nm	UV at 254 nm	UV at 350 nm
Data recording	FFFractionation software	FFFractionation software	strip chart recorder	strip chart recorder	strip chart recorder
Pump	Isochrom LC Spectra-Physics, (San Jose, CA)	Isochrom LC Spectra-Physics (San Jose, CA)	Minipuls 2 Gilson, (Middleton, WI)	Model LC 414 Kontron Electrolab (London, UK)	Model QD-1 Fluid Metering (Oyster Bay, NY)
SdFFF type	standard	standard	dual outlet	standard	slow-flow injection

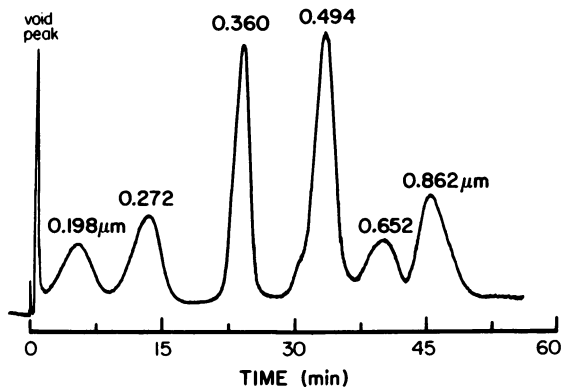


Figure 2. High resolution separation of polystyrene latex standards of indicated diameters by sedimentation FFF.

other details of the size distribution curve that may have an important bearing on product quality. Any method or instrument that cannot resolve close lying latex standards is likely to gloss over significant details characterizing the particulate material. The ability to resolve monodisperse latex samples is recommended as a standard test for all methodologies designed to provide accurate and detailed particle size distributions.

More typical of an industrial latex sample is the acrylic based latex material whose fractogram is shown in Figure 3a. This run was obtained with system I using  $G_0 = 169.0$  gravities,  $t_1 = 10$  min,  $t_a = -80$  min,  $\dot{V} = 1.25$  mL/min, and  $t_{sf} = 20$  min. A 0.05% (w/v) SDS solution with 0.01 (w/v) sodium azide was used as carrier liquid. Using a particle density of 1.1 g/mL, eqs 2, 3, and 5 can be combined to provide a unique value of the particle diameter  $d$  for particles eluting at any specified retention time  $t_r$ . This exercise makes it possible to affix a diameter scale (along with the observed time scale) to the fractogram of Figure 3a, making it easy to visualize the emerging particle peak in terms of constituent diameters. However, in order to arrive at a particle size distribution (PSD) for the sample, a standard scale correction procedure must be employed (16). When this procedure, implemented through the S101 software (FFFractionation, Inc.), is applied to the fractogram of Figure 3a, the PSD shown in Figure 3b emerges.

Sedimentation FFF can be applied with equal facility to dense inorganic and metallic particles. Figure 4a, for example, shows a fractogram obtained from system IV for a finely divided zirconia powder having a particle density of 6.0 g/mL. The carrier was 0.1% (v/v) FL-70 solution with 0.01% (w/v) sodium azide. The size distribution calculated (as above) for this material is shown in Figure 4b. The run was carried out using power programming (in which the variation of rpm with time is shown by the broken line) with  $G_0 = 7.05$  gravities,  $t_1 = 5$  min, and  $t_a = -40$  min, and with  $\dot{V} = 9.5$  mL/min and  $t_{sf} = 10$  min.

The validity of the size-based fractionation and of the resulting size distribution curves obtained from sedimentation FFF can be verified in several ways. One of these is to collect fractions and examine them by electron microscopy. A second means of validation is to compare size distribution results obtained under different conditions, perhaps even by using different FFF systems. Both of these approaches are illustrated in Figure 5 where a Teflon sample is examined. A 0.1% (v/v) Aerosol-OT solution with 0.01% (w/v) sodium azide was used as carrier liquid for the analysis of Teflon particles. The upper fractogram (a) was obtained from system III using a constant field strength of 10.7 gravities with  $\dot{V} = 1.33$  mL/min and  $t_{sf} = 19$  min. Fractions (corresponding to the shaded areas) were collected from this run and subjected to electron microscopy. The resulting micrographs are shown at the top of Figure 5. The mean diameters for the particles eluted in these cuts are calculated from eqs 2, 3, and 5 (with a Teflon density of 2.20 g/mL) to be 0.21, 0.27, and 0.32  $\mu\text{m}$ , respectively. These sizes show good correspondence with those obtained from the electron micrographs. (This comparison is simple to quantify with spherical particles but less simple for the somewhat elongated Teflon particles.)

The lower fractogram (b) of Figure 5 was obtained from system II at a constant field strength of 15.2 gravities and with  $\dot{V} = 1.68$  mL/min and  $t_{sf}$

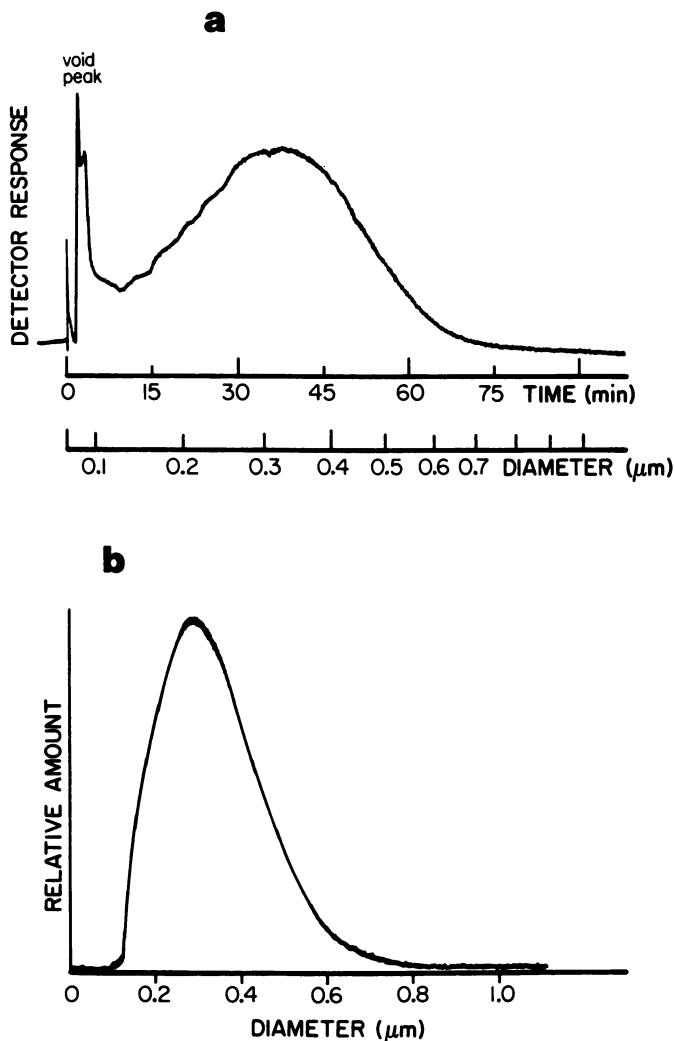


Figure 3. Fractionation of a broad acrylic based latex dispersion by sedimentation FFF. (a) Fractogram with diameter scale. The diameter scale is based on a particle density of 1.1 g/mL. (b) Particle size distribution of acrylic latex dispersion derived from the fractogram in (a).

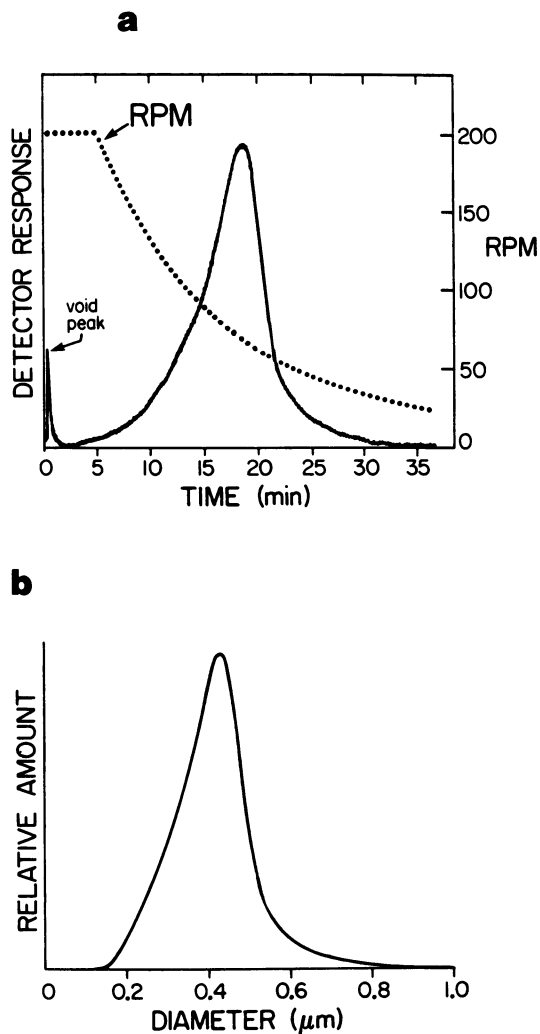


Figure 4. Sedimentation FFF of zirconia. (a) Fractogram; (b) Particle size distribution.

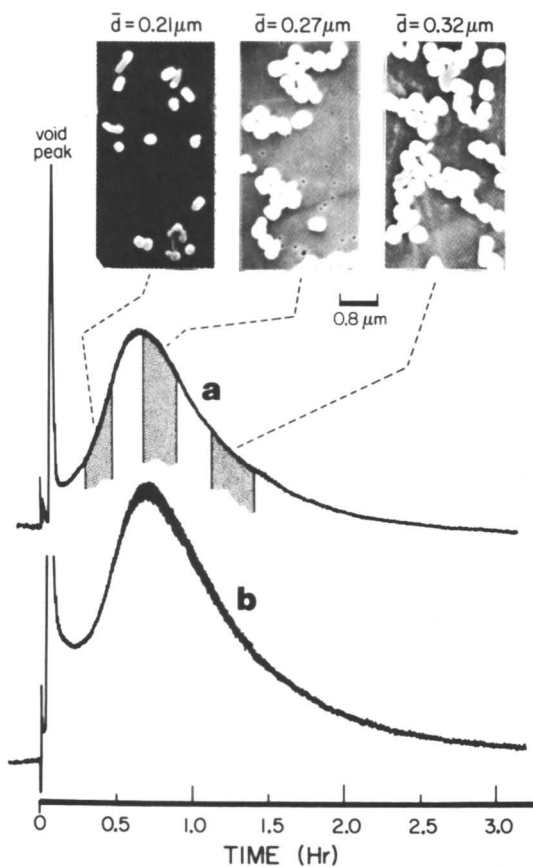


Figure 5. Fractograms of Teflon particles obtained from (a) system III and (b) system II under different experimental conditions (see text). The electron micrographs (top) of particles collected in the indicated shaded areas of fractogram (a) verify fractionation and size scaling.

= 15 min. The two fractograms are obviously similar despite the use of different systems and conditions. However the results become meaningful only when the two particle size distribution curves are compared. Such a comparison is provided in Figure 6. The agreement between the two curves is quite satisfactory.

FFF, of course, does not require spherical particles for analysis. Separation in the normal mode of sedimentation FFF is based strictly upon effective particle mass,  $m' = m\Delta\rho/\rho_p$ , as is apparent from Equation 4. For spherical particles,  $m'$  relates directly to sphere diameter  $d$ . For nonspherical particles, one can either obtain a particle mass (or volume) distribution from the fractogram or (more commonly) proceed with the calculation of a particle size distribution with the understanding that the "diameter" scale refers to the effective spherical diameter of emerging particles. This approach was used for the nonspherical Teflon particles in Figure 6. A more extreme example is provided by clay.

Figure 7 shows three fractograms of a sample of kaolin clay obtained from system I. Because of the high aspect ratio of the clay particles and the consequent enhanced risk of steric perturbations, the three runs were made under quite different experimental conditions to check the self-consistency of the results. The conditions for the three runs, all utilizing power programming, were as follows: (a)  $G_0 = 6.7$  gravities,  $t_1 = 5$  min,  $t_a = -40$  min; (b)  $G_0 = 15.2$  gravities,  $t_1 = 5$  min,  $t_a = -40$  min; (c)  $G_0 = 27$  gravities,  $t_1 = 10$  min, and  $t_a = -80$  min. For all three runs a 0.1% (v/v) Displex A40 solution was used as carrier liquid. The flow rate  $\dot{V}$  was  $1.50 \pm 0.02$  mL/min and the field, once it reached a level of 0.95 gravities, was held constant for the remainder of the run.

The fractograms of Figure 7 show little resemblance to one another except for a slight hint of bimodality. However when the size distribution curves (where one must keep in mind that size is measured in terms of effective spherical diameter) are compared for the three runs, very similar distributions are obtained as shown in Figure 8. A density value of 2.55 g/mL was used for the clay sample. While there are a few specific differences in the three curves of Figure 8, particularly in the vicinity of the first mode, the overall agreement is quite satisfactory considering the complexity of the sample and the diversity of experimental conditions. We note that the modality features of the above distribution would not be clearly represented by any method providing significantly less resolution than FFF. Electron micrographs obtained from another run on kaolin clay (not shown here) demonstrate a clear size fractionation. We conclude that sedimentation FFF is generally a suitable method for the size characterization of clay but caution that the diameter scale must be carefully interpreted as described above.

For completeness, we show in Figure 9 a fractogram of metallic copper particles (mainly spheres) with diameters greater than 1  $\mu\text{m}$  obtained from system V. The original powder sample was first dispersed in an aqueous solution containing 0.07% (w/v) sodium salt of naphthalene sulfonic acid-formaldehyde. The resulting dispersion was then analyzed in 0.1% (v/v) FL-70 solution with 0.02% (w/v) sodium azide. A constant field of 29.9 gravities and a flow rate of 29.4 mL/min were used. For these larger particles the steric mode of operation is utilized (without stop-flow) and the retention time of individual subpopulations is determined by Equation 7. For steric FFF, the flow rates can be very high and the runs correspondingly short without a significant loss of resolution. Thus the

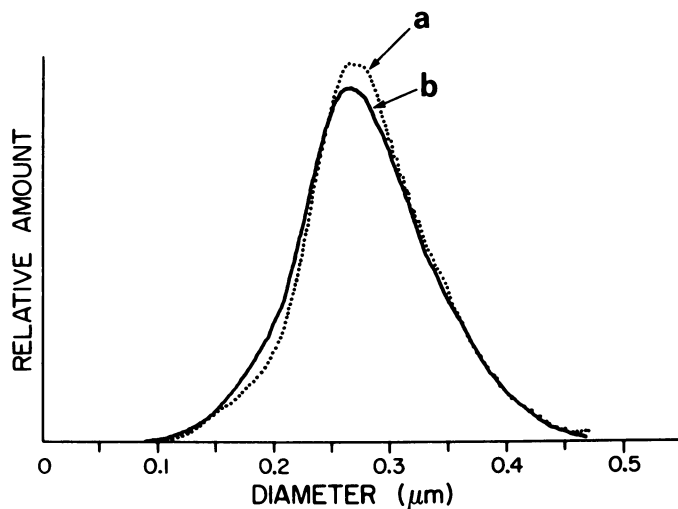


Figure 6. Comparison of particle size distribution curves obtained from fractograms (a) and (b) of Figure 5.

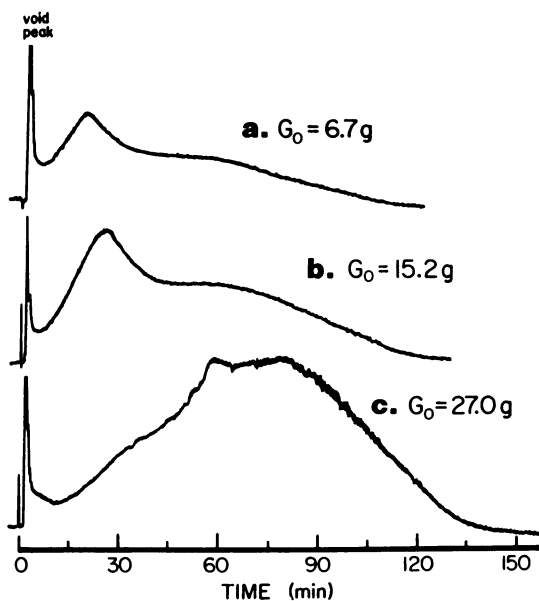


Figure 7. Fractograms of a kaolin clay sample obtained under different experimental conditions.



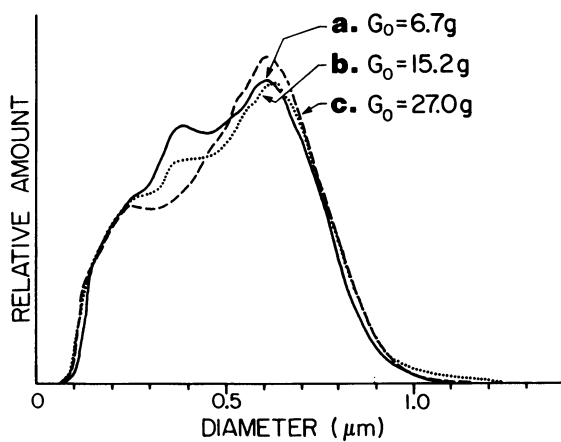


Figure 8. Particle size distributions of a kaolin clay sample derived from the three fractograms shown in Figure 7.

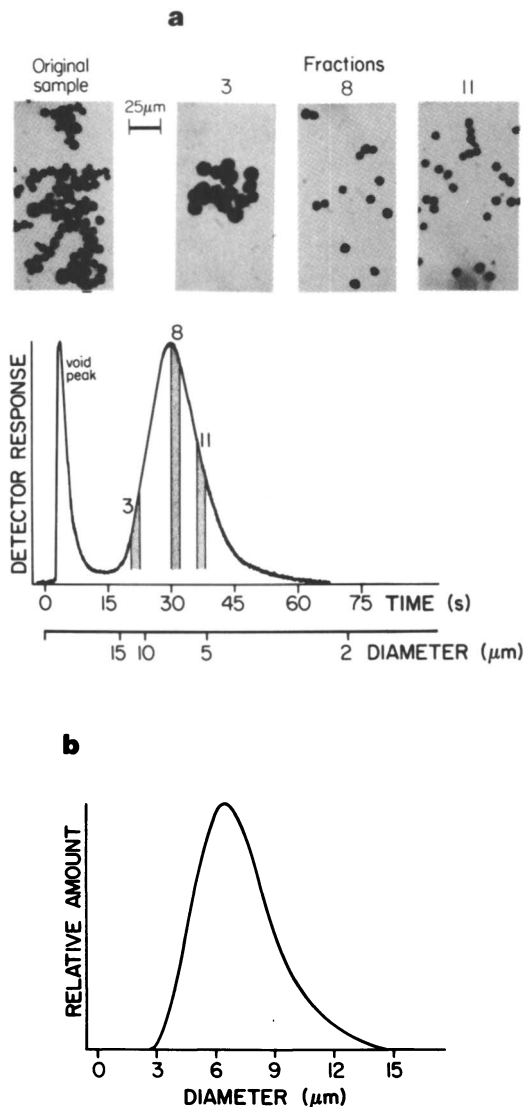


Figure 9. Sedimentation steric FFF of copper particles. (a) Fractogram; (b) Particle size distribution. The inserted micrographs obtained from cuts 3, 8, and 11 verify steric mechanism and size scaling.

run shown in Figure 9a is completed within about one minute of sample injection. The resulting size distribution for this material, obtained by a specially modified software package, is shown in Figure 9b. The density of copper particles was assumed to be 8.92 g/mL.

The steric mode separation of copper particles is verified by subjecting fractions collected at different positions of the fractogram to optical microscopy (see Fig. 9a). Inserted micrographs obtained from cuts 3, 8, and 11 provided particle diameters of  $11.6 \pm 0.6 \mu\text{m}$ ,  $7.0 \pm 0.7 \mu\text{m}$ , and  $5.3 \pm 0.4 \mu\text{m}$ , respectively, in good agreement with the diameter scale (see figure) obtained by calibration.

The steric FFF analysis of larger particles (such as those of copper shown above) is applicable to practically any particulate material for which diameters exceed  $1 \mu\text{m}$  and for which particle density is known. Applications in our laboratories have included latex spheres, glass beads, fly ash, and other metallic particles including those of palladium, silver, and gold.

For the PSD curves shown in the various figures, the curve height is weighted by light scattering since the detector for the system is a UV detector of the type used in liquid chromatography, which for colloids and particles produces its primary signal as a consequence of light scattering. Light scattering corrections have been described in the literature (17, 18) but were not utilized for the PSD curves of this study. (Such corrections are essential when wavelength  $\lambda \gg d$ , but less significant when  $\lambda \sim d$  or  $\lambda \ll d$  as found generally here.) It is likely that effective detectors will eventually be developed that respond more directly to sample mass or volume. Such detectors might include the evaporative light scattering mass detector first tested with FFF in 1984 (19). It could also include density detectors, a version of which was proposed for coupling with FFF in discussions with Dr. Bernd Trathnigg in 1987 (Trathnigg, B., personal correspondence, July 20, 1987). Other possibilities exist.

### Conclusions

The examples described here illustrate the application of sedimentation FFF to a variety of particulate materials. However, the true scope of FFF is much broader than suggested by these examples; FFF has been applied to particles much smaller and much larger than those described here and it has been applied to nonaqueous suspensions of particles as well. For most of these applications, FFF has the advantage of high resolution and a degree of flexibility that makes simple self-consistency tests possible. The ability to collect fractions and examine them by electron microscopy and other tools, both to confirm the results calculated from FFF and to extend the analysis to include other property distributions (e.g., shape, elemental content, etc.), significantly broadens the capability of FFF. The flexibility of operation can also be utilized in trading speed for resolution; if less resolution is needed in the submicron size range, the speed of the run can be correspondingly increased. For the larger particles subject to steric FFF, the runs are already extraordinarily fast as illustrated in Figure 9.

### Acknowledgment

This work was supported by National Science Foundation Grant CHE-8800675.

Literature Cited

1. Giddings, J. C. Sep. Sci. 1966, **1**, 123.
2. Giddings, J. C. Anal. Chem. 1981, **53**, 1170A.
3. Giddings, J. C. Sep. Sci. Technol. 1984, **19**, 831.
4. Caldwell, K. D. Anal. Chem. 1988, **60**, 959A.
5. Giddings, J. C. Chem. Eng. News 1988, **66**, 34.
6. Caldwell, K. D.; Karaiskakis, G.; Myers, M. N.; Giddings, J. C. J. Pharm. Sci. 1981, **70**, 1350.
7. Yonker, C. R.; Jones, H. K.; Robertson, D. M. Anal. Chem. 1987, **59**, 2573.
8. Liu, G.; Giddings, J. C. Anal. Chem., in press.
9. Giddings, J. C.; Caldwell, K. D.; Kesner, L. F. In Molecular Weight Determination; Cooper, A. R., Ed.; Wiley-Interscience: New York, 1989; Chapter 12.
10. Giddings, J. C.; Myers, M. N. Sep. Sci. Technol. 1978, **13**, 637.
11. Giddings, J. C.; Myers, M. N.; Caldwell, K. D.; Fisher, S. R. In Methods of Biochemical Analysis; Glick, D., Ed.; John Wiley: New York, 1980; Vol. 26, pp. 79-136.
12. Lee, S.; Myers, M. N.; Beckett, R.; Giddings, J. C. Anal. Chem. 1988, **60**, 1129.
13. Giddings, J. C.; Yoon, Y. H.; Caldwell, K. D.; Myers, M. N.; Hovingh, M. E. Sep. Sci. 1975, **10**, 447.
14. Koch, T.; Giddings, J. C. Anal. Chem. 1986, **58**, 994.
15. Williams, P. S.; Giddings, J. C. Anal. Chem. 1987, **59**, 2038.
16. Giddings, J. C.; Myers, M. N.; Yang, F. J. F.; Smith, L. K. In Colloid and Interface Science; Kerker, M., Ed.; Academic Press: New York, 1976; Vol. IV, pp. 381-398.
17. Kirkland, J. J.; Rementer, S. W.; Yau, W. W. Anal. Chem. 1981, **53**, 1730.
18. Yang, F.-S.; Caldwell, K. D.; Giddings, J. C. J. Colloid Interface Sci. 1983, **92**, 81.
19. Oppenheimer, L. E.; Mourey, T. H. J. Chromatogr. 1984, **298**, 217.

RECEIVED January 14, 1991

## Chapter 14

# Overview of Colloidal Aggregation by Sedimentation Field-Flow Fractionation

Bhajendra N. Barman<sup>1</sup> and J. Calvin Giddings

Field-Flow Fractionation Research Center, Department of Chemistry,  
University of Utah, Salt Lake City, UT 84112

Sedimentation field-flow fractionation (SdFFF) is shown to have an extraordinary ability to probe aggregation phenomena and to track particle size distribution changes caused by aggregation in colloidal samples. This technique separates particles and particulate clusters based on particle mass and provides equal-mass fractions that can be further characterized by electron microscopy. The effects of experimental parameters such as flow rate and field strength on the resolution and speed of aggregate fractionation are examined here. Details are provided for the application of SdFFF to: (a) detection of both trace and large amounts of aggregated clusters, (b) monitoring of latex clusters broken up by sonication and formed by the addition of appropriate surfactant, and (c) tracking changes in the relative population of clusters due to aging.

Colloidal or particulate aggregation is common in many industrial, biological, and environmental materials. The physical state of a suspension of individual particulate entities is perturbed due to cluster formation in these materials. As a consequence of this, the apparent particle size changes and at the same time bulk properties that depend on the particle size distribution are altered, thus affecting the quality and performance of the material. Therefore methods that provide both a detailed size characterization of aggregated samples and augment the understanding of aggregation phenomena have great practical importance.

The unique capability of sedimentation field-flow fractionation (SdFFF) applied to the problem of low order colloidal aggregation lies largely in its ability to provide the high-resolution mass-based separation of individual aggregated clusters according to well-defined principles.

<sup>1</sup>Current address: FFFractionation, Inc., P.O. Box 58718, Salt Lake City, UT 84158-0718

The SdFFF fractogram (plot of detector signal versus time) of monodisperse populations that have undergone aggregation consists of well-resolved peaks of singlet, doublet, and higher order aggregates. Such a fractogram provides direct and detailed information on the physical state of aggregation. The relative peak areas, for example, reflect the amounts of various aggregates in the sample; changes in peak areas show how the populations of different clusters change with time, with altered conditions, or with processing.

Another advantage of SdFFF in the study of aggregation is that it provides isolated fractions of constant particle mass (e.g., doublets in one fraction, triplets in another) that can be subjected to additional characterization by electron microscopy (EM) or other tools. By combining SdFFF with EM, it is possible to correlate particle mass (obtained from SdFFF retention) with morphology and dimensions (from EM), invaluable information in describing complex aggregates.

In recent publications we have demonstrated that the presence of different sized latex aggregates can be easily established by their separation in an SdFFF system (1-3). Aggregation is confirmed by retention calculations that establish approximate cluster mass and by the EM examination of the fractions collected from each eluted peak. A number of commercially available polymethylmethacrylate (PMMA) latex samples were found to have clusters composed of multiples of monodisperse primary particles. Both experimental and theoretical studies related to the formulation of resolution criteria (1) and aggregate polydispersity (2) were carried out with these samples.

In this study we report representative SdFFF results that show the ability of FFF methodology to track changes in cluster (apparent particle size) distribution caused by variable levels of aggregation in some monodisperse PMMA and polystyrene (PS) latex samples. The scope and limitations of this method for the characterization of aggregates from polydisperse samples are also discussed. The application of SdFFF for detecting trace levels as well as large populations of aggregates in colloidal dispersions is emphasized. The method is demonstrated in model studies involving the monitoring of latex clusters broken up by ultrasonication and formed by the addition of selective surfactant, and for tracking changes in the relative population of clusters due to aging. The importance of experimental SdFFF parameters such as carrier flow rate and field strength in carrying out these studies is also established. Examples are provided showing the effects of applied field and flow rate on the resolution and speed of aggregate separation.

### Theory

The theory of sedimentation FFF describing the fractionation and resolution of colloidal aggregates can be found elsewhere (1, 2). However, a few essential elements are addressed here for completeness.

The basic retention equation in FFF (applicable generally whether the field is sedimentation, electrical, cross flow, etc.) relates retention volume  $V_r$  to the theoretically obtained retention parameter  $\lambda$  as follows

$$V_r = \frac{V^0}{6\lambda[\coth(1/2\lambda) - 2\lambda]} \quad (1)$$

where  $V^0$  is the channel void volume. Equation 2 relates the parameter  $\lambda$  to particle mass  $m$  or particle diameter  $d$  (for spherical particles) in a form that applies specifically to sedimentation FFF

$$\lambda = \frac{kT}{mwG|\Delta\rho|/\rho_s} = \frac{6kT}{\pi wG|\Delta\rho|d^3} \quad (2)$$

where  $k$  is the Boltzmann constant,  $T$  is the absolute temperature,  $G$  is the centrifugal acceleration,  $w$  is the channel thickness,  $\rho_s$  is the particle density, and  $\Delta\rho$  is the difference in density between the particle and carrier liquid. For nonspherical particles,  $d$  is the effective spherical diameter.

For high levels of retention,  $\lambda$  is small and the following approximation to Equation 1 is valid

$$V_r \cong \frac{V^0}{6\lambda} \quad (3)$$

From Equations 2 and 3 we find that the retention volume (therefore retention time) is approximately proportional to particle mass. Since particle clusters in an aggregated sample will differ from one another by one elementary particle mass, SdFFF should provide a series of peaks with nearly equal spacing for the low order aggregates of a monodisperse latex population. Such regularly spaced peaks are illustrated in Figure 1 for aggregated PMMA latex. The successive peaks in the SdFFF fractogram correspond to singlets, doublets, triplets, and so on.

The above equations are for "normal" SdFFF operation where the centrifugal field is opposed by Brownian motion which drives particles away from the accumulation wall to yield a steady state particle cloud or layer (4). The layer thickness, differing from component to component, depends upon the interaction of the colloidal component with the centrifugal field and upon the opposing Brownian motion. In the normal mode, sample particle size  $d$  (usually submicron) is less than the mean layer thickness  $\ell$  (often 2-20  $\mu\text{m}$ ). Steric perturbations become apparent with increasing particle diameter as the increasing  $d$  approaches the decreasing  $\ell$ . In this situation, the position of particles in the flow stream is determined both by their physical size and by their Brownian motion. As a consequence of this dual influence, particles elute earlier than the "normal" mechanism would have allowed. As has been pointed out elsewhere, the steric effect is particularly significant for aggregates which can have relatively large and extended configurations (1). The normal SdFFF retention equations (Equations 1 and 3) can be modified to incorporate the steric mechanism to yield

$$V_r = \frac{V^0}{6\lambda + 3\gamma d'/w} \quad (4)$$

where  $d'$  is an effective particle diameter and  $\gamma$  is the steric correction factor of order unity (5).

Combining Equations 2 and 4, we obtain

$$V_r = \frac{AmG}{1 + Byd'mG} \quad (5)$$

where A and B are constants. The second term in the denominator results from the incorporation of steric perturbations. If steric effects were negligible, this term, for all practical purposes, would vanish. In this case one would expect the retention volume or time to be proportional either to particle mass  $m$  at constant field strength  $G$ , or to  $G$  for a particular cluster size of a fixed mass.

We note that field programming is not used in this study. Field programming is essential to fractionate broad particle populations (where particle diameters vary widely) to minimize run time (6-9). However, resolution is generally sacrificed in a field-programmed run (9). For colloidal aggregates, the effective spherical diameters of doublets, triplets, quadruplets, and quintuplets are 1.26, 1.44, 1.59, and 1.71 times the diameter of singlets, respectively. Since the effective spherical diameters of the successive higher order clusters differ only slightly, high resolution run conditions using a constant field strength are preferable for resolving these aggregates.

### Experimental

Three SdFFF systems were used in this study. System I is a model S101 sedimentation FFF instrument from FFFractionation, Inc. (Salt Lake City, UT). In this apparatus a channel 0.0254 cm thick, 89.4 cm long, and 1.90 cm in breadth is used. The distance between the channel and axis of rotation is 15.1 cm. The channel void volume measured as the elution volume of a nonretained sodium benzoate peak is 4.25 mL. The sample accumulation wall is a highly polished stainless steel surface. This system was coupled with a Model 8815 IsoChrom isocratic pump from Spectraphysics (San Jose, CA) and a Model 153 UV detector from Beckman Instruments (Berkeley, CA). The detector response was recorded and collected by built-in SdFFF data collection and analysis software (FFFractionation, Inc.).

System II is an apparatus similar in most technical respects to the system I instrument and was described elsewhere (1, 10). The apparatus consists of a single inlet and two outlets, the latter capable of providing stream-splitting at the outlet end of the channel to enhance detector signal (11). The system II channel has a length of 90.5 cm, thickness 0.0254 cm, breadth 2.0 cm, radius of rotation 15.3 cm, and a void volume of 4.50 mL. The sample accumulation wall in this channel consists of a highly polished Hastelloy C surface. In this system, a Beckman UV detector working at 254 nm was used; the detector response was transcribed onto a Houston Instrument (Austin, TX) strip chart recorder.

The third SdFFF system (III) consists of all the components of the system I apparatus except for the channel, which was replaced by a new channel with the same nominal dimensions as the system I channel but with a measured void volume of 4.52 mL.

Three PMMA samples were analyzed in this work. A nominal 0.230  $\mu\text{m}$  latex sample was obtained from Seradyn (Indianapolis, IN). Another sample, a nominal 0.207  $\mu\text{m}$  PMMA latex, was a gift from Dr. T. Provder of



The Glidden Company (Strongsville, OH). A third PMMA sample obtained from Polysciences (Warrington, PA) was reported to have particle diameter of 0.325  $\mu\text{m}$ . The polystyrene sample used in this study is a blended mixture of four distinct populations (0.225, 0.551, 1.003, and 1.347  $\mu\text{m}$ ), and was supplied by Seradyn as a polydisperse PS sample with nominal diameter of 0.478  $\pm$  0.215  $\mu\text{m}$ .

The carrier used for the latex analysis was doubly distilled water containing 0.05% (w/v) sodium dodecyl sulfate (SDS) and 0.01% (w/v) sodium azide.

## Results and Discussion

Optimization of Field Strength and Flow rate. According to Equations 2 and 3, we predict that the retention volume (and consequently the retention time) of a particular cluster will increase proportionately with an increase in centrifugal field strength. Normal FFF theory also predicts that the resolution between successive cluster peaks will be higher in the fractogram obtained with a higher centrifugal field (higher rpm) (4, 12). The effect of field strength on the fractionation and resolution of 0.207  $\mu\text{m}$  PMMA aggregates in system I is illustrated in Figure 1. The three representative fractograms in this figure were obtained with different field strengths at a constant flow rate of 1.10 mL/min. We observe that the above predictions are apparently valid for the earlier eluting aggregates. However, major departures, including the loss of resolution for larger size aggregates, are observed that can be attributed to steric effects (1, 13).

Previously we studied the dependence of retention volume on the flow rate at constant field (1). For this we plotted experimental data of  $V_r/V^0$  against aggregation number  $n$ , proportional to cluster mass. We observed significant deviations from the equations of normal SdFFF, which predict that  $V_r$  is independent of flow rate (see Equations 1-3). The deviations were attributed to the velocity dependence of the steric correction factor  $\gamma$  which reflects hydrodynamic lift force effects. For an interpretation of the anomalous behavior, an equation valid for constant field operation similar to Equation 5 was used.

According to Equation 5, we expect a significant deviation from a linear dependence of  $V_r$  on  $G$  as  $G$  is increased. This is particularly true for large size clusters for which serious steric perturbations are expected to result in a negative curvature in the plot of  $V_r$  versus  $G$ . The plots for the singlets and six clusters of 0.207  $\mu\text{m}$  PMMA beads are shown in Figure 2.

Representative fractograms illustrating the effect of carrier flow rate on cluster resolution for the 0.230  $\mu\text{m}$  PMMA latex are provided in Figure 3. Fractograms a, b, and c were obtained from system II at a constant field of 42.8 gravities but with carrier flow rates of 1.73, 1.23, and 0.44 mL/min, respectively. A considerable loss of resolution with increasing flow rate is observed in these fractograms. These results are consistent with the resolution criteria developed in earlier work where we predicted that sharper peaks and better resolution can be achieved by decreasing the carrier liquid flow rates (1). The loss of resolution at higher flow conditions can be attributed to nonequilibrium band broadening (1, 2), to a steric mechanism particularly for larger cluster sizes (1), and to the peak broadening effects of the finite polydispersity of the primary latex particles and thus of the clusters (2).

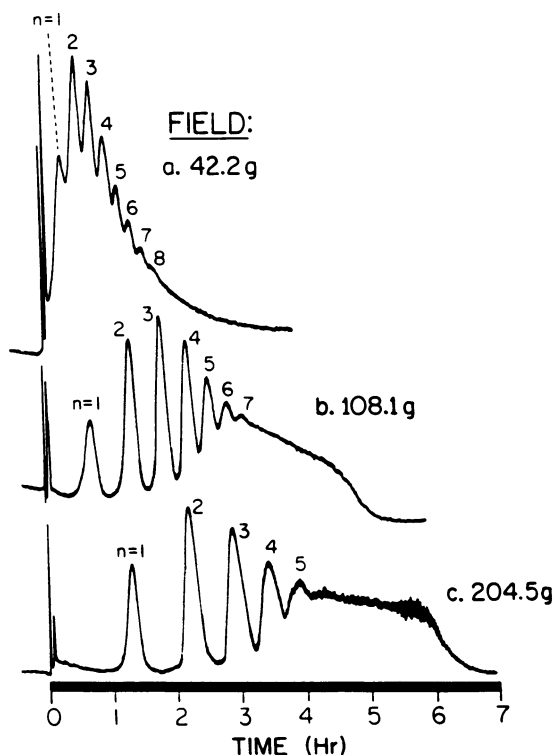


Figure 1. Fractograms of partially aggregated nominal  $0.207 \mu\text{m}$  PMMA latex spheres obtained with SdFFF system I at different field strengths (expressed as number of gravities  $g$ ) with a constant flow rate of  $1.10 \pm 0.02 \text{ mL/min}$ . The number of spheres per cluster is shown as  $n$ . Sample volumes: (a)  $40 \mu\text{L}$ , (b)  $45 \mu\text{L}$ , and (c)  $40 \mu\text{L}$ .

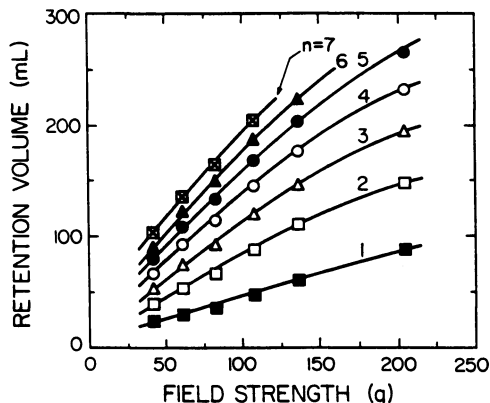


Figure 2. Plots of retention volume versus field strength (in gravities) for seven different clusters of  $0.207 \mu\text{m}$  PMMA latex spheres identified by their aggregation number  $n$ . Fractograms were obtained with SdFFF system I at a carrier flow rate of  $1.10 \pm 0.03 \text{ mL/min}$ .

In Particle Size Distribution II; Prover, T.;

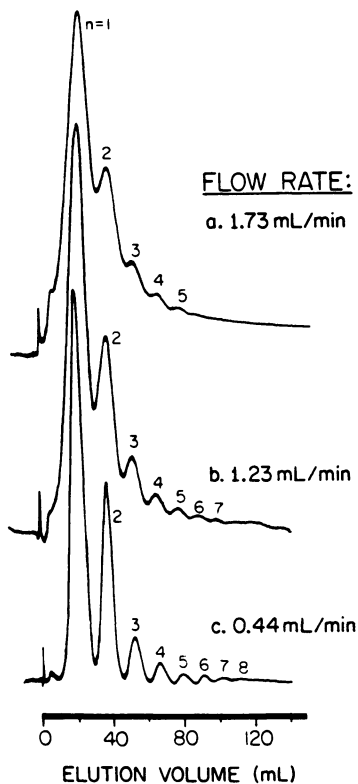


Figure 3. Fractograms of nominal 0.230  $\mu\text{m}$  PMMA latex aggregates obtained with SdFFF system II with different flow conditions. Field strength was kept constant at 42.8 g. Sample volumes: (a) 20  $\mu\text{L}$ , (b) 15  $\mu\text{L}$ , and (c) 14  $\mu\text{L}$ .

From both Figures 1 and 3, we find that the shorter run time in sedimentation FFF is compromised with a lower resolution level. However, it is expected that good resolution of the low-order aggregates can be obtained at high speed by moderate increases in  $G$  and large increases in flow rate.

**Scope of the Analysis of Aggregated Samples by SdFFF.** Aggregates from both monodisperse and polydisperse samples can be analyzed by SdFFF. So far, our attention has been focussed primarily on latex aggregates formed from monodisperse latex beads for simplicity. Latex aggregates have fixed composition and density and therefore their separation by SdFFF is based approximately on particle mass according to Equations 2 and 3. Moreover, the low polydispersity of the primary latex particles minimizes band broadening and provides better resolution between successive cluster peaks (2). The areas of well separated cluster peaks provide a clear picture of the extent of aggregation in such samples.

The SdFFF analysis of aggregates resulting from polydisperse samples is more difficult. Clusters of a given mass eluting at a specified time will accompany clusters of the same mass with different aggregation numbers and elementary particle size. (Mixed clusters made up of different sized elementary particles are likely to be found as well.) As a result of the aggregation, the elution profile and particle size distribution of the aggregated population will be different from those of the original polydisperse nonaggregated sample. However, a clear picture of the details of aggregation will not emerge unless fractions are collected for examination by other means such as electron microscopy. As noted earlier, SdFFF provides fractions of equal mass that can then be characterized structurally and dimensionally by EM.

The fractograms shown in Figures 1 and 3 indicated that the 0.207 and 0.230  $\mu\text{m}$  PMMA samples are extensively aggregated. However it is possible to observe very small amounts of aggregated clusters by sedimentation FFF if the primary particles are monodisperse and thus provide separate cluster peaks. Figure 4 provides an example where the doublets of the major component of a blended sample of four PS beads elute as a separate peak. The sample is reported to be polydisperse with a mean diameter of  $0.478 \pm 0.215 \mu\text{m}$ . The sample is shown by SdFFF (Figure 4) to consist of four distinct populations. Their diameters were reported as  $0.225 \pm 0.004$ ,  $0.551 \pm 0.011$ ,  $1.003 \pm 0.017$ , and  $1.347 \pm 0.014 \mu\text{m}$  with number fractions of 0.318, 0.625, 0.043, and 0.014, respectively (Bangs, L. B., Seradyn Inc., Indianapolis, IN, private communication, March 17, 1988). We note that the resolution between peaks achieved by SdFFF is very high. The experimental conditions chosen for the fractionation are such that we could separate 1.00 and 1.35  $\mu\text{m}$  PS beads by avoiding the steric transition normally found in that region. Using Equations 1 and 2 for the first fraction and Equations 2 and 4 for the rest, we determine mean diameters of particles eluting at the positions where cuts were taken (see Figure 4). The five mean diameters are as follows: 0.20, 0.52, 0.64 (for the doublets), 0.89, and 1.2  $\mu\text{m}$ . These values are consistent with but somewhat smaller than the reported values. For a rigorous comparison, particularly in the vicinity of 1.0  $\mu\text{m}$  particle size, it may be necessary to use  $\gamma$  values other than unity.

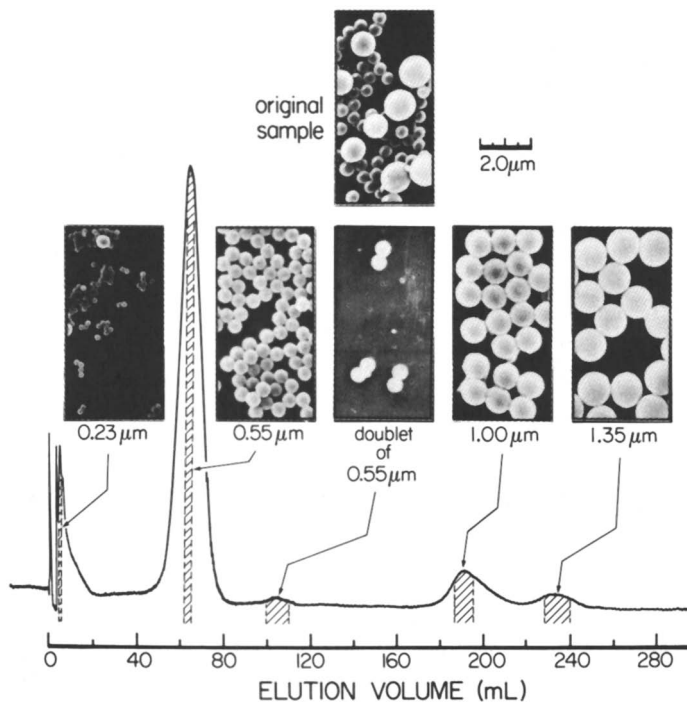


Figure 4. Fractogram showing components of nominal  $0.478 \pm 0.215$   $\mu\text{m}$  PS sample. This blended sample contains trace amounts of aggregated doublets formed from its major component. Experimental conditions: SdFFF system II was used with a field strength of 42.8 g and a flow rate of 0.97 mL/min.

**Model Studies Involving Cluster Breakup and Formation.** The disruption of aggregated species in the 0.299  $\mu\text{m}$  PMMA sample by ultrasonication was monitored by SdFFF (14). For this, the sample was agitated for a specific period and then analyzed by SdFFF. The same sample was sonicated again for other specified periods to repeat the analysis. The effects of sonication time on the breakup of aggregated clusters are reflected in the changing elution patterns with sonication time. With these experiments we could follow a gradual destruction of higher order aggregates to produce a singlet population. We note that due to the remarkable resolving power of SdFFF, individual clusters were resolved and the breakup kinetics of these clusters could be followed in detail (Barman, B. N.; Giddings, J. C. Langmuir, to be submitted).

Sedimentation FFF was also applied to track the formation of aggregated species in PS and PMMA populations (14, Barman, B. N.; Giddings, J. C. Langmuir, to be submitted). For this purpose, tetra-hexyl ammonium bromide (THAB) was used as a cationic surfactant to induce the aggregation of these negatively charged latex spheres. An original 0.327  $\mu\text{m}$  PS latex dispersion was prepared in sodium dodecyl sulfate (SDS) solution (0.05% w/v). Different amounts of cationic surfactant were added to vials containing the original dispersion and mixed well. The resulting dispersions with 0.12, 0.45, and 1.03 mM THAB were found to be stable (without observable precipitates or flocculates). The sample from each vial of stable suspension was subjected to analysis by SdFFF. The fractograms of the original and the three samples containing different amounts of THAB provided data on the relative increase in the population of doublets and higher order aggregates with increasing amount of THAB in the colloidal dispersion. Similar results were obtained when different amounts of THAB were added in a monodisperse 0.299  $\mu\text{m}$  PMMA dispersion containing 0.05% (w/v) SDS.

**Change in Aggregate Population Due to Aging.** The deterioration of latex samples upon aging was studied by SdFFF. By way of example, two fractograms of the 0.325  $\mu\text{m}$  PMMA beads obtained at two different times are shown in Figure 5. Fractogram a was obtained more than 2.5 years before fractogram b. (We note that peak positions do not coincide exactly because experimental conditions are slightly different in the two cases). In both fractograms, peaks for the singlet through quadruplet clusters are observed, followed by a tailing end for the unresolved higher order aggregates. A cursory examination suggests that the peak areas of doublets through quadruplets are nearly the same in these fractograms. However, the difference in the singlet peak areas is quite significant, indicating a loss of singlet population due to sample aging.

A more quantitative comparison is provided by the normalized (with respect to unit area) size distributions obtained from the fractograms of Figure 5 and shown in Figure 6. The overlaid size distributions of the original and aged samples indicate that the singlet through quadruplet peak positions are brought into registry when converted to a diameter scale, showing that none of the clusters has changed in size. The observed changes are due instead to aggregation. Thus the loss of the singlet population in the original sample (shown by the reduced area of the singlet peak in Figure 6) is reflected in the increase in the populations of doublets, triplets, and higher order aggregates. We note that there are some uncertainties (due to steric effects) in the calculation of effective

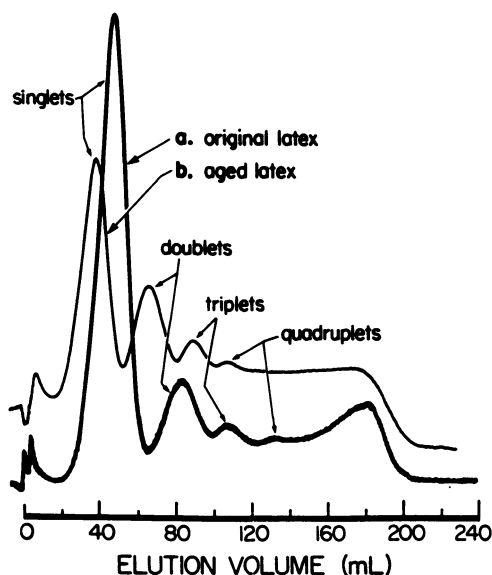


Figure 5. Effects of sample aging are reflected by the two fractograms of nominal 0.325  $\mu\text{m}$  diameter PMMA latex sample. The sample was run in (a) August, 1987, and (b) March, 1990. Experimental conditions: (a) SdFFF system II was used with a flow rate of 0.59 mL/min and a field strength of 19.8 g; (b) SdFFF system III was used with a flow rate of 0.56 mL/min and a field strength of 15.2 g.

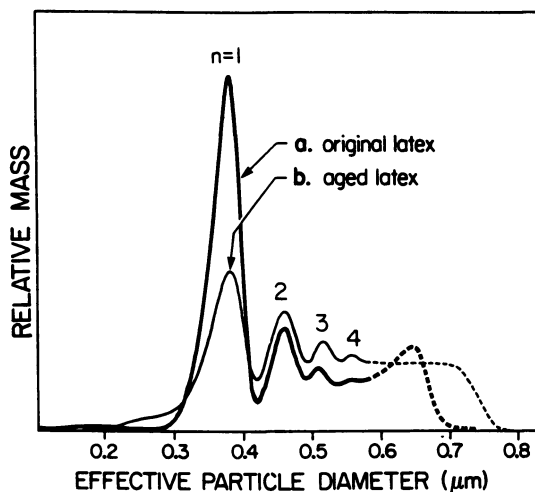


Figure 6. Particle size distributions derived from fractograms of Figure 5. A portion of each size distribution curve indicated by a dashed line has considerable uncertainty due to the interplay of steric exclusion and inversion mechanisms.

particle diameter in the tailing end of the size distribution curves as indicated by the broken lines.

### Conclusions

Because of its high intrinsic resolution, SdFFF is capable of resolving aggregated colloidal clusters from one another based on differences in their mass. The ability to collect fractions of constant (and known) particle mass and to subject them to electron microscopy adds another dimension to the characterization of aggregates.

The flexibility of SdFFF makes it possible to achieve different resolution levels by controlling both carrier flow rate and centrifugal field strength. Using optimized conditions, one can achieve desired level of separation of individual clusters in an aggregated sample.

The SdFFF technique is effective for monitoring from trace up to extensive levels of aggregation occurring in colloidal samples. Some demonstrated applications of this method include the following: (a) finding and measuring the relative content of aggregates in different monodisperse latex samples, (b) studying the breakdown of aggregated species to singlets and lower order aggregates by sonication, (c) tracking the controlled aggregation from monodisperse latex populations induced by the addition of a cationic surfactant, and (d) observing changes of the population of different latex aggregates caused by aging.

### Acknowledgment

This work was supported by U.S. Public Health Service Grant GM10851-33 from the National Institutes of Health.

### Literature Cited

1. Jones, H. K.; Barman, B. N.; Giddings, J. C. *J. Chromatogr.* 1989, **455**, 1-15.
2. Giddings, J. C.; Barman, B. N.; Li, H. *J. Colloid Interface Sci.* 1989, **132**, 554-565.
3. Schure, M. R.; Barman, B. N.; Giddings, J. C. *Anal. Chem.* 1989, **61**, 2735-2743.
4. Giddings, J. C.; Yang, F. J. F.; Myers, M. N. *Anal. Chem.* 1974, **46**, 1917-1924.
5. Lee, S.; Giddings, J. C. *Anal. Chem.* 1988, **60**, 2328-2333.
6. Yang, F. J. F.; Myers, M. N.; Giddings, J. C. *Anal. Chem.* 1974, **46**, 1924-1930.
7. Williams, P. S.; Giddings, J. C. *Anal. Chem.* 1987, **59**, 2038-2044.
8. Yau, W. W.; Kirkland, J. J. *Sep. Sci. Technol.* 1981, **16**, 577-605.
9. Giddings, J. C.; Williams, P. S.; Beckett, R. *Anal. Chem.* 1987, **59**, 28-37.
10. Jones, H. K.; Phelan, K.; Myers, M. N.; Giddings, J. C. *J. Colloid Interface Sci.* 1987, **120**, 140-152.
11. Giddings, J. C. *Anal. Chem.* 1985, **57**, 945-947.
12. Giddings, J. C. *Sep. Sci.* 1973, **8**, 567-575.
13. Myers, M. N.; Giddings, J. C. *Anal. Chem.* 1982, **54**, 2284-2289.
14. Barman, B. N.; Giddings, J. C. *Polym Mater. Sci. Eng.* 1990, **62**, 186-190.

RECEIVED January 14, 1991



## Chapter 15

# Separation and Characterization of 0.01–50- $\mu\text{m}$ Particles Using Flow Field-Flow Fractionation

S. Kim Ratanathanawongs, Inho Lee<sup>1</sup>, and J. Calvin Giddings

Field-Flow Fractionation Research Center, Department of Chemistry,  
University of Utah, Salt Lake City, UT 84112

Flow field-flow fractionation has been used to characterize particles with diameters ranging from 0.01  $\mu\text{m}$  to 50  $\mu\text{m}$ . Two different modes of operation are utilized for this diameter range: the normal mode for the small particle region (0.01  $\mu\text{m}$  to 2 or 3  $\mu\text{m}$ ) and the steric-hyperlayer mode for the large particle domain (0.3  $\mu\text{m}$  and up). Theoretical and experimental results are in good agreement for particle retention in normal mode flow FFF. In the steric-hyperlayer mode, empirical calibration curves are used to relate particle diameters to retention. Examples of flow FFF applications to colloidal silicas, polystyrene latex beads, pollen and spores, and chromatographic silicas are given.

Field-flow fractionation (FFF) is a particle (or polymer) separation and characterization technique that utilizes an external field to induce migration of a suspended (or dissolved) sample in a direction perpendicular to that of flow in a narrow conduit, usually formed between plane parallel bounding walls. Different degrees of retention are achieved depending on the particles' equilibrium distributions in the parabolic flow profile. Some of the common fields that have been employed include sedimentation, thermal, crossflow, and electrical (1-3). The type of field to be used in a particular analysis is selected according to the characteristics of the sample and the information desired.

Flow field-flow fractionation (flow FFF) utilizes a crossflow as the driving force to induce retention and separation. Since this driving force applies to all macromolecules and particles, flow FFF is the most universal of FFF techniques. It has been used to separate and characterize a wide variety of samples including biological, environmental, and industrial materials (see Figure 1). The versatility and range of this technique is evident upon examination of the abscissa of Figure 1. The various samples that have been characterized (to date) by flow FFF span 15 orders of magnitude with respect to particle mass or 5 orders of magnitude with respect to diameter.

Presently, the largest particles that have been separated and characterized in a flow FFF system are polystyrene latex beads with a diameter of 50  $\mu\text{m}$  (4). The

<sup>1</sup>Current address: Chemistry Department, Yonsei University, Seoul, Korea

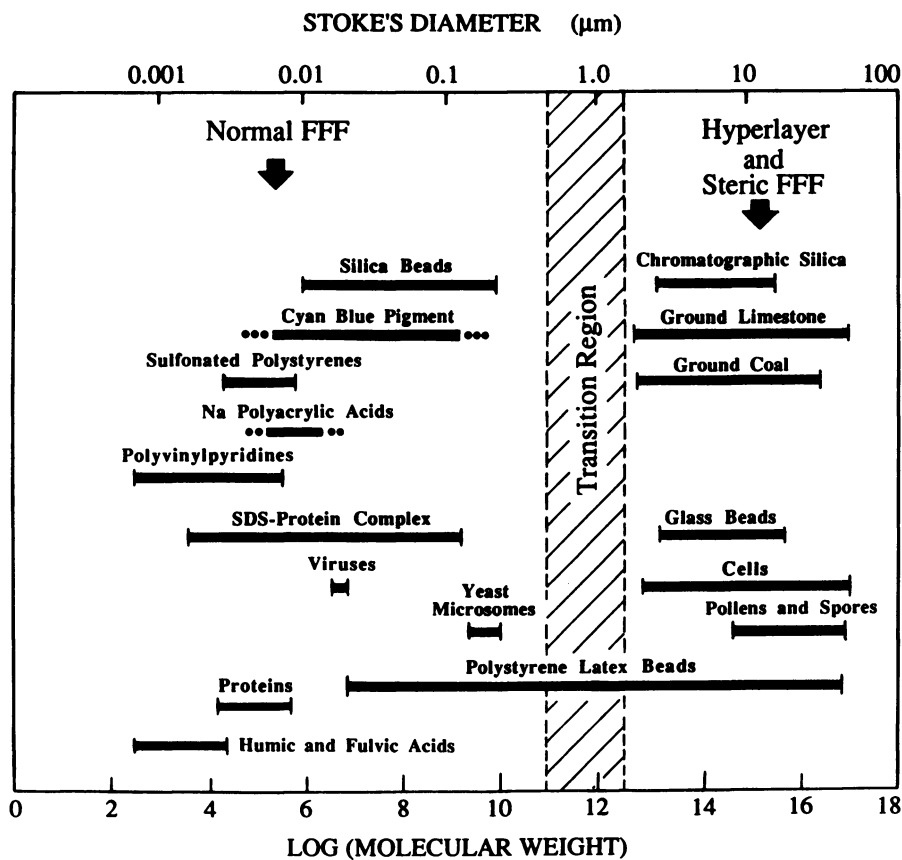


Figure 1. Range of flow FFF applications.

upper limit is determined by the thickness of the FFF channel, which can be arbitrarily increased; particles with diameters up to one-third the channel thickness may be evaluated without undue complications. This extension of the upper size limit has been demonstrated by Liu and Giddings using the earth's gravitational field as the driving force (thus sedimentation FFF) in a 1 mm thick FFF channel (Liu, G.; Giddings, J.C. *Anal. Chem.*, in press). Glass beads with diameters up to 500  $\mu\text{m}$  were successfully separated with retention times the order of minutes.

In flow FFF, components are driven across the channel by the crossflow of the carrier. Thus, in theory, there is no lower diameter/molecular weight limit to the applicability of flow FFF. However, in practice, a limit is established by the pressure build-up in the system due to the necessary use of low molecular weight cut-off membranes and the high cross flowrates needed to counteract the fast diffusion of low molecular weight compounds. The lowest molecular weight application reported to date was carried out by Beckett, Zhang, and Giddings (5) who utilized flow FFF in the characterization of aquatic humic and fulvic acids with molecular weights ranging from 300 to 20,000.

### Theory

The separation mechanisms of three different modes of FFF--normal, steric, and hyperlayer--are shown in Figure 2. The general features include the external cross-flow field applied perpendicular to the axis of separation and the parabolic flow profile that exists in the thin channel bounded by plane parallel porous walls. The parabolic flow profile in the FFF channel is described by

$$v = 6\langle v \rangle \left[ \frac{x}{w} - \left( \frac{x}{w} \right)^2 \right] \quad (1)$$

where  $v$  is the local carrier fluid velocity,  $\langle v \rangle$  is the mean fluid velocity,  $x$  is the distance from the accumulation wall, and  $w$  is the channel thickness. At the center of the channel ( $x = w/2$ ) the flow velocity  $v$  is 3/2 times  $\langle v \rangle$ . Lower flow velocities are found closer to the walls because of frictional drag along the walls;  $v$  approaches zero at the fluid-wall interface. Thus various degrees of retention will be observed depending on the positioning of the particles across the flow velocity profile.

**Normal Mode.** The field-induced migration of particles towards the accumulation wall in normal FFF is counteracted by diffusion (represented by  $D$ ) away from the wall as shown in Figure 2a. The result is the formation of steady-state layers that have an exponential concentration profile. The mean thickness  $\ell$  of each of the component clouds is determined by the ratio of the field-induced velocity  $U$  and the component diffusion coefficient  $D$ . The general FFF expression for the retention

parameter  $\lambda$ ,  $\lambda = \frac{\ell}{w}$ , can be written specifically for flow FFF as (6)

$$\lambda = \frac{D}{Uw} = \frac{DV^0}{\dot{V}_c w^2} \quad (2)$$

where  $V^0$  is the channel void volume and  $\dot{V}_c$  is the cross flowrate. The diffusion coefficient can be calculated from the Stokes-Einstein equation

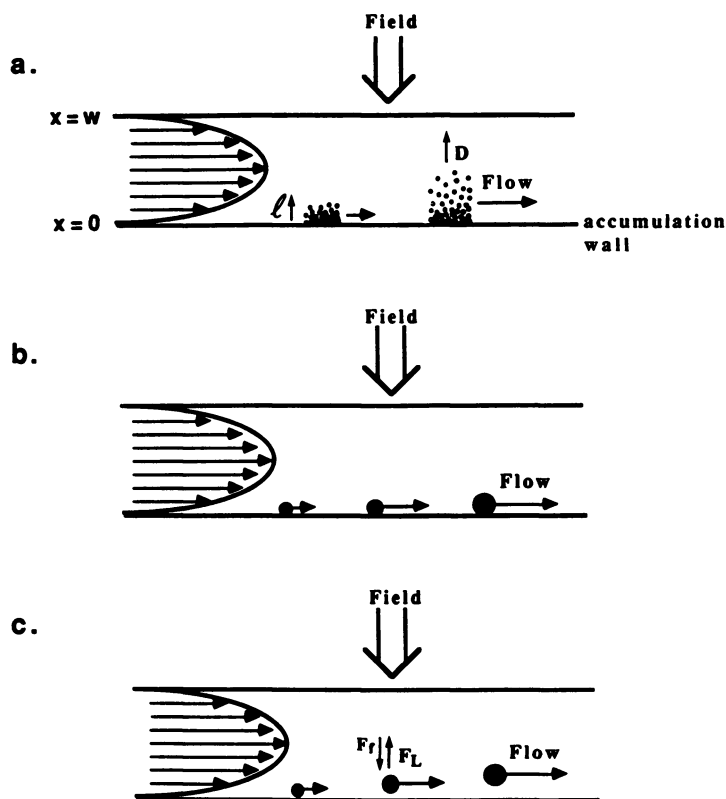


Figure 2. Separation mechanism of a) normal mode, b) steric mode, and c) hyperlayer mode of FFF.

$$D = \frac{kT}{3\pi\eta d} \quad (3)$$

where  $k$  is the Boltzmann constant,  $T$  is the temperature,  $\eta$  is the carrier viscosity, and  $d$  is the particle diameter.

The retention ratio  $R$ , which is equal to the ratio of the void time  $t^0$  to the retention time  $t_r$ , may be expressed in terms of  $\lambda$  by (7)

$$R = \frac{t^0}{t_r} = 6\lambda \left[ \coth\left(\frac{1}{2\lambda}\right) - 2\lambda \right] \quad (4)$$

Depending on the degree of retention, various approximations to Equation 4 can be used to calculate  $R$  (8). The most common is the  $6\lambda$  approximation ( $R = 6\lambda$ ) which is valid at high retentions for which  $\lambda \rightarrow 0$ . Using  $R = 6\lambda$  and the equalities expressed in Equations 2 and 3,  $t_r$  for flow FFF can be written as

$$t_r = \frac{\dot{V}_c w^2 \pi \eta d}{2 \dot{V} k T} \quad (5)$$

Equation 5 predicts a linear dependence of  $t_r$  on  $d$ . Thus small particles will elute prior to large particles. Furthermore, retention times can be decreased by decreasing the cross flowrate and/or increasing the channel flowrate.

**Steric Mode.** As shown in Figure 2b, large particles are driven very close to the accumulation wall by the field such that their centers of mass are approximately one radius away from the wall. (Diffusion away from the wall can be made negligible for particles with diameters greater than  $\sim 1 \mu\text{m}$ .) Differential migration along the separation axis occurs as a result of the different physical sizes and thus different extents of protrusion of the particles into the parabolic flow profile. Specifically, the center of mass of a large particle occupies a faster flowing streamline than that of a small particle. This results in elution of large particles prior to small particles, a reversal of the normal mode elution order.

The retention ratio for the steric mode of operation is given by (9, 10)

$$R = 3\gamma \frac{d}{w} \quad (6)$$

where  $\gamma$  is the dimensionless steric correction factor of order unity. The significance of this factor will be discussed in more detail below.

**Steric-Hyperlayer Mode.** The hyperlayer mode is realized when two opposing forces act on the sample such that each component is driven into a focussed equilibrium layer positioned at some specific distance above the accumulation wall (Figure 2c). The two forces in the present case are the crossflow force  $F_f$  and the hydrodynamic lift forces  $F_L$  (11). The lift forces cause particles to be elevated some finite distance above the accumulation wall. The elution order is the same as that observed in the steric mode but the retention times can be significantly shorter (11, 12) as particles have equilibrium positions in relatively faster flowing streamlines.

Williams, Koch, and Giddings (Williams, P. S.; Koch, T.; Giddings, J. C., *J. Fluid Mech.*, submitted) have empirically determined that the magnitude of the lift

forces increases with shear rate and particle diameter and decreases with increasing particle distance from the wall. The  $\gamma$  factor of Equation 6 is indicative of the magnitude of these lift forces relative to the applied crossflow force, that is,  $\gamma$  increases with  $F_L$  and decreases with  $F_f$ . When  $\gamma < 2$ , the mechanism is considered still to be steric; when  $\gamma \geq 2$ , it is hyperlayer.

The retention theory for steric and hyperlayer FFF is intricately intertwined with hydrodynamic lift forces which have yet to be fully characterized. Since the equilibrium positions of the particle bands cannot be accurately predicted from first principles, empirical calibration curves must be used to determine the diameter distribution of an unknown material.

The calibration process makes use of a plot of  $\log t_r$  versus  $\log d$ , which generally yields a straight line. The slope of the line equals the diameter-based selectivity  $S_d$ , expressed by

$$S_d = \left| \frac{d \log t_r}{d \log d} \right| \quad (7)$$

The parameter  $S_d$  may be thought of as the percentage change in retention time that results from a one percent change in diameter (13).

The calibration plots are obtained by measuring  $t_r$  for standards of different diameters. The diameter of the unknown is calculated from its measured retention time by means of Equation 8

$$\log d = \frac{\log t_r - C}{S_d} \quad (8)$$

where  $C$  is the intercept along the ordinate of the selectivity plot.

Sample polydispersity is measured in terms of the percent coefficient of variation (%C.V.), which is defined as the standard deviation in particle diameter  $\sigma_d$  divided by the mean particle diameter  $\bar{d}$  multiplied by 100. The %C.V. can be related to the peak standard deviation (in units of time)  $\sigma_t$  as shown by Equation 9 (14)

$$\%C.V. = \frac{\sigma_d}{\bar{d}} \times 100 = \frac{\sigma_t}{S_d t_r} \times 100 \quad (9)$$

The underlying assumption in Equation 9 is that the sample polydispersity is the major contributor to the observed band spreading, true in most cases for C.V. > 5%.

It is important to note that the retention mechanisms for all modes of flow FFF is independent of density. Transport of sample components to the accumulation wall occurs via positive displacement by the crossflow carrier. This freedom from density is reflected by the absence of the density term in equations that relate retention times (or ratios) to particle diameters.

**Particle Size Distributions.** The FFF fractogram is converted into a particle size distribution curve by applying a scale correction factor to the detector response. This correction is generally necessary because in most cases there is a nonlinear relationship between particle diameter and retention times (an exception is provided by Equation 5). The particle size distribution  $m(d)$  is expressed as (8, 15)

$$m(d) = c(t_r) \left| \frac{\delta t_r}{\delta d} \right| \quad (10)$$

where  $c(t_r)$  is the concentration of particles in the eluting stream at time  $t_r$  and  $\delta t_r$  is the small change in retention time corresponding to the small change in diameter  $\delta d$ . The ratio  $\delta t_r/\delta d$  reduces to the derivative of  $t_r$  with respect to  $d$ . By specifying the absolute value of  $dt_r/dd$ , we validate the use of Equation 10 for both the normal and steric-hyperlayer modes.

### Experimental

**Apparatus.** A schematic diagram of the flow FFF system is shown in Figure 3. The carrier is pumped down the length of the channel as well as across the channel by two separately controlled pumps. A Spectra-Physics (San Jose, California) Isochrom LC pump is used to drive the axial channel flow and a pulseless syringe pump (built in-house) serves as the crossflow pump. A variable pressure restrictor (Optimization Technologies, Bend, Oregon) is used to balance the channel and cross flowrates by providing a means of adjusting relative back pressures at the two outlets. Depending on the sample characteristics, injection is accomplished via a loop injector (Rheodyne 7010, Cotati, California) or directly on-channel with a syringe. Detection is achieved using a Spectroflow 757 UV-visible detector (Applied Biosystems, Ramsey, New Jersey) set at either 254 nm or 350 nm.

Separation takes place in the FFF channel. The channel system is comprised of a membrane, a spacer, and two Lucite blocks with inset frit panels. The layers, as encountered by the crossflow carrier, are frit, channel, membrane, and frit. The top (depletion) and bottom (accumulation) walls of the channel are defined by the frit and the membrane, respectively. The membrane serves as the accumulation wall and retains sample inside the channel.

Two different membranes were employed to obtain the results presented in this paper, namely, Amicon YM10 (Amicon, Danvers, Massachusetts) and Celgard 2400 (Hoeschst Celanese, Separations Products Division, Charlotte, North Carolina). The spacers from which the channel volumes were cut are made of Mylar and are 127  $\mu\text{m}$  or 254  $\mu\text{m}$  thick. Channel dimensions are 27.2 cm tip-to-tip length and 2 cm breadth.

In the process of a run, sample is injected followed by a momentary stop of the channel flow. This stopflow stage is accomplished by switching valves 1 and 2 ( $V_1$  and  $V_2$  in Figure 3) which routes the longitudinal channel flow around the channel. The relaxation process takes place as the crossflow force induces migration of the sample to the accumulation wall. Separation proceeds when  $V_1$  and  $V_2$  are switched back to their original positions and flow through the channel is resumed.

The stopflow period required in flow FFF is equal to the time ( $V^0/V_c$ ) that it takes for just one column volume to be displaced by the crossflow.

**Reagents and Samples.** The carrier liquid is doubly distilled water containing 0.02 % sodium azide and 0.1 % surfactant. Both FL-70 (Fisher Scientific, Fairlawn, New Jersey) and sodium dodecyl sulfate (SDS) were employed as surfactants.

Polystyrene latex standards varying in size from 0.021  $\mu\text{m}$  to 49.4  $\mu\text{m}$ , along with pollen grains and spores, were purchased from Duke Scientific (Palo Alto, California). The colloidal silica samples characterized are the Ludox series produced by E. I. DuPont & de Nemours (Wilmington, Delaware). The commercially available chromatographic packings examined here were manufactured by various companies as specified in reference 14.

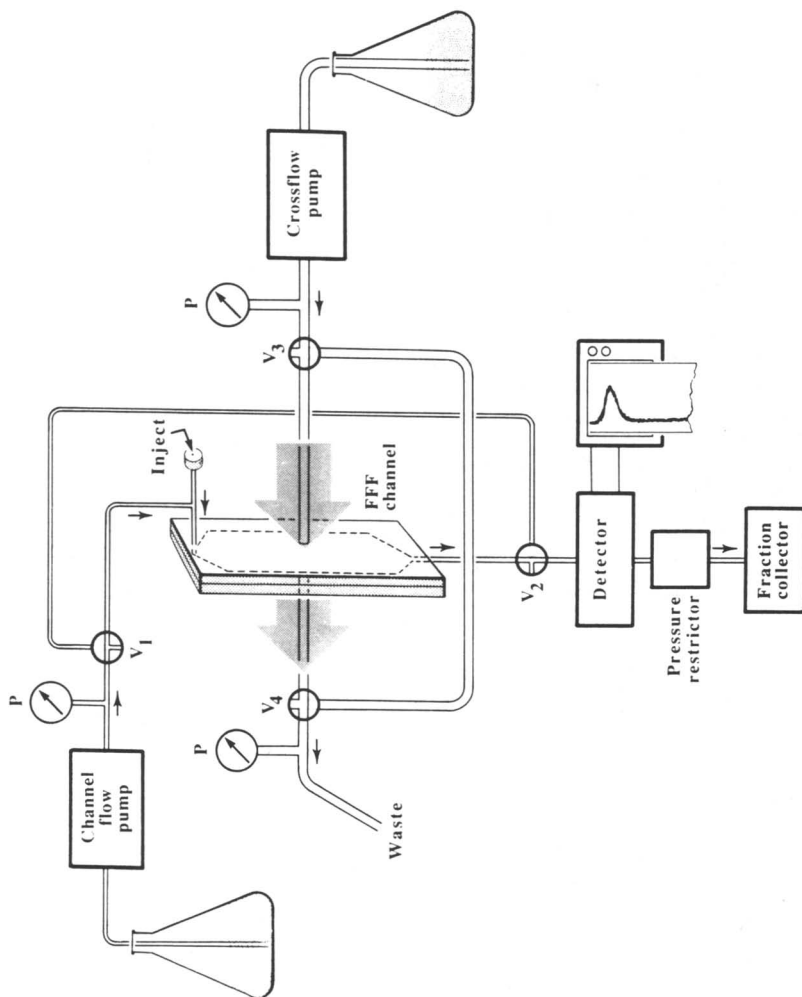


Figure 3. Schematic diagram of a flow FFF system. The terms P and  $V_1$ ,  $V_3$  refer to pressure gauges and valves 1 to 3, respectively. (Reproduced with permission from Ref. 14. Copyright 1989 Elsevier Science Publishers.)



Prior to injection, the sub- and supramicron polystyrene latex standard suspensions were diluted forty and five times, respectively. The Ludox silicas which are available as suspensions were diluted fifty fold. The HPLC silica samples were ~5 mg per mL of carrier and the mixture of pollens and spores consisted of ~2 mg/mL of each component. Injection volumes were 20  $\mu\text{L}$  in all cases.

### Results and Discussion

The particle size range is broken into two parts for discussion. Particles with diameters between 0.01 and about 1  $\mu\text{m}$  (up to 2 or 3  $\mu\text{m}$  in special cases) are subject to the normal operating mode of flow FFF. The steric or hyperlayer mode of flow FFF is generally applicable, depending upon conditions, from 1  $\mu\text{m}$  (down to 0.3  $\mu\text{m}$  in some circumstances) up to 50  $\mu\text{m}$  and beyond.

**Normal Mode.** A study was performed to compare the theoretical and experimental values of retention time  $t_r$  of submicron particles under different flow conditions. The latex particle standards used in this study (injected one at a time) had nominal diameters of 0.021, 0.054, 0.107, 0.155, 0.198, 0.232, 0.272, 0.330, and 0.426  $\mu\text{m}$ . The 127  $\mu\text{m}$  thick channel with the polypropylene membrane was used. The results, illustrated in Figure 4, show good agreement between experimental and theoretical  $t_r$  values, the latter calculated using Equations 2-4. These results suggest that standards are not generally needed in normal mode (submicron) particle characterization since diameters of unknowns may be calculated directly from their retention times.

The influence of channel and cross flowrates are also demonstrated in Figure

4. The retention times decrease as  $\dot{V}$  is increased or when  $\dot{V}_c$  is decreased, as suggested by the simplified form of Equation 5. The slope of the log  $t_r$  versus log  $d$  plots yields the diameter based selectivity which in the normal mode approaches a value of unity (16).

A positive deviation from theory is observed for highly retained (large) particles when  $\dot{V} = 1.03 \text{ mL/min}$  and  $\dot{V}_c = 1.60 \text{ mL/min}$ . The increased retention is probably due to some kind of interaction of the particles with the membrane. These interactions were not apparent when higher channel flowrates were employed, probably because of the counteracting effects of lift forces.

The results shown in Figure 4 were obtained using a polypropylene membrane in a 127  $\mu\text{m}$  thick channel--the thinnest channel reported (up to 1988) for flow FFF. This polypropylene membrane (Celgard 2400) possesses a number of desirable characteristics for flow FFF, such as thinness (25  $\mu\text{m}$ ) and flatness, that make possible the fabrication of thin high-performance channels. Unlike the ultrafiltration membranes (e.g., Amicon YM10) that have been used in other studies, this microporous membrane does not appear to be compressed when clamped in a flow FFF system. The channel thickness can therefore be assumed to be uniform, equal in value to the spacer thickness. Accordingly, the geometric void volume can be used in calculations of theoretical  $t_r$  values. The resulting good agreement between experimental and theoretical  $t_r$  values under the different flowrate conditions confirms the effectiveness of the thin channel configuration using a polypropylene membrane.

The fractionation of 0.054  $\mu\text{m}$ , 0.155  $\mu\text{m}$ , 0.232  $\mu\text{m}$ , and 0.330  $\mu\text{m}$  polystyrene latex beads shown in Figure 5 illustrates the high speed and resolving power of the thin flow FFF channel for submicron particles. The flowrates for this run were

$\dot{V} = 4.29 \text{ mL/min}$  and  $\dot{V}_c = 1.49 \text{ mL/min}$ . Baseline separation is achieved in 16 minutes; an additional 0.5 minutes is utilized for stopflow. The analysis time could be decreased further but only at the expense of resolution. (The system transient

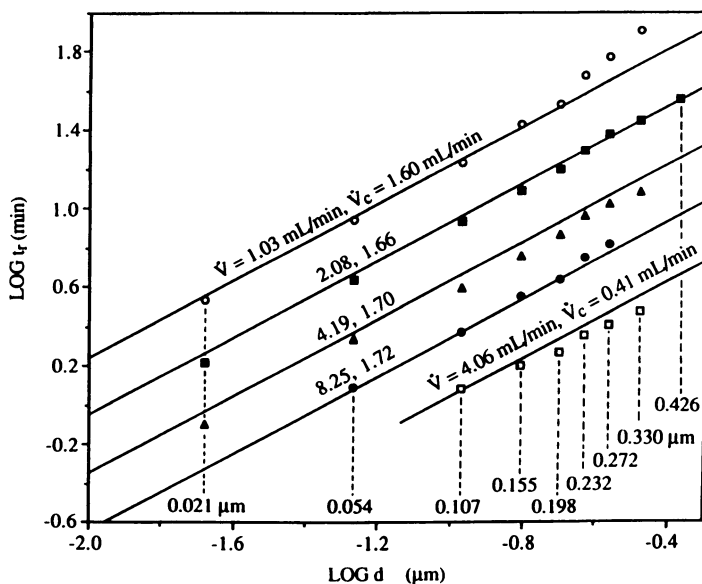


Figure 4. Comparison of theoretical and experimental retention time in normal mode flow FFF for nine submicron latex diameters at different channel flowrates  $\dot{V}$  and cross flowrates  $\dot{V}_c$ . System: spacer thickness = 127  $\mu\text{m}$ ; polypropylene membrane; carrier is 0.1% SDS, 0.02%  $\text{NaN}_3$ .

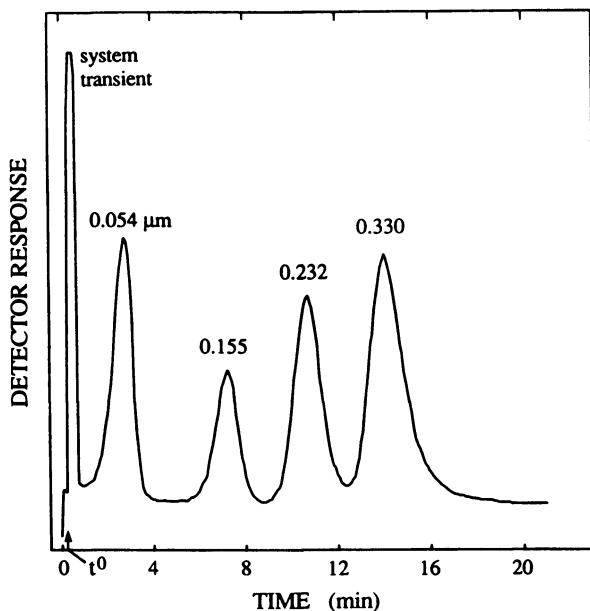


Figure 5. Normal mode separation of submicron polystyrene latex beads. System: same as that described in Figure 4 caption.

shown in the figure, caused by an abrupt change in the flowrate as the carrier flow through the channel is resumed at the end of the stopflow period, does not interfere with separation.)

Flow FFF was used in another set of experiments to characterize a series of Ludox colloidal silicas with (nominal) particle diameters ranging from 0.007  $\mu\text{m}$  (7 nm) to 0.022  $\mu\text{m}$  (22 nm). The 254  $\mu\text{m}$  thick spacer with the YM10 membrane was utilized for these materials. This membrane was selected for this particular application (rather than the polypropylene membrane) on the basis of pore size. The YM10 membrane has a molecular weight cutoff of 10,000 while the Celgard 2400 membrane has pore dimensions of 50 nm x 125 nm. Due to the compressibility of the YM10 membrane, the actual channel thickness was 230  $\mu\text{m}$  (calculated using PS standards).

The fractograms are shown in Figure 6. Experimental conditions were  $\dot{V} = 5.67$  mL/min and  $\dot{V}_c = 1.70$  mL/min. Under these conditions, the total run time (including a 1 min stopflow period) was less than 5 minutes per sample. The dissimilarity among the fractograms reflects the variation in the size distribution among samples.

As discussed in the Theory section (see Equation 10), the FFF fractograms are converted to particle size distribution curves by multiplying the measured concentration (assumed proportional to the detector response) at different times  $t_r$  by the factor  $1/dt_r/ddl$ . The resulting size distribution curves are shown in Figure 7. The mean particle diameters, uncorrected for light scattering (thus turbidimetric averages), are shown as  $d_{FFF}$  in Table I. These values are compared with those listed on DuPont's data sheet ( $d_{nom}$ ) and those obtained by Giddings, Lin, and Myers (17) through personal communications with J.J. Kirkland ( $d_{ref}$ ). The  $d_{FFF}$  values are in good agreement with those obtained from the sources noted above. The  $d_{ref}$  results were obtained using transmission electron microscopy.

Table I. Summary of Ludox Colloidal Silica Diameters

Type	$d_{nom}$ (nm)	$d_{ref}$ (nm)	$d_{FFF}$ (nm)	%C.V. <sub>FFF</sub>
AS-40	22	-	29	8.9
HS-40	12	10 - 20	15	18
		(few 40)		
HS-30	12	10 - 20	15	18
		(few 40)		
TM	22	10 - 50	23	16
SM	7	8-20	11	20
		(mostly 10 - 14)		

**Steric-Hyperlayer.** An example of the separation capability of flow FFF in the steric-hyperlayer (mainly hyperlayer) mode is shown in Figure 8. Here the 254  $\mu\text{m}$  thick channel with the YM10 membrane was used to separate polystyrene latex standards with nominal diameters of 49.4 (49)  $\mu\text{m}$ , 41.9 (42)  $\mu\text{m}$ , 29.4 (29)  $\mu\text{m}$ , 19.58 (20)  $\mu\text{m}$ , 15.00 (15)  $\mu\text{m}$ , 9.87 (10)  $\mu\text{m}$ , and 7.04 (7)  $\mu\text{m}$  in less than 6 minutes. Very rapid separations are commonly achieved in this mode of operation. The flow

conditions were  $\dot{V} = 3.93$  mL/min and  $\dot{V}_c = 3.33$  mL/min.

In order to work with unknown particle populations (see below), calibration plots must be established. For this purpose the retention time of each standard is

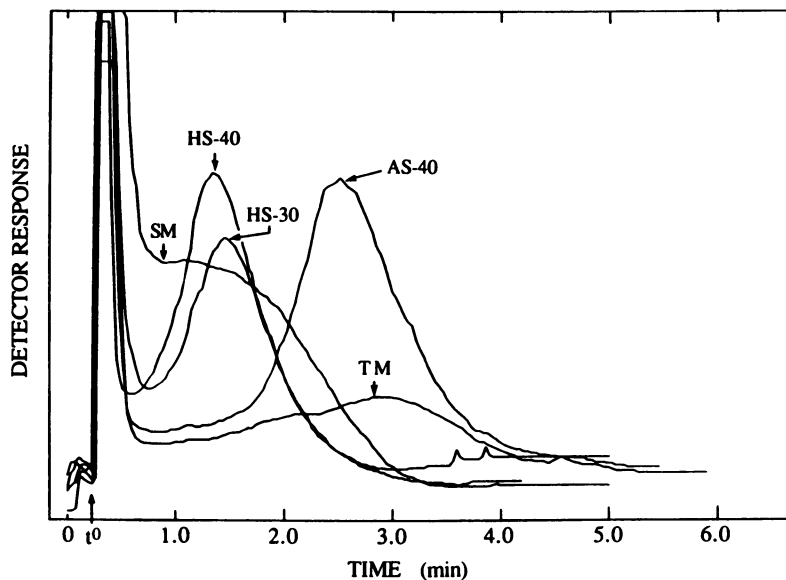


Figure 6. Fractograms of Ludox colloidal silicas. System: spacer thickness = 254  $\mu\text{m}$ ; Amicon YM10 membrane; carrier is 0.1% FL-70, 0.02%  $\text{NaN}_3$ .

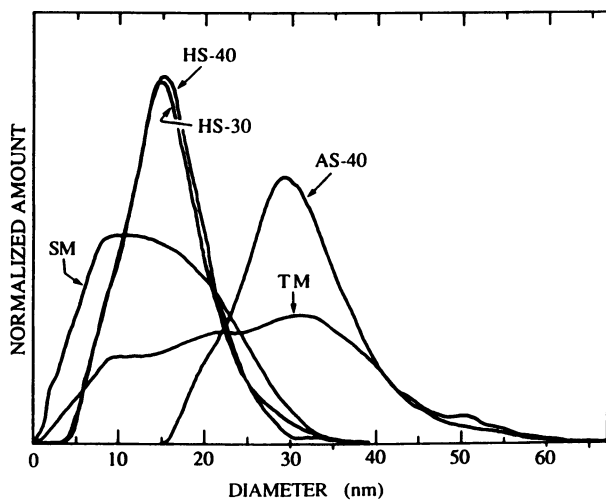


Figure 7. Particle size distribution curves of Ludox colloidal silicas (corresponds to fractograms shown in Figure 6).

measured and  $\log t_r$  is plotted against  $\log d$ . The slope of the line through these points yield the diameter-based selectivity  $S_d$ . For the steric-hyperlayer mode of flow FFF,  $S_d$  is generally greater than unity (4).

Figure 9 illustrates the resolving power and speed of analysis of flow/hyperlayer FFF applied to the separation of (a) paper mulberry pollen and (b) Johnson grass smut spores. Using a channel flowrate of 6.32 mL/min and a cross flowrate of 3.32 mL/min, the total analysis time is less than 2 min (including 0.7 min stopflow time). Superimposed on the sample fractogram is a fractogram of polystyrene standards, from which an  $S_d$  value is calculated. Using this  $S_d$  value (1.16) and the measured retention times of the paper mulberry pollen and the grass spores, the diameters of these two components were calculated via Equation 8 to be 14.6  $\mu\text{m}$  and 8.3  $\mu\text{m}$ , respectively. This is in good agreement with the supplier's values of 10.9–14.4  $\mu\text{m}$  for the paper mulberry pollen and  $7.4 \pm 0.8 \mu\text{m}$  for the grass spores.

Commercially available high performance liquid chromatography silica packing materials have been surveyed and their nominal diameters compared to those calculated from FFF retention measurements using the above noted calibration plots (14). Fractograms obtained using a 254  $\mu\text{m}$  thick spacer and a YM10 membrane are shown for spherical packings in Figure 10a and irregular packings in Figure 10b.

The experimental conditions were  $\dot{V} = 7.75 \text{ mL/min}$  and  $\dot{V}_c = 1.58 \text{ mL/min}$ . The letters beside each fractogram can be cross referenced to the trade names of the support materials in Table II. Both the spherical and irregular 5  $\mu\text{m}$  materials eluted within 1 min while the spherical 3  $\mu\text{m}$  particles required 1.7 min.

The mean particle diameter  $\bar{d}$  and the polydispersity of each chromatographic silica sample are reported in Table II. The FFF results for  $\bar{d}$  were calculated using the  $t_r$  value corresponding to the first moment of the peak (center of mass) rather than the  $t_r$  value at the maximum peak height. The resulting  $\bar{d}$  was compared to that obtained by scanning electron microscopy (SEM). The SEM values are number averages of at least 200 measurements each. The agreement between the FFF and SEM diameters is within 3%. The  $S_d$  value used in the FFF polydispersity calculations (Equation 9) is 1.05.

Particle size distribution curves corresponding to fractograms of silicas shown in Figure 10 were obtained as described in the Theory section. These distribution curves are shown in Figure 11. It should be noted that these results have not been corrected for light scattering in the detector and that these corrections are not highly significant in this size range. Without correction, the distributions and mean diameters are weighted by surface area.

The upper abscissa scale of Figure 10 is the diameter scale determined using polystyrene standards. The independence of the crossflow driving force on particle density allows the use of calibration standards having different densities from those of the samples. In addition, the resulting size distribution, unlike that obtained from sedimentation FFF, is free of the requirement to know the density. This characteristic is of particular importance in applications involving materials (such as chromatographic silica) that may have a porosity and thus a density distribution as well as a particle size distribution.

## Conclusions

The applicability of flow FFF to the separation and characterization of particles over a wide diameter range has been demonstrated. The good agreement between theoretical and experimental results in the normal mode validates the use of current FFF theory in

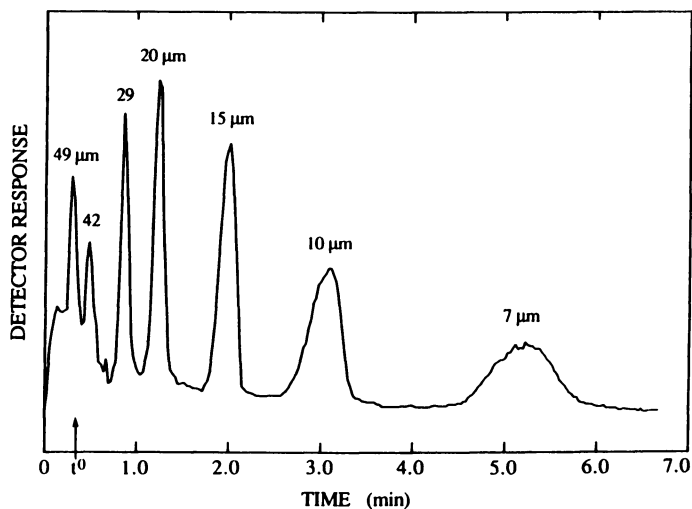


Figure 8. Separation of polystyrene latex standards of indicated diameters using flow/hyperlayer FFF. System: same as that described in Figure 6 caption.

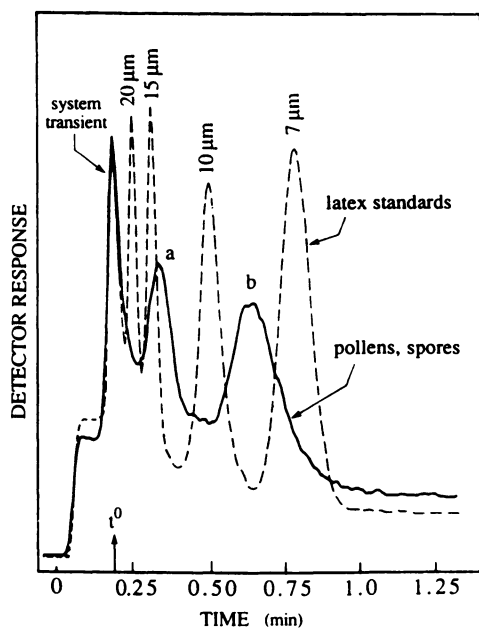


Figure 9. Separation of pollen and spores and of latex standards. a) paper mulberry pollen and b) Johnson grass smut spores. System: same as that described in Figure 6 caption.

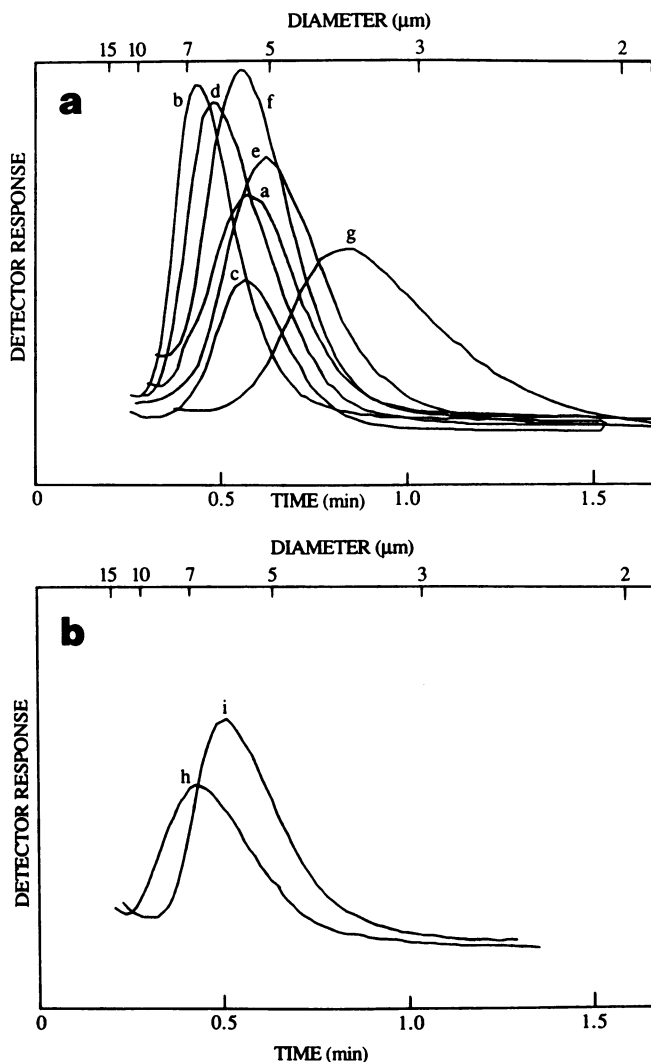


Figure 10. Fractograms of commercially available chromatographic silicas a) spherical 3  $\mu\text{m}$  and 5  $\mu\text{m}$  and b) irregular 5  $\mu\text{m}$ . (Reproduced with permission from Ref. 14. Copyright 1989 Elsevier Science Publishers.)

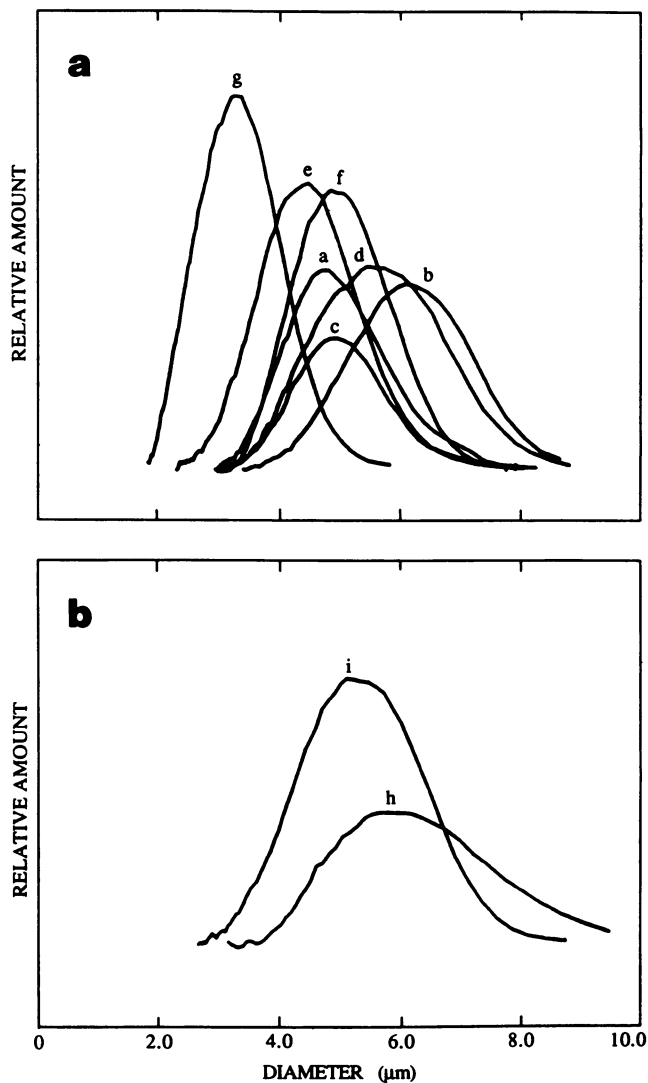


Figure 11. Particle size distribution curves of chromatographic silicas (corresponds to the fractograms shown in Figure 10). a) spherical 3  $\mu\text{m}$  and 5  $\mu\text{m}$  and b) irregular 5  $\mu\text{m}$ .



Table II. Summary of the Mean Retention Times, Diameters, and Polydispersities (C.V.) of Various Chromatographic Silicas

	$t_r$ (s)	dFFF	dSEM	%C.V.FFF
<i>nominal 5 <math>\mu\text{m}</math> spherical particles</i>				
a. Spherex	38.0	4.78	4.72	17.2
b. Hypersil	30.2	5.97	6.11	16.6
c. Nucleosil	36.3	5.00	5.15	15.3
d. IB-Sil	32.9	5.42	5.54	18.4
e. W-Porex	42.3	4.31	4.26	20.0
f. Spherisorb	36.9	4.87	4.94	15.1
<i>nominal 3 <math>\mu\text{m}</math> spherical particles</i>				
g. Hypersil	59.0	3.19	3.29	20.5
<i>nominal 5 <math>\mu\text{m}</math> irregularly shaped particles</i>				
h. Partisil	30.7	5.97	-	21.3
i. Lichrosorb	35.9	5.10	-	19.4

SOURCE: Reproduced with permission from Ref. 14. Copyright 1989 Elsevier Science Publishers.

the calculation of submicron diameters from the retention time. Analysis times are relatively short, particularly for the steric-hyperlayer mode where two and three minute experiments are common. The density independence of the crossflow force allows for the rapid and accurate characterization of porous materials.

### Acknowledgements

The authors wish to acknowledge Troy Holly for writing the software used in determining particle size distributions and Dr. P. Stephen Williams for many helpful discussions.

This work was supported by National Science Foundation Grant CHE-8800675.

### Legend of Symbols

C	ordinate intercept of selectivity plot
d	particle diameter
D	diffusion coefficient
k	Boltzmann constant
$\ell$	mean layer thickness
R	retention ratio
S <sub>d</sub>	diameter based selectivity
$t^0$	void time
$t_r$	retention time
T	temperature
U	field-induced velocity
v	local fluid velocity
$\langle v \rangle$	mean fluid velocity

$V^0$	channel void volume
$\dot{V}$	channel flowrate
$\dot{V}_c$	cross flowrate
$w$	channel thickness
$\gamma$	steric correction factor
$\lambda$	retention parameter
$\eta$	carrier viscosity

### Literature Cited

1. Giddings, J. C. Chem. & Eng. News 1988, **66**, 34.
2. Caldwell, K. Anal. Chem. 1988, **60**, 959A.
3. Kesner, L. F.; Giddings, J. C. In High Performance Liquid Chromatography; Brown, P. R.; Hartwick, R. A., Eds.; John Wiley & Sons: New York, 1989; Chapter 15.
4. Giddings, J. C.; Chen, X., Wahlund, K.-G; Myers, M. N. Anal. Chem. 1987, **59**, 1957.
5. Beckett, R.; Jue, Z.; Giddings, J. C. Environ. Sci. Technol. 1987, **21**, 289.
6. Wahlund, K.-G.; Winegarner, H. S.; Caldwell, K. D.; Giddings, J. C. Anal. Chem. 1986, **58**, 573.
7. Giddings, J. C.; Yang, F. J., Myers, M. N. Anal. Chem. 1976, **48**, 1126.
8. Giddings, J. C.; Caldwell, K. D. In Physical Methods of Chemistry, Vol. IIIB; Rossiter, B. W.; Hamilton, J. F., Eds.; John Wiley & Sons: New York, 1989; Chapter 8.
9. Koch, T.; Giddings, J. C. Anal. Chem. 1986, **58**, 994.
10. Peterson, R. E., II; Myers, M. N.; Giddings, J. C. Sep. Sci. Technol. 1984, **19**, 307.
11. Caldwell, K. D.; Nguyen, T. T.; Myers, M. N.; Giddings, J. C. Sep. Sci. Technol. 1979, **14**, 935.
12. Giddings, J. C.; Myers, M. N., Caldwell, K. D.; Pav, J. W. J. Chromatogr. 1979, **185**, 261.
13. Myers, M. N.; Giddings, J. C. Anal. Chem. 1982, **54**, 2284.
14. Ratanathanawongs, S. K.; Giddings, J. C. J. Chromatogr. 1989, **467**, 341.
15. Yang, F.-S.; Caldwell, K. D.; Giddings, J. C. J. Colloid Interface Sci. 1983, **92**, 81.
16. Giddings, J. C.; Caldwell, K. D.; Jones, H. K. In Particle Size Distribution: Assessment and Characterization, T. Provder, Ed.; ACS Symposium Series No. 332; American Chemical Society: Washington, D.C., 1987; Chapter 15.
17. Giddings, J. C.; Lin, G. C.; Myers, M. N. J. Colloid Interface Sci. 1978, **65**, 67.

RECEIVED January 14, 1991

## Chapter 16

# Size Analysis of a Block Copolymer-Coated Polystyrene Latex

Jenqthun Li<sup>1</sup>, Karin D. Caldwell<sup>1,3</sup>, and Julia S. Tan<sup>2</sup>

<sup>1</sup>Center for Biopolymers at Interfaces, Department of Bioengineering,  
University of Utah, Salt Lake City, UT 84112

<sup>2</sup>Life Sciences Research Laboratories, Eastman Kodak Company,  
Rochester, NY 14650

A PEO-PPO-PEO triblock surfactant of type F108 (MW 14,600, the ratio of PEO/PPO/PEO is 129/56/129) has been adsorbed to two polystyrene standard particles with diameters of 272 nm and 69 nm respectively; the complex is found to be stable in several different media, including physiological saline containing 0.8% human serum albumin. The thickness of the ad-layer is determined by PCS after isolation of the monomer fraction of the coated particles by sedimentation FFF, or by flow FFF. Differences in layer thickness are found for the two particles, with the smaller particles showing a thinner coating. A direct PCS evaluation of the composite size without prior fractionation gives values which are larger than those measured on the monomer fraction, a fact explained by the presence of aggregates identified through the fractionation process and subsequently by SEM. SedFFF is found to permit quantification of the amount of surfactant adsorbed to each particle; these amounts are in good agreement with adsorption and quantification studies using radio-isotope labelled surfactant.

In recent years, the use of colloidal systems as vehicles for drug delivery has received much attention. It is particularly the slow release of drug from such carriers, and the possibility to attach specific targeting moieties such as antibodies with a desired tissue affinity to these particles that is responsible for the attention. The ability of a colloidal carrier to reach its target before being cleared from the system depends primarily on its size; while particles in the 100-200 nm range are small enough to escape from the vascular system, larger particles are confined within this system and eventually end up in the liver or spleen. From recent studies of the systemic distribution of colloids, however, it is becoming clear that not only size, but also surface composition has a strong effect on this distribution. For example, Illum et al. (1,2) have shown that surfactant Pluronic F108 are only to a minor degree trapped in the

<sup>3</sup>Corresponding author

American Chemical Society  
Library

© 1991 American Chemical Society

1155 16th St., N.W.

Washington, D.C. 20036

In Particle Size Distribution II: Proceedings, T.;

ACS Symposium Series; American Chemical Society: Washington, DC, 1991.

liver, the major portion being found elsewhere in the carcass. Accumulation in the liver is the final result of a process that begins with the sequential adsorption of an array of plasma proteins to the particle. The suppression of protein adsorption by different surface treatments is therefore a major goal in current research on targeted drug delivery.

Numerous research groups have shown that surfaces coated with polyethyleneoxide (PEO), in either grafted or adsorbed form, are significantly less prone to protein adsorption than their untreated counterparts (3-5). The effect is thought to be the result of steric exclusion and is strongly correlated with the chain length of the polymer. Just as a repulsion of protein is accomplished by the dynamics of the PEO chains in the surface coating, the steric exclusion effect is also responsible for reducing inter-particle attraction and suppressing aggregation.

Because of its importance in colloid stabilization, the steric exclusion effect created by adsorption of polymeric surfactants onto particles of different surface composition has been studied extensively. Aside from surface densities of adsorbed polymer, and stabilities of the adsorption complex upon changes in composition of the suspension medium, the parameter most frequently studied is the thickness of the adsorbed layer. Since, for a given molecular weight, this thickness bears an inverse relationship to the mobility of the polymer chains ( $\xi$ ), it may constitute a measure of the stabilizing effect of the coating. If so, one may question whether the layer thickness is the same regardless of substrate geometry or whether the different curvatures presented by core particles of different diameters in any way affect the thickness of the coating.

On particulate surfaces, coating thicknesses are frequently analyzed by photon correlation spectroscopy (PCS). As long as dust contamination can be minimized, this technique offers a rapid and convenient way of determining the Z-average of particle diameters present in a suspension, and the thickness of an adsorbed layer can, in principle, be determined from the size difference between coated and uncoated particles. For monodisperse populations, the PCS technique reproducibly yields diameters in good agreement with values from other well accepted methods, such as analytical ultracentrifugation ( $Z$ ), and electron microscopy ( $\mu$ ). However, for polydisperse samples of unknown distribution the technique is less well suited as a characterization tool, as it only provides values for the average diameter together with a polydispersity index. This index is derived by assuming the recorded autocorrelation function to be the sum of the several specific exponential functions, generated by each size present in the population and weighted by the concentration of particles of this size. The second moment of this fitted distribution is then reported as the polydispersity index for the distribution. Since larger particles scatter light more strongly than fines, even minor contaminations of particles larger than the average tend to shift the average size toward larger values without noticeably affecting the measured polydispersity.

Several comparative studies of polymer coatings on particles and on flat surfaces indicate a lack of agreement between coating thicknesses determined by PCS, on the one hand, and by ultracentrifugation, ellipsometry, and neutron scattering, on the other (2). Various geometrical correction factors are applied to the non-PCS measurements to bring them into conformity with the PCS data, often with less than satisfactory result (10).

In order to develop a better understanding of the question of polymer conformation on the surface of colloidal particles, we have

used two forms of the field-flow fractionation (FFF) technique, namely the subtechniques of sedimentation and flow FFF, to fractionate adsorbates into cuts of uniform particle size. Due to the uniformity of these cuts, PCS could be expected to give reliable information about the size of particles in each cut. For particles fractionated by flow FFF the retention volume is a direct measure of particle size, and the combination of FFF and PCS therefore yields two independent measurements of particle size.

Although the size selectivity of the sedimentation FFF technique is higher than that of the flow analogue and separations by this method produces highly uniform fractions, the interpretation of retention data in terms of particle diameter is complicated by the required input of an exact value for the particle density. While this poses no problems for uncoated particles whose composition is uniform throughout, it is impossible to implement for coated particles where the coating density differs from that of the core. Since the composite density depends on the unknown degree of solvation of the adsorbed layer, the size of a composite particle can not be determined from sedFFF retention data, although it is readily measured on collected sedFFF fractions using PCS. While the thickness of an adsorbed layer eludes measurement by this technique, the present study explores the possibility of determining the amount of polymer adsorbed to the surface. As will be shown below, this can be done provided the density of the unsolvated polymer is known.

The fractionation of coated particles ideally takes place in a carrier free of soluble surfactant. In order for the recorded diameter values to be meaningful, one must make sure that the coating is stably adsorbed so that no desorption of polymer takes place during the sizing process. Since an additional interest of ours is to better understand the protein resistance given a polymeric surface upon treatment with PEO-containing surfactants, we have also examined the stability of the coating in a protein environment.

## Experimental

### Sizing Methods. Sedimentation Field-Flow Fractionation (sedFFF).

Under the influence of an applied centrifugal field, a particulate sample is transported by a flowing carrier through the thin FFF channel with a velocity which directly reflects its buoyant mass. The relationship between the sample characteristics mass and density, and the resultant migration velocity has been described in detail by Giddings and others (11-13). For all FFF techniques operating in the "normal" mode (14), a sample's retention ratio  $R$  is exactly related to the thickness  $l$  of the layer that forms as the field concentrates the sample particles near the accumulation wall.

$$\frac{V_{\text{zone}}}{\langle V \rangle} = R = \frac{6l}{w} \left\{ \coth\left(\frac{w}{2l}\right) - \frac{2l}{w} \right\} \quad (1)$$

Here,  $V_{\text{zone}}$  is the average migration rate of a given particle type,  $\langle V \rangle$  is the average carrier velocity, and  $w$  is the thickness of the channel. For convenience, the dimensionless relative layer thickness  $l/w$ , which is characteristic of each particle type, is given the symbol  $\lambda$ . Each subtechnique of FFF is associated with a specific relationship between parameter  $\lambda$ , on the one hand, and the product of field strength and sample characteristics on the other; in the case of sedFFF, these characteristics are mass  $m$  and density  $\rho_p$ , as noted above

$$\lambda = \frac{kT}{m(\Delta\rho/\rho_p)Gw} \quad (2)$$

In this equation,  $kT$  has the usual meaning of Boltzmann constant and temperature,  $\Delta\rho$  symbolizes the difference in density between particle and carrier, and  $G$  is the centrifugal acceleration. For spherical particles of uniform density, the mass  $m$  in Equation 2 may be expressed as the product of volume and density. Under such circumstances,  $\lambda$  is a simple function of particle size  $d$

$$\lambda = \frac{6kT}{d^3 \pi \Delta\rho Gw} \quad (3)$$

Equation 3 applies only to particles of uniform density or to composite particles whose overall density is exactly known. This is not the case for adsorption complexes, where a core particle of known size and density is covered by a solvated ad-layer of unknown thickness and density. However, if the density of the unsolvated coating is known, the measured  $\lambda$ -value can be used to calculate the dry mass of the coating, as seen from a rearrangement of Equation 2 in which total mass  $m$  is replaced by the sum of masses for the core ( $m_1$ ), the unsolvated coat ( $m_2$ ), and the mass of bound solvent ( $m_3$ ), and the particle density is expressed as total mass divided by total volume  $V$ , in turn calculated from masses  $m_1$ ,  $m_2$ , and  $m_3$ , and densities  $\rho_1$ ,  $\rho_2$  and  $\rho$ , respectively. By writing the buoyant mass as  $(m - V\rho)$ , i.e. the difference between the total mass and the mass of displaced suspension medium, and expressing  $V$  as  $[(m_1/\rho_1) + (m_2/\rho_2) + (m_3/\rho)]$ , one arrives at the following relationship:

$$\frac{kT}{\lambda Gw} = (m_1 + m_2) - \rho \{ (m_1/\rho_1) + (m_2/\rho_2) \} \quad (4)$$

where  $\rho$  symbolizes carrier density.

The sedimentation FFF unit used in this work was built in house, essentially according to (15). The nominal dimensions of the flow channel are  $96.0 \times 2.0 \times 0.0254$  cm<sup>3</sup>, and the measured void volume  $V^0$  of this unit is 4.76 mL. The emergence of particles from the separator was monitored by a Linear UV detector with a 254 nm light source. Experimental retention ratios  $R$  were computed in the usual way as ratios of  $V^0$  and elution volumes  $V_e$ . All analyses were performed under a field of 173 gravities (1000 rpm) and a channel flow of 2.7 mL/min. Samples of 5  $\mu$ L volume were injected directly onto the channel and relaxed at zero flow for 15 min.

*Flow Field-Flow Fractionation (flow FFF)*. This subtechnique accomplishes retention and selectivity by allowing a flow of carrier across the semi-permeable walls of the channel to concentrate the sample particles in thin layers near one of the walls. The longitudinal carrier velocity, which is typically around two orders of magnitude higher than that of the cross-flow, performs the transport of particles from inlet to outlet at relative rates which are determined by the thickness of each particle layer. As in the case of sedFFF, Equation 1 above relates an observed retention ratio  $R$  to its corresponding  $\lambda$ -value, i.e. to the dimensionless thickness of the sample layer. However, in contrast to sedFFF, retention in flow FFF is a function of a single particle characteristic, namely the diffusivity (16).

$$\lambda = \frac{DV^{\circ}}{V_w^2} = \left( \frac{kTV^{\circ}}{3\pi\eta V_w^2} \right) \frac{1}{d} \quad (5)$$

The "field strength" in this case is the rate of cross-flow,  $V$ ; the column void volume is  $V^{\circ}$  and  $D$  is the sample's diffusion coefficient. In the right hand formulation, the Stokes-Einstein equation is used to express  $D$  in terms of the carrier viscosity  $\eta$  and the hydrodynamic diameter  $d$  of the sample particle

$$D = \frac{kT}{3\pi\eta d} \quad (6)$$

A comparison of Equations 3 and 5 reveals that sedFFF, where  $\lambda$  varies with  $d^{-3}$ , is more selective to samples of different sizes than its flow counterpart for which  $\lambda$  is proportional to  $d^{-1}$ . The absence of any influence on retention by a second sample characteristic, e.g. density, and the significantly larger separation range (typically 1-1000 nm for flow FFF as compared to 100-1000 nm for sedFFF) makes the flow analogue an attractive complement to the sedimentation subtechnique.

The flow FFF instrument used in this study was purchased from FFFractionation; the dimensions of its flow channel are 27.6 X 2.0 X 0.0254 cm<sup>3</sup>, and its measured void volume is 1.17 mL. Samples of 5  $\mu$ L were injected and relaxed at zero axial flow for a time period sufficient to let 1.5 void volumes of cross flow pass through the channel. As in the sedFFF experiment, the effluent from the flow FFF channel was monitored by UV detection (Linear) at 254 nm.

**Photon Correlation Spectroscopy (PCS).** Light from a monochromatic source which impinges on a particulate suspension is scattered to varying degrees in all different directions. The scattered light from neighboring particles will interfere constructively or destructively depending upon the wavelength of this light, the observation angle and the distance between particles. This distance is not constant, but varies in time as a result of Brownian motion; by mapping the time course of registered intensity fluctuations through the use of an autocorrelator one can establish an average diffusivity for the sample. As in the case of flow FFF above, the Stokes-Einstein equation can then be used to convert values for the diffusivity  $D$  into corresponding values for the diameter  $d$  (17).

The autocorrelator assembles a correlation function  $G(\tau)$  from pairs of measurements of scattered photons, recorded at times  $t_0$  and  $t_0 + t$ . For samples of uniform size and composition, the autocorrelation function is given by

$$G(\tau) = 1 + \beta \exp(-\Gamma\tau) \quad (7)$$

where  $\Gamma$  is the shorthand notation for the product of the sample's diffusion coefficient  $D$  and the factor  $(4\pi n \sin(\theta/2)/\lambda')^2$ , whose value depends on the refractive index  $n$  of the suspension medium, the observation angle  $\theta$ , and the wavelength  $\lambda'$  of the incident light. Factor  $\beta$  in Equation 7 is a system specific constant. From the diffusion coefficient  $D$  one calculates a hydrodynamic diameter  $d$  for the sample using the Stokes-Einstein relationship (Equation 6).

In this work, PCS sizing was performed using either the fixed angle (90-degree) BI-90, or the multiangle BI-2030AT particle sizers

from Brookhaven Instruments. All liquids used for sample dilution were previously passed through a Millipore filter with a 200 nm pore size.

**Other Methods. Scanning Electron Microscopy.** Fractions from sedFFF and flow FFF were collected on Nucleopore filters with pore sizes of either 200 nm or 100 nm. After air drying, these filters were cut to size, mounted on stubs, and sputter coated with gold. Specimens treated in this way were then subjected to electron microscopy using a JEOL model JFM 35 scanning electron microscope.

**Measurements of Surfactant Adsorption and Leakage.** The PEO side-arms of the Pluronic F108 surfactant were radioisotope labelled with  $^{125}\text{I}$  using a method to be described in detail elsewhere (Li, J.; Lin, J.; Caldwell, K.D. Manuscript is in preparation). Following adsorption of labelled surfactant from a 4% F108 solution, which is well into the plateau region of the adsorption isotherm (3), the coated polystyrene spheres were pelleted in a Fisher Microcentrifuge, model 235A, and the supernatant was removed. After resuspension in phosphate buffered saline (PBS, 0.15M, pH 7.4) the particles were again centrifuged and the supernatant collected for measurement of its radioactivity using a Beckman 170M Radiocounter. These washing cycles were repeated until no radioactivity was measured in the supernatant. Samples were run in triplicate. By suspending the coated particles for different lengths of time in media of different composition, centrifuging, and measuring the radioactivity in the supernatant, the relative rate of surfactant desorption/displacement was assessed for each medium. The smaller PS particle (69 nm) coated with  $^{125}\text{I}$ -labelled F108 can not be forced to settle using the above method. Instead, a centrifuge tube containing a filter with MW 30,000 cut off (Amicon, Centricon-30) was used to separate solids from supernatant. During careful washing of the solids collected on the filter, the filtrate was continuously counted for radioactivity; the washing continued until no radioactivity could be detected in the filtrate. At this point, the radioactivity of the filter was counted and related to the known amount of particles present. From the radioactivity measured on a given amount of particles, their surface density of F108 was determined.

**Measurements of Latex Concentration and Surfactant Density.** The density of the polystyrene latex is known to be 1.053 g/mL (value  $\rho_2$  in the equation below). By measuring the density  $\rho$  of a suspension of PS latex in a medium of known density  $\rho_1$ , one determines the mass concentration  $c_2$  (g/mL) of polymeric particles from the following relationship

$$\rho = \left[ c_2 + \left( 1 - \frac{c_2}{\rho_2} \right) \rho_1 \right] \quad (8)$$

The density ( $\rho_2$ ) of the F108 surfactant was similarly measured from solutions of known concentration  $c_2$ , obtained by careful weighing of the dry polymer and dissolving in accurately determined volumes of distilled water. All densities were determined to 6-th place accuracy using a Mettler PAAR model DMS 60 high precision densitometer.

### **Materials**

Two types of polystyrene latex spheres with nominal diameters of 69 and 272 nm (Seradyn) were used as substrates in the adsorption



experiments; in addition, other PS latex standards from the same manufacturer were used to verify the performance of the sizing equipment.

The polymeric surfactant focused on in this study was Pluronic F108, generously donated by the BASF corporation. This material is a triblock with a molecular weight of 14,600 dalton, consisting of PEO/PPO/PEO in the monomeric ratio of 129/56/129. The density of this material was determined to be 1.186 g/mL, as described above.

All standard particles were sized prior to any exposure to the polymeric surfactant, using a 0.1% aqueous solution of the FL-70 (low molecular weight) surfactant from Fisher Scientific. This suspension medium has been used extensively in FFF particle characterization experiments, and has been found to yield diameters in good agreement with other techniques. During the adsorption experiments, the latex particles (2.5% w/w) were incubated with F108 (4.0% w/w) in PBS for periods of 24 hours under constant end-over-end shaking. The coated latex particles were then sized using carriers containing either 0.1% FL-70, or 0.1% F108 in deionized water alone or with the addition of 12 mM NaCl. The desorption of F108 surfactant was studied in media consisting of deionized water, F108 in DI water, 0.1% aqueous FL-70, and 0.1% human serum albumin (HSA, ICN 82-301-1) in PBS.

### Results and Discussion

The generally good agreement between particle sizes determined by FFF and other methods has been discussed previously (11-13). In Figure 1a we have compiled data from a study by Li, J-M.; Caldwell, K.D., and Mächtle, W. (18) in which 9 PS latex standards were characterized using analytical ultracentrifugation (AUC), sedFFF, PCS, and SEM. The good correlation between the manufacturer's (BASF) AUC data, and data from the other techniques supports the notion that particle diameters are accurately determined using either of the techniques, provided the samples are uniform in size and of known density. However, while polydisperse samples are readily sized by sedFFF and AUC, and somewhat less easily sized by SEM, their detailed size distribution can not be established using the PCS technique (17). Instead, this method is generally limited to providing a Z-average of all sizes present in the sample as well as a polydispersity index for the population. Only for bimodal samples with a larger than 100% size difference between the modes is it possible to size the two populations separately (17). Conversely, since the centrifugal force affecting the suspended particles depends both on their size and density (19), the two sedimentation techniques AUC and sedFFF are by themselves unsuited for sizing samples with nonuniform density. It is, however, possible to utilize the high fractionating power of the sedFFF technique to produce narrow fractions of such samples, and to subsequently let the PCS provide a size assignment for the now uniform particles present in each fraction.

Flow FFF presents an altogether different situation, since from Equation 5 above it is clear that size is the only particle characteristic which affects retention in this technique. For monodisperse standard particles, Figure 1b illustrates the good agreement found between diameters determined by flow FFF and those determined by PCS.

Adsorption of the F108 triblock to two PS standard latex samples with nominal diameters of 69 and 272 nm was performed at a surfactant concentration well above the onset of the plateau region of the adsorption isotherm (20) and resulted in significant size increases,

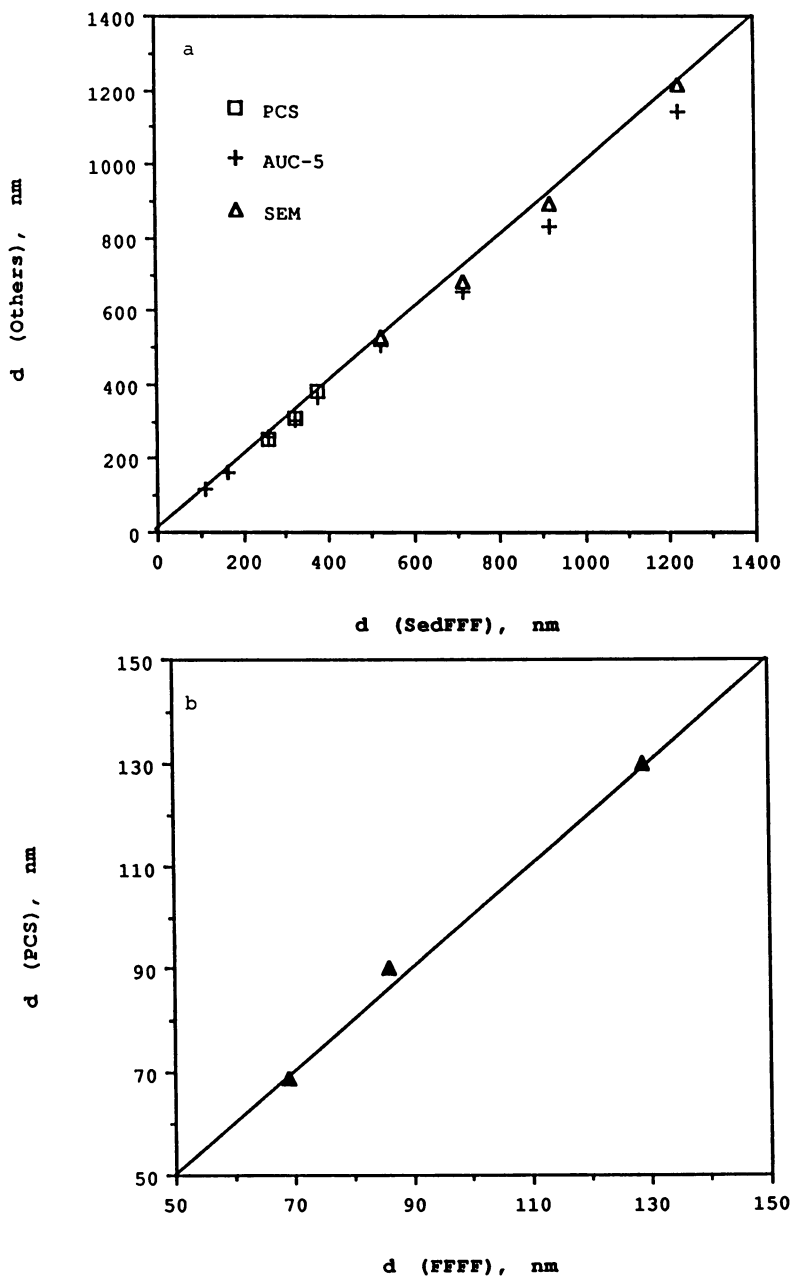


Figure 1. a) Comparison of particle sizes determined by *sedFFF* and other techniques;  
 b) Comparison of size determinations by PCS and flow FFF.

as judged from PCS at a fixed observation angle. Indeed, this technique showed the diameters of the (filtered) adsorption complexes to be 84 and 320 nm, respectively. In PCS, the angular dependence of the scattering intensity is known to differ markedly with particle size. A good way to monitor a sample for changes in its polydispersity, such as might occur during the adsorption of a polymeric surfactant, is therefore to scan for angular variations in the diffusion coefficient  $D$  of Equation 6 before and after the adsorption (10). If there is no change in the polydispersity as a result of the coating, the relationships between  $D$  and  $\sin^2\theta/2$  should remain constant in both cases throughout all observation angles. Although Figure 2 shows a slight scatter in the  $D$  values recorded for the F108-coated PS 272 nm at different observation angles, the data give no clear indication of any increase in sample polydispersity.

An altogether different conclusion is reached when the sample is examined by sedFFF. The fractograms in Figure 3 show the elution profiles of PS 272 before and after coating. In the "before" case, the fractogram contains one single peak indicative of a unimodal size distribution. As the density of the naked polystyrene particles is well known, their average size can be calculated from the elution position using Equations 1 and 2. This value, reported in Table I, is seen to be in close agreement with the size determined from PCS. By contrast, the fractogram representing the F108-coated particles displays quite a bit of complexity, with the major peak being trailed by several minor components. Since the density of the coated particles is unknown, no size can be assigned to these components based on their sedFFF elution behavior. However, electron micrographs of fractions collected under each peak very clearly revealed the presence of monomers, dimers, trimers, and higher order aggregates. The monomer fraction is by far the most abundant, and an average diameter for particles in this fraction is easily determined by PCS (see Table I). A direct PCS analysis of the F108-coated PS particles had shown an average diameter of 365 nm; after passage through a Nucleopore filter with 0.8  $\mu\text{m}$  pore size, the average PCS size was reduced to 320 nm indicative of a coating thickness of 24 nm. However, by exposing the sample to the sedFFF procedure and thereby removing all aggregates from the coated particles, one arrives at the much smaller value of 14 nm for this thickness, as seen in Table I.

Table I. Sizes of Bare and F108-Coated PS Particles, and the Relative Coating Thickness,  $\delta$

	d, Nominal (nm)	d, PS (nm)	d, F108 coated PS (nm)	$\delta$ (nm)
FFF	272	275 $\pm$ 2	-	-
	69	69 $\pm$ 2	82 $\pm$ 2	7 $\pm$ 2
PCS	272	272 $\pm$ 3	301 $\pm$ 2*	14 $\pm$ 3
	69	68 $\pm$ 3	84 $\pm$ 2**	8 $\pm$ 3

\* Measured on collected fraction

\*\* Measured on filtered solution

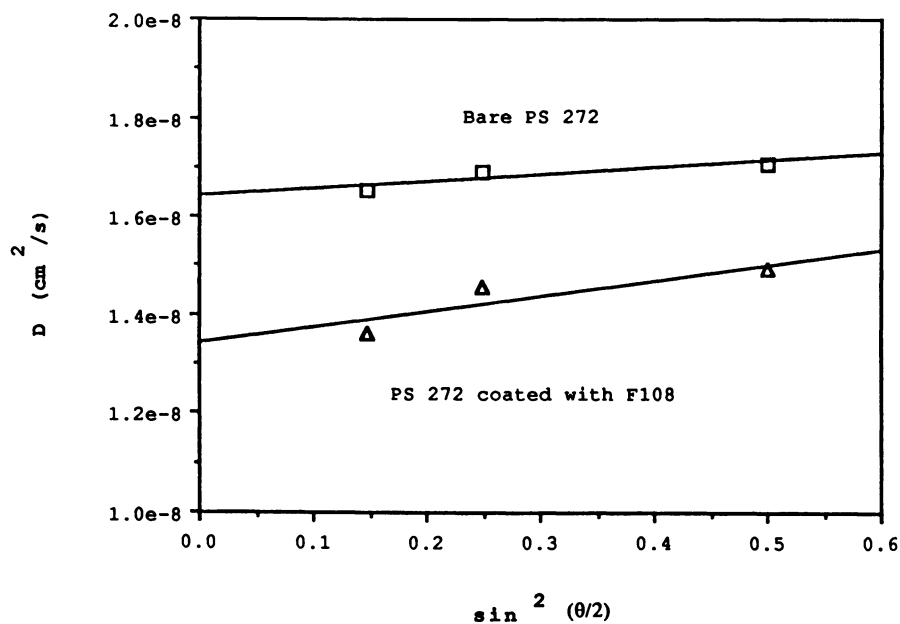


Figure 2. Angle dependence of diffusion coefficients for the PS 272-F108 adsorption complex determined by PCS.

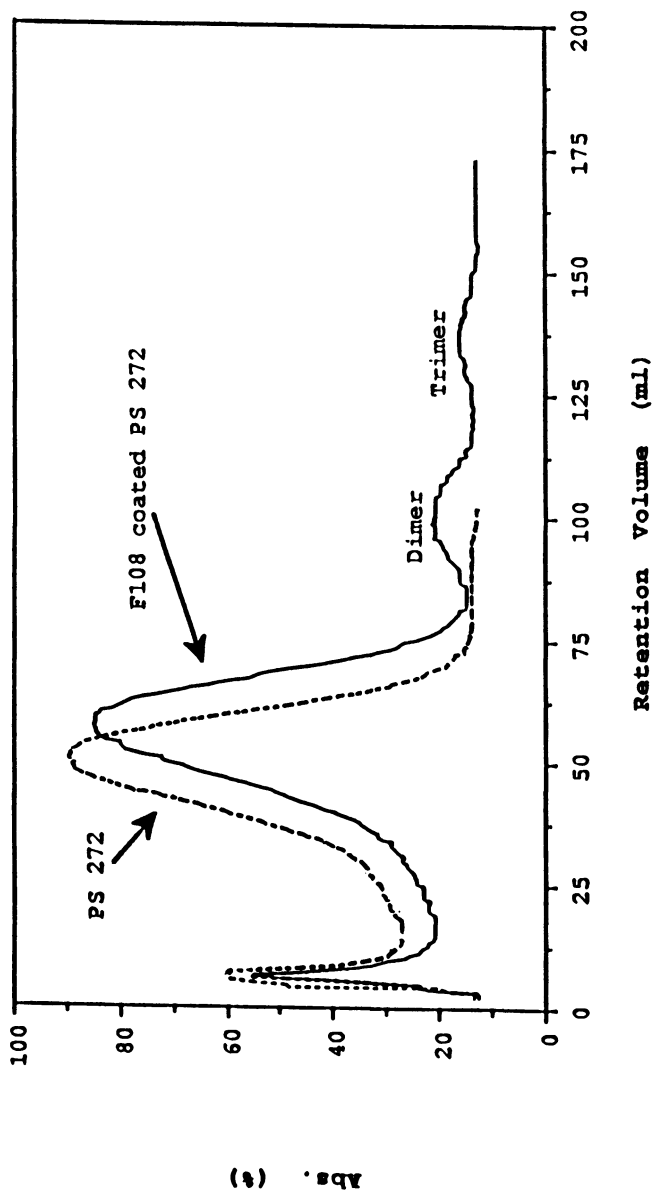


Figure 3. SedFFF fractogram of PS 272 before and after coating with the F108 surfactant. Carrier: 0.1% F108, 12 mM NaCl; flow rate 2.7 mL/min; field strength 173 gravities.

A similar situation is found for the smaller latex, whose diameter of 69 nm is outside the range of resolution by our sedFFF instrument, but is well within range for resolution by the flow FFF technique. Although less size selective than its sedimentation counterpart, this technique has the advantage of establishing a direct relationship between retention and size (Equation 5), without influence of a second sample characteristic (e.g. density in case of sedFFF). Figure 4 illustrates the flow FFF elution patterns collected for a 69 nm PS latex, before and after coating with F108. The naked latex is seen to elute as a relatively narrow peak commensurate with a diameter of 69 nm, while the coated particles elute with a tailing peak indicative of the presence of aggregates. The elution position of the peak maximum suggests a size for the coated monomer of 82 nm (see Table I), while a PCS analysis of the filtered, unfractionated sample suggested an average size of 84 nm.

From Table I it appears that the F108 surfactant forms a thicker layer on the surface of the larger particles as compared to the smaller analogue. While this observation stems from at least three batches of adsorbate of each of the two sizes reported on here, a general statement regarding the relationship between coating thickness and substrate curvature will have to wait until latex particles of several other sizes have been examined. Interestingly, a trend of increased coating thickness with increasing particle size was observed for a series of Pluronic-coated PS latex of a wide range of diameters using capillary hydrodynamic fractionation (21). As these findings differ from previous observations based on PCS alone (3), the present study using a combination of FFF and PCS is being expanded to include a wider range of particle diameters and different incubation conditions.

It may be instructive to examine the surface area occupied per surfactant molecule when adsorbed to either the 272 nm or the 69 nm polystyrene latex. This can be done after adsorption of radioisotope-labelled surfactant to particles of each size, and quantification of the amount of surfactant residing on each particle. For the larger particles, retention measurements in sedFFF represent an independent means of determining the amount of surfactant adsorbed to each particle. This procedure, which is outlined in Equation 4 above, represents a novel way of extracting information from sedFFF regarding the relative composition of adsorption complexes under conditions where the densities of both core and (unsolvated) coating are known. Table II shows the surface areas per F108 molecule determined from both the sedFFF and the  $^{125}\text{I}$ -labelling experiments. From this table one finds the two methods to be in good agreement for the 272 nm particle, while the small size of the 69 nm particle precludes analysis by sedFFF and a resultant verification of the isotope quantification. The surfactant appears more compactly adsorbed on the larger particles, where the area per adsorbed F108 molecule is 7-8 nm<sup>2</sup>, as compared to the smaller particles where the corresponding area is 20 nm<sup>2</sup>. The small area per adsorbent molecule found for the larger particles is surprising. In a similar study involving F108 adsorption to carboxylated PS latex particles with a 312 nm diameter, Kayes and Rawlins (20) found the surface area per molecule to be 24 nm<sup>2</sup>. From an extrapolation to zero PEO chain length of surface areas determined for a series of triblocks with a PPO half the size of that present in F108 (30 monomer units vs. 56), these authors concluded that the 30 unit PPO block occupied an area of 2.4 nm<sup>2</sup>. If correct, our measurements would indicate that on

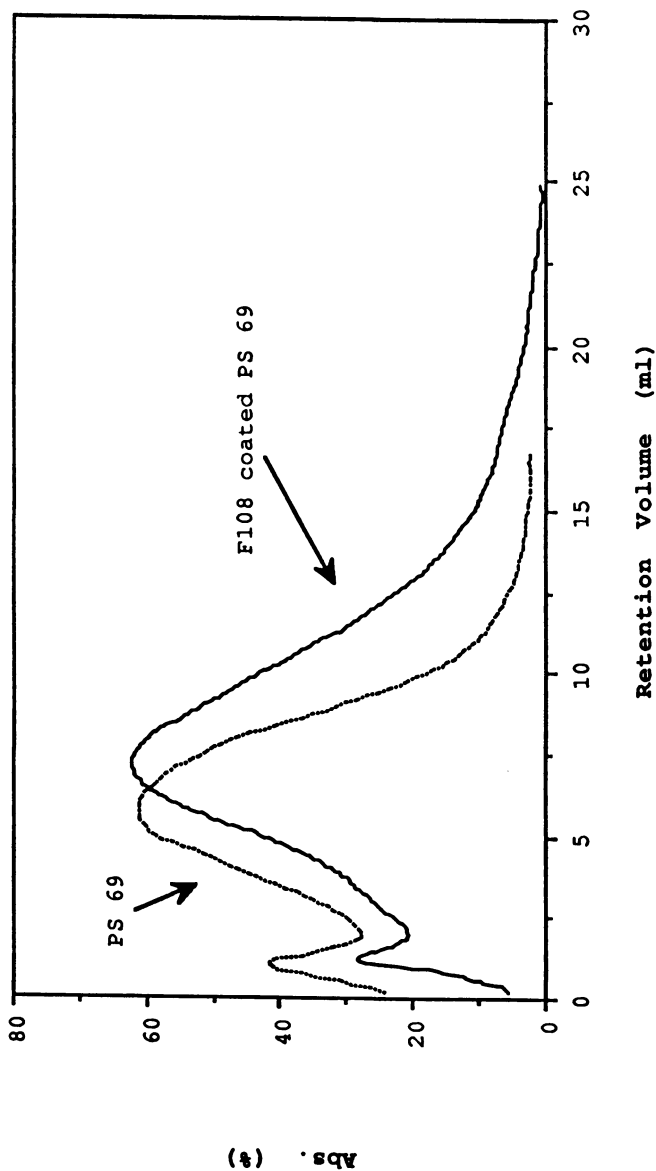


Figure 4. Flow FFF fractogram of PS 69 before and after coating with the F108 surfactant. Carrier: PBS (0.15 M, pH 7.4); cross flow 15.6 mL/h; longitudinal flow 6.5 mL/h.

unsubstituted PS 272, the area per molecule is just about twice that of the central PPO-block.

Table II. Amount of Adsorbed F108 on PS Particles

	Adsorbed Amount (mg/particle)	Surface Area/Molecule (nm <sup>2</sup> /molecule)
PS 272		
125I-labelled	7.16±0.09x10 <sup>-13</sup>	7.9±0.1
SedFFF	8.07±0.35x10 <sup>-13</sup>	7.0±0.3
PS 69		
125I-labelled	1.81±0.03x10 <sup>-14</sup>	20.1±0.3

Throughout this study, the adsorption of F108 resulted from a 24 h exposure of the PS latex particles to a 4% solution of surfactant in physiological saline. Since both the PCS and FFF analyses were carried out in highly diluted solutions of the surfactant, it was essential to determine whether the surfactant were stably adsorbed, or whether the surface concentration of F108 on the latex particles were reduced during the sizing process due to leakage into the less concentrated suspension medium. For this purpose, <sup>125</sup>I-labelled F108 surfactant was adsorbed onto the latex particles in the usual way. After 24 h the beads were carefully washed in phosphate buffered saline (PBS), via a series of suspensions and centrifugations, until no radioactivity was detected in the supernatant. After a final spin, the particles were suspended in either of a number of media (see Table III), and kept under slow shaking for several days; once a day, the supernatant was temporarily removed and analyzed for <sup>125</sup>I by means of a  $\gamma$ -counter. In analogy with observations on adsorbed polymers studied by other authors (22), we found no leakage of F108 from an adsorbate suspended in PBS. Even in the presence of 0.8% human serum albumin (HSA), there was no leakage seen during a three-day period. Although this observation does not prove that the surfactant treatment has rendered the particles resistant to protein adsorption, it does indicate that HSA is unable to displace F108 from its adsorption complex with polystyrene, even during extended exposure to the protein in solution. These results are in agreement with a previous study by one of us (23), based on observations of the fluorescence anisotropy of several labelled proteins.

As expected, suspension media containing F108 in soluble form showed substantial displacement of surfactant molecules by others of the same kind (see Table III); this process of zero free energy change is characteristic of the dynamic equilibrium. A significant leakage was also recorded in 0.1% FL-70, which is the medium most frequently used in the FFF characterization of regular latex spheres. In order to avoid leakage during the size analyses, all characterizations of the adsorbate, whether by PCS or FFF, were therefore performed either in straight PBS, or in PBS with a 0.1% F108 additive.



Table III. Stability of the PS 272-F108 Adsorption Complex in Different Environments

Solution Composition	Day 1	Day 2	Day 3
PBS (0.15M, pH 7.4)	1.0	1.0	1.0
0.8% HSA in PBS	1.0	1.0	1.0
4.0% F108 in PBS	0.59	0.55	0.54

### Conclusion

Adsorption of the polymeric surfactant F108 to polystyrene latex spheres, under the experimental conditions chosen here, leads to the formation of aggregates which push the PCS-value of the composite diameter to artificially high numbers. Pre-fractionation by FFF removes these aggregates and permits an accurate PCS based determination of the thickness of the coating layer. In addition, the flow FFF procedure itself provides a value for the diameter of the coated latex particles from the observed retention; there is good agreement between the PCS and FFF derived sizes for the purified monomer fraction. From a combination of FFF and PCS we conclude that the polymeric surfactant F108 appears to form a thicker coating on the larger latex particles. This observation needs to be further examined using a wide range of particle diameters and different incubation conditions.

In the case of sedimentation FFF, the observed retention does not translate into a size of the adsorption complex due to the unknown value of its hydrated density. Here, the retention measurement is shown to yield information about the amount of polymeric surfactant associated with each particle, and thus the surface area occupied by each surfactant molecule adsorbed to the latex core. Such information can be obtained by an entirely different approach involving the adsorption and quantification of radio-isotope labelled surfactant to known amounts of uncoated latex particles. The good agreement between values for the amount of surfactant per particle determined, on the one hand, by the isotope technique and on the other hand by sedFFF, supports this novel use of the analytical information contained in the sedFFF retention measurement. Surface densities determined by the two techniques indicate the surfactant to be more highly concentrated on the larger particles.

From leakage studies of PS latex coated with  $^{125}\text{I}$ -labelled F108 surfactant one finds no measurable desorption when the particles are suspended in phosphate buffered saline. This is true even in the presence of 0.8% human serum albumin, which does not appear to displace any surfactant from the adsorption complex. Suspension in an F108 containing medium leads to a detachment of labelled surfactant, as expected from the dynamic nature of the adsorption equilibrium. The polymeric surfactant is also shown to desorb in a medium containing the low molecular weight surfactant FL-70 which is otherwise frequently used as carrier in particle analysis by FFF, but shown to be unsuitable for the present study.

### Acknowledgements

This work was supported by grant No. GM 38008-03 from the National Institutes of Health. One of us (JTL) gratefully acknowledges support from a fellowship awarded by the Eastman Kodak Corporation.

### Literature Cited

1. Iillum, L.; Davis, S.S. Life Science 1987, **40**, 1553.
2. Iillum, L.; Davis, S.S. FEBS Letters 1984, **167**, 79.
3. Lee, J.; Martic, P.A.; Tan, J.S. J. Colloid Interface Sci. 1989, **131**, 252.
4. Andrade, J.D.; Hlady, V. Adv. Polymer Sci. 1986, **79**, 1.
5. O'Mullane, J.E.; Davison, C.J.; Petrak, K.; Thomlinson, E. Biomaterials 1988, **9**, 203.
6. Nagaoka, S.; Mori, Y.; Takiuchi, H.; Yokota, K.; Tanzawa, H.; Nishiumi, S. In Polymers as Biomaterials; Shalaby, S.W.; Hoffman, A.S.; Ratner, B.D.; Horbett, T.A., Eds.; Plenum Press: New York, 1984; p 361.
7. Mächtle, W. Makromol. Chem. 1984, **185**, 1025.
8. Bradford, E.B.; Vanderhoff, J.W. J. Appl. Phys. 1955, **26**, 864.
9. Garvey, M.J.; Tadner, T.F.; Vincent, B. J. Colloid Interface Sci. 1976, **55**, 440.
10. Killman, E.; Maier, H.; Baker, J.A. Colloids and Surfaces 1988, **31**, 51.
11. Giddings, J.C.; Yang, F.J.F.; Myers, M.N.; Anal. Chem. 1974, **46**, 1917.
12. Giddings, J.C.; Karaiskakis, G.; Caldwell, K.D. Sep. Sci. Technol. 1981, **16**, 607.
13. Caldwell, K.D. In Modern Methods of Particle Size Analysis; Barth, H., Ed.; John Wiley & Sons: New York, 1984; p 211.
14. Myers, M.N.; Giddings, J.C. Anal. Chem. 1982, **54**, 2284.
15. Giddings, J.C.; Myers, M.N.; Caldwell, K.D.; Fisher, S.R. In Methods of Biochemical Analysis; Glick, D., Ed.; John Wiley & Sons: New York, 1980; Vol. 26, p 79.
16. Giddings, J.C.; Yang, F.J.; Myers, M.N. Science 1976, **193**, 1244.
17. Weiner, B.B. In Modern Methods of Particle Size Analysis; Barth, H., Ed.; John Wiley & Sons: New York, 1984; p 93.
18. Li, J.; Caldwell, K.D. J. Chromatography 1990, **517**, 361.
19. Caldwell, K.D.; Li, J. J. Colloid Interface Sci. 1989, **132**, 256.
20. Kayes, J.B.; Rawlins, D.A. Colloid & Polymer Sci. 1979, **257**, 622.
21. Venkatesan, J.; DosRamos, J.G.; Silebi, C. Published elsewhere in this volume.
22. Pfefferkorn, E.; Carroy, A.; Varoqui, R.; J. Polymer Sci. Phys. 1985, **23**, 1997.
23. Tan, J.S.; Martic, P.A. J. Colloid Interface Sci. 1990, **136**, 415.

RECEIVED February 19, 1991

## Chapter 17

# Efficiency of Particle Separation in Capillary Hydrodynamic Fractionation (CHDF)

J. G. DosRamos<sup>1</sup>, R. D. Jenkins<sup>2</sup>, and C. A. Silebi<sup>2</sup>

<sup>1</sup>Matec Applied Sciences, Hopkinton, MA 01748

<sup>2</sup>Department of Chemical Engineering and Emulsion Polymers Institute, Lehigh University, Bethlehem, PA 18015-3590

This paper presents a fundamental analysis from which we can determine the minimum residence time required to fully develop the concentration profile of a colloidal species in laminar flow through a capillary, and the specific resolution of the separation. Our analysis is based on the full development of the radial concentration profile of particles in the capillary. To estimate the minimum residence time required to fully develop the radial concentration profile, we evaluated the smallest eigenvalue of the particle diffusion equation from the Rayleigh quotient while taking into account the radial migration of particles caused by fluid inertial forces and the colloidal potential of interaction between the dispersed particles and the capillary wall. Measurements of the variance of the fractogram and of the average elution time of the colloidal species determined the specific resolution. The ionic strength of the eluant and the lift forces exerted on the colloidal particles by the inertia of the fluid can either increase or decrease the specific resolution, depending on the value of the product of the particle Reynolds number and the Peclet number. Fundamental theoretical calculations for the specific resolution agree well with experimentally measured values.

When submicron colloidal particles of different sizes are transported by a fluid through an open capillary tube under laminar flow conditions, they fractionate and emerge in order of decreasing diameter. The rate at which the particles are transported downstream (as measured by their elution times) can be quantified in terms of the eluant velocity and ionic strength, particle diameter, and capillary diameter. This difference in the rate of transport for particles of different sizes can be used to obtain the particle size distribution (PSD) of a broad distribution of particle sizes. Unfortunately, a sample composed of monodisperse particles elutes within a range of elution times rather than at a single elution time, this effect is referred to as axial dispersion or "instrumental band broadening". Axial dispersion is a serious obstacle to obtaining the PSD, and is the main cause of imperfect resolution in CHDF and in other fractionation methods.

0097-6156/91/0472-0264\$06.00/0  
© 1991 American Chemical Society

Taylor [1] developed the theoretical framework from which the longitudinal dispersion of molecular species in laminar flow through capillary tubes could be evaluated in terms of fundamental parameters. Shortly afterwards, Aris [2] used the method of moments to generalize Taylor's analysis to include non-circular cross sections. In 1970 DiMarzio and Guttman [3] applied Taylor's analysis to evaluate the longitudinal dispersion coefficient of finite size spherical particles. DiMarzio and Guttman assumed that a Brownian particle suspended in a viscous fluid undergoing Poiseuille flow within a capillary tube samples all radial positions accessible to it with equal probability, provided that the residence time of the particle in the flow field is long. However, the finite size of the particle limits the approach of the particle center to a distance equal to its radius from the inner surface of the capillary wall. As a consequence of this, the particle is excluded from the slowest moving streamlines; this implies that the longitudinal dispersion of particles decreases somewhat with increasing particle size.

Polymer colloids are useful as a model system because they have a broad range of well characterized, uniform particle sizes that can be used to investigate dispersion phenomena of particles flowing through capillary tubes under laminar flow conditions. Several experimental studies have been reported which demonstrate that, contrary to Taylor and Aris' results for solutes, when colloidal particles with diameters greater than 1- $\mu\text{m}$  are pumped through a capillary tube, their axial dispersion decreased with increasing eluant velocities. Noel et al. [4], using capillary tubes of 250- and 500  $\mu\text{m}$  inside diameter, reported such behavior for 10 $\mu\text{m}$  silica particles. In a similar study of particle fractionation by flow through capillaries, Brough et al. [5] found the same behavior for 2  $\mu\text{m}$  diameter particles. According to McHugh [6], this phenomena results from the tubular pinch effect, where fluid inertial forces induce a radial migration of the particles toward a non-central radial position [7]. Moreover, based on Taylor's minimum residence time criteria, McHugh also indicated that, for the experimental conditions of Noel et al., the steady state radial concentration profile did not fully develop because of the small diffusion coefficient of the particles and the relatively large eluant velocity and capillary diameters. He concluded that a more detailed analysis was needed to explain the reduction in axial dispersion with increasing particle size and eluant velocity.

Recently, Silebi and DosRamos [8] used CHDF to obtain analytical separations of submicron sized particles using capillaries with diameters as small as 7 microns. In contrast to previous studies, these investigators found that, in addition to the effect of inertial forces on the particles, ionic strength influences the fractionation and the axial dispersion of particles in microcapillaries. Because of the well defined geometry of the microcapillary, CHDF is amenable to rather exacting theoretical analysis [9]. For laminar flow, the parabolic velocity profile provides an exact description of the flow distribution; the inertial and colloidal forces, which apply uniformly throughout the capillary tube, are equally well-defined in terms of particle size, capillary radius, eluant velocity and composition. In the present work, we apply Taylor's method of analysis of the dispersion phenomena in laminar flow to capillary hydrodynamic fractionation of submicron colloidal particles, and incorporate size exclusion, wall effects, and colloidal and inertial forces into the theory because all of these phenomena affect the particle displacement through the capillary and its radial distribution. The most important feature of the theory of dispersion as introduced by Taylor is that it describes the average concentration distribution in a complex three-dimensional system by the solution of the one-dimensional convective diffusion equation. As a result, the primary problem is to determine from first principles the dispersion coefficient associated with the one-dimensional dispersion equation.

### Theory

Including fluid inertial forces and electrostatic repulsion between the particles and the capillary wall, the diffusion equation that governs the development of the particle concentration profile for the separation process described above is [9,10]:

$$\frac{\partial c}{\partial t} + \frac{1}{r} \frac{\partial}{\partial r} \left[ -r D_r \frac{\partial c}{\partial r} + rc \left\{ v_{pr} - \frac{D_r}{kT} \frac{\partial \Phi}{\partial r} \right\} \right] + (v_{pz} - \langle v_{pz} \rangle) \frac{\partial c}{\partial Z_1} = 0 \quad (1)$$

The particle radial velocity  $v_{pr}$ , the particle velocity in the axial direction  $v_{pz}$ , the radial component of the particle diffusion coefficient tensor  $D_r$ , and the colloidal interaction potential  $\Phi$  are given by the expressions used by Silebi and DosRamos [10] in their analysis of axial dispersion.  $Z_1$  defines a coordinate system which translates with the average velocity of the colloidal particles,  $\langle v_{pz} \rangle$ . The average velocity of the particles in the axial direction  $\langle v_{pz} \rangle$  is given by [9,10]:

$$\langle v_{pz} \rangle = \frac{\int_0^{R_o - R_p} v_{pz}(r) e^{-E(r)} r \, dr}{\int_0^{R_o - R_p} e^{-E(r)} r \, dr} \quad (2)$$

where

$$E(r) = \frac{\Phi}{kT} - \int_0^r \frac{v_{pr}(r)}{D_r(r)} \, dr \quad (3)$$

The rate of transport of colloidal particles is characterized by the dimensionless separation factor  $R_f$ , which is defined as the ratio of the average velocity of the particles (evaluated from Equation 2) to the mean velocity of the eluant  $\langle v_{pz} \rangle / v_m$ . In Poiseuille flow, the velocity of a particle suspended in a fluid is slightly slower than the axial velocity of the undisturbed fluid evaluated at the same distance from the tube wall as the particle's center of mass. The particle streamline velocity at  $r$ ,  $v_{pz}(r)$ , is given by [11]:

$$v_{pz}(r) = 2v_m(1 - \bar{r}^2) - v_{ps} \quad (4)$$

where the first term is the familiar laminar velocity profile for the unperturbed eluant stream velocity which has a mean velocity  $v_m$ , at the dimensionless radial position  $\bar{r}$  (given by the ratio of radial position to capillary radius) of the center of mass of the particle. The slip velocity  $v_{ps}$  accounts for the wall retardation effect and depends on the ratio of particle to capillary radius  $\kappa$  and the dimensionless radial position  $\bar{r}$ . The slip velocity for a neutrally buoyant particle is given by [9,10]:

$$v_{ps} = \frac{4}{3} v_m \kappa^2 + \frac{5}{2} v_m \kappa^3 (1 + \bar{r}) \left[ \frac{1}{(1 - \bar{r})^2} - \frac{1}{(1 + \bar{r})^2} \right] \quad (5)$$

The particle velocity in the radial direction  $v_{pr}$  results from lateral hydrodynamic forces that drive the particles to an equilibrium position away from the centerline of the capillary. Hence, the integral term in the exponential of Equation 3 accounts for the particle migration caused by this inertial hydrodynamic force. Describing this inertial migration in dimensionless variables the integral expression yields a front factor given by the product of the particle Reynolds number ( $R_{ep} = 2R_p v_{ps}(0)/\nu$ ) and the Peclet number ( $P_e = R_o v_m/D_\infty$ ).

After the concentration profile has fully developed, the variation of the average particle concentration with axial position is described by [9]:

$$\frac{\partial C_m}{\partial t} = D^* \frac{\partial C_m}{\partial Z_1^2} \quad (6)$$

where  $D^*$  is the effective axial dispersion coefficient that is obtained from the moments of the diffusion equation in the presence of an external force field as described by Equation 1. The minimum residence time of the solute flowing through the capillary required to fully develop the particle radial concentration profile  $t_{min}$  is governed by the eigenvalues of Equation 1. Thus, the smallest (and most important) eigenvalue provides an estimate as to when Equation 6 is valid:

$$t_{min} \gg \frac{R_o^2}{\lambda_{sm} D_\infty} \quad (7)$$

where the smallest eigenvalue  $\lambda_{sm}$  equals 14.7 for a molecular solute [1]. Ananthakristan and Gill [12] concluded from their numerical simulations that Equation 6 is valid when the average residence time for a molecular solute in a capillary tube is at least  $0.7R_o^2/D_\infty$ , and a symmetric Gaussian distribution of residence times centered about the average residence time of the solute results. This indicates that a value of 10 times the right hand side of Equation 7 could be used as a good estimate of the minimum residence time  $t_{min}$ . Equation 1 is a separable partial differential equation that, together with boundary conditions that describe the symmetry of the capillary and no mass flux through the capillary wall, is a Sturm-Liouville system. Therefore, the minimum of the Rayleigh quotient for the class of equations that satisfy the boundary conditions equals the smallest eigenvalue of Equation 1. The appendix presents the details of the derivation.

Expressions to evaluate the effective axial diffusion coefficient  $D^*$  have been developed in detail by Brenner and Gaydos [13], who used the method of moments, and more recently by Silebi and DosRamos [9], who followed Taylor's method of analysis. The principal results are given below.

$$D^* = \frac{\int_0^{R_o - R_p} \frac{H^2(r) dr}{r D_r(r) e^{-E(r)}}}{\int_0^{R_o - R_p} e^{-E(r)} r dr} + \frac{\int_0^{R_o - R_p} D_z(r) e^{-E(r)} r dr}{\int_0^{R_o - R_p} e^{-E(r)} r dr} \quad (8)$$

where

$$H(r^*) = \int_0^{r^*} \{ v_{pz}(r') - \langle v_{pz} \rangle \} e^{-E(r')} r' dr' \quad (9)$$

The solution of Equation 6 for  $N$  particles that are concentrated over a small length  $dZ$  at the entrance of the capillary ( $Z = 0$ ) at time  $t = 0$  is given by:

$$C_m = \frac{N}{2 R_0^2 \sqrt{\pi^3 D^* t}} e^{-\frac{Z_1^2}{4D^*t}} \quad (10)$$

The degree of axial dispersion in capillary tubes can be determined experimentally from the fractogram (time distribution of the concentration of the sample in the eluting stream) generated by the injected sample as it exits from the capillary tube. The axial dispersion coefficient characterizes the spreading of the fractogram, as evaluated from the variance of the fractogram  $\sigma_c^2$ :

$$\sigma_c^2 = \frac{\int_0^\infty C_m (t - \langle t_p \rangle)^2 dt}{\int_0^\infty C_m dt} \quad (11)$$

where  $\langle t_p \rangle$  is the average elution time of the particles, given by the ratio of capillary length to the average velocity of the particle calculated from Equation 2, and  $C_m(t)$  is the average concentration of the particles over the cross-section of the tube as given by Equation 10. The total axial dispersion quantified in terms of the second moment of the fractogram,  $\sigma_T^2$ , associated with the convected motion of submicron particles in the CHDF system is given by the superposition of the contributions from the dispersion in the capillary tube,  $\sigma_c^2$ , and the non-ideal mixing at the injection valve and the detector,  $\sigma_{n-i}^2$ . Thus,

$$\sigma_T^2 = \sigma_c^2 + \sigma_{n-i}^2 \quad (12)$$

The contribution from the non-idealities were obtained from the difference between the ideal degree of axial dispersion of a solute (sodium dicromate) flowing through the capillary according to Taylor's theory and the total experimental dispersion of this solute in our CHDF system. The degree by which two different size particle populations (subscripts 1 and 2) are separated determines the efficiency of separation, which is quantified using the internationally accepted definition of the specific resolution,  $R_s$ :

$$R_s = \frac{\langle t_1 \rangle - \langle t_2 \rangle}{2(\sigma_{T,t_1} + \sigma_{T,t_2})} \quad (13)$$

$\langle t_i \rangle$  is the average residence time, and  $\sigma_{T,t_i}$  is the total axial dispersion of the  $i$ th size particle population. The magnitude of colloidal forces relative to fluid inertial forces, as characterized by the product of the particle Reynolds number and the Peclet number, has a significant effect on  $R_s$ , as described in the discussion below.

### Results and Discussion

As shown in Figures 1 and 2, the eigenvalue can become much larger than 14.7 (the value for molecular solutes), and it increases as the particle size increases under the flow conditions typically used for the separation of particles in capillary hydrodynamic fractionation. Hence, under these conditions, the minimum residence time needed to develop the radial concentration profile for larger particles may be less than for smaller particles. The smallest eigenvalue increases as the capillary radius decreases or as the average eluant velocity increases. This is expected since the product of the particle Reynolds number and the Peclet number ( $Re_p Pe$ ), which quantifies the significance of inertial forces relative to colloidal forces, increases with increasing mean eluant velocity and with decreasing capillary radius. At  $Re_p Pe$  near 10.5, inertial forces are large enough to accelerate the development of particle radial concentration profile, which produces an abrupt increase in the eigenvalue. Figure 2 shows that colloidal forces can significantly influence the approach to full development of the radial concentration profile when  $Re_p Pe$  is less than 10.5. As the ionic strength of the eluant decreases, the eigenvalue increases because the electrostatic interaction between the capillary wall and the particles provides an additional force which excludes particles from the slower velocity streamlines near the capillary wall. When  $Re_p Pe$  is greater than 30, inertial lift forces eclipse the colloidal forces in importance, and the curves for different ionic strengths in Figure 2 merge at large particle sizes and large mean eluant velocities. Thus, the minimum residence time that is required to develop the

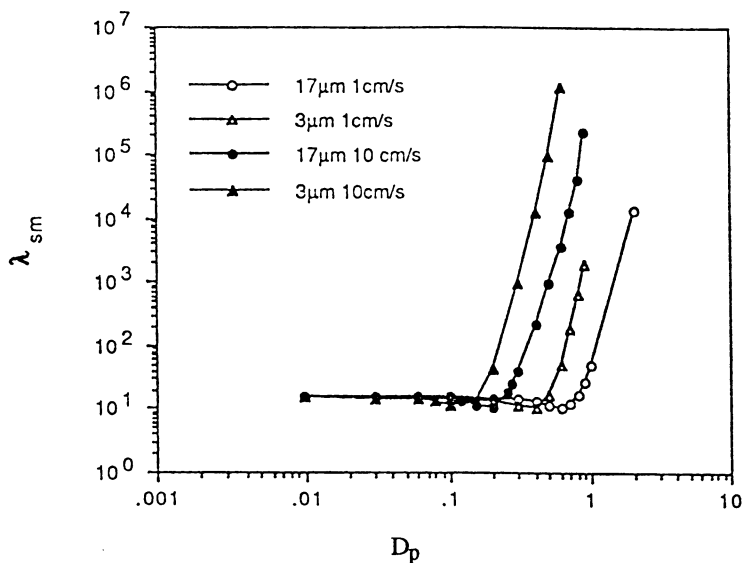


Figure 1: Minimum eigenvalue of the diffusion equation, neglecting the colloidal potential, for various capillary radii and mean eluant velocities.



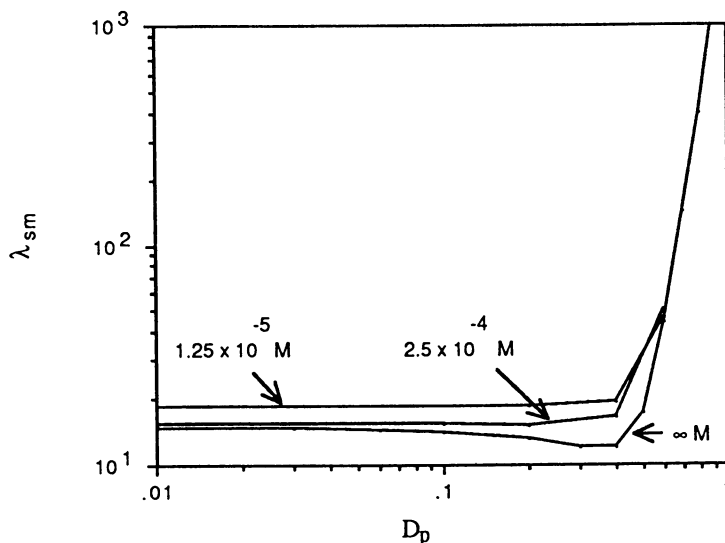


Figure 2: Minimum eigenvalue of the diffusion equation for various ionic strengths (in Molarity).  
Capillary radius: 3  $\mu\text{m}$ ; Eluant velocity: 1 cm/s;

radial concentration profile of the particle flowing through the capillary decreases under the following conditions: increasing electrostatic repulsion between the capillary wall and particles; increasing ratio of particle size to capillary diameter; and increasing average eluant velocity. Table I compares the range of residence times for several particle sizes under the conditions used in this study with the minimum time (10 times the value obtained from Equation 7) required for the particles to develop their radial concentration profile. These results demonstrate that the residence times of the particles in our experiments are sufficient to fully develop the steady state radial particle concentration profile. As a consequence, Equations 2 and 6 can be applied to describe the rate of transport and the dispersion of the colloidal particles in the capillary.

Figures 3 and 4 illustrate the effect of electrolyte in the eluant on  $R_f$  and  $R_g$ . Figure 3 shows that, at low ionic strengths ( $5 \times 10^{-4}$  M), varying the surface potential for both the particle and the surface of the capillary from 20 to 150 mV does not affect  $R_f$ , resulting in a single line representing the relationship between the separation factor and the particle diameter. Similar results were obtained, at this low ionic strength, when values of Hamaker's constant (a variable that accounts for the

Table I. Range of Minimum Residence Times for Various Particle Diameters for an Operating Pressure Drop of 5000 psi

Tube radius ( $\mu\text{m}$ )	Range of Marker Elution Time (s)	$t_{\text{min}}$ Particle diameter		
		88 nm	357 nm	1100 nm
3.75	16-1200	1.9-1.9	4.5 - 7.8	7.2 - 24.1
6.5	50-1500	5.8-5.8	23.6 - 23.5	50. - 72.5
17.0	240-1300	39.4-39.4	95. - 161.	49. - 496.

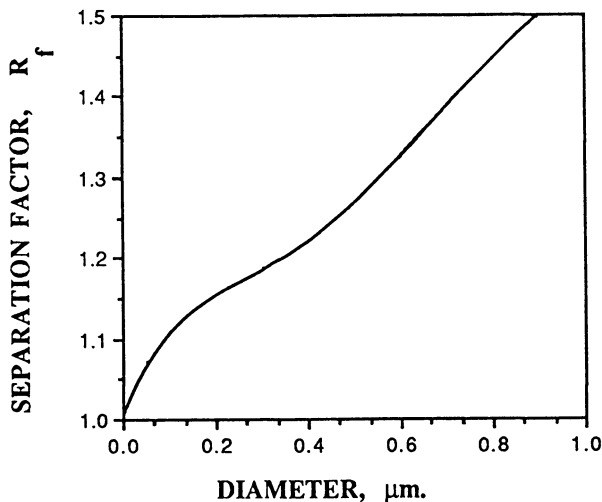


Figure 3: Theoretical computation showing the separation factor for values of the electric surface potential of the particle ranging from 20 to 150 mV at an ionic strength of 0.5 mM. Capillary radius: 3  $\mu\text{m}$  Eluant velocity: 1 cm/s

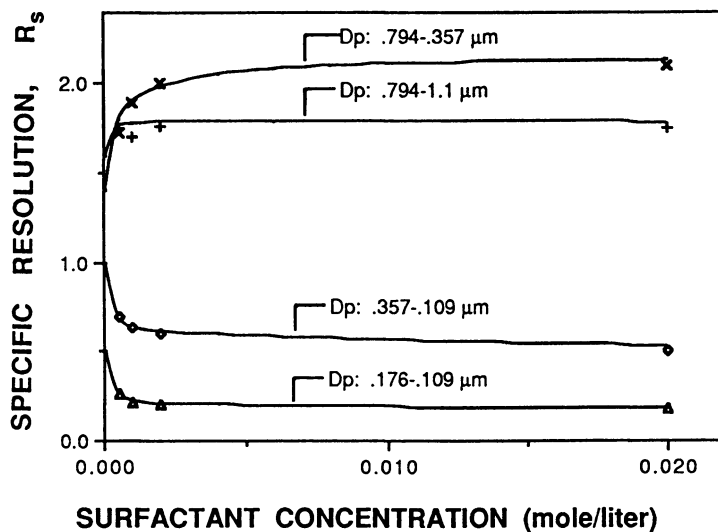


Figure 4: Influence of Sodium Dodecyl Sulfate concentration on the specific resolution of various pairs of particles. Capillary length: 5 m; Capillary radius: 3.6  $\mu\text{m}$ ; Eluant velocity: 1.3 cm/s

van der Waals' attractive force), in the range  $(.5 - 20) \times 10^{-14}$  ergs were used. This is of practical interest because the separation of the particles is then based solely on size, and not on electrokinetic characteristics. Conversely, at high ionic strengths ( $\geq 10^{-2}$  M), our theoretical calculations have shown that the average velocity of the particle is sensitive to both Hamaker's constant and surface charge density [9]. But because colloidal particles tend to coagulate at high eluant ionic strengths, this is not a practical operating condition in CHDF. Figure 4 presents the influence of the ionic strength of the eluant on the specific resolution  $R_s$ . At concentrations of sodium lauryl sulfate (SLS) above the critical micelle concentration ( $8 \times 10^{-3}$  M), the ionic strength of the eluant used in the calculations includes the ionic contributions of the micellar "macroions" [14]. For the range of ionic strength smaller than  $10^{-2}$  M,  $R_s$  decreases when the ionic strength of the eluant increases because an increase in the number of counterions in the eluant diminishes the electrostatic repulsion between the capillary wall and the particles. This allows the particles to sample the slower velocity streamlines near the capillary wall, which increases axial dispersion and decreases the specific resolution. Increasing the concentration of ions in the eluant beyond that required to effectively eliminate the electrostatic interaction between the particles and the capillary wall has no effect on the efficiency of separation  $R_s$ , and  $R_s$  reaches a limiting value for large eluant ionic strengths. Since large particles are comparatively less influenced by colloidal interactions than small particles, and since the average velocity of the smaller particles becomes slower as the ionic strength of the eluant increases, the efficiency of separation for mixtures of large and small particles increases. The curves for the mixture of .791 and .375  $\mu\text{m}$  particles in Figure 4 demonstrates this.

Figures 5 and 6 present results from theoretical calculations for the specific resolution, and Figures 7 and 8 compare theory and experimental results. The specific resolution increases as capillary radius decreases, and can either increase or decrease as the average eluant velocity increases, depending on the magnitude of the hydrodynamic radial force exerted on the particles by the fluid inertia. At small

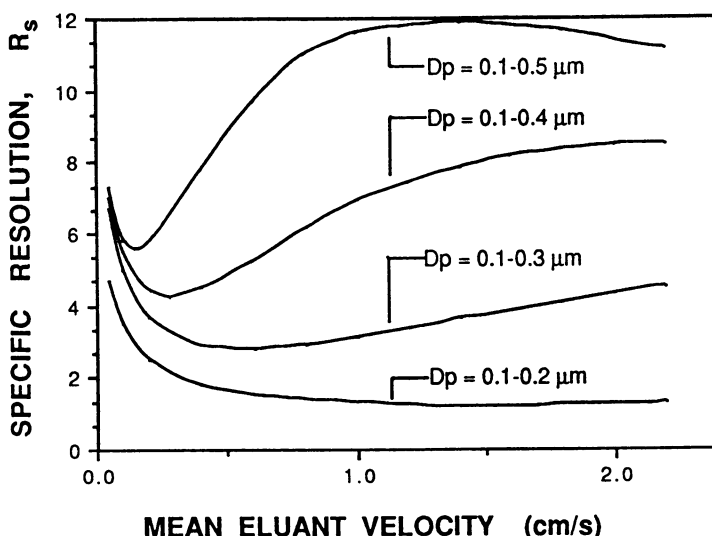


Figure 5: Theoretical calculation of the influence of eluant velocity on the specific resolution of various pairs of particles. Capillary radius: 3  $\mu\text{m}$ ; Capillary length: 20 m; Ionic Strength:  $1 \times 10^{-3}$  M.

average eluant velocities,  $R_s$  decreases because the degree of axial dispersion increases sharply as the average eluant velocity increases, until the hydrodynamic force exerted on the particles in the radial direction by the fluid become significant. This onset of the radial hydrodynamic force occurs when  $Re_p P_e$  is equal to 3. For a given capillary radius, the hydrodynamic force from fluid inertia increases strongly with the size of the particles and the mean eluant velocity. Thus, as the eluant velocity of the fluid increases, the radial hydrodynamic force affects the larger particles first, increasing their average velocity to increase the difference in residence times among particles of different sizes and to decrease the axial dispersion of the larger particles. Hence, the efficiency of separation reaches a minimum when  $Re_p P_e$  equals 3, and increases as the average velocity of the eluant increases. The increase in  $R_s$  as the eluant velocity increases continues until  $Re_p P_e$  based on the larger particles in the mixture equals 40; this is where  $R_f$  of these larger particles reaches its limiting value. As the average eluant velocity increases further, the separation factor for the smaller species increases, while the separation factor for the larger particles remain constant at its limiting value. Consequently, the efficiency of separation reaches a maximum, and then decreases as the average eluant velocity increases, at the point when  $Re_p P_e > 40$  for the larger particles in the mixture and  $Re_p P_e < 40$  for the smaller particles in the mixture. As the eluant velocity increases further,  $Re_p P_e$  for the smaller sized particle reaches a value of 40. Then the separation factors for both species have reached their limiting values, and further increases in average eluant velocity decreases the axial dispersion of both particle sizes to increase the specific resolution. For submicron particles, the efficiency of separation decreases with increasing average eluant velocity, since very large eluant velocities are required before  $Re_p P_e$  exceeds 3. This is especially significant for small inner diameter capillaries, where the large pressure drops encountered in the microcapillaries places an upper limit on the average eluant velocity. Thus, under this limiting condition, smaller velocities will give a better separation for mixtures of the smaller particles.

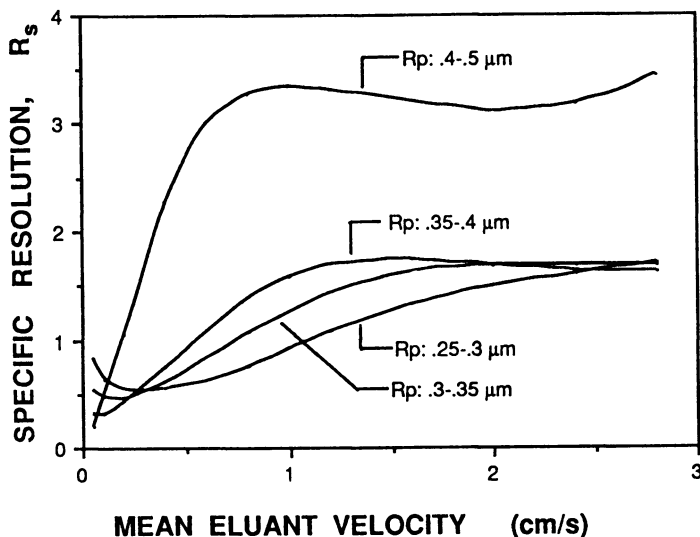


Figure 6: Theoretical calculation of the influence of the eluant velocity on the specific resolution for various pairs of particles. Capillary radius:  $3 \mu\text{m}$ ; Capillary length:  $20 \text{ m}$ ; Ionic strength:  $1 \times 10^{-3} \text{ M}$ .

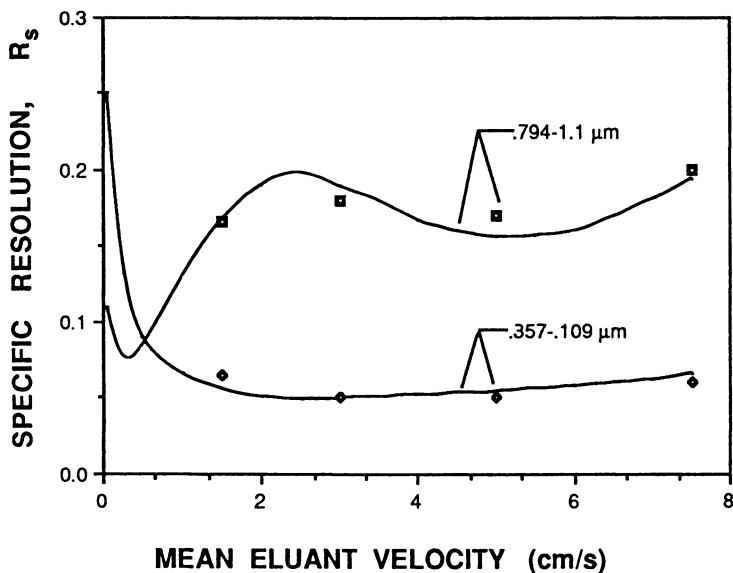


Figure 7: Comparison between theoretical and experimental results of the specific resolution as a function of eluant velocity. Capillary radius:  $17.4 \mu\text{m}$ ; Capillary length:  $17.4 \text{ m}$ ; Ionic strength:  $1 \times 10^{-3} \text{ M}$ .

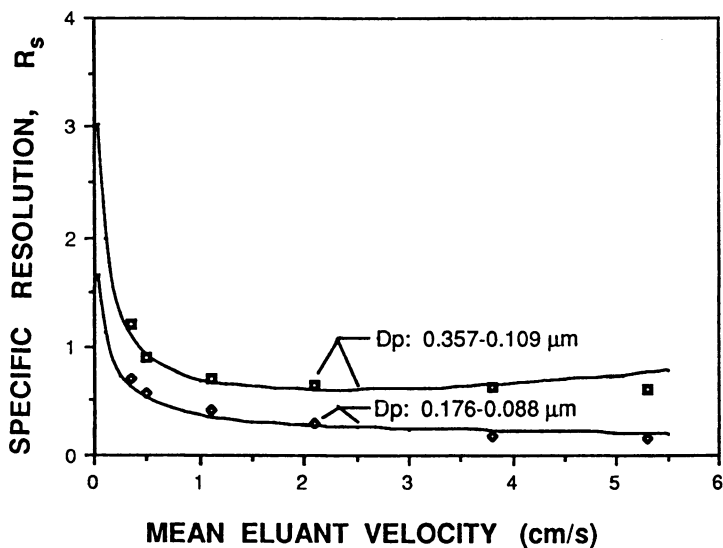


Figure 8: Comparison between theoretical and experimental results of the specific resolution as a function of eluant velocity. Capillary radius:  $3.5 \mu\text{m}$ ; Capillary length:  $8.5 \text{ m}$ ; Ionic strength:  $1 \times 10^{-3} \text{ M}$ .

### Conclusions

The appropriate criteria for the development of the steady state radial concentration profile has been established based on the evaluation of the smallest eigenvalue of the convective diffusion equation for the particles. The results show good agreement between the calculated and experimental values of  $R_f$  and  $R_s$ . For mixtures of particles in which  $R_{ep}P_e$  is smaller than 3 for all species in the mixture, the specific resolution decreases as the eluant velocity increases. At ionic strengths greater than  $10^{-3}M$ , the experimental specific resolution of several pairs of particles was essentially constant as predicted by the theoretical analysis. The analysis provides a natural explanation for universal calibration:  $R_f$  becomes independent of particle type (as indicated by the particle's surface potential and Hamaker's constant) at very low eluant ionic strength because the double layer repulsive force dominates the van der Waals attractive force.

### Appendix

Rewriting Equation 1 in dimensionless form yields:

$$\frac{\partial \bar{c}}{\partial \bar{t}} + \frac{1}{\bar{r}} \frac{\partial}{\partial \bar{r}} \left[ -\bar{r} \bar{D} \left( \frac{\partial \bar{c}}{\partial \bar{r}} + \bar{c} \frac{\partial \bar{E}}{\partial \bar{r}} \right) \right] + \left( \bar{v}_{pr} - R_f \right) \frac{\partial \bar{c}}{\partial \bar{Z}_1} = 0 \quad (A1)$$

where

$$\bar{c} = \frac{c(r,t)}{c_o}, \quad \bar{t} = \frac{t D_\infty}{R_o^2}, \quad \bar{D} = \frac{D_r}{D_\infty}, \quad \bar{\Phi} = \frac{\Phi}{kT}, \quad \bar{v}_{pr} = \frac{v_{pr} v}{R_p v_m^2 \kappa^2} \quad (A2)$$

$$\bar{Z}_1 = \frac{D_\infty}{v_m R_o^2} \{ Z - \langle v_{pz} \rangle t \}, \quad \bar{E} = \bar{\Phi} - \frac{3}{8} R_{ep} P_e \int_0^{\bar{r}} \frac{\bar{v}_{pr}}{\bar{D}} d\bar{r}$$

$c_o$  is the particle concentration at the entrance of the capillary,  $Z$  is the axial distance from the entrance of the capillary,  $R_{ep}$  is the particle Reynolds number, and  $P_e$  is the Peclet number. The boundary conditions which accompany the diffusion equation correspond to symmetry around the capillary centerline and to no mass flux across the capillary wall:

$$\left. \frac{\partial \bar{c}}{\partial \bar{r}} \right|_{\bar{r}=0} = 0 \quad (A3)$$

$$\left[ \frac{\partial \bar{c}}{\partial \bar{r}} - \bar{c} \frac{\partial \bar{E}}{\partial \bar{r}} \right] \Big|_{\bar{r}=1-\kappa} = 0 \quad (A4)$$

Equations A1, A2, and A3 constitute a Sturm–Liouville system. To find the conditions under which radial variations of concentration are reduced to a small fraction of their initial value through the action of molecular diffusion, it is necessary to calculate how rapidly the radial concentration profile approaches a time independent form. The solution of Equation A1 that gives the dependence of  $\bar{c}$  upon  $\bar{r}$  and  $\bar{t}$  can be obtained by assuming a functionality dependence of the form

$\bar{c}(\bar{r}, \bar{t}) = \rho(\bar{r}) \tau(\bar{t})$ . Substitution of this product solution into Equation A1 after separating variables and integrating yields for the time and radial functions:

$$\tau(\bar{t}) = A e^{-\lambda \bar{t}} \quad (\text{A5})$$

$$[\bar{r} \bar{D} \rho' - \rho \bar{r} \bar{D} \bar{E}']' - \lambda \rho \bar{r} = 0 \quad (\text{A6})$$

where the primes indicate ordinary differentiation with respect to radial position, and  $\lambda$  is the separation constant or eigenvalue. As seen in Equation A5, the eigenvalue  $\lambda$  governs approach to full development of the particle radial concentration profile.

It is difficult to solve Equations A6 analytically for the eigenvalue, so we instead form the Rayleigh quotient to quantify the upper bound of the smallest eigenvalue, which is used to examine the influence of particle size and flow conditions on entrance length. The following development presents the mathematical details for forming the Rayleigh ratio for Equation A6. To form the Rayleigh quotient, we first put Equation A6 into Sturm–Liouville form:

$$[p(\bar{r}) \rho']' + [\lambda q(\bar{r}) + w(\bar{r})] \rho = 0 \quad (\text{A7})$$

where

$$p(\bar{r}) = \exp \left\{ \int \left( \frac{(\bar{r} \bar{D})'}{\bar{r} \bar{D}} + \bar{E}' \right) d\bar{r} \right\} \quad (\text{A8})$$

$$q(\bar{r}) = \frac{p(\bar{r})}{\bar{D}} \quad (\text{A9})$$

$$w(\bar{r}) = p(\bar{r}) \left[ \frac{\bar{D} \bar{E}' + \bar{r} (\bar{D} \bar{E}')'}{\bar{r} \bar{D}} \right] \quad (\text{A10})$$

Following Silebi and McHugh [15], we multiply Equation A7 by an arbitrary estimating function  $F$  for  $\rho$ , integrate by parts, and rearrange to form the Rayleigh quotient:

$$\lambda = \frac{\int_0^{1-\kappa} [p(F')^2 - wF^2] d\bar{r} - (pFF')|_0^{1-\kappa}}{\int_0^{1-\kappa} q F^2 d\bar{r}} \quad (\text{A11})$$

As long as  $F$  satisfies the symmetry and no-flux boundary conditions, and is twice continuously differentiable, numerical integration of Equation A11 calculates the upper bound of the smallest eigenvalue. An appropriate estimating function for the radial concentration profile of the particles is:

$$F(\bar{r}) = [1 + a\bar{r} + b\bar{r}^2 + c\bar{r}^3] e^{-\bar{E}} \quad (\text{A12})$$

The exponential factor is the fully developed concentration profile, obtained by solving the radial component of the diffusion equation when the total radial flux is

zero. The constants in Equation A12 are found by applying the boundary conditions and the orthogonality condition:

$$\int_0^{1-\kappa} \bar{F} \bar{r} \, d\bar{r} = 0 \quad (\text{A13})$$

Thus result Equations A14 through A16:

$$a = \bar{\Phi}' \Big|_{\bar{r}=0} \quad (\text{A14})$$

$$b = \frac{\left| \begin{array}{cc} -\bar{\Phi}' \Big|_{\bar{r}=0} & 3(1-\kappa)^2 \\ -\int_0^{1-\kappa} \bar{r}(1 + \bar{r}(\bar{\Phi}')) \Big|_{\bar{r}=0} e^{-\bar{E}} \, d\bar{r} & \int_0^{1-\kappa} \bar{r}^4 e^{-\bar{E}} \, d\bar{r} \end{array} \right|}{\left| \begin{array}{cc} 2(1-\kappa) & 3(1-\kappa)^2 \\ \int_0^{1-\kappa} \bar{r}^3 e^{-\bar{E}} \, d\bar{r} & \int_0^{1-\kappa} \bar{r}^4 e^{-\bar{E}} \, d\bar{r} \end{array} \right|} \quad (\text{A15})$$

$$c = \frac{\left| \begin{array}{cc} 2(1-\kappa) & -\bar{\Phi}' \Big|_{\bar{r}=0} \\ \int_0^{1-\kappa} \bar{r}^3 e^{-\bar{E}} \, d\bar{r} & -\int_0^{1-\kappa} \bar{r}(1 + \bar{r}(\bar{\Phi}')) \Big|_{\bar{r}=0} e^{-\bar{E}} \, d\bar{r} \end{array} \right|}{\left| \begin{array}{cc} 2(1-\kappa) & 3(1-\kappa)^2 \\ \int_0^{1-\kappa} \bar{r}^3 e^{-\bar{E}} \, d\bar{r} & \int_0^{1-\kappa} \bar{r}^4 e^{-\bar{E}} \, d\bar{r} \end{array} \right|} \quad (\text{A16})$$

Direct numerical integration of Equation A11 calculates the smallest eigenvalue of the diffusion equation, and hence, the minimum residence time required to fully develop the radial particle concentration profile. In the absence of colloidal and inertial forces, and assuming constant diffusivity, the analytical solution of the above equations results in  $\lambda = 14.7 D/(1 - \kappa)^2$ . For zero particle size, this is the same result obtained from Taylor's analysis of the dispersion of a molecular species in laminar flow.



Literature Cited

1. Taylor, G.I. Proc. R. Soc. Lond. 1954, **A225**, 473.
2. Aris, R. Proc. Roy. Soc. A 1956, **235**, 67.
3. DiMarzio, E. A.; Guttman, C. M., Macromolecules 1970, **3**, 131.
4. Noel, R.J.; Gooding, K. M.; Regnier, F.E.; Ball, D.M.; Orr, C.; Mullins, M.E. J.Chromat. 1978, **166**, 373.
5. Brough, A.W.J.; Hillman, D.E.; Perry, R.W. J. Chromat. 1981, **208**, 175.
6. McHugh, A.J. CRC Critical Reviews in Analytical Chemistry 1984, **15**, 63.
7. Segre, G.; Silberberg, A. J. Fluid Mech. 1962, **14**, 136.
8. Silebi, C. A.; DosRamos, J. G. J. Coll. and Interf. Sci. 1989, **130**, 14.
9. DosRamos, J. G.; Silebi, C. A. J. Coll. and Interf. Sci. 1989, **133**, 302.
10. Silebi, C. A.; DosRamos, J. G. AIChE J. 1989, **35**, 1351.
11. Brenner, H. Progress in Heat and Mass Transfer 1972, **6**, 509.
12. Ananthakristan, V. ; Gill, W. N.; Barduhn, A. J. AIChE J. 1965, **11**, 1063.
13. Brenner, H.; Gaydos, L.J. J. Colloid Interf. Sci. 1977, **58**, 312.
14. Nagy, D. J., Silebi, C.A.; McHugh, A.J. J. Colloid Interf. Sci. 1981, **79**, 264.
15. Silebi, C. A.; McHugh, A. J. J. Polymer Sci: Physics 1979, **17**, 1469.

RECEIVED January 14, 1991

## Chapter 18

# Eluant Composition Effects on the Separation Factor in Capillary Hydrodynamic Fractionation (CHDF)

J. Venkatesan<sup>1</sup>, J. G. DosRamos<sup>2</sup>, and C. A. Silebi<sup>1</sup>

<sup>1</sup>Department of Chemical Engineering and Emulsion Polymers Institute, Lehigh University, Bethlehem, PA 18015-3590

<sup>2</sup>Matec Applied Sciences, Hopkinton, MA 01748

The effects of the molecular weight, concentration and eluant velocity on the separation factor of monodisperse polystyrene latexes in CHDF are reported for several surfactants. The surfactants used include ionic and nonionic surfactants with different hydrophobic groups and hydrophilic-lipophilic balance (HLB). The results show that the molecular weight and concentration of the nonionic surfactants have a significant effect on the separation factor. When the high molecular weight surfactant contains considerable amounts of ionic impurities, their separation factor is smaller than either the cleaned surfactant or a lower molecular weight surfactant relatively free of ionic impurities. With the lower molecular weight ionic surfactant, sodium lauryl sulfate (SLS), a decrease in its concentration results in increases in the separation factor. In general, at equivalent ionic strengths the values of the separation factor were greater with nonionic surfactants than with the low molecular weight ionic surfactant. The separation factors determined with the lower molecular weight anionic surfactant were used to determine the hydrodynamic thickness of the layer of non-ionic surfactants adsorbed on the latex particles. An estimation of the thickness of the adsorbed nonionic surfactant led us to conclude that the osmotic repulsion is effective at distances greater than the thickness of the adsorbed surfactant.

The application of flow through packed column methods to characterize the size of colloidal particles was first described in 1971 by Krebs and Wunderlich (1), who observed a difference in elution times when polymer latex particles were suspended in a fluid pumped through columns packed with porous silica. Five years later H. Small(2), using columns packed with nonporous beads, pioneered the development of column particle chromatography; this technique has come to be known as hydrodynamic chromatography (HDC). One important characteristic of HDC is that it allows the size analysis of colloidal particles in different environments, such as

0097-6156/91/0472-0279\$06.00/0

© 1991 American Chemical Society

those used in the final formulation of polymer latexes in which different pH, surfactants, thickeners and electrolytes are used at various concentrations. The separation mechanism in HDC has been described in terms of the convected Brownian motion of the particles through the interstitial region, modeled as an array of interconnected capillary tubes, and subject to colloidal forces and steric exclusion effects(3-5). According to the theoretical analysis, the mechanism of size separation by flow through conduits is due to two effects: (i) the laminar velocity profile of the fluid inside the conduit and (ii) the steric exclusion of the particles from the slower velocity streamlines next to the wall of the capillary. Because the smallest particles can approach the wall most closely, where the velocity approaches zero, they will on the average be the slowest to move down the capillary. Thus, because of these two effects, the average velocity of the particles will be greater than that of the eluant, with the average velocity of the particle increasing with the size of the particle. In addition to these two effects, the average velocity of the particle is also affected by the interaction between the particles and the wall of the capillary arising from the double layer electrostatic repulsion and the van der Waals attraction. Increasing the electrostatic repulsion between the particles and the surface of the packing will force the particles to radial positions further away from the wall of the capillary.

Not surprisingly, a few years later, narrow bore capillary tubes were used to separate by size micrometer sized particles(6-8). Although these studies reported differences in elution times of different size submicron particles, the resolution obtained was not good enough to obtain analytical separations of bimodal mixtures of submicrometer sized particles, primarily due to the large diameters of the capillaries used. In all these earlier investigations, the diameter of the capillaries used were greater than 100 micrometers. Recently, de Jaeger et al. (9) improved the resolution of particle separation in capillary tubes by using gelatines of high molecular weights and several synthetic water soluble polymers which, when dissolved in the eluant stream, adsorb on both the capillary wall (reducing the effective capillary diameter) and the particle surface (increasing the effective particle size). These investigators were able to obtain partial separations of submicrometer particles from samples containing mixtures of different monodisperse standards. Although the values of the separation factor,  $R_f$  (dimensionless rate of transport, experimentally obtained from the ratio of peak elution time of a molecular species to the peak elution time of the colloidal particle), reported by de Jaeger et al. were greater than those obtained by Small (2) in separations by flow through non-porous packed columns (HDC), the fractionation obtained was not better than that in HDC, primarily due to excessive axial dispersion caused by the increase in eluant viscosity and the large diameter of the capillary tube.

Although the best gelatine based eluant system used by De Jaeger et al. (9) in their capillary hydrodynamic separations was a high molecular weight gelatine, these investigators found that the differences observed were not due solely to variations in the molecular weight of the gelatine in the eluant, which creates a steric barrier both on the capillary wall and the particles, but also to the fact that the gelatine is an amphoteric polyelectrolyte, providing an electrostatic repulsion between the particles and the capillary wall which forces the particles to travel in higher velocity streamlines away from the capillary wall. In their experiments with polyvinylalcohol and carboxymethylcellulose in the eluant, the separation obtained resulted in smaller values of  $R_f$  than those obtained for the gelatines. Furthermore, the use of polystyrene sulfonic acid in the eluant made it impossible to obtain a stable baseline. Nonionic surfactants have also been used by de Jaeger et al. in order to increase the separation factor in capillary tubes. In particular, De Jaeger et al. also studied the effect of concentration of Pluronic F109, a nonionic water-soluble block copolymer

surfactant (molecular weight 14,600 Daltons and HLB >24) produced by BASF, and found that a 1.5% by weight concentration of Pluronic gave the highest  $R_f$  value and the narrowest fractogram. Results with other nonionic surfactants in flow through packed columns HDC have also shown a very small increase in the separation factor (10).

Apart from these studies, no systematic studies have been carried out on the effect of well-defined long chain nonionic surfactants on the separation factor. In particular, the influence of the molecular weight of a specific polymer and the length of either the hydrophobic or hydrophilic groups in the molecule of different homologues on the same latex can be expected to affect the separation behavior. We have recently reported the analytical separation of submicrometer particles by capillary hydrodynamic fractionation using smaller diameter capillaries (11-14). Our theoretical results show that the repulsive interaction between the surface of the capillary and the colloidal particles play a significant role on the fractionation. Knowledge of the interaction potential between the particles and the wall of the capillary in the presence of adsorbed layer of polymer thus provide important information for the prediction of the separation factor of the colloidal particles. Thus, a more detailed understanding of the adsorption characteristics on colloidal particles would also make it possible to predict the effect of adsorbed polymers on the elution behavior of the colloidal particles in capillary hydrodynamic fractionation (CHDF).

Interfacial properties of polymer solutions are of interest in many fields. One aspect which has attracted great interest is the interaction between solid surfaces separated by a polymer solution. The presence of polymer chains may influence the forces between the surfaces in two different ways, depending on the nature of the interactions between the macromolecules and the surfaces:

(i) if this interaction is attractive to both surfaces, the polymer chains are adsorbed. In such a case, the effective interaction between the surfaces is repulsive (15-17).  
(ii) When the surface-polymer interaction is repulsive or vanishes, the situation is quite different. The concentration of polymer vanishes at the surface and increases with the distance from the surface, reaching the bulk concentration at a distance of the order of the correlation length of the polymer in solution. This leads to a positive interfacial energy and therefore to an attraction between the surfaces since the system tends to minimize its total free energy (18).

Since both the ionic strength and the presence of nonionic surfactants in the eluant can affect the separation factor, in this study we used eluant solutions containing different concentrations of an anionic surfactant: sodium lauryl sulfate (SLS); as well as solutions of two nonionic water-soluble surfactants of different molecular weights: Pluronic (BASF) and Triton (Rohm and Haas). These two nonionic surfactants were chosen for our study since nonionic surfactants of the poly(ethylene oxide)/alkyl ether type are extensively used as emulsifiers and dispersants of polymer latexes and are known to be adsorbed onto most of them including polystyrene latexes (19,20) as well as silica surfaces (20). Another important factor in the selection of the nonionic surfactants is based on the interaction between the particle surface and the surfactant molecules. It has been reported that, in the adsorption of anionic and nonionic emulsifier on polystyrene latex particles, the adsorption decreases with decrease in hydrophobicity of the surfactant i.e. increasing HLB. An optimum HLB range was found to be 14-15 for maximum adsorption of nonionic surfactants at a polystyrene latex particle. The effects of the surfactant's molecular weight, concentration and type on the separation factor at different eluant average velocities are reported. Several studies in our labs and elsewhere on the adsorption of these anionic and nonionic surfactants on latex particles of different chemical composition have been published (19-21), allowing us to choose the appropriate concentration of the surfactants in the eluant.

## Experimental

**Instrument.** The CHDF flow system used has been described previously (6,7); a schematic diagram of the instrument is shown in Figure 1. It can be described briefly as follows: from a reservoir, a dilute solution of surfactant is pumped by a Laboratory Data Control Mini-Pump (Model 2396) equipped with a pulse dampener. The surfactant solution flows through the injection valve (Rheodyne 7125), where 20  $\mu\text{l}$  of the sample is loaded and injected into the continuously flowing surfactant solution. The sample is diluted before injection to a weight fraction of approximately 1% solids with a solution having the same composition as the eluant pumped through the microcapillary. In this study, the eluant used is an aqueous solution of either a nonionic or an anionic surfactant. Prior to use, the eluting solution is filtered through a 1.0 micrometer Nucleopore filter membrane to prevent extraneous material from fouling the system. The eluting solution is delivered to the microcapillary at a constant pressure using a Milton Roy Mini-Pump. Since the flow in the microcapillary is laminar (the calculated Reynolds numbers were always less than 1), and the eluant is a newtonian fluid, the inside diameter of the fused silica capillary tube used in this study was determined hydrodynamically from pressure drop-average fluid velocity measurements, using the Hagen-Poiseuille equation (22). The inside diameter obtained from the Hagen-Poiseuille equation was 6.5  $\mu\text{m}$ . The length of the microcapillary used was 2 m. The detector used is a Laboratory Data Control Model SM4000 variable wavelength spectrophotometer.

**Materials.** A series of very uniform polystyrene latices with diameters ranging from 0.088–0.357  $\mu\text{m}$  were used in this study. Typical sample preparation consisted of diluting a few drops of the concentrated latex dispersion in about 2 ml of the corresponding eluant used in the CHDF unit. Following sonication for about 1 minute, the sample was injected into the CHDF eluting stream.

Sodium lauryl sulfate (SLS), 98% pure (Stephan Chemical Company), was purified by recrystallization from boiling ethanol, followed by extraction with anhydrous ethyl ether (Fisher, certified grade) and then dried in a vacuum oven.

In this study we used two kinds of commercially available nonionic surfactants: Pluronic (BASF Corp.) surfactant and Triton (Rohm and Haas) surfactant. Pluronics are water soluble polyethylene oxide-polypropylene oxide-polyethylene oxide block copolymers where the propylene oxide is the hydrophobic group which will be preferentially adsorbed onto the surface of the more

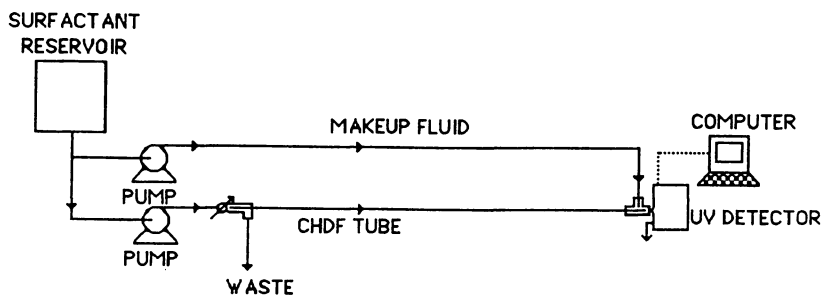


Figure 1: Schematic diagram of CHDF apparatus.

hydrophobic polymer surface of the latex particles. The molecular structures of these surfactants are: Pluronic HO-(CH<sub>2</sub>CH<sub>2</sub>O)<sub>X</sub>-CH<sub>2</sub>CH(CH<sub>3</sub>)O<sub>Y</sub>-(CH<sub>2</sub>CH<sub>2</sub>O)<sub>X</sub>-H, polyethylene oxide-polypropylene oxide-polyethylene oxide block copolymer. Pluronics of three molecular weights were used in this work: Pluronic (BASF) L35, F68 and F127 with molecular weights of 1900 (hydrophobe: 950), 8400 (hydrophobe: 1680) and 12600 (hydrophobe: 3780) respectively, their corresponding HLB values are: 18-23, >24 and 18-23 in order of increasing molecular weight. The Triton surfactant used are octyl phenol polyether alcohols. The molecular structure of the Triton used in this work is: C<sub>8</sub>H<sub>17</sub>C<sub>6</sub>H<sub>4</sub>(OC<sub>2</sub>H<sub>4</sub>)<sub>X</sub>OH with values of x = 10, 40 and 70 (with commercial names Triton X100, X408 and X705); their molecular weights are: 628, 1966 and 3286 respectively, with corresponding HLB values of 13.5, 17.9 and 18.7. They will be denoted OP-E10, OP-E40 and OP-E70, respectively. The Pluronic surfactants were used in two forms: first, as received from the manufacturer and second, after removing the ionic species present in the commercial surfactant. The presence of ionic species, as impurities or byproducts from the manufacturing process of the surfactant, in some of these nonionic surfactants was made evident by comparing the conductance measurements (shown in Table I for the three molecular weights used in this study) for aqueous solutions using the cleaned and the commercial Pluronic and Triton surfactants at a concentration of 0.5% by weight. Also included in Table I are the conductivities of several concentrations of the anionic surfactant SLS.

The electrolytes in the surfactant solution were removed by stirring an ion exchange resin in the solution until the electrolyte level was brought down to the desired concentration. The electrolyte level was monitored by conductance measurements. The ion exchange resin comprised of a mixture of a cationic exchange resin (20-50 mesh hydrogen form) and an anionic exchange resin (20-50 mesh chlorine form), manufactured by Bio-Rad laboratories. The total amount of ion exchange resin used was approximately 10% of the weight of surfactant in solution. The cationic and anionic resins were mixed in 50:50 weight ratio. The water was distilled and deionized, with a conductivity less than 1 μS.

Table I. Conductance of 0.5% by Weight Aqueous Solutions of Nonionic Surfactants and several Molar Concentrations of SLS

Surfactant	Molecular weight (Daltons)	Conductivity (μS)	
		Commercial	Cleaned
Pluronic L35	1900	0.9	0.9
Pluronic F68	8400	7.3	1.5
Pluronic F127	12600	100.0	1.3
Triton X100	628	7.5	---
Triton X405	1966	11.0	---
Triton X705	3286	8.7	---
SLS 1 mM	288		57.5
SLS 0.5 mM	288		33.0
SLS 0.1 mM	288		7.8

**The Separation Factor:** Particle separation has been quantified experimentally in terms of the separation factor,  $R_f$ , determined experimentally by the ratio of elution times associated with the marker peak and the particle peak. Thus

$$R_f = \frac{t_m}{t_p} \quad (1)$$

where  $t_m$  and  $t_p$  denote the elution time of the marker and particle peaks respectively. In order to prevent flocculation of the latexes, induced by the ionic marker species, both the marker species and the monodisperse standards are injected separately and their elution times measured.

### Results and Discussion

The long chain nonionic surfactant should be used at a concentration at which the latex particles will be completely covered with the adsorbed long chain nonionic surfactant, since it is well known that partial coverage may result in flocculation of the colloidal dispersion by particle bridging. Adsorption studies have shown that a concentration range of 1.5-3 times the critical micellar concentration of the nonionic surfactant will be sufficient to completely cover the particle surface with the adsorbed surfactant (19). Since full coverage is not reached at the critical micelle concentration but at slightly higher concentrations, the affinity of the hydrocarbon tail to itself must be greater than its affinity to the slightly more polar surface of the polymer particle.

The effect of the ionic strength on the separation factor in CHDF has been previously reported (11) and is further illustrated in Figure 2 for the microcapillary used in this study. As shown in this figure, the separation factor increases with both increasing particle size and decreasing eluant ionic strength.

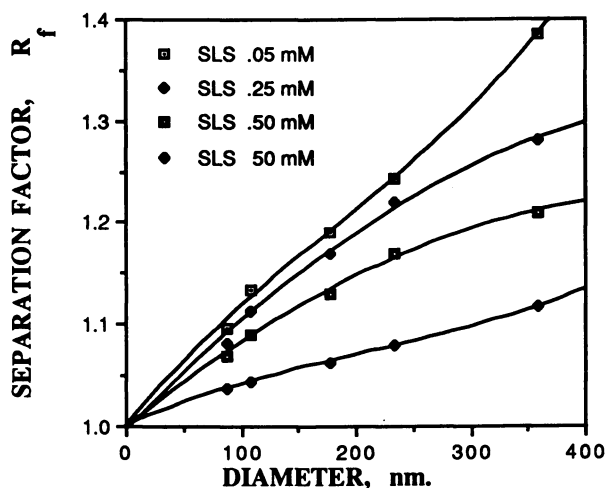


Figure 2: Separation factor-particle diameter for Sodium Lauryl Sulfate (SLS) at several molar concentrations. Eluant velocity: 2.7 cm/s

This ionic strength effect has been explained in terms of the double layer repulsive potential, which increases as the ionic strength decreases, pushing the particles away from the capillary surface into faster streamlines, and consequently increasing the particle separation factor (12).

The separation factor for the low (L35) and high (F127) molecular weight Pluronic used as received without any further purification is shown in Figure 3. Contrary to expectations, the separation factor is larger with the lower molecular weight surfactant. This may be attributed to the high concentration of ions in the solution of the higher molecular weight Pluronic, detected by the solution conductivity (see Table I). The high concentration of ions will both decrease the size of the electrostatic double layer and compress the size of the steric layer (due to a decrease in the solvency) of the adsorbed nonionic surfactant; as a consequence, the particles will be able to get closer to the wall of the capillary, sampling streamlines of slower velocities, thus decreasing their average velocity (i.e. their separation factor). On the other hand, when the ions or electrolytes present in the high molecular weight surfactant have been removed, the separation factor increases as the molecular weight of the surfactant increases, as shown in Figure 4.

Figures 5 and 6 show the variation of the separation factor with particle diameter at two eluant average velocities. The experimental results shown in Figure 5 were obtained using the uncleaned surfactant solution. The results obtained at the higher velocity display significantly greater separation factors than at lower velocity. The relatively high ionic strength of the surfactant solution compresses the ionic double layer around the colloidal particles. This decreases the influence of colloidal forces on the flow behavior of the particles. The radial hydrodynamic force (the tubular pinch effect (23, 24)) experienced by the particles at higher velocities leads to higher separation factors. At the lower velocity ( $v = 1.2$  cm/sec), the Brownian motion of the particles overcome the effect of the radial hydrodynamic force resulting in lower separation factors. Similar behavior is observed when ionic surfactant

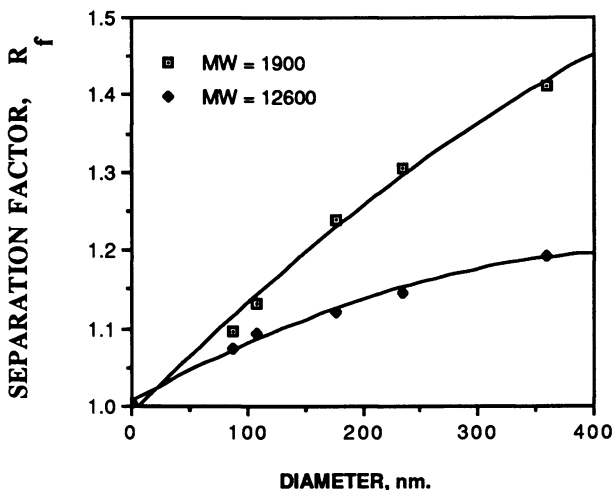


Figure 3: Separation factor-particle diameter data for uncleaned high and low molecular weight surfactants. Concentration: 0.5% Eluant velocity: 1.25 cm/s



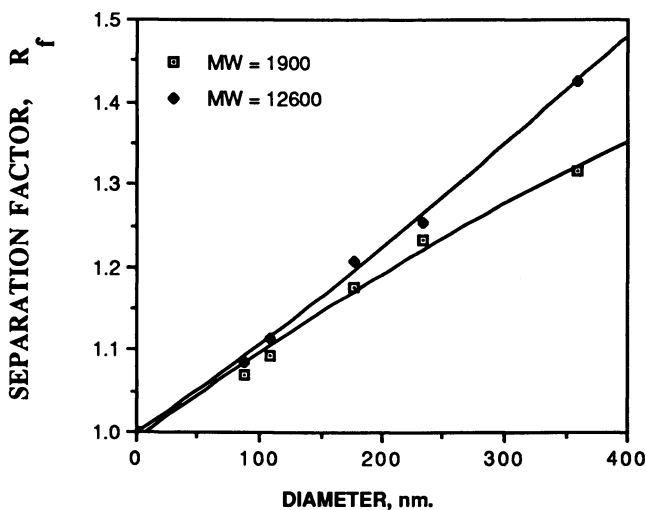


Figure 4: Separation factor-particle diameter data for cleaned high and low molecular weight surfactant. Concentration: 0.05% Eluant velocity: 1.25 cm/s

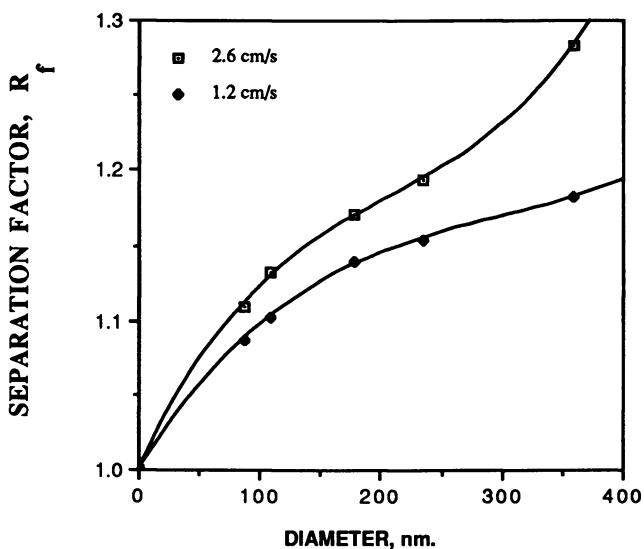


Figure 5: Separation factor-particle diameter at two eluant velocities. Surfactant: uncleaned Pluronic F127 Concentration: 0.05%

solutions are used as the eluant (12). Figure 6 shows the variation of the separation factor with particle diameter using the cleaned surfactant. Because the conductivity is now about two orders of magnitude smaller, there is a smaller concentration of ions in the solution; which will increase the thickness of the ionic double layer around the particles which increases the electrostatic repulsion between the particles and the wall of the capillary pushing the particles into faster streamlines away from the wall of the capillary. Under these conditions, the colloidal forces appear to dominate the tubular pinch effect, and the average velocity of the particles (i.e. the separation factor) is not significantly affected by the fluid inertial forces.

Figure 7 shows the variation of the separation factor with particle diameter for two different concentrations (weight percent) of the Pluronic F68 surfactant in the eluant. In this concentration range, a higher concentration of the surfactant produces higher values of the separation factors. More concentrated surfactant solutions allow for a more uniform adsorption of the surfactant on the particle and the capillary wall, thus reducing the effective diameter of the capillary tube. Therefore, surfactant solutions with higher concentrations of the surfactant result in higher separation factors up to a saturation concentration beyond which further increase of the surfactant concentration does not affect the separation factor. This concentration effect has also been observed with the other molecular weight Pluronic surfactants. However, when aqueous solutions of Triton are used in the eluant the effect of surfactant concentration is dependent on the critical micellar concentration of the particular surfactant. Figure 8 shows the variation of the separation factor with concentration of OP-E40 for five different particle sizes. The separation factors reach a maximum at an intermediate concentration around 0.3-0.5%, which corresponds to approximately 1.5 to 3 times the cmc of OP-E40. This behavior has also been observed with OP-E10 and OP-E70. This may appear to contradict the conclusions discussed earlier on the Pluronic surfactant concentration effect. It should, however, be noted that triblock copolymers of ethylene oxide and propylene oxide (Pluronics) have been shown to possess anomalous association behavior in aqueous solution due to the enhanced dehydration with temperature (25, 26).

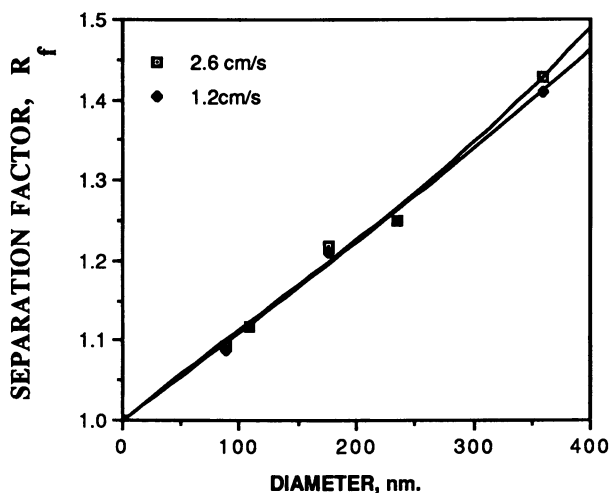


Figure 6: Separation factor-particle diameter at two eluant velocities. Surfactant: cleaned Pluronic F127 Concentration: 0.05%

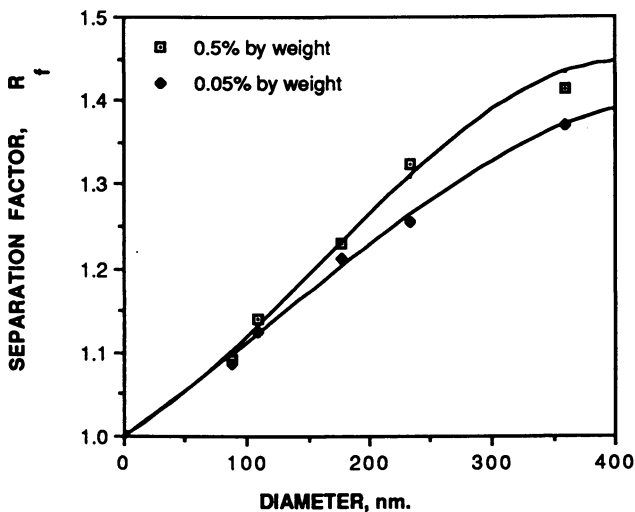


Figure 7: Separation factor-particle diameter at two concentrations. Surfactant: cleaned Pluronic F68. Eluant velocity: 1.2 cm/s

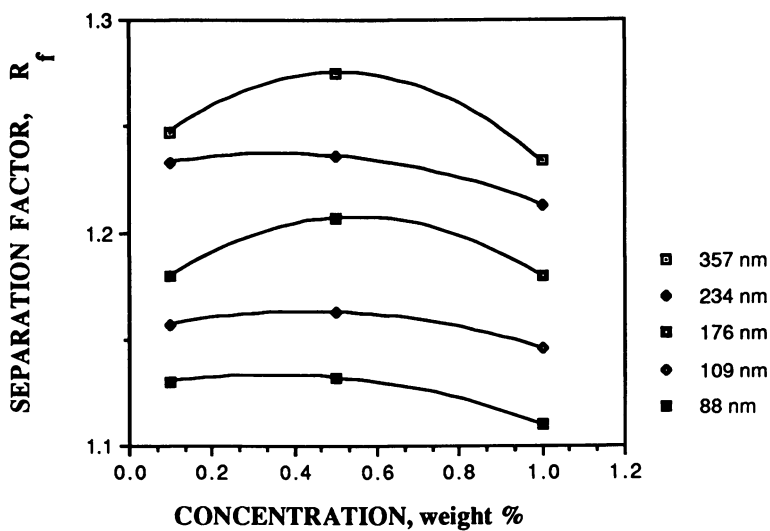


Figure 8: Separation factor-concentration for nonionic (OP-E40) surfactant. Eluant velocity: 1cm/s

At room temperature, Zhou and Chu (25, 26) found that these surfactants essentially exist in solution unassociated and do not exhibit micellization until higher temperatures (above  $\sim 50^{\circ}\text{C}$ ) are attained. As a result of this, any conclusions inferred on the surfactant concentration effects based on the cmc of the surfactant cannot apply in the case of the Pluronics.

A comparison between the 1% Pluronic F127 solution as eluant and two concentrations of the ionic surfactant Sodium Lauryl Sulfate (SLS) is made in Figure 9. As expected, the clean Pluronic surfactant gives larger separation factors than SLS solutions. It should be noted that, unlike the concentration effect observed with nonionic surfactants (Figure 7), for the ionic surfactant decreasing the concentration of SLS will increase the separation factor due to the increase in the electrostatic repulsion between the particle and the wall of the capillary.

When particles are coated with an adsorbed polymer layer, the rate of transport, (i.e average elution time), which depends on the size of the particles, must reflect the size of the particle core as well as the thickness of the adsorbed layer. Therefore the separation factor of a particle coated with an adsorbed layer should be greater than that of an uncoated particle. A simplistic interpretation of this increase in the separation factor by the adsorbed layer of nonionic surfactants is that this effect is due solely to an increase in the effective size of the colloidal particle. If this is the case, then we should be able to determine the thickness of the adsorbed layer by measuring the particle size. The procedure we followed for determining the thickness of the adsorbed layer around the latex particle consists of running two separate experiments in which the eluants have the same ionic strength (so that the electrostatic repulsion is the same): one containing the nonionic surfactant and the other free of the nonionic surfactant.

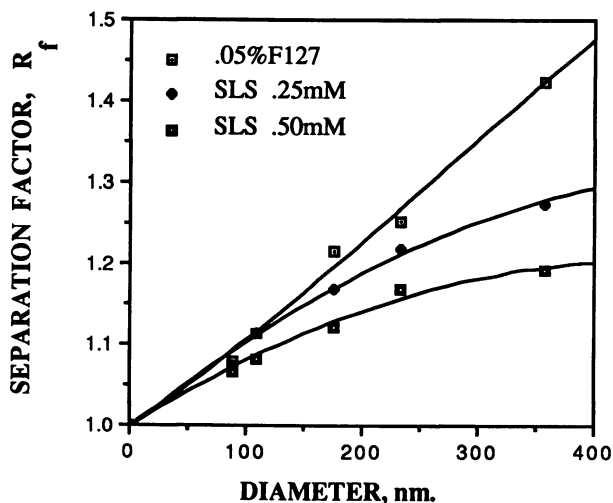


Figure 9: Separation factor–particle diameter for ionic (SLS) and nonionic (Pluronic F127) surfactants. Eluant velocity: 2.7 cm/s.

The results are shown in Figure 10 for OP-E10 and OP-E70. For OP-E10 (Triton X100), we found that the layer thickness ranged from 13 to 30 nm; considering the low molecular weight of this surfactant, we cannot attribute the increase in the separation factor to be solely due to an increase in the effective size of the particles due to the adsorbed layer. For both Triton and Pluronic surfactants, the adsorbed layer thickness for all these nonionic surfactants ranged from 13 to 74 nm, depending on the surfactant, the molecular weight, and the average velocity of the eluant. These values are 3 to 18 times greater than the thickness reported by Connor and Ottewill (27) who found a thickness of 4 nm for polyethylene oxide (molecular weight: 450) adsorbed on polystyrene latexes. Because these thicknesses are considerably larger than the random coiled size of the adsorbed surfactants, we conclude that the thickness of the adsorbed layer determined by CHDF reflects not only the steric effect but also the osmotic repulsive interaction between the particles and the surface of the capillary. It may also be argued that the large thickness of the adsorbed layer may be due to coagulation effects; however an increase in electrolyte concentration, which should enhance coagulation, did not result in a larger apparent diameter. Moreover, experimental studies by Doroszkowski and Lambourne (28) have shown that the range of repulsive forces between sterically stabilized spheres extended much further than the end-to-end distance of the adsorbed polymer molecules. We also found that for a homologous series of surfactants, an increase in molecular weight results in an increase in the thickness of the adsorbed layer; this is seen in Figure 10, and this can also be concluded for the Pluronics from Figure 4. However, comparing the Pluronic and Triton, we found that the Pluronic, with a molecular weight of 12600, gives a thickness essentially identical to that of the Triton, with a molecular weight of 3286. This result may be explained on the basis of the size of the hydrophilic groups in each of these surfactant molecules. In both surfactants the size of the hydrophilic groups, which extend into the aqueous medium, are nearly equal and as a consequence the thickness of the adsorbed layers should be similar.

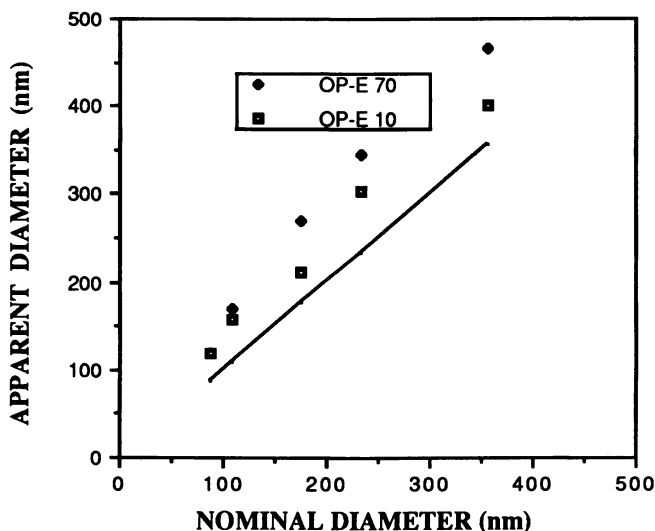


Figure 10: Apparent diameter for OP-E10 (M.W. 628) and OP-E70 (M.W. 3286); Concentration: 0.5% Eluant velocity: 1.0 cm/sec

### Conclusions

The results show that the molecular weight and concentration of the nonionic surfactants adsorbed on the latex particles have a significant effect on their separation factor. Moreover, our results show that a decrease in the concentration of a particular nonionic surfactant may result in either larger or smaller values of the separation factor, depending on whether ions are present in the solution. On the other hand, with the lower molecular weight ionic surfactants, the general trend is that a decrease in their concentration results in increases in the separation factor. In general, values of the separation factor were greater with nonionic surfactants than with ionic surfactants. The high resolution of CHDF can be used to determine the range of steric and osmotic repulsive effects induced by the adsorption of polymeric surfactants on the surface of dispersed colloidal particles.

### Literature Cited

1. Krebs, V. K.F., and Wunderlich, W. Angew. Makromol. Chem. 1971, **20**, 203.
2. Small, H. J. J. Colloid Interface Sci. 1974, **48**, 147.
3. Silebi, C. A., and McHugh, A. J. AIChE J. 1978, **24**, 204.
4. Prieve, D. C., and Hoysan, P. M. J. Colloid Interface Sci. 1978, **64**, 201.
5. Buffham, B. A. J. Colloid Interface Sci. 1978, **67**, 154.
6. Noel, R. J.; Gooding, K. M.; Regnier, F. E.; Ball, D. M.; Orr, C.; Mullins, M.E. J. Chromatogr. 1978, **166**, 373.
7. Mullins, M. E., and Orr, C. Int. J. Multiphase Flow 1979, **5**, 79.
8. Brough, A.W.J., Hillman, D.E., Perry, R.W. J. Chromatogr. 1981, **208**, 175.
9. DeJaeger, N. C., Trappers, J. L., and Lardon, P. Part. Charact. 1986, **3**, 187.
10. Small H.; Saunders, F. L.; Solc, J. Adv. in Colloid and Interface Sci., 1976, **6**, 237.
11. Silebi, C. A., and DosRamos, J.G. J. Colloid Interface Sci. 1989, **130**, 14.
12. DosRamos, J. G., and Silebi, C. A. J. Colloid and Interface Science 1989, **133**, 302.
13. Silebi, C. A., and DosRamos, J.G. AIChE J. 1989, **35**, 1351.
14. DosRamos, J. G., and Silebi, C. A. J. Colloid and Interface Science 1990, **136**, 3.
15. Edwards, S. F. Proc. Royal Soc. Ser. A 1978, **343**, 427.
16. Gerber, P. R.; Moore, M. A. Macromolecules 1976, **9**, 478.
17. Middlemiss, K. M.; Torrie, G. M.; Whittington, S. G. J. Chem. Phys. 1977, **66**, 3327.
18. Asakura, H.; Oosawa, A. J. Chem. Phys. 1954, **22**, 1255.
19. Krongberg, B.; Kall, L.; Stenius P. J. Dispersion Science and Technology 1981, **2**, 215.
20. Killmann, E.; Maier, H.; Baker, J. A. Colloids and Surfaces 1988, **31**, 51.
21. Ahmed, M. Ph. D. Thesis, Lehigh University, Bethlehem 1984.
22. Bird, R. B.; Stewart, E. N.; Lightfoot, W. Transport Phenomena, John Wiley: New York, 1960.
23. Segre, G.; Silberberg, A. Nature (London) 1961, **189**, 209.
24. Segre, G.; Silberberg, A. J. Fluid Mech. 1962, **14**, 136.
25. Zhou, Z; Chu, B. Macromolecules 1988, **21**, 2548
26. Zhou, Z; Chu, B. J. Colloid Interface Sci. 1988, **126**, 171.
27. Connor, P.; Ottewill, R. H. J. of Colloid and Interface Science 1971, **37**, 642.
28. Doroszkowski, A., and Lambourne, R. J. of Colloid and Interface Sci. 1973, **43**, 97.

RECEIVED January 14, 1991

## Chapter 19

# Size Analysis of Simple and Complex Mixtures of Colloids in the Submicrometer Range Using Capillary Hydrodynamic Fractionation

J. G. DosRamos<sup>1</sup> and C. A. Silebi<sup>2</sup>

<sup>1</sup>Matec Applied Sciences, Hopkinton, MA 01748

<sup>2</sup>Department of Chemical Engineering and Emulsion Polymers Institute, Lehigh University, Bethlehem, PA 18015-3590

The application of capillary hydrodynamic fractionation (CHDF) to mixtures of monodisperse particle samples is described. The particle size distribution of several polymer latexes with diameters ranging from 20 nm to 1000 nm was determined in less than 10 minutes using the fractograms obtained with the CHDF system. The distributions obtained were compared with those using electron microscopy. The reproducibility of the instrument is illustrated by successive analyses of several samples of different particle sizes. Capillary hydrodynamic fractionation is compared to two other fractionation techniques: hydrodynamic chromatography and sedimentation field flow fractionation. It is shown, using an example, that capillary hydrodynamic fractionation is sufficiently versatile to separate by size complex colloidal mixtures which have particles of different chemical composition and density.

Particle size analysis is important to the various fields of colloid science and technology because of the many properties which are directly related to the average particle size (PS) and particle size distribution (PSD). The stability and viscosity of colloidal suspensions and the opacity or gloss of films are just a few examples of properties affected by the size of the colloidal particles. Consequently there is widespread interest in methods for determining particle size and size distribution which are applicable to colloids. Although the number of methods used for particle size measurements is very large, all these methods can be divided into two major categories: (i) fractionation methods; and (ii) nonfractionation methods. A review of these techniques have been published by Barth et al. (1). CHDF belongs to the category of fractionation methods. As has also been indicated by Giddings et al. (2), an important advantage of fractionation methods over non-fractionation methods is that fractionation methods can, within certain limits, break down broad particle populations into their components, allowing further characterization by other methods such as the non-fractionation method of turbidimetric detection at several wavelengths. This paper will be concerned primarily with one relatively new method, capillary hydrodynamic fractionation (CHDF), which is applicable in the submicrometer range. Like most particle size methods, CHDF has a limited range

0097-6156/91/0472-0292\$06.00/0

© 1991 American Chemical Society

of usefulness, which for the system used in this investigation extends from about two hundredths of a micron up to about one micron. However, this is a range which presents problems for many other methods, especially if the dispersion has a multimodal distribution. Recently this technique has been developed to calculate accurate size distributions from the elution time-detector response data.

In capillary hydrodynamic fractionation, submicrometer colloidal dispersions are separated according to size by flow through a microcapillary tube (3-8). A size separation based on the laminar flow through capillaries was first proposed by DiMarzio and Guttman (9,10) as the separation mechanism in size exclusion chromatography (SEC). According to their theoretical analysis, the mechanism of size separation by flow through conduits is due to two effects: (i) the laminar velocity profile of the fluid inside the conduit and (ii) the steric exclusion of the particles from the slower velocity streamlines next to the wall of the capillary. Because the smallest particles can approach the wall most closely, where the velocity approaches zero, they will move most slowly down the capillary. Thus, because of these two effects, the average velocity of the particles will be greater than that of the eluent, with the average velocity of the particle increasing with the size of the particle. In addition to these two effects, the separation is also affected by the following: radial forces acting on the particles due to the fluid inertial effect; and the electrostatic repulsion and van der Waals attraction between the particles and the wall of the capillary. These two additional effects force the particles to radial positions further away from the wall of the capillary. Because this separation mechanism is based on a single liquid phase and does not involve the partitioning of the fractionating species between two phases, as in typical chromatographic separations, a separation due to hydrodynamic effects in a microcapillary tube is not a form of chromatography, as has been discussed previously by Giddings et al. (2). We have recently reported the analytical separations of synthetic mixtures of monodisperse polystyrene latex particles by capillary hydrodynamic fractionation (4). Under typical operating conditions in CHDF, larger latex particles elute from the capillary ahead of smaller ones, and water soluble molecular species (such as sodium benzoate) which are used as marker species elute last. Since different sized particles move at different velocities in this system, broad particle populations are sorted into different fractions as they elute from the capillary tube. Although the emphasis of our work has been on spherical polymer latexes, we have also applied the method to other spherical and nonspherical colloids.

The relevant experimental parameters involved in the CHDF separation process are: the particle diameter; ionic strength of the eluant; surfactant species and concentration; capillary diameter; and eluant average velocity. Theoretical and experimental studies of the effect of these parameters on the axial dispersion and the separation factor have been carried out previously (3-8). These aspects of CHDF will be discussed in another chapter in this volume.

This paper summarizes the fractionation capabilities of CHDF and the practical applications of CHDF for particle size determination for a variety of colloidal systems. Direct comparison to other well known fractionation methods is needed so that potential users might have a point of reference about the capabilities of CHDF. Recent results are presented which illustrate how CHDF is also useful as a means of obtaining average particle size and particle size distributions of complex colloids and commercial polydisperse latex systems.

### Experimental

Particle size distributions were determined using a CHDF 1100 (Matec Applied Sciences, Hopkinton, Massachusetts). The instrument consists of modular-type components, including a solvent delivery pump, pressure gauge, electronic high



pressure relief safety valve, prefilter, sample injection valve, separation microcapillary, ultraviolet flow-through detector, microcomputer, and a printer. A sample of each colloidal dispersion was prepared for CHDF particle size analysis. Each dispersion was first agitated slightly by shaking, then a few drops of the sample was diluted with the surfactant solution used as eluant in the CHDF system (typically having an ionic strength of 1 millimolar or less). Final weight percent concentration of the dispersions injected ranged from 0.3 to 2% by weight, depending on the strength of its response to UV light in order to generate CHDF detector signals in the appropriate range. In the case of carbon black, which was in a dried powder form, a dispersion was prepared by adding the same solution used as the mobile phase in the CHDF system to a few milligrams of the carbon black sample giving a final solid content of approximately 1% by weight. Finally, just prior to analysis, each one of the diluted samples were ultrasonicated for two minutes before injecting them into the eluting stream in the CHDF system.

SFFF measurements were performed using the programmed DuPont SFFF-1000 Particle Size Analyzer. In this unit, the field strength is reduced continuously during the run to condense broad particle distributions to a reasonable range of elution volumes (11-13). In this study, SFFF fractionations were obtained at two programmed operating conditions: (i) Standard operation mode, in which the initial spin velocity is 5000 rpm and decays exponentially with a time constant of 4 min. and, (ii) High resolution mode, in this case the initial spin velocity is 12000 rpm and the decay time constant is 4 min.

HDC measurements were made with a column 9 mm. ID, 0.5 m. in length packed in our laboratory with non-porous 18  $\mu$ m Styrene Divinyl Benzene beads. Band broadening was minimized by using the on-column injection system described elsewhere (14,15).

In practice, resolution in these fractionation methods can be amplified by increasing either the length of the separation path or, in the case of SFFF, the intensity of the applied force field. In the case of SFFF, we choose to run the fractionations at two programmed force fields so that the total elution time was under one hour. As for CHDF and HDC, we have arbitrarily chosen the separation pathlength such that the time of analysis is limited to no more than 10 minutes.

### Fractionation Efficiency

One of the most commonly used definition of the specific resolution between two species in chromatography theory is given by the difference between the mean elution times of the two species divided by the average of the widths of the fractograms at the base:

$$R_s = \frac{t_{p1} - t_{p2}}{2(\sigma_{p1} + \sigma_{p2})} \quad (1)$$

where  $t_{p1}$  and  $t_{p2}$  are the peak elution times of species 1 and 2 respectively, and  $\sigma_{p1}$  and  $\sigma_{p2}$  are the standard deviations of the fractograms of each species. Therefore  $R_s$  measures the ability of a fractionation method to resolve two populations. The significance of  $R_s$  in evaluating the efficiency of a separation stems from the well established fact that a complete fractionation is associated with a value of  $R_s$  equal to 1.5.

### Particle Size Analysis by CHDF

In CHDF, a flow-through detection system connected to the outlet of the capillary tube monitors the concentration of the fractionated particles. The passage of the

fractionated sample through the detector provides a signal output trace,  $F(t)$ , which will be referred to as the fractogram. A fractogram can never fully represent the distribution of colloid sizes in the injected sample: instrumental spreading and axial dispersion cause elution of a single species to occur over a range of elution times. Interpretation of a fractogram must therefore account for the axial dispersion, and requires an evaluation of instrumental spreading and correction of the detector response to obtain the true distribution of the injected sample.

The detector response at elution time  $t$ ,  $F(t)$ , can be expressed as (16):

$$F(t) = \int_0^{\infty} W(y)G(t,y)dy \quad (2)$$

where  $W(y)$  is the area under the total fractogram due to the species eluting with a mean residence time  $y$ , and  $G(t,y)$  is the normalized detector response for a truly monodisperse system with mean residence time  $y$ ;  $G(t,y)$  is called the instrumental spreading function. Considering the discrete version of Equation 2, and bearing in mind that all intervening functions are of finite length, for a polydisperse sample, the fractogram,  $F(t)$ , will be given by the sum of the contributions of each individual species, Equation 2 reduces to:

$$F(t) = \sum_{j=1}^n W_j G_j(t) \quad (3)$$

where  $W_j$  and  $G_j(t)$  are the contributions to the total fractogram area and the normalized spreading function of species eluting at a mean residence time  $t_j$ , respectively. The deconvolution of the fractogram which is simply the solution of Equation 3 in order to obtain  $W_j$ , requires an appropriate form of the spreading function. The total number of particles  $N_j$  of diameter  $D_j$  is related to  $W_j$  by:

$$N_j = \frac{2.303W_j}{R_{ext}\chi} \quad (4)$$

where  $\chi$  is the optical pathlength and  $R_{ext}$  is the extinction cross section. The extinction coefficient may be determined using the Mie theory of light scattering or experimentally with different particle sizes of well characterized standards of the sample being analyzed. When the injected sample is monodisperse, peak broadening occurs solely due to axial dispersion and instrumental nonidealities; if  $t_j$  is the mean residence time of the fractogram,  $F_j(t)$ , generated by the monodisperse sample, then the instrumental spreading function for this particle size is given by:

$$G_j(t) = \frac{F_j(t)}{\int_0^{\infty} F_j(t)dt} \quad (5)$$

Furthermore, to convert  $W(y)$  into a size distribution requires a relationship between the mean elution time of the particle  $t_j = y$  and the corresponding particle diameter  $D_j$  (i.e., a calibration curve). The fractograms of standard monodisperse samples may be used to construct a calibration curve relating the particle diameter  $D_j$  with its mean residence time,  $t_j$ , by:

$$\frac{t_m}{t_j} = 1 + aD_j + bD_j^2 + cD_j^3 \quad (6)$$

where the coefficients  $a$ ,  $b$  and  $c$  depend on the diameter of the capillary, ionic strength, eluent velocity, and surfactant concentration and type. While deconvolution techniques can provide particle size distribution curves from partially resolved peaks, the deconvolution must be based on assumptions about instrumental

band broadening and band shape. However, the use of a numerical method for deconvoluting the fractogram will allow us to use directly the normalized fractograms of the monodisperse standards, thus eliminating the need for a specific spreading function to characterize them. With varying degrees of success, several analytical and numerical methods have been suggested for deconvoluting (solving for  $W$ ) either Equations 2 or 3. We have applied several of these methods to determine particle size distributions from the chromatograms obtained by HDC(17), and have found that the numerical method proposed by Ishige et al. (18) seems to be not only the most simple but the most effective deconvolution method. It is a numerical method that does not require significant computing time. The method is based on the fact that  $F(t)$  always has a broader distribution than the input distribution  $W(y)$ . Consequently, if the calculated fractogram,  $F_i^*(t)$ , after the  $i$ -th iteration is broader than the experimental fractogram,  $F(t)$ , the assumed  $W_{j,i}$  must be sharpened to give a response closer to  $F(t)$ . The algorithm starts using  $F(t_j)$  as a first estimate of  $W_j$  that is assuming no axial dispersion (i.e.  $G(t,y) = \delta(t-y)$ , where  $\delta$  is the Dirac function), subsequent estimates are calculated by:

$$W_{j,i+1} = \frac{F_i^*(t_j)}{F(t_j)} W_{j,i} \quad (7)$$

where  $F_i^*(t_j)$  is the fractogram calculated using  $W_{j,i}$  and the subscript  $i$  indicates the iteration number. The procedure is repeated until  $F_i^*$  satisfies a convergence criterion or a limiting number of iterations is reached.

## Results

Table I summarizes the range of particle diameters and the type of colloidal dispersions which have been analyzed by CHDF. A variety of eluant ionic strengths, pH levels, and surfactant concentrations and types were used in these characterizations.

Figure 1 shows an example of a fractogram output of a mixture of unimodal samples (each one produced single peaks when run separately) of polystyrene particles each having 91- and 60-nm (nanometer) average diameters. The differential and cumulative particle size distributions have been obtained from this fractogram by

**Table I.** Summary of Colloidal Dispersions Analyzed by CHDF

Dispersion	Particle Diameter Range (nm)	Characteristics
Polystyrene	20-1100	Narrow and broad distributions
Neoprene	50-300	Polydisperse
Butadiene-styrene copolymer	20-400	Polydisperse
Carboxylated styrene latexes	20-700	Polydisperse
Polybutadiene	20-400	Polydisperse
Polyvinyl chloride	40-600	Narrow and broad distributions
Polyvinyl acetate	70-300	Polydisperse
Polymethyl methacrylate	20-1000	Narrow and broad distributions
Styrene miniemulsions	80-300	Polydisperse
Carbon black	40-400	Polydisperse
Silver Halide	40-800	Polydisperse
Dyaryl Yellow pigment	40-600	Polydisperse
Medium Chrome Yellow pigment	70-700	Polydisperse
Diamond powder	40-300	Polydisperse

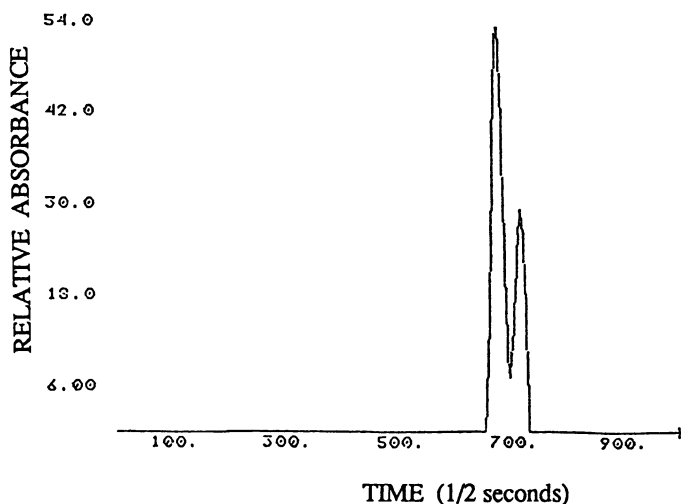


Figure 1: Fractogram from CHDF Data System.

two approaches: first by neglecting the instrumental spreading effect (that is, no deconvolution was applied, so  $W_j = F(t_j)$ ) and second by carrying out the deconvolution of the fractogram, using the method developed by Ishige et al. (18). The particle size distributions obtained with and without deconvolution are shown in Figures 2a and 2b. Figure 3 shows the fractogram for a mixture of polystyrene latex particles with average diameters of 91, 176, 234 and 400 nm. The presence of these four size populations is clearly seen in the fractogram. Noticeable is the nearly complete separation of the fractions with average diameters of 176 and 234 nm. Figures 4 show the differential and cumulative particle size distributions obtained from the deconvolution of this fractogram. Complete size distributions of synthetic latex mixtures and commercial samples having broad distributions have also been obtained by CHDF, and these results have been compared to those obtained by transmission electron microscopy. The PSD obtained by CHDF have been found to agree with those obtained by TEM. The fractogram for a commercial styrene-butadiene sample is shown in Figure 5. The cumulative particle size number distribution obtained by deconvoluting this fractogram is shown in Figure 6 along with the PSD obtained with the transmission electron microscope. Other comparisons with TEM particle size distributions have also been made using mixtures of well characterized standards and these results have shown good agreement between the two PSDs (7).

The particle size distribution of eight different carbon black dispersions (specific gravity = 1.86) were analyzed by CHDF (using monodisperse polystyrene latices as standards) and their volume averaged diameter compared with the corresponding average diameter determined using a Nicomp Model 270 Photon Correlation Spectroscopy (PCS). The results of these analyses are summarized in Table II, which presents the results of the volume, surface and number particle diameter averages determined by CHDF and the corresponding volume average diameter obtained from PCS. In addition, an average diameter obtained by dibutyl phthalate adsorption (DBPA) is also shown in Table II. A synthetic mixture of the CB2 polydisperse carbon black colloidal dispersion and the Dow standard narrow polystyrene with a nominal diameter of 234 nm were injected into the CHDF system, yielding the fractogram appearing in Figure 7.

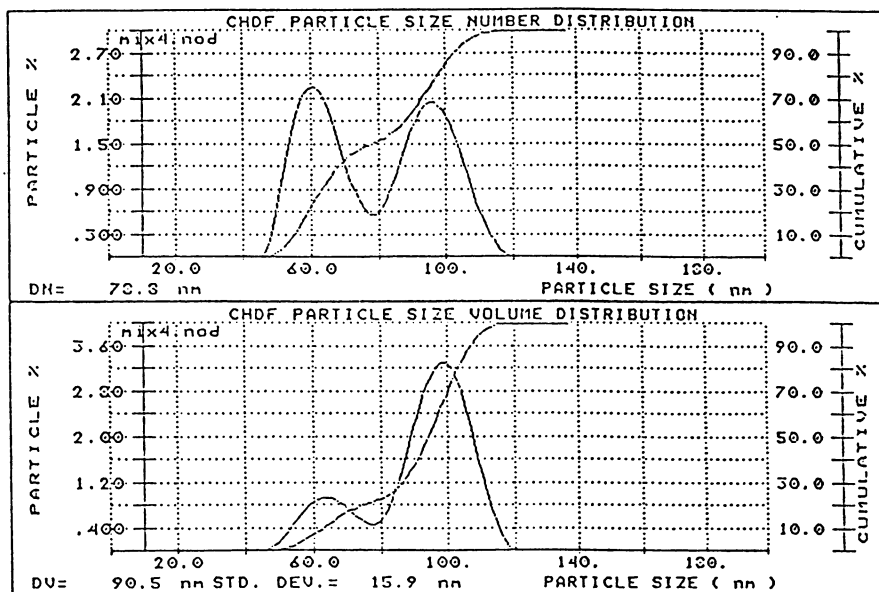


Figure 2a: Calculated PSD without deconvolution for the fractogram shown in Figure 1.

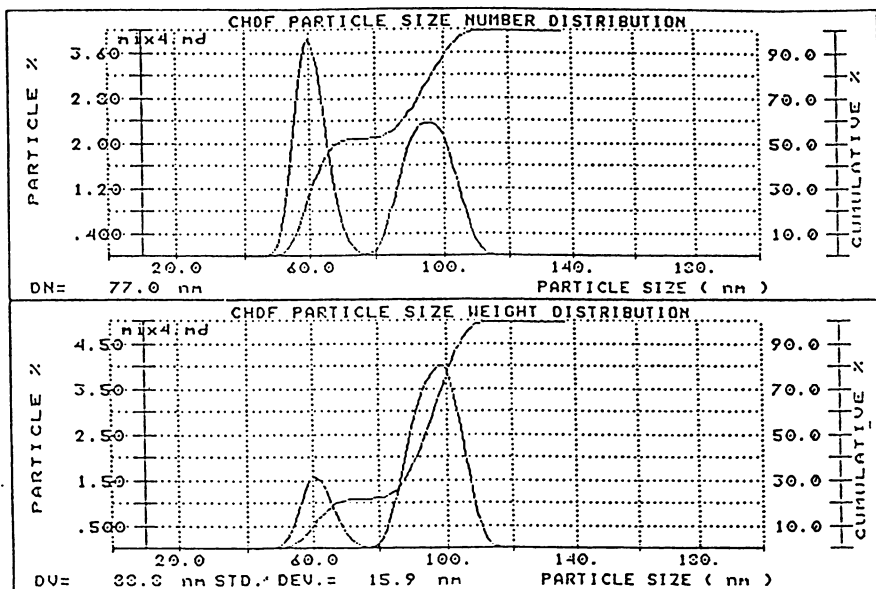


Figure 2b: Calculated PSD by deconvolution of the fractogram shown in Figure 1.

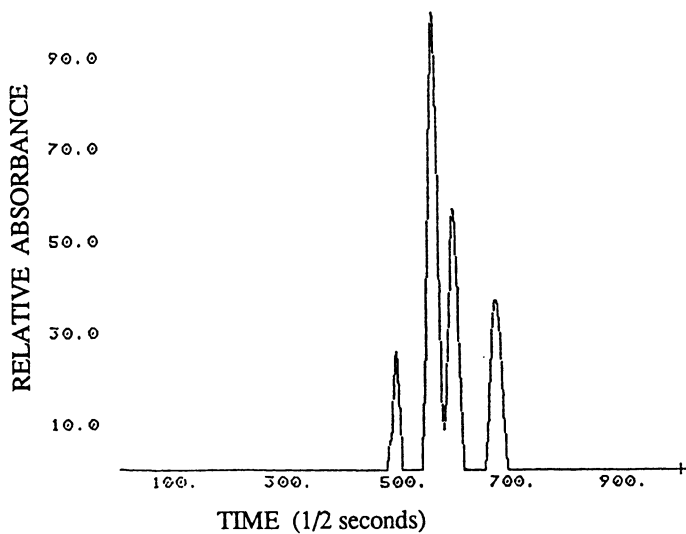


Figure 3: Fractogram from CHDF Data System.

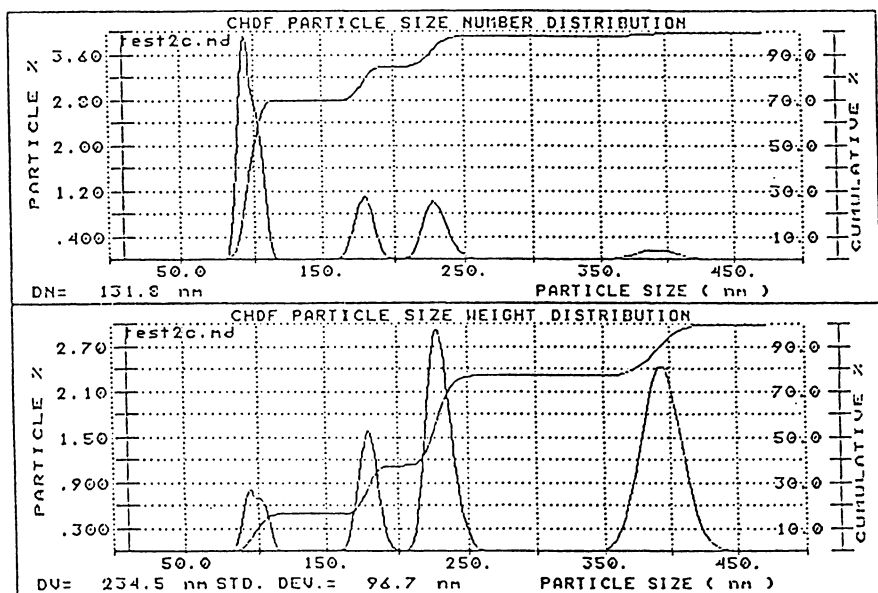


Figure 4: CHDF calculated PSD for the fractogram shown in Figure 3

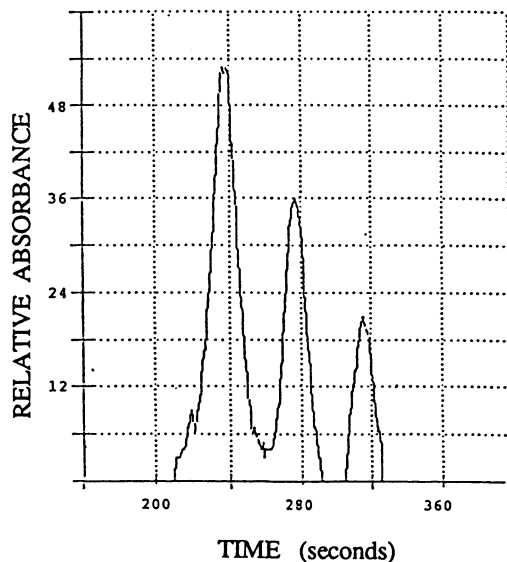


Figure 5: CHDF Fractogram of a commercial polystyrene-butadiene latex.

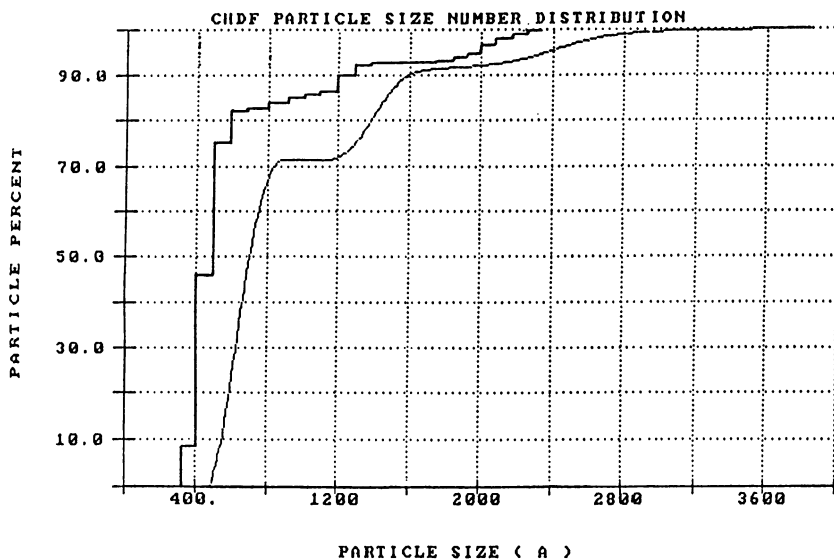


Figure 6: PSD for the sample in Figure 5. Continuous curve: Calculated PSD from the Fractogram in Figure 5. Bar Histogram: Electron Microscope data.

**Table II.** Particle Size Distribution Analysis of Carbon Black Colloidal Dispersions

Sample	Sizing Technique				
	CHDF		PCS	DBP	
	Number Ave. Diameter (nm)	Surface Ave. Diameter (nm)			
CB1	58	119	196	177	131
CB2	52	92	141	140	84
CB3	148	180	227	212	167
CB4	111	147	205	197	136
CB5	105	161	227	200	137
CB6	101	148	191	200	137
CB7	61	121	170	195	124
CB8	98	128	171	173	101

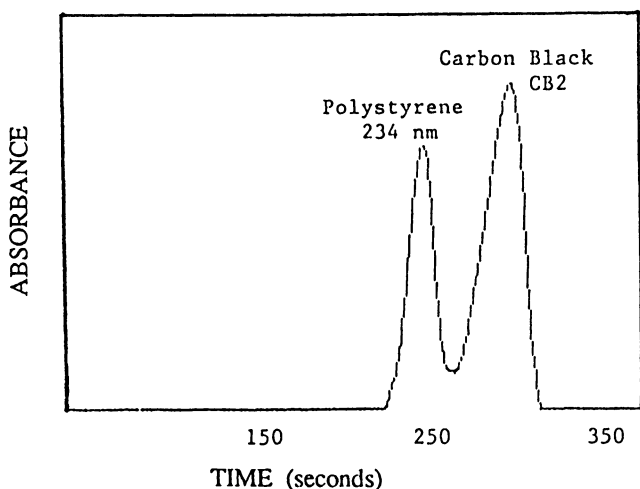


Figure 7: Fractogram of mixture of 234 nm polystyrene and CB2 carbon black.

Table III shows the number and weight average particle sizes and the standard deviation obtained after repeated injections of three different samples. The reproducibility in particle size analysis of latexes demonstrates the precision of the CHDF analysis (Table III). The experimental uncertainty in elution time corresponds to considerably less than 5% uncertainty in establishing the particle size of a latex with a narrow particle size distribution.

As an illustration of the resolving power of the fractionation in CHDF we have compared it with two other fractionation techniques: sedimentation field flow fractionation and hydrodynamic chromatography. Figures 8-11 illustrate the fractograms obtained from a trimodal latex mixture fractionated through the HDC column, the SFFF unit, and the CHDF system. We should mention that the PSDs (not shown) obtained for this sample for the two operating conditions of SFFF were different probably because deconvolution was not applied.



**Table III.** Particle Size Distribution Analysis: Reproducibility of CHDF

Sample Injection #		Number Average Diameter (nm)	Volume Average Diameter (nm)	Standard Deviation (nm)
PS1	1	33.5	45.6	10.5
	2	35.0	45.3	9.9
	3	36.6	44.7	9.4
	4	34.4	45.8	10.4
PS2	1	87.5	92.7	11.8
	2	87.4	93.6	12.5
	3	90.4	96.5	12.6
	4	89.9	94.4	12.5
PS3	1	249	250	11.0
	2	244	246	11.9
	3	245	246	11.4
	4	245	246	11.1

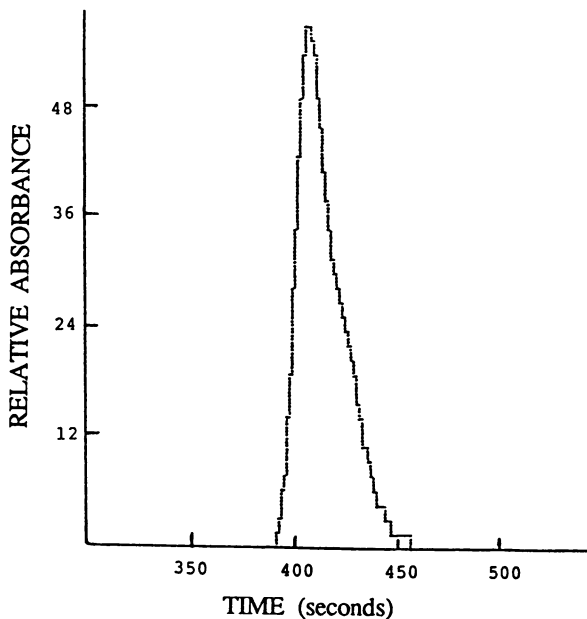


Figure 8: HDC Fractogram of mixture of 109, 176 and 234 nm. polystyrene standards.

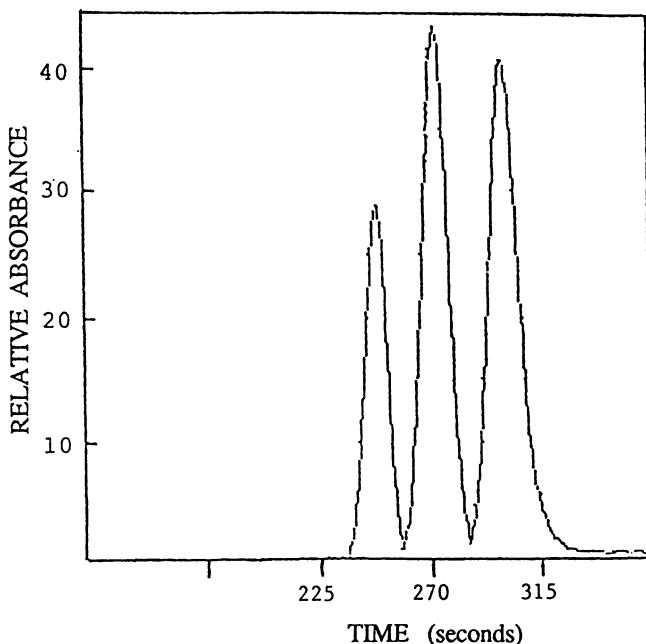


Figure 9: CHDF Fractogram of mixture in Figure 8.

In Table IV, we show the specific resolution of the three fractionation methods for several pairs of particle sizes. These specific resolutions were calculated from the fractograms obtained for each standard. In the case of SFFF, we have included results obtained at its normal (or standard) and high resolution operating condition. The second characteristic listed in Table IV is the elution time required for complete elution of the bimodal mixture.

### Discussion

In general, the accuracy of the determination of a size distribution curve will increase with the specific resolution exhibited by the system. A short time of analysis and high resolution is desirable to reach the ultimate goal of speed and accuracy in the determination of particle size distribution. Based on the results shown in these fractograms, one can conclude that the deconvolution is absolutely necessary to resolve or identify the partially separated populations in the case of HDC, because its specific resolution is low, but this is not the case for CHDF or SFFF where the different populations are easily identified because of their significantly greater specific resolution. However, as illustrated in Figures 2 and 4 deconvolution helps in resolving partially separated peaks. As we mention when the field strength was varied in SFFF the PSD obtained for the same sample also varied probably because of the lack of band broadening correction. Thus, even for these high resolution methods, deconvolution should always be applied in order to correct for band broadening due to the velocity distribution of the carrier fluid and the non-idealities in the injection and detection cells.

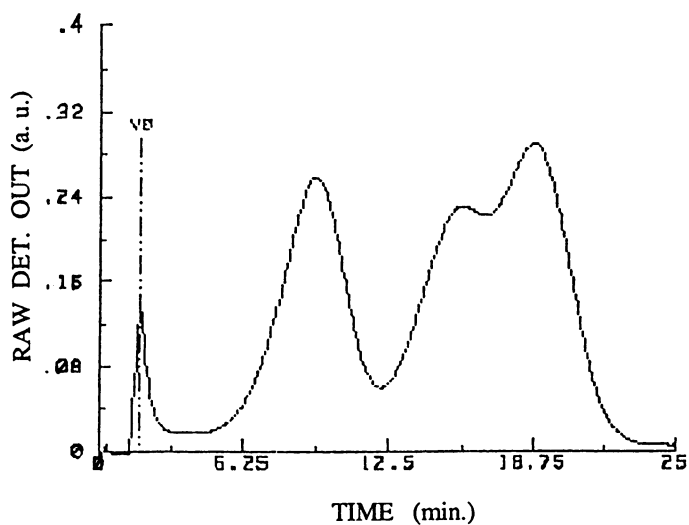


Figure 10: SFFF Fractogram of mixture in Figure 8 at 5000 rpm.

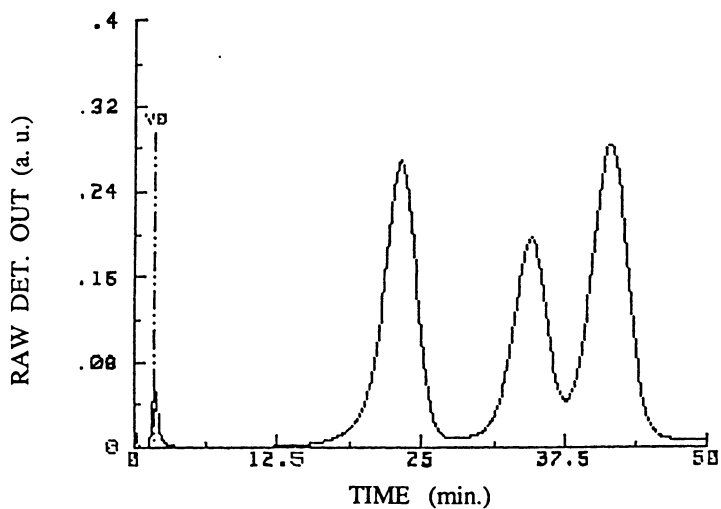


Figure 11: SFFF Fractogram of mixture in Figure 8 at 12000 rpm.

**Table IV.** Comparison of fractionation techniques with respect to: (i) specific resolution  $R_s$  of bimodal populations and (ii) the time (in minutes) for complete elution of the mixture  $t_{\max}$

Methods	Relative Particle Sizes							
	88/109		109/176		176/234		234/357	
	$R_s$	$t_{\max}$	$R_s$	$t_{\max}$	$R_s$	$t_{\max}$	$R_s$	$t_{\max}$
HDC	.22	6.5	.36	6.5	.35	6.0	.34	6.0
CHDF	.83	7.0	1.40	6.5	1.46	5.5	1.65	5.0
SFFF								
High Rsltn	1.08	27.0	1.69	38.0	.96	46.5	1.13	55.0
Standard Rsltn	.51	12.5	.93	19.0	.56	23.0	.71	28.5

One characteristic of CHDF is that the separation factor (the ratio of marker species and particle elution times, given by Equation 6) increases as the electrolyte concentration of the eluant decreases (3-5). This ionic strength effect certainly implies that the surface charge density of the particle plays a role and it might be expected to affect the separation factor of a latex, especially in the case of complex systems consisting of particles with varying surface charge densities. However, based on the following observations, we can conclude that the surface charge density has no effect on the separation factor: At eluant ionic strengths of  $10^{-3}$  M (molar) or less, dispersions of polymer latexes and carbon black particles of quite different electrophoretic mobility and similar particle sizes elute at a rate which is determined solely by their size, eluting at a rate consistent with the polystyrene calibration curve and with their size determined by other methods.

Therefore, although all latex particles undergo charge-induced electrostatic repulsion from the surface of the capillary, the thickness of the excluded region is dependent only on the ionic strength of the environment and is relatively insensitive to the charge of the colloid. This behavior can be understood by examining the electrostatic interaction energy associated with the overlapping ionic double layers, which at low ionic strength overwhelms the van der Waals attraction, making the electrostatic interaction to dominate the total potential of interaction between the wall and the particles which then will be insensitive to Hamaker's constant when the ionic strength of the eluant is low ( $10^{-3}$  M or less). Calculations of the separation factor based on the theoretical analysis of the separation mechanism in CHDF have shown that at low ionic strengths (less than  $10^{-3}$  M), neither surface charge nor Hamaker's constant significantly affect the average velocity of the particles (5). Similar theoretical and experimental conclusions were reached by several investigators in the case of separation by flow through packed columns (19-23). Therefore, the residence time of the particles in the capillary depends solely on their size and the ionic strength of the eluant but not on the particle's chemical composition. When CHDF is operated under the low ionic strength conditions, the interaction potential between the particles and the wall of the capillary is no longer significantly affected by variations in the surface potential of the particles, and at a particular average eluant velocity the separation depends only on particle size and ionic strength.

Density of the colloidal particles is another factor which might be expected to affect the separation factor if their sedimentation velocities can produce significant hydrodynamic effects on the velocity of the particles. Efforts to check this effect have been hampered by lack of suitable well characterized standards; but at the present time, based on limited observations with particles having a diameter smaller than or equal to  $0.5 \mu\text{m}$ , as shown in Table II for carbon black, density appears to have essentially no effect on the separation in this particle size range. It is clear from these results that all of these samples were polydisperse, as demonstrated by

evaluating the ratios of volume to number average diameters. The agreement between the particle size averages obtained by CHDF and PCS is quite good as seen in Table II, indicating that a calibration based on polystyrene particles may be used to accurately determine the size of the considerably more dense carbon black particles. It can also be seen that the particle diameter obtained by DBPA agrees very well with the surface average particle diameter obtained by CHDF.

While many experimental challenges and data reduction problems must be resolved in order to extend the application of CHDF to other complex colloids, no practical barrier appears to exist which would block progress in this direction. Using considerably more dense monodisperse particles, such as some inorganic colloids, with a wider range of particle sizes would help in exploring the effect of density on the separation factor and the efficiency of the fractionation.

### Conclusions

These results show that CHDF is a valuable technique for particle sizing in the submicron range. It offers advantages compared to other techniques in this size range, especially for dispersions with broad distributions. Typical analysis requires less than 10 minutes for the fractionation process and the evaluation of the particle size distribution of a polydisperse sample. The results obtained show a very close agreement with the average sizes obtained with other conventional sizing techniques, as well as with the complete particle size distributions obtained by transmission electron microscopy. The resolution obtained in CHDF is such that bimodal mixtures of narrow distribution particle sizes having ratios less than 1.5:1 have been resolved analytically. Complete size distributions of synthetic latex mixtures and commercial samples having broad distributions have also been obtained by CHDF and these results have been compared to those obtained by transmission electron microscopy. The PSD obtained by CHDF have been found to agree with those obtained by TEM. Shear deformation has been found to have little or no effect on particle size characterization when the particle is relatively rigid, as in film forming latexes of the styrene-butadiene or acrylate types. The ability of CHDF to measure the size of film forming latexes gives this method a distinct advantage over electron microscopy, where the tendency of soft particles to deform and sinter on drying is a problem, especially if prehardening has not been done. Therefore, a CHDF system calibrated with polystyrene standards can be used to obtain size data for a variety of polymer latexes which are in very good agreement with data obtained by conventional methods, such as for latexes formed from styrene-butadiene, methyl methacrylate, styrene-butylacrylate and vinyl acetate.

This work has placed an emphasis on the practical aspects of CHDF analysis for particle size, and no attempt has been made to give an overview of the field of particle size analysis *per se*. However, a perspective for the impact of CHDF as a sizing technique can be gained by reference to the comparison to two other fractionation methods which are available. Comparisons with SFFF at normal operating conditions indicate that resolution in CHDF is significantly better. When SFFF is operated at its highest resolution the efficiency of the separation is very similar to that obtained in CHDF. However, the time for the fractionation process in SFFF is considerably longer (25-55 minutes) than in CHDF (7 minutes or less). Thus CHDF, because of its speed, accuracy, and relatively low cost, is clearly one of the most attractive methods for submicron latex sizing, and its use as a routine characterization tool should continue to expand.

### Acknowledgements

The authors wish to thank Dr. Jesse R. West for the DBPA and PCS data on carbon black.

Literature Cited

1. Barth, H. G.; Sun, S. T., Anal. Chem. 1985, **57**, 151.
2. Giddings, J. C.; Caldwell, K. D.; Jones, H. K., In Particle Size Distribution Assessment and Characterization, Provder, T., Ed.; ACS Symposium Series No. 332; American Chemical Society: Washington, DC, 1987; pp 215-239.
3. DosRamos, J. G. Ph. D. Thesis, Lehigh University, Bethlehem, 1988.
4. Silebi, C. A.; DosRamos, J. G. J. Colloid Interf. Sci., 1989, **130**, 14.
5. DosRamos, J. G.; Silebi, C. A. J. Colloid Interf. Sci., 1989, **133**, 302.
6. Silebi, C. A.; DosRamos, J. G. AIChE J., 1989, **35**, 1351.
7. DosRamos, J.G.; Silebi, C. A. J. Colloid Interf. Sci., 1990, **135**, 165.
8. DosRamos, J.G.; Silebi, C. A. Polymeric Mat. Sci. and Eng. 1989, **61**, 855.
9. DiMarzio, E. A.; Guttman, C.M. Macromol. 1970, **3**, 681.
10. Guttman, C. M.; DiMarzio, E. A. Macromol. 1970, **3**, 131.
11. Yang, F. J. F.; Myers, M. N.; Giddings, J. C. Anal. Chem. 1974, **46**, 1924.
12. Yau, W. W.; Kirkland, J. J. J. Chromat. 1981, **218**, 217.
13. Kirkland, J. J.; Yau, W. W.; Szoka, F. C. Science 1982, **215**, 296.
14. DosRamos, J. G.; Silebi, C. A. Polym. Mat. Sci. and Eng. 1986, **54**, 268.
15. DosRamos, J. G. M.S. Thesis, Lehigh University, Bethlehem, 1985.
16. Tung, L.H. J. Appl. Polym. Sci. 1966, **10**, 375.
17. Silebi, C. A.; McHugh, A. J. J. Appl. Polym. Sci. 1979, **23**, 1699.
18. Ishige, T.; Lee, S. I.; Hamielec, A. E. J. Appl. Poly. Sci. 1971, **15**, 1607.
19. Small, H. J. Colloid and Interf. Sci. 1974, **48**, 147.
20. Small, H.; Saunders, F.; Solc, J. Adv. Colloid and Interf. Sci. 1976, **6**, 237.
21. Prieve, D. C.; Hoysan, P. M. J. Colloid and Interf. Sci. 1978, **64**, 201.
22. Silebi, C. A.; McHugh, A. J. AIChE J. 1978, **24**, 204.
23. Buffham, B. J. Colloid and Interf. Sci. 1978, **67**, 154.

RECEIVED January 14, 1991

## Chapter 20

# Viscometry as a Detection Scheme for Particles in Separation Techniques for Size Distribution Analysis

Grant Von Wald and Martin Langhorst

Analytical Sciences Laboratory, The Dow Chemical Company, 1897  
Building, Midland, MI 48667

Viscometry was investigated as a possible size and composition independent detector for hydrodynamic chromatography. The specific viscosity was found to be linear with latex concentration from 0.01 to 0.4% solids, did not depend on particle composition, and was independent of particle size above roughly 100 nm. However, the specific viscosity increased 30% as the diameter of the latex decreased from 100 nm to 30 nm. This size dependence was ascribed to the presence of a surface layer on the latex in solution. Although the size dependence would not preclude its application, the utility of the viscometer was limited by low sensitivity and long time response.

A number of technologies, such as hydrodynamic chromatography (HDC) and the various techniques of field flow fractionation (FFF), can efficiently separate particles by size in order to quantitate the distribution of sizes in a sample. For any particle separation technique, it is necessary to determine the concentration of particles eluting from the separation element. The ideal detector could determine the concentration of particles without dependence on the particle diameter or composition. At the present time, the spectrophotometric detector operated in the ultra-violet wavelength range is the most widely applied detector for particle separation-distribution analysis instruments. Although spectrophotometric detectors have excellent sensitivity, they suffer from the disadvantage that the response of the detector is a strong function of the particle composition and of the particle size over the colloidal range of 20 to 2000 nm in diameter. The accuracy of particle size distribution measurements by separation techniques, such as HDC, would be greatly enhanced if a size and composition independent detector could be devised.

0097-6156/91/0472-0308\$06.00/0  
© 1991 American Chemical Society

One possible scheme for such a size and composition independent detector is suggested by the Einstein viscosity law which states that the specific viscosity of a particle suspension,  $\eta_{sp}$ , equals 2.5 times the fraction of the volume of the suspension occupied by particles,  $\phi$ , i.e.:

$$\eta_{sp} = 2.5\phi = (\eta_s - \eta_o) / \eta_o \quad (1)$$

where  $\eta_s$  is the viscosity of the suspension and  $\eta_o$  is the viscosity without particles present. If the Einstein viscosity law were rigorously true for the particle suspensions of interest in particle separation methods, a detector which measured  $\eta_{sp}$  would be the ideal composition and size independent detector. Deviations of this simple relationship between  $\eta_{sp}$  and  $\phi$  are expected for particle volume fractions above approximately 0.01 (1). An upper concentration limit of 0.01 volume fraction is not expected to be a significant limitation in this work as particle concentrations in HDC and FFF are at least an order of magnitude lower than 0.01.

A second complication in the relationship between  $\eta_{sp}$  and particle concentration arises from the surface layer of bound solvent and surface active agents which is present in stable colloidal suspensions in water (1). The surface layer complicates the relationship between the volume that the particles occupy in a suspension and the weight concentration of particles. For instance, if there were no surface layer, the weight fraction and the volume fraction of particles in a suspension would be directly related by the densities of the particles and the solvent. However, if there is a surface layer present, the effective volume of the particles in a suspension will be larger than the "dry" volume of the particles. In particular, as the diameter of the particles decreases and the surface area per mass increases, the contribution of a surface layer to the volume occupied by particles will increase.

The sensitivity requirements for a viscosity detector suitable for quantitating the particle concentrations eluting from HDC or FFF are stringent. The volume fraction of particles would be expected to be in the  $1 \times 10^{-3}$  to  $1 \times 10^{-7}$  range so that viscosity changes on the order of  $10^{-6}$  must be detected. Previous experience with other viscometer designs (2,3) indicates that a suitable viscometer design for detection of specific viscosities in the range of interest in particle separation technologies is the differential viscometer patented by Max Haney (4,5).

The purpose of this report was to determine if measurements of  $\eta_{sp}$  could provide the desired ideal particle concentration detector relationship and to evaluate the suitability of the differential viscometer for use in particle separations. HDC was used as the separation tool, although the principle of the measurements could be applied to other separation techniques. The  $\eta_{sp}$  of latices of varying composition and diameters from 20 nm to 1000 nm were studied to probe the generality of the Einstein viscosity law and the utility of the viscometer as a chromatographic detector.



### EXPERIMENTAL

**Apparatus.** The HDC apparatus that was employed was similar to the one described previously (6). The sample loop volume was 100  $\mu\text{L}$  which was the maximum loop volume permissible before significant peak broadening occurred due to the injection volume. The HDC eluent consisted of 0.2% Brij 35 non-ionic surfactant (polyoxyethylene(23) lauryl ether), 0.05% sodium lauryl sulfate (SLS), and 2 mM  $\text{NaH}_2\text{PO}_4$  adjusted to a pH of 3-3.4.

The differential viscometer was a model number 100, Viscotek, Inc. of Porter Texas. The hold-up reservoir in this viscometer was the original design, as opposed to the reservoir presently used in this model viscometer, in order to increase the sensitivity of the viscometer slightly. A spectrophotometric detector, Applied Biosystems 773, was used in series after the differential viscometer to assist in the evaluation of the viscometer.

The model 100 differential viscometer is intended to be used as a detector for gel permeation chromatography. In order to be able to directly measure  $\eta_{sp}$  for latex of known concentration without the HDC column present, the HDC apparatus was rearranged. The injection loop was increased to 1.4 mL using 310 cm of 0.030" I.D. tubing. The HDC column was removed and the injection valve was connected to the viscometer. It was necessary to put an additional pulse dampener between the valve and the viscometer. This pulse dampener consisted of a "T" connector (VALCO) with one leg of the "T" connected to a 35 cm long length of 1/16" I.D. tubing which was closed off to trap air in the end of the tubing. The trapped air, which was readily compressed, absorbed the pressure pulse when the valve was switched.

The diameter of four polystyrene latices were measured in 5 mM NaCl and in HDC eluent using the Coulter Scientific Instruments N4M photon correlation spectroscopy instrument. A measurement time of 180 sec and angle of 90° were used. A viscosity of 0.890 cP was used for the NaCl solution. The relative viscosity of the HDC eluent was measured to be  $1.021 \pm 0.005$  (Schott-Geräte Ubbelholde Automated Viscosity Measuring System) at 25°C. The index of refraction of the HDC eluent was measured to be the same as water to within 0.002 units (Bausch and Lomb, Inc., ABBE-3L). The average diameter reported in Table I was calculated by fitting a single exponential to the autocorrelation function (i.e., the "unimodal" mean diameter as described by Coulter Scientific Instruments).

**Samples.** The polystyrene and carboxylated polystyrene latices were purchased from Duke Scientific Corp. and Seradyn Diagnostics. A density of 1.05 g/mL was used for the polystyrene latex (7,8). The acrylate copolymer, styrene-butadiene copolymer, and polybutadiene latices were obtained from internal Dow sources.

The density of the copolymers was calculated using literature values for the density of pure polymers of each monomer (7) and assuming that the density of the copolymer was linear function of the composition of the polymer. A density of 0.913 g/mL was used for polybutadiene (7). The densities calculated for the styrene-butadiene latices agreed with published measurements (8). The polyvinyltoluene latex was obtained from Seradyn Diagnostics and a literature value of 1.03 g/mL was used for the polymer density (7).

The dry volume fraction,  $\Phi_d$ , of latex was calculated from the fraction of solids in the latex,  $S_1$ , and the density of the polymer in the latex,  $\rho_p$ , using the formula:

$$\Phi_d = S_1 / \rho_p \quad (2)$$

where the density of the eluent was assumed to be 1.00 g/mL. The percent solids of the latices was measured by weighing latex suspension in an Al pan, drying the latex at approximately 100°C for 20-40 minutes and then weighing the dried latex. Repeat measurements were within one percent relative. The percent solids of the latex suspension actually studied were calculated from the dilution ratio of the original latex with eluent. The diameter of the latices was either given by the vendor from electron microscopy or measured using HDC (6). Many of the diameter assignments from HDC or electron microscopy were verified using photon correlation spectroscopy.

## RESULTS

Figures 1 through 6 summarize the measurements which were performed to characterize the performance of the differential viscometer and to investigate the relationship between  $\eta_{sp}$  and particle concentration.

An example direct measurement of  $\eta_{sp}$  without the column is displayed in Figure 1 for a 0.412% solids 300 nm diameter polystyrene latex. Figure 1a presents the output of the two pressure transducers in the differential viscometer versus time. The sample was injected at the five minute point and was exhausted at roughly the 7 min point. The  $\eta_{sp}$  was calculated using the equation:

$$\eta_{sp} = 4P_d / (P_i - 2P_d) \quad (3)$$

where  $P_d$  is the change in the differential transducer reading from the background level (1.2 min to 5 min in Figure 1a) to the plateau reached after the sample injection (just after 6 min to 7 min) and  $P_i$  is the inlet pressure transducer reading (4,5). Figure 1b presents the  $\eta_{sp}$  calculated using Equation 3. The  $\eta_{sp}$  was averaged over the time period from just after 6 minutes to 7 minutes where the differential pressure was constant (between the solid vertical lines in Figure 1b).

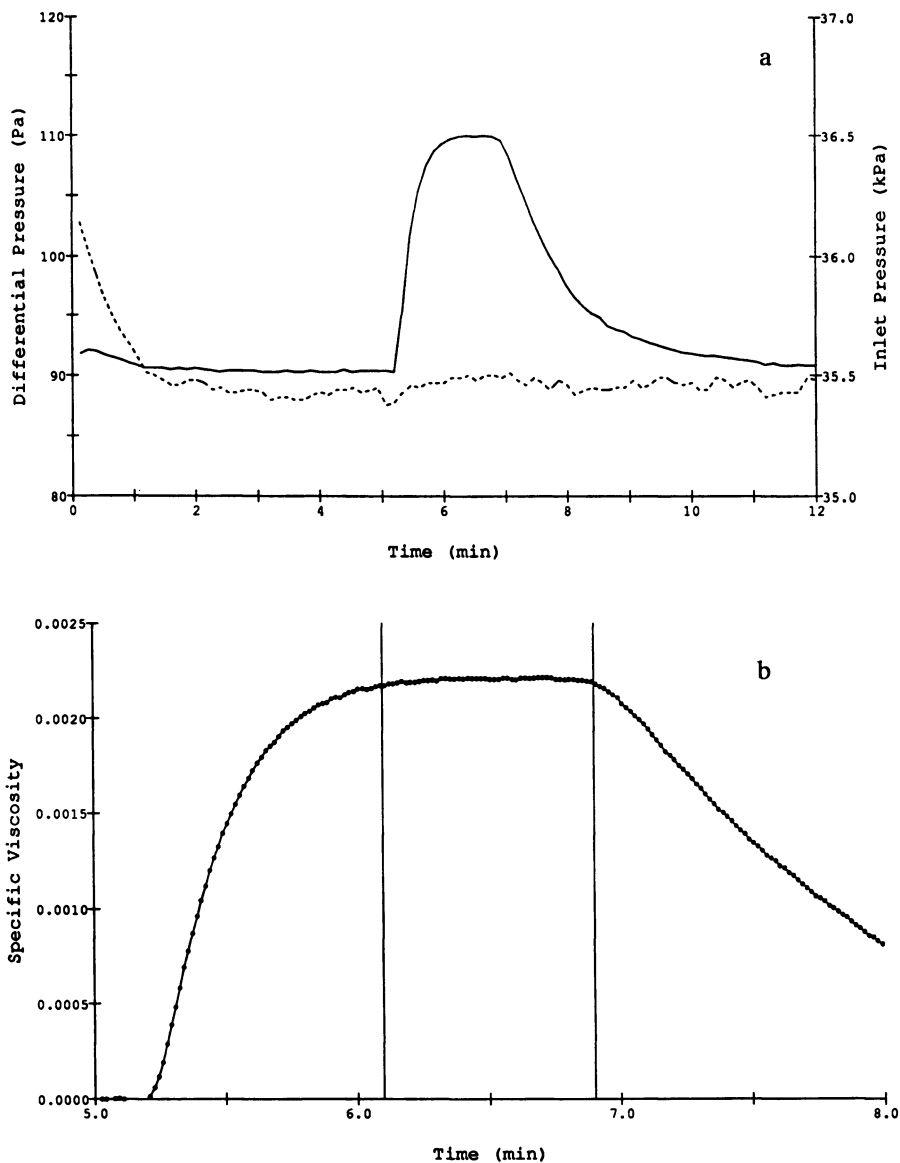


Figure 1.  $\eta_{sp}$  Measurement for 0.412% solids 300 nm diameter polystyrene latex.

(a) Differential and inlet pressure transducer output versus time.

Inlet pressure: ——— Differential pressure: - - - - -

(b) Calculated  $\eta_{sp}$  versus time.

Figure 2 presents data which demonstrates the sensitivity of the differential viscometer when it was used as a detector for HDC. Results collected with two concentrations of a 29 nm polystyrene latex, 0.099% solids and 0.0099% solids, are displayed. Both the differential pressure transducer output in Pa from the viscometer and the absorbance measured by the spectrophotometric detector were collected and are displayed in Figure 2. For all the suspensions studied, the change in the differential pressure was insignificant compared to the inlet pressure so that  $\eta_{sp}$  was directly proportional to the differential pressure (See Equation 3). Repeat measurements of the peak height of the differential pressure reading over a several day time period were within a 10% range. The reproducibility could have been improved by collecting the inlet pressure also in order to normalize out fluctuations in the pumping rate.

The effect of latex size on the viscometer response was studied by injecting a series of 0.412% solids polystyrene latices onto the HDC column. The results are summarized in Figure 3 where the peak differential pressure change is plotted versus the latex diameter. Figure 4 displays the peak differential pressure change in Pa versus the latex diameter for different types of latex.

Figures 5 and 6 present the results from direct measurements of  $\eta_{sp}$ . The linearity of the relationship between  $\eta_{sp}$  and latex concentration was evaluated. The measured  $\eta_{sp}$  is plotted against the dry volume fraction of 38 nm, 106 nm, and 300 nm diameter polystyrene latices in Figure 5. The least squares fit of the data to a straight line are reported in Figure 5 where "X 106 nm" stands for the dry volume fraction of latex. The dependence of  $\eta_{sp}$  on the latex diameter was also investigated in 0.002% Brij 35, 0.0005% SLS with 2 mM  $\text{NaH}_2\text{PO}_4$  and in 0.1% SLS with 2 mM  $\text{NaH}_2\text{PO}_4$ . The results are presented in Figure 6.

The effect of the surfactants in HDC eluent on the effective diameter of four polystyrene latices was measured using photon correlation spectroscopy following a similar study of the interaction of polyethylene oxide with the surface of polystyrene latex (9). The results are summarized in Table I where the mean diameter is given for measurements with polystyrene latices in 5 mM NaCl without any surfactant added, besides the surfactant in the stock latex suspensions, and in standard HDC eluent.

TABLE I. Photon Correlation Spectroscopy Measurements of the Diameter of Four Polystyrene Latices in 5 mM NaCl and HDC Eluent

Latex Identification	Latex Diameter From Vendor	Latex Diameter 5 mM NaCl	Latex Diameter HDC Eluent
Duke 5003	29 nm*	27.7, 27.3 nm	30.6, 30.4 nm
Duke 3030	30 nm**	30.7, 30.5 nm	35.8, 35.0 nm
Duke 5010	106 nm*	121, 122 nm	120, 122 nm
Seradyn 1B58	204 nm*	209, 210 nm	211, 202 nm

\* Determined from electron microscopy.

\*\* Determined by photon correlation spectroscopy.

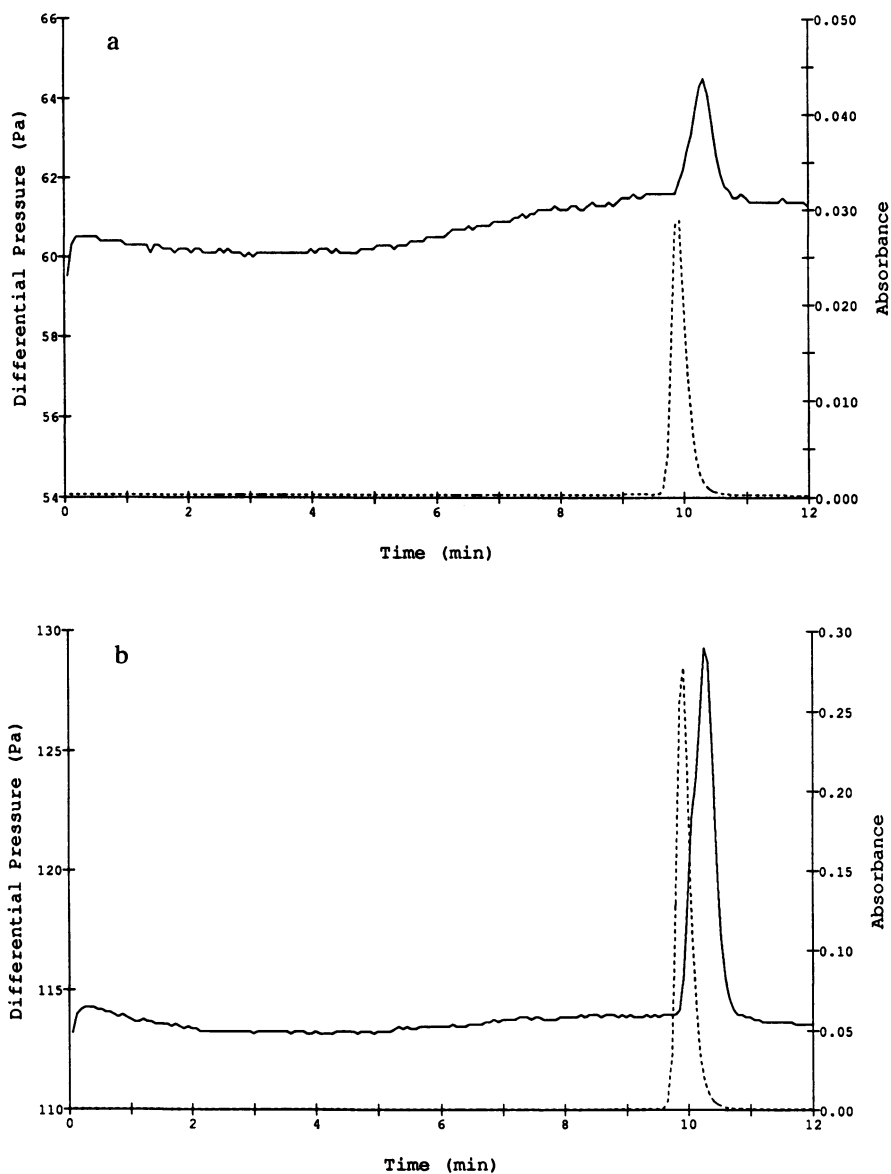


Figure 2. Responses of the differential pressure transducer and the spectrophotometric detector at a wavelength of 254 nm to injections of 29 nm diameter polystyrene latex. (a) 0.0099% solids injection. (b) 0.099% solids injection. Differential pressure: ——— Absorbance: - - - - -

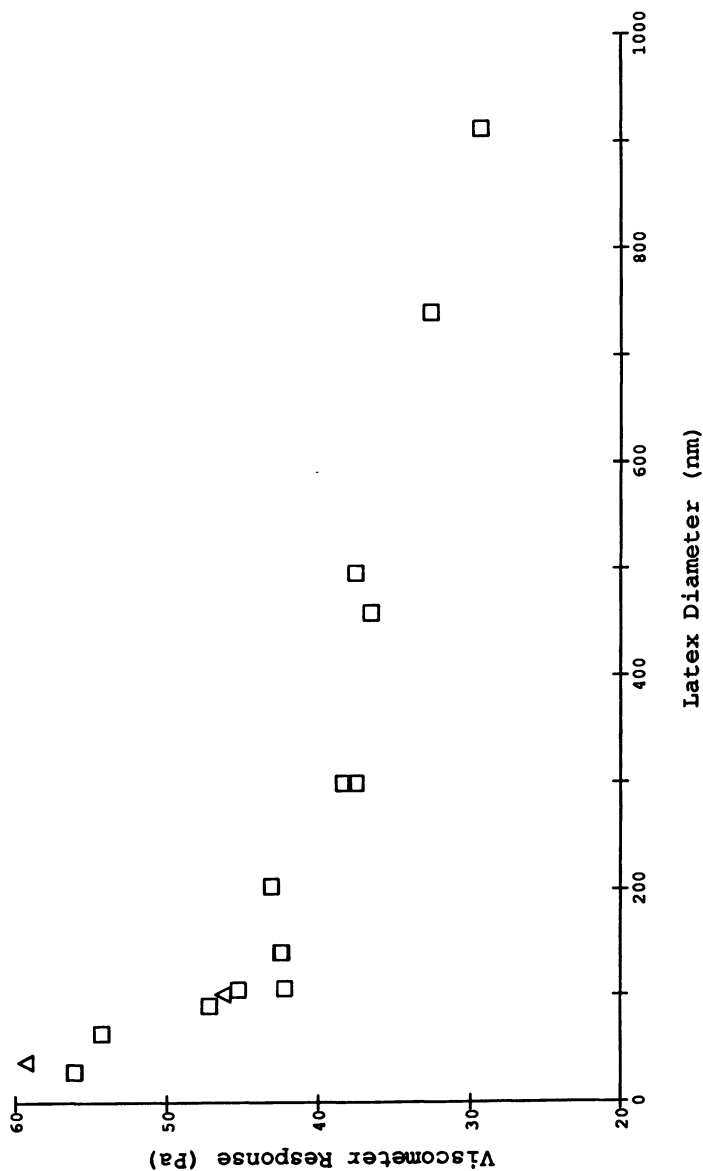


Figure 3. Dependence of the viscometric response to latex diameter for a series of polystyrene latices injected at 0.412% solids with HDC eluent measured as the change in differential pressure.

□ Polystyrene latices    △ Carboxylated polystyrene latices

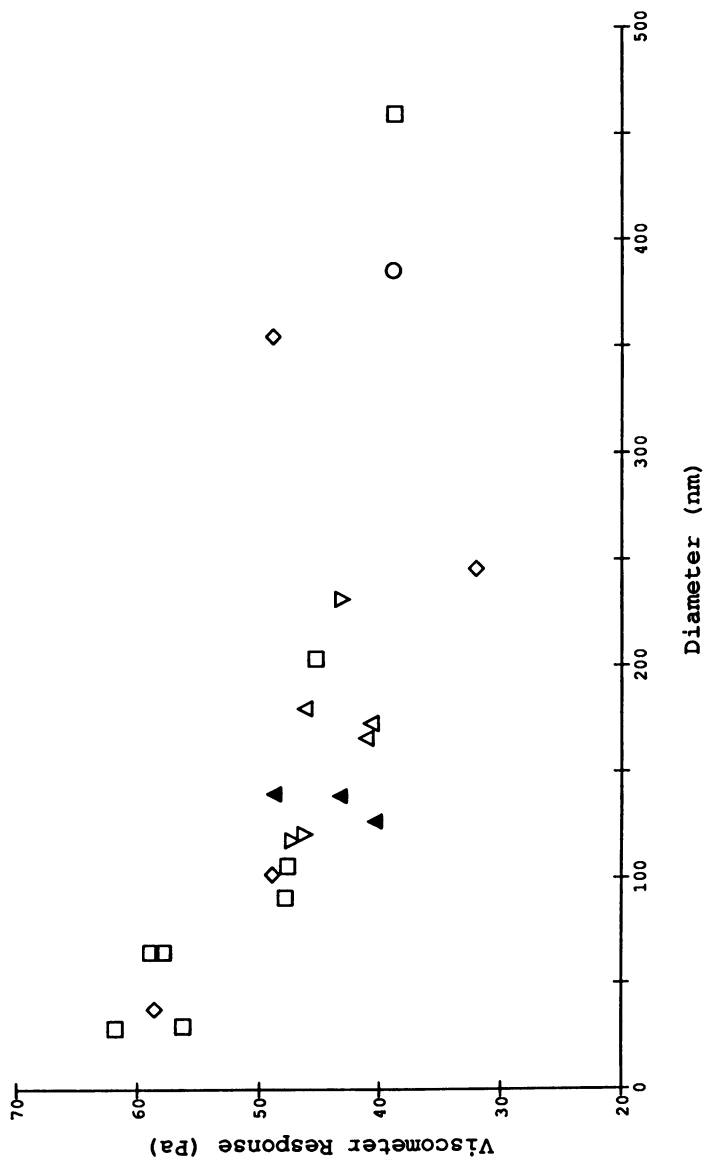


Figure 4. Response of the viscometer to injections of 0.0040 dry volume fraction of latices of different compositions measured as the change in differential pressure.

◇ Carboxylated polystyrene ○ Polyvinyltoluene  
 ▲ S/B copolymer ▼ Butadiene ▲ Acrylate □ Polystyrene

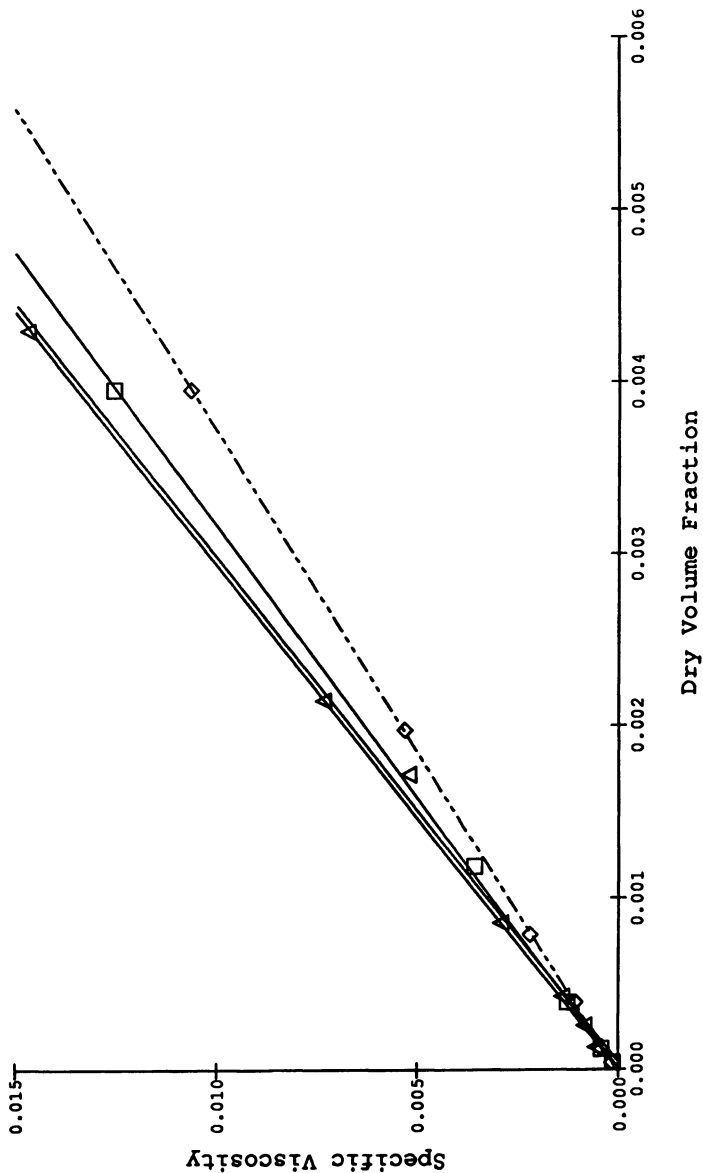


Figure 5.  $\eta_{sp}$  versus concentration for three polystyrene lattices in lower surfactant concentration HDC eluent.  
 □ Duke 5010 106 nm    △ Duke C004 38 nm    ◇ Duke 5030 300 nm  
 — 3.156\* (X 106 nm) -  $1.04 \times 10^{-5}$   
 — 3.398\* (X 38 nm) -  $7.08 \times 10^{-5}$   
 - - - 2.669\* (X 300 nm) -  $6.11 \times 10^{-5}$



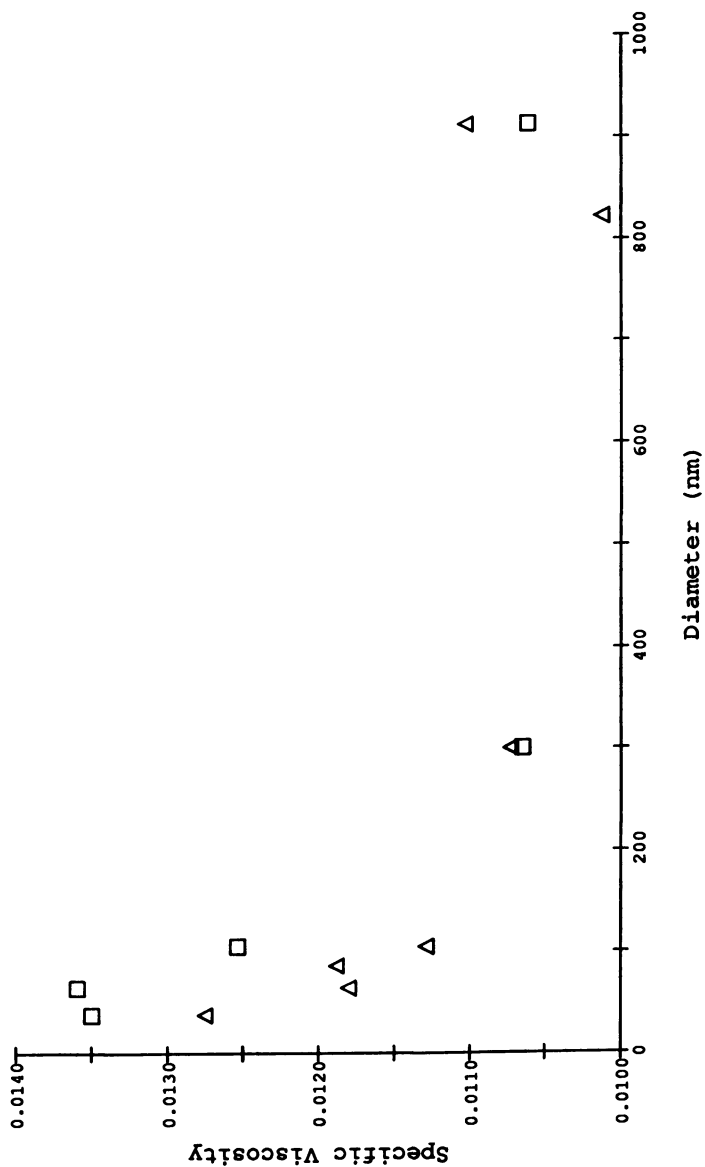


Figure 6.  $\eta_{sp}$  versus diameter measured for polystyrene latices.  
 □ 0.002% Brij 35, 0.005% SLS, 2 mM NaH<sub>2</sub>PO<sub>4</sub>  
 △ 0.1% SLS, 2 mM NaH<sub>2</sub>PO<sub>4</sub>

## DISCUSSION

Linearity and Sensitivity. In order to permit evaluation of the relationship between particle concentration and  $\eta_{sp}$ , the requisite sensitivity and linearity of the differential viscometer had to be verified. The sensitivity of the viscometer can be estimated to be approximately 0.001% solids injected from the measurements of the differential viscometer response to injections of 0.099 and 0.099% solids of a 29 nm polystyrene latex (Figure 2).

The differential viscometer was found to give a linear response to latex concentration over the range from 0.01-0.4% solids injected onto the column. Also,  $\eta_{sp}$  was found to be linear with latex concentration over the range of 0.01-0.4% solids without the HDC column present (See Figure 5).

Dependence on Diameter and Composition. Given acceptable sensitivity and linearity, the dependence of the viscometer signal on latex diameter and composition was investigated. The results for constant concentration of polystyrene latex injected onto the HDC column are summarized in Figure 3. The peak differential pressure resulting from injections of 0.412% solids polystyrene latices was observed to increase from 45.3 Pa for a 106 nm diameter latex to 56.1 Pa for a 29 nm diameter latex. The response also decreased to 29.3 Pa at 913 as expected because of the trapping of particles with diameters greater than roughly 500 nm by the HDC column (6,10). On the other hand, when latices of varying compositions were injected onto the column at 0.0040 dry volume fraction (See Equation 2), no dependence on the latex composition, within experimental error, could be discerned for the latex types studied (See Figure 4).

One possible hypothesis to explain the size dependence of the viscometer measurements could have been a non-linear relationship between  $\eta_{sp}$  and particle concentration as has been observed for higher particle concentrations (1). However, as discussed above and displayed in Figure 5, measurements of  $\eta_{sp}$  from 0.01 to 0.4 percent solids with three different latices, demonstrated the linearity of  $\eta_{sp}$  with concentration.

Another component of the size dependence of the viscometer results collected with the HDC column can be accounted for by the measurements of  $\eta_{sp}$  as a function of diameter. Figure 6 displays the  $\eta_{sp}$  for a series of polystyrene latices at 0.412% solids. Above roughly 200 nm the  $\eta_{sp}$  of latices measured without the column is constant (Figure 6) while a significant decrease was observed with the column present (Figure 3). The difference between the two sets of results in Figures 3 and 6 illustrates the influence of trapping by the HDC column as expected from previous work (6,10).

However, the most significant feature of the direct  $\eta_{sp}$  measurements displayed in Figure 6 is the increase in  $\eta_{sp}$  for latex diameter less than 100 nm. The dependence of  $\eta_{sp}$  on diameter for the suspensions with Brij 35 and SLS surfactants (Figure 6) is nearly identical to that observed with the HDC column (Figure 3). Thus, the dependence of viscometer response on latex diameter is not the consequence of a HDC column-particle interaction.

Proposed Cause for Size Dependence. The increase in  $\eta_{sp}$  as the particle diameter decreased from 100 nm to 30 nm suggests a more complex relationship between  $\eta_{sp}$  and particle concentration in the colloidal regime than the Einstein viscosity law indicates. Although a linear relationship exists between  $\eta_{sp}$  and latex concentration, the proportionality constant between  $\eta_{sp}$  and the "dry" volume fraction of latex calculated from weight concentration is larger than the value of 2.5 predicted by Einstein for every latex studied and increased from 2.67 for the 300 nm latex to 3.40 for the 29 nm latex.

The dependence of the proportionality constant between  $\eta_{sp}$  and particle concentration on particle diameter is hypothesized to be the consequence of the solvation layer on the surface of the particle (11). It has been well established that the surface of a lyophobic colloid in an aqueous dispersion, such as latex, will have associated with it a variety of species that will increase the effective diameter of the colloid (11). If the surface layer of a polystyrene latex particle in an aqueous solution were 1.5 nm thick, the volume of a 300 nm diameter particle would increase over the "dry" volume by 2.8%. The same thickness of solvation layer would change the volume of a 29 nm particle by 34%. A surface layer slightly greater than 1.5 nm in thickness would account for the observed increase of  $\eta_{sp}$  for latex diameters below 100 nm and the relatively small dependence of  $\eta_{sp}$  on latex diameter for sizes greater than 300 nm (e.g., See Figure 3 or 6).

Confirmation of Proposed Cause of Size Dependence. If the observed dependence of  $\eta_{sp}$  on particle diameter is the consequence of a surface layer, then it would not be correct to state that  $\eta_{sp}$  is a function of diameter. Rather, it would be more accurate to state that the effective diameter of a colloid is dependent on the suspension conditions which is an assertion already well established in the literature. Furthermore, it should be emphasized that the observed increase in  $\eta_{sp}$  as the particle diameter decreases is hypothesized to be the consequence of a difference in the effective diameter between the measurement conditions where the  $\eta_{sp}$  measurements were made and the conditions under which the diameter was assigned by the vendor for these polystyrene latices. For the latices larger than 100 nm in diameter, the experimental conditions of TEM measurements and HDC measurements are much different. However, for these larger latices the contribution of surface layers to the effective particle diameter is not expected to be large. Some of the smaller latices were assigned diameters using TEM. For these latices it would be expected that solution measurements might give different diameters than electron microscopy. On the other hand, some of the other latices with diameters less than 100 nm were sized using photon correlation spectroscopy. For these latices the change in effective diameter would be between the solution conditions for the photon correlation spectroscopy measurements and the conditions in the HDC eluent.

In order to test this hypothesis, the diameter of four latices were determined using photon correlation spectroscopy in 5 mM NaCl suspension which had no surfactant in it, besides the surfactant which was in the latex stock suspensions supplied by the vendor, and in HDC eluent. The results are summarized in Table I. For the 29 nm and 30 nm latices, a clear increase in the effective diameter in HDC eluent versus 5 mM NaCl was observed. The observed change in diameter between HDC eluent and 5 mM NaCl, approximately 3 nm, agreed with the 3 nm increase in diameter predicted from the  $\eta_{sp}$  measurements. No difference was observed for the 204 nm and 106 nm diameter latices. This is presumably the consequence of the relatively small effect a surface layer would have on the diameter of these latices.

#### Dependence of $\eta_{sp}$ , Size Relationship on Solution Conditions.

Given the strong dependence of the effective particle volume on latex diameter below 100 nm, it would be important to understand the dependence of the solvation layer thickness on the solvent conditions in order to apply viscometry to particle detection for separation methods. In addition to the solution conditions, the nature of the surface of the particle would be expected to affect the layer with which it is in contact. However, measurements of  $\eta_{sp}$  for a variety of latex types, summarized in Figure 4, did not depend on the latex composition. Also, the composition independence of particle elution in HDC indicates that at least at low ionic strengths, the effective particle diameter is not a strong function of particle composition (10).

The solution conditions which would be expected to affect size and structure of the surface layer on a latex include at least the ionic strength, surfactant type and surfactant concentration (11). When the surfactant concentration was reduced 100 fold at constant phosphate buffer concentration, the size dependence of the differential viscometer response to injections of polystyrene latex from 29 nm to 913 nm was unchanged. These results indicate that size of the surface layer does not depend strongly on surfactant concentration.

The  $\eta_{sp}$  of 300 nm and 913 nm diameter polystyrene latex was the same in 0.002% Brij 35 and 0.0005% SLS with 2 mM  $\text{NaH}_2\text{PO}_4$  and in 0.1% SLS with 2 mM  $\text{NaH}_2\text{PO}_4$  (Figure 6). However, below 100 nm in diameter the increase in  $\eta_{sp}$  as a function of nominal diameter was slightly greater in the solution with Brij 35. These results (Figure 6) suggest that SLS may have a slightly smaller surface layer thickness.

The ionic strength is also known to affect the structure and thickness of the surface layer on a colloid. However, for the application of viscometry to HDC, this dependence would not be important because of the requirement that the ionic strength be kept constant to maintain the calibration of HDC columns. It would be possible to calibrate the viscometer so that viscometer response was corrected from the effective volume the particles occupy in HDC eluent to a volume more reflective of the diameter assigned using TEM or photon correlation spectroscopy in solutions without SLS or Brij 35 present.

Limitations in the Performance of the Viscometer. However, further investigation of the practical utility of viscometry for particle detection was not undertaken because of other limitations in the performance of the Viscotek differential viscometer. The short term signal to noise ratio and long term stability of the viscometer sufficed to permit preliminary evaluation of the utility of viscometry. It is not certain that the differential viscometer signal to noise and stability would permit accurate size distribution calculation.

Another limitation in the performance of the Viscotek differential viscometer for chromatographic analyses was the broadening of peaks by the viscometer. The broadening due to the viscometer itself was studied by injecting a solution of 0.2% Brij 35 and 0.05% SLS surfactant when 0.002% Brij 35, 0.005% SLS with 2 mM  $\text{NaH}_2\text{PO}_4$  eluent was being pumped through the HDC column. Results were collected with both the viscometer and the spectrophotometric detector located after the viscometer. The full width at half maximum (FWHM) of the peak from the surfactants was measured to be 20 sec with an elution time of 614 seconds as detected at 210 nm with a flow rate of 1 mL/min. The FWHM for the same peak was 23 sec as measured by the viscometer. At a flow rate of 0.5 mL/min, the FWHM of the absorbance peak was 40 sec at an elution time of 1248 sec while the FWHM was 44 sec as detected by the viscometer. Clearly the additional broadening by the viscometer cannot be due to the dead volume of the viscometer because the peak width was narrower for the spectrophotometric detector which was located after the viscometer. Also, there was a slight reduction in the relative difference in the peak widths for the two detectors when the flow rate was decreased. This suggests that the broadening observed with the Viscotek differential viscometer is the consequence of the response time of the differential pressure transducer. For HDC where the fractionation power of the column just suffices to permit a useful size separation, broadening by the detector as was observed with the Viscotek viscometer causes an unacceptable loss of resolution. Deconvolution of the detector broadening, which is commonly practiced when this detector is used in gel permeation chromatography, cannot remedy this deficiency. The chromatograms are already deconvolved to remove as much broadening as is feasible (6). For other techniques, such as FFF and gel permeation chromatography which have greater resolving power, this broadening may not be significant, but should be considered when using the Viscotek detector.

### CONCLUSION

The application of viscometric detection to colloidal particle separation techniques has been found to be more complex than the Einstein viscosity law suggests. Although viscometric detection was found to meet one of the two criteria of the ideal particle quantitation detector, independence from particle composition, an increase in  $\eta_{sp}$  of 30% as the diameter of the latex decreased from 100 nm to 30 nm was observed. Evidence from photon correlation

spectroscopy and viscometry suggests this size dependence is the consequence of a 1.5 nm thick surface layer in HDC eluent. This size dependence does not preclude the application of viscometry for particle quantitation, particularly for particles with diameter greater than 100 nm where the  $\eta_{sp}$  was observed to be constant within 10% out to particle diameters of 913 nm. However, the minimal sensitivity and long time response of current pressure transducer technology limit the utility of viscometer for use with HDC. If more sensitive transducers were developed, viscometry should be reconsidered as this detection scheme could greatly enhance the accuracy of size determinations using particle size separation methods by providing composition, and at least above 100 nm in diameter, size independent detection.

#### Literature Cited

1. Vold, R. D.; Vold, M. J. Colloid and Interface Chemistry; Addison-Wesley: Reading 1983; p. 347.
2. Abbott, S. D.; Yau, W. W. U.S. Patent 4 578 990, 1986.
3. Chamberlin, A.; Tuinstra, H. E. J. Applied Polymer Sci. 1988, **35**, 1667-82.
4. Haney, M. A. U.S. Patent 4 463 598, 1984.
5. Haney, M. A. J. Applied Polymer Sci. 1985, **30**, 3023-36.
6. McGowan, G. R.; Langhorst, M. A. J. of Colloid and Interface Sci. 1982, **89**, 94-106.
7. Brandrup, J.; Immergut, E. H. Polymer Handbook, 2nd ed.; Wiley: New York, 1975.
8. Nagy, D. J. Anal. Chem. 1989, **61**, 1934-37.
9. Kato, T.; Nakamura, K.; Kawaguchi, M.; Takahashi, A. Polymer J., 1981, **13**, 1037-1043.
10. McHugh, A. J. CRC Critical Rev. in Anal. Chem. 1984, **15**, 63-117.
11. Hiemenz, P. C. Principles of Colloid and Surface Chemistry; Marcel Dekker: New York, 1977; pp. 62-75.

RECEIVED March 5, 1991

## Chapter 21

# Electrophoretic Fingerprinting for Surface Characterization of Colloidal Particles

R. L. Rowell, S.-J. Shiau, and B. J. Marlow

Department of Chemistry, University of Massachusetts,  
Amherst, MA 01003

The classical characterization of the surface chemistry of colloidal particles is by the zeta potential, a calculated quantity derived from measurements of the electrophoretic mobility. We show that the average mobility is a more fundamental and characteristic property and that the average mobility may be represented as a function of the characteristic state variables pH and  $p\lambda$  (the negative log of the specific conductance) in the form of an electrophoretic fingerprint (EF). The EF is therefore a contour diagram of mobility in pH- $p\lambda$  space. A variety of EFs are discussed in order to illustrate the use of the EF as a sensitive probe of the surface electrochemical state and a measure of colloid stability. The fingerprinting approach is extended to hydrodynamic fingerprinting (HF), a representation of the hydrodynamic particle size as a function of pH and  $p\lambda$ .

The zeta potential has been widely used as a characterizing parameter in colloid science (1). The zeta potential is the average potential at the surface of shear surrounding a moving colloidal particle so that it links the hydrodynamic radius with various theoretical models of the structure of the double layer. It is calculated from the measurable electrophoretic mobility  $u_E = v_E/E$  which is the particle velocity under unit field strength. Thus, the mobility is the directly measured quantity while the zeta potential is an interpretation requiring several assumptions.

In earlier work (2,3) we reported on modern instrumentation for measurement of the distribution of the electrophoretic mobility. Here we show that the average electrophoretic mobility may be represented as a function of two variables of state: the pH and the  $p\lambda$  which is the negative log of the specific conductance (S/m). The representation of  $u_E$  as a function of pH and  $p\lambda$  is called "electrophoretic topography" and yields a template or "fingerprint" (4,5) as well as details on the fine structure (2,3), i.e., the electrophoretic mobility distribution at a point in the pH- $p\lambda$  domain.

The advantage of pH and  $p\lambda$  as variables is that together they provide a complete and characteristic set as shown below. Historically pH has been used as an independent variable but varying pH necessarily varies  $p\lambda$  at the same time. The ionic strength has also been used as an independent variable but is unknown when dealing with a system of unknown electrolyte concentration. We show below the simplicity and advantage of using  $p\lambda$ , a directly measurable electrolyte variable that complements pH in the pH- $p\lambda$  domain.

0097-6156/91/0472-0326\$06.00/0

© 1991 American Chemical Society

It should be stressed that pH and  $\rho\lambda$  are regarded as characteristic variables for the colloidal system as a whole. The conductance, expressed by the measured  $\rho\lambda$ , may in general have contributions arising from the medium and the particle itself by translational motion or by surface conductance. We need to be aware of such contributions and the changes that take place as the conditions of pH and  $\rho\lambda$  change, but in general we do not possess detailed knowledge of those contributions. That is the principal advantage of the use of  $\rho\lambda$  as a variable; it is characteristic of the state of the total colloidal system. We replace elusive detailed microscopic knowledge by suitable thermodynamic state variables.

Finally, we note that while the main theme of this paper is electrophoretic fingerprinting, the approach logically leads to an analogous tool, hydrodynamic fingerprinting as discussed below.

### Experimental

**Materials.** The latex microspheres used were obtained from Interfacial Dynamics Corp., IDC #2-73-70, 0.865  $\mu\text{m}$  diameter, stock 4.1% solids. The manufacturers specifications were surfactant free and ultraclean. They were diluted with double-distilled deionized (DDD) water with no preservatives or other additives. Two drops of the standard latex were added to 250 mL DDD water and dispersed with a magnetic stirrer at medium speed for 10 min. The pH was adjusted with HCl or KOH using 3 min of fast stirring to equilibrate. The specific conductance was varied over a wide range using KCl.

Titanium dioxide powder, 99.999% Golden Label from Aldrich was added to DDD water (0.838 g/100 mL) to make a stock solution which was dispersed with a Fisher Model 300 Sonic Dismembrator at 35% of full power for 48 hours. The storage bottle was wrapped with aluminum foil to reduce photooxidation. Fifteen drops of stock solution were added to 250 mL of different concentrations of KCl. The pH was varied with HCl or KOH.

BLACK PEARLS L (oxidized carbon black) and REGAL 660 (non-oxidized carbon black) were obtained from the CABOT Corporation Research Center, Billerica, MA (6). Stock solutions were prepared from 2.4 g carbon black in 100 mL DDD water. The dispersions were covered with PARAFILM in a beaker and agitated with a magnetic stirrer for 24 hours to ensure dispersion. Samples for fingerprinting were prepared from 20 drops of the stock solution in 250 mL DDD water. The pH was varied using HCl and KOH while  $\rho\lambda$  was varied using KCl.

**Procedure.** The electrophoretic mobility was measured with a commercially available Pen Kem System 3000 Automated Electrokinetics Analyzer which has been described in some detail elsewhere (5,7,8). The moving images of particles relative to a rotating grating of constant and known speed creates frequency shifts which are converted by a fast Fourier transform analyzer to give a reproducible measurement of the mobility based on hundreds of particles moving in the stationary layer. The mean mobility, used in this work, was reproducible to within less than 3%.

**Analysis of Data.** The mean electrophoretic mobility from the Pen Kem 3000 from a sample at a given measured pH and  $\rho\lambda$  is represented as a three-dimensional graph as discussed below using an IBM compatible PC with software SURFER supplied by Golden Software, Inc., Golden, CO. The algorithm involves Kringing as described previously (4).



## Results

**Electrophoretic Fingerprinting.** In Figure 1 we show the template and fingerprint for a polystyrene latex containing acidic surface groups (carboxyl, R-CO<sub>2</sub>H) and basic surface groups (amidine, R-C(NH)(NH<sub>2</sub>)) so that the latex is zwitterionic. The experimental points from which the representations were prepared are shown as dots in the pH-p $\lambda$  domain of the fingerprint.

We have added a dashed envelope curve to Fig. 1 which gives a boundary in the pH-p $\lambda$  domain that separates the experimentally accessible region from the extrapolated lines that were generated by the curve-fitting routine. Below the dashed boundary the extrapolations are without physical significance because experimentally p $\lambda$  necessarily increases as the pH is increased or decreased from the pH of minimum p $\lambda$ . The offset in pH of the minimum p $\lambda$  in the dashed curve from neutral pH 7 is governed by the balance between the contributions from the acidic and basic groups as the dilution conditions cause the conductance to approach that of the preparatory DDD water, p $\lambda$  = -3.7 (2).

Some studies of the dependence of the fingerprint pattern on the number and distribution of experimental points have been carried out (9) so that the general features of the patterns reported here are reproducible. This is shown by the series of fingerprints shown in Figure 2 using respectively 106, 73, 58, and 38 data points. The number of data points was decreased by deleting randomly the data points from the original file. We note that compressed surfaces, shrink scale ranges, decreased isomobility line numbers, smaller maximum mobility domains, etc., are produced when the number of data points decreases. By examining the characteristics of the lines and shapes shown in Figure 2, we recommend that on the order of 70 data points are required to produce meaningful fingerprints. Note that contour lines obtained by extrapolation into the experimentally inaccessible or not-measured regions is especially sensitive to the number of data points. While 70 points seems to be a minimum for the test system, it is clear that a much larger number would be preferable for defining the finer details of the fingerprint. The number of data points required will in general vary with the complexity of the system and the level of detail required for a meaningful interpretation.

The fingerprint and template for the TiO<sub>2</sub>-KCl system is given in Figure 3. We have omitted the experimental points and have approximated the experimentally inaccessible regions by using the software to block out triangular regions in the corners of the pH-p $\lambda$  domain. The locus of the zero mobility contour line has been darkened for emphasis.

A set of fingerprints are shown in Figures 4 and 5 for two dispersions of carbon black which had a common ancestry. The oxidized carbon black powder, BLACK PEARLS, was manufactured by oxidation of the parent material, the non-oxidized REGAL 660. We have shown the experimental points and again have approximated the experimentally inaccessible regions by corner triangles.

## Discussion

The broad principal shown by our work is that the fingerprint is a characteristic of the surface electrical state of the system. The variables pH and p $\lambda$  are not independent but they are characteristic and measurable so that the fingerprint may be obtained on a colloidal dispersion of unknown ionic composition. Fingerprints for different systems are quite different as shown by the examples given.

We have said elsewhere (5) that the template or fingerprint is actually a self-consistent representation of the experimentally measured mobility in the experimentally measured pH-p $\lambda$  domain. From the fingerprint or self-consistent

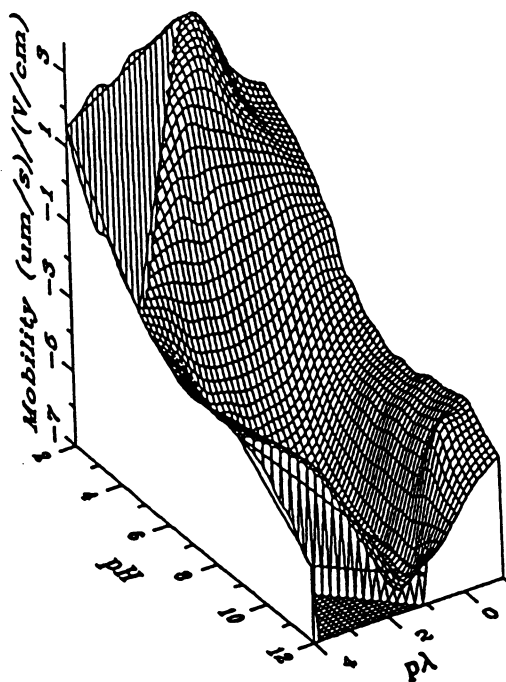
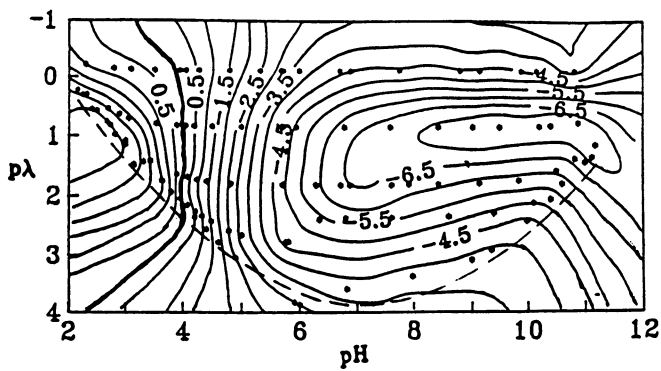


Figure 1. The electrophoretic fingerprint and template of the carboxyl-amidine zwitterionic latex (PL-7).

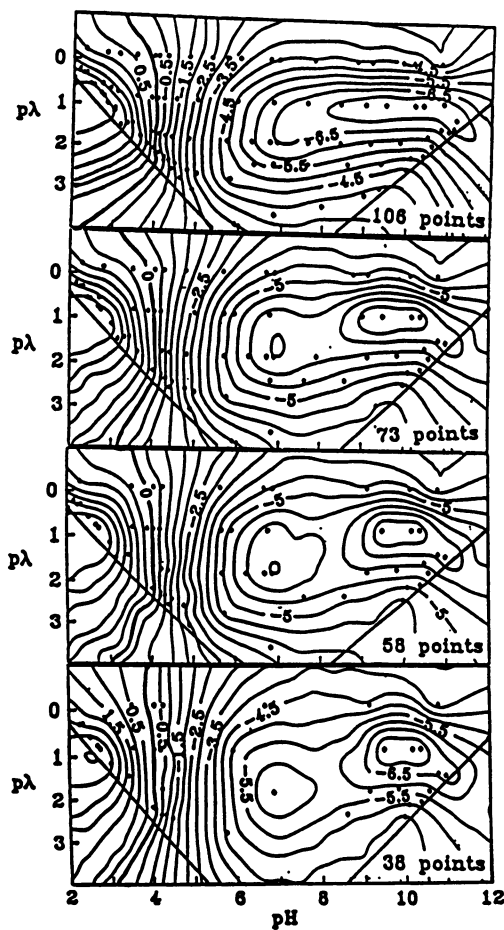


Figure 2. The influence of the number of data points on the electrophoretic fingerprint of the carboxyl-amidine zwitterionic latex (PL-7).

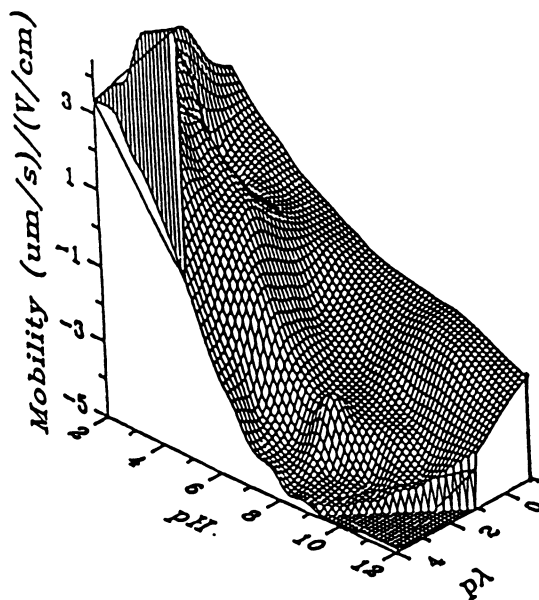
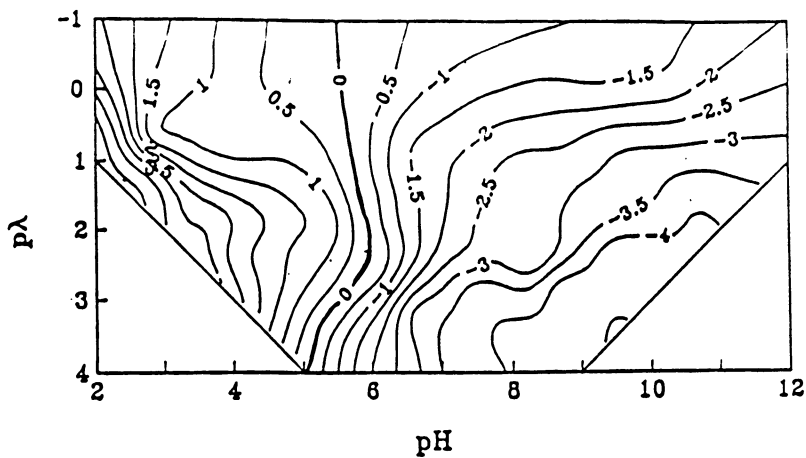


Figure 3. The electrophoretic fingerprint and template of the titanium dioxide-KCl system.

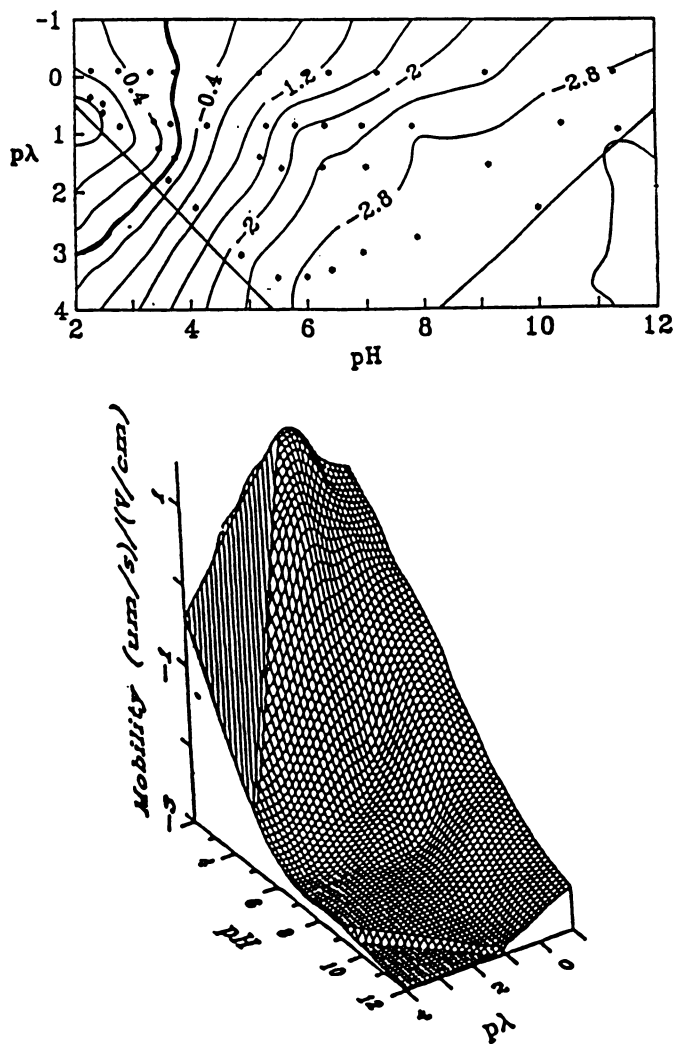


Figure 4. The electrophoretic fingerprint and template of the BLACK PEARLS (oxidized carbon black) dispersion.

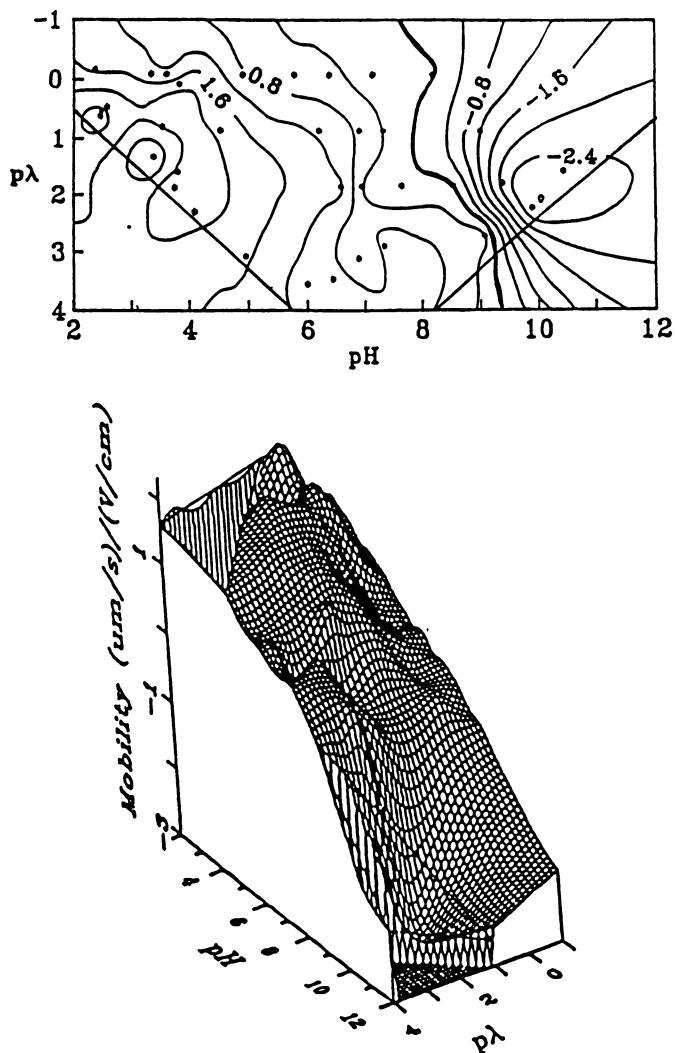


Figure 5. The electrophoretic fingerprint and template of the REGAL 660 (non-oxidized carbon black) dispersion.

mobility surface (SCMS), one can mathematically take cuts along any pH- $\rho\lambda$  path of experimental or theoretical interest.

Furthermore, if the SCMS varies when the order or manner of collecting the data is varied, then one can conclude that the dispersion is procedurally interactive with the acids, bases and salts used to vary pH and  $\rho\lambda$  and the variation in the SCMS can be used as a means of correlating the data and systematically studying the nature of the interaction in a highly controllable and experimentally well-founded manner. For example, from the SCMS, one can obtain a profile of the mobility along any desired pH- $\rho\lambda$  path. One can then sweep that mobility path independently and with a different experimental protocol. Any difference between the calculated cut and the directly measured cut will reveal the interactions that would make the mobility a path function and not a state function of pH and  $\rho\lambda$ .

The classical approach to electrophoresis is to measure mobility as a function of pH, usually in the presence of 10 mM to 20 mM added electrolyte which is used to "swamp out" the contribution from the colloid and allow one to calculate an experimental ionic strength. The mobility-pH profile thus obtained in reality follows some path in the pH- $\rho\lambda$  domain which may be visualized by noting the experimental points in the fingerprints shown here. At high ionic strength ( $\rho\lambda$  1 to 0) the pH- $\rho\lambda$  path is nearly parallel to the pH axis. However, at low ionic strength ( $\rho\lambda$  1 to 4) the pH- $\rho\lambda$  path becomes increasingly curved and in the limit of very low electrolyte, it approaches the dashed locus shown in Fig. 1. For this reason, comparison of mobility-pH profiles from different experiments or from different laboratories may lead to troublesome differences because in fact differences in procedure lead to different paths in the pH- $\rho\lambda$  domain.

On the other hand, if a fingerprint can be reproducibly prepared by different sampling patterns in the pH- $\rho\lambda$  domain then one indeed has a state property, the SCMS. The SCMS should be reproducible in different laboratories and if so, it follows that a mathematically interpolated mobility-pH cut at constant  $\rho\lambda$  will give a constant and reproducible profile.

The electrophoretic fingerprinting approach to obtain an SCMS removes the ambiguity in mobility-pH profiles in the same way that a mountain range will have a well-defined contour along a North-South or East-West hiking trail.

**Zeta Potential-Salt Concentration Maximum.** The SCMS approach sheds some understanding on an important problem that has arisen with the use of monodisperse polystyrene latexes as model colloids. Midmore and Hunter (10) state the problem this way: "One particular disappointment has been the failure to find a convincing explanation for the behavior of the  $\zeta$ -potential of polystyrene latices as a function of electrolyte concentration, and this has brought the ideality of the system into serious question. Various workers have reported a disconcerting maximum in the  $\zeta$ -potential/electrolyte concentration plot (11-13), and have offered a number of explanations. There seem to exist three possible reasons for the maximum: (i) adsorption of co-ions into the inner Helmholtz plane, (ii) crossing of the mobility/ $\zeta$ -potential maximum, and (iii) hairiness or surface roughness resulting in the shear plane moving away from the surface with decreasing electrolyte concentration."

The effect, the so-called electrokinetic maximum, has attracted considerable consideration by other groups as well (5,14-18) because classical double-layer theories predict only a continuous decrease in mobility with increasing ionic strength.

Goff and Luner (14) have fit the maximum with a three-parameter ion-exchange model while a theoretical treatment by Zukoski and Saville has introduced the dynamic Stern layer model (17). Recent work by Bijsterbosch et al. (15) has suggested that the effect may be due to adsorbed polyelectrolyte.

We would first like to point out that the problem can be simplified by using the measured mobility rather than the  $\zeta$ -potential since the  $\zeta$ -potential is a derived quantity whose calculation depends on a model for the charge distribution surrounding a colloidal particle. In simple limiting theories such as the Smoluchowski or Hückel equations (1) the  $\zeta$ -potential is directly proportional to the mobility with different constants of proportionality. More advanced theories (1) show that the mobility-zeta potential relation depends on the quantity  $\kappa a$  where  $a$  is the particle radius (actually the hydrodynamic radius defining the surface of shear) and  $\kappa$  is proportional to the square root of the ionic strength but is widely known in the form  $1/\kappa$  as the Debye length which is a measure of the extent of the double layer.

It is clear from all of the fingerprints shown here that it is easily possible to demonstrate a maximum in the mobility- $p\lambda$  profile (which is the fundamental curve underlying the zeta potential-salt concentration maximum) at a selected and constant pH. It is also clear that the nature of the mobility- $p\lambda$  profile will vary strongly with pH so that much of the controversy in the literature may simply be a consequence of an ill-defined path in the pH- $p\lambda$  domain. Indeed, some workers have considered the maximum as dependent on ionic strength which does not distinguish the  $p\lambda$  dependence from a pH dependence or some combination path in the pH- $p\lambda$  domain. Further understanding of the effect can clearly be facilitated by defining the path in the pH- $p\lambda$  domain where the measurements are made and interpreted.

**Hydrodynamic Fingerprinting.** Our experience with electrophoretic fingerprinting or the SCMS has led us to conclude that a logical complement to the SCMS is the hydrodynamic fingerprint (HF) or self-consistent diameter surface (SCDS) which is a three-dimensional representation of the measurable hydrodynamic diameter as a function of pH and  $p\lambda$ . If the diameter surface is independent of the order of data acquisition then the SCDS is an HF, a true state function.

The hydrodynamic diameter may be determined at high particle concentration by sedimentation or ultracentrifugation but it would be preferable to measure the hydrodynamic diameter by PCS (photon correlation spectroscopy, also known as QELS for quasi-elastic light scattering) because, in principal, measurements can be made at a particle concentration comparable to the electrophoresis measurements.

In such a case, a comparison of  $u_E$  can be made with  $d_h$  the hydrodynamic diameter at the same point in the pH- $p\lambda$  domain. Moreover, one can obtain a  $u_E$ -pH profile at constant  $p\lambda$  to compare with a  $d_h$ -pH profile at constant  $p\lambda$  and also, a  $u_E$ - $p\lambda$  profile at constant pH to compare with a  $d_h$ - $p\lambda$  profile at constant pH. Such profiles would add to our understanding of the electrokinetic maximum described above.

With SCMS and SCDS information available one can compare the dependence of the electrophoretic fingerprint and the hydrodynamic fingerprint on particle concentration to gain insight into the nature of electrokinetic and hydrodynamic interactions. At low particle concentration, the measurements will be controlled by particle-fluid interactions which may be used to define reference topologies (electrokinetic and hydrodynamic fingerprints) which may be used to measure the particle-particle interactions that arise with increasing particle concentration.

## Conclusions

1. We have shown that the electrokinetic fingerprint or self-consistent mobility surface is a powerful tool to determine a characteristic electrical state function.
2. The SCMS may be interpolated to give mobility profiles at constant pH and  $p\lambda$ .



3. By analogy with the SCMS, we have proposed the use of the SCDS or self-consistent diameter surface, a three-dimensional representation of the hydrodynamic diameter as a function of pH and  $p\lambda$ .
4. The SCDS may be interpolated to give diameter profiles at constant pH or  $p\lambda$ .
5. The electrokinetic maximum in the zeta potential vs. salt concentration could be better defined and better studied using pH or  $p\lambda$  profiles from a SCMS and a SCDS at comparable particle concentrations.

### Acknowledgments

This work was supported by grants from the CABOT Foundation and a contract with the AMOCO Corporation. Technical assistance and instrument support was provided by Pen Kem, Inc. The work is based on the Ph.D. thesis of S.-J. Shiau, presently at DuPont Taiwan Ltd., 7th Fl. International Bldg., 8 Tung Hua North Rd., Taipei, Taiwan, R.O.C.

### Literature Cited

1. Hunter, R. J. Zeta Potential in Colloid Science; Academic: New York, 1981.
2. Marlow, B. J.; Rowell, R. L. J. Energy & Fuels 1988, **2**, 125.
3. Marganski, R. E.; Rowell, R. L. J. Energy & Fuels 1988, **2**, 132.
4. Marlow, B. J.; Fairhurst, D.; Schutt, W. Langmuir 1988, **4**, 776.
5. Morfesis, A. A.; Rowell, R. L. Langmuir 1990, **6**, 1088.
6. Carbon black samples were kindly supplied by Dr. John Day.
7. Goetz, P. J. U.S. Patent 4 154 669.
8. Marlow, B. J.; Rowell, R. L. J. Energy & Fuels 1988, **2**, 125.
9. Shiau, S.-J. Ph.D. Thesis, University of Massachusetts, Amherst, 1989.
10. Midmore, B. R.; Hunter, R. J. J. Colloid Interface Sci. 1988, **122**, 521.
11. Meijer, A. E. J.; van Megen, W. J.; Lyklema, J. J. Colloid Interface Sci. 1978, **66**, 99.
12. Bensely, C. N.; Hunter, R. J. J. Colloid Interface Sci. 1983, **92**, 448.
13. Van der Put, A. G.; Bijsterbosch, B. H. J. Colloid Interface Sci. 1983, **92**, 499.
14. Goff, J. R.; Luner, P. J. Colloid Interface Sci. 1984, **99**, 468.
15. Boncamp, B. C.; Alvarez, R. H.; De Las Nieves, F. J.; Bijsterbosch, B. H. J. Colloid Interface Sci. 1987, **118**, 366.
16. Zukoski, C. F.; Saville, D. A. J. Colloid Interface Sci. 1985, **107**, 322.
17. ibid. 1986, **114**, 32.
18. ibid. 1986, **114**, 45.

RECEIVED January 29, 1991

## Chapter 22

# Zeta Potential Measurements of Irregular Shape Solid Materials

D. Fairhurst<sup>1</sup> and V. Ribitsch<sup>2</sup>

<sup>1</sup>Brookhaven Instruments Corporation, 750 Blue Point Road,  
Holtville, NY 11742

<sup>2</sup>Institute for Physical Chemistry, University of Graz, Austria

An instrument is described to measure the electrokinetic potential of solid bodies whose size and/or shape precludes determination by either conventional electrophoresis, or electroacoustic, techniques. Based on the established principles of streaming potential/current, and using specially designed measuring cells, the zeta potential of fibres and films is calculated from two simple methods. Examples of measurements are presented to demonstrate the straightforward use of the instrument for the investigation of industrially important applications.

The electrokinetic surface properties of materials are important to many industrial processes (1), and also biological and medical applications (2-4). These properties are generated by the electrochemical double layer (EDL) which exists at the phase boundary between a solid and a solution containing ionic moieties in which the solid is dispersed or suspended.

The net charge at the surface of a material in contact with a polar medium is governed by three processes viz ionization/dissociation of surface chemical groups, adsorption of ionic species and dissolution of ions from the material into solution.

The distribution of the electrical charges at the interface is different from that in the bulk phase. The simplest model is that of Stern (5). The charges at the surface are compensated by ions of opposite charge (counter-ions) in solution forming two different layers. Hence the term electrochemical double layer. The layer closest to the surface, (the Stern layer), is considered immobile whilst the outer layer, (the diffuse layer), allows diffusion of ions through thermal motion.(Figure 1).

The potential decreases linearly from  $\psi_0$ , (the surface, or wall, potential), to  $\psi_d$ , (the Stern potential), and then decays exponentially to zero in the diffuse

0097-6156/91/0472-0337\$06.00/0  
© 1991 American Chemical Society

layer. Unfortunately, the fundamental interfacial property  $\psi_0$ , (and hence charge density,  $\sigma_0$ ), is experimentally inaccessible (6). What can be derived is the electrokinetic, or zeta, potential (ZP). This quantity is defined as the potential at the surface of shear - so called because any relative movement of the surface with respect to the solution will cause some of the counter-ions to be sheared off resulting in only partial compensation of the surface charge. The location of the surface of shear is never precisely known. In reality it is a region of rapidly changing viscosity rather than a mathematical plane. Thus the ZP is not well defined. Nevertheless the ZP has become a useful parameter to monitor electrokinetic behavior, especially changes in such behavior (1). In theoretical calculations the ZP is frequently taken to be identical with the Stern potential.

**Methods to determine the Zeta Potential.** Any relative motion between the rigid and mobile parts of the EDL will result in one of four related electrokinetic effects (Figure 2). Measurements made using techniques based upon each effect should, in principle, result in the same calculated value for the ZP. Very often a variety of factors conspire to produce results that are not compatible. These include assumptions in the model for the EDL, inadequacies in the theory, experimental limitations in the design and construction of instrumentation and differences in sample preparation for each method (7).

Since the electrochemical properties at the solid-liquid interface are critically dependent upon the extent of that interface and the, concomitant, interfacial chemistry then it is crucially important that the correct measurement technique be used.

Instruments, based on the different electrokinetic effects, have practical working limits. The most common procedure used is (micro)electrophoresis. This requires that the material under investigation be in the form of a stable dispersion of microscopically visible particles. Only extremely dilute sols (typically less than 0.001%) can be studied and calculation of the ZP assumes a spherical particle. Most industrial dispersions are concentrates; dilution is, often, not an innocuous process. Also, the particles under investigation must not be so large, nor so dense, that they sediment from the field of view before the measurement can be completed. The new electroacoustic technique (8), which is an extension of the sedimentation potential method, will work with dispersion concentrations in the range 1w/w% to 50w/w%. However, the technique is in its infancy; various technical/practical complications arise as the particle concentration increases making calibration difficult. Furthermore, calculation of ZP values from the raw (vibration)potential data has not been definitively established.

Figure 3 is an example of the limitations of each electrokinetic technique using the constraints of particle density and solids volume fraction. Note, there is no completely satisfactory method for systems containing material of density less than approximately 2 g/cc and at concentrations between about 0.1% to about

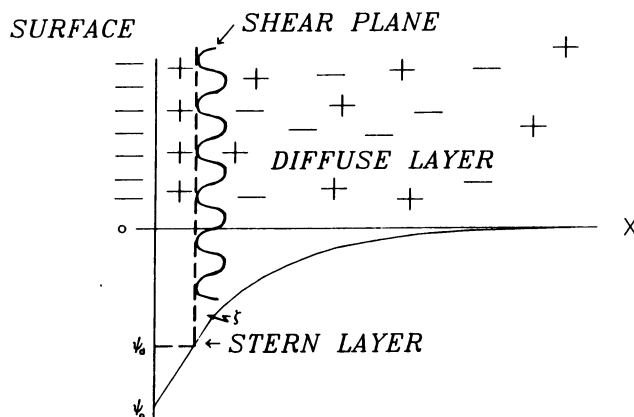


Figure 1. Stern Model of the Electrochemical Double Layer.

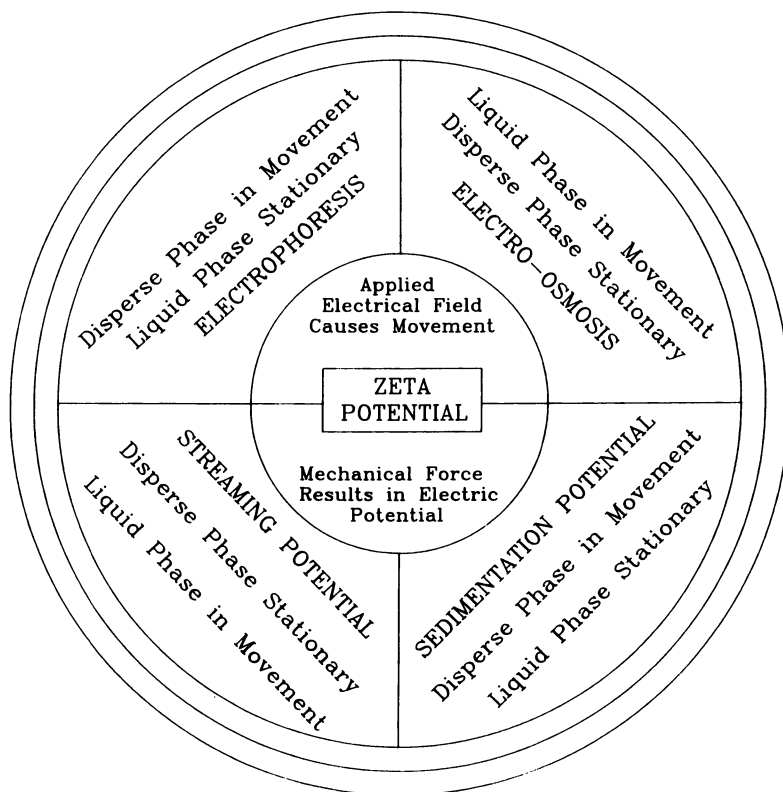


Figure 2. Relationship between the four types of electrokinetic phenomena.

August 2, 2012 | <http://pubs.acs.org>  
 Publication Date: September 24, 1991 | doi: 10.1021/bk-1991-0472.ch022

10%. Other constraints, such as refractive index and particle size, can also be used to construct alternative "technique limitation" diagrams.

The choice of method should be predicated primarily by the particular application that needs to be investigated. Too often, the system under investigation is adapted to fit the available instrumentation; care must be taken that the results of any measurement are not instrument dependent. This can be illustrated by the example of paper wet end chemistry. The ZP of the furnish must be measured and optimized in order to maximize process parameters such as drainage, water removal and retention (9-11).

The "furnish" is a fibrous wood pulp slurry from which paper is made. Wood fibres are thinner than human hair but can vary in length from tens of micrometres to tens of millimetres. The furnish can also contain various additives to provide desired physical and processing properties. These additives include fillers to provide opacity, sizing to give water resistance and dyes for colour. It is clear from Figure 3, however, that (micro)electrophoresis is only suitable for use with a small, selected, portion of the fines. This fraction will have different interfacial properties to the bulk furnish. Since the entire furnish cannot be assessed, results obtained using (micro)electrophoresis will be limited in their usefulness. Further, wood fibres are hollow and stiff so they are beaten ("refining") which causes them to roughen, fray and collapse. This gives the mixture better bonding quality, allowing the fibres to adhere to each other. The fibres are beaten to varying degrees of "freeness"; the freeness affects how quickly water can be removed from the pulp. The beating essentially changes the viscoelastic behaviour of the pulp. It also has the effect of exposing more surface functional groups. The major chemical constituents of wood fibre are cellulose and lignin. Thus, the surface groups are anionic (negatively charged).

It is common practice to add so-called "drainage aids" to neutralize this surface charge and create a structure which will have maximum drainage while maintaining the desired physical properties. These drainage aids are, in effect, cationic (positively charged) surfactants, polyelectrolytes and polymers. Thus, an important parameter which needs to be monitored is the cationic demand of the pulp. This can readily be made by measuring the ZP of the pulp as a function of added cationic chemical. Comprehension of the relation between cationic demand and the level of furnish freeness is fundamental to understanding wet end chemistry. A meaningful correlation clearly can not be obtained using (micro)electrophoresis.

Measurement of the ZP of materials of irregular size and shape, such as textile fibers, hair, polymer films, paper pulp, metal foil and coarse dispersions of mining material, can be made most satisfactorily using the streaming potential method. An intensive review of the theoretical background, and methodical details, of ZP measurements on fibers has been made by Jacobasch(12).

## Principles

**Measurement of Streaming Potential : Basic Theory.** When an electrolyte solution is forced, by external pressure, through a porous plug of material, or across a channel formed by two plates, or down a capillary, a streaming potential develops between the ends (Figure 4). The development of this potential which arises from the motion of ions in the diffuse layer is, in fact, a complex process - transfer of charge and mass occurring simultaneously by a number of mechanisms. The potential difference developed for a given applied pressure difference is measured by electrodes placed at either end of the plug or capillary. The fundamental equations relating mechanical and electrical forces were first derived by Helmholtz and Smoluchowski; an excellent review of the topic has been made by Hunter (1).

The ZP is calculated from :

$$\zeta = (E_s/\Delta p).(n / \epsilon \epsilon_0).(L/A).(1/R) \dots\dots\dots(1)$$

Where  $\zeta$  is the zeta potential,  $E_s$  is the streaming potential,  $\Delta p$  is the hydrodynamic pressure difference across the plug,  $n$  is the liquid viscosity,  $\epsilon$  is the liquid permittivity,  $\epsilon_0$  is the permittivity of free space,  $L$  is the length of the plug,  $A$  is the cross-sectional area of the plug and  $R$  is the electrical resistance across the plug. The inadequacies of the fundamental equation have recently been reviewed (13). For most practical systems Equation 1 is perfectly adequate. Practical problems, inherent in making the measurement, such as asymmetry potential, plug porosity and surface conductance are well documented (1,7,14,15).

The various terms in Equation 1 are known or must be measured. The first term,  $(E_s/\Delta p)$ , is determined by direct measurement of the potential generated for a given, constant, driving pressure. The precision and repeatability of detection can be significantly increased if the potential is monitored as a function of a continuously increasing pressure difference (16). The value of the quotient  $(E_s/\Delta p)$  is determined from the slope. For a given temperature the values of  $n$ ,  $\epsilon$ , and  $\epsilon_0$  are constant for the liquid used (usually water). The plug resistance,  $R$ , can be measured directly using an AC bridge at three different frequencies (500, 1000 and 2000 Hz) (17). However, if both the streaming potential,  $E_s$  and the streaming current,  $I_s$ , are measured simultaneously then the DC resistance,  $R$ , can be determined indirectly from the ratio of the two quotients,  $(E_s/\Delta p)/(I_s/\Delta p)$  (18).

The final term,  $(L/A)$ , consists of two parameters neither of which can be easily measured. Various approaches have been suggested to address the problem. Two different, but simple, methods are those of Fairbrother and Mastin (19) and Chang and Robertson (20). In the Fairbrother and Mastin (FM) approach the term  $(L/A)$  is replaced by  $(R_s K_s)$ , where  $R_s$  is the electrical resistance of the plug when the measurement cell is filled with an electrolyte

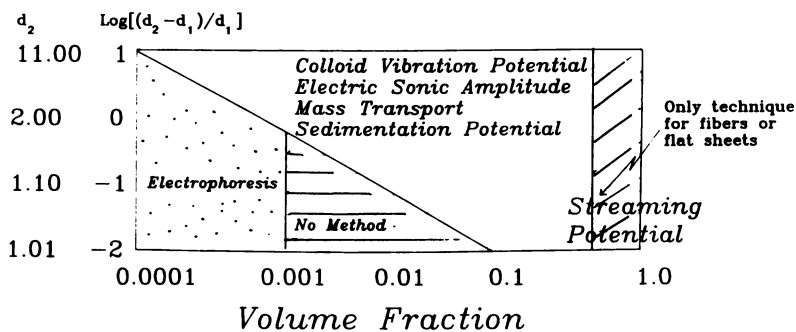
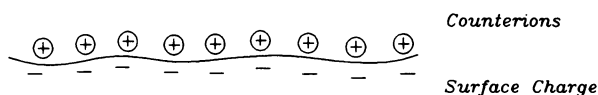
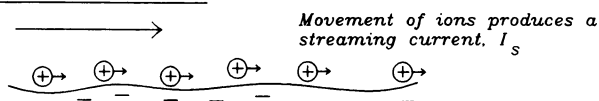


Figure 3. Operational Envelope for Electrokinetic Techniques under constraints of Density and Volume Fraction.

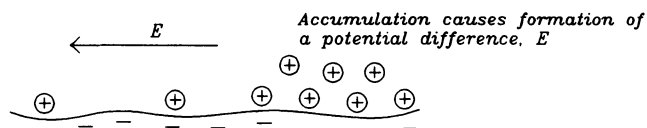
Electric Double Layer at Rest



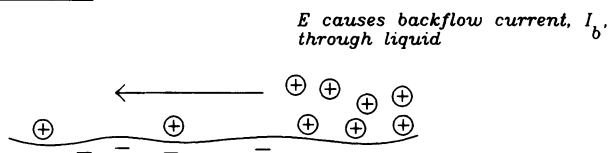
Liquid Caused to Move Relative to Surface



Accumulation of Ions Downstream



Backflow Current Through Liquid



A steady state is reached quickly where  $I_s - I_b = 0$  and the measured potential difference (the streaming potential) gives direct information about the electrostatic charge at the surface-solution interface.

Figure 4. Schematic representation of Streaming potential at the Solid-Solution Interface.

whose specific conductance,  $K_s$ , is accurately known (21). A 0.1M KCl solution is used to avoid the problem of surface conductance (22).

Thus,

$$\zeta = (E_s / \Delta p) \cdot (n / \epsilon \epsilon_0) \cdot (R_s \cdot K_s / R) \dots\dots\dots(2)$$

The measurements of  $R_s$  and  $R$  are usually made sequentially. The cell is first filled with the standard electrolyte and  $R_s$  measured. The cell is then flushed and refilled with the experimental liquid and  $R$  measured. Because a complete exchange of electrolyte may not be possible without changing the packing density of the plug, the FM approach is limited to streaming potential measurements through single channels (membranes), or across surfaces with well defined, fixed, open geometry (films).

For plugs of granular material and bundles of fibers, where the packing density is not well defined and cannot always be duplicated, the approach of Chang and Robertson (CR) can be adopted. Building on geometric considerations of Goring and Mason (23) they developed an empirical relationship between porosity and packing density. Using their approach Equation 1 can be written as :

$$\log_e(E_s / \Delta p) \cdot (L_m / R) = \log_e \zeta - Bd \dots\dots\dots(3)$$

Where  $L_m$  is the distance between the electrodes,  $B$  is a constant which depends upon the material under investigation and  $d$  is the (fibre) concentration in the cell in  $g/cm^3$  or "packing density".

The ZP is obtained from the intercept of a plot of streaming potential versus packing density (Equation 3).

## Methods and Materials

**Apparatus.** The measurements presented here were all performed using an instrument developed originally at the Technical University Graz, Austria. The design and operation addresses all the requirements discussed above. A schematic diagram and photograph are shown in Figure 5. The instrument comprises an analyzer, data control system and measuring cells. The analyzer consists of a mechanical drive unit to produce, and measure, the driving pressure which causes the electrolyte solution to flow from a reservoir into and through a measuring cell and out back into the reservoir, or to waste. The flow direction can be reversed. Operation is manual or under computer control. The streaming potential and the streaming current are both measured. Temperature, pH and conductivity sensors are also included. Plug resistance is measured by a choice of either AC or DC methods. The ZP is calculated from the streaming potential/streaming current data using either the CR or FM methods.

A commercial version of the instrument is now available as the BROOKHAVEN-Paar BI-EKA.



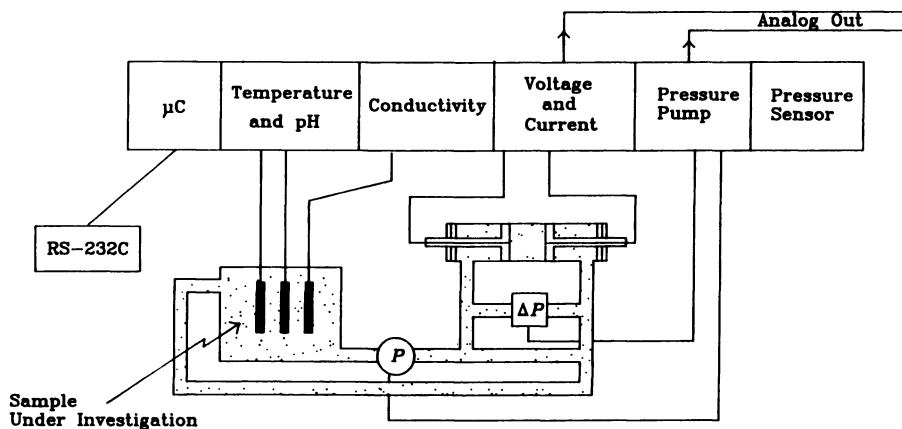
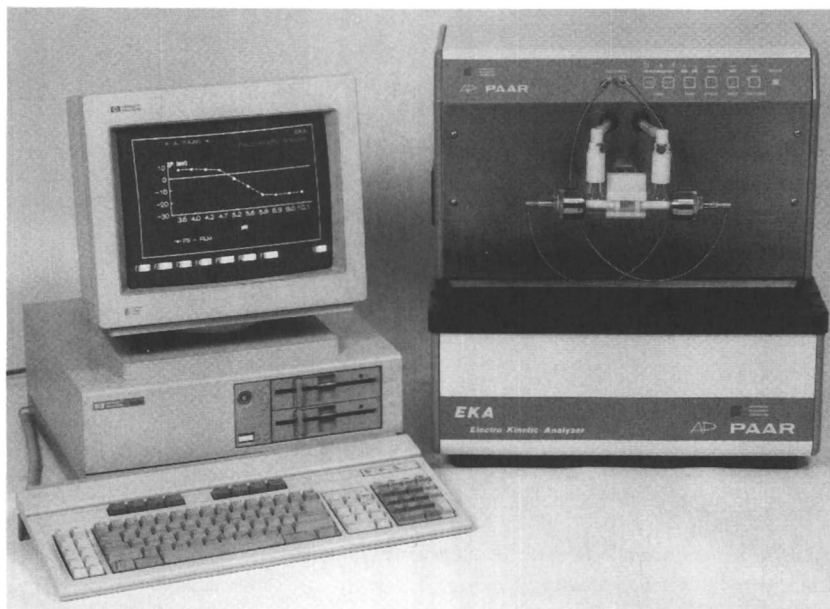


**Figure 5. Photograph and Schematic Diagram of the BROOKHAVEN - Paar Electrokinetic Analyser.**

**Measuring Cells.** The choice of cell design depends upon the nature of the sample under investigation.

1. A Cylindrical Cell (Figure 6a) based on earlier designs of Goring and Mason (23) and Joy et al (24), with modifications suggested by Schaumberger and Schurz (18). It has two perforated Ag/AgCl electrodes which are able to slide inside a glass body. A known weight of material in the form of fibers or granules is placed between the electrodes. The electrode spacing is measured precisely by means of micrometer screw drives. Either the FM or the CR method of ZP evaluation can be selected. In the latter method, the distance between the electrodes is decreased in a series of sequential steps to squeeze the plug and so change the packing density.

2. A Rectangular Cell (Figure 6b) made of PMMA based on an original idea by Andrade (25,26) with improvements adopted by Jacobasch (27). The necessary hydrodynamic requirements (28) were met to ensure reproducible determination of streaming potential. A channel of well defined dimensions is created by use of PTFE spacers. The sample is usually in the form of plates, film or foil and is cut to size (120mm x 50mm) to fit inside the PTFE formers. Irregular shaped, or formed, material can also be accommodated by mounting in a suitable sealing material such as beeswax in recesses in an optional, modified, version of the cell; each recess has dimensions 100mm x 20mm x 5mm. Ag/AgCl electrodes are mounted at each end of the channel. Only the FM method can be used to calculate the ZP.

It must be stressed that the streaming potential is valid only if certain hydrodynamic conditions are met. In any cell design the fluid flow must be steady, incompressible, laminar, and established (28). Ensuring such conditions exist is not trivial and, yet, is a basic assumption in the calculation of ZP from streaming potential measurements. Recently, Bowen (29) has extended the theory and provided correction factors to the classical Helmholtz-Smoluchowski equation under conditions where the capillary or channel dimensions are large relative to the double layer thickness.

**Procedure.** Ideally, before any measurement the material under investigation should be soaked overnight in the initial, or base, electrolyte with agitation to remove air bubbles adhered on the surface. This is more important for hydrophobic surfaces such as polymer/plastic sheets and bundles of polymer fibres. When the cell is assembled with the sample in place it must first be flushed in both directions to remove entrapped air. In the BROOKHAVEN-Paar EKA rinsing and flushing can be done manually or automatically (under computer control).

All parts of each cell must also be cleaned on a regular basis not only for good laboratory practice but also to achieve the best reproducibility in measurements. For the glass (cylindrical) cell soaking in a suitable laboratory detergent

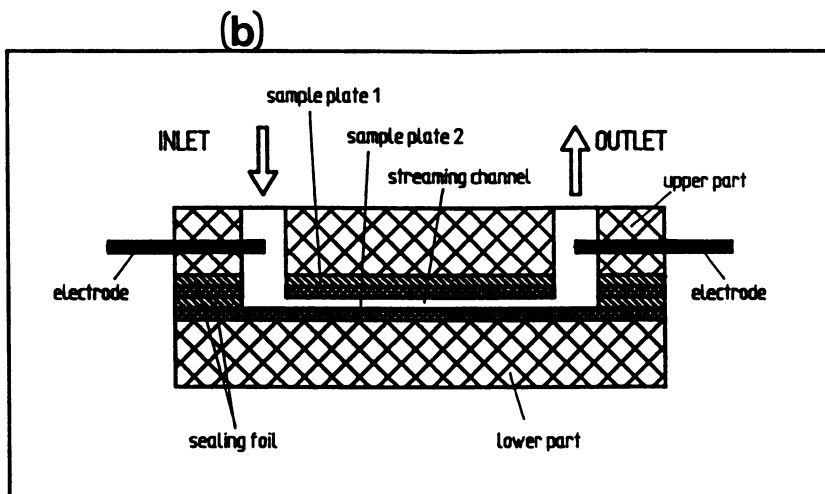
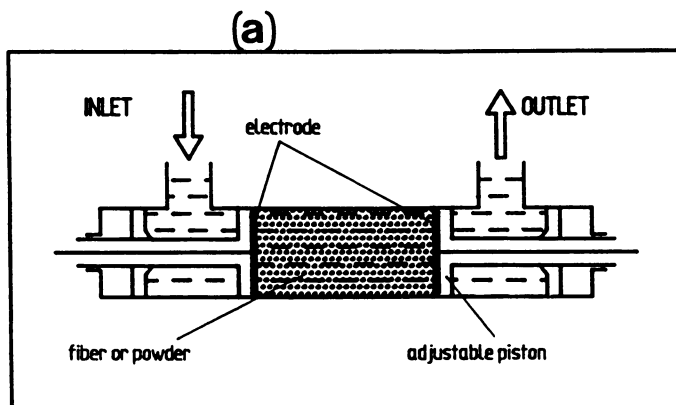


Figure 6. Measurement Cells for the Electrokinetic Analyser.  
 (a) For the investigation of fibers and granulates.  
 (b) For the investigation of films and plates.

followed by a thorough rinsing in distilled water is usually sufficient. The inner surfaces of the PMMA (rectangular) cell can be cleaned using 5% sodium carbonate followed by a detergent wash (after Joy et al).

The Ag/AgCl electrodes must also be regenerated from time to time. A convenient preparation of such electrodes has been described by Ives and Janz (30).

**Materials.** All materials were used as supplied. No special precautions or cleaning procedure was adopted other than the initial soaking prior to measurement. All reagents were Analar grade.

### Results and Discussion

Four examples are presented. These demonstrate the versatility, and utility, of the streaming potential technique for the investigation of the electrokinetic properties of surfaces of materials which are directly used in important industrial processes.

**Example 1.** The quality of offset printing is affected by the surface chemistry of the printing plates (31). The bright metal surface is dimmed as corrosion proceeds. Various oxidative species are produced on the surface and these reduce the hydrophobic character. The oxide groups can be ionic and so will dissociate in solution to a degree which depends upon the pH of the solution and, to a lesser extent, on the ionic strength. The magnitude of the ZP is a sensitive measure of the dissociative nature of surface groups ; a ZP of zero indicates an isoelectric point (IEP) and a plateau in the plot of ZP vs pH is indicative of complete dissociation (1,32).

Figure 7 shows the pH dependency of the ZP determined for two samples of printing plate which have received different surface treatments. Two pieces of each sample were cut to size to fit into the standard rectangular cell. Surface A is clean with a bright metallic luster. Surface B has been exposed to corrosive elements and appears dim. The oxidized surface exhibits an IEP near pH6 and total dissociation of surface groups can be attained at around pH7. In contrast, dissociation is not complete for the clean surface until around pH10 and there is no evidence of an IEP.

Both the wetting and adhesive properties of solids depend on the dissociation constant (pK-value) of the surface chemical composition (33-35); the pK-value of such surface groups can be estimated from ZP measurements (36). Thus, the effects of chemical and physical treatment of surfaces can readily be monitored and analysed using streaming potential measurements.

The flow through nature of the streaming potential method also makes it ideal for the study of long term corrosion or oxidation processes using different solution formulations - one example would be printing ink fountain solution.

American Chemical Society  
Library

1155 16th St., N.W.

In Particle Size Distribution II, Powder, T.;  
ACS Symposium Series; Washington, D.C.: American Chemical Society, 1991.

**Example 2.** The lifetime of paper machine felts is highly dependent upon the degree of contamination which occurs during paper manufacture (37). The "paper felt" is a felt blanket which conveys the newly formed paper through press rollers (and steam heated driers) where excess water is squeezed out of the paper and into the felt. The tendency of the felt to become polluted is controlled by the felt surface charge (38). The least contamination is found for very low, but negative, values of the ZP. Usually cationic synthetic resins are added to felts during their manufacture to achieve this low ZP condition.

Table 1 lists results of ZP measurements made using samples of polyester fiber felt treated with different levels of resin. Pieces of felt were cut to fit the recesses of the modified rectangular cell and the ZP was determined using distilled water as the flow fluid. The results show that increasing amounts of resin lead to a decrease in the primary negative ZP. Overdosing with the resin produces a positive ZP - an equally undesirable situation.

**Table 1. Polyester Paper Machine Felt Samples**

Resin Treatment	Zeta Potential (mV)
Untreated	-28
0.1%	-17
0.5%	-2
1.0%	+10

Thus, streaming potential measurements can be used to optimize felt manufacturing and also to improve the filtration process in paper production. In addition it is possible to study variations in surface charge behaviour caused by contamination which occurs during paper manufacture as well as cleaning procedures for the felts.

**Example 3.** In the textile industry fibers are coated with agents that reduce the tendency for surface oxidation which will affect processibility of the fiber (39).

Figure 8 shows the pH dependency of two samples of viscose fibers. Sample A is coated and Sample B is untreated. No difference can be observed. Thus the nature of any dissociable groups is unaffected by the coating treatment.

Cationic quaternary ammonium salts are used as anti-static agents for fibers (40-42). Figure 9 shows the result of titrating the same two viscose fiber samples with cetylpyridinium bromide (CPyBr) solution. There is a dramatic difference in the number of titratable groups between the two fiber surfaces. The untreated fiber required almost three times the concentration of CPyBr (12mg) to obtain an IEP compared with the protected fiber (4mg). The maximum surface coverage was also significantly different.

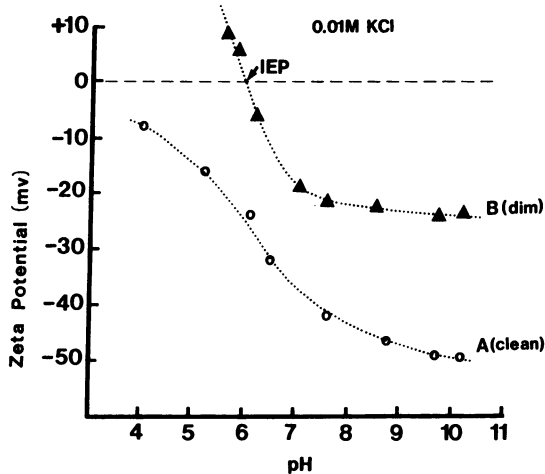


Figure 7. Variation of the Zeta Potential with pH for two pieces of Offset Printing Plate.

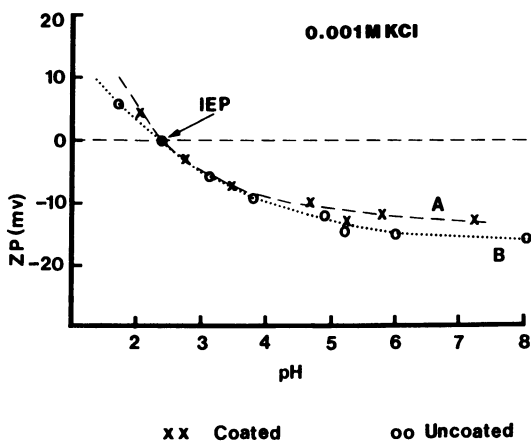


Figure 8. Comparison of the pH dependency of the Zeta Potential for two samples of Viscose fibers.

The protected fiber has a 50% larger ZP value than the uncoated fiber and would, therefore, exhibit much better anti-static properties.

Thus, streaming potential is an effective tool to study both deviations in the chemical composition of fibres and the activity of the preparation agents used in textile processing.

**Example 4.** In the mining industry rock destruction or machining uses high speed drills with diamond bits. The rate of diamond abrasion is a function of the machining speed. Drilling fluids which are used as coolants are formulated to contain auxiliary additives (43) which critically affects both parameters viz drill abrasion and machine speed. Optimum conditions i.e. minimum diamond abrasion and maximum machining speed are achieved when the zeta potential of the rock surface is zero with respect to the liquid coolant (44,45). To date this "enhanced drilling phenomenon" is not well understood; the economic implications are, however, enormous. Also, no statistically reliable trend exists between rock property tests (such as hardness) and mechanisms proposed to explain this point of zero charge phenomenon (46).

For negatively charged rock surfaces cationic surface active agents are used in the coolant formulation. Figure 10 shows the result of an experiment which used two plate-like pieces of granite rock. The ZP was measured as a function of the concentration of dodecylpyridinium chloride (DoPyCl). For the material under investigation only a relatively low concentration (less than 0.01M DoPyBr) was needed to completely reverse the sign of the charge on the rock surface.

Thus, streaming potential measurements can be used to directly determine optimum additive concentrations for zero point of charge conditions of mineral surfaces.

For geological material, fracture of the surface can expose a completely different surface chemistry. Measurement of fines alone, using (micro) electrophoresis, can give incomplete, and possibly misleading, information. This may be one reason for the varied, often contradictory, ZP data for mineral surfaces. The streaming potential method uses material of macroscopic dimensions and is, thus, more appropriate for real, practical systems.

## Conclusion

A new instrument, the BROOKHAVEN-Paar BI-EKA, is available to measure the ZP of materials of industrial importance whose size, or shape, precludes measurement by (micro)electrophoresis. Reproducibility and comparability of results is ensured through the measuring cell geometries. However, the precision of ZP values from the streaming potential method is typically about 10% and so is less than that obtained using (micro)electrophoresis.

Investigation as to the nature, and type, of various processing agents for selected applications - such as optimization of surface chemical composition - can readily be made. A major advantage of the technique is the ability to

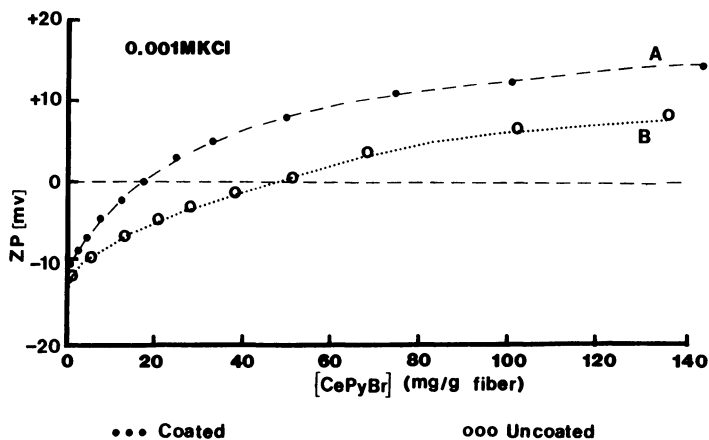


Figure 9. Effect of the Adsorption of Cetylpyridinium Bromide on the Zeta Potential of Viscose fiber.

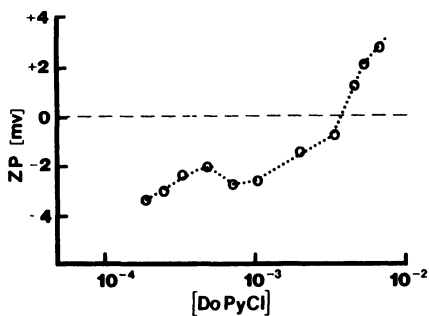


Figure 10. The Reversal of Charge of a Granite Surface using a Quaternary Ammonium Salt.



investigate adsorption phenomena in situ. The flow through nature of the method makes it ideal for the study of long term corrosion or oxidation processes. The use of material of macroscopic dimensions provides data which is more appropriate to process conditions.

### Literature Cited

1. Hunter,R.J.,Zeta Potential in Colloid Science; Academic Press, New York, 1981.
2. Richmond,D.V. and Fisher,D.J., Advances in Microbial Physiology, 9, 1, 1973.
3. Seaman,G.V.F., in "The Red Blood Cell", Volume 2, Academic Press, New York, 1975.
4. Berreta,D.A. and Pollock,S.R., Journal of Orthopaedic Research, 4, 337, 1986.
5. Kruyt,H.R.(Ed), Colloid Science, Volume 1, Elsevier, London, 1949.
6. Guggenheim,E.A., J.Phys.Chem., 33, 842, 1924.
7. Shaw,D.J., "Electrophoresis", Academic Press, London, 1969.
8. Marlow,B.J., Fairhurst,D. and Pendse,H.P., Langmuir, 4, 611, 1988.
9. McKague,J.F., et at., TAPPI Papermakers Conference, Boston, 1974.
10. Melzer,J., Das Papier, 26, 305, 1972.
11. Anderson,R.G. and Penniman,J.G., Paper Trade Journal, January 14, 1974.
12. Jacobasch,H-J., et al., Coll. and Polym. Sci., 263, 3, 1988.
13. Christoforou,C.C., et al., J.Coll. and Int. Sci., 106, 1, 1985.
14. Somasundaran,P. and Kulkarni,R.D., J.Coll. and Int.Sci., 45, 591, 1973.
15. van den Hoven,T.J.J., Thesis, Wageningen Agricultural University, 1984.
16. Ball,B. and Fuerstenau,D.W., Miner.Sci.Eng., 5, 267, 1973.
17. Ferse,A. and Paul,M., Z.Phys.Chem., 252, 198, 1973.
18. Schausberger,A. and Schurz,J., Ange.Makromol.Chem., 80, 1, 1979.
19. Fairbrother,F. and Mastin,H., J.Chem.Soc., 75, 2318, 1924.
20. Chang,M. and Robertson,A., Can.J.Chem-Eng., 45, 66, 1967.
21. von Stackelberg et al, Kolloid Z.,135, 67, 1954.
22. Bull,H.B. and Gortner,R.A., J.Phys.Chem., 35, 309, 1931.
23. Goring,D. and Mason,S., Can.J.Res., Sect.B., 28, 307, 1950.
24. Joy,A.S., Watson,D. and Botten,R., Res.Techniques in Instr., 1, 6, 1965.

25. Van Wagenen, R.A., Andrade, J.D. and Hibbs, J.B., J. Electrochem. Soc., 123, 1438, 1976.
26. Van Wagenen, R.A. and Andrade, J.D., J. Coll. and Int. Sci., 76, 305, 1980.
27. Schurz, J., et al., GIT Fachz. Lab., 2, 98, 1986.
28. Van Wagenen, R.A., PhD Thesis, University of Utah, 1976.
29. Bowen, B.D., J. Coll. and Int. Sci., 106, 367, 1985.
30. Ives, D. and Janz, G., Reference Electrodes, Academic Press, New York, 1961.
31. Bassemir, R.W., in "Colloids and Surfaces in Reprographic Technology (Eds. M.Hair and M.L.Croucher)", ACS Symposium Series 200, 1982.
32. Ottewill, R.H. and Shaw, J.N., Disc. Faraday Soc., 42, 154, 1966.
33. Bolger, J.C., in "Adhesion Aspects of Polymeric Coatings (Ed. K.Mittal), Plenum Press, New York, 1983.
34. Fowkes, F.M., in "Physicochemical Aspects of Polymer Surfaces (Ed. K.Mittal), Plenum Press, New York, 1983.
35. Jacobasch, H.-J., Angew. Makromol. Chemie, 128, 47, 1984.
36. Schurz, J., et al., Wochenblatt f. Papierfabrik., 525, 1989.
37. Saltman, D., "Paper Basics", Van Nostrand, New York, 1978.
38. Weigl, J. and Kaestner, M., Wochenblatt f. Papierfabrik., 16, 559, 1982.
39. Linfield, W., "Fatty Acids and their Industrial Application", Marcel Dekker, New York, 1968.
40. Schwartz, A.M. and Perry, J.W., "Surface Active Agents", Vol.1, Interscience, New York, 1949.
41. Jungerman, E. (Ed), "Cationic Surfactants", Marcel Dekker, New York, 1970.
42. Johnson, D.H., J. Am. Oil Chem. Soc., 55, 438, 1977.
43. Appl, F.C., et al., Ind. Diamond Rev., 41, 312, 1981.
44. Westwood, A.R.C., et al., Colloids and Surfaces, 2, 1, 1981.
45. Engelmann, W.H., et al., J. Electrochem. Soc., 135, 1043, 1988.
46. Tuzinski, P.A., US Dept. of the Interior, Bureau of Mines, private communication.

RECEIVED July 22, 1991

## Chapter 23

# Operational Protocols for Efficient Characterization of Arrays of Deposited Fineparticles by Robotic Image Analysis Systems

Brian H. Kaye

Physics Department, Laurentian University, Sudbury, Ontario P3E 2C6,  
Canada

Efficient characterization of the size distribution of a sample of fineparticles as viewed through a microscope requires the estimate of the population frequency in each size group. To achieve comparable efficiency in each section of the population an automated system (cybernetic instrument) should initially search large areas of a field of view to establish the range of sizes to be characterized and then establish an appropriate search algorithm for each size group so that the confidence to be placed in the data can be predicted. Procedures for automating this so called "Stratified count strategy" are discussed.

### Primary Count Loss and Secondary Count Gain in Fineparticle Characterization by Image Analysis

The problem of coincidence effects has been extensively studied in stream methods of fineparticle characterization. In stream methods of characterization coincidence effects occur in one dimensional data space that is in the one-dimensional train of fineparticles in the fluid stream present in the measurement zone of the instrument. To understand the generation of coincidence effects in stream methods consider the idealized sketch of an interrogation zone of stream counter such as the Coulter Counter or the Elzone counter as shown in Figure 1 (1,2). The actual physical effects of multiple occupancy of the sensitive zone varies from instrument to instrument but in general multiple occupancy results in the under counting of a smaller size, this error is called primary count loss and the false registering of the presence of a large pseudo fineparticle created by the signal generated by multiple occupancy of the zone. This latter effect is known as Secondary Count gain. The two effects are known as coincidence errors. Early in the days of the development of stream counters such as the Coulter Counter it was appreciated that the only safe way to avoid coincidence errors in a fineparticle characterization study was to continuously dilute the concentration of the suspension being used in the stream counter until the measured fineparticle size distribution function was independent of the further dilution of the suspension.

0097-6156/91/0472-0354\$06.00/0  
© 1991 American Chemical Society

In the characterization of fineparticle systems by inspection of deposited fineparticles on a filter, or other flat surface, coincidence effects arise by the chance positioning of deposited fineparticles close enough to each other to pose an interpretive problem as to whether a given profile constitutes a single fineparticle or if the profile should be treated in the logic of the characterization study as two separate fineparticles. Consider for example, the stylized fields of view for a coal dust sample and a polyurethane foam sample of respirable dusts described by Walkenhorst (3) and by Laskin et al (4) shown in Figure 2.

Although image analysis of deposited fineparticles has been considered to be the ultimate reference method for many fineparticle studies it is somewhat surprising that there have been virtually no studies of the effect of coincidence effects on the accuracy of the fineparticle characterization study in two-dimensional space. Pioneers in the studies of the size distribution of respirable dust were aware of the problem and recommended correction factors for surface covered estimates if the build up of dust from a long term sampler was such that a large fraction of the surface of the filter became covered with dust (5).

When carrying out characterization studies by studying deposited fineparticles the pioneer workers recommended, in any attempt to keep coincidence errors to an acceptable minimum, that analysts keep the percentage of the filter paper covered by dust to below 5% area coverage. There are two problems with this recommendation. First of all, most analysts have very little experience enabling them to judge what constitutes 5% coverage (see discussion of the problem in the next section of this communication) and secondly, as will be shown in the second part of this communication coincidence errors at 5% coverage can be a significant feature of the characterization study. The elimination of spatial coincidence effects is of vital importance when assessing the exposure of industrial workers to respirable dust hazards. For example, if the fineparticles noted by A, B, and C in Figure 2(a) are treated as separate entities, then the respirable dust level could be much higher than if they are considered to be part of the larger units adjacent to them in the field of view. Perhaps one of the reasons for the scarcity of studies of coincidence effects in image analysis studies stems from the fact that operators have been overly confident of their ability to take decisions with respect to the integrity of individual profiles and have relied on electronic logic to separate what they consider to be adjacent profiles rather than integral entities deposited as a whole on the filter paper. Thus, they have developed erosion-dilation logic in automated image analysis to separate what are considered contiguous profiles even if the justification for such processing of the image is minimal (6).

Even if one can rely on erosion logic to separate the contiguous profiles in a field of view this places considerable extra burden on, and hence increases the expense of, the logic available in the processing of deposited profiles. From a cost effectiveness point of view it would appear desirable to arrange the experimental strategies so that there are no contiguous profiles in the field of view. That is to simplify the logic process demanded of the image analysis system.

A basic problem arising in the study of respirable dusts deposited on the filter is an economic one. As will be shown in this communication if one attempts to keep the area density of dust deposited on a filter below the level at which significant coincidence effects occur then there is a need to use a sequence of many filters during a working period. This is usually

technically and financially unacceptable with currently available equipment. Therefore, the analyst is often forced to make subjective decisions with regard to what constitutes an individual profile when looking into the microscope at relatively dense fields of view. As a consequence many studies on respirable dust characteristics are of doubtful value. The situation with respect to the interpretation and assessment of data and respirable dusts reported in the scientific literature is further complicated by the fact that sometimes workers in the field actually report the size distribution of visible subunits present in the dust as distinct from the size distribution of the observable units since they feel that the primary unit constitutes the health hazard. Consider for example the outlines of lead fume generated from an electric furnace studied in a recent publication by Tohno and Takahashi (7). These authors report a logic for separating the profiles of Figure 3(a) into the constituent units displayed in Figure 3(b). This probably grossly over estimates the health hazard of the dust.

Again consider the alumina profiles shown in Figure 4 the authors of this study report that they treated visible subunits as having been formed by chance during the deposition process of the capture of the aerosol by the fibres of the filter (8). In this latter case, the problem is not a simple one of spatial random chance coincidence effects; the problem is compounded by the fact that surface forces for such very fine dust encourage the building of capture trees which deliberately interfere with single fineparticle deposition dynamics (9). Because of the difficulties associated with coincidence effects both by simple random deposition and by enhanced growth of pseudo agglomerates during the deposition process it becomes essential when assessing the true levels of respirable dust to have a physical understanding of the frequency with which simple coincidence effects occur and how the growth of capture trees distort fineparticle characterization studies in two-dimensional space. It may well be that many respirable dust studies have both either under and over estimated the health hazards of a specific dust due to the arbitrary way in which apparent agglomerates have been treated by the logic of the characterization procedure and the anticipation of the operator carrying out the study. In this communication, attention will be focussed on spatial deposition coincidence effects. The problem of the distortion of the size distribution of very fine respirable dust by capture trees growth will be the subject of a future communication. The simulation studies presented in this communication indicate that spatial coincidence effects in dust characterization studies can only be considered to be negligible at much lower filter coverage than previously anticipated or used in industrial hygiene practice. In the final portion of this communication the implications of the studies presented here for the future design of image analysis systems for studying health hazard dust and other powders are explored and future research outlined.

### Monte Carlo Studies of Chance Clustering in Deposited Fineparticle Arrays

To gain a physical understanding of the importance of chance clustering in a deposited array of monosized fineparticles in two-dimensional space one can use Monte Carlo routines in which a random number table is converted into a simulated field of view of fineparticles. Monte Carlo is a general name used by mathematicians to describe the mathematical modelling of procedures which are subject to random variations such as the success (or lack of it) of a gambler playing roulette at Monte Carlo.

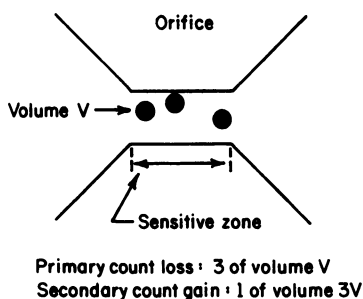


Figure 1: When more than 1 fineparticle occupies the sensitive region of the interrogation zone of a stream counter coincidence effects reduce the accuracy of the fineparticle characterization study.

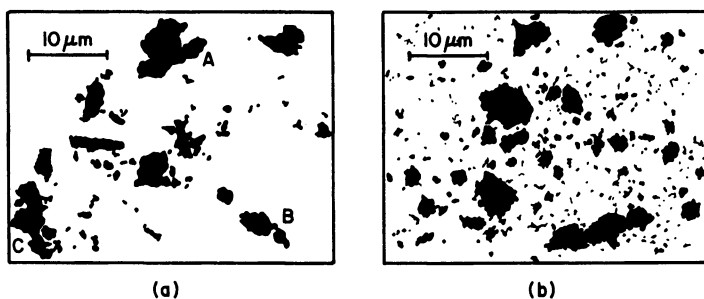


Figure 2: Deciding which items in a field of view of deposited fineparticle constitute separate functional entities is a critical decision in studies of the levels of respirable dust in industrial areas. (a) A sample of coal dust (Reproduced with permission from ref. 3. Copyright C. C. Thomas 1972.) (b) A sample of polyurethane foam dust. (Reproduced with permission from ref. 4. Copyright C. C. Thomas 1972.)

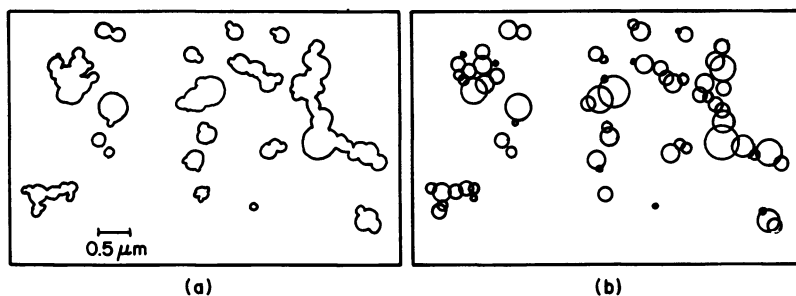


Figure 3: In some occupational health studies observed fineparticles are resolved into “obvious?” constituent units. (Reproduced with permission from ref. 7. Copyright Hosokawa Mikron International 1988.)

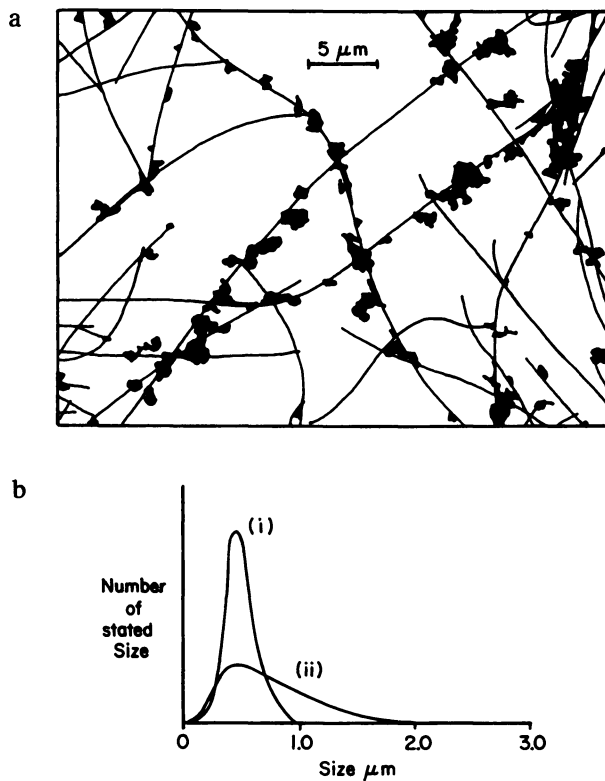


Figure 4: In a recent study of airborne alumina dusts the authors treated apparently contiguous fineparticles and operationally independent units when characterized by analysis of electron micrographs of the captured fineparticles. (a) Size distribution by image analysis and (b) size distribution by laser aerosol spectrometer. (Reproduced with permission from ref. 8. Copyright 1988 VCH Publishers.)

Thus the simulation of the arrival of pesticide droplets on a leaf would be modelled by a Monte Carlo routine (10). In view of the fact that many early studies of deposited fineparticles recommend that one can safely use 5% by area fields of view to carry out size distribution studies the first study carried out was to simulate the clustering occurring by chance in a deposited monosized aerosol at a 5% coverage expectation. The random number table used in the experiments reported in this study is shown in Figure 5 (12). (Note - many personal computers have random number generator programs however, the generation of truly random numbers is a difficult task. For this reason we used the table of Figure 5 which is taken from an extensive study and tabulation of random number tables (6).

Each of the digits in the table of figure 5 occur with a frequency of 0.1. Therefore, to simulate the appearance of a fineparticle field of view covered by monosized profiles up to 5% of the field one needs an unbiased method for converting half of any given digit into simulated fineparticles.

An objective routine for changing a digit into a simulated fineparticle at a 5% level of area coverage is to take a digit as representing a fineparticle if a digit in another random number table is odd, since on average 50% of the digits in the other reference table will be odd. Thus every 9 in the table of Figure 5 could become a dust particle if when we encounter a 9 in the table a digit in a companion random number table is odd. One could also use the criterion that the digit in the other table had to be even when again half of the digits in the first table would be converted into simulated fineparticles. In Figure 6 six simulated fields of view at 5% coverage are shown. The notation in the top left hand corner indicates the rule used to generate the simulated field of view. Thus, in the field of view of Figure 6(a) zero was converted to a simulated deposited fineparticle if the conversion reference digit in a companion table was odd. In Figure 6(b) the digit 1 was converted to a simulated dust particle whenever the conversion reference digit was even and so on. It is interesting to note the fluctuations in real coverage when the anticipated coverage is 5% by area. It can be seen that the actual area coverage varied from a low of 4.56% to a high 6.28%. It is also interesting to note in view of the current interest in fractal geometry that these 6 fields of view constitute statistically self similar systems (2,11). These fields of view can be used to train operators in what constitutes a given level of coverage and what statistically self similar systems look like. Initially operators when shown these fields of view vary widely in their estimate of the area coverage. In an informal experiment with people new to the field of size characterization answers ranging from 10% to 1% were given.

From the point of view of this communication the important aspect of the simulated fields of view of Figure 6 is the level of clustering that has occurred. Thus, clusters as high as 4 units have occurred and clusters of 3 and 2 occur relatively frequently. In Figure 7 the size distribution of the simulated clusters representing secondary count gain clusters at 5% coverage can be seen. It is obvious that primary count loss and secondary count gain are significant factors effecting the accuracy of the characterization study at 5% coverage. If the pixel size represented a size which was considered to be the threshold of the size constituting a respirable hazard the number of respirable dust fineparticles would be under estimated by a factor of 1.4, a factor which could result in a dangerous level of dust being reported as a safe acceptable level.

To explore the density of coverage which is desirable, if one must seek out a coverage at which significant spatial coincidence effects on a filter surface are avoided, the appearance of filter papers at an anticipated



95429	05023	42445	81479	06582	57832	19864	09655	46091	89898
54933	30376	60217	12916	71034	41493	00810	40746	22328	98099
49242	61815	36878	72093	63479	15847	81812	72644	85935	82053
41240	22056	66879	48908	44909	12820	75666	70382	86600	21025
02049	38223	10899	13677	14360	74016	06527	80281	53788	70695
27000	12588	72677	50662	96047	51209	61781	22706	94834	24773
91285	54345	34034	37310	55291	63399	98036	17711	15957	26772
44887	26995	74237	88921	18037	92664	90519	13201	54268	92950
72892	36748	42544	00765	29826	04582	16897	05507	00115	95513
17812	43757	07029	78410	93762	09606	33152	81105	79698	22892
95921	10413	86215	85039	35246	27026	13873	35350	94513	38339
40023	28286	92943	41583	27563	73009	52091	86401	64081	10484
80560	81722	72870	86454	57429	72880	60952	61152	02839	30079
47712	67899	21900	18132	29785	26865	42058	97353	43889	41507
80406	13822	81956	08991	95359	03425	39700	53545	16848	26169
56642	53730	56710	70241	10522	30170	47951	28314	84072	86847
74682	44393	69167	41446	43982	45485	23758	88922	76378	76329
45524	46409	12928	46822	21407	04653	03029	95903	71550	87652
57139	42113	85637	92492	06469	35989	92453	68124	98263	75567
00705	17743	58687	88502	80485	22352	93014	94452	18065	42134
05549	70101	92945	27189	95527	49801	05829	59762	74343	51864
22327	55480	95907	77989	88732	93567	75074	32414	81044	77751
86018	85835	88367	10506	33585	31568	93165	63832	06743	65506
70839	18951	33484	00091	74367	72892	04084	59770	82641	32061
67411	88645	77789	72757	59927	39876	87841	51595	96364	60506
28259	11822	53058	16516	20196	71098	63699	63075	68394	32666
04503	79028	63404	03482	76677	23288	39594	66119	81274	99982
63288	93134	91378	91988	12157	34581	79674	85790	22454	87109
63701	54429	86992	02004	28351	13700	89012	70678	92686	89488
96540	71159	93478	97919	43501	65527	82167	15386	33527	12041
16744	20236	89506	63437	81051	56704	59752	67516	93433	82926
75423	86481	84147	82941	47088	75897	62126	14258	15839	82679
48129	76751	53494	04187	79955	30747	81231	26399	40379	16182
81433	53248	63646	64467	48089	89590	15504	16287	02513	03315
81800	27936	60474	34712	90626	62663	68616	39411	28219	98681
07751	33731	44285	96913	33077	93006	52025	19420	77286	92896
26480	31002	93898	49074	16354	28824	09677	57532	14898	43899
09458	04923	17904	70053	69033	81766	54408	03819	04008	69508
91478	94042	90945	63299	86572	67303	55861	78772	46641	20170
36033	56105	41641	23328	59888	47185	72830	71950	59564	97746
22404	60701	89749	20791	60898	06962	75470	23908	18351	08554
94658	81609	05446	72224	93683	52224	17750	48138	41620	90644
39921	05493	34544	93414	02831	02695	06558	13437	91279	30904
36744	75178	91131	27882	87981	82359	62162	72337	98921	74546
16956	15978	46143	32638	46917	23087	69066	99985	01735	20241
33291	76222	52088	07482	83308	98960	40993	84206	76311	91982
63079	72605	89507	42852	14681	18795	78102	30630	16175	77998
47767	52203	62663	32254	31966	15805	99528	34002	69239	77643
76432	63190	29948	04588	27277	11393	09048	55210	71579	95191
04180	18717	58573	32422	38615	85666	03020	27931	01660	44950

Figure 5: Random number table used in simulation experiments. (Reproduced with permission from ref. 12. Copyright Free Press Publishers.)

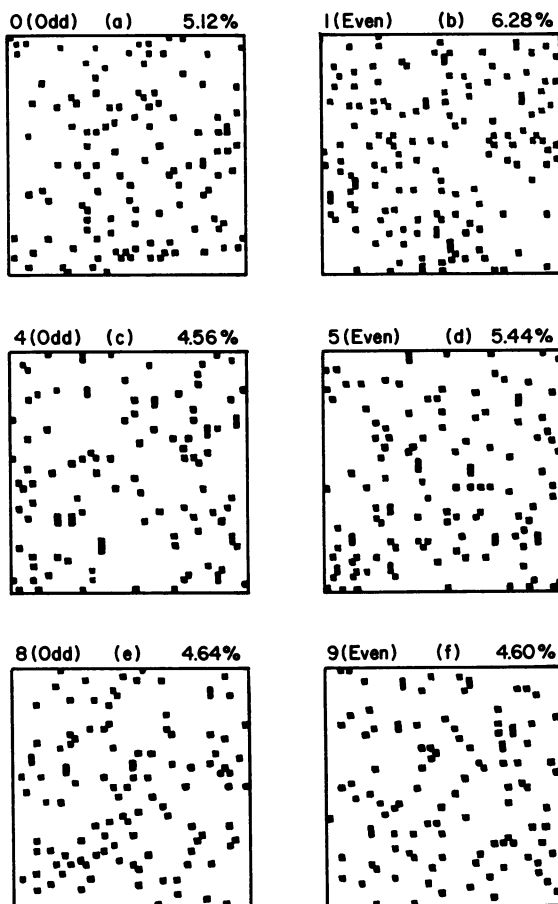


Figure 6: Simulated fields of deposited fineparticles at 5% area coverage show significant coincidence effects.

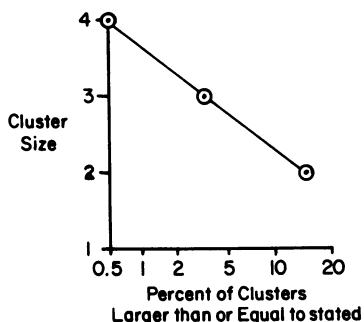


Figure 7: The size distribution of clusters formed by chance contiguity at 5% coverage could mislead the analyst. (Reproduced with permission from ref. 6. Copyright 1989 VCH Publishers.)

deposition coverage of 1% was simulated using the random number table. In this case any given digit was transformed into a simulated fineparticle if the digit in the conversion reference table was a specific digit since this resulted on average of 1/10th of any given digit being converted into a simulated deposited fineparticle. Thus, one could turn a 6 into a simulated fineparticle whenever the conversion reference digit was 5. The six simulated 1% coverage filter papers are shown in Figure 8. Again the conversion procedure is noted at the top left hand corner of a given field of view and the measured percentage cover is noted in the top right hand corner. Thus, for Figure 8(a) the digit 0 was converted into a simulated fineparticle if the conversion reference digit was 1. From a visual inspection of the six simulated fields of view it can be seen that the occurrence of a doublet is on average once per field of view. In Figure 9 the simulated appearance of fineparticle fields with 0.1% coverage is shown. The conversion routine is again noted in the top left hand corner and the measured density of coverage shown at the top right hand corner. The appearance of these 6 fields of view is encouraging in that it appears that coincidence effects appear to have been reduced to a relatively low level however one cannot build final conclusions on such a limited data set. However, the overall picture indicated by the simulated data of Figures 7,8 and 9 is that most certainly coincidence effects can be quite significant at 5% coverage, a widely used figure, and that one should go to much lower deposition densities to avoid interpretive problems, and hence subjective bias, when evaluating the levels of respirable dust by microscope inspection of deposited fineparticles. To show how severe the problem can be if one operates at levels higher than 5% coverage (note that the percentage coverage of 2(a) and 2(b) are respectively 10 and 15% ) the appearance of the field of view at 20% coverage was generated and this simulated field of view is shown in Figure 10. To generate this field of view all 6's and all 7's of the random number table were converted into simulated fineparticles. It can be seen that apparent agglomerates containing up to 17 units can appear by chance juxtaposition in a deposited field of view. If we again assume that this single square represents the threshold of respirable hazard in such a field of view an automated microscope unable to differentiate between single units and agglomerates would report the respirable dust level as 86 units instead of 478 units. Furthermore, the size distribution function of the clusters would obey a log-log size distribution which has been reported from time to time for deposited dust. It is obvious from this simulation study that only if such a distribution function of the type shown in Figure 11 is proven to be independent of the density of dust on the filter should its existence be treated as a real phenomena and not an artifact created by the use of an overloaded filter paper. Very rarely have people reported the density of coverage used in their studies of respirable dust and many operators would consider the 20% field of view of Figure 10 to be a not unreasonable filter deposit to be used in image analysis studies.

### Discussion of Data

The occurrence of coincidence effects in two-dimensional space appears to have been neglected in many studies of the hazards represented by respirable dust. At the very least one should treat with caution any data on size distribution of deposited dust fineparticles which does not carry with it a statement of the density of deposition permitted on the filter used to carry the dust prior to the size analysis study. However it is difficult to believe that operators would be willing to use many sparsely populated filter

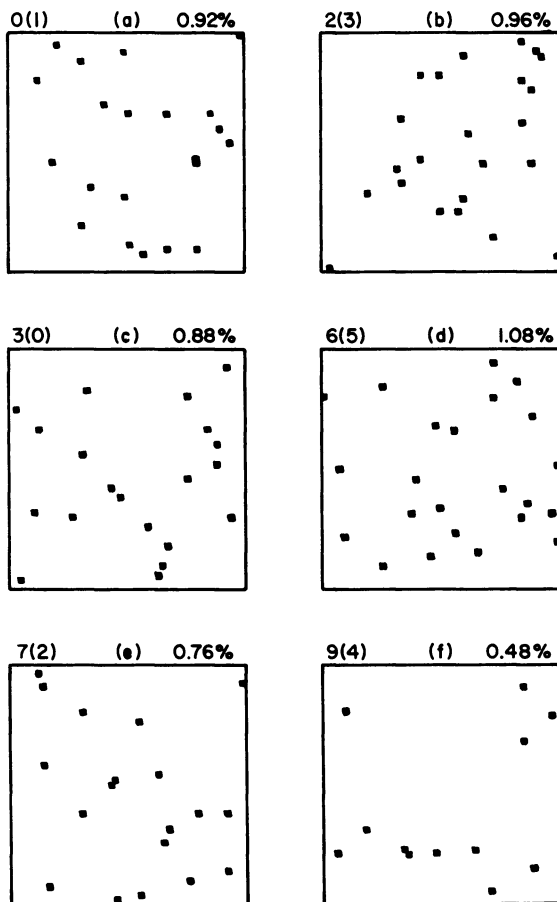


Figure 8: Simulated fields of view at an anticipated coverage level of 1.0%.

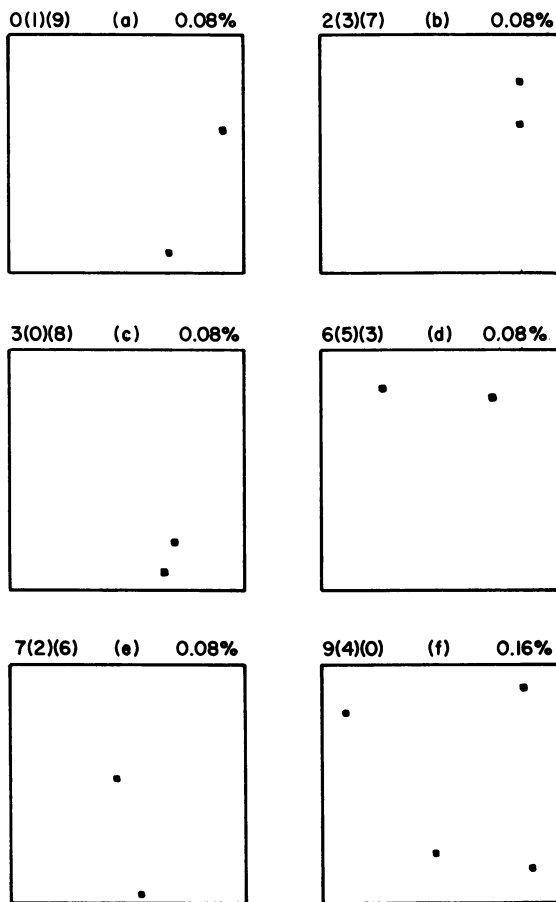


Figure 9: Simulated fields of view at an anticipated coverage level of 0.1%.

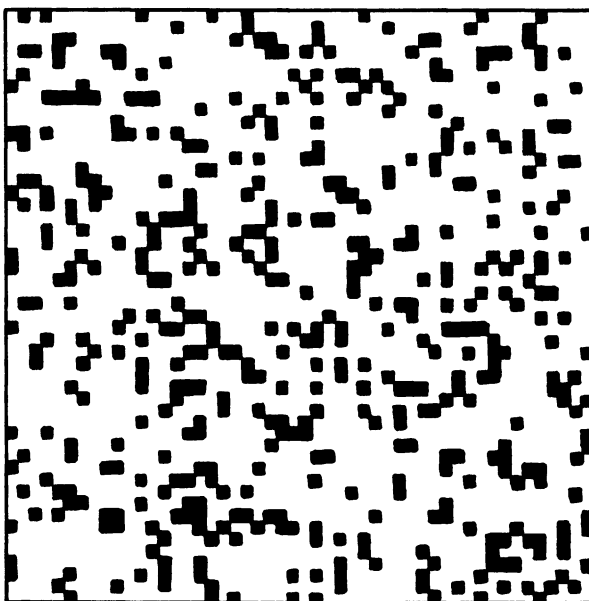


Figure 10: Simulated 20% coverage field of view.

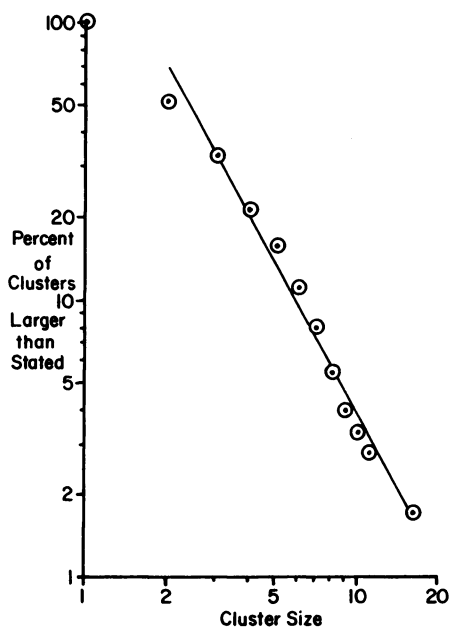


Figure 11: Size distribution of the clusters formed by chance in Figure 10.

papers of the type illustrated in Figure 9. It appears therefore that one needs to have a radically different strategy than those previously used if image analysis of filter captured fineparticles is to prove to be a viable technique for monitoring dust. Either one must arrange to use electrostatic manipulation of the dust fineparticles to deposit them on the filter paper in such a way that contiguity is forbidden or alternatively one must use a different logic in the image analyzer. Currently at Laurentian University we are working on an intelligent image analysis system which will be able to carry out continuous monitoring of dust and sprays. Initially this instrument is envisioned as being used in a research situation but with the falling costs and miniaturization trends currently manifested in electronic design it is feasible that the instrument may be available for in work place use in the not too distant future. The logic of the system is outlined in Figure 12. The basic logic of the system will be presented here and a more complete description of its logic is in preparation. A continuously moving filter strip or thin plastic surface moves under an active deposition orifice from which the fineparticles are deposited on the inspection strip. Hydrodynamic fractionation, as in a cascade impactor, may be used at this stage. This strip moves continuously so that one can accept relatively sparse deposition on the surface as it moves towards a primary inspection photo electric line array. This one line array inspects the filter to discover the location and basic size category of fineparticles deposited on the moving surface. Data from this primary inspection line array is stored in a short term memory and generates the co-ordinates of the approximate center of gravity of the deposited fineparticle. This information is used to control the positioning of high resolution matrix with regard to y movement and anticipates the arrival from the x co-ordinate of the deposited fineparticle. The high resolution information from the profile is then sent to processing logic and can also be sent to a video tape or high capacity memory bank. In this way the high resolution part of the image analyzer does not spend its time collecting information on empty space.

It should be noted that if one were to use sparse field deposition with current automated microscope systems one would spend a great deal of time looking at empty space and wasting the sophisticated electronics deciding to throw away space information it should not have collected in the first place. After the fineparticles have passed the high resolution matrix there could be a collector and/or cleaner for the deposition tape which could form an endless belt. This design of automated image analysis system has many other advantages. For example it is ideally suited to implement stratified count logic which is discussed in some detail in the next section.

### Stratified Count Logic for Robotic Image Analyzers

When faced with the task of characterizing an array of profiles such as those shown in Figure 13 many workers start to characterize every fineparticle encountered in the field of view as one starts from the inspection line A and moves across the field of view in the direction of the arrow as shown in Figure 13. Thus by the time they have reached the position shown by the arrow B they have tallied the number of four different sized fineparticles as shown by the tally given underneath the tally area. It can be seen that the analyst has encountered many more of the smallest fineparticles than the larger profiles. If the analyst continues such a characterization strategy the net effect will be to gain a great deal of information on the population on the smallest sizes per unit area of the field of view whereas they will have only sparse information on the

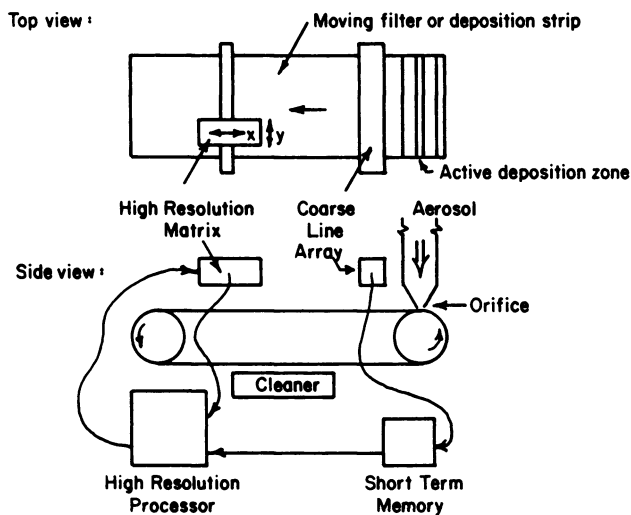
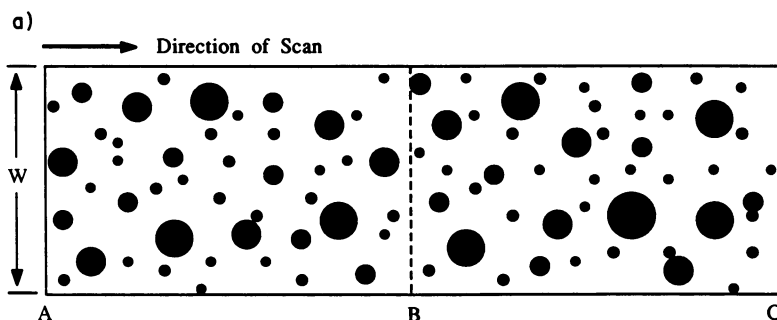


Figure 12: Logic flow chart for a cybernetic system for characterizing fineparticle images (C.A.F.I.) currently under development at Laurentian University.





b)

Tally for A to B			Tally for A to C		
Size		Number	Size		Number
1	●	28	1	●	59
2	●	8	2	●	15
3	●	6	3	●	10
4	●	3	4	●	7
5	●		5	●	1

c)

Size	Scan Length (cm)	Scan Area (cm <sup>2</sup> )	Unit Area Density
d	$l$	$A = l \times W$	$\alpha = (A_u/A) \times 10$
1	2.7	13.5 = $A_u$	10
2	9.0	45	3
3	16	80	1.69
4	22.8	114	1.18
5	160	800	0.17

Note that in this case  $W = 5$  cm

Figure 13: In the stratified count logic size distribution procedure one seeks to estimate the population density of each size of fineparticle.

population density of the largest profiles. Thus by the time the simulated field of view of figure 13 is completed the distribution of the various sizes encountered in the search will be as shown in the tally given in Figure 13. If the size distribution of the fineparticles encountered up until the point C is converted into a weight distribution, the distribution function from the data of tally A to C is as shown in Figure 14(a). A useful way of deciding if one has really gained useful information on the size distribution function when carrying such a transformation is to plot the curves for +1 and - 1 conversion curves in which one takes one from all the observed tallies in the size groups and adds one to the size groups. This would generate the set of curves shown in Figure 14. The data of the tally up to the point C shows that there would be wild fluctuations in the distribution of the curve generated for +1 and -1 which is caused by the fact that we know so little about the population density of the larger fineparticles which are rare events if one continues the search strategy illustrated in Figure 13. A far more efficient strategy for characterizing the size distribution of an array of profiles such as that of Figure 13 is a procedure known as stratified logic count. The stratified logic count is not only more efficient but is more appropriate for a robotic analyzer as compared to a human being. For example if the profiles of Figure 13 were to be evaluated in total as the search scan moves from A through B to C then the microscope or television camera being used by the robot would have to be focussed differently for each size of fineparticle. In the stratified logic procedure the robot will seek to characterize one size group at a time. Thus the camera is initially set to see the largest fineparticle known to be present in the slide or field of view. Then the field of view is inspected for only this largest fineparticle and a linear search is inspected until 10 of the largest profiles have been located. If in this search one discovers a larger profile, as for example the large profile encountered between B and C, then after it has inspected the field of view for the initial size for which it was focussed it could then repeat the search for ten of the new largest profile. Assuming that this has been achieved one now looks for the line scan length needed to discover ten of the next size of fineparticle and so on. By adopting this strategy the camera and/or microscope is only adjusted at each switch to a new size group. The strategy results in information on the population density of each size of fineparticle with approximately the same confidence levels. The data is transformed into a size distribution function by first calculating the population density of each size per unit area. The calculation is illustrated in Figure 13. When this strategy is adopted the plus and minus one curves for the data are much more compatible with each other. In theory the robot can be programmed to adjust its search strategy to increase the confidence levels to any desired limits. Or alternatively it can be instructed to access how much work would have to be done if would wished to increase ones confidence to any given level. By using very low density of coverages to eliminate co-incidence effects and by adopting a stratified logic procedure with a moving field of view as suggested by the system in Figure 12 one can considerably lower the cost of automated image analysis since only very low level decisions will have to be taken by the image processing system. A very important area of fineparticle science in which information is needed on the size distribution of a fineparticle system is that for inspecting the droplets produced by fuel injection systems of engines, paint spray systems and pesticide spray systems. Currently at Laurentian University we are starting work on systems which will be used for automatic inspection of spray systems in which the droplets are deposited on a moving strip of

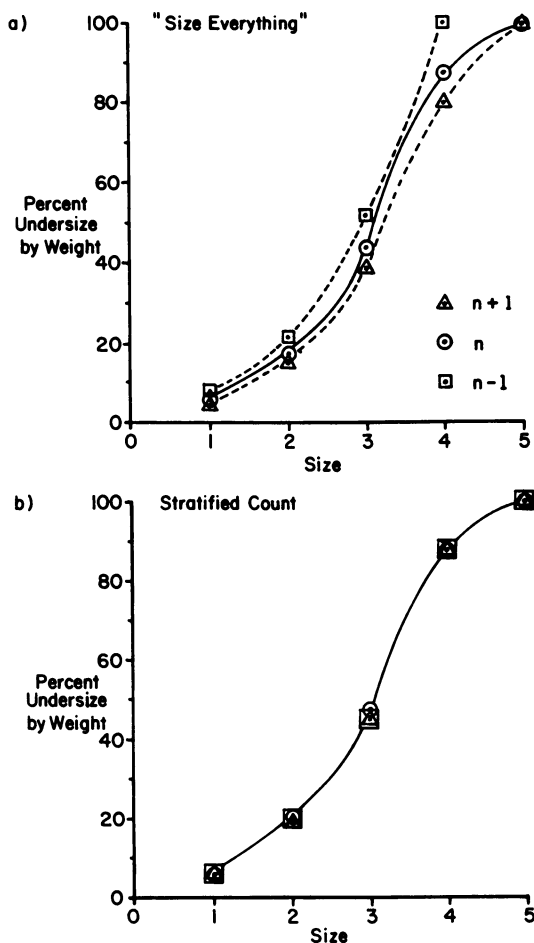


Figure 14: Stratified count logic results in more confidence in the measured size distribution function for less data collection as compared to "size everything" strategies.

filter paper and then presented to a robotic eye using the concepts of Figure 12 and that of stratified logic systems. Prototype data should be available in the near future.

#### Literature Cited

1. Kaye, B.H. Direct Characterization of Fineparticles; J. Wiley and Sons: New York, 1981.
2. Allen, T. Particle Size Analysis; Chapman and Hall; Third Edition, 1981.
3. Walkenhorst, A.W. "New Sampling Method For Particulate Matter With Finely Porous Filters", Chapter 26, in Assessment of Airborne Particles, edited by Mercer, T.T.; Morrow, P.W.; Stober, W.; proceedings of a conference on toxic aerosols, published by C.C. Thomas: Springfield, Illinois, 1972.
4. Laskin, S.; Drew, R.T.; Cappiello, V.P.; Kurschner, M.; "Inhalation Studies With Freshly Generated Polyurethane Foam Dust", Chapter 19 in Assessment of Airborne Particles, edited by Mercer, T.T.; Morrow, P.E.; Stober, W.; proceedings of a conference on toxic aerosols, published by C.C. Thomas: Springfield, Illinois, 1972.
5. Timbrell, V.; "An Aerosol Spectrometer and Its Applications", Assessment of Airborne Particles, Charles C. Thomas, 1972.
6. A Randomwalk Through Fractal Dimensions, Kaye, B.H.; VCH Publishers: Weinheim, Germany, September 1989.
7. Tohno, S.; Takahasi, K.; "Shape Analysis of Particles by Image Scanner and Microcomputer Application to Agglomerated Aerosol Particles", Kona No. 6, 1988, pp. 2-14, this journal is published by Hosokawa Mikron International Inc.: 780 Third Avenue, New York, N.Y., 10017.
8. Schafer, H.J., Pfeifer, H.J., "Sizing of Submicron Aerosol Particles by the Whisker Particle Collector Method", Particle and Particle Systems Characterization, Vol. 4, 1988, pp. 174-178.
9. Ensor, D.S.; Mullins, M.E.; "The Fractal Nature of Dendrites Formed by the Collection of Particles on Fibres", Particle Characterization 2, 1985, pp. 77-78.
10. B.H. Kaye, "Characterizing The Structure of Fumed Pigments Using the Concepts of Fractal Geometry", submitted for publication in Particle & Particle Systems Characterization.
11. The use of Monte Carlo routines to model many fineparticle structures are discussed in detail in Reference 6. The practical details of Monte Carlo routines for modelling dust deposition studies are presented indepth in the forthcoming book "Discovering the Surprising Patterns of Chaos and Complexity", B.H. Kaye to be published by VCH Publishers, Weinheim, Germany (Anticipated publishing date Spring, 1992.)
12. "A Million Random Digits with 100,000 Normal Deviates," Rand Corporation, published by Free Press Publishers: Glencoe, Illinois.

RECEIVED July 22, 1991

## Chapter 24

### Formation Dynamics Information

#### Can It Be Derived from the Fractal Structure of Fumed Fineparticles?

Brian H. Kaye and G. G. Clark

Physics Department, Laurentian University, Sudbury, Ontario P3E 2C6,  
Canada

In recent years several publications have described the fractal structure of aerosol systems. In this communication a study of the distribution of boundary fractal dimensions of two populations of two commercially available carbonblack profiles are reported. Both sets of carbonblack profiles manifested structural and textural fractals. It is suggested that the type of distribution function describing the many different fractal boundaries manifest by the profiles indicates that the systems are produced by the interaction of many small causes of the same magnitude. It is also suggested that the difference between the two populations indicates possible differences in the formation dynamics for the two sets of carbonblack profiles.

Fractal geometry is the study of the structure of rugged systems. It has been shown by several workers that the structure of fineparticles created by a fuming process results in agglomerated fineparticles which have fractal structure (1,2,3). These fineparticle systems include important commercial pigments such as carbon black and titanium dioxide (4). It has been shown that the various aspects of the structure of an agglomerated fineparticle formed by the collision and sticking together of unit spheres can be described by the use of fractal dimensions. The fractal dimension of a system is an addendum to the topological dimension of a system which describes the space filling ability of the curve. Thus in Figure 1 the fractal dimensions and topological dimensions of a series of rugged lines are shown. High resolution electron micrographs show that carbonblack agglomerates are formed by spheres of the same size which collide with each other in the turbulent regions of the flame to produce agglomerates of various shape and size. In Figure 2 a digitized carbonblack profile which has been studied by several workers is shown (5,6,7,8,9). To characterize the fractal dimension of the boundary of the agglomerate, it should be noted that some other workers who have studied the internal structure of agglomerates have also used a fractal dimension related to the internal structure of the agglomerates. This fractal dimension which is

0097-6156/91/0472-0372\$06.00/0  
© 1991 American Chemical Society

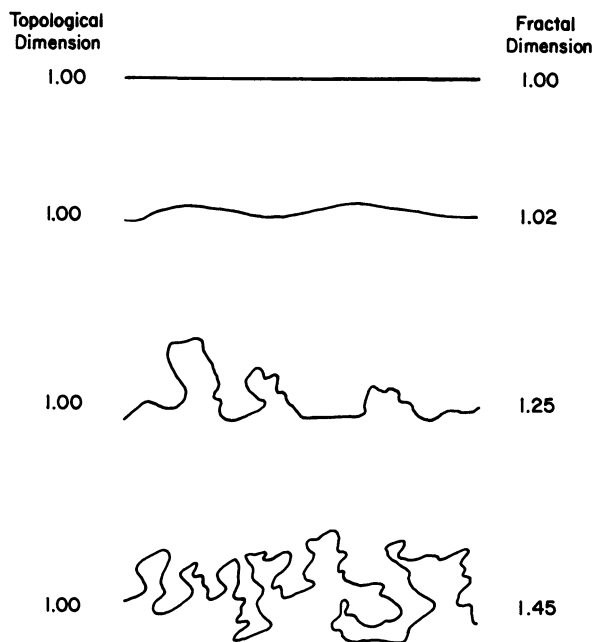


Figure 1: The ruggedness of a line can be described by a fractional addendum to the topological dimension. The combination is known as the fractal dimension of the line. (Reproduced with permission from ref. 2. Copyright 1990 VCH Publishers.)

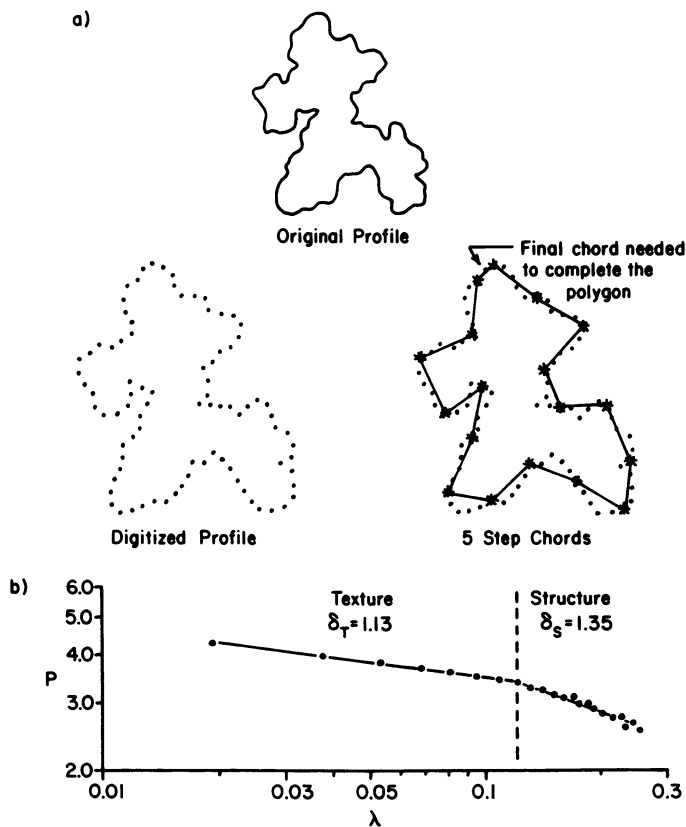


Figure 2: In the equipaced method for deducing the fractal dimension of a boundary, polygons of increasing side length are constructed on a digitized version of the boundary. (a) Various polygons used to estimate the perimeter of the carbonblack profile. (b) Richardson plot of normalized perimeter—resolution parameter data generated by equipaced exploration of the carbonblack profile.

$\lambda$  = number of digitized steps along the profile to form a chord;

$P$  = perimeter estimate; and

$\delta$  = fractal dimension over a given range of inspection resolutions.

$\lambda$  and  $P$  are normalized with respect to the maximum projected length of the profile. (Reproduced with permission from ref. 2. Copyright 1990 VCH Publishers.)

described as a density or mass fractal dimension is different from the boundary fractal discussed in this communication (3,4). When studying the boundary fractal dimension of an agglomerate such as a carbonblack profile, one is studying a two dimensional projection of the structure of the system. For this reason the projected boundary fractal dimension is often less rugged than the fractal dimension that would be characterized by embedding the carbonblack in a resin and taking a section through the agglomerate. Although information is lost by studying projected boundary fractal dimensions it appears that there is still a useful amount of information in such fractal boundaries. Obtaining electron micrographs of carbonblacks is an expensive process. Techniques for looking at sections through carbonblack agglomerates set in resin will require a different set of boundary fractals to describe such structures. All of the fractal dimensions discussed in this communication are boundary fractals of projected images. This fact should be remembered when evaluating the information presented in this communication. Essentially the fractal dimension of a boundary such as that of the carbonblack profile shown in Figure 2 is studied by estimating the boundary at a series of resolutions. These boundary estimates and an appropriate resolution parameter, in normalized format, are plotted on a log-log graph which is known as a Richardson plot (10). It has been shown that the slope of the data lines on such a graph can be used to deduce the fractal dimension of the boundary.

### Experimental Studies

The experimental procedure used in this communication to characterize the boundaries of the carbonblack profiles is the equipaced polygon exploration technique (2). The basic concepts of this technique can be appreciated from Figure 2. The digitized outline of the profile is stored in a computer memory and then polygons of decreasing resolution are constructed on the original profile by drawing cords to the beginning and end of the distances paced out around the profile. Thus in part (a) of Figure 2 the basic digitization of the profile and three different polygons used to estimate the profile are shown. For many carbonblack profiles it has been discovered experimentally that the data lines for the exploration of the profile manifest two or more linear relationships leading to the estimation of at least two different fractal dimensions as shown in the Figure 2. It is becoming apparent that the fractal dimension  $\delta$  for systems such as boundary fractals of aerosol fineparticles contain information on the formation dynamics and the detailed structure of the profile at different resolutions (2,6). Thus the data line of Figure 2 at high resolution corresponds to high level scrutiny of the texture of the boundary of the agglomerates whereas the data line at coarse resolution comes from exploring the coarse structure of the agglomerate. (the fractal dimension of the graph is related to the slope of the data line by the relationship  $\delta = 1 + |m|$  where  $m$  is the slope of the line (2)) The data line on the Richardson plot for coarse resolution is related to the gross structural features of the agglomerate and this fractal dimension is described as the structural boundary fractal dimension.

### Discussion

The physical significance of the structural fractal dimension can be appreciated from the data presented for three model profiles in Figure 3



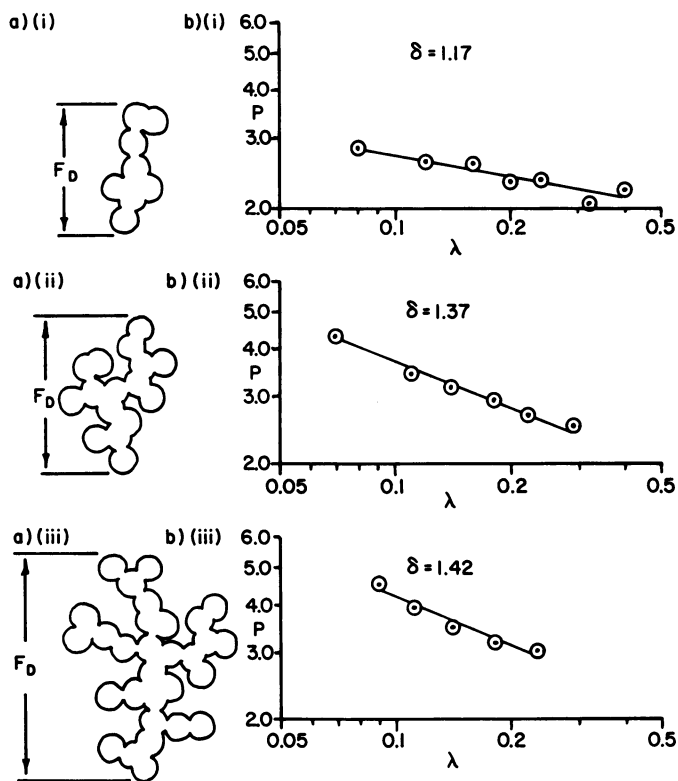


Figure 3: The magnitude of the boundary fractal dimension at coarse resolution is related to the gross structure of the profile. (Reproduced with permission from ref. 2. Copyright 1990 VCH Publishers.)

created by joining glass spheres together to create different types of agglomerates. A simple compact agglomerate has a structural fractal dimension of the order of 1.17 whereas more complex agglomerates formed by the collision of several compact agglomerates have higher boundary fractal dimensions of the order of 1.37 to 1.42. The quantity denoted by  $F_D$  of Figure 3 is the normalizing factor used to prepare the data of the Figure 3. Experimental studies show that at high resolution the packing of the spheres for real carbonblack agglomerates produces a textural fractal of the order 0.08 (2). Thus in Figure 4 some high resolution data for the carbonblack of Figure 2 obtained by a technique known as erosion dilation logic is shown (2). This shows a textural fractal of 1.07 and a structural fractal of 1.34 indicating that the agglomerate has probably been formed by the collision of several sub-agglomerates as suggested by the sketch given in Figure 4. (2).

In erosion treatment of an image of an agglomerate the computer control of the image analysis system strips off a layer of pixels (the image screen is divided by the computer into a mosaic of small squares and the basic small square of such a mosaic is known technically as a pixel). A computer can repeat this operation several times. When subjected to the stripping routine the agglomerate structure changes as indicated in the diagrams of Figure 5(a). We can interpret this as that by stage 9 the structure looks as if it has 5 subsidiary agglomerates. By the time we get to 14 pixel strips some contributory agglomerates have disappeared only 3 basic contributing structures remain and one of those (the bottom right hand agglomerate) looks as if it will break down into 2 with further erosion. By using pixel stripping to estimate the possible number of contributory primary agglomerates to a secondary agglomerate one can deduce information on the formation dynamics and match it with the measured fractal dimensions. The second approach to understanding the physical significance of the carbonblack structure is to model the growth of various agglomerates on a computer and match the resultant structure of the model system to systems generated experimentally (11). The modelling process used to simulate agglomerate growth can be illustrated in two-dimensions by considering the system as shown in Figure 6(b). The systems of Figure 6(b) have been greatly simplified to explain the actual process rather than to depict detailed experiments. A real modelling experiment would use a much smaller pixel size with the modelling area containing at least 500 x 500 picture elements. A picture element is taken to be representative of the sub-units joining the growing agglomerates. The centre of the pixel space is designated as a nucleating centre for the growing agglomerate. A black pixel representing a basic unit of the agglomerate structure is then allowed to approach the nucleating centre by a randomwalk process until by chance it impinges on the nucleating centre. As this time a decision is taken as to the probability of the impinging pixel joining the growing agglomerate. Thus in the simplest case it is assumed that every staggering pixel approaching the nucleating centre has 100% chance of joining the agglomerate if it impinges orthogonally on the nucleating centre. A two-dimensional model of this type of growth generates the type of agglomerate shown in Figure 6(a) which is known as Whitten and Sander agglomerate (12).

If one now changes the sticking rules so that for example when the staggering pixel encounters the growing agglomerate there is only a 50% chance of joining the agglomerate and the staggering pixel may move away until it again encounters the growing agglomerates. In Figure 6(b) the appearance of the two-dimensional agglomerates grown with different

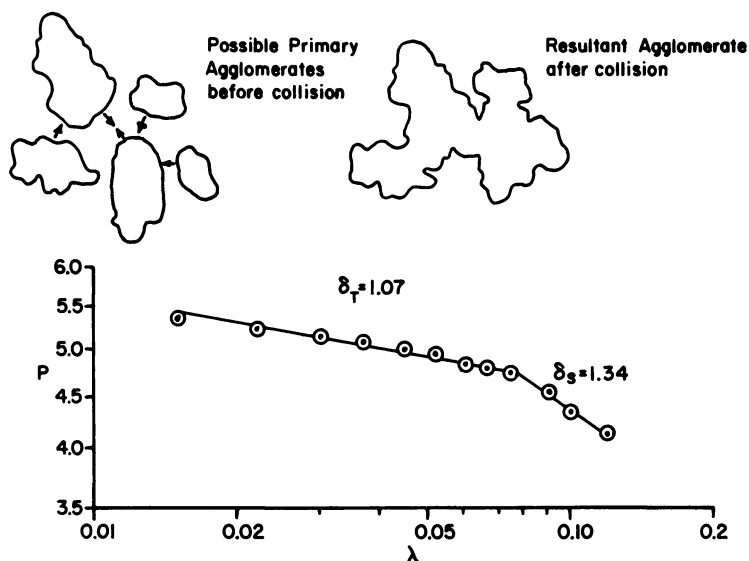


Figure 4: A boundary structural fractal dimension of the order of 1.40 is manifest by agglomerates which appear to have been formed by the collision of several compact agglomerates. (Reproduced with permission from ref. 2. Copyright 1990 VCH Publishers.)



Figure 5: Pixel stripping routines called erosion routines can “dissolve” the image of a profile into probable constituent parts. (Reproduced with permission from ref. 2. Copyright 1990 VCH Publishers.)

In Particle Size Distribution II; Provder, T.;

ACS Symposium Series; American Chemical Society: Washington, DC, 1991.

sticking rules are shown. Studies on the three-dimensional structure of agglomerates modelled in this way are being carried out by several groups of scientists (13,14). The modelling process of Figure 6(a) obviously matches the growth of agglomerates in turbulence of a flame. It may be that the growth of a complex agglomerate can take place in two stages with the sticking rules changing during the formation period. In Figure 6(c) the growth of an agglomerate modelled on a computer when after a certain period the sticking rules change show how the agglomerate can have a spindly centre with denser formations toward the outside. If one looks at the series of profiles shown in Figure 6(b) it would seem to be a reasonable hypothesis to suggest that 100% sticking agglomerate would be the most desirable commercial pigment since it would offer the greater surface area to the interaction of photons impinging upon its structure in a paint film. Furthermore, under the conditions of shear operating during the physical manufacture of paint the agglomerate is likely to break down to produce more independent scattering centres. The possibility that this is a working hypothesis aimed at optimizing is under investigation (15).

If one examines a set of profiles from a commercial product it soon becomes apparent that within any one set of fineparticles there is a whole range of boundary fractal dimensions. Thus in Figure 7 the profiles of two different commercially available carbonblack systems are shown. These profiles were traced from high magnification electron micrographs of the carbonblack provided by N. Mace of the Cabot Corporation (16).

The trade names of these two different carbonblacks manufactured and sold by the Cabot Corporation are Vulcan 7H and Sterling NSI (16). A population of profiles taken from a series of high magnification electron micrographs are shown in Figure 8. The problem addressed in this communication is an exploration of the possibility that the boundary fractal dimension distribution function of the two sets of pigments are characteristic of the two products. Each of the Figure 8 profiles of the two sets of pigments were characterized by using the equipaced technique for exploring the structure of the profile.

Typical data plots for representative profiles from the two sets of fineparticles are shown in Figure 9. These profiles exhibit two ranges of linearity in their Richardson's plots defining the structural and textural fractal dimension of the profile. Thus at coarse resolution the structural boundary fractal dimension of the Vulcan profile shown in Figure 9 is 1.41. At high resolution the textural boundary fractal dimension of the profile is 1.12 and this is described as the textural fractal of the profile. The structural and textural fractal for the representative Sterling black profiles are shown in Figure 9(b) are 1.23 and 1.08 respectively. The information on the population structural and textural boundary fractals for the two arrays of Figure 8 have been plotted in Figure 10. The structural and textural distribution data appears to be describable by a Gaussian distribution with the distribution for the two pigments being clearly different. The data presented in these two graphs is admittedly sparse but it should be appreciated that the cost and difficulty of acquiring the necessary electron micrographs and the cost of carrying out the analysis of each profile is an expensive operation. In fact it was only possible to carry out this experiment because students were asked to characterize the profiles of Figure 8 as part of their undergraduate laboratory projects. The mean fractal dimension and standard deviation seem to be quite characteristic of the two different populations. The data of Figure 10 appears to suggest that the variation in the fractal dimensions of a population of fineparticles is a potential method for characterizing the

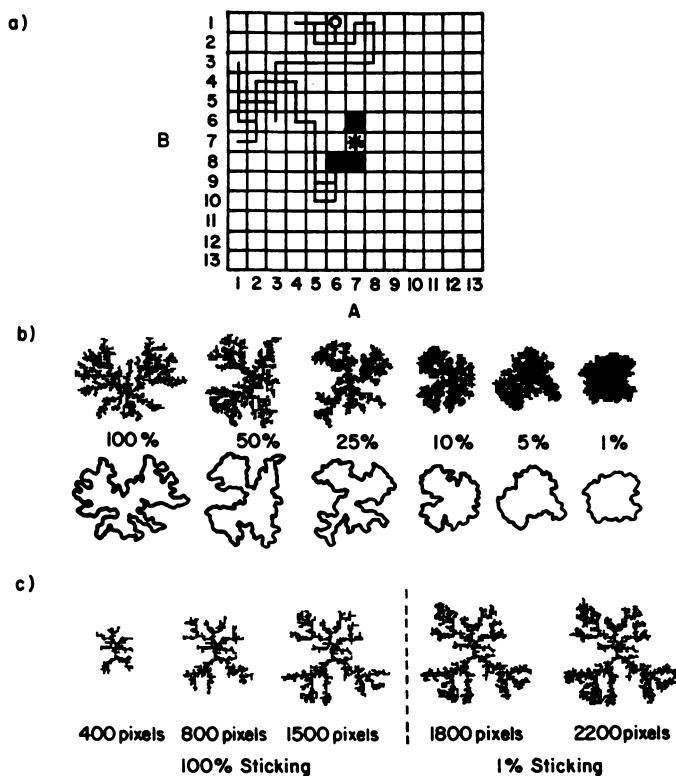


Figure 6: Randomwalk modeling of cluster growth can be used to create models of agglomerates which may be useful when interpreting the physical significance of observed rugged structures. (a) Basic modeling proceeding and Whitten and Sander agglomerate; (b) agglomerates grown using different sticking probabilities; and (c) agglomerates whose structure manifest changing sticking probabilities.

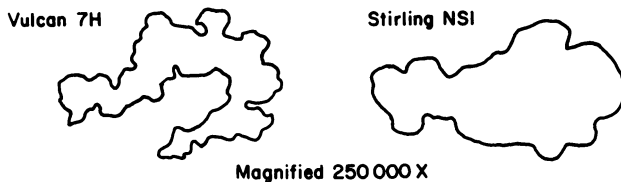
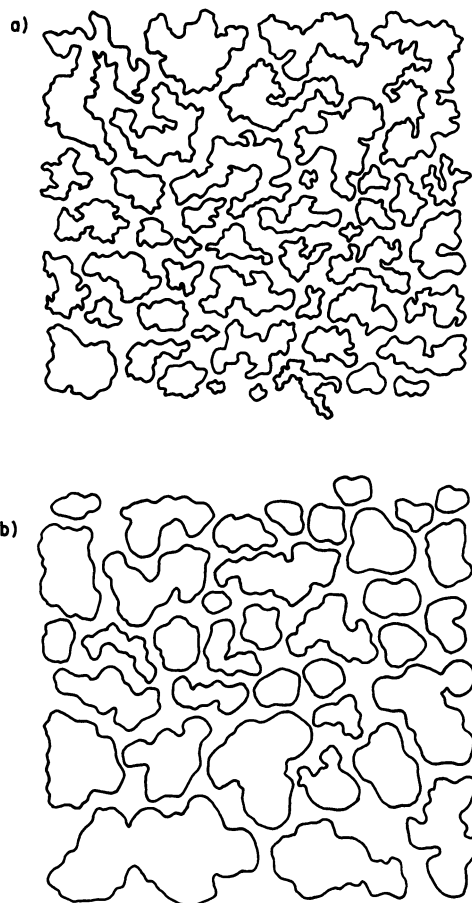


Figure 7: Typical profiles of carbonblacks traced from electron micrographs.



**Figure 8:** Carbonblack profiles taken from high magnification electron micrographs of two commercially available carbonblacks (5) from the Cabot Carbon Corporation. (a) Vulcan 7H and (b) Sterling NSI. (Reproduced with permission from ref. 16. Copyright Cabot Corporation.)

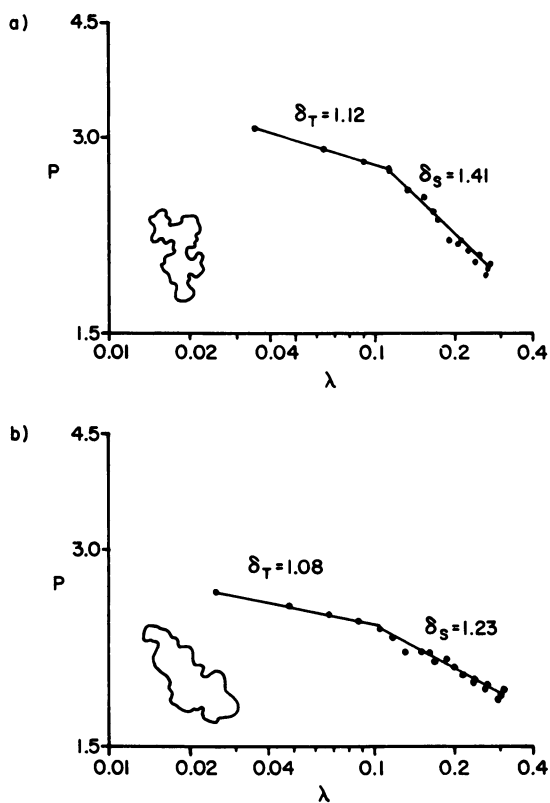


Figure 9: Typical Richardson plots for representative carbonblack profiles. (a) Vulcan 7H and (b) Sterling NSI.

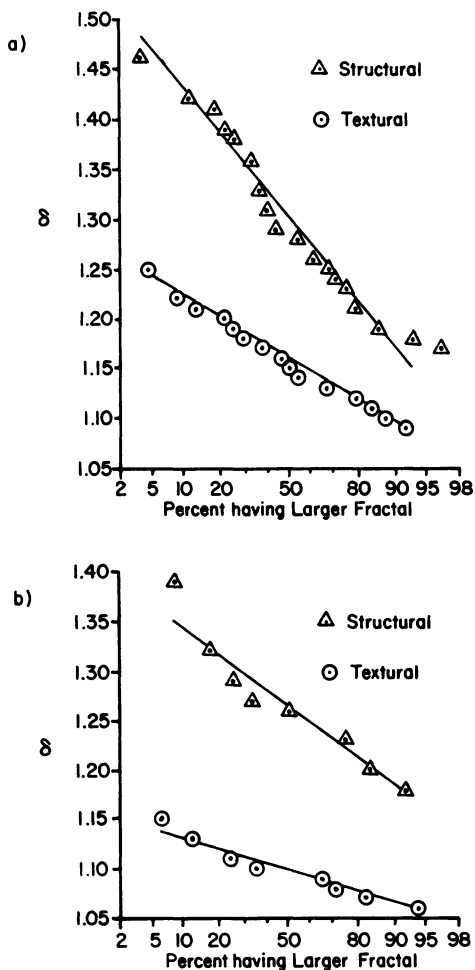


Figure 10: Distribution data for the variation of structural and textural boundary fractal dimensions of the two populations of carbonblack profiles displayed in Figure 1. (a) Vulcan 7H and (b) Sterling NSI.



differences in populations of commercial pigments. This is a method that will become more feasible as a research and quality control tool as more sophisticated image characterization equipment becomes available for fractal boundary characterization and automated image analysis systems.

The fact that the textural and structural distribution functions for both sets of profiles are probably Gaussian distributed would indicate that they have been formed by the random interaction of many causes of approximately equal strength i.e. there is no dominant formation mechanism. The fact that the structural fractal dimension of the Vulcan 7H carbonblacks is considerably higher than the structural fractal dimension of the Sterling carbonblacks would seem to indicate that in the formation process agglomerates were colliding with each other for a longer period in the production of the Vulcan carbonblack than in the case of the Sterling carbonblack. In other words the formation of the agglomerates was quenched more quickly in the case of the Sterling product than for the Vulcan product. Further work is in progress to test the hypotheses that less rugged profiles have been created by preventing the agglomeration process from continuing (17).

#### Literature Cited

1. Mandelbrot, B.B. The Fractal Geometry of Nature; W. Freeman: San Francisco, 1983.
2. Kaye, B.H. A Randomwalk Through Fractal Dimensions; VCH Publishers; Weinheim, Federal Republic of Germany, 1990.
3. Meakin, P.: "Simulations of Aggregation Process," Chapter 3, in the Fractal Approach to Heterogeneous Chemistry, edited by Avnir, D., John Wiley and Sons Limited, 1989.
4. Kaye, B.H. "Characterizing the Structure of Fumed Pigments Using the Concepts of Fractal Geometry", (In press), Particle & Particle Systems Characterization.
5. A.I. Medalia, G.J. Hornik, "Pattern Recognition Problems in the Study of Carbonblack", Pattern Recognition, 4 (1975) 155.
6. A.I. Medalia, "Dynamic Shape Factors of Particles", Powder Technol., 4 (1970-1971) Pgs.. 117-138
7. A.G. Flook, "The Use of Dilation Logic on the Quantimet to Achieve Fractal Dimension Characterization of Texture and Structure of Profiles", Powder Technol., 21 (1978) Pgs. 295-298.
8. H. Schwarz, H.E. Exner, "The Implementation of the Concept of Fractal Dimensions on a Semi-automatic Image Analyzer", Powder Technol., 27 (1980) Pgs. 207-213.
9. B.H. Kaye, "Multi Fractal Description of A Rugged Fineparticle Profile", Part. Charact. 1 (1984), 14-21
10. B.H. Kaye Direct Characterization of Fineparticles, Wiley & Sons, New York, 1981, See Chapter 10
11. The relationship between the fractal dimension and the formation dynamics of a system has recently been discussed in a lecture entitled "Fractalicious Structures and Probable Events" an address given to the Math Educators of Canada Conference held in Vancouver, May 23-25 by Professor B.H. Kaye, copies of the lecture are available from Laurentian University.
12. T.A Whitten, L.M. Sander, "Diffusion Limited Aggregation; A Kinetic Critical Phenomenon", Phys. Rev. Lett., 47 (1981) 1400.

13. R. Richter, L.M. Sander, Z. Cheng, "Computer Simulations of Soot Aggregation", J. Colloid Interface Sci., 100 (1984) Pgs. 203-209.
14. P. Meakin, R. Jullien, "The Effects of Random Bond Breaking on Diffusion Limited Cluster-Cluster Aggregation", J. Phys., 46, (1985) Pg. 1543.
15. B.H. Kaye, G.G. Clark, "Evaluating the Physical Significance and Health Hazards of Agglomerate Structure in Combustion Generated Aerosols", in preparation.
16. Cabot Corporation, Concord Road, Billerica, MA, U.S.A., 01821.
17. Experimental work in fractal systems has been developing faster than the appearance of detailed scientific publications which are presented in scientific journals. The information on the formation dynamics embedded in the distribution functions of systems such as carbonblack are explored in a publication in preparation entitled "Discovering the Surprising Patterns of Chaos and Complexity" by B.H. Kaye.

RECEIVED April 12, 1991

## Chapter 25

# Dispersion and High-Resolution Electrozone Analysis of Magnetic Particles

Richard F. Karuhn

Particle Data Laboratories, 115 Hahn Street, Elmhurst, IL 60126

Accurate analysis of magnetic materials are difficult due to agglomeration. The electric sensing zone or other state-of-the-art technologies that do not induce high shear to the analytical suspension fluid will therefore generate oversize distributions. The unstable analytical suspension will:

1. Lose "counts" at an increasing rate with time
2. The primary mass mode will be oversized and sub-populations of the primary mode will be evident.

Two samples of a commercially ball milled magnetic oxide were dispersed using a high viscosity media. It holds deagglomerated particles apart until analysis is started on an electric sensing zone particle size analyzer. Data reveal the analytical suspension is stable during the analysis period and the technique can easily follow the decrease in particle size during milling.

The producers of magnetic products have a fine particle analytical problem which is unique to their industry -reagglomeration of dispersed powder due to magnetic attraction. The finest colloidal material can generally be kept dispersed by coating the particles with long chain organics such as sodium oleate but the larger material such as that used in permanent magnets presents a difficult challenge. Since the interparticle magnetic attraction for large particles cannot be overcome by chemical means, several other approaches have been used over the years to achieve analytical dispersion stability. In addition to ultrasonic treatment in the presence of surfactants, researchers have heated samples to the Curie point under nitrogen (1), degaussed in a 20 ampere A.C. current (2) and even induced shear forces by high speed pumping of low concentration slurries.

Each of the above methods to demagnetize or disperse a powder sample has a difficulty associated with it. Heating a sample to an elevated temperature of 850° C under a nitrogen blanket and cooling it again can cause a change in the particle size due to sintering. A wide variation of residual magnetism has been noted in various magnetic materials after passage through an alternating magnetic field. Finally, we have seen this sample processed on a light diffraction analyzer in which the suspension

0097-6156/91/0472-0386\$06.00/0  
© 1991 American Chemical Society

was pumped around in a closed loop with data being reported every 30 seconds. At each of 10 reporting intervals, the particle size distribution shifted downward and finally stabilized. Data is presented which shows that the steady trend toward a smaller median size is due to deagglomeration of the large end of the distribution induced by high shear forces of the analyzer's centrifugal pump.

The purpose of this investigation was to develop a sample preparation technique for a "soft" (low flux density) magnetic powder that would allow a rapid high resolution analysis to take place using the electric sensing zone detection principle. Presently, the industry uses scanning electron microscopy and the Fisher Sub sieve Sizer for research and quality control.

The techniques discussed in this paper were designed to provide our client with a means of following the progress of his ball milling operation. We were asked to answer the questions, "Could we determine the difference between a 13 hour and a 24 hour ball milled sample by following a size reduction of the large end of the distribution? Also, are subpopulations evident?" The task of following the size reduction of the larger particles was ideal for the Elzone(3) particle size analyzer because a majority of the population by frequency for this sample type is usually below the lower detection limit of the electric sensing zone technique.

### ANALYTICAL MEASUREMENT PRINCIPLE

The electric sensing zone analytical technique has developed rapidly over the past twenty years. In this technique, particles suspended in a conductive fluid, flow serially through an orifice under a differential pressure. A constant current is applied to two electrodes which are immersed on each side of the orifice. As each particle passes through the orifice, it replaces its own volume of electrolyte within the orifice, momentarily changing the resistance value between the electrodes. The impedance change results in a voltage pulse of short duration having a magnitude proportional to particle volume. The resulting series of pulses is electronically amplified, counted and scaled prior to storage in the memory of a PC computer. Raw data processing is performed by the PC in such a manner that a population histogram of 128 channels of information is acquired. Following a typical collection of 50,000 electronic pulses (particles), frequency population data is conditioned by applying calibration information. The frequency data is then stored in memory while the original data is converted to a volume (mass) basis. Data is then reported in a format requested by the researcher.

Since the electric sensing zone analytical method simultaneously yields both a size distribution analysis and the particle concentration per unit volume of carrier electrolyte, we can tell if magnetic reagglomeration is occurring. We would note a loss of count rate per unit volume and the size distribution curve would shift upward on succeeding analytical trials.

### ANALYTICAL CONSIDERATIONS

There were several analytical considerations required of the sample preparation and instrument operation technique in order to assure us of a useable and repeatable methodology. These were:

1. Loose agglomerates must be broken.
2. Individual particles in a moderately high concentration must be held at some finite distance from their neighbor.

3. The quality of the initial viscous phase dispersion must be capable of being viewed under a 100X dark field microscope.
4. The initial viscous phase dispersion must be stable for 15 minutes or more.
5. The final analytical aqueous dispersion for instrumental analysis must be stable for up to 3 minutes or more.
6. The final analytical aqueous particle suspension must not exceed a 1% coincidence rate at the instruments detector orifice in order to achieve a high resolution analysis.

We found that the above requirements could be achieved by suspending magnetic powders in HONEY and then subjecting the suspension to high viscous shear forces. The exact dispersion methodology and associated analytical procedure using the Elzone particle size analyzer is discussed below.

### DISPERSION AND ANALYTICAL TECHNIQUE

Typically, samples arrive at our service lab in a dry powder state because they have been prepared for quality control analysis by scanning electron microscopy or the Fisher Subsize Sizer. Our experience with samples in this dry state is that HARD agglomerates are formed during the drying process. They resist the combined dispersion forces of an aqueous surfactant and ultrasonic probe and are therefore to be avoided. When using our technique, the analyst should obtain samples that are moist in order to avoid dealing with the hard agglomerates.

The recommended sample preparation and analytical steps are listed below:

1. Place a small portion of the sample into about one c.c. of pure commercial honey. Mix well in a suitable container to obtain a homogenous suspension and then place a drop of the mix onto a precleaned microscope slide. Cross contamination can easily be eliminated by mixing the sample and honey in a single use, disposable 20cc sample vial. These vials are designed for use in automatic blood cell counters and like precleaned microscope slides are available from all major lab supply houses.
2. Overlap a second clean slide 3/4 of the way over the first one. Use the remaining 1/4 of each slide as handles for the following operations.
3. Place the combination down on a clean surface and press the two slides together thereby creating a thin film that will spread out uniformly under the slides.
4. Since the concentration of the material between the slides is probably too concentrated, separate the two and set one aside for future use. We prepare our samples in a laminar flow bench so that the exposed honey does not become contaminated with atmospheric dust.
5. Overlay another clean slide on top of one of the split two slides and press together again. The compression and resulting shear disperses the magnetically attracted particles. In order to increase the shear forces, pull the slides along a common a plane and then push them back again.
6. Place the combined slides on a 100X microscope and examine the material for the quality of the dispersion as well as concentration. A high particle loading is to be avoided because the interparticle distances will be very small. If the concentration is too high, appropriate steps must be taken to reduce it. If the concentration is moderate and dispersion good, rinse the slide combination with filtered water. Rinse all sides, top and bottom so that any acquired surface contamination will not interfere with the analysis. Set the washed slide combination aside while the analytical instrument is prepared.

7. We used a standard computerized Elzone particle size analyzer, model 112, a 38 micron detection orifice, and aqueous 4% by weight sodium pyrophosphate solution as an electrolyte. The analytical span was 1.33 through 17.5 microns.
8. After it has been determined that the electrolyte is free of background contamination, separate the two washed slides and simply place one into the stirring electrolyte on the instrument platform. The sample preparation technique assures that a bubble free suspension is presented to the detection orifice.
9. Begin the analysis immediately and acquire at least 50,000 particles over the designated analytical range.

## RESULTS AND DISCUSSION

The apparent success of this technique is based upon the fact that sample dispersion is achieved by shear forces and the very material transmitting the shear will hold the dispersed particles apart until analyzed. Finally, the particles on the slide which are originally very close to each other are slowly liberated from the 0.10 cc of dissolving honey into 100 cc volume of electrolyte. The 1000 : 1 change in volumetric dilution vastly increases the inter-particle distances thereby promoting suspension stability for a long enough period to easily complete the analysis.

Figure 1 provides the information detailing the suspension concentration requirements to maintain a stable analytical fluid. Note that by increasing the concentration of particles per unit volume, the rate of magnetic reagglomeration also increases as we would expect. A typical analysis time for 50000 particles using a 38 micron orifice at the 1% coincidence level of particles in the detection aperture was about 1.3 minutes. Figure 2 presents the log probability plots of data expressed on a mass basis from milled unlabeled samples taken at 13 hours and then again after 24 hours. Note the bimodal nature of the data and that both data sets converge to a common distribution below 3.4 microns. Clearly, the upper size ranges of the 24 hour sample has been reduced by the milling operation and the fact that both sets converge at the 3.4 micron level provides information regarding the mill characteristics.

The fact that we were able to correctly distinguish significant differences between two samples that arrived in unmarked jars gave us a high degree of confidence in the analytical techniques. In order to confirm the accuracy of the analysis, we asked the Leeds and Northrup Company to analyze the 13 Hour sample in their Microtrac using a dispersion technique of their choice. They used an ultrasonic probe, Tamol surfactant and water to disperse the sample. Power levels and surfactant concentrations were not available to us when the data was reported. The dispersed sample was then analyzed in conjunction with their small volume sample recirculation system with data being reported every 30 seconds for 10 consecutive runs.

Table 1 presents the data summary from the Microtrac analyzer. Note that with each successive run, the indicated percentage at 22.0, 16.0, 11.0, and 7.8 microns decreased until about the ninth run. While these percentages decreased, the percentage figures at 5.50, 3.90, 2.80 and 1.90 microns increased. It should also be noted that the mass median diameter of 6.43 microns for this work agrees well with the Elzone median of 6.87 microns diameter.

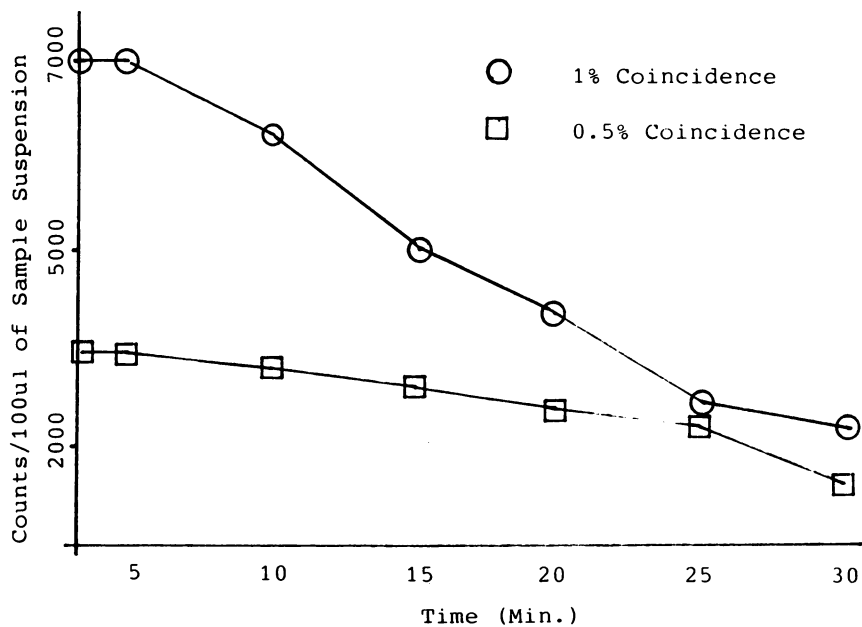


Figure 1. Dispersion stability of Elzone analytical suspension as a function of time and concentration.

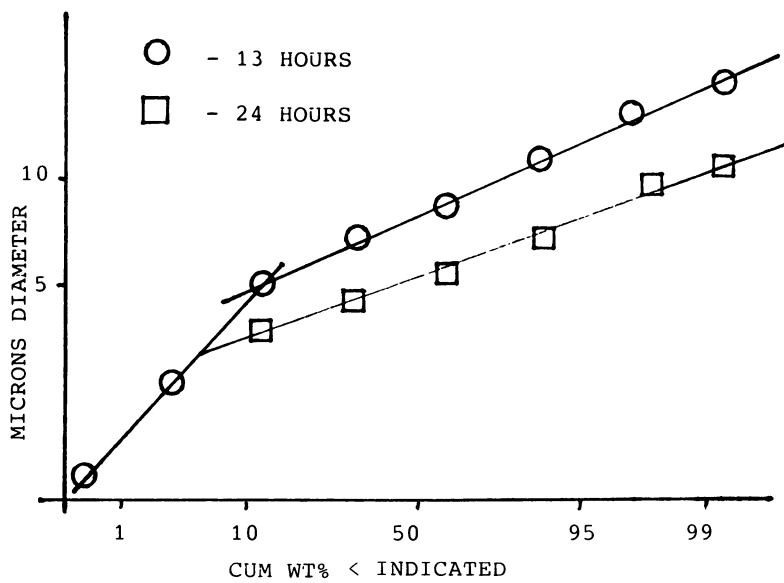


Figure 2. Particle size distributions as a function of milling time.

TABLE 1. MICROTRAC ANALYSIS OF 13 HOUR SOFT FERRITE SAMPLE

MICRONS	RUN NUMBER									
	1	2	3	4	5	6	7	8	9	10
22.0	1.1	0.5	0.3	0.2	0.1	0.2	0.1	0.2	0.2	0.2
16.0	13.6	13.1	12.8	12.6	12.4	12.4	12.3	12.3	12.4	12.4
11.0	22.1	21.1	20.7	20.5	20.4	20.2	20.1	20.0	19.9	19.8
7.0	28.0	28.0	28.0	27.9	27.8	27.8	27.8	27.7	27.6	27.6
5.5	21.9	23.2	23.7	24.0	24.2	24.3	24.3	24.5	24.4	24.4
3.9	6.0	6.6	6.9	7.1	7.2	7.3	7.3	7.4	7.4	7.4
2.8	2.1	2.0	2.0	2.0	1.9	2.0	2.1	2.1	2.1	2.1
1.9	2.8	2.9	3.0	3.0	3.1	3.1	3.2	3.2	3.2	3.2



Data would seem to indicate that shear forces from the impeller pump are indeed continuing to disperse the sample beyond what was possible with a surfactant and an ultrasonic probe. Also, we suspect that dispersion of the magnetically reagglomerated particles is being achieved due to this force. A user of this analytical instrument type should be aware that a good stable dispersion is possible to achieve provided that a suitable recirculation time is used prior to reporting data.

Due to the unique analytical problems associated with the analysis of magnetic particles, the industry relies on two classical analytical techniques. The scanning electron microscope and the Fisher Subsieve sizer are presently the instruments of choice. Scanning electron microscopy data suffers four major problem areas for this sample type:

1. Long sample prep time
2. Labor intensive
3. Typically only 100 - 200 particles are sized and counted as individuals from photographs of the agglomerated material.
4. Usually, the concept of "Stratified Counting"<sup>(4)</sup> to estimate the population density of each size present in the sample is not used. This lack of data concerning the larger size results in a biasing of the frequency distribution analysis towards the fines.

Fisher Sub-Sieve Sizer data provides a simple number relative to the entire sample. However, it offers no information as to what part of the distribution curve has changed when the average particle diameter of one sample is different than the previous sample.

### CONCLUSION

The present work has restated that the main problem encountered when measuring the particle size of magnetic powders is reagglomeration following dispersion. We have described a simple dispersion and analytical method designed to follow changes in the upper particle size ranges of these ball milled products. The technique is not appropriate for the determination of the frequency median size of a ball milled magnetic material since it usually lies below the detection limit of the electric sensing zone technique.

### LITERATURE CITED

1. Langberg, D.E., Measurement of Magnetite Particle Size Distribution; University of Newcastle, Australia, personal correspondence of preprint
2. Smith, F., Demagnetization of Ferromagnetic Particles; 1961, British Journal of Applied Physics, Vol. 12, pp. 155-159
3. Elzone is a registered trademark of Particle Data Inc., P.O. Box 265, Elmhurst, IL, 60126
4. Kaye, B.H., Operational Protocols for Efficient Characterization of Arrays of Deposited Fineparticles by Robotic Image Analysis Systems; 1991, ACS Symposium Series, in print

RECEIVED June 11, 1991

## Author Index

- Barman, Bhajendra N., 198,217  
Bott, S. E., 106  
Brandolin, A., 20,64  
Caldwell, Karin D., 247  
Chang, Yu-Jain, 86  
Clark, G. G., 372  
Devon, Michael J., 134,154  
DosRamos, J. G., 264,279,292  
Fairhurst, D., 184,337  
Garcia-Rubio, L. H., 20,64  
Giddings, J. Calvin, 198,217,229  
Gossen, Paul, 86  
Groves, M. J., 123  
Hamielec, Archie E., 2  
Hansen, Finn Knut, 169  
Hart, W. H., 106  
Jenkins, R. D., 264  
Karuhn, Richard F., 386  
Kaye, Brian H., 354,372  
Koehler, M. E., 20  
Kourti, Theodora, 2,34,86  
Kuo, C., 20  
Langhorst, Martin, 308  
Lee, Inho, 229  
Li, Jenqthun, 247  
MacGregor, John F., 2,34,86  
Marlow, B. J., 326  
Meyer, Edwin, 154  
Moon, Myeong Hee, 198  
Myers, Marcus N., 198  
Nicoli, David F., 86  
Provder, Theodore, 20,134,154  
Ratanathanawongs, S. Kim, 229  
Ribitsch, V., 337  
Rowell, R. L., 326  
Rudin, Alfred, 134,154  
Shiau, S.-J., 326  
Silebi, C. A., 264,279,292  
Tan, Julia S., 247  
Thomas, John C., 98  
Tscharnuter, W. W., 184  
Venkatesan, J., 279  
Von Wald, Grant, 308  
Weiner, Bruce B., 154,184  
Wu, Jau-Sien, 86

## Affiliation Index

- Brookhaven Instruments Corporation,  
98,154,184,337  
Coulter Electronics, Inc., 106  
Dow Chemical Canada Inc., 134,154  
The Dow Chemical Company, 308  
Eastman Kodak Company, 247  
FFFractionation, Inc., 198  
The Glidden Company, 20, 134,154  
Laurentian University, 354,372  
Lehigh University, 264,279,292  
Matec Applied Sciences, 264,279,292  
McMaster University, 2, 34, 86  
Nicomp Particle Sizing Systems, 86  
Particle Data Laboratories, 386  
University of Graz, 337  
University of Illinois at Chicago, 123  
University of Massachusetts, 326  
University of Oslo, 169  
University of South Florida, 20, 64  
University of Utah, 198,217,229,247  
University of Waterloo, 134,154

## Subject Index

### A

- Absorbance in detector zone, 158
- Adsorbed layer thickness, measurement of stabilizing effect of coating, 248
- Apparent diameters, definition, 10–11
- Autocorrelation function, definition for photon correlation spectroscopy, 251
- Average diameter
  - determination, 42–43
  - estimation using turbidimetry, 50–52
- Average integrated extinction efficiency, definition, 186
- Axial dispersion, definition, 264
- Axial dispersion coefficient, 268

### B

- Boundary fractal dimension, study method, 375
- Broad size distributions
  - light flux patterns, 109–112
  - limited angular range, 112–113,114f

### C

- Capillary hydrodynamic fractionation
  - axial diffusion coefficient, 267–268
  - axial dispersion coefficient, 268
  - development, 280–281
  - efficiency, 269–274,294
  - eluant composition, effect on separation factor, 280–290
  - experimental procedure, 293–294
  - ionic strength, 265
  - limitations, 292–293
  - long-chain nonionic surfactants, effect on separation factor, 281
  - minimum residence time, 267
  - particle concentration, variation with axial position, 267
  - particle size analysis theory, 294–296
  - particle velocity, 266–267
  - size separation mechanism, 293
  - slip velocity, 266

- Chance clustering in deposited fineparticle arrays, 356,359–365
- Coating thicknesses, analysis by photon correlation spectroscopy, 248
- Coincidence effect
  - fineparticle characterization, 356,359–365
  - stream methods of fineparticle characterization, generation, 354
- Coincidence errors, definition, 354
- Colloidal aggregation, occurrence, 217
- Colloidal aggregation analysis
  - aggregated samples, scope of analysis, 224,225f
  - cluster breakup and formation, 226
  - experimental systems, 220–221
  - optimization of field strength and flow rate, 221,222–223f,224
  - particle size distribution, original and aged samples, 226,227f,228
  - poly(methyl methacrylate) latex aggregates, fractogram, 221,223f,224
  - polystyrene latex samples, fractogram, 224,225f
  - retention parameter, 218–219
  - retention volume, 218–219
  - retention volume vs. field strength, 221,222f
  - sample aging, effect on aggregate population, 226,227f
  - sedimentation field-flow fractionation, 217–218
  - theory, 218–220,222f
- Colloidal particles, electrophoretic fingerprinting for surface characterization, 326–335
- Colloidal systems
  - size, effect on targeting, 247
  - surface composition, effect on targeting, 247–248
  - use in drug delivery, 247
- Column particle chromatography, 279
- Coulter principle, particulate ]
  - detection, 127
- Cyclical-field field-flow fractionation, 202

### D

- Decay constant, definition, 100

- Degree of dilution, on-line measurements using turbidimetry, 56
- Density  
copolymers, calculation, 311  
disc centrifuge, 172,173*t*  
measurement, 252
- Deposited fineparticle arrays, chance clustering, 356,359–365
- Detector response, capillary hydrodynamic fractionation, 295
- Detector slit width error in disc centrifuge measurement of latex particle size distributions  
absorbance in detector zone, 158  
differential number distribution, 161–162  
emulsion polymerization of polymer particle from seed particle, 164  
emulsion polymerization of seed polymer, 163–164  
experimental procedure, 162–163  
extinction coefficient, 156  
finite slit width in detector zone, geometry, 156,157*f*,158  
geometric dimensions of disc cavity, 166,167*t*  
normalized differential weight distribution in diameter space, 161  
number-average diameter, 162  
particle cross section  
annular ring, 160  
beam, 158–159  
particle diameter calculation, 163  
particle settling, 155–156  
particle size  
bimodal sample, 164,167*t*  
monodisperse latices, 164,165*f*  
narrow distribution latices and blends, 164,165*t*  
percentage deviation, 166  
polymerization procedures, 163–164  
theory, 155–162  
transmittance, 156  
turbidity, 156,158  
volume fraction of particles in detector zone, 158  
weight-average diameter, 161–162
- Diameter-based selectivity, definition for flow field-flow fractionation, 234
- Differential number distribution in time-space, disc centrifuge, 161–162
- Diffraction, description, 106
- Diffusion coefficient, flow field-flow fractionation, 231,233,251
- Disc centrifuge  
detector slit width error, measurement of latex particle size distribution, 154–167  
extinction efficiency, importance in particle size analysis, 184–195  
measurement of particle size distribution diameter averages, optically corrected, 150,151*t*  
differential weight distribution for particle sizes, normalized, 137  
distribution averages, formulas for calculation, 139,140*t*  
experimental procedure, 138–139  
extinction coefficient, 136  
extinction coefficient and inverse time vs. diameter, 143,144–149*f*,150  
integrated extinction coefficients, calculation, 139  
number-average diameter, 137  
particle diameter vs. integrated extinction coefficient, 139,142*f*  
particle settling, 135  
percent error, 136–137  
photosedimentometer trace, 150,152*f*  
polystyrene mixture, actual vs. calculated averages, 150,152*t*  
Stokes law plot for polystyrene and poly(methyl methacrylate) latices, 139,141*f*  
turbidity, 135–136  
weight-average diameter, 138  
optical corrections, 134–135  
particle size distribution  
measurement, 134  
theory, 135–138
- Disc centrifuge with density gradient, particle size distributions  
application, 169  
averaging process, 180,181*f*  
calibration curves for extinction efficiencies, 177–178  
coefficient of variation determination, 179–180  
data logging and presentation, 171  
density, 172,173*t*  
experimental procedure, 170–171  
gradient constants, 171,173*t*

Disc centrifuge with density gradient, particle size distributions—*Continued*  
 Joyce–Loebl disc, schematic representation, 171,174f  
 light scattering, problems, 169–170  
 particle diameter, 171–172  
 particle number calculation from turbidity, 173,175–177  
 particle size distribution calculation from particle numbers, 179  
 spin fluid volume, 180,182f  
 viscosity, 172,173t  
 volume fraction, 172  
 weight fraction, 172  
 Dispersion and high-resolution electric sensing zone analysis of magnetic particles  
 accuracy, 389  
 analytical considerations, 387–388  
 comparison to other techniques, 392  
 Microtrac analysis of 13-h soft ferrite sample, 389,391t  
 particle size distributions vs. milling time, 389,390f  
 sample preparation and analytical procedure, 388–389  
 success, 389  
 suspension concentration requirements for stable analytical fluid, 389,390f  
 Dispersion-quotient method for particle size distribution determination, 44  
 Distributional form, particle size, *See* Particle size distributional form  
 Dry volume fraction of latex, calculation, 311  
 Dynamic light scattering  
 advantages and disadvantages, 98  
 autocorrelation function of scattered light intensity, 87  
 decay constants of scatterers in suspension, 87–88  
 first-order autocorrelation function, 87–88  
 Gaussian analysis, 88–89  
 hydrodynamic radius, 87  
 need for on-line measurement of particle size distribution, 86  
 Nicomp distribution analysis, 88–89  
 off-line measurement of particle size distribution, 86  
 on-line applications, 67,89–90  
 scattering wave vector, 87  
 theory, 87–89,99–100

Dynamic light scattering on-line particle size distribution determination  
 advantages, 89–90  
 autodilution, 90  
 autodilution and light scattering sensor, 95,96f  
 continuous latex reactor, 91,92–93f,94  
 errors, lack of sensitivity, 90  
 experimental setup for continuous latex reactor, 91,92f  
 measured and manipulated variables vs. reaction time, 91,92f,94  
 modification of instrumentation for industrial environments, 94–95,96f  
 photomultiplier detector, 95,96f  
 sampler and prediluter, 91,93f,95  
 sampling device, 90  
 suitability, 89–90  
 theoretical background, 87–89

## E

Effective axial diffusion coefficient, capillary hydrodynamic fractionation, 267  
 Efficiency of particle separation in capillary hydrodynamic fractionation  
 comparison of theoretical and experimental results, 272,273,274f  
 electrolyte, effect on specific resolution, 270,271f,272  
 eluant velocity, effect on specific resolution, 272–273f  
 minimum eigenvalue of diffusion equation vs. capillary radii and mean eluant velocities, 269f  
 vs. ionic strength, 269,270f  
 minimum residence times for particle diameters, 270t  
 Rayleigh quotient, derivation of minimum, 275–277  
 separation factor for different electric surface potentials, 270,271f,272  
 theory, 266–269  
 Einstein viscosity law, equation, 309  
 Electric sensing zone analytical technique, analysis of magnetic particles, 387–392  
 Electrochemical double layer  
 description, 337  
 electrokinetic phenomena, 338,339f  
 Stern model, 337,339f

- Electrokinetic maximum, description, 334
- Electrokinetic surface properties of materials, 337
- Electrokinetic techniques, limitations, 338,340,342*f*
- Electrophoretic fingerprinting for surface characterization of colloidal particles
- data analysis procedure, 327
  - experimental procedure, 327
  - fingerprint and template
    - carbon black dispersion, 328,332*f*
    - carboxyl–amidine zwitterionic latex, 328,329*f*
    - TiO<sub>2</sub>–KCl system, 328,331*f*
  - hydrodynamic fingerprinting, 335
  - number of data points, effect on fingerprint of carboxyl–amidine zwitterionic latex, 328,330*f*
  - self-consistent mobility surface, determination, 328,334
  - zeta potential–salt concentration maximum, 334–335
- Electrophoretic mobility, 326–327
- Electrophoretic topography, 326
- Eluant composition effects on separation
- factor in capillary hydrodynamic fractionation
  - adsorbed layer thickness, determination using particle size, 290*f*
  - apparatus, 282*f*
  - conductivity and molecular weights of nonionic surfactants, 283*t*
  - eluant velocity, 285,286–287*f*
  - experimental materials, 282,283*t*
  - ionic strength, 284*f*,285
  - ionic vs. nonionic surfactants, 289*f*
  - molecular weight, 285–286*f*
  - separation factor determination, 282
  - surfactant concentration, 287,288*f*,289
- Equipped polygon exploration technique, concepts, 375
- Extinction coefficient, definition for disc centrifuge, 136,156
- Extinction efficiency
- calculations, 187,188–189*f*
  - calibration curves, 177–178
  - carbon black results, 193*f*,195
  - cumulative undersize distribution by mass, 191,192*f*,193*f*
  - definition, 177,186
- Extinction efficiency—*Continued*
- experimental procedure, 187,190
  - extinction efficiency vs. diameter
    - carbon black, 187,188*f*
    - natural quartz, 187,188*f*
    - polystyrene latex, 187,189*f*
  - latex results, 191*t*,194*t*
  - latex standards, diameters, 191*t*,194
  - light scattering correction, 185
  - limiting cases, 186
  - mean and standard error of samples, 190*t*
  - quartz powder results, 191,192–193*f*
  - theory, 185–186
  - Treasure correction and refractive index variations, 190,194–195
  - weight-average diameter(s)
    - mixed latex standards, 194*t*
    - natural quartz powder, 191,192*f*
- Extremely wide dynamic range high-resolution particle sizing by light scattering
- broad size distributions, 109–114
  - double Fourier lens optical collection system, 113,114*f*
- Fraunhofer diffraction approximation for light pattern, 107
- loss of resolution at small size end, 113,115*f*
  - optical system, 107,108*f*
  - polarization intensity differential scattering, 113–122
  - scattered light flux patterns, 107,108*f*
- F
- Fiber optic dynamic light scattering from concentrated dispersions
- apparent diffusion coefficient and time-dependent amplitude vs. volume fraction, 101,102*f*
  - dynamic light scattering theory, 99–100
  - experimental procedure, 100–102*f*
  - latex particle size vs. reaction time, 103,104*f*
  - particle size measurements during pigment crystallization, 103*t*,104
- Field-flow fractionation
- advantages, 198
  - applications, 202
  - channel structure, 199,201*f*
  - characterized particles, 199,200*t*
  - description, 198,229

**Field-flow fractionation—Continued**

- field selection, 229
  - force exerted on single particle by field, 203
  - mean retention time, 203–204
  - particle distribution relative to
    - accumulation wall of channel, 202–203
  - principal operating modes, 202
  - principles, 199,202
  - properties that control elution times,
    - dependence on subtechnique, 198
  - range of applicability, 199
  - retention parameter, 203
  - sedimentation field, 199,202
  - theory, 202–204
  - velocity of transport, 202
- Field strength, sedimentation field-flow fractionation, 204**
- Fineparticle(s)**
- profiles of alumina dusts, 356,358f
  - resolution of lead fume into constituent units, 356,357f
- Fineparticle characterization, image analysis**
- coal dust sample, stylized fields of view, 355,357f
  - logic flow chart for cybernetic system, 366,367f
  - Monte Carlo studies of chance clustering, 356,359–365
  - primary count loss and secondary count gain, 354–356,357–358f
  - stratified count logic for robotic image analyzers, 366,368–371
- Fineparticles with fractal structure, examples, 372**
- Flow field-flow fractionation**
- applications, 202,229
  - channel and cross-flow rates, 237,238f
  - chromatographic silicas
    - commercially available, 241,243f
    - particle size distribution curves, 241,244f
  - coefficient of variation, 234
  - cross flow, use as driving force, 229
  - diameter-based selectivity, 234
  - diffusion coefficient, 231,233
  - experimental procedure, 235,236f,237
  - lower size limit, 231
  - Ludox colloidal silicas
    - diameters, 239f
    - particle size distribution curves, 239,240f

**Flow field-flow fractionation—Continued**

- mean retention times, diameters, and polydispersities of chromatographic silicas, 241,245f
  - normal mode, 231,233
  - normal mode separation of submicrometer polystyrene latex beads, 237,238f,239
  - parabolic flow profile, 231
  - particle size distribution determination, 234–235
  - retention parameter, 231
  - retention ratio, 233
  - retention time, 233,237,238f
  - separation mechanisms, 231,232f
  - separation of pollen and spores and of latex standards, 241,242f
  - separation of polystyrene latex standards, 239,241,242f
  - sizing theory, 250–251
  - steric-hyperlayer mode, 233–234
  - theory, 231–235
  - upper size limit, 229,231
- Flow-through packed column methods, size characterization of colloidal particles, 279**
- Force exerted on single particle by field, field-flow fractionation, 203**
- Formation dynamics derivation from fractal structure of fumed fineparticles**
- agglomerate formation by collision of compact agglomerates, 377,378f
  - boundary fractal dimension vs. gross structure, 375,376f,377
  - carbon black profiles
    - distribution data for variation, 379,383f,384
    - electron micrographs, 379,380–381f
    - Richardson plots, 379,382f
  - cluster growth simulation from random walk modeling, 377,379,380f
  - experimental procedure, 375
  - pixel stripping routines, constituent parts, 377,378f
- Forward scattering, effect on turbidimetric measurements, 57–58**
- Fractal dimension of system**
- description, 372,373f
  - digitized carbon black profile, 372,374f
  - types, 372,375
- Fractal geometry, definition, 372**

- Fractal structure of fumed fineparticles, derivation of formation dynamics information, 372–384
- Fraunhofer diffraction approximation, description of light pattern, 107
- G**
- Gaussian analysis, 88
- Generalized cross-validation technique, selection of  $\gamma$ , 21
- H**
- HIAC counter, use for particulate determination, 126
- Hydrodynamic chromatography development, 279
- separation mechanism, 280
- size analysis of colloidal particles, 279–280
- Hydrodynamic fingerprinting, 335
- I**
- Instrumental band broadening, definition, 264
- Instrumental particle size analysis procedures for parenteral solutions
- Coulter principle, 127
- future concerns, 129–130
- light extinction methodology, 127–129
- microscopic method, 126–127
- particulates, 125–126
- size distributions in parenteral solutions, 124–125
- Instrumental spreading function, capillary hydrodynamic fractionation, 295
- Intensity of transmitted light, definition, 185
- Inversion turbidimetric techniques for latex particle size distribution determination
- experimental procedures, 22
- narrow polystyrene standards, 23,24f,25f,t,26
- normalized measured turbidity spectra of polystyrene latices, 23,24f
- optical property measurements, 22
- poly(methyl methacrylate) latices, 26–30
- Inversion turbidimetric techniques for latex particle size distribution determination—*Continued*
- small molecules, 22–23,24f
- styrene–butadiene latices, 29,30t
- vinyl acetate–butyl acrylate latices, 29,31f,32t
- J**
- Joint confidence regions, estimation, 6
- L**
- Latex particle size distribution(s)
- detector slit width error in measurement with disc centrifuge, 154–167
- inversion turbidimetry, experimental validation, 20–32
- Latex reactors
- on-line particle size distribution measurements, 64–83
- particle growth, 53,54f
- turbidimetry, potential for on-line applications, 53,54f,55
- weight-average diameters, 53,54f
- Light extinction methodology, particulate detection, 127–129
- Light scattering
- corrections for disc centrifuge, 184–185
- extremely wide dynamic range, high-resolution particle sizing, 106–122
- Longitudinal dispersion of molecular species in laminar flow, evaluation using fundamental parameters, 265
- M**
- Magnetic particles, dispersion and high-resolution electric sensing zone analysis, 386–392
- Magnetic products
- analytical dispersion stability, 386–387
- fineparticle analytical problem, 386
- Mean retention time, definition for field-flow fractionation, 203–204



Method of moments, determination of particle size distribution, 45  
 Microelectrophoresis, determination of  $\zeta$  potential, 338  
 Microscopic method, particulate detection, 126–127  
 Minimum residence time, capillary hydrodynamic fractionation, 267  
 Monodisperse suspension, specific turbidity, 3,41  
 Monte Carlo studies of chance clustering in deposited fineparticle arrays  
 density of coverage, 359,362,363–365f  
 deposited fineparticles, simulated fields, 359,361f  
 random number table used in simulation experiments, 359,360f  
 size distribution of clusters  
 chance contiguity, 359,361f  
 20% coverage, 362,365f  
 Monte Carlo technique, description, 356,359  
 Multimodal distributions from turbidity spectra, 45–46

## N

Narrow polystyrene standards  
 particle size distributions, inversion turbidimetric technique, 23,24f,25f,t  
 turbidity spectra, 23,24f  
 Nicomp distribution analysis, 88–89  
 Normal mode of flow field-flow fractionation results, 237,238f,239t,240f  
 theory, 231,233  
 Normalized differential weight distribution  
 diameter space, 161  
 particle sizes, 137  
 Number-average diameter in time–space  
 definition for disc centrifuge, 137,162

## O

Off-line particle size distribution measurements, examples, 67  
 On-line particle size distribution measurements for latex reactors  
 batch sampling times, 70,72  
 block diagram, 65,66f

On-line particle size distribution measurements for latex reactors—  
*Continued*  
 continuous dilution system, 72–83  
 deconvolution of turbidity spectra, 69  
 design problems, 64–65  
 dilution factor calculated as function of time, 72,73f  
 dynamic light scattering, 86–96  
 leading moments of particle size distribution in reactor and at exit of second dilution vessel, 72,76–77f,78  
 simulated and recovered, 78–83f  
 measurement system, 67  
 particle size distribution  
 beginning and end of formation, 72,74f  
 recovery in reactor, 69–70  
 residence time, 72,75f  
 time deconvolution, 69–70  
 reactor model, 65  
 sampling–dilution system, 67–69  
 styrene polymerization simulation, 70,71f  
 On-line particle size measurements using turbidimetry, historical perspective, 56–57  
 Optical properties, on-line measurements using turbidimetry, 55  
 Optical properties of latex suspensions, turbidimetric measurements, 57

## P

Parabolic flow profile, flow field-flow fractionation, 231  
 Parenteral solutions  
 definition, 123  
 inadvertent particulates, physiological dangers, 124  
 particulate content, 123–124  
 particulate detection methods, 126–129  
 size distributions, probable, 124–125  
 standards of cleanliness, 129–130  
 Particle cross section in annular ring, definition for disc centrifuge, 160  
 Particle diameter, definition for disc centrifuge, 171–172  
 Particle diffusion coefficient, definition, 100  
 Particle–light interactions, phenomena, 106

- Particle numbers, calculation from turbidity, 173,175–177
- Particle radial velocity, capillary hydrodynamic fractionation, 266–267
- Particle separation, capillary hydrodynamic fractionation, 264–274
- Particle separation and characterization, flow field-flow fractionation, 229–245
- Particle settling, definition for disc centrifuge, 135,155–156
- Particle size, role in industrial applications of polymeric and colloidal materials, 98
- Particle size analysis, colloidal science and technology, 292
- Particle size analysis by capillary hydrodynamic fractionation  
colloidal dispersions, summary, 296*t*  
colloidal particle density, effect on separation factor, 305–306  
commercial polystyrene–butadiene latex, fractogram, 297,300*f*  
data system, fractogram, 296,297*f*  
deconvolution, 303  
detector response, 295  
instrumental spreading function, 295  
ionic strength  
  effect on separation factor, 305  
  effect on thickness of excluded region, 305  
particle(s), total number, 295  
particle size distributions  
  carbon black colloidal dispersions, 297,301*t*  
  commercial polystyrene–butadiene latex, 297,300*f*  
  polystyrene latex particles, 297,299*f*  
  with and without deconvolution, 297,298*f*  
  polystyrene and carbon black, fractogram, 297,301*f*  
  polystyrene latex particles, fractogram, 297,299*f*  
  reproducibility, 301,302*t*  
  resolving power, 301,302–304*f*,305*t*  
  theory, 294–296
- Particle size determination  
disc centrifuge, extinction efficiency, 184–195  
flow field-flow fractionation, 234–235  
  definition, 4  
  disc centrifuge, 134–152  
Particle size determination—*Continued*  
flow field-flow fractionation—*Continued*  
  regularization techniques, 20  
  sedimentation field-flow fractionation, 198–215  
  specific turbidity measurements, 3  
  turbidimetric technique determination, 3–19  
  turbidimetry, 39  
  viscometry, 308–322  
  turbidimetry, 34–59
- Particle size distribution measurement  
objective, 184  
size- and composition-independent detector, increase in accuracy, 308
- Particle size distributional form  
error in assumed form, 47–48  
typical distributional functions, 46–47
- Particle sizing  
instrument specifications, 184  
limitation to dilute solutions, 98–99  
measurement methods, 292  
turbidimetric techniques, 2
- Particle streamline velocity, capillary hydrodynamic fractionation, 266
- Particulate(s)  
contamination of parenteral solutions, 125–126  
detection methods, 126–129
- Particulate aggregation, 217
- Percent coefficient of variation, flow field-flow fractionation, 234
- Photocount autocorrelation function, calculation, 99
- Photon correlation spectroscopy  
analysis of coating thicknesses, 248  
sizing theory, 251–252  
*See also* Dynamic light scattering
- Pluronic copolymer-coated polystyrene latex, size analysis, 247–261
- Polarization intensity differential scattering  
electric field from oscillating dipole, 113,116,117*f*  
experimental geometry, 113,115*f*  
optical train, 116,118*f*  
patterns for small particles, 116,119–120*f*  
signal for particles comparable to light wavelength, 116,117*f*  
size distributions from polystyrene latex spheres, 116,121–122*f*

**Polydisperse system**  
 specific turbidity, definition, 41–42  
 turbidity, definition, 39  
**Polydispersity index**, assumptions, 248  
**Poly(ethylene oxide)-coated surfaces**,  
 protein adsorption, 248  
**Polymer colloids**, particle elution  
 behavior from capillary tubes, 265  
**Polymer solution**, effect on interaction  
 between solid surfaces, 281  
**Polymeric volume fraction**, calculation, 55  
**Poly(methyl methacrylate) latices**  
 particle size distributions, 26,28f,29,30f  
 typical turbidity spectra, 26,27f  
 weight particle size distribution, 26,28f  
**Primary count loss**, definition, 354  
**Probable size distributions in parenteral**  
 solutions, 124–125

**R**

**Regularization techniques for particle**  
 size distribution estimation,  
 turbidity equation, 20–21  
**Respirable dusts**, study problems, 355–356  
**Retention parameter**  
 field-flow fractionation, 203,250–251  
 flow field-flow fractionation, 231  
 sedimentation field-flow fractionation,  
 218–219,249–250  
**Retention ratio**  
 flow field-flow fractionation, 233  
 sedimentation field-flow  
 fractionation, 249  
**Retention time**, flow field-flow  
 fractionation, 233  
**Retention volume**, sedimentation field-flow  
 fractionation, 218–220  
**Robotic image analyzers**, stratified count  
 logic, 366,368–371

**S**

**Scattering**, definition, 106  
**Scattering angle**, definition, 107  
**Scattering coefficient**  
 calculation, 38  
 dependence on diameter, 10

**Scattering factor**, light scattering  
 correction, 185  
**Secondary count gain**, definition, 354  
**Sedimentation field-flow fractionation**  
 colloidal aggregation studies, 217–218  
 particle size distribution  
 description of devices, 204,205t  
 experimental procedure, 204  
 field strength, 204  
 fractionation  
 broad acrylic-based latex dispersion,  
 207,208f  
 copper particles, 211,214f,215  
 kaolin clay sample, 211,212f  
 Teflon particles, 207,210f,211  
 zirconia, 207,209f  
 high-resolution separation of polystyrene  
 latex standards, 204,206f,207  
 illustrative applications, 204–215  
 kaolin clay sample, particle size  
 distributions, 211,213f  
 light scattering corrections, 215  
 principles, 199,201f,202  
 Teflon particles, size distribution  
 curves, 211,212f  
 theory, 202–204  
 size selectivity, 249  
 sizing theory, 249–250  
**Sedimentation in density gradient**, theory,  
 171–173,174f  
**Self-consistent mobility surface**,  
 electrophoretic fingerprinting, 328,334  
**Separation factor in capillary**  
 hydrodynamic fractionation, eluant  
 composition effects, 280–290  
 capillary hydrodynamic fractionation, 284  
 eluant velocity, 285,286–287f  
 ionic strength, 284f,285  
 ionic vs. nonionic surfactants, 289f  
 molecular weight, 285–286f  
 surfactant concentration, 287,288f,289  
**Size analysis of pluronic copolymer coated**  
 polystyrene latex  
 adsorption complex, stability in different  
 environments, 260,261t  
 amount of coating adsorbed on polystyrene  
 particles, 258,260t  
 angle dependence of diffusion coefficients,  
 255,256f  
 bare and coated particles, sizes, 255t

- Size analysis of pluronic copolymer coated polystyrene latex—*Continued*  
experimental procedure, 249–253  
flow field-flow fractionation sizing method, 250–251  
latex concentration measurement, 252  
particle sizes, determined by different techniques, 253,254f,255  
photon correlation spectroscopic sizing method, 251–252  
polystyrene latex before and after coating  
flow field-flow fractogram, 258,259f  
sedimentation field-flow fractogram, 255,257f  
relative coating thickness for coated particles, 255t  
scanning electron microscopic procedure, 252  
sedimentation field-flow fractionation sizing method, 249–250  
sizing methods, 249–252  
surfactant adsorption and leakage measurements, 252  
surfactant density measurement, 252
- Size distribution analysis, viscometry as detection scheme for particles in separation, 308–322
- Slip velocity, capillary hydrodynamic fractionation, 266
- Spatial coincidence effects, dust hazard exposure, 355
- Specific resolution, capillary hydrodynamic fractionation, 268–269
- Specific turbidity  
application, 39  
average diameter, determination, 42–43  
behavior for polydisperse systems, 4–9,13–14  
behavior for systems with different refractive index ratios, 8t,9f  
equation for monodisperse suspension, 3  
equation for spherical particles, 2–3  
monodisperse system, 41  
particle size determination, 2  
particle size distribution, 3  
polydisperse system, 41–42
- Specific viscosity of particle suspension  
calculation, 311  
definition, 309  
particle concentration, 309
- Spherical, nonabsorbing, isotropic particle suspension, definition of turbidity, 35,38
- Steric exclusion effect, importance in colloidal stabilization, 248
- Steric–hyperlayer mode of flow field-flow fractionation  
results, 239,241–245  
theory, 233–234
- Steric mode of flow field-flow fractionation, theory, 233
- Stratified count logic for robotic image analyzers  
application, 369,371  
distribution procedures, 366,368f,369  
useful information vs. that from size-everything strategies, 369,370f
- Stream counter, idealized representation of interrogation zone, 354,357f
- Stream methods of fineparticle characterization, coincidence effects, 354
- Styrene–butadiene latices  
particle size distribution, 29,30t  
refractive index estimation, 29,30t
- Submicrometer colloidal particles, rate of particle transport, 264
- Submicrometer particle sizing instruments  
examples, 184  
light scattering corrections, 184–185
- Surface characterization of colloidal particles, electrophoretic fingerprinting, 326–335
- T**
- Thermal field-flow fractionation, 202
- Total axial dispersion, capillary hydrodynamic fractionation, 268
- Total number of particles, capillary hydrodynamic fractionation, 295
- Total particle cross section in beam, disc centrifuge, 158–159
- Transmittance, disc centrifuge, 156
- Treasure correction, description, 190
- Turbidimetric technique capability for determination of full particle size distribution  
apparent, 8

Turbidimetric technique capability for determination of full particle size distribution—*Continued*  
 constant specific turbidity curves  
 vs. wavelength, 4,5f  
 vs. weight-average diameters, 4  
 diameter exponent, 11,12f,13  
 experimental verification of weight-average diameter from apparent diameter, 14,15t  
 exponents  $y$  and  $z$  vs.  $\alpha$ , 11,12f,13  
 joint confidence regions for estimated parameters with error in specific turbidity, 6,7f,8  
 maximum percent error in estimated parameters for 3% experimental error, 8t  
 parameters with error in specific turbidity, estimation, 6t,7f,8,9f  
 particle size distribution when random error is added to specific turbidities, 8,9f  
 polydisperse systems, behavior of specific turbidity, 4–9  
 scattering coefficient vs.  $\alpha$ , 11,12f  
 specific turbidity behavior, 13–14  
 specific turbidity behavior for systems with different refractive index ratios, 8t,9f  
 specific turbidity values per diameter, 19  
 theoretical values of specific turbidities, calculation, 4  
 turbidity ratio method, 14–15,16t,17  
 Turbidimetry for particle size determination  
 advantages, 34  
 controversies and contradictory reports, 35  
 definition of turbidity, 35,38–39,40f  
 dispersion-quotient method, 44  
 estimation of particle size distribution, 39  
 specific turbidity, 39,41–43  
 turbidity ratio, 43  
 wavelength exponent, 44  
 work on application using different materials, 34,36–37t  
 Turbidity  
 definition, 35,38–39,185  
 definition for disc centrifuge, 135–136,156,158  
 exponents  $y$  and  $z$  vs.  $\alpha$ , 39,40f  
 Turbidity-average diameters, 50–51

Turbidity for particle size distribution determination  
 accuracy of measurements, 58  
 average diameters, estimation, 50–52  
 controversy in literature, resolution, 49–50  
 corroboration of results, 59  
 error in refractive index ratios, 49  
 error on estimated particle size distribution, 48–49  
 forward scattering, 57–58  
 measurement errors, effect on particle size distribution, 49  
 method of moments, 45  
 multimodal distributions from turbidity spectra, 45–46  
 on-line applications to latex reactors, investigation of potential, 53,54f,55  
 on-line measurements and data analysis, requirements, 55–56  
 on-line particle size measurements, historical perspective, 56  
 optical properties of latex suspensions, 57  
 particle size distribution, choice of form, 46–48  
 wavelength choice, 58–59  
 Turbidity of monodisperse suspension, definition, 10  
 Turbidity ratio, 43  
 Turbidity ratio method for particle size distribution determination  
 equation, 14  
 experimental values, 15,16t  
 explanation of behavior, 16–17  
 sensitivity to experimental error, 14  
 turbidity measurements needed, 15

## V

Vinyl acetate–butyl acrylate latices  
 normalized measured turbidity spectra, 29,31f  
 particle size distribution, 29,31f,32t  
 refractive index estimation, 29  
 Viscosity, disc centrifuge, 172,173t  
 Viscosity detector for hydrodynamic chromatographic particle size distribution determination  
 apparatus, 310  
 average diameter, calculation, 310

Viscosity detector for hydrodynamic chromatographic particle size distribution determination—*Continued*  
copolymer density, calculation, 311  
dry volume fraction of latex, calculation, 311  
experimental samples, 310  
latex size, effect on viscometer response, 313,315–316f  
linearity, 319  
performance limitations, 322  
sensitivity, 319  
sensitivity of differential viscometer, 313,314f  
sensitivity requirements, 309  
signal dependence on composition, 319  
signal dependence on diameter, 319  
size dependence of specific viscosity, confirmation of proposed cause, 320–321  
specific viscosity, direct measurement without column, 311,312f  
specific viscosity–size relationship, solution conditions, 321  
specific viscosity vs. concentration, 313,317f  
specific viscosity vs. diameter, 313,318f  
surfactants, effect on effective diameter, 313t  
Volume fraction, 41,172  
Volume–surface average diameters, determination, 51–52

## W

Wavelength, effect on turbidimetric measurements, 58–59  
Wavelength exponent, determination of particle size distribution, 44  
Weight-average diameter, 52  
Weight-average diameter in diameter space, disc centrifuge, 161–162

Weight-average diameter in time–space, disc centrifuge, 138  
Weight fraction, disc centrifuge, 172

## Z

Zeta potential  
application, effect on measurement method choice, 340  
calculation, 326  
characterizing parameter, 326  
definition, 326,338  
determination methods, 338–342f  
zeta potential–salt concentration maximum, 334–335  
Zeta potential measurements of irregularly shaped solid materials  
apparatus, 343,344f  
cell design, 345  
cetylpyridinium bromide adsorption, effect on  $\zeta$  potential of viscose fiber, 348,350,351f  
cylindrical cell, 345,346f  
equation, 341,343  
examples, 347–351  
experimental procedure, 345,347  
measurements for polyester paper machine felt samples, 348t  
pH dependency of  $\zeta$  potential for viscose fibers, 348,349f  
principles, 341,342f,343  
rectangular cell, 345,346f  
reversal of granite surface charge using quaternary ammonium salt, 350,351f  
streaming potential, schematic representation, 341,342f  
streaming potential measurement, theory, 341,342f,343  
variation with pH for offset printing plate, 347,349f